# NEW INSIGHTS ON NEURON AND ASTROCYTE FUNCTION FROM CUTTING-EDGE OPTICAL TECHNIQUES

EDITED BY: Srdjan D. Antic, Bradley James Baker and Marco Canepari
PUBLISHED IN: Frontiers in Cellular Neuroscience

frontiers Research Topics

ISSN 1664-8714
ISBN 978-2-88963-267-1
DOI 10.3389/978-2-88963-267-1

## About Frontiers

Frontiers is more than just an open-access publisher of scholarly articles: it is a pioneering approach to the world of academia, radically improving the way scholarly research is managed. The grand vision of Frontiers is a world where all people have an equal opportunity to seek, share and generate knowledge. Frontiers provides immediate and permanent online open access to all its publications, but this alone is not enough to realize our grand goals.

## Frontiers Journal Series

The Frontiers Journal Series is a multi-tier and interdisciplinary set of open-access, online journals, promising a paradigm shift from the current review, selection and dissemination processes in academic publishing. All Frontiers journals are driven by researchers for researchers; therefore, they constitute a service to the scholarly community. At the same time, the Frontiers Journal Series operates on a revolutionary invention, the tiered publishing system, initially addressing specific communities of scholars, and gradually climbing up to broader public understanding, thus serving the interests of the lay society, too.

## Dedication to Quality

Each Frontiers article is a landmark of the highest quality, thanks to genuinely collaborative interactions between authors and review editors, who include some of the world's best academicians. Research must be certified by peers before entering a stream of knowledge that may eventually reach the public - and shape society; therefore, Frontiers only applies the most rigorous and unbiased reviews.
Frontiers revolutionizes research publishing by freely delivering the most outstanding research, evaluated with no bias from both the academic and social point of view. By applying the most advanced information technologies, Frontiers is catapulting scholarly publishing into a new generation.

## What are Frontiers Research Topics?

Frontiers Research Topics are very popular trademarks of the Frontiers Journals Series: they are collections of at least ten articles, all centered on a particular subject. With their unique mix of varied contributions from Original Research to Review Articles, Frontiers Research Topics unify the most influential researchers, the latest key findings and historical advances in a hot research area! Find out more on how to host your own Frontiers Research Topic or contribute to one as an author by contacting the Frontiers Editorial Office: researchtopics@frontiersin.org

# NEW INSIGHTS ON NEURON AND ASTROCYTE FUNCTION FROM CUTTING-EDGE OPTICAL TECHNIQUES

Topic Editors:
**Srdjan D. Antic,** University of Connecticut Health Center, United States
**Bradley James Baker,** Korea Institute of Science and Technology (KIST), South Korea
**Marco Canepari,** UMR5588 Laboratoire Interdisciplinaire de Physique (LIPhy), France

**Citation:** Antic, S. D., Baker, B. J., Canepari, M., eds. (2019). New Insights on Neuron and Astrocyte Function from Cutting-Edge Optical Techniques. Lausanne: Frontiers Media SA. doi: 10.3389/978-2-88963-267-1

# Table of Contents

frontiers
in Cellular Neuroscience

EDITORIAL
published: 15 October 2019
doi: 10.3389/fncel.2019.00463

# Editorial: New Insights on Neuron and Astrocyte Function From Cutting-Edge Optical Techniques

*Srdjan D. Antic*[1]*, *Bradley James Baker*[2]* *and Marco Canepari*[3,4,5]*

[1] Department of Neuroscience, Institute for Systems Genomics, Stem Cell Institute, UConn Health, Farmington, CT, United States, [2] The Center for Functional Connectomics, Korea Institute of Science and Technology, Seoul, South Korea, [3] Division of Bio-Medical Science and Technology, KIST School, Korea University of Science and Technology (UST), Seoul, South Korea, [4] Laboratories of Excellence, Ion Channel Science and Therapeutics, Valbonne, France, [5] Institut National de la Santé et Recherche Médicale, Paris, France

**Keywords: optogenetic, voltage imaging, calcium imaging, GCaMP, voltage-sensitive dye**

OPEN ACCESS

***Edited and reviewed by:***
*Arianna Maffei,*
*Stony Brook University, United States*

****Correspondence:***
*Srdjan D. Antic*
*antic@uchc.edu*
*Bradley James Baker*
*bradley.baker19@gmail.com*
*Marco Canepari*
*marco.canepari@*
*univ-grenoble-alpes.fr*

***Specialty section:***
*This article was submitted to*
*Cellular Neurophysiology,*
*a section of the journal*
*Frontiers in Cellular Neuroscience*

***Received:*** *05 September 2019*
***Accepted:*** *30 September 2019*
***Published:*** *15 October 2019*

***Citation:***
*Antic SD, Baker BJ and Canepari M*
*(2019) Editorial: New Insights on*
*Neuron and Astrocyte Function From*
*Cutting-Edge Optical Techniques.*
*Front. Cell. Neurosci. 13:463.*
*doi: 10.3389/fncel.2019.00463*

**Editorial on the Research Topic**

**New Insights on Neuron and Astrocyte Function From Cutting-Edge Optical Techniques**

One of the most coveted goals of science is to elucidate the cellular bases of complex brain functions. How does a piece of biological tissue produce accurate cognitive insights, or succumbs to a devastating neurological disease? Neurons and astrocytes are the most numerous cells in the brain, comprising >95% of the brain parenchyma, and are responsible for all aspects of rapid information processing in the mammalian brain. Monitoring of physiological changes at the individual cell level, as well as in cell populations, is essential (Popovic M. et al., 2015; Nakajima et al., 2016). Early explorations of cellular physiology entailed metal (or glass and metal) electrodes. However, due to their highly invasive and tissue-harming nature, all electrodes, no matter how small, are limited experimental tools. While understanding brain circuits ultimately relies on the analyses of multiple and well-identified cells and subcellular compartments, the required information at high spatial and temporal resolution is not achievable using only electrode techniques for several reasons. First, the necessity for simultaneous measurements from ensembles of cells seems to be the most agreed upon aspect of the modern neuroscience (Barbera et al., 2016; Cai et al., 2016; Ji et al., 2016). Unfortunately, electrode arrays are limited in the number of cells they can monitor simultaneously. Second, the other reason for choosing optical imaging technologies over standard electrode recordings is that this is the only available approach to explore in detail thin processes of neurons and astrocytes, i.e., the essential cellular compartments underlying brain function (Larkum et al., 2018; Sheffield and Dombeck, 2019). In particular, in thin dendritic branches of neurons and astrocytes, optical measurements perform better than electrode recordings, in terms of calcium activity (Schiller et al., 1995; Kampa et al., 2006), membrane potential transients (Zhou et al., 2008), and also for recording ion currents (Jaafari et al., 2014; Jaafari and Canepari, 2016; Ait Ouares et al., 2019). In summary, the places where electrodes cannot go, optical measurements are taking over (Popovic M. A. et al., 2015; Bindocci et al., 2017; Gordleeva et al., 2019).

In the last decades, neuroscience research has been driven by the development of novel technologies interfacing scientists with molecules, cells, neuronal tissues, or the entire brain. Certainly, optical techniques have played a major role in this progress opening the gate to unprecedented information on living neurons and astrocytes. Innovative illumination and light recording strategies (Müllenbroich et al.; Ronzitti et al.; Battefeld et al.; Miyazaki et al.) advanced our knowledge on signaling in submicron structures (Francavilla et al.; Kuhn and Roome; Miyazaki et al.) while permitting the investigations in semi-intact tissues (Tominaga et al.; Kajiwara et al.; Quicke et al.). In parallel, the new emerging field of optogenetics allowed the selected expression of light-activated proteins that can be used for precisely targeted photostimulation (Baker and Flannery). Other optical strategies that recently progressed include combined $Ca^{2+}$ and $Na^{+}$ measurements (Miyazaki et al.), membrane potential recordings from individual cells (Francavilla et al.; Kuhn and Roome; Quicke et al.), or cell populations (Tominaga et al.; Kajiwara et al.; Li et al.), and chemical stimulation of targeted receptors using caged compounds (Palma-Cerda et al.).

## STUDIES USING ORGANIC INDICATORS

In the early days of functional optical imaging, organic dyes were used for studying membrane potential changes in excitable cells and were dubbed voltage-sensitive dyes (Davila et al., 1973; Cohen et al., 1978). Later on, compounds were synthesized for measuring calcium or sodium transients in the cytosol (Brown et al., 1975; Grynkiewicz et al., 1985). Tominaga et al. have developed a voltage-sensitive dye imaging method for measuring compound synaptic potentials (population signals) from the entire hippocampus CA1 area for extended periods of time (experiments lasting up to 12 h). Their results shed light on a rarely discussed spatial aspect of long term potentiation (LTP) induction (e.g., magnitude of LTP increases with distance from the stimulation site) (Tominaga et al.). Using the same experimental approach, based on extracellular labeling of brain slices with voltage-sensitive dye and state-of-the-art wide-field single-photon voltage imaging at 2,000 frames per s, Kajiwara et al. showed that the efficacy of propagation of electrical activity between two critical brain regions, from perirhinal cortex to entorhinal cortex, is strongly dependent on membrane excitability and is malleable by synaptic plasticity (Kajiwara et al.). Miyazaki et al. have developed a robust method for simultaneous imaging of $[Ca2^{+}]_i$ and $[Na^{+}]_i$ changes in neurons at high speed and high spatial resolution. Via whole-cell electrode attached to the cell body, the authors co-inject two different pairs of spectrally orthogonal $Ca^{2+}$ and $Na^{+}$ indicators and excite the two dyes by illuminating at two wavelengths either using LEDs or laser spots. This method allowed them to monitor synaptically evoked $Ca^{2+}$ and $Na^{+}$ transients in individual dendritic spines (Miyazaki et al.). The review article by Dong et al. describes several techniques for studying gap junctions in the central nervous system. Fluorescent compounds and dyes are at the heart of several experimental approaches designed to probe the existence, strength, or nature of gap junction coupling: injection of small tracer molecules, scrape loading/dye transfer method, and recovery after photobleaching method (e.g., membrane-permeable fluorescein-AM). The review article by Kuhn and Roome, describes experimental design for performing dendritic voltage imaging in awake behaving animals. The authors also provide a very detailed account of the physical chemistry and quantum mechanics of charge-shift voltage-sensitive dyes with a special emphasis on two dyes from the Fromherz group (ANNINE-6 and ANNINE-6+). Physical chemistry and quantum mechanics of the organic dyes explains certain practical issues of working with fluorescent dyes, such as signal-to-noise ratio, phototoxicity, shape of the emission spectrum, dye flipping from one membrane leaf to another, etc. (Kuhn and Roome).

## STUDIES USING GENETICALLY ENCODED INDICATORS

Genetically encoded optical sensors of cell activity have become very popular in recent years, because they can be targeted to specific cell types. This is especially important in studies of the brain circuitry, because individual brain regions always include a multitude of different cell types, each type bestowed with a specific set of afferents and efferents, as well as rules for synaptic integration and patterned action potential firing. Francavilla et al. used viral transfection to label hippocampal GABAergic interneurons with the calcium indicator GCaMP6f. Two photon imaging of dendritic calcium transients (CaTs) was carried out in head-restrained mice running on a circular treadmill. Data showed that $Ca^{2+}$ signals had larger amplitude and could invade the entire dendritic tree during locomotion, while during immobility, the signal amplitude was significantly lower in both soma and dendrites, and a significant fraction of dendrites showed spatially restricted CaTs, which were not seen in the soma. The authors proposed that strong dendrite-soma coupling, associated with animal locomotion, may facilitate the spike-timing-dependent or Hebbian forms of synaptic plasticity in interneurons. In contrast, during animal quiet state, this type of activity can be reduced or even replaced by local dendritic $Ca^{2+}$ signaling, which may facilitate the anti-Hebbian plasticity mechanisms (Francavilla et al.). Another group working with GCaMP used the transgenic animal Thy1-GCaMP6f, expressing GCaMP6f in cortical pyramidal neurons (Li et al.). These authors showed that they can monitor sharp waves (SWs), carbachol-induced theta oscillations, and interictal-like spikes in brain slices. Furthermore, the authors claim that population GCaMP6f signals are fast enough for monitoring theta and beta oscillations (<25 Hz), which is an advancement for $Ca^{2+}$ imaging. Quicke et al. also use a transgenic animal approach for delivery of a genetically encoded indicator to neurons. However, instead of GCaMP which is a calcium indicator, they use voltage indicator (VSFP Butterfly 1.2) to monitor membrane potential changes (Quicke et al.). Unlike the cytosolic molecule GCaMP, voltage indicators are membrane proteins (Kannan et al.). Their expression in brain tissue produces fluorescently labeled neuropil made of densely intermingled dendrites and axons, hence cellular resolution is lost. To achieve single cell resolution in voltage imaging, Quicke et al. combine recently developed sparse transgenic expression strategy (Song et al., 2017) and patch clamp recordings to demonstrate optical recordings of action potentials in individual neurons (Quicke et al.). Unlike GCaMP, genetically encoded voltage indicators have poor signal to noise ratio (Antic et al., 2016; Storace et al., 2016). But the signal-quality gap between GCaMP and GEVI is becoming narrower each year (Adam et al., 2019; Qian et al., 2019). A set of the state-of-the-art strategies for improving GEVI properties (sensitivity, brightness, SNR, fast kinetics, etc.) is described in an excellent article by Kannan et al., together with the overview of the pallet of currently available GEVIs (Kannan et al.). Finally, Storace et al. illustrate how membrane potential imaging using GEVIs (e.g., Arclight) can be utilized to decode the activity of the mammalian olfactory bulb, a goal that has been elusive for decades using older experimental approaches. Here, the authors used a clever strategy to simultaneously monitor input and output of a brain region in awake animal responding to controlled odor presentations. Afferent inputs to the olfactory glomeruli were assessed by calcium imaging from axon terminals of olfactory receptor cells (impinging onto the tufts of the mitral cells in the olfactory bulb glomerulus). Olfactory bulb outputs, on the other hand, were monitored by GEVI labeling of the mitral cells, whose axons project from the olfactory bulb into other brain regions. Simultaneous calcium and voltage imaging revealed that the output activity maps and the output signal size are much less concentration dependent than are the input maps and signals (Storace et al.). These results contribute immensely to our current understanding of the cellular mechanism for concentration invariance of odor recognition. The Storace et al. study is an excellent example of how applications of advanced imaging technologies (dual anatomical and genetic targeting leading to simultaneous calcium voltage imaging in an awake behaving animal) will impact systems neuroscience in the future.

## ADVANCES OF OPTICAL TECHNOLOGIES

The ability of functional imaging to address fundamental questions depends on novel cutting-edge technologies and instrumentation. Battefeld et al. describe a versatile and open-source rapid LED switching system for one-photon imaging and photo-activation, that can be used either for quantitative ratiometric $Ca^{2+}$ imaging or to combine $Ca^{2+}$ imaging with optogenetic stimulation. Miyazaki et al. present an upgraded version of an imaging system, based on high speed multiplexing of light LEDs, to combine $Na^{+}$ and $Ca^{2+}$ imaging, a powerful approach to advance our knowledge on neuronal excitability and synaptic transmission. Ronzitti et al. review strategies for light shaping in three dimensions, including SLM-based multiplexing illumination, temporal focusing and other approaches. These rapidly developing illumination technologies open the gate to all-optical manipulation of neural circuits involving simultaneous stimulation of well-defined targets and simultaneous functional imaging of the resulting activity. Among light shaping approaches, light-sheet microscopy represents one of the most promising strategies. Using this technique, Müllenbroich et al. present an interesting improvement for imaging the transparent nervous system of zebra fish. In this application, Bessel beams are used to remove artifacts and dramatically improve sensitivity in $Ca^{2+}$ imaging measurements (Müllenbroich et al.). Finally, a novel caged glutamate receptor antagonist is presented by Palma-Cerda et al. This compound combines the fast photolysis and hydrolytic stability of this family of photoactivatable molecules with fast-equilibrating competitive action on glutamate receptors, enabling deep investigation of postsynaptic functions at the molecular level (Palma-Cerda et al.).

## AUTHOR CONTRIBUTIONS

All authors listed have made a substantial, direct and intellectual contribution to the work, and approved it for publication.

## FUNDING

SA has been supported by National Institutes of Health (NIH) grants MH109091, NS099573, EB022903; and Cure Alzheimer's Fund. MC has been supported by the *Agence Nationale de la Recherche* through the grants ANR-14-CE17-0006 and ANR-11-LABX-0015. BB has been supported by the National Institute of Neurological Disorders And Stroke of the National Institutes of Health under Award Number U01NS099691. The content is solely the responsibility of the authors and does not necessarily represent the official views of the National Institutes of Health. BB has also been funded by the Korea Institute of Science and Technology (KIST) grants 2E26190 and 2E26170.

## REFERENCES

Adam, Y., Kim, J. J., Lou, S., Zhao, Y., Xie, M. E., Brinks, D., et al. (2019). Voltage imaging and optogenetics reveal behaviour-dependent changes in hippocampal dynamics. *Nature* 569, 413–417. doi: 10.1038/s41586-019-1166-7

Ait Ouares, K., Filipis, L., Tzilivaki, A., Poirazi, P., and Canepari, M. (2019). Two distinct sets of $Ca^{2+}$ and $K^{+}$ channels are activated at different membrane potentials by the climbing fiber synaptic potential in purkinje neuron dendrites. *J. Neurosci.* 39, 1969–1981. doi: 10.1523/JNEUROSCI.2155-18.2018

Antic, S. D., Empson, R. M., and Knopfel, T. (2016). Voltage imaging to understand connections and functions of neuronal circuits. *J. Neurophysiol.* 116, 135–152. doi: 10.1152/jn.00226.2016

Barbera, G., Liang, B., Zhang, L., Gerfen, C. R., Culurciello, E., Chen, R., et al. (2016). Spatially compact neural clusters in the dorsal striatum encode locomotion relevant information. *Neuron* 92, 202–213. doi: 10.1016/j.neuron.2016.08.037

Bindocci, E., Savtchouk, I., Liaudet, N., Becker, D., Carriero, G., and Volterra, A. (2017). Three-dimensional $Ca^{2+}$ imaging advances understanding of astrocyte biology. *Science* 356:eaai8185. doi: 10.1126/science.aai8185

Brown, J. E., Cohen, L. B., De Weer, P., Pinto, L. H., Ross, W. N., and Salzberg, B. M. (1975). Rapid changes in intracellular free calcium concentration. Detection by metallochromic indicator dyes in squid giant axon. *Biophys. J.* 15, 1155–1160. doi: 10.1016/S0006-3495(75)85891-7

Cai, D. J., Aharoni, D., Shuman, T., Shobe, J., Biane, J., Song, W., et al. (2016). A shared neural ensemble links distinct contextual memories encoded close in time. *Nature* 534, 115–118. doi: 10.1038/nature17955

Cohen, L. B., Salzberg, B. M., and Grinvald, A. (1978). Optical methods for monitoring neuron activity. *Annu.Rev. Neurosci.* 1, 171–182. doi: 10.1146/annurev.ne.01.030178.001131

Davila, H. V., Salzberg, B. M., Cohen, L. B., and Waggoner, A. S. (1973). A large change in axon fluorescence that provides a promising method for measuring membrane potential. *Nat. New Biol.* 241, 159–160. doi: 10.1038/newbio241159a0

Gordleeva, S. Y., Ermolaeva, A. V., Kastalskiy, I. A., and Kazantsev, V. B. (2019). Astrocyte as spatiotemporal integrating detector of neuronal activity. *Front. Physiol.* 10:294. doi: 10.3389/fphys.2019.00294

Grynkiewicz, G., Poenie, M., and Tsien, R. Y. (1985). A new generation of $Ca^{2+}$ indicators with greatly improved fluorescence properties. *J. Biol. Chem.* 260, 3440–3450.

Jaafari, N., and Canepari, M. (2016). Functional coupling of diverse voltage-gated $Ca^{2+}$ channels underlies high fidelity of fast dendritic $Ca^{2+}$ signals during burst firing. *J. Physiol.* 594, 967–983. doi: 10.1113/JP271830

Jaafari, N., De Waard, M., and Canepari, M. (2014). Imaging fast calcium currents beyond the limitations of electrode techniques. *Biophys. J.* 107, 1280–1288. doi: 10.1016/j.bpj.2014.07.059

Ji, N., Freeman, J., and Smith, S. L. (2016). Technologies for imaging neural activity in large volumes. *Nat. Neurosci.* 19, 1154–1164. doi: 10.1038/nn.4358

Kampa, B. M., Letzkus, J. J., and Stuart, G. J. (2006). Requirement of dendritic calcium spikes for induction of spike-timing-dependent synaptic plasticity. *J. Physiol.* 574, 283–290. doi: 10.1113/jphysiol.2006.111062

Larkum, M. E., Petro, L. S., Sachdev, R. N. S., and Muckli, L. (2018). A perspective on cortical layering and layer-spanning neuronal elements. *Front. Neuroanat.* 12:56. doi: 10.3389/fnana.2018.00056

Nakajima, R., Jung, A., Yoon, B. J., and Baker, B. J. (2016). Optogenetic monitoring of synaptic activity with genetically encoded voltage indicators. *Front. Synaptic. Neurosci.* 8:22. doi: 10.3389/fnsyn.2016.00022

Popovic, M., Vogt, K., Holthoff, K., Konnerth, A., Salzberg, B. M., Grinvald, A., et al. (2015). Imaging submillisecond membrane potential changes from individual regions of single axons, dendrites and spines. *Adv. Exp. Med. Biol.* 859, 57–101. doi: 10.1007/978-3-319-17641-3_3

Popovic, M. A., Carnevale, N., Rozsa, B., and Zecevic, D. (2015). Electrical behaviour of dendritic spines as revealed by voltage imaging. *Nat. Commun.* 6:8436. doi: 10.1038/ncomms9436

Qian, Y., Piatkevich, K. D., Mc Larney, B., Abdelfattah, A. S., Mehta, S., Murdock, M. H., et al. (2019). A genetically encoded near-infrared fluorescent calcium ion indicator. *Nat. Methods* 16, 171–174. doi: 10.1038/s41592-018-0294-6

Schiller, J., Helmchen, F., and Sakmann, B. (1995). Spatial profile of dendritic calcium transients evoked by action potentials in rat neocortical pyramidal neurones. *J. Physiol.* 487, 583–600. doi: 10.1113/jphysiol.1995.sp020902

Sheffield, M. E., and Dombeck, D. A. (2019). Dendritic mechanisms of hippocampal place field formation. *Curr. Opin. Neurobiol.* 54, 1–11. doi: 10.1016/j.conb.2018.07.004

Song, C., Do, Q. B., Antic, S. D., and Knöpfel, T. (2017). Transgenic strategies for sparse but strong expression of genetically encoded voltage and calcium indicators. *Int. J. Mol. Sci.* 18:E1461. doi: 10.3390/ijms18071461

Storace, D., Sepehri Rad, M., Kang, B., Cohen, L. B., Hughes, T., and Baker, B. J. (2016). Toward better genetically encoded sensors of membrane potential. *Trends Neurosci.* 39, 277–289. doi: 10.1016/j.tins.2016.02.005

Zhou, W. L., Yan, P., Wuskell, J. P., Loew, L. M., and Antic, S. D. (2008). Dynamics of action potential backpropagation in basal dendrites of prefrontal cortical pyramidal neurons. *Eur. J. Neurosci.* 27, 923–936. doi: 10.1111/j.1460-9568.2008.06075.x

**Conflict of Interest:** The authors declare that the research was conducted in the absence of any commercial or financial relationships that could be construed as a potential conflict of interest.

frontiers in Cellular Neuroscience

MINI REVIEW
published: 19 September 2018
doi: 10.3389/fncel.2018.00320

# Gap Junctions in the Nervous System: Probing Functional Connections Using New Imaging Approaches

*Ao Dong*[1,2,3]*, *Simin Liu*[1,2] *and Yulong Li*[1,2,3]*

[1] *State Key Laboratory of Membrane Biology, Peking University School of Life Sciences, Beijing, China,*
[2] *PKU-IDG/McGovern Institute for Brain Research, Beijing, China,* [3] *Peking-Tsinghua Center for Life Sciences, Beijing, China*

Gap junctions are channels that physically connect adjacent cells, mediating the rapid exchange of small molecules, and playing an essential role in a wide range of physiological processes in nearly every system in the body, including the nervous system. Thus, altered function of gap junctions has been linked with a plethora of diseases and pathological conditions. Being able to measure and characterize the distribution, function, and regulation of gap junctions in intact tissue is therefore essential for understanding the physiological and pathophysiological roles that gap junctions play. In recent decades, several robust *in vitro* and *in vivo* methods have been developed for detecting and characterizing gap junctions. Here, we review the currently available methods with respect to invasiveness, signal-to-noise ratio, temporal resolution and others, highlighting the recently developed chemical tracers and hybrid imaging systems that use novel chemical compounds and/or genetically encoded enzymes, transporters, channels, and fluorescent proteins in order to map gap junctions. Finally, we discuss possible avenues for further improving existing techniques in order to achieve highly sensitive, cell type-specific, non-invasive measures of *in vivo* gap junction function with high throughput and high spatiotemporal resolution.

**Keywords: gap junction, electrical synapse, fluorescence imaging, genetically encoded methods, nervous system**

OPEN ACCESS

***Edited by:***
*Bradley James Baker,*
*Korea Institute of Science and Technology (KIST), South Korea*

***Reviewed by:***
*Bela Volgyi,*
*University of Pécs, Hungary*
*Pablo Jose Saez,*
*Institut Curie, France*

***Correspondence:**
*Ao Dong*
*aodong@pku.edu.cn*
*Yulong Li*
*yulongli@pku.edu.cn*
*orcid.org/0000-0002-9166-9919*

***Received:*** *01 July 2018*
***Accepted:*** *03 September 2018*
***Published:*** *19 September 2018*

***Citation:***
*Dong A, Liu S and Li Y (2018) Gap Junctions in the Nervous System: Probing Functional Connections Using New Imaging Approaches. Front. Cell. Neurosci. 12:320. doi: 10.3389/fncel.2018.00320*

## INTRODUCTION

Multicellular organisms rely on cell-cell communication to coordinate a wide range of physiological processes and maintain homeostasis. Most organisms have evolved a rich diversity of mechanisms to achieve this communication, including long-distance signaling through the release, and binding of hormones (Ansar Ahmed et al., 1985; Giustina and Veldhuis, 1998; Meier and Gressner, 2004), spatially confined synaptic transmission between two neurons (Krnjevic, 1974; Pereda, 2014), and gap junctional coupling between neighboring cells (Kumar and Gilula, 1996; Sohl et al., 2005; Mese et al., 2007). In the central nervous system, billions of neurons are intermingled and communicate with each other through a specialized structure called the synapse, forming a complex signaling network. Although synapses are predominantly chemical in nature, with neurotransmitters released from the presynaptic terminal and sensed by the postsynaptic neuron via surface receptors, gap junction–based electrical synapses are also widely distributed, and play an essential role in regulating both the development and function of the nervous system (Pereda, 2014).

Gap junctions, composed of connexins in vertebrates and innexins in invertebrates, are intercellular channel complexes between connected cells (Kumar and Gilula, 1996; Phelan et al., 1998). Pannexins are vertebrate homologs to the innexins (Baranova et al., 2004), form hemi-channels connecting cytosol and extracellular space (D'hondt et al., 2009), and could mediate gap junctional connection in cells when overexpressed (Bruzzone et al., 2003; Vanden Abeele et al., 2006; Lai et al., 2007; Ishikawa et al., 2011), although their *in vivo* role in forming functional gap junction is unclear (Sosinsky et al., 2011). Ions and other small molecules with a molecular mass up to approximately 1 to 2 kDa can freely diffuse through gap junctions (Loewenstein, 1981; Kumar and Gilula, 1996; Neijssen et al., 2005). Thus, signals such as action potentials can propagate directly between gap junction–coupled neurons, resulting in virtually no delay in signal transmission (Furshpan and Potter, 1957;Bennett and Zukin, 2004); in contrast, signal transmission via a chemical synapse has a delay on the order of milliseconds (Katz and Miledi, 1965; Sabatini and Regehr, 1996). Gap junctions therefore allow organisms to respond extremely rapidly under certain conditions, for example in the escape reflex in crayfish (Antonsen and Edwards, 2003) and the retina's response to visual stimuli in vertebrates (Bloomfield and Volgyi, 2009). Gap junctions are also expressed in glial cell types, including astrocytes (Wallraff et al., 2004), microglia (Garg et al., 2005), oligodendrocytes and Schwann cells (Nualart-Marti et al., 2013), and insect blood-brain barrier glial cells (Speder and Brand, 2014), which is essential for the buffering of ions and transmitters, inflammatory response, myelination and neural stem cell proliferation. Gap junctions also connect glia and neurons (Dobrenis et al., 2005; Meng et al., 2016). Given their highly varied and important roles, it is therefore not surprising that malfunctions in gap junctions can disrupt communication among neurons and glia, thus giving rise to a variety of diseases and neurological disorders, including hereditary deafness (Martinez et al., 2009), uncorrelated motor neuron firing (Personius et al., 2007), and Charcot-Marie-Tooth disease (Kleopa, 2011).

Extensive studies of gap junctions in the nervous system have been carried out by various research groups over the past few decades; the expression of gap junction forming subunits were detected by northern blot (Paul et al., 1991; White et al., 1992), RT-PCR (Wrenzycki et al., 1996; Xia et al., 1998), western blot (Stauffer, 1995; Giepmans and Moolenaar, 1998), and immunohistochemistry (Beyer et al., 1989; Dermietzel et al., 1989). In this review, we focus on functional methods that can detect gap junctional coupling, first briefly summarizing current approaches relying on electrophysiological recording, tracer-based assays, and hybrid methods using genetic tools (**Figure 1**), mainly focusing on recently developed imaging methods. We summarize the performance and properties of these methods, including their invasiveness, throughput, feasibility, sensitivity, spatial resolution, and temporal resolution (**Table 1**). As new *in vivo* methods are being developed, new features of gap junction regulation will likely be revealed, yielding important new insights into the role that gap junctions play in both health and disease.

## ELECTROPHYSIOLOGICAL RECORDING

Gap junctional coupling can be measured using dual-electrode whole-cell current-clamp recordings (Furshpan and Potter, 1959). This method requires two microelectrodes; one electrode is used to inject current into one cell, and the other electrode is used to measure the resulting change in membrane potential in a connected neighboring cell. Because the two cells are electrically coupled, current injection leads to a change in the membrane potential of both cells (**Figure 1A**). Alternatively, dual-electrode whole-cell voltage clamp can also be used to measure gap junctional coupling; in this configuration, inducing a change in membrane potential between the two cells drives an electrical current through the gap junctions (Spray et al., 1979). Electrophysiological recording has millisecond resolution, picoampere current detection sensitivity, and the ability to measure conductance and rectification, both of which are important properties of electrical synapses in neurons. However, this method has obvious limitations, including the need for relatively high technical expertise, specialized equipment, high invasiveness due to disruption of the cell membrane integrity, relatively low throughput, and one-off recording. Moreover, this method by itself cannot discriminate distinct cell types, which is particularly problematic given the heterogeneous nature of the nervous system. In addition, the recordings are usually performed at the cell body, which does not take into account the subcellular localization of gap junctions, particularly in neurons and other cell types with complex morphology.

## TRANSFER OF TRACERS

To assay the gap junction communications, tracers including fluorescent dyes, and bioactive small molecules can be introduced to one cell or a group of cells. The diffusion of tracers from the primary targeted cells to other connected cells reflects the gap junctional couplings.

### Microinjection of the Tracer

The injection of a tracer, followed by measuring its transfer, is usually the first step in identifying the location and morphology of cells within a tissue. Because small molecules can pass freely through gap junctions, the diffusion of an injected small tracer molecule can be used to measure gap junctional coupling between cells (**Figure 1B**). With respect to the study of gap junction–mediated communication, the most commonly used fluorescent dye is Lucifer Yellow, with a molecular weight of 457 Da (Stewart, 1978), and the most commonly used bioactive small molecule is biocytin, with a molecular weight of 372 (Horikawa and Armstrong, 1988). The transfer (i.e., diffusion) of an injected tracer to neighboring cells can be observed either directly (in the case of a fluorescent dye) or *post hoc* using immunohistochemistry (in the case of a bioactive

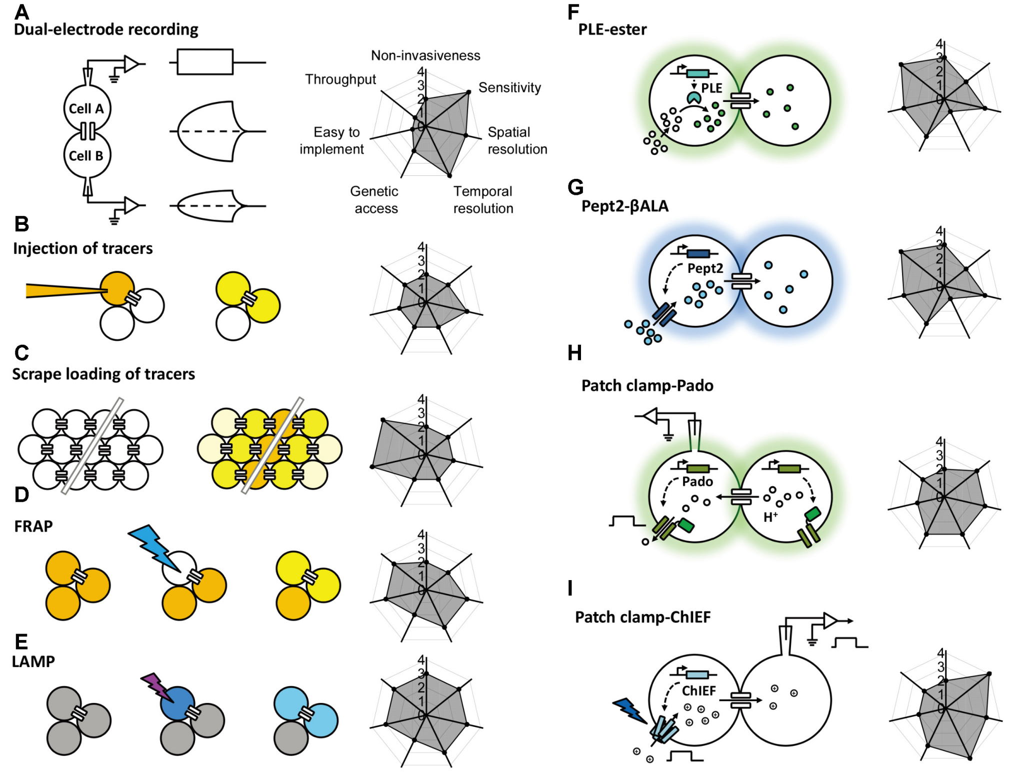

**FIGURE 1 |** Schematic overview of the currently available methods for studying gap junctions. The principle behind each method is shown schematically on the left with a radar graph on the right that summarizes its corresponding performance index (e.g., sensitivity, throughput, resolution) in arbitrary units ranging from 0 to 4. Further details are provided in the text. FRAP, fluorescence recovery after photobleaching; LAMP, local activation of a molecular fluorescent probe; PLE, porcine liver esterase; Pept2, peptide transporter 2; βALA, AMCA-labeled dipeptides β-Ala-Lys; ChIEF, an engineered version of a channelrhodopsin.

**TABLE 1 |** Overview of the methods used to probe gap junctional communication.

| | **Property/characteristic** | | | | | | |
|---|---|---|---|---|---|---|---|
| **Method** | **Sensitivity** | **Throughput** | **Ease of implementation** | **Genetic access** | **Temporal resolution** | **Spatial resolution** | **Invasiveness** |
| Dual-electrode recording | + ++ | Two cells each time | Technically demanding | No | Milliseconds | Cellular level | Invasive |
| Injection of tracers | + | Limited number of cells | Technically demanding | No | 5–20 min | Cellular level | Invasive |
| Scrape loading of tracers | + | Dozens of cells | Relatively easy | No | 2 min | Cellular level | Invasive |
| FRAP | + | Dozens of cells | High-power laser | No | ∼50 s | Cellular level | Photo damage |
| LAMP | + + | Dozens of cells | Relatively easy | No | ∼200 s | Cellular level | Non-invasive |
| PLE-ester | + | Dozens of cells | Relatively easy | Yes | Hours | Cellular level | Non-invasive |
| Pept2-βALA | + | Dozens of cells | Relatively easy | Yes | Hours | Cellular level | Non-invasive |
| Patch clamp-Pado | + + | Limited number of cells | Technically demanding | Yes | Sub-second | Cellular level | Invasive |
| Patch clamp-ChIEF | + ++ | Limited number of cells | Technically demanding | Yes | Milliseconds | Cellular level | Invasive |

*FRAP, fluorescence recovery after photobleaching; LAMP, local activation of a molecular fluorescent probe; PLE, porcine liver esterase; Pept2, peptide transporter 2; βALA, AMCA-labeled dipeptides β-Ala-Lys; ChIEF, an engineered version of a channelrhodopsin.*

small molecule). The tracers used in these experiments are not membrane-permeable, thereby reducing non-specific diffusion through the cell membrane. This method is technically easier to perform compared to electrophysiology, which requires multiple electrodes and a sophisticated recording setup. However, it still lacks cell type specificity, requires the microelectrode, and the dye diffusion is irreversible, thus preventing the ability to study gap junctions repeatedly in the same cells. Moreover, the injection process requires either mechanical pressure or iontophoresis, and immunohistochemistry takes a relatively long time, thus reducing both the temporal resolution and the throughput.

## Scrape Loading of the Tracer

In addition to the one-by-one injection, the tracer can be introduced into a large population of cells via the scrape (McNeil et al., 1984). Cultured cells in one layer are incubated with gap junction-permeable but cell membrane impermeable dyes as mentioned above and are scraped by a needle or a scalpel. Dye molecules therefore get into wounded cells, and can further diffuse to adjacent cells that are intact but coupled with the scraped cells by gap junctions (**Figure 1C**; el-Fouly et al., 1987). The scrape loading/dye transfer method is the easiest one to implement among all methods discussed here. Because of its simplicity, gap junctional communications were evaluated using this method in many cell types, including fibroblasts (Azzam et al., 2001), germ cells in testis (Decrouy et al., 2004), and astrocytes (Giaume and McCarthy, 1996). The limitations of this method include that it is mostly effective in adherent cells and therefore mainly applied in cultured cells or tissue slices *in vitro*. The scraping procedure in conjunction of cell fixation protocol offers qualitative rather than quantitative data for gap junctional connections.

## Fluorescence Redistribution/Recovery After Photobleaching (FRAP)

To overcome the high invasiveness and technical expertise associated with microelectrode-based methods, Wade et al. (1986) developed the gap-FRAP technique (**Figure 1D**), an all-optical strategy used to study gap junctions. Rather than injecting fluorescent molecules into individual cells, cultured cells are incubated with membrane-permeable fluorescein-AM; upon entering the cell, the ester bond is hydrolyzed by intracellular esterases, leaving the hydrophilic fluorescein molecule trapped within the cell (Rotman and Papermaster, 1966). After an intense focused laser is used to bleach the fluorescein in one cell, the bleached fluorescein molecules and the unbleached fluorescein molecules in neighboring cells diffuse through the gap junctions, leading to the recovery of fluorescence in the original bleached cell. Compared to the methods described above, FRAP is less invasive and easier to perform. Importantly, this method provides both qualitative and quantitative information regarding the strength of the gap junctions, which is reflected by the kinetics of fluorescence recovery (Lee et al., 1995; Soroceanu et al., 2001). This method also provides satisfactory temporal resolution, as the photobleaching can be performed extremely rapidly using a high-power laser (Lippincott-Schwartz et al., 2003). One potential drawback of FRAP is that the intense laser illumination may damage the cell. In addition, in order to quantitatively characterize the FRAP kinetics which reflect the strength of the gap junctional communication, the recovery event needs to be monitored until the fluorescence recover to the plateau, which takes much longer time than the half-time for recovery (Lippincott-Schwartz et al., 2003). This requirement makes FRAP not suitable for measuring very fast dynamics of the gap junctions as can be done by electrophysiological recording (Abbaci et al., 2008). Finally, similar to tracer tracking methods, FRAP by itself lacks cell type specificity, constraining its application mainly to homogenous cell cultures.

## Local Activation of a Molecular Fluorescent Probe (LAMP)

To avoid potential phototoxicity associated with photobleaching while still leaving the cell intact, Dakin et al. (2005) developed LAMP, which uses the caged fluorescent dye NPE-HCCC2-AM (**Figure 1E**; Zhao et al., 2004). After the cell is loaded as described above for NPE-HCCC2-AM, UV illumination is used to uncage NPE-HCCC2 in specific cells and release HCCC2, which has a molecular weight of 450 Da and emits blue fluorescence. The uncaged HCCC2 can then diffuse to neighboring cells connected via gap junctions. In a sense, LAMP is a combination between FRAP and tracer tracking in that it generates a fluorescent signal (the "tracer") in one cell and then tracks the movement of the tracer through gap junctions, while maintaining cell integrity. In this respect, LAMP has the combined advantages of both methods in that it is non-invasive, provides quantitative data, and has relatively high temporal resolution. In addition, LAMP allows for multicolor imaging, as the uncaging of NPE-HCCC2 requires a small pulse of UV light and is therefore compatible with fluorescent indicators in the visible spectrum (Dakin et al., 2005; Dakin and Li, 2006; Abbaci et al., 2008). This method can be improved further by incorporating caged fluorescent molecules with higher uncaging efficiency and a more penetrable red-shifted emission spectrum. Unfortunately, LAMP still requires loading of an exogenous dye, which limits its applications in *in vivo* preparations. Moreover, uncaging of NPE-HCCC2 is irreversible, making it less suitable for studying the dynamics of gap junctions repeatedly over a prolonged period of time.

# HYBRID APPROACHES COMBINED WITH GENETIC TOOLS

In order to obtain more cell type-specific information, genetically encoded proteins can be incorporated into the method being used to map gap junctions; this is particularly important for studying gap junctions in a specific cell population within the heterogeneous central nervous system.

## Esterase-Ester Pair

This enzyme-substrate pair has been used successfully to map gap junctions (**Figure 1F**). The enzyme is expressed in specific cell types; the substrate, which is water-soluble, membrane-permeable, unaffected by endogenous enzymes but catalyzed by the ectopically expressed enzyme, is able to diffuse through gap junctions. One example of this approach is the highly selective esterase-ester pair developed by Tian et al. (2012). In this approach, they synthesized a series of esters that fluoresce upon hydrolysis, and identified one substrate (called "substrate **6**") that was stable in several different cell types in a range of species, including flies, rodents, and humans. They also identified porcine liver esterase (PLE) (Lange et al., 2001) as the most potent at catalyzing the hydrolysis of substrate **6** and used the PLE-substrate **6** pair to map the distribution of gap junctions. PLE hydrolyzes substrate **6** to produce a fluorescent product, and the diffusion of this fluorescent product causes fluorescence in the cells that were connected via gap junctions to the PLE-expressing cells (**Figure 1F**). Thanks to genetic manipulation, this strategy provides higher cell type specificity using a relatively simple approach. The bio-specificity of substrate **6** ensures that this strategy can be used in a wide variety of organisms and cell types; however, it is still possible that endogenous esterases can cause a non-specific background signal under certain conditions. Thus, the system can be optimized by modifying the PLE enzyme and/or the substrate, or by identifying a more bioorthogonal enzyme-substrate pair (Sletten and Bertozzi, 2009; Ritter et al., 2015). At the same time, robust control experiments (for example, using knockout models) are an essential step in testing for non-specific background due to endogenous enzymes (Qiao and Sanes, 2015). Another drawback of this method is the relatively low temporal resolution, which requires up to 30 min of incubation in the substrate, thereby limiting its value in terms of studying the dynamics and regulation of gap junctions (Tian et al., 2012). In addition, this method has only been tested in cultured cell lines, and its feasibility in primary cells (e.g., neurons and cardiomyocytes) and *in vivo* applications has not been investigated.

## Transporter-Substrate Pairs

An alternative strategy is to use a transporter-substrate pair in which a genetically encoded transporter is expressed in one cell, which then transports a fluorescent substrate into the cytoplasm; diffusion of the fluorescent substrate to neighboring cells indicates the presence and distribution of gap junctions. In 2015, Qiao and Sanes reported the use of human Pept2 (a peptide transporter) (Biegel et al., 2006) and the AMCA-labeled dipeptide β-Ala-Lys (βALA, the substrate) (Dieck et al., 1999) as a strategy for mapping gap junctions (**Figure 1G**; Qiao and Sanes, 2015). Using this innovative tool, they successfully mapped functional gap junctions in cultured HEK293 cells and quantified the diffusion properties of βALA, which reflects the strength of the gap junctions. Taking advantage of the CreER system and sparse labeling in Pept2 knockout mice, they then confirmed the presence of gap junctional communication between J-RGCs (a subset of retinal ganglion cells) and amacrine cells in the mouse retina (Bloomfield and Volgyi, 2009; Hoshi and Mills, 2009; Volgyi et al., 2009), and they demonstrated the presence of gap junctions in horizontal cells. Importantly, the authors also characterized the light-dependent electrical coupling of horizontal cells by mapping the pattern of gap junctional communication before and after illumination with light (Xin and Bloomfield, 1999). Thus, the Pept2-βALA pair provides a powerful tool for mapping the distribution and strength of gap junction connectivity both in cultured cells and in an *ex vivo* retinal preparation. On the other hand, a clear drawback associated with this method is that the temporal resolution (which is on the order of hours) is not sufficient to track the dynamics of the strength of gap junction connections.

## Genetically Encoded Fluorescent Sensors/Optogenetics Combined With Patch-Clamp Recording

Genetically encoded fluorescent sensors provide another means to map gap junctions by monitoring the concentration change of a chemical during diffusion through gap junctions. In 2016, Kang and Baker reported the development of a novel genetically encoded fluorescent sensor called Pado, which can be used to track the diffusion of protons through gap junctions (**Figure 1H**; Kang and Baker, 2016). Pado is a dual-function protein created by fusing an engineered voltage-gated proton channel from *Clonorchis sinesis* with a pH-sensitive fluorescent protein (Super Ecliptic pHluorin 227A, or SE227A) (Jin et al., 2012). To demonstrate proof-of-principle, Kang and Baker expressed Pado in HEK293 cells, then used the whole-cell patch-clamp technique to depolarize one cell. The change in voltage opened the voltage-gated proton channels, facilitating the efflux of protons from the cell and creating an electrochemical gradient between this cell and neighboring cells connected via gap junctions. Protons then diffused from the neighboring cells down this electrochemical gradient, and the change in SE227A fluorescence was detected in both the clamped cell and the adjacent cells. While this method is promising, the data should be taken carefully and some calibrations allowing for quantitative analysis should be performed. A similar strategy utilizing a hybrid calcium indicator Calcium Green FlAsH could also enable detection of gap junctional couplings, by monitoring the intercellular propagation of calcium waves in gap junction coupled cells (Tour et al., 2007). Given that Calcium Green FlAsH needs to be applied exogenously, further improvements can be achieved by using pure genetically encoded calcium indicators such as GCaMP6 (Chen et al., 2013).

Given the electrical properties of gap junctions, optogenetics is yet another useful tool for mapping gap junctions, as an electrical signal generated by light-activated channelrhodopsins (Nagel et al., 2003, 2005) can propagate to coupled cells and be detected using patch clamp. Recently, Wang et al. (2014) combined an improved version of the channelrhodopsin ChIEF (Lin et al., 2009) with electrophysiology in order to map gap junction connections in the *Drosophila* olfactory system (**Figure 1I**). They performed patch-clamp recordings on cholinergic projection neurons (mPNs) while expressing ChIEF in mediolateral antennocerebral tract projection neurons (mlPNs) labeled by *Mz699-Gal4* (Ito et al., 1997). Applying blue laser illumination to the mlPNs induced depolarization of some mPNs; this effect was not altered by the nicotinic receptor antagonist mecamylamine but was sensitive to the *shakB*$^2$ mutation (which affects innexin-8) (Thomas and Wyman, 1984; Phelan et al., 1996; Zhang et al., 1999; Song and Tanouye, 2006), leading to the conclusion that mPNs and mlPNs are electrically coupled. The finding that blocking cholinergic receptors had no effect on the mlPN-mPN coupling indicates that when using this tool, it is important to distinguish chemical and electrical synapses using genetics and/or pharmacology, as ChIEF induced depolarization of presynaptic neurons can drive postsynaptic responses in both chemical and electrical synapses. Moreover, unlike the dual-electrode whole-cell patch-clamp technique, the ChIEF-based method is unidirectional and cannot be used to identify rectifying gap junctions. To overcome this limitation, a light-gated chloride pump such as the Halorhodopsin isolated from *Natronomonas* (NpHR) (Han and Boyden, 2007; Zhang et al., 2007) can be used to hyperpolarize the presynaptic terminal, thereby reversing the direction of the current across the electrical synapse.

Compared to previous methods, these two strategies (exemplified by Pado and ChIEF) do not require an exogenously applied substrate, which simplifies the experimental protocol and makes them more feasible for use in *in vivo* applications. In addition, because they have relatively faster kinetics (on the order of milliseconds to seconds), these methods can be used to collect repeated measurements, which is essential for studying the dynamics of the strength of gap junctional connections at high temporal resolution. On the other hand, these approaches require the use of glass micropipettes, reducing their throughput. Moreover, one needs to block chemical synapses when using ChIEF to detect electrical synapses, which may alter the normal state of the nervous system.

## PERSPECTIVES

Gap junctions play an extremely important role in mediating cell-cell communication, and their distribution and dynamics are essential for maintaining normal physiological function and homeostasis. Although researchers have been able to link genetic mutations with these conditions, identifying precisely which cell populations are affected by these mutations has been far more difficult. In a more physiological context, single-cell transcriptomics has revealed that both neurons and glia are more heterogeneous than previously believed (Lake et al., 2016; Tasic et al., 2016). In addition, connexins and innexins are encoded by multiple genes, giving rise to a wide diversity of gap junctions. For example, the mouse and human genomes contain 20 and 21 connexin-encoding genes, respectively (Sohl and Willecke, 2003), and the *Caenorhabditis elegans* and *Drosophila melanogaster* genomes contain 25 and 8 innexin-coding genes, respectively (Starich et al., 2001; Stebbings et al., 2002). Therefore, investigating the function of gap junctions in distinct cell types and in an isoform-specific manner remains extremely challenging. To overcome these challenges, new methods providing improved genetic specificity, high spatial resolution, and functionally relevant temporal resolution are urgently needed. Ideally, these methods should be non-invasive and technically simple to perform, thereby facilitating their use in *in vivo* applications, allowing researchers to study gap junctions in a more physiological setting.

In principle, using genetically encoded tools provides a possible solution. For example, the PLE-ester and Pept2-βALA strategies discussed above eliminate the need to manually manipulate the cells with glass pipettes, while providing the advantages associated with fluorescence imaging (Tian et al., 2012; Qiao and Sanes, 2015). On the other hand, the patch-clamp–based Pado and ChIEF strategies provide faster kinetics and do not require an exogenous substrate, making the background signal easier to control by regulating the expression level (Wang et al., 2014; Kang and Baker, 2016). However, each of these methods includes a non-genetically encoded component (e.g., an exogenous substrate or whole-cell patch-clamp recording), which have inherent limitations as discussed above.

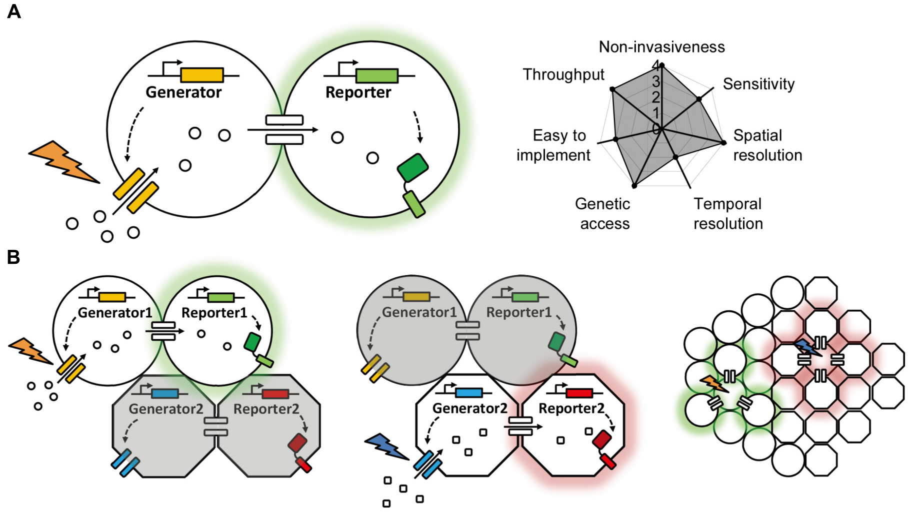

**FIGURE 2 |** A proposed ideal optogenetics-based system for mapping gap junctions. **(A)** The principle behind the proposed optogenetics-based system shown on the left with its theoretical performance index on the right, similar to **Figure 1**. **(B)** A proposed multiplex, optogenetic system for mapping gap junction using two pairs of bio-orthogonal generators and reporters and its application in an intact tissue with heterogeneous cell types.

The vast majority of genetically encoded methods used to date are based on the diffusion of target molecules such as esters, ions, peptides, or synthetic dyes through gap junctions. In each case, the electrochemical gradient that drives this diffusion is generated exogenously (e.g., by patch clamp, tracer introduction, or substrate application), and the chemical transfer is usually detected using fluorescent probes. Thus, we can summarize the entire system as consisting of a "generator" and a "reporter"; the generator produces the electrochemical gradient between coupled cells, and the reporter reports the transfer of molecules through the gap junctions (**Figure 2A**). In a system comprised exclusively of genetically encoded optogenetics-based components, both the generator and the reporter would be proteins (e.g., a light-activated channel or transporter and a fluorescent sensor). In this idealized system, the generator would be controlled by light and would use the cel's endogenous ions or chemicals to generate the electrochemical gradient, and the reporter would sense the change in concentration and change its fluorescence intensity. This non-invasive optogenetics-based system could be used to control and image a large number of cells simultaneously, and the background fluorescence could be minimized greatly by controlling the expression of the generator and reporter. More importantly, multicolor imaging could be achieved—at least in theory—by using a combination of generators with non-overlapping action wavelengths and/or reporters with non-overlapping excitation and emission spectra (**Figure 2B**). Given the wide range of clear benefits associated with this approach, genetically encoded optogenetics represents one of the most promising strategies for studying gap junctions in the future.

## AUTHOR CONTRIBUTIONS

YL, AD, and SL conceived and wrote the manuscript.

## FUNDING

This work was supported by the National Basic Research Program of China (973 Program; grant 2015CB856402 to YL), the General Program of National Natural Science Foundation of China (projects 31671118 and 31371442 to YL), and the Junior Thousand Talents Program of China (to YL).

## ACKNOWLEDGMENTS

We thank the members of the Li lab for providing feedback on the manuscript.

## REFERENCES

Abbaci, M., Barberi-Heyob, M., Blondel, W., Guillemin, F., and Didelon, J. (2008). Advantages and limitations of commonly used methods to assay the molecular permeability of gap junctional intercellular communication. *Biotechniques* 45, 33–52, 56–62. doi: 10.2144/000112810

Ansar Ahmed, S., Penhale, W. J., and Talal, N. (1985). Sex hormones, immune responses, and autoimmune diseases. Mechanisms of sex hormone action. *Am. J. Pathol.* 121, 531–551.

Antonsen, B. L., and Edwards, D. H. (2003). Differential dye coupling reveals lateral giant escape circuit in crayfish. *J. Comp. Neurol.* 466, 1–13. doi: 10.1002/cne.10802

Azzam, E. I., De Toledo, S. M., and Little, J. B. (2001). Direct evidence for the participation of gap junction-mediated intercellular communication in the transmission of damage signals from alpha -particle irradiated to nonirradiated cells. *Proc. Natl. Acad. Sci. U.S.A.* 98, 473–478. doi: 10.1073/pnas.011417098

Baranova, A., Ivanov, D., Petrash, N., Pestova, A., Skoblov, M., Kelmanson, I., et al. (2004). The mammalian pannexin family is homologous to the invertebrate innexin gap junction proteins. *Genomics* 83, 706–716. doi: 10.1016/j.ygeno.2003.09.025

Bennett, M. V., and Zukin, R. S. (2004). Electrical coupling and neuronal synchronization in the Mammalian brain. *Neuron* 41, 495–511. doi: 10.1016/S0896-6273(04)00043-1

Beyer, E. C., Kistler, J., Paul, D. L., and Goodenough, D. A. (1989). Antisera directed against connexin43 peptides react with a 43-kD protein localized to gap junctions in myocardium and other tissues. *J. Cell Biol.* 108, 595–605. doi: 10.1083/jcb.108.2.595

Biegel, A., Knutter, I., Hartrodt, B., Gebauer, S., Theis, S., Luckner, P., et al. (2006). The renal type H + /peptide symporter PEPT2: structure-affinity relationships. *Amino Acids* 31, 137–156. doi: 10.1007/s00726-006-0331-0

Bloomfield, S. A., and Volgyi, B. (2009). The diverse functional roles and regulation of neuronal gap junctions in the retina. *Nat. Rev. Neurosci.* 10, 495–506. doi: 10.1038/nrn2636

Bruzzone, R., Hormuzdi, S. G., Barbe, M. T., Herb, A., and Monyer, H. (2003). Pannexins, a family of gap junction proteins expressed in brain. *Proc. Natl. Acad. Sci. U.S.A.* 100, 13644–13649. doi: 10.1073/pnas.2233464100

Chen, T. W., Wardill, T. J., Sun, Y., Pulver, S. R., Renninger, S. L., Baohan, A., et al. (2013). Ultrasensitive fluorescent proteins for imaging neuronal activity. *Nature* 499, 295–300. doi: 10.1038/nature12354

Dakin, K., and Li, W. H. (2006). Local Ca2 + rise near store operated Ca2 + channels inhibits cell coupling during capacitative Ca2 + influx. *Cell Commun. Adhes.* 13, 29–39. doi: 10.1080/15419060600631425

Dakin, K., Zhao, Y., and Li, W. H. (2005). LAMP, a new imaging assay of gap junctional communication unveils that Ca2 + influx inhibits cell coupling. *Nat. Methods* 2, 55–62. doi: 10.1038/nmeth730

Decrouy, X., Gasc, J. M., Pointis, G., and Segretain, D. (2004). Functional characterization of Cx43 based gap junctions during spermatogenesis. *J. Cell. Physiol.* 200, 146–154. doi: 10.1002/jcp.10473

Dermietzel, R., Traub, O., Hwang, T. K., Beyer, E., Bennett, M. V., Spray, D. C., et al. (1989). Differential expression of three gap junction proteins in developing and mature brain tissues. *Proc. Natl. Acad. Sci. U.S.A.* 86, 10148–10152. doi: 10.1073/pnas.86.24.10148

D'hondt, C., Ponsaerts, R., De Smedt, H., Bultynck, G., and Himpens, B. (2009). Pannexins, distant relatives of the connexin family with specific cellular functions? *Bioessays* 31, 953–974. doi: 10.1002/bies.200800236

Dieck, S. T., Heuer, H., Ehrchen, J., Otto, C., and Bauer, K. (1999). The peptide transporter PepT2 is expressed in rat brain and mediates the accumulation of the fluorescent dipeptide derivative beta-Ala-Lys-Nepsilon-AMCA in astrocytes. *Glia* 25, 10–20. doi: 10.1002/(SICI)1098-1136(19990101)25:1<10::AID-GLIA2>3.0.CO;2-Y

Dobrenis, K., Chang, H. Y., Pina-Benabou, M. H., Woodroffe, A., Lee, S. C., Rozental, R., et al. (2005). Human and mouse microglia express connexin36, and functional gap junctions are formed between rodent microglia and neurons. *J. Neurosci. Res.* 82, 306–315. doi: 10.1002/jnr.20650

el-Fouly, M. H., Trosko, J. E., and Chang, C. C. (1987). Scrape-loading and dye transfer. A rapid and simple technique to study gap junctional intercellular communication. *Exp. Cell Res.* 168, 422–430. doi: 10.1016/0014-4827(87)90014-0

Furshpan, E. J., and Potter, D. D. (1957). Mechanism of nerve-impulse transmission at a crayfish synapse. *Nature* 180, 342–343. doi: 10.1038/180342a0

Furshpan, E. J., and Potter, D. D. (1959). Transmission at the giant motor synapses of the crayfish. *J. Physiol.* 145, 289–325. doi: 10.1113/jphysiol.1959.sp006143

Garg, S., Md Syed, M., and Kielian, T. (2005). *Staphylococcus aureus*-derived peptidoglycan induces Cx43 expression and functional gap junction intercellular communication in microglia. *J. Neurochem.* 95, 475–483. doi: 10.1111/j.1471-4159.2005.03384.x

Giaume, C., and McCarthy, K. D. (1996). Control of gap-junctional communication in astrocytic networks. *Trends Neurosci.* 19, 319–325. doi: 10.1016/0166-2236(96)10046-1

Giepmans, B. N., and Moolenaar, W. H. (1998). The gap junction protein connexin43 interacts with the second PDZ domain of the zona occludens-1 protein. *Curr. Biol.* 8, 931–934. doi: 10.1016/S0960-9822(07)00375-2

Giustina, A., and Veldhuis, J. D. (1998). Pathophysiology of the neuroregulation of growth hormone secretion in experimental animals and the human. *Endocr. Rev.* 19, 717–797. doi: 10.1210/er.19.6.717

Han, X., and Boyden, E. S. (2007). Multiple-color optical activation, silencing, and desynchronization of neural activity, with single-spike temporal resolution. *PLoS One* 2:e299. doi: 10.1371/journal.pone.0000299

Horikawa, K., and Armstrong, W. E. (1988). A versatile means of intracellular labeling: injection of biocytin and its detection with avidin conjugates. *J. Neurosci. Methods* 25, 1–11. doi: 10.1016/0165-0270(88)90114-8

Hoshi, H., and Mills, S. L. (2009). Components and properties of the G3 ganglion cell circuit in the rabbit retina. *J. Comp. Neurol.* 513, 69–82. doi: 10.1002/cne.21941

Ishikawa, M., Iwamoto, T., Nakamura, T., Doyle, A., Fukumoto, S., and Yamada, Y. (2011). Pannexin 3 functions as an ER Ca(2 + ) channel, hemichannel, and gap junction to promote osteoblast differentiation. *J. Cell Biol.* 193, 1257–1274. doi: 10.1083/jcb.201101050

Ito, K., Sass, H., Urban, J., Hofbauer, A., and Schneuwly, S. (1997). GAL4-responsive UAS-tau as a tool for studying the anatomy and development of the *Drosophila* central nervous system. *Cell Tissue Res.* 290, 1–10. doi: 10.1007/s004410050901

Jin, L., Han, Z., Platisa, J., Wooltorton, J. R., Cohen, L. B., and Pieribone, V. A. (2012). Single action potentials and subthreshold electrical events imaged in neurons with a fluorescent protein voltage probe. *Neuron* 75, 779–785. doi: 10.1016/j.neuron.2012.06.040

Kang, B. E., and Baker, B. J. (2016). Pado, a fluorescent protein with proton channel activity can optically monitor membrane potential, intracellular pH, and map gap junctions. *Sci. Rep.* 6:23865. doi: 10.1038/srep23865

Katz, B., and Miledi, R. (1965). The measurement of synaptic delay, and the time course of acetylcholine release at the neuromuscular junction. *Proc. R. Soc. Lond. B Biol. Sci.* 161, 483–495. doi: 10.1098/rspb.1965.0016

Kleopa, K. A. (2011). The role of gap junctions in Charcot-Marie-Tooth disease. *J. Neurosci.* 31, 17753–17760. doi: 10.1523/JNEUROSCI.4824-11.2011

Krnjevic, K. (1974). Chemical nature of synaptic transmission in vertebrates. *Physiol. Rev.* 54, 418–540. doi: 10.1152/physrev.1974.54.2.418

Kumar, N. M., and Gilula, N. B. (1996). The gap junction communication channel. *Cell* 84, 381–388. doi: 10.1016/S0092-8674(00)81282-9

Lai, C. P., Bechberger, J. F., Thompson, R. J., Macvicar, B. A., Bruzzone, R., and Naus, C. C. (2007). Tumor-suppressive effects of pannexin 1 in C6 glioma cells. *Cancer Res.* 67, 1545–1554. doi: 10.1158/0008-5472.CAN-06-1396

Lake, B. B., Ai, R., Kaeser, G. E., Salathia, N. S., Yung, Y. C., Liu, R., et al. (2016). Neuronal subtypes and diversity revealed by single-nucleus RNA sequencing of the human brain. *Science* 352, 1586–1590. doi: 10.1126/science.aaf1204

Lange, S., Musidlowska, A., Schmidt-Dannert, C., Schmitt, J., and Bornscheuer, U. T. (2001). Cloning, functional expression, and characterization of recombinant pig liver esterase. *Chembiochem* 2, 576–582. doi: 10.1002/1439-7633(20010803)2:7/8<576::AID-CBIC576>3.0.CO;2-Y

Lee, S. H., Magge, S., Spencer, D. D., Sontheimer, H., and Cornell-Bell, A. H. (1995). Human epileptic astrocytes exhibit increased gap junction coupling. *Glia* 15, 195–202. doi: 10.1002/glia.440150212

Lin, J. Y., Lin, M. Z., Steinbach, P., and Tsien, R. Y. (2009). Characterization of engineered channelrhodopsin variants with improved properties and kinetics. *Biophys. J.* 96, 1803–1814. doi: 10.1016/j.bpj.2008.11.034

Lippincott-Schwartz, J., Altan-Bonnet, N., and Patterson, G. H. (2003). Photobleaching and photoactivation: following protein dynamics in living cells. *Nat. Cell Biol.* 5(Suppl.), S7–S14.

Loewenstein, W. R. (1981). Junctional intercellular communication: the cell-to-cell membrane channel. *Physiol. Rev.* 61, 829–913. doi: 10.1152/physrev.1981.61.4.829

Martinez, A. D., Acuna, R., Figueroa, V., Maripillan, J., and Nicholson, B. (2009). Gap-junction channels dysfunction in deafness and hearing loss. *Antioxid. Redox Signal.* 11, 309–322. doi: 10.1089/ars.2008.2138

McNeil, P. L., Murphy, R. F., Lanni, F., and Taylor, D. L. (1984). A method for incorporating macromolecules into adherent cells. *J. Cell Biol.* 98, 1556–1564. doi: 10.1083/jcb.98.4.1556

Meier, U., and Gressner, A. M. (2004). Endocrine regulation of energy metabolism: review of pathobiochemical and clinical chemical aspects of leptin, ghrelin, adiponectin, and resistin. *Clin. Chem.* 50, 1511–1525. doi: 10.1373/clinchem.2004.032482

Meng, L., Zhang, A., Jin, Y., and Yan, D. (2016). Regulation of neuronal axon specification by glia-neuron gap junctions in *C. elegans*. *eLife* 5:e19510. doi: 10.7554/eLife.19510

Mese, G., Richard, G., and White, T. W. (2007). Gap junctions: basic structure and function. *J. Invest. Dermatol.* 127, 2516–2524. doi: 10.1038/sj.jid.5700770

Nagel, G., Szellas, T., Huhn, W., Kateriya, S., Adeishvili, N., Berthold, P., et al. (2003). Channelrhodopsin-2, a directly light-gated cation-selective membrane channel. *Proc. Natl. Acad. Sci. U.S.A.* 100, 13940–13945. doi: 10.1073/pnas.1936192100

Nagel, G., Szellas, T., Kateriya, S., Adeishvili, N., Hegemann, P., and Bamberg, E. (2005). Channelrhodopsins: directly light-gated cation channels. *Biochem. Soc. Trans.* 33, 863–866. doi: 10.1042/BST0330863

Neijssen, J., Herberts, C., Drijfhout, J. W., Reits, E., Janssen, L., and Neefjes, J. (2005). Cross-presentation by intercellular peptide transfer through gap junctions. *Nature* 434, 83–88. doi: 10.1038/nature03290

Nualart-Marti, A., Solsona, C., and Fields, R. D. (2013). Gap junction communication in myelinating glia. *Biochim. Biophys. Acta* 1828, 69–78. doi: 10.1016/j.bbamem.2012.01.024

Paul, D. L., Ebihara, L., Takemoto, L. J., Swenson, K. I., and Goodenough, D. A. (1991). Connexin46, a novel lens gap junction protein, induces voltage-gated currents in nonjunctional plasma membrane of *Xenopus* oocytes. *J. Cell Biol.* 115, 1077–1089. doi: 10.1083/jcb.115.4.1077

Pereda, A. E. (2014). Electrical synapses and their functional interactions with chemical synapses. *Nat. Rev. Neurosci.* 15, 250–263. doi: 10.1038/nrn3708

Personius, K. E., Chang, Q., Mentis, G. Z., O'donovan, M. J., and Balice-Gordon, R. J. (2007). Reduced gap junctional coupling leads to uncorrelated motor neuron firing and precocious neuromuscular synapse elimination. *Proc. Natl. Acad. Sci. U.S.A.* 104, 11808–11813. doi: 10.1073/pnas.0703357104

Phelan, P., Bacon, J. P., Davies, J. A., Stebbings, L. A., Todman, M. G., Avery, L., et al. (1998). Innexins: a family of invertebrate gap-junction proteins. *Trends Genet.* 14, 348–349. doi: 10.1016/S0168-9525(98)01547-9

Phelan, P., Nakagawa, M., Wilkin, M. B., Moffat, K. G., O'kane, C. J., Davies, J. A., et al. (1996). Mutations in shaking-B prevent electrical synapse formation in the Drosophila giant fiber system. *J. Neurosci.* 16, 1101–1113. doi: 10.1523/JNEUROSCI.16-03-01101.1996

Qiao, M., and Sanes, J. R. (2015). Genetic method for labeling electrically coupled cells: application to retina. *Front. Mol. Neurosci.* 8:81. doi: 10.3389/fnmol.2015.00081

Ritter, C., Nett, N., Acevedo-Rocha, C. G., Lonsdale, R., Kraling, K., Dempwolff, F., et al. (2015). Bioorthogonal enzymatic activation of caged compounds. *Angew. Chem. Int. Ed. Engl.* 54, 13440–13443. doi: 10.1002/anie.201506739

Rotman, B., and Papermaster, B. W. (1966). Membrane properties of living mammalian cells as studied by enzymatic hydrolysis of fluorogenic esters. *Proc. Natl. Acad. Sci. U.S.A.* 55, 134–141. doi: 10.1073/pnas.55.1.134

Sabatini, B. L., and Regehr, W. G. (1996). Timing of neurotransmission at fast synapses in the mammalian brain. *Nature* 384, 170–172. doi: 10.1038/384170a0

Sletten, E. M., and Bertozzi, C. R. (2009). Bioorthogonal chemistry: fishing for selectivity in a sea of functionality. *Angew. Chem. Int. Ed. Engl.* 48, 6974–6998. doi: 10.1002/anie.200900942

Sohl, G., Maxeiner, S., and Willecke, K. (2005). Expression and functions of neuronal gap junctions. *Nat. Rev. Neurosci.* 6, 191–200. doi: 10.1038/nrn1627

Sohl, G., and Willecke, K. (2003). An update on connexin genes and their nomenclature in mouse and man. *Cell Commun. Adhes.* 10, 173–180. doi: 10.1080/cac.10.4-6.173.180

Song, J., and Tanouye, M. A. (2006). Seizure suppression by *shakB*$^2$, a gap junction mutation in *Drosophila*. *J. Neurophysiol.* 95, 627–635. doi: 10.1152/jn.01059.2004

Soroceanu, L., Manning, T. J. Jr., and Sontheimer, H. (2001). Reduced expression of connexin-43 and functional gap junction coupling in human gliomas. *Glia* 33, 107–117. doi: 10.1002/1098-1136(200102)33:2<107::AID-GLIA1010>3.0.CO;2-4

Sosinsky, G. E., Boassa, D., Dermietzel, R., Duffy, H. S., Laird, D. W., Macvicar, B., et al. (2011). Pannexin channels are not gap junction hemichannels. *Channels* 5, 193–197. doi: 10.4161/chan.5.3.15765

Speder, P., and Brand, A. H. (2014). Gap junction proteins in the blood-brain barrier control nutrient-dependent reactivation of *Drosophila* neural stem cells. *Dev. Cell* 30, 309–321. doi: 10.1016/j.devcel.2014.05.021

Spray, D. C., Harris, A. L., and Bennett, M. V. (1979). Voltage dependence of junctional conductance in early amphibian embryos. *Science* 204, 432–434. doi: 10.1126/science.312530

Starich, T., Sheehan, M., Jadrich, J., and Shaw, J. (2001). Innexins in *C. elegans*. *Cell Commun. Adhes.* 8, 311–314. doi: 10.3109/15419060109080744

Stauffer, K. A. (1995). The gap junction proteins beta 1-connexin (connexin-32) and beta 2-connexin (connexin-26) can form heteromeric hemichannels. *J. Biol. Chem.* 270, 6768–6772.

Stebbings, L. A., Todman, M. G., Phillips, R., Greer, C. E., Tam, J., Phelan, P., et al. (2002). Gap junctions in *Drosophila*: developmental expression of the entire innexin gene family. *Mech. Dev.* 113, 197–205. doi: 10.1016/S0925-4773(02)00025-4

Stewart, W. W. (1978). Functional connections between cells as revealed by dye-coupling with a highly fluorescent naphthalimide tracer. *Cell* 14, 741–759. doi: 10.1016/0092-8674(78)90256-8

Tasic, B., Menon, V., Nguyen, T. N., Kim, T. K., Jarsky, T., Yao, Z., et al. (2016). Adult mouse cortical cell taxonomy revealed by single cell transcriptomics. *Nat. Neurosci.* 19, 335–346. doi: 10.1038/nn.4216

Thomas, J. B., and Wyman, R. J. (1984). Mutations altering synaptic connectivity between identified neurons in Drosophila. *J. Neurosci.* 4, 530–538. doi: 10.1523/JNEUROSCI.04-02-00530.1984

Tian, L., Yang, Y., Wysocki, L. M., Arnold, A. C., Hu, A., Ravichandran, B., et al. (2012). Selective esterase-ester pair for targeting small molecules with cellular specificity. *Proc. Natl. Acad. Sci. U.S.A.* 109, 4756–4761. doi: 10.1073/pnas.1111943109

Tour, O., Adams, S. R., Kerr, R. A., Meijer, R. M., Sejnowski, T. J., Tsien, R. W., et al. (2007). Calcium Green FlAsH as a genetically targeted small-molecule calcium indicator. *Nat. Chem. Biol.* 3, 423–431. doi: 10.1038/nchembio.2007.4

Vanden Abeele, F., Bidaux, G., Gordienko, D., Beck, B., Panchin, Y. V., Baranova, A. V., et al. (2006). Functional implications of calcium permeability of the channel formed by pannexin 1. *J. Cell Biol.* 174, 535–546. doi: 10.1083/jcb.200601115

Volgyi, B., Chheda, S., and Bloomfield, S. A. (2009). Tracer coupling patterns of the ganglion cell subtypes in the mouse retina. *J. Comp. Neurol.* 512, 664–687. doi: 10.1002/cne.21912

Wade, M. H., Trosko, J. E., and Schindler, M. (1986). A fluorescence photobleaching assay of gap junction-mediated communication between human cells. *Science* 232, 525–528. doi: 10.1126/science.3961495

Wallraff, A., Odermatt, B., Willecke, K., and Steinhauser, C. (2004). Distinct types of astroglial cells in the hippocampus differ in gap junction coupling. *Glia* 48, 36–43. doi: 10.1002/glia.20040

Wang, K., Gong, J., Wang, Q., Li, H., Cheng, Q., Liu, Y., et al. (2014). Parallel pathways convey olfactory information with opposite polarities in *Drosophila*. *Proc. Natl. Acad. Sci. U.S.A.* 111, 3164–3169. doi: 10.1073/pnas.1317911111

White, T. W., Bruzzone, R., Goodenough, D. A., and Paul, D. L. (1992). Mouse Cx50, a functional member of the connexin family of gap junction proteins, is the lens fiber protein MP70. *Mol. Biol. Cell* 3, 711–720. doi: 10.1091/mbc.3.7.711

Wrenzycki, C., Herrmann, D., Carnwath, J. W., and Niemann, H. (1996). Expression of the gap junction gene connexin43 (Cx43) in preimplantation bovine embryos derived in vitro or in vivo. *J. Reprod. Fertil.* 108, 17–24. doi: 10.1530/jrf.0.1080017

Xia, J. H., Liu, C. Y., Tang, B. S., Pan, Q., Huang, L., Dai, H. P., et al. (1998). Mutations in the gene encoding gap junction protein beta-3 associated with autosomal dominant hearing impairment. *Nat. Genet.* 20, 370–373. doi: 10.1038/3845

Xin, D., and Bloomfield, S. A. (1999). Dark- and light-induced changes in coupling between horizontal cells in mammalian retina. *J. Comp. Neurol.* 405, 75–87. doi: 10.1002/(SICI)1096-9861(19990301)405:1<75::AID-CNE6>3.0.CO;2-D

Zhang, F., Wang, L. P., Brauner, M., Liewald, J. F., Kay, K., Watzke, N., et al. (2007). Multimodal fast optical interrogation of neural circuitry. *Nature* 446, 633–639. doi: 10.1038/nature05744

Zhang, Z., Curtin, K. D., Sun, Y. A., and Wyman, R. J. (1999). Nested transcripts of gap junction gene have distinct expression patterns. *J. Neurobiol.* 40, 288–301. doi: 10.1002/(SICI)1097-4695(19990905)40:3<288::AID-NEU2>3.0.CO;2-O

Zhao, Y., Zheng, Q., Dakin, K., Xu, K., Martinez, M. L., and Li, W. H. (2004). New caged coumarin fluorophores with extraordinary uncaging cross sections suitable for biological imaging applications. *J. Am. Chem. Soc.* 126, 4653–4663. doi: 10.1021/ja036958m

**Conflict of Interest Statement:** The authors declare that the research was conducted in the absence of any commercial or financial relationships that could be construed as a potential conflict of interest.

frontiers in Cellular Neuroscience

ORIGINAL RESEARCH
published: 20 September 2018
doi: 10.3389/fncel.2018.00315

# Bessel Beam Illumination Reduces Random and Systematic Errors in Quantitative Functional Studies Using Light-Sheet Microscopy

*M. Caroline Müllenbroich [1,2*†], Lapo Turrini [2], Ludovico Silvestri [1,2], Tommaso Alterini [2], Ali Gheisari [2], Natascia Tiso [3], Francesco Vanzi [2,4], Leonardo Sacconi [1,2] and Francesco S. Pavone [1,2,5]*

*[1] National Institute of Optics, National Research Council, Sesto Fiorentino, Italy, [2] European Laboratory for Non-linear Spectroscopy, LENS, Sesto Fiorentino, Italy, [3] Department of Biology, University of Padova, Padua, Italy, [4] Department of Biology, University of Florence, Sesto Fiorentino, Italy, [5] Department of Physics and Astronomy, University of Florence, Sesto Fiorentino, Italy*

**Edited by:**
*Marco Canepari,*
*UMR5588 Laboratoire Interdisciplinaire de Physique (LIPhy), France*

**Reviewed by:**
*Knut Holthoff,*
*Friedrich-Schiller-Universität Jena, Germany*
*Markus Rothermel,*
*RWTH Aachen Universität, Germany*
*Martin Oheim,*
*Centre National de la Recherche Scientifique (CNRS), France*

***Correspondence:**
*M. Caroline Müllenbroich*
*caroline.muellenbroich@glasgow.ac.uk*

**†Present Address:**
*M. Caroline Müllenbroich,*
*School of Physics & Astronomy,*
*University of Glasgow, Glasgow,*
*United Kingdom*

**Received:** *23 April 2018*
**Accepted:** *29 August 2018*
**Published:** *20 September 2018*

**Citation:**
*Müllenbroich MC, Turrini L, Silvestri L, Alterini T, Gheisari A, Tiso N, Vanzi F, Sacconi L and Pavone FS (2018) Bessel Beam Illumination Reduces Random and Systematic Errors in Quantitative Functional Studies Using Light-Sheet Microscopy. Front. Cell. Neurosci. 12:315. doi: 10.3389/fncel.2018.00315*

Light-sheet microscopy (LSM), in combination with intrinsically transparent zebrafish larvae, is a method of choice to observe brain function with high frame rates at cellular resolution. Inherently to LSM, however, residual opaque objects cause stripe artifacts, which obscure features of interest and, during functional imaging, modulate fluorescence variations related to neuronal activity. Here, we report how Bessel beams reduce streaking artifacts and produce high-fidelity quantitative data demonstrating a fivefold increase in sensitivity to calcium transients and a 20-fold increase in accuracy in the detection of activity correlations in functional imaging. Furthermore, using principal component analysis, we show that measurements obtained with Bessel beams are clean enough to reveal in one-shot experiments correlations that can not be averaged over trials after stimuli as is the case when studying spontaneous activity. Our results not only demonstrate the contamination of data by systematic and random errors through conventional Gaussian illumination and but,furthermore, quantify the increase in fidelity of such data when using Bessel beams.

**Keywords: spontaneous activity, zebrafish, principle component analysis, light-sheet microscopy, functional imaging, Bessel beams, flickering artifacts, striping**

## 1. INTRODUCTION

Light-sheet microscopy (LSM) in combination with intrinsically transparent samples like zebrafish larvae, is a choice method to elucidated neuronal activity on a organ-wide scale at cellular resolution and has yielded fast volumetric calcium activation maps over the entire encephalon (Vladimirov et al., 2014). In LSM Siedentopf and Zsigmondy (1902), a technique which affords intrinsic optical sectioning, fast acquisition rates and low photobleaching, fluorescence is excited in a thin sheet of excitation light that coincides with the focal plane of a perpendicularly placed detection objective (Huisken et al., 2004).

This very nature of uncoupled, perpendicular optical pathways for fluorescence excitation and detection entails, however, a set of drawbacks unique to LSM in the form of dark shadows that appear whenever the fluorescence-exciting light sheet is interrupted by scattering or absorbing obstacles. These refractive heterogeneities, always present to some extent even in extremely well clarified or intrinsically transparent samples, have been shown to lead to a loss of spatial resolution and a concomitant degradation in sensitivity and contrast (Chen et al., 2016). At best, dark shadowing severely affects image homogeneity, at worst, it completely obscures any feature of interest in the affected area. Considering the increasingly large dataset sizes now routinely produced in high-throughput light-sheet microscopy, high demands are placed on the automated tools to count, trace or segment the fluorescent features of interest. Consequently, background uniformity and indeed high-fidelity imaging are paramount to facilitate the extraction of meaningful insights from terabytes of data.

Furthermore, if the obstacles that obstruct the light sheet are not static, their shadows dynamically modulate the fluorescence intensity, causing an artifact here termed "flickering." For example, hemodynamic absorption (Ma et al., 2016) of the light sheet can be particularly problematic for *in-vivo* $Ca^{2+}$-imaging where the variation of fluorescence signal over time quantifies neuronal activity. We hypothesize that artifacts due to streaky shadows are non-negligible and cause loss or corruption of data obtained in light-sheet microscopy experiments. This premise is supported by a previous functional study in zebrafish which had to manually exclude neurons affected by severe flickering from further flickering from further analysis (Panier et al., 2013). We argue that dynamic flickering constitutes an inherent source of artifact potentially falsifying in light-sheet microscopy experiments and therefore any theory inferred from such observations might have to be questioned.

Aiming for an optical solution to streaking artifacts, here, we apply Bessel beams (Durnin et al., 1987, see **Supplementary Materials** for further information), to LSM to functional imaging of zebrafish larvae for high-fidelity interrogation of their neuronal activity.

Bessel beams have been previously applied to microscopy to extend the useful field of view or depth of field (Lorenser et al., 2014; Lu et al., 2017) or to image in scattering media either to study the scattering properties of the sample or the self-reconstructing properties of the Bessel beam itself (Fahrbach et al., 2010, 2013a). Since a Bessel beam's central core can be extremely narrow without being subject to diffraction (McGloin and Dholakia, 2005), Bessel beams have also been applied to LSM to obtain isotropic resolution (Planchon et al., 2011; Gao et al., 2014) or to increase spatio-temporal resolution (Chen et al., 2014, however mostly demonstrating results from cell cultures or *C. elegans* at a very early developmental stage. Finally, two groups have published technological development concerning Bessel beams applied to LSM (Zhang et al., 2014; Zhao et al., 2016).

Here, we report on the application of Bessel beams to functional imaging in zebrafish larva in LSM, and more specifically to the study of spontaneous activity. The investigation of spontaneous activity, by definition, implies measurements in complete absence of stimuli and therefore precludes the possibility to clean up data by averaging of repeated trials. Using a direct comparative analysis between Bessel and Gaussian illumination we first provide supporting evidence and quantification of artifacts introduced by Gaussian illumination. Further, we demonstrate that Bessel beams provide the superior accuracy and sensitivity needed to reveal strong correlations in spontaneous activity in one-shot measurements otherwise lost when using conventional Gaussian illumination.

## 2. RESULTS

### Light-Sheet Microscope for *in-vivo* Imaging

A custom-made light-sheet microscope (**Figure 1A** and **Figure S2**), specifically designed for *in-vivo* imaging of zebrafish larva, was used for all functional imaging experiment. In brief, a 488 nm continuous-wave diode-pump solid state laser (Excelsior, Spectra Physics, Santa Clara, USA) with 50 mW output power was used as light source and an acousto-optical tunable filter (AOTF) was used as a shutter and power regulator. Two different illumination paths could be selected by the use of flip mirrors. The first illumination path, expands the output of the laser onto a galvanometric mirror (galvo, 6220H, Cambridge Technology, Bedford, USA). The galvo is re-imaged with a 4f telescope onto the back aperture of the excitation objective (4x, 0.13 NA, air immersion, Olympus, Tokyo, Japan). The excitation objective focused the illumination beam into the sample chamber and by applying a sawtooth waveform to the galvo the beam was rapidly scanned to form a virtual light sheet which coincided with the focal plane of a perpendicularly placed detection objective (20x, 1 NA, water immersion, Olympus, Tokyo, Japan). The sample was mounted on an x−, y−, z−, Θ-stage (M-122.2DD and M-116.DG, Physik Instrumente, Karlsruhe, Germany) which allowed its precise positioning and the acquisition of z-stacks. Fluorescence was detected in a wide-field scheme with a tube lens forming an image onto the chip of a sCMOS camera (OrcaFlash4.0, Hamamatsu, Hamamatsu city, Japan). Appropriate filters are used to bandpass filter the fluorescence and reject excitation light. The camera was operated in rolling shutter mode thereby creating a virtual confocal slit. In the second illumination path a telescope adjusted the beam diameter of the Gaussian beam before the axicon (AX251-A, $\alpha = 1^\circ$, Thorlabs, Newton, USA) to minimize the Gaussian contribution produced by the round tip. The self-reconstruction length of the resulting Bessel beam (see also **Figure S1**) was then re-imaged with 3 additional lenses, each placed at 2f from each other respectively, into the common Gaussian light path. A circular spatial filter was used close to a Fourier plane near the galvo to filter out any residual Gaussian contribution to the Bessel beam. A heating system kept the sample chamber at a constant temperature of 28.5 °C. The microscope was controlled via custom software written in LabVIEW 2012 (National Instruments, Austin, USA) using the Murmex library (Distrio, Amsterdam, The Netherlands).

### Streaking Artifacts Obscure Microscopic Features of Interest

The effects of streaking artifacts are visualized in **Figure 2**. All images were acquired using a custom-built light-sheet microscope (**Figure 1**) which provided cellular resolution over the entire encephalon within one field of view. The image obtained using Gaussian illumination (**Figure 2a**) shows degraded image homogeneity and dark shadows obscuring microscopic anatomical features of interest which are further

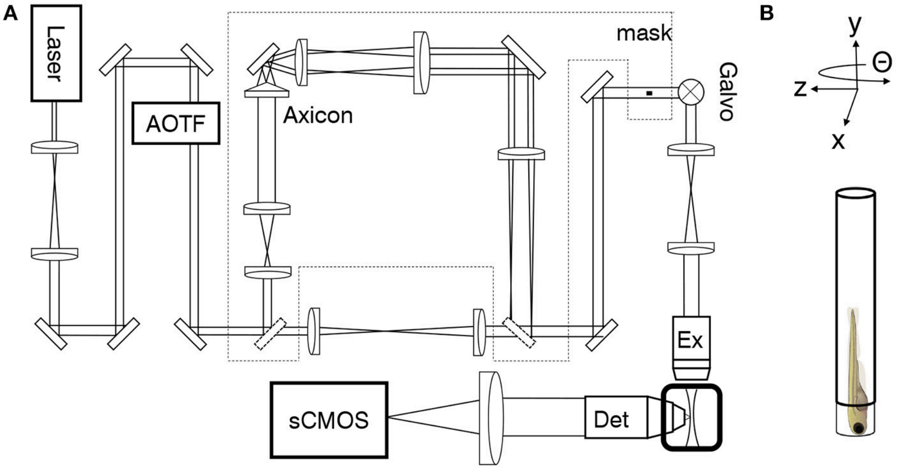

**FIGURE 1 |** Light-sheet microscope for *in-vivo* imaging. **(A)** As an alternative to standard Gaussian illumination, a Bessel beam created by an axicon could be used. **(B)** The larva was mounted vertically on an x−, y−, z−, Θ-stage.

illustrated in an inset detailing the hindbrain (**Figure 2b**). Notably those same features remain clearly visible when using Bessel beam illumination (**Figures 2c,d**). In order to quantify the extent of the area affected by strong striping, we calculated the normalized line profiles obtained over the entire width (along the illumination direction) of the image for Gauss and Bessel illumination respectively (**Figure 2e**) and further binarised their absolute difference (**Figure 2f**) with respect to a user-selected threshold to obtain a pattern similar to a bar code. By superimposing this bar pattern to the original image the percentage of 2D area affected by streaking inhomogeneity was estimated (Müllenbroich et al., 2018)). Using a threshold of 15%, we estimated that 72.8 ± 12.5% (error is standard deviation, $n = 20$ planes throughout the encephalon, $N = 11$ larvae) of the volume was affected by streaking.

The sensitivity of the area percentage on the threshold is reported in **Figure 2g** (using the same sample size, error is sem). The percentage area when considering only the proximal or distal half of the zebrafish respectively shows no statistically relevant difference (**Figure 2h**, $p$=0.6467, paired $t$-test of $n = 20$ planes in $N = 11$ larvae aged 4–5 dpf, error is sem) highlighting the limitation of double-sided illumination.

## Dynamic Flickering Modifies Functional Traces

In the following, we consider functional imaging in zebrafish where neuronal activity is quantified by a relative change in fluorescence of the calcium indicator with respect to a baseline value. Additionally to previously discussed static shadows also present in intrinsically transparent zebrafish larva, dynamic shadowing caused by the movement of red blood cells leads to a fluctuation of this baseline, here termed flickering. As early as 3 days post fertilization (dpf), fully formed blood vessels (**Figures 3a–c**, green arrow heads) can be easily distinguished by the flow of individual blood cells (red arrow heads). Hemodynamic absorption and scattering represents a multiplicative noise source (Ma et al., 2016) and therefore has the potential to modulate significantly the sensitivity to fluorescence variations related to neuronal activity in adjacent neurons (white arrow heads). A projection of the standard deviation for ≈ 100 ms of the trace (**Figure 3b**) clearly evidences blood vessels by superimposing the trajectories of blood cells and further highlights the strong variations in gray values in corresponding adjacent regions (see **Videos S1–S4**). Notably, when displayed on the same brightness scale, the corresponding areas are free of strong flickering when using Bessel beam illumination (**Figures 3c,d**).

In this section, we evaluate to which extent flickering potentially masks or even falsifies neuronal activity when using Gaussian illumination. Furthermore we directly compare each quantification with its Bessel beam counterpart. Based on an approach employing standard deviation projections, we devised an automated methodology detailed in the methods section 4 and **Figures S3, S4**. Tricaine, a general anesthetic that blocks voltage sensitive $Na^+$ channels preferentially in neurons, was added to the fish water. The 2D area fraction affected by strong flickering was quantified at 23.8 ± 6.5% for Gaussian and 0.8 ± 0.5% for Bessel beam illumination respectively (**Figure 3e**, error is sem, $p < 0.0001$, paired $t$-test, $n = 18$ planes in $N = 10$ larvae aged 4–5 dpf).

### Hemodynamic Baseline Contamination

Due to the irregular flow of blood cells, the traversing excitation light sheet is either absorbed or scattered out of its trajectory such that the baseline fluorescence in adjacent neurons is no longer steadily generated, both because of direct shadowing of in-focus fluorophores and of spurious excitation of out-of-focus ones. In the following, dF/F traces of pairwise identical neurons, imaged with either a Gaussian or Bessel beam, located in areas affected by strong flickering and located as described in the previous section, were compared. Larvae were treated with tricaine ($160\,\mathrm{mg\,l^{-1}}$), a commonly used general anesthetic

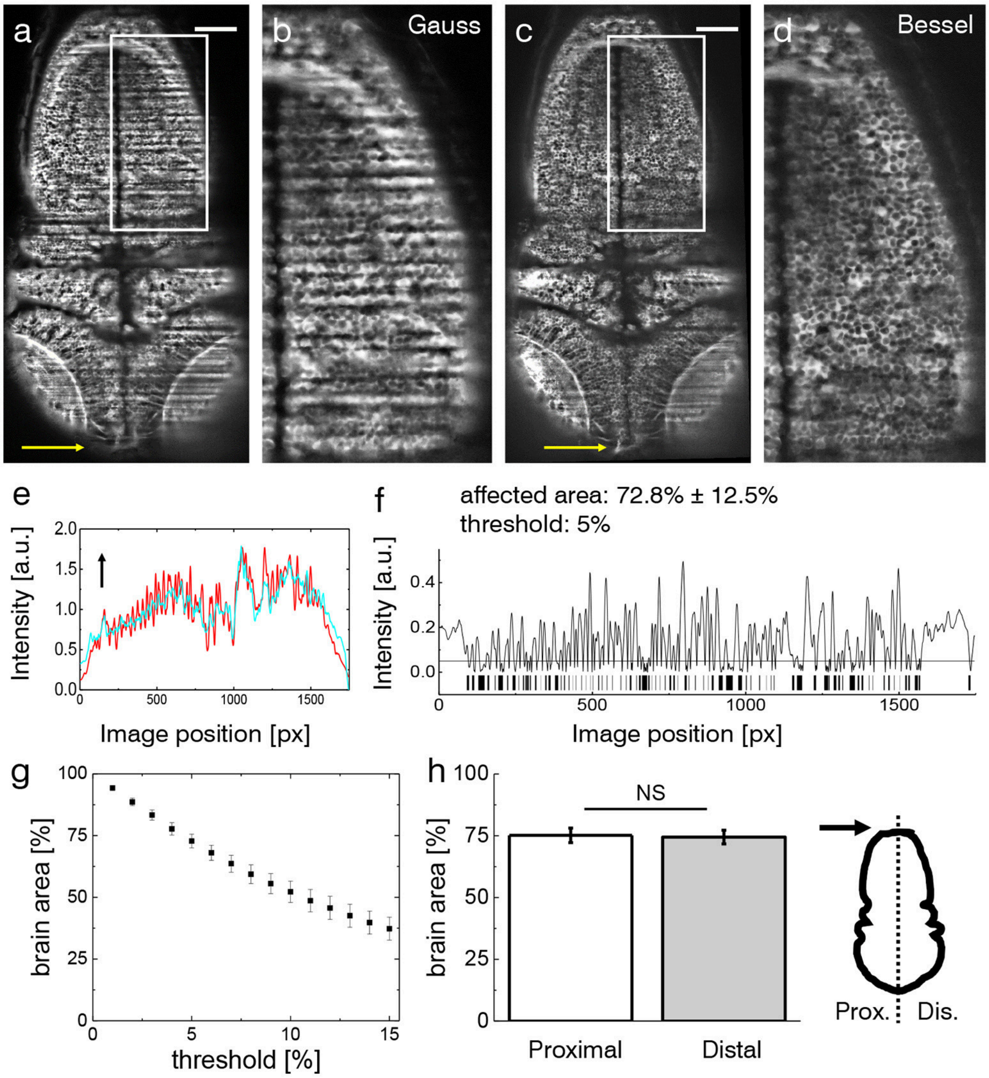

**FIGURE 2 |** Shadow artifacts in zebrafish imaging. **(a,c)** Static shadows in the encephalon of a 3 dpf Tg(elavl3:GCaMP6s) zebrafish with cytoplasmatic expression of GCaMP imaged with Gaussian and Bessel beam illumination. Yellow arrow indicates light-sheet propagation. Scale bar: 100 μm. **(b,d)** Details showing the hindbrain. The contrast in both images has been enhanced over the entire image using Contrast-Limited Adaptive Histogram Equalization (CLAHE) in ImageJ for better visualization. **(e)** Normalized line profile averaged over the entire width of the image for Gaussian (red) and Bessel beam illumination (cyan) evidences the shadows as drops in the red curve. Arrow indicates light-sheet propagation. **(f)** Absolute difference of the line profiles in **(e)** and the resulting bar code when applying a threshold of 5%. With this threshold 72.8 ± 12.5% (error is standard deviation, $n = 20$ planes throughout the encephalon in $N = 11$ larvae) was affected by streaking artifacts. **(g)** Sensitivity of the affected area on the threshold. Each point is the average of $n = 20$ planes in $N = 11$ larvae, error is standard error of the mean (sem). **(h)** The difference between the half of the larva proximal and distal to the light-sheet source is not statistically significant ($p = 0.6467$, paired $t$-test of $n = 20$ planes in $N = 11$ larvae, error is sem).

to globally lower neuronal activity (Attili and Hughes, 2014; Turrini et al., 2017), to ensure that any changes in baseline fluorescence were only due to dynamic flickering and not neuronal activity. A transversal section of the encephalon of a 4 dpf Tg(elavl3:H2B-GCaMP6s) zebrafish larva is shown in **Figures 4a,b**. Three representative neurons are marked with red (cyan) circles for the Gaussian (Bessel) case and their dF/F traces are shown in **Figure 4c**. Different positions in the encephalon display different levels of baseline noise; however, in general, the noise obtained in Bessel traces was consistently lower than that in traces obtained with Gaussian illumination. Quantified by their standard deviation, we analyzed traces measured with Gaussian and Bessel beam illumination respectively to obtain the level of baseline noise in the absence of neuronal activity (**Figure 4d**). The baseline noise was 19.65 ± 0.18% of dF/F for Gaussian and 3.90 ± 0.07% for Bessel beam illumination ($p < 0.0001$, paired $t$-test, $n = 625$ cells, 15 time lapses at various depths in $N = 7$ larvae of 4–5 dpf, error is sem) constituting a 5-fold increase in sensitivity.

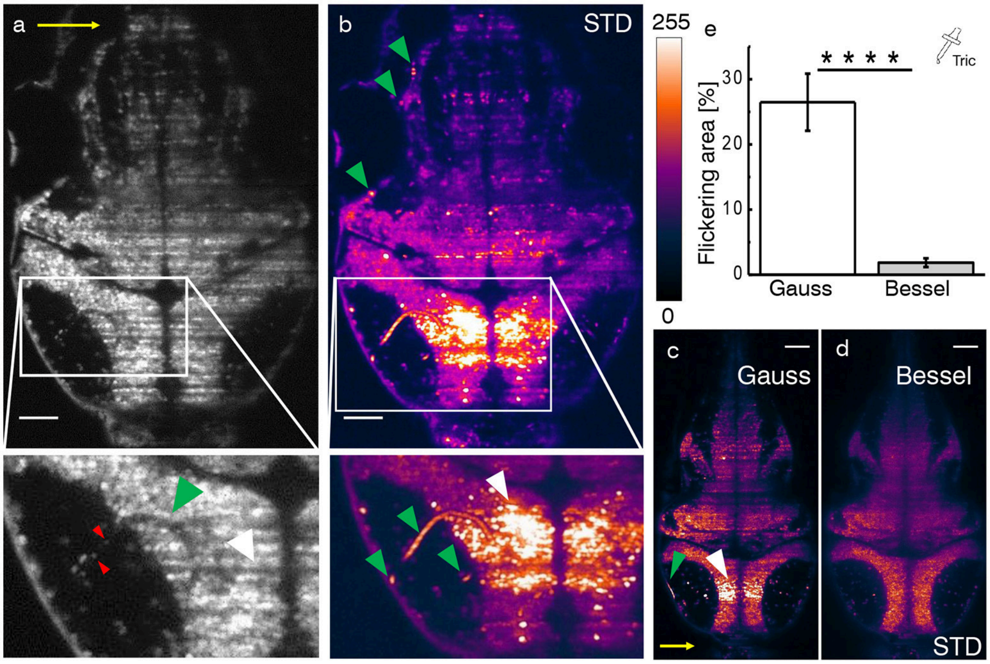

**FIGURE 3 |** Hemodynamic flickering in zebrafish imaging. **(a)** Transverse plane of a 4dpf Zebrafish larva [Tg(elavl3:H2B-GCaMP6s)]. Red blood cells (red arrow heads) passing through vasculature (green arrow head) dynamically absorb or scatter the excitation light sheet (yellow arrow) and create areas of strongly fluctuating shadow artifacts (white arrow head). Scale bar: $50\,\mu\mathrm{m}$. **(b)** Projection of the standard deviation over $\approx 100\,\mathrm{ms}$ of a time lapse recording on the plane shown in **(a)**. Each of the three segments of vasculature (green arrow heads, inset) causes a corresponding area of high standard deviation of the fluorescence intensity (white arrow head). A look-up table has been applied for clarity ranging from 0 (black) to 255 (white) for the 8-bit gray pixel value. **(c,d)** Displayed on the same brightness scale, corresponding flickering is much reduced with Bessel beam illumination. **(e)** Quantification of 2D area strongly affected by flickering for Gaussian ($23.8 \pm 6.5\,\%$) and and Bessel beam illumination ($0.8 \pm 0.5\,\%$) (****$p \leq 0.0001$, paired *t*-test of $n = 18$ planes in $N = 10$ larvae aged 4–5 dpf, error is sem). Tricaine ($160\,\mathrm{mg\,l^{-1}}$) was added to the fish water.

## Statistical Analysis of Reduced Sensitivity and Accuracy

The previously reported increase in baseline noise directly reduces the sensitivity to calcium transients. In this section, using statistical arguments, we quantify the loss in peak detection and activity correlation due to time-varying hemodynamic flickering.

Exemplary traces in **Figure 4e** illustrate a peak counting routine (see Methods section 4) which counted peaks above Gaussian baseline noise (red triangles) and again above Bessel beam baseline noise (cyan triangles) on identical traces obtained with Bessel beam illumination. Peaks of sub-threshold prominence (black arrow head) were discarded. The total number of peaks per minute detected above their respective baseline noise levels are reported in **Figure 4f** ($p < 0.0001$, paired *t*-test, $n = 586$ cells, in $N = 1$ larva, error is sem). The cells were located at 12 different depths throughout the encephalon of a 4 dpf larva. Whereas on average 6.6 peaks per minute could be detected above Bessel beam noise levels, only 0.5 peaks per minute were high enough to surpass the Gaussian baseline noise. This means that, statistically, if a given cell were to be located in an area affected by strong flickering, then less than 1 out of 12 peaks would be detected due to the higher associated baseline noise when using Gaussian compared to Bessel beam illumination.

To further illustrate the influence of increased baseline noise on dF/F traces, we generated random white noise of an amplitude corresponding to the Gaussian and Bessel baseline noise respectively, and multiplied it pairwise to traces obtained with Bessel beam illumination, see **Figure S5**. The native data set without synthetic noise was considered as ground truth and allowed an absolute comparison between Gaussian and Bessel beam illumination. The absolute cross correlation coefficients reported in **Figure S5d** reveal that while the mean of the Gaussian and native data set differ significantly (0.0978 vs. 0.1309), the difference between the mean of the Bessel and the native data set is not statistically significant (0.1308 vs. 0.1309) ($p < 0.0001$, *t*-test, $n = 27{,}7885$ corresponding to 746 cells in $N = 1$ larva, error is too small to be displayed). Next, the difference in cross correlation coefficients between the native traces and the traces with synthetic noises was calculated (**Figures S5e,f,i**). The histograms of these distributions give some important insights; whereas the mean value represents the bias of each modality, the standard deviation gives a measure of its accuracy. For Gaussian illumination, we obtained a mean value of 0.0127 (**Figure S5g**) whereas this value is 5.29E-5 for Bessel beam illumination (**Figure S5j**). This result indicates the introduction of a systematic error by Gaussian illumination which is approximately one tenth of the average absolute correlation coefficient. Furthermore, the standard deviations of the histograms give a direct measure of the random error

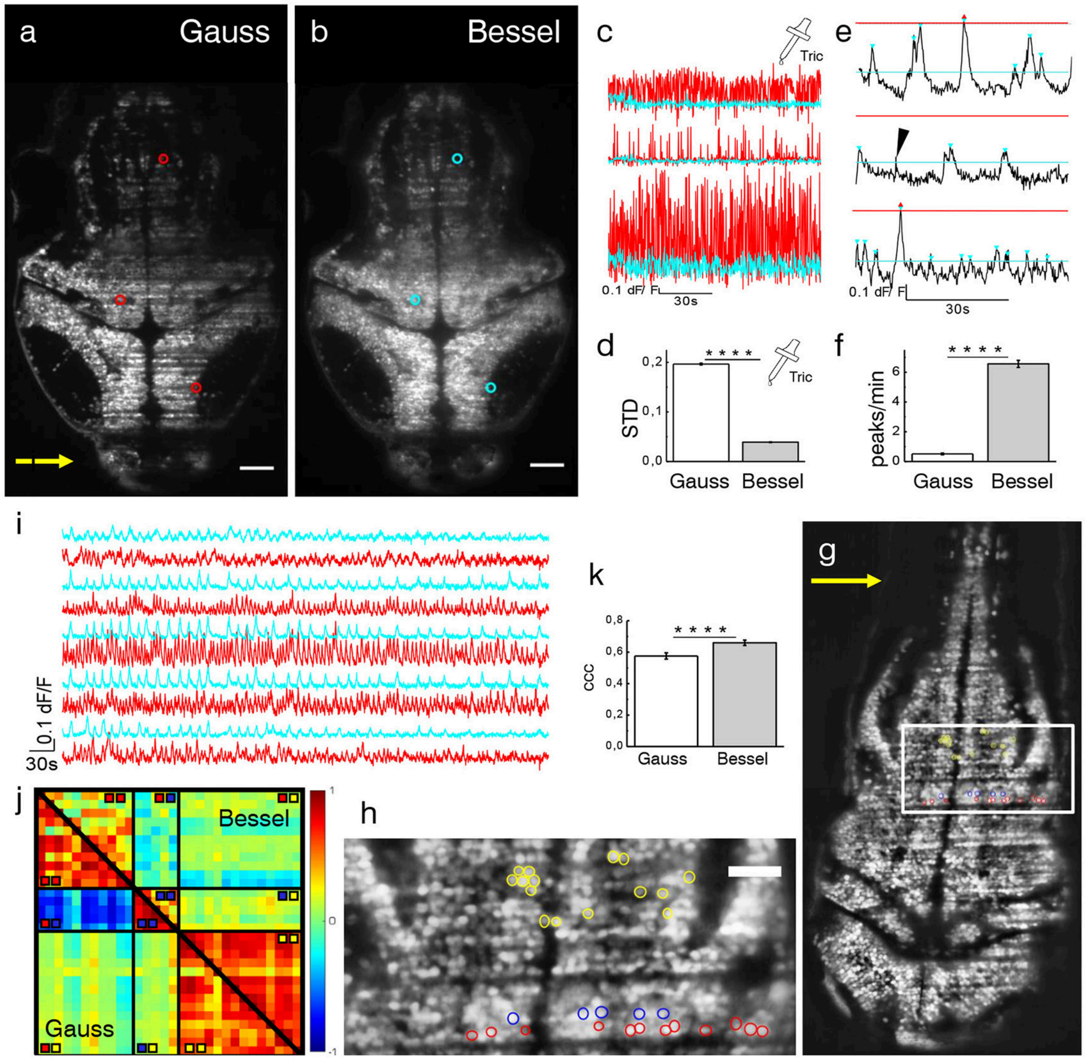

**FIGURE 4** | Ca$^{2+}$-imaging. Transverse plane of a 4 dpf elavl3:H2B-GCaMP6s larva imaged with Gaussian **(a)** and Bessel beam illumination **(b)**. Scale bar is $50\,\mu\text{m}$. Yellow arrow indicates direction of light sheet. Indicated are three exemplary cells with red (cyan) circles which have been illuminated with a Gaussian (Bessel) beam and whose traces can be seen in **(c)**. **(d)** Mean standard deviation (STD) of traces without neuronal activity ($p < 0.0001$, paired $t$-test, $n = 625$ cells in $N = 7$, error is sem). **(e)** Exemplary dF/F traces measured with Bessel beam illumination during neuronal activity. Indicated are peaks (triangles) above the noise level for Gaussian (red) and Bessel beam illumination (cyan). Peaks with prominence below threshold were discarded (black arrow head). **(f)** Peaks per minute detected above noise level using appropriate thresholding to exclude Gaussian and Bessel baseline noise ($p < 0.0001$, paired $t$-test, $n = 586$, in $N = 1$ larva, error is sem). **(g)** Transverse plane of a 4dpf larva imaged with Gaussian illumination. Indicated are cells located on two adjacent excitation lines (red, blue) and randomly in the hindbrain as part of an active network (yellow, see also zoomed view in **h**). **(i)** Exemplary traces of cells (marked yellow in **h**) measured with Gaussian (red) and Bessel beam illumination (cyan). **(j)** Correlation matrix of cells measured with Gaussian (lower triangular) and Bessel beam illumination (upper triangular matrix). The color scale ranges from −1 (blue) to +1 (red). **(k)** Averaged coefficient of cross correlations (ccc) of yellow yellow quadrant ($p < 0.0001$, paired $t$-test, $n = 91$, $N = 1$, error is sem).

introduced by each method and therefore a measure of accuracy. The standard deviation was 0.0682 for Gaussian and 0.0033 for Bessel beam illumination (**Figure 4g**, **Figure S5e**) which constitutes an 20-fold increase in accuracy compared to Gaussian illumination.

## Real Neuronal Correlation Is Masked by Spurious Correlation

The previous section evaluated the reduction of sensitivity from a statistical point of view by distinguishing peaks with respect to numerical thresholds and by including baseline noise of typical amplitude both obtained by averaging hundreds of cells affected by flickering. We showed that the contamination with both systematic and random errors is significantly higher when using Gaussian beam compared to Bessel beams. In the following section, we present measurements of spontaneous neuronal activity in individual cells in the presence of flickering in one exemplary larva.

As indicated in **Figures 4g,h**, several cells have been manually selected in the hindbrain of a 4dpf larva to generate a scenario in which spurious correlations due to flickering significantly alter the correlation amongst cells in a circuit. The red and blue cells where chosen in an area determined by the methodology described in **Figure 3e** and corresponded to lines in which nearby flowing blood cells cast alternating shadows whereas the yellow cells have been randomly chosen among a circuit of cells that showed strong spontaneous activity (see **Videos S5, S6**). It is apparent from the correlation matrix (**Figure 4j**) that, when using Gaussian illumination, a strong correlation between cells on one line (sector marked 🟥🟥 in the correlation matrix) can be observed which strongly anti-correlates with cells from the line immediately next to it (🟥🟦), an obvious hemodynamic artifact. Notably when using Bessel beam illumination this strong spurious correlation is not observed (average cross correlation $-0.571 \pm 0.025$ for Gauss vs. $-0.013 \pm 0.023$ for Bessel beam illumination, $n = 55$, error is sem, see table in **Figure S6**). Exemplary traces of spontaneous activity outside an area strongly affected by flickering (cells marked yellow) are shown in **Figure 4i**. It is worthwhile pointing out, that when looking at correlations entirely outside flickering areas (🟨🟨), average correlation obtained with Gaussian beams was $0.576 \pm 0.020$ and $0.660 \pm 0.017$ (an increase of 15 %, $n = 91$) for Bessel beams (**Figure 4k**). This result demonstrates that even when steering clear of problematic areas with evident strong flickering, correlations of neuronal activity can be significantly affected by residual flickering, less evident to the human eye, when using Gaussian illumination. Since Bessel beams have a fivefold increased sensitivity to calcium transients compared to Gaussian beams, they are more likely to detect calcium transients in multiple functionally connected cells and this leads to a higher average correlation as seen in **Figure 4j**. A more comprehensive analysis based on automatic segmentation rather than manual selection of cells is presented in **Figure S7**.

## Principle Component Analysis of Spontaneous Activity

In this last section we compare the first principal components of spontaneous activity in the hindbrain and the cerebellum for Gaussian (top) and Bessel beam illumination (bottom row of **Figure 5**) at two different depths (left and right hand side) in one exemplary larva. The cells in **Figures 5a,b,g,h** are color-coded according to the standard deviation of their mean correlation with every other cell. While the emerging pattern shows lateral symmetry over the rostral-caudal axis of the larva for Bessel beam illumination, the pattern using Gaussian illumination is quasi identical in color along the illumination direction of the light sheet and mostly following a symmetry along the dextro-sinister axis of the larva. The 10 % of cells mostly contributing to the first principal component of the hindbrain and cerebellum respectively are shown in **Figures 5c,d,i,j**. Whereas with Bessel beam illumination a symmetric distribution of cells is apparent, Gaussian illumination leads to an agglomeration of cells mainly located on the far side with respect to the illumination and clustered around strong shadows which indicate the presence of flickering artifacts (white arrows). Accordingly, the time traces of the first principal component of the hindbrain (navy) and the cerebellum (green, **Figures 5e,f,k,l**) are less noisy and show higher correlation with each other when obtained from measurements with Bessel beam compared to Gaussian illumination.

# 3. DISCUSSION

Large-scale neuronal recordings and their interpretation have been a paradigm shift toward understanding circuit function during behavior (Ahrens et al., 2012). With substantial improvements in imaging technology and a concurrent increase in the size and complexity of neuronal data, pressure now shifts toward data analysis as a fundamental bottleneck for neuroscience (Freeman et al., 2014). A common approach in large-scale imaging in zebrafish larvae is to apply an automatic segmentation algorithms which identifies ROIs associated with individual neurons (Panier et al., 2013; Kawashima et al., 2016) and extracts the dF/F traces from the contained pixel values.

Isolating fluorescent features of interest in a heterogeneous background places higher computational demands on the algorithms used, often with concurrent increase in computation time and complexity of the parameters to be tuned. A recent study showed that very simple algorithms like global thresholding or high pass filtering require uniform background intensity and fail to segment simple fluorescent forms like cell nuclei when a striated background simulating muscle fibers is added to the image (Chitalia et al., 2016). As the complexity of the fluorescent feature increases, so do the demands on the algorithms tasked to isolate them. Another recent study compared automated segmentation of a simple synthetic interrupted tube with progressively added salt and pepper noise by a range of published algorithm and their failure to accurately trace this simulated neurite at noise levels of five percent (Liu et al., 2016). In **Figure 2**, we show how a threshold of 5 % leads to more than a three quarters of the larva encephalon to be affected by a striated background, jeopardizing hours of microscope acquisition time, data post-processing and sample preparation if the data cannot be accurately segmented in an automated fashion.

Furthermore, the results presented in this paper demonstrate the contamination of data by artifacts created by hemodynamic flickering that threaten the automated extraction of calcium transients over the entire larva encephalon. Here, we have shown a reduction of the flickering area by a factor of ≈ 30 when using Bessel beam illumination (**Figure 3**). Whereas a previous publication (Panier et al., 2013) manually excluded severely affected neurons from further analysis, using Bessel beams would allow to include substantially more cells in a move from large-scale imaging toward true brain-wide analysis.

The deleterious effect of flickering artifacts caused by passing blood cells has been previously reported (Panier et al., 2013) but not quantified. Here, we present a statistical analysis to estimate the baseline noise associated hemodynamic modulation in most adversely affected neurons and report a STD of ≈ 20 % dF/F for Gaussian illumination compared to ≈ 4 % for Bessel beams. This represents a 5-fold increase in sensitivity to accurately reveal $Ca^{2+}$

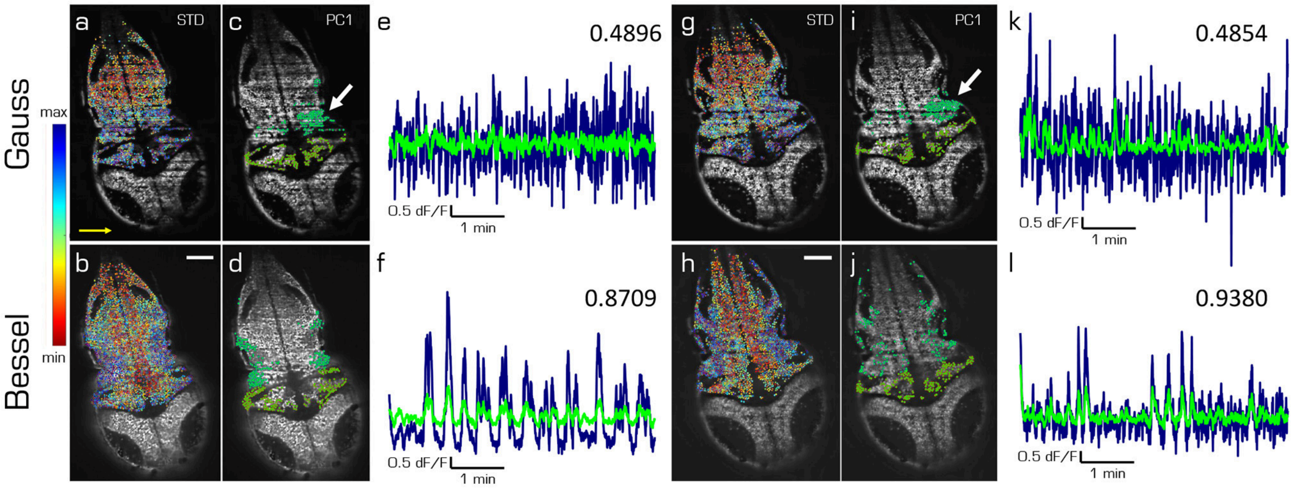

**FIGURE 5 |** Principal components of spontaneous activity in the hindbrain and the cerebellum. Transverse planes of a 5dpf elavl3:H2B-GCaMP6s larva imaged with Gaussian (top) and Bessel illumination (bottom row) at two different depth (left and right half). Scale bar is $50\,\mu\text{m}$. Yellow arrow indicates direction of light sheet. **(a,b,g,h)** Standard deviation of the mean correlation to every other cell color-coded from blue (maximum) to red (minimum). **(c,d,i,j)** Indicate the $10\,\%$ of cells most contributing to the first principal component in the hindbrain and cerebellum respectively. **(e,f,k,l)** Time traces of the first principal component of the hindbrain (navy) and the cerebellum (light green) and the correlation between both traces (top right).

transients when using Bessel beam illumination that otherwise would have been buried in noise.

Notably, this sensitivity gain cannot be achieved simply by using standard double-sided illumination (Ahrens et al., 2012). Indeed, in the hypothesis of Gaussian noise distribution, the process of summing up two independent variables (the two illuminations) increases the signal-to-noise ratio only by a factor $\sqrt{2}$, about 3.5 times less than what we found with Bessel beams. The use of two-photon excitation in the light-sheet microscope (Wolf et al., 2015; Piksarv et al., 2017) might mitigate the problem, but is prone to shadowing artifacts even more than Bessel beam illumination (Fahrbach et al., 2013b). Furthermore, upgrading a single-photon LSM to Bessel beam illumination is substantially less expensive than introducing two-photon excitation.

The STD values presented here represent a worst-case scenario; in the best case, at least in 2D studies, the plane of interest contains no or very little vessels and therefore no flickering and consequently the baseline noise in Gaussian and Bessel beam are identical. For true 3D brain-wide acquisitions however, it will be impossible to fully avoid hemodynamic contamination.

To illustrate the effect of increased baseline noise, we have presented a statistical analysis applying peak counting and cross correlation to identical traces. By counting peaks due to spontaneous neuronal activity above the Gaussian baseline noise and the Bessel baseline noise we estimated that less than 1 out of 12 peaks would be detected. This is a conservative estimate since usually higher thresholds of signal to noise ratio (SNR), e.g., Rose criterion: SNR=5 (Rose, 1973), are common. Furthermore, using synthetic white noise, we have demonstrated that the randomizing effect of hemodynamic noise leads to a loss of correlation which cannot be hoped to be recovered by clever engineering of ever brighter calcium indicators due to its multiplicative nature.

Blood flow in the brain is regulated to match neuronal demand based on activity by restricting and dilating the diameter of vessels, a phenomenon known as neurovascular coupling (Attwell et al., 2010). Assuming HagenPoiseuille law of fluidic dynamics, this results in varying volumetric flow rates and therefore speeds of red blood cells. This plus other randomizing effects like vessel orientation and location means that neurons more than just a few cell diameters away from each other experience entirely uncorrelated noise. More strikingly however, the opposite is true as well: neurons which lie in close proximity on a line parallel to the excitation light will experience a baseline noise that is very strongly correlated and capable of generating spurious correlations that are not due to activity. Playing the devil's advocate, we "created" a correlation matrix in which the positive correlation between cells on one line and their anti-correlation with cells on a neighboring line were so strong as to mask actual correlation due to activity in an area not severely affected by flickering. This result is important because it shows that not only do Bessel beams reduce the area affected by strong flickering in which they also generate a significantly lower baseline noise. Additionally, even in areas that are not strongly affected by flickering due to immediately close by vessels, Bessel beams reveal neuronal activity that is lost when using Gaussian illumination.

We point out that while PCA is not suited to isolate hemodynamic flickering due to the dependent nature of the components, independent component analysis (ICA) has been used previously to identify various artifact sources (Vigário et al., 1998) and might be useful not only to contain flickering artifacts but also to extract information on local blood flow.

A prerequisite to understanding how the brain interacts with the outside world is to understand its intrinsic spatio-temporal dynamics in complete absence of external stimuli. Activity patterns are spontaneously produced in the brain and have been demonstrated to influence brain function (Romano et al., 2015), which is why neuronal interactions underlying spontaneous activity and its biological relevance have been gaining interest in recent years (Ringach, 2009; Deco et al., 2011, 2013; Destexhe, 2011).

This complete absence of external stimuli has a far-reaching consequence for the imaging setups designed to reveal the underlying mechanism of spontaneous activity. It is fundamentally impossible to average responses over triggering trials to clean up the signal. Single one-shot measurements of functional traces therefore need to be intrinsically clean enough to allow extraction of meaningful data without averaging. In **Figure 5** we have demonstrated how hemodynamic noise leads to a reduction to 56 % of correlation between the first principal component of the hindbrain and the cerebellum when using Gaussian compared to Bessel beam illumination.

Although we do not claim biological reproducibility as only one fish has been investigated, these results serve as a proof of principle that applying Bessel beams to quantitative light-sheet microscopy is indeed an enabling technique capable to reveal correlations in functional traces that might otherwise remain buried in noise.

In conclusion, we have illustrated how flickering can adversely affect and even falsify data extracted from LSM images. We compared the performance of Gaussian and Bessel beam illumination in functional studies employing $Ca^{2+}$ imaging in larval zebrafish. We have identified sources of contamination in the form of true correlation lost in a multiplicative baseline noise and spurious correlation overpowering correlation due to actual neuronal activity when using standard illumination. We have shown how the use of Bessel beams can provide an optical solution to correct for these artifacts on the microscope system side and allow for high-fidelity imaging in light-sheet microscopes. The results given here present a new quality standard for quantitative single-neuron sensitivity measurements in LSM opening up novel experiments on spontaneous activity.

# 4. MATERIALS AND METHODS

## Zebrafish Husbandry and Larva Mounting

We generated two stable zebrafish transgenic lines using a Tol2 construct with elavl3 promoter that drives the expression of the genetically encoded calcium indicator GCaMP6s in all neurons (Freeman et al., 2014). Tg(elavl3:GCaMP6s) line showed a cytoplasmic expression of the transgene whereas line Tg(elavl3:H2B-GCaMP6s) expressed GCaMP6s in fusion with histone H2B and consequently showed nuclear localization. Larvae were kept according to standard procedures (Westerfield, 1995). Each 4-5dpf Tg(elavl3:H2B-GCaMP6s) larva, of unknown sex, used in the experiments was transferred into a reaction tube containing 1.5 % low gelling temperature agarose (A9414, Sigma) in fish water (150 mg Instant Ocean, 6.9 mg $NaH_2PO_4$, 12.5 mg $Na_2HPO_4$ per 1 l of $dH_2O$), kept at 38 °C. The zebrafish larva was then drawn with a syringe into a glass capillary (O.D. 1.5 mm); after gel polymerization, the agarose cylinder containing the larva was gently extruded until the head protruded from the glass (**Figure S1b**). The glass capillary was then mounted onto an x−, y−, z−, Θ-stage (M-122.2DD and M-116.DG, Physik Instrumente, Germany) and immediately immersed into the sample chamber containing fish water. The fish water was kept at a constant temperature of 28.5 °C.

## Calcium Imaging

For *in-vivo* $Ca^{2+}$ imaging a line exposure time of 0.3 ms was used, resulting in a frame rate of 44 Hz. When using Bessel beam illumination, power was increased by a factor of three compared to Gaussian illumination. Typical laser power at the back focal plane of the excitation objective was 0.7 mW for Gaussian illumination and 2 mW for Bessel illumination. These power levels have been already reported in the literature to be safe in term of photo-toxicity (Panier et al., 2013). The 16bit depths images constituting each time lapse were first converted from the proprietary Hamamatsu file format to a multi-page tiff and simultaneously temporally down sampled by a factor of 8 to save disc space resulting in an effective frame rate of 5.5 Hz. When tricaine was added to the fish water and the traces therefore were used to analyze flickering, no temporal downsampling was performed. Z profiles of regions of interests were then extracted with a FIJI macro over a hand selected circular area covering the cell nucleus or else using a Matlab script for automated segmentation (Kawashima et al., 2016). The dF/F traces were obtained with a custom-written Matlab script in which, firstly, the background, measured over a ROI outside the larva on the proximal side to the laser, was subtracted and secondly, the baseline of the traces were calculated using the *msbackadj* function. Thirdly, the baseline was subtracted from the trace and finally, the trace was divided by the baseline to normalize it (Freeman et al., 2014).

## Estimation of the Area Affected by Flickering

The area affected by primary flickering for Gaussian and Bessel beam illumination was estimated in a plane by using a sequence of custom-made macros (FIJI) and programs (LabVIEW). By primary flickering is intended strong variations in baseline fluorescence intensity directly attributable to a large, nearby blood vessel. The more subtle, yet noticeable, effect of smaller peripheral blood vessels was neglected as it was much harder to quantify. Using this automated method 2D maps of severe flickering areas were obtained which allowed us to calculate the percentage of the entire encephalon that were prone to a substantial source of additive noise. To assure that the evidenced changes in pixel brightness were not due to activity, Tricaine ($160\,\mathrm{mg\,l^{-1}}$), a general anesthetic that blocks voltage sensitive $Na^+$ channels preferentially in neurons, was added to the fish water.

The methodology (**Figure S3**), based predominantly on a temporally down-sampled time lapse in which each frame corresponded to the standard deviation (STD) of a certain frame window of the original raw data, evidenced the characteristic shape of long horizontal stripes. A custom-written FIJI macro was used to calculate the STD time lapse of the raw data time lapse with window size 5 and step size 5. After adjusting both time lapses to the same brightness scale, an additional macro automatically compared the STD time lapses of the Gaussian and Bessel beam by running through a sequence of functions to enhance the features of the images that changed most in brightness value using the exact same parameters in both cases. With both time lapses displayed on the same brightness scale, first a gamma of 1.1, second a bandpass filter and third a variance filter were applied over the entire image. After again adjusting both time lapses to the same brightness scale, each time lapse was collapsed to a single image using using a z projection of the STD. The resulting images were thresholded to a common value and converted to 8 bit binary where dark spots indicating the parts of the encephalon that had changed the most during high frame rate (44 Hz) acquisition. The binary images where then analyzed in a custom-written LabVIEW program that automatically found the bounding boxes of each identified particle (**Figure S4**). In the case of Gaussian illumination, the horizontal dimension of the bounding box of each particle was extended up to a mask corresponding to the free-hand selection of the encephalon of the larva. In the case of the Bessel beam illumination, the bounding box was extended to a length corresponding to the theoretically calculated reconstruction length of the Bessel beam which follows from simple trigonometric considerations:

$$x = \frac{\tan \beta}{0.5 * h} \tag{1}$$

where $\beta$ is the angle of the cone in the sample chamber, and $h$ is the height of the bounding box. The LabVIEW program then automatically calculated the sum of all bounding boxes and their percentile of the free-hand selection of the entire encephalon. The characteristic horizontal stripes of the resulting areas, confirmed that the method indicated primarily shadowing artifacts and not individual neuronal activity.

## Peak Counting and Correlation Analysis

For peak counting, the dF/F traces were loaded into a custom-written Matlab program and smoothed using the *sgolayfilt* function (order 5, framelen 7). The *findpeaks* function was then used to automatically detect peaks above the Gaussian and Bessel noise level respectively with a minimum peak prominence of 8.5 % of dF/F. The correlation matrices were calculated using a custom-written Matlab program using the *corr2* function. Noise (see **Figure S5**) was generated according to the following pseudo Matlab code to produce random noise that oscillates around an average of unity:

```
noise = STD .* randn + 1;
```

The noise vector was than point-wise multiplied to the trace vector which was averaged to zero using:

```
y = (trace - μ) .* noise;
```

## Principle Component Analysis

For principle component analysis, all time lapses were temporally downsampled by a factor of 10 to a final frame rate of 4.4 Hz, binned (2 × 2, average) and converted to 8bit. The resulting time lapses were registered to a reference frame using the TurboReg plugin in FIJI. After automated segmentation using the script in Kawashima et al. (2016) and extraction of the dF/F traces for all segmented cells, the principal components were calculated using the *pca* function in Matlab.

## Experimental Design and Statistical Analysis

To assess the area affected by flickering, which we assumed would have some variability between larvae, a sample size of N=10 larva was chosen. To assess the baseline contamination with random noise, again assuming some variability between larva, but mostly expecting variability between different cells, a sample size of N=7 larva was used. To obtain "native" traces of spontaneous activity in which we counted peaks above certain thresholds and to which we added synthetic noise, we concentrated our study on the variability between cells taking advantage of the single cell resolution afforded by the microscope, which is why a sample size of N=1 larva was used. The cross correlation of traces of spontaneous activity in areas affected by strong flickering represents a specifically constructed case study, which is why a sample size of N=1 larva was used. The comparison between the principle components of spontaneous activity were exemplified in N=1 larva specifically to demonstrate the strength of Bessel beam illumination for one-shot experiments. Each experiment was performed first in Gaussian modality and then immediately again in Bessel beam modality. An experiment constitutes the acquisition of a time-lapse. Experiments were repeated on several transversal planes in the larva encephalon. The biological replication of experiments occurs each time we changed the larva. The technical replication occurs when experiments were repeated in the same larva but in a different transversal plane. There were no outliers. There was no inclusion/exclusion of data. Each graph clearly states the statistical analysis method used (mostly paired t-test to directly compare Gaussian and Bessel illumination), the sample size N (animals) or n (cells/planes), the mean, the standard error of the mean and the $p$-value in the figure legend as well as in the main result text.

## ETHICS STATEMENT

All experiments were carried in accordance to Italian law on animal experimentation (D.L. 4 March 2014, n.26), under authorization n. 407/2015-PR from the Italian Ministry of Health.

## AUTHOR CONTRIBUTIONS

MM, LSi, and LSa conceived the experiments. LT, FV, and NT generated the transgenic zebrafish lines. LT prepared the samples. MM, TA, and AG built the microscope. MM and LT conducted the experiments. MM analyzed the results. MM wrote the manuscript with input from all co-authors. FP acquired all funding and supervised the project.

## FUNDING

This project received funding from the European Union's H2020 research and innovation programme under grant agreements No. 720270 (Human Brain Project) and 654148 (Laserlab-Europe), and from the EU programme H2020 EXCELLENT SCIENCE-European Research Council (ERC) under grant agreement ID n.692943 (BrainBIT). The project has also been supported by the Italian Ministry for Education, University, and Research in the framework of the Flagship Project NanoMAX and of Eurobioimaging Italian Nodes (ESFRI research infrastructure), and by Ente Cassa di Risparmio di Firenze (private foundation).

## ACKNOWLEDGMENTS

The authors would like to thank Riccardo Ballerini and Ahmed Hajeb from the mechanical workshop at LENS for the production of custom pieces and advise on structural stability in sample mounting. The authors are grateful to Mauro Giuntini and Marco De Pas from the electronic workshop for the construction of the sample heating and electronics in the light-sheet microscopes. We further thank Misha Ahrens for providing the tol2-elavl3-H2B GCaMP6s and the tol2-elavl3 GCaMP6s plasmids (Addgene plasmid #59530 and #59531).

## SUPPLEMENTARY MATERIAL

The Supplementary Material for this article can be found online at: https://www.frontiersin.org/articles/10.3389/fncel.2018.00315/full#supplementary-material

## REFERENCES

Ahrens, M. B., Li, J. M., Orger, M. B., Robson, D. N., Schier, A. F., Engert, F., et al. (2012). Brain-wide neuronal dynamics during motor adaptation in zebrafish. *Nature* 485, 471–477. doi: 10.1038/nature11057

Attili, S., and Hughes, S. M. (2014). Anaesthetic tricaine acts preferentially on neural voltage-gated sodium channels and fails to block directly evoked muscle contraction. *PLoS ONE* 9:e103751. doi: 10.1371/journal.pone.0103751

Attwell, D., Buchan, A. M., Charpak, S., Lauritzen, M., MacVicar, B. A., and Newman, E. A. (2010). Glial and neuronal control of brain blood flow. *Nature* 468, 232–243. doi: 10.1038/nature09613

Chen, B. C., Legant, W. R., Wang, K., Shao, L., Milkie, D. E., Davidson, M. W., et al. (2014). Lattice light-sheet microscopy: imaging molecules to embryos at high spatiotemporal resolution. *Science* 346:1257998. doi: 10.1126/science.1257998

Chen, Y., Glaser, A., and Liu, J. T. (2016). Bessel-beam illumination in dual-axis confocal microscopy mitigates resolution degradation caused by refractive heterogeneities. *J. Biophoton* 10, 68–74. doi: 10.1002/jbio.201600196

Chitalia, R., Mueller, J., Fu, H. L., Whitley, M. J., Kirsch, D. G., Brown, J. Q., et al. (2016). Algorithms for differentiating between images of heterogeneous tissue across fluorescence microscopes. *Biomed. Opt. Expr.* 7, 3412–3424. doi: 10.1364/BOE.7.003412

Deco, G., Jirsa, V. K., and McIntosh, A. R. (2011). Emerging concepts for the dynamical organization of resting-state activity in the brain. *Nat. Rev. Neurosci.* 12:43. doi: 10.1038/nrn2961

Deco, G., Jirsa, V. K., and McIntosh, A. R. (2013). Resting brains never rest: computational insights into potential cognitive architectures. *Trends Neurosci.* 36, 268–274. doi: 10.1016/j.tins.2013.03.001

Destexhe, A. (2011). Intracellular and computational evidence for a dominant role of internal network activity in cortical computations. *Curr. Opin. Neurobiol.* 21, 717–725. doi: 10.1016/j.conb.2011.06.002

Durnin, J., Miceli J. Jr., and Eberly, J. H., (1987). Diffraction-free beams. *Phys. Rev. Lett.* 58:1499. doi: 10.1103/PhysRevLett.58.1499

Fahrbach, F. O., Gurchenkov, V., Alessandri, K., Nassoy, P., and Rohrbach, A. (2013a). Light-sheet microscopy in thick media using scanned bessel beams and two-photon fluorescence excitation. *Opt. Express* 21, 13824–13839. doi: 10.1364/OE.21.013824

Fahrbach, F. O., Gurchenkov, V., Alessandri, K., Nassoy, P., and Rohrbach, A. (2013b). Self-reconstructing sectioned bessel beams offer submicron optical sectioning for large fields of view in light-sheet microscopy. *Opt. Express* 21, 11425–11440. doi: 10.1364/OE.21.011425

Fahrbach, F. O., Simon, P., and Rohrbach, A. (2010). Microscopy with self-reconstructing beams. *Nat. Photon.* 4, 780–785. doi: 10.1038/nphoton.2010.204

Freeman, J., Vladimirov, N., Kawashima, T., Mu, Y., Sofroniew, N. J., Bennett, D. V., et al. (2014). Mapping brain activity at scale with cluster computing. *Nat. Methods* 11, 941–950. doi: 10.1038/nmeth.3041

Gao, L., Shao, L., Chen, B.-C., and Betzig, E. (2014). 3d live fluorescence imaging of cellular dynamics using bessel beam plane illumination microscopy. *Nat. Protoc.* 9, 1083–1101. doi: 10.1038/nprot.2014.087

Huisken, J., Swoger, J., Del Bene, F., Wittbrodt, J., and Stelzer, E. H. (2004). Optical sectioning deep inside live embryos by selective plane illumination microscopy. *Science* 305, 1007–1009. doi: 10.1126/science.1100035

Kawashima, T., Zwart, M. F., Yang, C.-T., Mensh, B. D., and Ahrens, M. B. (2016). The serotonergic system tracks the outcomes of actions to mediate short-term motor learning. *Cell* 167, 933–946. doi: 10.1016/j.cell.2016.09.055

Liu, S., Zhang, D., Liu, S., Feng, D., Peng, H., and Cai, W. (2016). Rivulet: 3d neuron morphology tracing with iterative back-tracking. *Neuroinformatics* 14, 387–401. doi: 10.1007/s12021-016-9302-0

Lorenser, D., Christian Singe, C., Curatolo, A., and Sampson, D. D. (2014). Energy-efficient low-fresnel-number bessel beams and their application in optical coherence tomography. *Opt. Lett.* 39, 548–551. doi: 10.1364/OL.39.000548

Lu, R., Sun, W., Liang, Y., Kerlin, A., Bierfeld, J., Seelig, J. D., et al. (2017). Video-rate volumetric functional imaging of the brain at synaptic resolution. *Nature Neurosci.* 20:620. doi: 10.1038/nn.4516

Ma, Y., Shaik, M. A., Kim, S. H., Kozberg, M. G., Thibodeaux, D. N., Zhao, H. T., et al. (2016). Wide-field optical mapping of neural activity and brain haemodynamics: considerations and novel approaches. *Phil. Trans. R. Soc. B* 371:20150360. doi: 10.1098/rstb.2015.0360

McGloin, D., and Dholakia, K. (2005). Bessel beams: diffraction in a new light. *Contem. Phys.* 46, 15–28. doi: 10.1080/0010751042000275259

Müllenbroich, M. C., Silvestri, L., Di Giovanna, A. P., Mazzamuto, G., Costantini, I., Sacconi, L., et al. (2018). High-fidelity imaging in brain-wide structural studies using light-sheet microscopy. *eNeuro*. doi: 10.1117/12.2251471. [Epub ahead of print].

Panier, T., Romano, S. A., Olive, R., Pietri, T., Sumbre, G., Candelier, R., et al. (2013). Fast functional imaging of multiple brain regions in intact zebrafish larvae using selective plane illumination microscopy. *Front. Neural Circ.* 7:65. doi: 10.3389/fncir.2013.00065

Piksarv, P., Marti, D., Le, T., Unterhuber, A., Forbes, L. H., Andrews, M. R., et al. (2017). Integrated single-and two-photon light sheet microscopy using accelerating beams. *Sci. Reports* 7:1435. doi: 10.1038/s41598-017-01543-4

Planchon, T. A., Gao, L., Milkie, D. E., Davidson, M. W., Galbraith, J. A., Galbraith, C. G., et al. (2011). Rapid three-dimensional isotropic imaging of living cells using bessel beam plane illumination. *Nat. Methods* 8, 417–423. doi: 10.1038/nmeth.1586

Ringach, D. L. (2009). Spontaneous and driven cortical activity: implications for computation. *Curr. Opin. Neurobiol.* 19, 439–444. doi: 10.1016/j.conb.2009.07.005

Romano, S. A., Pietri, T., Pérez-Schuster, V., Jouary, A., Haudrechy, M., and Sumbre, G. (2015). Spontaneous neuronal network dynamics reveal circuit's functional adaptations for behavior. *Neuron* 85, 1070–1085. doi: 10.1016/j.neuron.2015.01.027

Rose, A. (1973). *Vision: Human and Electronic.* New York, NY: Plenum Press.

Siedentopf, H., and Zsigmondy, R. (1902). Uber sichtbarmachung und größenbestimmung ultramikoskopischer teilchen, mit besonderer anwendung auf goldrubingläser. *Annalen Physik* 315, 1–39. doi: 10.1002/andp.19023150102

Turrini, L., Fornetto, C., Marchetto, G., Müllenbroich, M. C., Tiso, N., Vettori, A., et al. (2017). Optical mapping of neuronal activity during seizures in zebrafish. *Sci. Reports* 7:3025. doi: 10.1038/s41598-017-03087-z

Vigario, R., Jousmaki, V., Hamalainen, M., Hari, R., and Oja, E. (1998). "Independent component analysis for identification of artifacts in magnetoencephalographic recordings," in *Advances in Neural Information Processing Systems,* eds M. I. Jordan, M. J. Kearns, and S. A. Solla (Cambridge, MA: MIT Press).

Vladimirov, N., Mu, Y., Kawashima, T., Bennett, D. V., Yang, C.-T., Looger, L. L., et al. (2014). Light-sheet functional imaging in fictively behaving zebrafish. *Nat. Methods* 11, 883–884. doi: 10.1038/nmeth.3040

Westerfield, M. (1995). *Westerfield The Zebrafish Book. Guide for the Laboratory Use of Zebrafish (Danio rerio),* 3rd Edn. Eugene, OR: University of Oregon Press.

Wolf, S., Supatto, W., Debrégeas, G., Mahou, P., Kruglik, S. G., Sintes, J.-M., et al. (2015). Whole-brain functional imaging with two-photon light-sheet microscopy. *Nature Methods* 12:379. doi: 10.1038/nmeth.3371

Zhang, P., Phipps, M. E., Goodwin, P. M., and Werner, J. H. (2014). Confocal line scanning of a bessel beam for fast 3d imaging. *Opt. Lett.* 39, 3682–3685. doi: 10.1364/OL.39.003682

Zhao, T., Lau, S. C., Wang, Y., Su, Y., Wang, H., Cheng, A., et al. (2016). Multicolor 4d fluorescence microscopy using ultrathin bessel light sheets. *Sci. Reports* 6:26159. doi: 10.1038/srep26159

**Conflict of Interest Statement:** The authors declare that the research was conducted in the absence of any commercial or financial relationships that could be construed as a potential conflict of interest.

frontiers
in Cellular Neuroscience

MINI REVIEW
published: 21 September 2018
doi: 10.3389/fncel.2018.00316

# Innovative Optogenetic Strategies for Vision Restoration

*Cameron K. Baker*[1] *and John G. Flannery*[2]*

[1] *Department of Molecular and Cell Biology, University of California, Berkeley, Berkeley, CA, United States,* [2] *School of Optometry, University of California, Berkeley, Berkeley, CA, United States*

The advent of optogenetics has ushered in a new era in neuroscience where spatiotemporal control of neurons is possible through light application. These tools used to study neural circuits can also be used therapeutically to restore vision. In order to recapitulate the broad spectral and light sensitivities along with high temporal sensitivity found in human vision, researchers have identified and developed new optogenetic tools. There are two major kinds of optogenetic effectors employed in vision restoration: ion channels and G-protein coupled receptors (GPCRs). Ion channel based optogenetic therapies require high intensity light that can be unsafe at lower wavelengths, so work has been done to expand and red-shift the excitation spectra of these channels. Light activatable GPCRs are much more sensitive to light than their ion channel counterparts but are slower kinetically in terms of both activation and inactivation. This review article examines the latest optogenetic ion channel and GPCR candidates for vision restoration based on light and temporal sensitivity.

**Keywords: optogenetics, vision restoration, retina, opsin, GPCR, retinal degeneration**

OPEN ACCESS

***Edited by:***
*Srdjan D. Antic,*
*University of Connecticut Health Center, United States*

***Reviewed by:***
*Fabio Benfenati,*
*Fondazione Istituto Italiano di Technologia, Italy*
*Kai Zhang,*
*University of Illinois at Urbana-Champaign, United States*

***Correspondence:***
*John G. Flannery*
*flannery@berkeley.edu*

***Received:*** *29 June 2018*
***Accepted:*** *30 August 2018*
***Published:*** *21 September 2018*

***Citation:***
*Baker CK and Flannery JG (2018) Innovative Optogenetic Strategies for Vision Restoration. Front. Cell. Neurosci. 12:316. doi: 10.3389/fncel.2018.00316*

## INTRODUCTION

Shortly after the popularization of optogenetic tools in neuroscience began in the early 2000s (Nagel et al., 2003, 2005; Boyden et al., 2005), researchers began evaluating their use in a novel *in vivo* application: vision restoration. In America, over 1,000,000 people are currently considered blind, with that number expected to double by 2030 (National Eye Institute, 2010). Most patients suffering from retinal degenerative diseases, like retinitis pigmentosa and macular degeneration, often first lose their light sensitive photoreceptors, the rods and cones, leaving the remaining retinal tissue light insensitive (**Figure 1**). However, the surviving cells can retain functionality and connections to the brain long after photosensitivity disappears. For decades researchers have attempted to activate this remaining tissue with prosthetic electrical stimulation (Margalit et al., 2002). With the advent of optogenetics, photosensitivity and vision can be restored at cellular resolution.

The first successful attempt at bestowing light sensitivity to non-photoreceptor retinal cells with optogenetic tools was in 2006 (Bi et al., 2006). In this pioneering work they heterologously expressed a microbial opsin, channelrhodopsin-2 (ChR2) from *Chlamydomonas reinhardtii* (**Figure 2A**), in thalamic projecting retinal ganglion cells (RGCs; **Figure 1B**) via adeno associated virus (AAV) serotype 2. This groundbreaking article showed that endowing surviving retinal cells with light sensitive proteins can restore light responses both retinally and cortically. Furthermore, it was one of the first articles to use AAV as a retina delivery vector and to demonstrate long term expression and safety. For over a decade researchers have been improving upon this basic method of virally expressing optogenetic proteins in surviving retinal cells, using new effectors to improve light and temporal sensitivity.

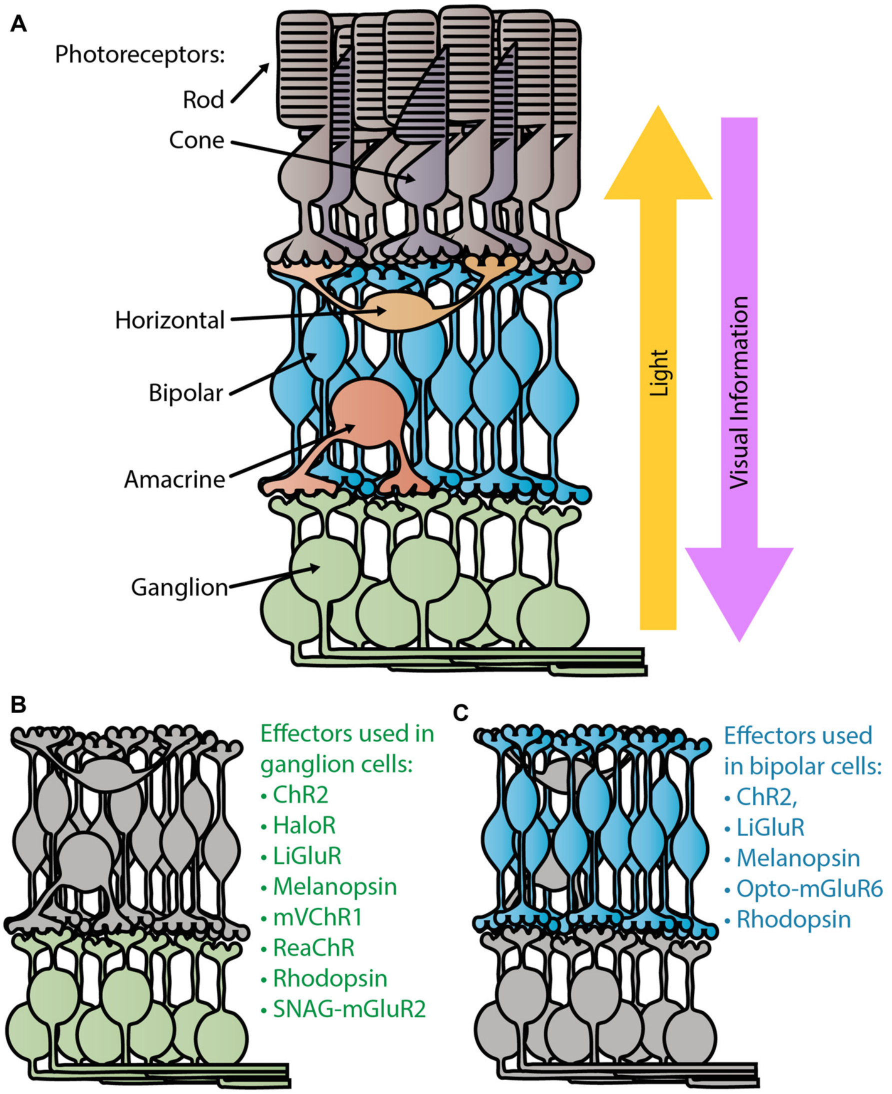

**FIGURE 1 |** Retina schematic. **(A)** Diagram of a normal healthy retina. Light passes through the retina, entering through the retinal ganglion cell (RGC) layer to reach the light sensitive photoreceptors, the rods and cones, in the outer retina. Visual information is sent from the photoreceptors to the bipolar cells where the ON/OFF processing begins. Ganglion cells are the terminal retinal signal recipients and they relay onto neurons in the lateral geniculate nucleus in the thalamus. Panels **(B,C)** depict the degenerate retina without photoreceptors. Panel **(B)** lists the optogenetic therapies that have been tested in ganglion cells (Bi et al., 2006; Lin et al., 2008; Zhang et al., 2009; Caporale et al., 2011; Tomita et al., 2014; Sengupta et al., 2016; Berry et al., 2017), while **(C)** lists those tested in bipolar cells (Lagali et al., 2008; Gaub et al., 2014, 2015; Macé et al., 2015; Scalabrino et al., 2015; van Wyk et al., 2015).

The ambitious aim to cure blindness optogenetically has driven light sensitive protein development, benefiting neuroscience as a whole with new effectors. Human vision has broad spectral (400–700 nm) and light sensitivity ($10^4$ to $10^{16}$ photons $cm^{-2}$ $s^{-1}$) with high temporal resolution (up to 60 Hz for long cone opsins; Kalloniatis and Luu, 1995). In order to restore sight, researchers have had to step beyond ChR2 to find and engineer new optogenetics that can better recapitulate human vision. In this review article, we will compare the latest optogenetic ion-channel and G-protein coupled receptor (GPCR) based technologies in their effectiveness at restoring sight to blind retinas based on the amount of light required for activation and temporal sensitivity.

## ION CHANNELS

The main advantage of optogenetic ion channel based therapies is temporal sensitivity. Photoactivation allows ions to flow through the channel activating or inhibiting the neural host. Upon light stimulus removal, inactivation is quick. With an opening and closing rate on the order of milliseconds, optogenetic ion channels have the potential for successive high frequency stimulation required for normal human vision

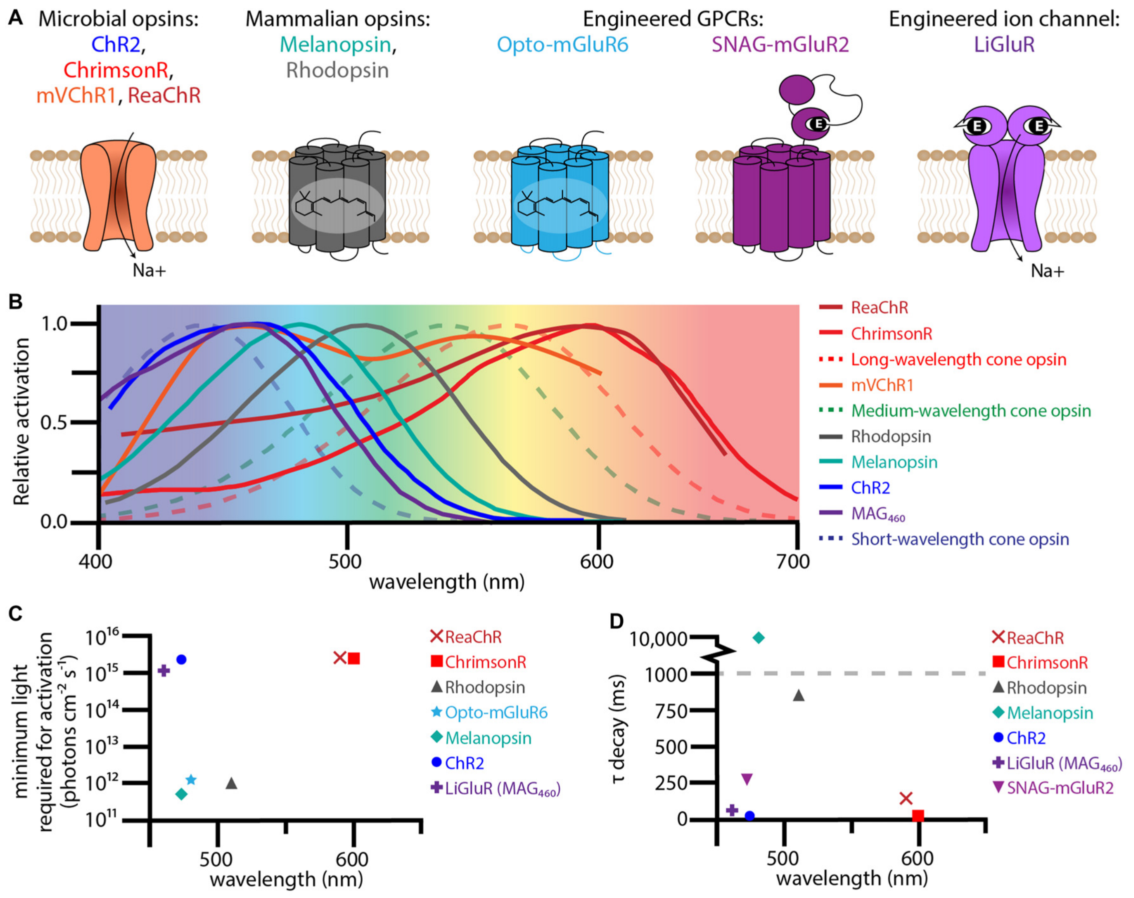

**FIGURE 2 |** Therapeutic optogenetic effectors used to restore the visual response in degenerate retinas. **(A)** Structural diagrams of optogenetic microbial opsins, mammalian opsins, and engineered GPCRs and ion-channels. The microbial opsins are all sodium permeable ion channels. The mammalian opsins, melanopsin and rhodopsin, are GPCRs with six transmembrane domains containing the chromophore 11-cis retinal. The engineered GPCR Opto-metabotropic glutamate receptor 6 (mGluR6) is comprised of the transmembrane domains from melanopsin with the intracellular loops from mGluR6. SNAG-mGluR2 is mGluR2 with a N-terminal SNAP-tag that tethers the PORTL BGAG. Upon light stimulation, the azobenzene in BGAG isomerizes allowing the distal glutamate to bind to the active site of mGluR2. The engineered ion channel LiGluR is iGluR6 with a cysteine mutation that allows for the covalent binding of the photoswitch maleimide-azobenzene-glutamate (MAG). Light isomerizes the azobenzene in MAG forcing the glutamate into the binding pocket. **(B)** Excitation spectra for optogenetic effectors used for vision rescue (solid lines) and human cone opsins (dotted lines). **(C)** The minimum light required for activation for various optogenetic effectors when used for vision rescue plotted against wavelength. **(D)** The τ decay constant plotted against wavelength for various optogenetic effectors. The excitation spectra, minimum light requirements, and τ decay constants were collected from the following publications: Lin et al. (2008, 2009); Gaub et al. (2014, 2015); Tomita et al. (2014); van Wyk et al. (2015); Pruneau et al. (2016); Sengupta et al. (2016); Berry et al. (2017).

(**Figure 2D**). However, light sensitivity is sacrificed for temporal sensitivity, with most channels requiring at least $10^{15}$ photons $cm^{-2}$ $s^{-1}$ to activate their neural hosts (**Figure 2C**; Bi et al., 2006; Sengupta et al., 2016). This amount of light is dangerous at shorter wavelengths, like the 470 nm that maximally activates ChR2 (International Commission on Non-Ionizing Radiation Protection, 2013). Of growing interest is "red-shifting" these ion channels to safer long wavelengths.

One such ion channel that was successfully red-shifted is the modified mammalian ion channel LiGluR (**Figure 2A**; Volgraf et al., 2006). Based on the human ionotropic glutamate receptor 6, LiGluR has a mutated cysteine residue that allows Maleimide-Azobenzene-Glutamate (MAG), a photoswitchable tethered ligand (PTL), to covalently bind to the outside of the ion channel. Certain wavelengths of light isomerize the azobenzene from trans to cis, forcing the distal glutamate into the protein's binding pocket opening the ion channel. The first generation of MAG, MAG0, was bistable and used 380 nm light to open and 500 nm to close. While this ultraviolet bistable channel was able to restore the visual response (Caporale et al., 2011), including the pupillary response, the amount and wavelengths of light required are dangerous to humans. To circumvent these problems, a second generation MAG, MAG460, was developed (Kienzler et al., 2013). No longer bistable and activated at 460 nm (**Figure 2B**), MAG460 was also able to restore the visual response in both mice and dogs (Gaub et al., 2014). While the LiGluR-MAG460 system requires a similar amount and spectrum of light as ChR2 (**Figures 2C,D**), its modular design is advantageous. Since LiGluR requires the PTL to be delivered in trans, patients would have the option of which one to have delivered and when, which would be especially beneficial if other PTLs with different activation spectrums are developed in the future.

Currently, in order to achieve activation using wavelengths above 550 nm, different opsins are required. In 2008 the Deisseroth group discovered the red-shifted ChR2 ortholog VChR1 from *Volvox carteri* (Zhang et al., 2008). This cation channel's excitation spectrum is red shifted approximately 70 nm when compared to ChR2, with a peak excitation at 535 nm and a capacity to produce spiking at 589 nm. While this red-shifted spectrum was promising, this channel does not express well due to inefficient plasma membrane integration.

Various groups have tackled this expression problem by generating chimeras with other microbial ion channels. Of these chimeric microbial channels, ReaChR (Lin et al., 2013) and mVChR1(Tomita et al., 2014) have demonstrated vision restoration efficacy in rodents, and in the case of ReaChR, primates (**Figures 1B**, **2A**; Sengupta et al., 2016). ReaChR, which used the N-terminus of ChiEF to facilitate membrane trafficking, the transmembrane domain from VChR2 to increase expression, and a L171I point mutation to reduce desensitization above 600 nm, has a red-shifted activation spectrum with a peak excitation ∼600 nm and is capable of generating photocurrent at 630 nm (**Figure 2B**; Lin et al., 2013). In mice this channel could produce spiking frequencies up to 30 Hz in ganglion cells and 22 Hz in macaque retinal explants (Sengupta et al., 2016). Considering that film often uses 24 frames per second, the temporal sensitivity of ReaChR seems sufficient for vision rescue. While ReaChR still requires light on the same order of magnitude as ChR2 at $10^{15}$ photons $\text{cm}^{-2}$ $\text{s}^{-1}$ (**Figure 2C**), light at this portion of the spectrum is safe up to $10^{17-18}$ photons $\text{cm}^{-2}$ $\text{s}^{-1}$ (International Commission on Non-Ionizing Radiation Protection, 2013).

The other red-shifted chimeric channel, mVChR1, is a fusion of VChR1 and the N-terminus *Chlamydomonas* channelrhodopsin-1 (not to be confused with C1V1) and has the largest activation spectrum of the ion channel based opsins tested thus far, ranging from 468 nm to 640 nm (**Figure 2B**; Tomita et al., 2014). The conductance of mVChR1 is not as efficient as ChR2 and it also requires a similar amount of light to open the channel. However, it is the only ion channel responsive to light throughout the whole human visual spectrum, making it a promising gene therapy candidate. To further improve spectral sensitivity, the same group used both mVChR1 with ChR2 to restore vision in blind mice (Sato et al., 2017). Unsurprisingly, the use of multiple opsins generated greater light responses across the spectrum than one opsin alone.

In 2014 another red-shifted microbial ion channel was discovered in *Chlamydomonas noctigama*, termed ChrimsonR (**Figure 2A**; Klapoetke et al., 2014). With a similar activation spectrum and light requirements of ReaChR but with a faster deactivation time constant (**Figures 2B–D**), ChrimsonR is another strong vision restoration gene therapy candidate and is currently in clinical trials (ClinicalTrials.gov, 2015).

Even though the red-shifted opsin variants use a safer wavelength of light, they still require extremely bright light on the order of $10^{15}$ photons $\text{cm}^{-2}$ $\text{s}^{-1}$ (**Figure 2C**). Since the light is the direct effector of these ion channels, there is no way to increase light sensitivity of the system other than increasing the light sensitivity of the opsin itself. Currently, the best strategy to increase light sensitivity is to use a light sensitive effector with the capacity to amplify the light response, like GPCRs.

## GPCRs

While there have been great improvements in spectral sensitivity and conductance for light activated ion channels, they still pale in comparison to the signal generated by optogenetic GPCRs. The pay-off for this increased light sensitivity is a loss in temporal sensitivity, with optical GPCRs lagging behind their ion channel in terms of both activation and inactivation (Lin et al., 2008; Cehajic-Kapetanovic et al., 2015; Gaub et al., 2015; Berry et al., 2017; De Silva et al., 2017). However, the slower kinetics of the optogenetic GPCR could be well tolerated due the loss of a synaptic layer. Compared to wild type, the light signal was able to reach V1 faster for the optogenetic ion channel gene therapies by tens of milliseconds (Bi et al., 2006; Lagali et al., 2008; Caporale et al., 2011; Macé et al., 2015; Sengupta et al., 2016). The loss of the photoreceptors and their synapse means that there are fewer cells the light signal has to pass between before reaching the brain in these animals with restored vision. Due to this, the slowness of the GPCRs can be partially compensated for by signal generation in downstream cells.

The first GPCR to be adapted for vision restoration was the light sensor for intrinsically photosensitive RGCs, melanopsin (**Figure 2A**; Lin et al., 2008). Responsible for the pupillary light response and maintenance of circadian rhythms (Provencio et al., 1998), melanopsin is a clear candidate for vision restoration due to its established ability to generate light responses in non-photoreceptor retinal cells. When delivered intravitreally to the ganglion cell layer (Lin et al., 2008), or subretinally to outer retinal cells (De Silva et al., 2017), melanopsin treated retinas are three fold more light sensitive than any microbial opsin, only requiring $10^{12}$ photons $\text{cm}^{-2}$ $\text{s}^{-1}$ to generate a signal (**Figure 2C**). While melanopsin treated mice are able to perform some basic light response behavior and show an increased pupillary light response, the GPCR's kinetics are incredibly slow. It takes hundreds of milliseconds to several seconds to activate melanopsin, and even longer for it to turn off (**Figure 2D**; De Silva et al., 2017). This slow response time is sufficient for basic perception (i.e., is it daytime or not), but makes it a poor tool for the high acuity vision associated with humans.

Another candidate for vision rescue is rhodopsin, the exceedingly light sensitive GPCR found in rod photoreceptors (Cehajic-Kapetanovic et al., 2015; Gaub et al., 2015). Rod photoreceptors are capable of responding to a single photon thanks to the phototransduction cascade. Light isomerizes the chromophore 11-*cis* retinal into all-*trans* retinal, inducing a conformational change in the GPCR which activates its G-protein, transducin. The α-subunit of transducin dissociates and activates phosphodiesterase (PDE), which lowers the concentration of cGMP, closing cyclic nucleotide gated channels and hyperpolarizing the cell. When expressed in non-photoreceptor cells, rhodopsin has a similar light sensitivity to melanopsin of $10^{12}$ photons $cm^{-2}$ $s^{-1}$ (**Figure 2C**), but importantly responds to light 10 times faster than melanopsin (**Figure 2D**; Cehajic-Kapetanovic et al., 2015; Gaub et al., 2015). However, when compared to rod photoreceptors, rhodopsin activation in ganglion cells or bipolar cells is much slower. When heterologously expressed, it is unlikely that the time to isomerize 11-*cis* or activate rhodopsin itself has changed, but rather the lack of other phototransduction cascade proteins increases cellular response times. Rod photoreceptors have specialized discs which contain all the phototransduction cascade proteins to promote efficient signaling. While other cells lack this specific structure and phototransduction cascade, photoactivation of other existing signaling cascades could improve temporal sensitivity.

What is impressive is that the rhodopsin protein is photosensitive at all. Many believed that rhodopsin outside a photoreceptor would be unable to attain its 11-*cis* retinal chromophore. 11-*cis* is tightly regulated being recycled from all-*trans* in retinal pigment epithelium (RPE) and Müller cells, which have developed specialized mechanisms to deliver the incredibly photosensitive pigment to photoreceptors (Kiser et al., 2014). While some teams have had to supply the 11-*cis* for the multielectrode array (MEA) experiments, *in vivo* assays demonstrated effective iterative activation of rhodopsin without the use of exogenous chromophore (Cehajic-Kapetanovic et al., 2015). Perhaps in the degenerate retina, the RPE and Müller cells still produce 11-*cis* and can aberrantly deliver it. Considering that photoreceptors contain approximately a thousand discs each with thousands of rhodopsin molecules (Nathans, 1992), the concentration of rhodopsin ectopically expressed in ganglion cells or bipolar cells would pale in comparison to wild type levels, perhaps low enough to ensure chromophore delivery despite being non-target cells. Furthermore, there might be alternative chromophore delivery mechanisms. It was recently determined that melanopsin also uses 11-*cis* (Walker et al., 2008), so whatever mechanism delivers the 11-*cis* to melanopsin could potentially also deliver it to rhodopsin when expressed in ganglion or bipolar cells.

Recently, optically controlled GPCRs have been engineered by multiple groups (Airan et al., 2009; Karunarathne et al., 2013; Levitz et al., 2013; Broichhagen et al., 2015; van Wyk et al., 2015; Morri et al., 2018). Unlike melanopsin or rhodopsin, these GPCRs have been constructed or modified to become light sensitive. One particularly interesting candidate, Opto-metabotropic glutamate receptor 6 (mGluR6), is a chimeric protein composed of the chromophore-adhering transmembrane domains of melanopsin with the regulatory transmembrane domains of mGluR6, the ON-bipolar specific GPCR (**Figure 2A**; van Wyk et al., 2015). Opto-mGluR6 is the most light sensitive construct tested so far, eliciting a light response at $5 \times 10^{11}$ photons $cm^{-2}$ at 473 nm (**Figure 2C**). In degenerate animals expressing Opto-mGluR6 in their bipolar cells (**Figure 1C**), the light responses generated signals in bipolar cells and ganglion cells had similar timing to photoreceptor evoked light responses in wild type animals. Expressing a photoactivable version of the naturally occurring GPCR in the target cell type is an enticing goal, however, the Opto-mGluR6 group had to resort to transgenic animals to show any function or behavior. In order for any of these therapies to be a viable option for people, non-transgenic routes must be pursued.

## DELIVERY METHODS

The goal of these ambitious projects is to cure blindness in humans. While transgenic animals are an invaluable laboratory tool, they are not applicable to humans. Viral transduction is currently the best method to constitutively express heterologous proteins in mammals. Other methods like electroporation have been shown to successfully deliver transgenes in mice (de Melo and Blackshaw, 2011), but the AAV method has been demonstrated to be safe, effective and long lasting, as evidenced by the recent FDA approval for the first vision restoration gene therapy for LCA2 (Maguire et al., 2009; Simonelli et al., 2010; Jacobson et al., 2012; FDA, 2017).

The current trend in many laboratories is to try and recapitulate the ON/OFF light response by infecting ON-bipolar cells with improved viral capsids and promoters (**Figure 1C**; Doroudchi et al., 2011; Cronin et al., 2014; Gaub et al., 2014, 2015; Cehajic-Kapetanovic et al., 2015; Macé et al., 2015; van Wyk et al., 2015). The hypothesis is that infecting the furthest upstream cells preserves the circuitry and processing resulting in a better final signal sent to the brain. By using the mGluR6 promoter, the ON-bipolar cell specific metabotropic glutamate receptor, optogenetic gene expression is limited to these upstream cells. ChR2 (Doroudchi et al., 2011; Cronin et al., 2014; Macé et al., 2015), LiGluR (Gaub et al., 2014), rhodopsin (Cehajic-Kapetanovic et al., 2015; Gaub et al., 2015) and Opto-mGluR6 (van Wyk et al., 2015) mediated light activation of bipolar cells (**Figure 1C**) can produce ON and OFF responses in ganglion cells and diverse responses in V1, unlike the simple ON response produced by photosensitive ganglion cells.

While this is an admirable goal, bipolar cells are one of the hardest cell types to infect in the retina (Dalkara et al., 2009). Laboratories have engineered new and improved AAV variants with unprecedented retinal penetration (Dalkara et al., 2013), and even the best capsid variants do not efficiently transduce bipolar cells. AAV never achieves complete infection and is normally "patchy," so complete restoration of a receptive field looks unlikely. Furthermore, the mGluR6 promoters used to restrict expression to the ON-bipolar cells may not work in many retinal dystrophies due to dis- and downregulation of mGluR6 (van Wyk et al., 2017). mGluR6 is tonically activated by the continuous release of glutamate by photoreceptors in the dark. Upon photoreceptor cell death, mGluR6 is no longer stimulated and the ON-bipolar cells undergo transcriptional changes that limit mGluR6 expression and potentially other genes under that promoter (Jones et al., 2016).

Instead of trying to restrict expression to bipolar cells, it might be more advantageous to use ubiquitous promoters that would allow expression in bipolar cells and other retinal cells to increase light sensitivity. This way some greater processing is preserved allowing for the generation of ON and OFF light responses, while generally increasing the light sensitivity of the retina as a whole.

## MULTI-EFFECTOR THERAPY

Bipolar cells direct the ON and OFF pathways in healthy tissue, but that does not mean that bipolar derived signal is the only way to generate ON and OFF signals. There are a variety of inhibitory optogenetic ion channels (Berndt et al., 2014, 2016; Govorunova et al., 2015), pumps (Schobert and Lanyi, 1982; Gradinaru et al., 2008; Chow et al., 2010) and GPCRs (Levitz et al., 2013; Broichhagen et al., 2015) that could emulate an "OFF" response. This was first demonstrated by Zhang et al. (2009) by combining the inhibitory ion pump HaloR with ChR2 to produce ON and OFF and ON/OFF light responses. While HaloR requires 20 times more light than ChR2, which already requires an unsafe amount of light, this study importantly shows that the retina can produce multiple types of light responses without bipolar cell transduction.

Recently, Berry et al. (2017) improved upon Zhang's original work by using their engineered SNAG-mGluR2 and LiGluR combination therapy. Similar to LiGluR, SNAG-mGluR2 is a modified version of the mGluR2 with a N-terminal SNAP tag that allows stable conjugation of the azobenzene-glutamate photoswitch by a selective benzylguanine-reactive group (**Figure 2A**; Broichhagen et al., 2015). SNAG-mGluR2 is one of the fastest optogenetic GPCRs with kinetics on the order of hundreds of milliseconds (**Figure 2**D), but it unfortunately requires a similar amount of light as ChR2 (**Figure 2C**). The combination of the excitatory LiGluR ion channel and inhibitory SNAG-mGluR2 GPCR generates diverse light responses including ON, OFF and ON/OFF responses. These diverse responses improved visual behavior in treated mice compared to LiGluR or SNAG-mGluR2 alone. While this combination therapy still requires bright light, it importantly shows that multi-effector therapy has the potential to restore complex and diverse cellular light responses similar to natural vision.

## CONCLUSIONS

The audacious goal of genetically restoring vision to the blind is now possible. Newly discovered and developed optogenetics have improved upon the original ChR2 studies. By red-shifting ion channels, researchers have made safer alternatives with broader spectrums. And new GPCRs are gaining speed to allow for the temporal precision required for high acuity vision. The new trend to use multiple effectors to generate diverse responses should be expanded further. Humans use three different cone opsins and one rod opsin to generate vivid visual perception. With so many optogenetics with diverse excitation spectra, combination therapies using multiple effectors producing excitatory and inhibitory responses at different wavelengths could generate the complex visual information comparable to responses naturally derived in healthy tissue. With new and innovative therapies constantly being developed, vision restoration is within sight.

## AUTHOR CONTRIBUTIONS

CB devised the review article. CB and JF wrote it.

## FUNDING

This work was supported by FFB—Award # TA-GT-0314-0641-UCB-WG—Development of Optogenetic Tools with Increased Light Sensitivity for Vision Restoration. Lowy Medical Research Institute Limited—Award # 036414—AAV-Mediated Delivery of Angiogenic and Neurotrophic Factors to The Retina. Hope for Vision—Award # WU-15-230—Optogenetic Vision Restoration Using Opsins for Increased Sensitivity. FFB—Award # C-GT-0711-0532-UCB03—Viral Mediated Gene Therapy for Retinal Degenerations.

## ACKNOWLEDGMENTS

We would like to thank Emilia Araujo Zin for her help in editing this manuscript.

## REFERENCES

Airan, R. D., Thompson, K. R., Fenno, L. E., Bernstein, H., and Deisseroth, K. (2009). Temporally precise *in vivo* control of intracellular signalling. *Nature* 458, 1025–1029. doi: 10.1038/nature07926

Berndt, A., Lee, S. Y., Ramakrishnan, C., and Deisseroth, K. (2014). Structure-guided transformation of channelrhodopsin into a light-activated chloride channel. *Science* 344, 420–424. doi: 10.1126/science.1252367

Berndt, A., Lee, S. Y., Wietek, J., Ramakrishnan, C., Steinberg, E. E., Rashid, A. J., et al. (2016). Structural foundations of optogenetics: determinants of channelrhodopsin ion selectivity. *Proc. Natl. Acad. Sci. U S A* 113, 822–829. doi: 10.1073/pnas.1523341113

Berry, M. H., Holt, A., Levitz, J., Broichhagen, J., Gaub, B. M., Visel, M., et al. (2017). Restoration of patterned vision with an engineered photoactivatable G protein-coupled receptor. *Nat. Commun.* 8:1862. doi: 10.1038/s41467-017-01990-7

Bi, A., Cui, J., Ma, Y.-P., Olshevskaya, E., Pu, M., Dizhoor, A. M., et al. (2006). Ectopic expression of a microbial-type rhodopsin restores visual responses in mice with photoreceptor degeneration. *Neuron* 50, 23–33. doi: 10.1016/j.neuron.2006.02.026

Boyden, E. S., Zhang, F., Bamberg, E., Nagel, G., and Deisseroth, K. (2005). Millisecond-timescale, genetically targeted optical control of neural activity. *Nat. Neurosci.* 8, 1263–1268. doi: 10.1038/nn1525

Broichhagen, J., Damijonaitis, A., Levitz, J., Sokol, K. R., Leippe, P., Konrad, D., et al. (2015). Orthogonal optical control of a g protein-coupled receptor with a snap-tethered photochromic ligand. *ACS Cent. Sci.* 1, 383–393. doi: 10.1021/acscentsci.5b00260

Caporale, N., Kolstad, K. D., Lee, T., Tochitsky, I., Dalkara, D., Trauner, D., et al. (2011). LiGluR restores visual responses in rodent models of inherited blindness. *Mol. Ther.* 19, 1212–1219. doi: 10.1038/mt.2011.103

Cehajic-Kapetanovic, J., Eleftheriou, C., Allen, A. E., Milosavljevic, N., Pienaar, A., Bedford, R., et al. (2015). Restoration of vision with ectopic expression of human rod opsin. *Curr. Biol.* 25, 2111–2122. doi: 10.1016/j.cub.2015.07.029

Chow, B. Y., Han, X., Dobry, A. S., Qian, X., Chuong, A. S., Li, M., et al. (2010). High-performance genetically targetable optical neural silencing by light-driven proton pumps. *Nature* 463, 98–102. doi: 10.1038/nature08652

ClinicalTrials.gov. (2015). RST-001 phase I/II trial for advanced retinitis pigmentosa. Available online at: https://clinicaltrials.gov/ct2/show/study/NCT02556736.

Cronin, T., Vandenberghe, L. H., Hantz, P., Juttner, J., Reimann, A., Kacsó, A.-E., et al. (2014). Efficient transduction and optogenetic stimulation of retinal bipolar cells by a synthetic adeno-associated virus capsid and promoter. *EMBO Mol. Med.* 6, 1175–1190. doi: 10.15252/emmm.201404077

Dalkara, D., Byrne, L. C., Klimczak, R. R., Visel, M., Yin, L., Merigan, W. H., et al. (2013). *In vivo*-directed evolution of a new adeno-associated virus for therapeutic outer retinal gene delivery from the vitreous. *Sci. Transl. Med.* 5:189ra76. doi: 10.1126/scitranslmed.3005708

Dalkara, D., Kolstad, K. D., Caporale, N., Visel, M., Klimczak, R. R., Schaffer, D. V., et al. (2009). Inner limiting membrane barriers to AAV-mediated retinal transduction from the vitreous. *Mol. Ther.* 17, 2096–2102. doi: 10.1038/mt.2009.181

de Melo, J., and Blackshaw, S. (2011). *In vivo* electroporation of developing mouse retina. *J. Vis. Exp.* 52:2847. doi: 10.3791/2847

De Silva, S. R., Barnard, A. R., Hughes, S., Tam, S. K. E., Martin, C., Singh, M. S., et al. (2017). Long-term restoration of visual function in end-stage retinal degeneration using subretinal human melanopsin gene therapy. *Proc. Natl. Acad. Sci. U S A* 114, 11211–11216. doi: 10.1073/pnas.1701589114

Doroudchi, M. M., Greenberg, K. P., Liu, J., Silka, K. A., Boyden, E. S., Lockridge, J. A., et al. (2011). Virally delivered channelrhodopsin-2 safely and effectively restores visual function in multiple mouse models of blindness. *Mol. Ther.* 19, 1220–1229. doi: 10.1038/mt.2011.69

FDA. (2017). FDA approves novel gene therapy to treat patients with a rare form of inherited vision loss. Available online at: https://www.fda.gov/newsevents/newsroom/pressannouncements/ucm589467.htm.

Gaub, B. M., Berry, M. H., Holt, A. E., Isacoff, E. Y., and Flannery, J. G. (2015). Optogenetic vision restoration using rhodopsin for enhanced sensitivity. *Mol. Ther.* 23, 1562–1571. doi: 10.1038/mt.2015.121

Gaub, B. M., Berry, M. H., Holt, A. E., Reiner, A., Kienzler, M. A., Dolgova, N., et al. (2014). Restoration of visual function by expression of a light-gated mammalian ion channel in retinal ganglion cells or ON-bipolar cells. *Proc. Natl. Acad. Sci. U S A* 111, E5574–E5583. doi: 10.1073/pnas.1414162111

Govorunova, E. G., Sineshchekov, O. A., Janz, R., Liu, X., and Spudich, J. L. (2015). Natural light-gated anion channels: a family of microbial rhodopsins for advanced optogenetics. *Science* 349, 647–650. doi: 10.1126/science.aaa7484

Gradinaru, V., Thompson, K. R., and Deisseroth, K. (2008). eNpHR: a Natronomonas halorhodopsin enhanced for optogenetic applications. *Brain Cell Biol.* 36, 129–139. doi: 10.1007/s11068-008-9027-6

International Commission on Non-Ionizing Radiation Protection. (2013). "On limits of exposure to incoherent visible and infrared radiation," in *Health Physics*, 74–96. Available online at: https://www.icnirp.org/cms/upload/publications/ICNIRPVisible_Infrared2013.pdf.

Jacobson, S. G., Cideciyan, A. V., Ratnakaram, R., Heon, E., Schwartz, S. B., Roman, A. J., et al. (2012). Gene therapy for leber congenital amaurosis caused by *RPE65* mutations. *Arch. Ophthalmol.* 130, 9–24. doi: 10.1001/archophthalmol.2011.298

Jones, B. W., Pfeiffer, R. L., Ferrell, W. D., Watt, C. B., Marmor, M., and Marc, R. E. (2016). Retinal remodeling in human retinitis pigmentosa. *Exp. Eye Res.* 150, 149–165. doi: 10.1016/j.exer.2016.03.018

Kalloniatis, M., and Luu, C. (1995). Temporal resolution. *Webvision Organ. Retin. Vis. Syst.* Available online at: http://www.ncbi.nlm.nih.gov/pubmed/21413411.

Karunarathne, W. K. A., Giri, L., Kalyanaraman, V., and Gautam, N. (2013). Optically triggering spatiotemporally confined GPCR activity in a cell and programming neurite initiation and extension. *Proc. Natl. Acad. Sci. U S A* 110, E1565–E1574. doi: 10.1073/pnas.1220697110

Kienzler, M. A., Reiner, A., Trautman, E., Yoo, S., Trauner, D., and Isacoff, E. Y. (2013). A red-shifted, fast-relaxing azobenzene photoswitch for visible light control of an ionotropic glutamate receptor. *J. Am. Chem. Soc.* 135, 17683–17686. doi: 10.1021/ja408104w

Kiser, P. D., Golczak, M., and Palczewski, K. (2014). Chemistry of the retinoid (visual) cycle. *Chem. Rev.* 114, 194–232. doi: 10.1021/cr400107q

Klapoetke, N. C., Murata, Y., Kim, S. S., Pulver, S. R., Birdsey-Benson, A., Cho, Y. K., et al. (2014). Independent optical excitation of distinct neural populations. *Nat. Methods* 11, 338–346. doi: 10.1038/nmeth.2836

Lagali, P. S., Balya, D., Awatramani, G. B., Münch, T. A., Kim, D. S., Busskamp, V., et al. (2008). Light-activated channels targeted to ON bipolar cells restore visual function in retinal degeneration. *Nat. Neurosci.* 11, 667–675. doi: 10.1038/nn.2117

Levitz, J., Pantoja, C., Gaub, B., Janovjak, H., Reiner, A., Hoagland, A., et al. (2013). Optical control of metabotropic glutamate receptors. *Nat. Neurosci.* 16, 507–516. doi: 10.1038/nn.3346

Lin, J. Y., Knutsen, P. M., Muller, A., Kleinfeld, D., and Tsien, R. Y. (2013). ReaChR: a red-shifted variant of channelrhodopsin enables deep transcranial optogenetic excitation. *Nat. Neurosci.* 16, 1499–1508. doi: 10.1038/nn.3502

Lin, B., Koizumi, A., Tanaka, N., Panda, S., and Masland, R. H. (2008). Restoration of visual function in retinal degeneration mice by ectopic expression of melanopsin. *Proc. Natl. Acad. Sci. U S A* 105, 16009–16014. doi: 10.1073/pnas.0806114105

Lin, J. Y., Lin, M. Z., Steinbach, P., and Tsien, R. Y. (2009). Characterization of engineered channelrhodopsin variants with improved properties and kinetics. *Biophys. J.* 96, 1803–1814. doi: 10.1016/j.bpj.2008.11.034

Macé, E., Caplette, R., Marre, O., Sengupta, A., Chaffiol, A., Barbe, P., et al. (2015). Targeting channelrhodopsin-2 to ON-bipolar cells with vitreally administered AAV restores ON and OFF visual responses in blind mice. *Mol. Ther.* 23, 7–16. doi: 10.1038/mt.2014.154

Maguire, A. M., High, K. A., Auricchio, A., Wright, J. F., Pierce, E. A., Testa, F., et al. (2009). Age-dependent effects of RPE65 gene therapy for Leber's congenital amaurosis: a phase 1 dose-escalation trial. *Lancet* 374, 1597–1605. doi: 10.1016/S0140-6736(09)61836-5

Margalit, E., Maia, M., Weiland, J. D., Greenberg, R. J., Fujii, G. Y., Torres, G., et al. (2002). Retinal prosthesis for the blind. *Surv. Ophthalmol.* 47, 335–356. doi: 10.1016/S0039-6257(02)00311-9

Morri, M., Sanchez-Romero, I., Tichy, A.-M., Kainrath, S., Gerrard, E. J., Hirschfeld, P. P., et al. (2018). Optical functionalization of human Class A orphan G-protein-coupled receptors. *Nat. Commun.* 9:1950. doi: 10.1038/s41467-018-04342-1

Nagel, G., Brauner, M., Liewald, J. F., Adeishvili, N., Bamberg, E., and Gottschalk, A. (2005). Light activation of channelrhodopsin-2 in excitable cells of *Caenorhabditis elegans* triggers rapid behavioral responses. *Curr. Biol.* 15, 2279–2284. doi: 10.1016/j.cub.2005.11.032

Nagel, G., Szellas, T., Huhn, W., Kateriya, S., Adeishvili, N., Berthold, P., et al. (2003). Channelrhodopsin-2, a directly light-gated cation-selective membrane channel. *Proc. Natl. Acad. Sci. U S A* 100, 13940–13945. doi: 10.1073/pnas.1936192100

Nathans, J. (1992). Rhodopsin: structure, function and genetics. *Biochemistry* 31, 4923–4931. doi: 10.1021/bi00136a001

National Eye Institute. (2010). Blindness. Available online at: https://nei.nih.gov/eyedata/blind.

Provencio, I., Jiang, G., De Grip, W. J., Hayes, W. P., and Rollag, M. D. (1998). Melanopsin: an opsin in melanophores, brain and eye. *Proc. Natl. Acad. Sci. U S A* 95, 340–345. doi: 10.1073/pnas.95.1.340

Pruneau, D., Douar, A., Dalkara, D., Duebel, J., Caplette, R., Gauvin, G., et al. (2016). Optogenetic visual restoration using chrimson. Available online at: https://patents.google.com/patent/WO2017187272A1/en.

Sato, M., Sugano, E., Tabata, K., Sannohe, K., Watanabe, Y., Ozaki, T., et al. (2017). Visual responses of photoreceptor-degenerated rats expressing two different types of channelrhodopsin genes. *Sci. Rep.* 7:41210. doi: 10.1038/srep41210

Scalabrino, M. L., Boye, S. L., Fransen, K. M. H., Noel, J. M., Dyka, F. M., Min, S. H., et al. (2015). Intravitreal delivery of a novel AAV vector targets ON bipolar cells and restores visual function in a mouse model of complete congenital stationary night blindness. *Hum. Mol. Genet.* 24, 6229–6239. doi: 10.1093/hmg/ddv341

Schobert, B., and Lanyi, J. K. (1982). Halorhodopsin is a light-driven chloride pump. *J. Biol. Chem.* 257, 10306–10313.

Sengupta, A., Chaffiol, A., Macé, E., Caplette, R., Desrosiers, M., Lampič, M., et al. (2016). Red-shifted channelrhodopsin stimulation restores light responses in blind mice, macaque retina and human retina. *EMBO Mol. Med.* 8, 1248–1264. doi: 10.15252/emmm.201505699

Simonelli, F., Maguire, A. M., Testa, F., Pierce, E. A., Mingozzi, F., Bennicelli, J. L., et al. (2010). Gene therapy for Leber's congenital amaurosis is safe and effective through 1.5 years after vector administration. *Mol. Ther.* 18, 643–650. doi: 10.1038/mt.2009.277

Tomita, H., Sugano, E., Murayama, N., Ozaki, T., Nishiyama, F., Tabata, K., et al. (2014). Restoration of the majority of the visual spectrum by using modified Volvox channelrhodopsin-1. *Mol. Ther.* 22, 1434–1440. doi: 10.1038/mt.2014.81

van Wyk, M., Hulliger, E. C., Girod, L., Ebneter, A., and Kleinlogel, S. (2017). Present molecular limitations of ON-bipolar cell targeted gene therapy. *Front. Neurosci.* 11:161. doi: 10.3389/fnins.2017.00161

van Wyk, M., Pielecka-Fortuna, J., Löwel, S., and Kleinlogel, S. (2015). Restoring the ON switch in blind retinas: opto-mGluR6, a next-generation, cell-tailored optogenetic tool. *PLoS Biol.* 13:e1002143. doi: 10.1371/journal.pbio.1002143

Volgraf, M., Gorostiza, P., Numano, R., Kramer, R. H., Isacoff, E. Y., and Trauner, D. (2006). Allosteric control of an ionotropic glutamate receptor with an optical switch. *Nat. Chem. Biol.* 2, 47–52. doi: 10.1038/nchembio756

Walker, M. T., Brown, R. L., Cronin, T. W., and Robinson, P. R. (2008). Photochemistry of retinal chromophore in mouse melanopsin. *Proc. Natl. Acad. Sci. U S A* 105, 8861–8865. doi: 10.1073/pnas.0711397105

Zhang, Y., Ivanova, E., Bi, A., and Pan, Z.-H. (2009). Ectopic expression of multiple microbial rhodopsins restores ON and OFF light responses in retinas with photoreceptor degeneration. *J. Neurosci.* 29, 9186–9196. doi: 10.1523/JNEUROSCI.0184-09.2009

Zhang, F., Prigge, M., Beyrière, F., Tsunoda, S. P., Mattis, J., Yizhar, O., et al. (2008). Red-shifted optogenetic excitation: a tool for fast neural control derived from *Volvox Carteri*. *Nat. Neurosci.* 11, 631–633. doi: 10.1038/nn.2120

**Conflict of Interest Statement**: The authors declare that the research was conducted in the absence of any commercial or financial relationships that could be construed as a potential conflict of interest.

frontiers in Cellular Neuroscience

ORIGINAL RESEARCH
published: 24 October 2018
doi: 10.3389/fncel.2018.00389

# Overall Assay of Neuronal Signal Propagation Pattern With Long-Term Potentiation (LTP) in Hippocampal Slices From the CA1 Area With Fast Voltage-Sensitive Dye Imaging

***Yoko Tominaga, Makiko Taketoshi and Takashi Tominaga****

*Laboratory for Neural Circuit Systems, Institute of Neuroscience, Tokushima Bunri University, Sanuki, Japan*

Activity-dependent changes in the input-output (I-O) relationship of a neural circuit are central in the learning and memory function of the brain. To understand circuit-wide adjustments, optical imaging techniques to probe the membrane potential at every component of neurons, such as dendrites, axons and somas, in the circuit are essential. We have been developing fast voltage-sensitive dye (VSD) imaging methods for quantitative measurements, especially for single-photon wide-field optical imaging. The long-term continuous measurements needed to evaluate circuit-wide modifications require stable and quantitative long-term recordings. Here, we show that VSD imaging (VSDI) can be used to record changes in circuit activity in association with theta-burst stimulation (TBS)-induced long-term potentiation (LTP) of synaptic strength in the CA1 area. Our optics, together with the fast imaging system, enabled us to measure neuronal signals from the entire CA1 area at a maximum frame speed of 0.1 ms/frame every 60 s for over 12 h. We also introduced a method to evaluate circuit activity changes by mapping the variation in recordings from the CA1 area to coordinates defined by the morphology of CA1 pyramidal cells. The results clearly showed two types of spatial heterogeneity in LTP induction. The first heterogeneity is that LTP increased with distance from the stimulation site. The second heterogeneity is that LTP is higher in the stratum pyramidale (SP)-oriens region than in the stratum radiatum (SR). We also showed that the pattern of the heterogeneity changed according to the induction protocol, such as induction by TBS or high-frequency stimulation (HFS). We further demonstrated that part of the heterogeneity depends on the I-O response of the circuit elements. The results show the usefulness of VSDI in probing the function of hippocampal circuits.

**Keywords: voltage-sensitive dye, hippocampus, LTP, optical recording, L-LTP, HFS, TBS**

***Edited by:***
*Srdjan D. Antic,*
*University of Connecticut Health Center, United States*

***Reviewed by:***
*Katsushige Sato,*
*Komazawa Women's University, Japan*
*Jian-young Wu,*
*Georgetown University, United States*

****Correspondence:***
*Takashi Tominaga*
*tominagat@kph.bunri-u.ac.jp*

***Received:*** *24 August 2018*
***Accepted:*** *10 October 2018*
***Published:*** *24 October 2018*

***Citation:***
*Tominaga Y, Taketoshi M and Tominaga T (2018) Overall Assay of Neuronal Signal Propagation Pattern With Long-Term Potentiation (LTP) in Hippocampal Slices From the CA1 Area With Fast Voltage-Sensitive Dye Imaging.*
*Front. Cell. Neurosci. 12:389.*
*doi: 10.3389/fncel.2018.00389*

## INTRODUCTION

Brain function depends on neural circuit activity. Understanding the circuit behavior of *in vitro* specimens is essential to address the physiology and pathology of the normal and diseased brain. Conventional electrophysiological methods, such as field potential recordings, sharp electrode intracellular recordings and patch clamping, are useful for determining the activity of the cells in the circuit and the synaptic connections between elements. However, there is increasing demand to directly elucidate the circuit activity, as the excitation/inhibition (E/I) balance of neural circuits has gained attention (Isaacson and Scanziani, 2011). The E/I imbalance should affect the control and synchrony among various circuit elements and cause a diverse range of psychiatric disorders, including autism spectrum disorders (ASDs; Persico and Bourgeron, 2006), schizophrenia (Canitano and Pallagrosi, 2017) and Alzheimer's disease (AD; Busche and Konnerth, 2016). One must evaluate the activity across the broad span of the circuit to understand neural circuit mechanisms of brain malfunction (Uhlhaas and Singer, 2012; Anticevic and Murray, 2017).

Optical recordings of membrane potential changes in neurons could be an ideal measurement technique to achieve this goal. Optical recording began with a single point observation of the optical characteristic changes by membrane excitation (Hill and Keynes, 1949; Cohen et al., 1968, 1970), which later led to an imaging technique that employed synthetic voltage-sensitive dye (VSD; Davila et al., 1973; Ross et al., 1974) that could capture the real-time activity of brain circuit function in the 1980's (Grinvald et al., 1981, 1982, 1988; Ichikawa et al., 1993; Vranesic et al., 1994). Wide-field large-scale voltage imaging can probe the circuit mechanism in animal models of healthy and disease states (Tanemura et al., 2002; Mann et al., 2005; Suh et al., 2011; Juliandi et al., 2016). However, there are several technical challenges that prevent wide-field imaging from meeting experimental requirements, namely, the low sensitivity of the dye and the fast signaling of neurons.

Comparing the voltage dependence of the VSD in a single membrane (∼%/100 mV; Loew et al., 1992) to the signal size from the bulk-stained brain tissue, the VSD signal is usually small ($10^{-2}$–$10^{-3}$; Peterka et al., 2011). The low optical signal is due to the ratio of the fluorescence from the membrane with constant (unaffected), and sub-threshold potential change; this is more significant than that produced by a substantial potential-change such as action potential (Tominaga et al., 2009). Additionally, the camera must have a high frame rate that can capture membrane potential events that occur in the millisecond range. The camera should also be able to capture a large amount of light during the limited timeframe to avoid photon-shot noise, i.e., the randomness of the number of photons proportional to the square root of total photons. Ultimately, the camera must fulfil these essential characteristics, i.e., having low noise (at least 60 dB at $10^{-3}$ change), a high-speed (sub-millisecond) frame rate, and the ability to capture a large amount of light (at least $10^5$ photons). Several commercially available imaging systems can meet these requirements. Optics are also crucial, especially in the low-magnification range, and slice handling is essential to avoid mechanical noise and to maintain proper physiology.

In the present article, we present how our imaging system can be used with hippocampal slices prepared via well-known methodology. We demonstrate an imaging analysis of long-term potentiation (LTP; Bliss and Gardner-Medwin, 1973; Bliss and Collingridge, 1993) in the hippocampal CA1 area, which is a key indicator of brain function in many disease models (Monday and Castillo, 2017; Monday et al., 2018).

# MATERIALS AND METHODS

## Slice Preparation and Staining With VSD

All animal experiments were performed according to protocols approved by the Animal Care and Use Committee of Tokushima Bunri University. Hippocampal slices (350 μm thick) were prepared from 4- to 5-week-old male mice (C57BL6), decapitated under deep isoflurane anesthesia. The brains were quickly cooled in iced artificial cerebrospinal fluid (ACSF; 124 mM NaCl, 2.5 mM KCl, 2 mM $CaCl_2$, 2 mM $MgSO_4$, 1.25 mM $NaH_2PO_4$, 26 mM $NaHCO_3$ and 10 mM glucose, pH 7.4, after bubbling with mixed 95%/5% $O_2/CO_2$ gas). After cooling for 5 min, the hippocampus was dissected out along with the surrounding cortex and sliced in 350-μm-thick sections with a vibratome (Leica VT-1000 and VT-1200s). Each slice was transferred onto a fine-mesh membrane filter (Omnipore, JHWP01300, 0.45 μm pores, Merk Millipore Ltd., MA, USA) held in place by a thin plexiglass ring (inner diameter, 11 mm; outer diameter, 15 mm, thickness 1–2 mm). Slices placed in the plexiglass ring were transferred to a moist chamber continuously supplied with a humidified mixture of $O_2$ and $CO_2$ gas. The temperature was held at 28°C for 25 min and then at room temperature. After 1 h of incubation in the chamber, slices were stained with an aliquot of the staining solution (100–110 μl for each slice) of VSD [0.1 mM Di-4-ANEPPS (D-1199, Molecular Probes Inc. OR, USA) in a mixture of 2.7% ethanol, 0.13% Cremophor EL (Sigma), 50% fetal bovine serum (Sigma) and 50% ACSF] for 20 min. The slices were subjected to experiments after at least 1 h of incubation at room temperature.

## Recording

A slice sustained with the plexiglass ring was placed in an immersion-type recording chamber. Slices were continuously perfused with ACSF at a rate of 1 ml $min^{-1}$. The ACSF was continuously bubbled with an $O_2/CO_2$ gas mixture. Before placing in the recording chamber, the ACSF was warmed to 31°C with an electronic temperature-controlling heating block (**Figure 1**). Epifluorescence optics (Tominaga et al., 2000), consisting of two principal lenses [an $f$ = 20 mm objective lens (NA = 0.35; Brainvision Inc., Tokyo, Japan) or ×5 MyCAM lens (NA = 0.60; custom made by Olympus) and a ×1.0 Leica Microsystems projection lens], a dichroic mirror (575 nm), absorption (530 nm) and excitation (590 nm) filters, were mounted above the slice. Fluorescence was measured and projected onto a CMOS camera (MiCAM Ultima or MiCAM02, Brainvision Inc., Tokyo, Japan). The ratio of the fractional change in VSD fluorescence to the initial amount of fluorescence (ΔF/F) was used as the optical signal. The frame rate was 0.1 ms/frame on the MiCAM Ultima camera (14 bit ADC, $1.5 \times 10^6$ well depth, 80 dB; **Figures 2**, **3**) and 0.6 ms/frame on the MiCAM02 camera (12 bit ADC, $4.5 \times 10^5$ well depth, 70 dB; **Figures 4–6**). The optical signals presented in the following sections are signals that have been spatially and temporally filtered with a Gaussian kernel of 5 × 5 × 3 (horizontal × vertical × temporal directions) two times. The analysis of the optical signals was performed with a procedure developed on the Igor Pro software (WaveMetrics Inc., OR, USA).

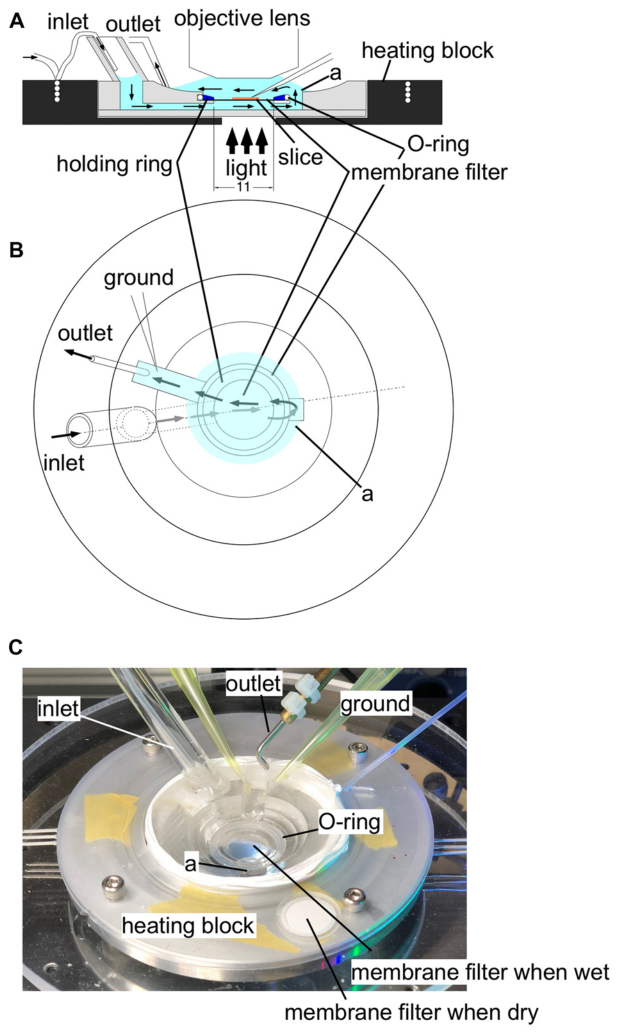

**FIGURE 1 |** An illustration of the experimental recording chamber system. **(A)** A side view of the recording chamber. An aluminum heating block (black) surrounds the plexiglass recording chamber. A thin tubing embedded in the heating block supplies gassed ACSF to the recording chamber through a wide bubble-trapping tube. The ACSF then flows beneath the specimen held by a polytetrafluoroethylene (PTFE) membrane filter (13 mm in diameter) fixed to a thin (1 mm in height) plexiglass holding ring. The ACSF flows upward through a connecting channel and over the specimen. The tight sealing of the O-ring and the plexiglass holding ring ensures a single stream of ACSF, so that the ACSF supply gas and glucose from both sides of the specimen. The ACSF is then sucked by the outlet tubing. **(B)** A top view of the chamber system. Arrows represent the flow of ACSF. **(C)** A photograph of the experimental recording system. In the center of the recording chamber, a wet membrane filter was placed to show that the membrane filter becomes transparent so that transmitted illumination is possible. A membrane filter was placed outside the recording chamber before use to show the membrane filter when it is dry for comparison. Label (a) shows the well connecting the fluid channel beneath the membrane filter and the top space to cover a slice.

A glass microcapillary tube (5-µm opening diameter, filled with ACSF, 1 MOhm) was used as a monopolar stimulating electrode and a recording electrode for field potential recordings. The electrophysiological recording system was controlled with a procedure developed for Igor Pro (WaveMetrics Inc., OR, USA).

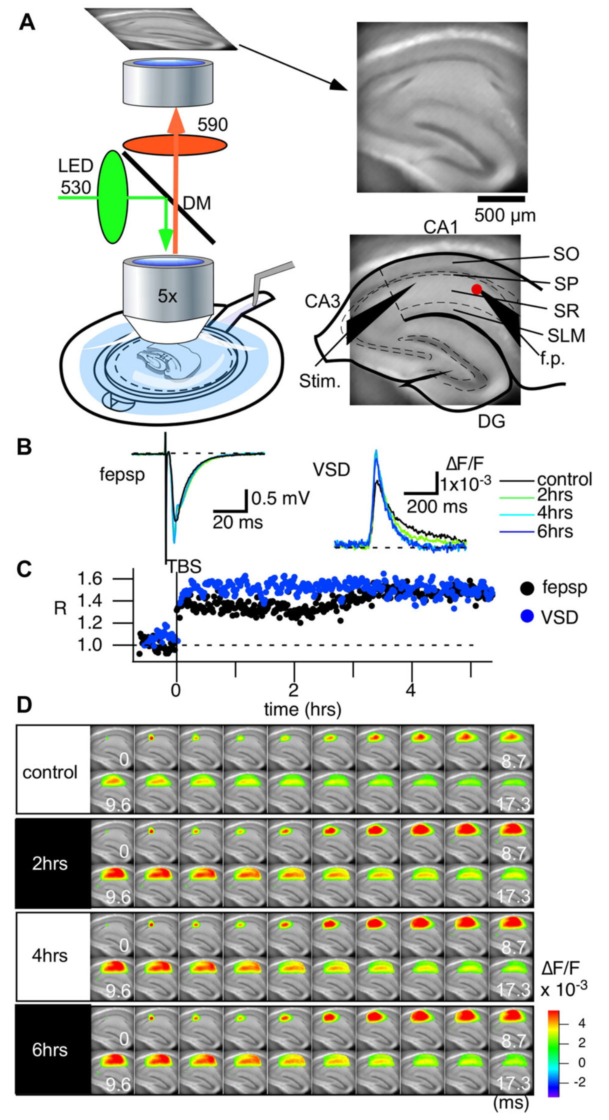

**FIGURE 2 |** Voltage-sensitive dye (VSD) imaging can follow the long-term circuit activity changes of hippocampal slices caused by theta-burst stimulation (TBS). **(A)** An illustration showing the recording setup of the optical recording system. A membrane filter attached to a thin plastic ring holds a slice preparation. The ring is then held in place with a recording chamber, in which adequate ACSF is provided from the bottom of the experimental chamber and flows over the slice towards the outlet tubing. A water immersion objective lens (5× Olympus, NA 0.35) of a tandem-lens configured epifluorescent optics unit is placed above the slice preparation. An imaging device (MiCAM Ultima and MiCAM02, Brainvision Inc., Tokyo, Japan) captures the fluorescent images of the slice (right). The configuration of the electrodes (Stim., the stimulation electrode; f.p., the field potential electrode) and an illustration of the hippocampus are superimposed. Abbreviations: SO, stratum oriens-alveus; SP, stratum pyramidale; SR, stratum radiatum; SLM, stratum lacunosum-moleculare. **(B)** Traces of field excitatory postsynaptic potentials (fEPSPs) recorded with the field electrode before and after TBS-induced long-term potentiation (LTP) and the optical signal at the corresponding pixel. Both traces are average of eight traces. **(C)** Time course of LTP with the fEPSP slope (black) and the optical signal (blue) at the tip of the field potential electrode. **(D)** The panel shows consecutive images of the response for the control recording and for recordings made at 2 h, 4 h and 6 h. We recorded the optical signals every 60 s at a frame rate of 0.1 ms/frame.

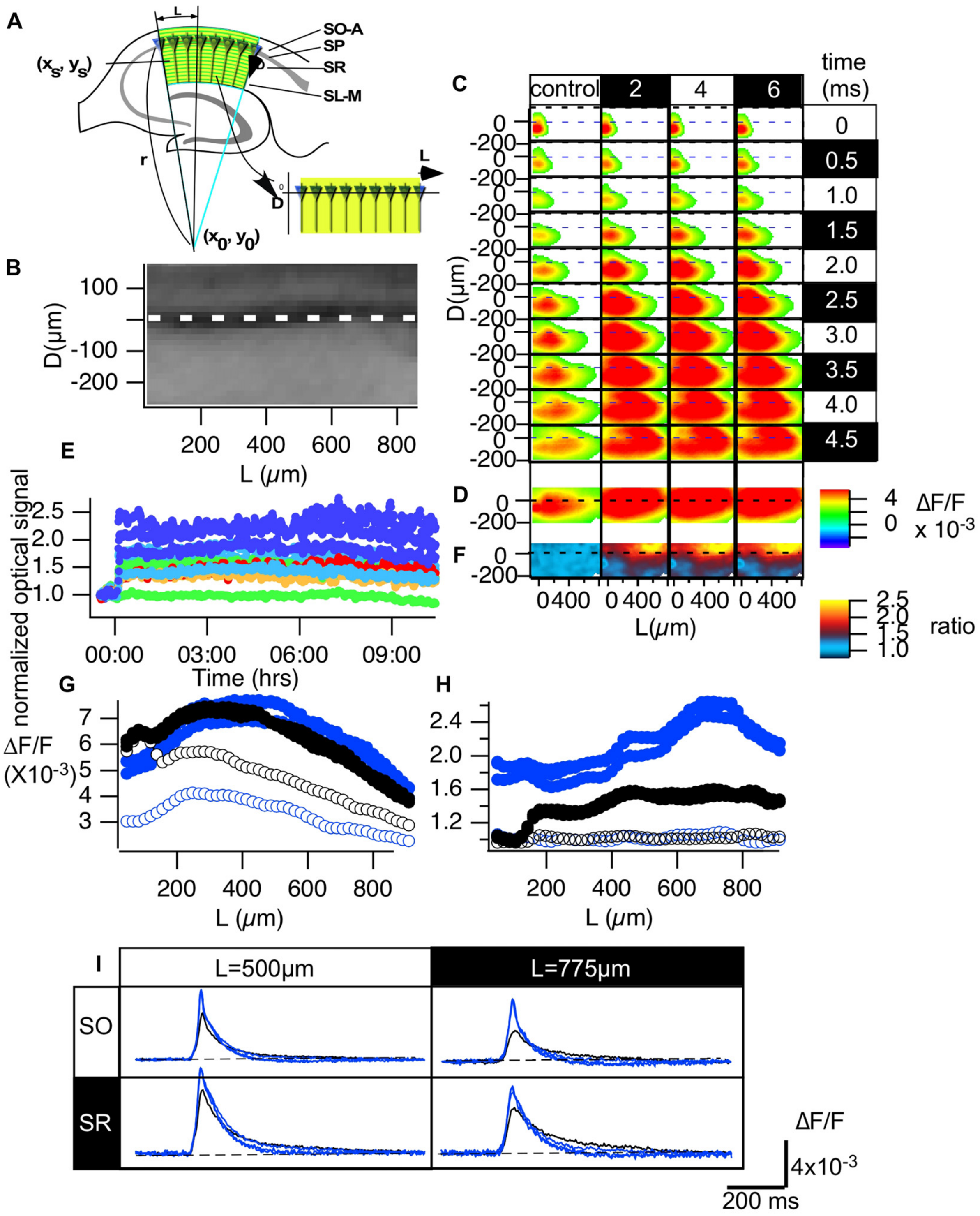

**FIGURE 3 |** Normalization made it possible to evaluate the optical signals in the CA1 area of hippocampal slices. **(A)** An illustration of how we converted the hippocampal CA1 area to the distance from the start of the CA1 (L) and the distance from the pyramidale cell layer (D) plane **(B)**. **(C)** Representative propagation pattern of the optical signal spread along the CA1 area converted to the D-L plane in each time frame for the control recording and recordings made 2, 4 and 6 h from TBS. **(D)** The peak value of each pixel in the D-L plane. **(E)** The time course of the normalized optical signals in pixels of the D-L plane for 10 h. **(F)** The amplitude of the normalized degree of LTP mapped to the D-L plane at each time point. **(G)** The line profile of the optical signal along the line at $D = -75$ μm (SO) and $D = 150$ μm (SR) at each time point (control, 2, 4 and 6 h). **(H)** The line profile of the normalized degree of LTP along the same lines. **(I)** The time course of the optical signal at the representative points ($L = 500$ and 775 μm, respectively) in each line of the SO ($D = -75$ μm) and the SR ($D = 150$ μm) at each time point.

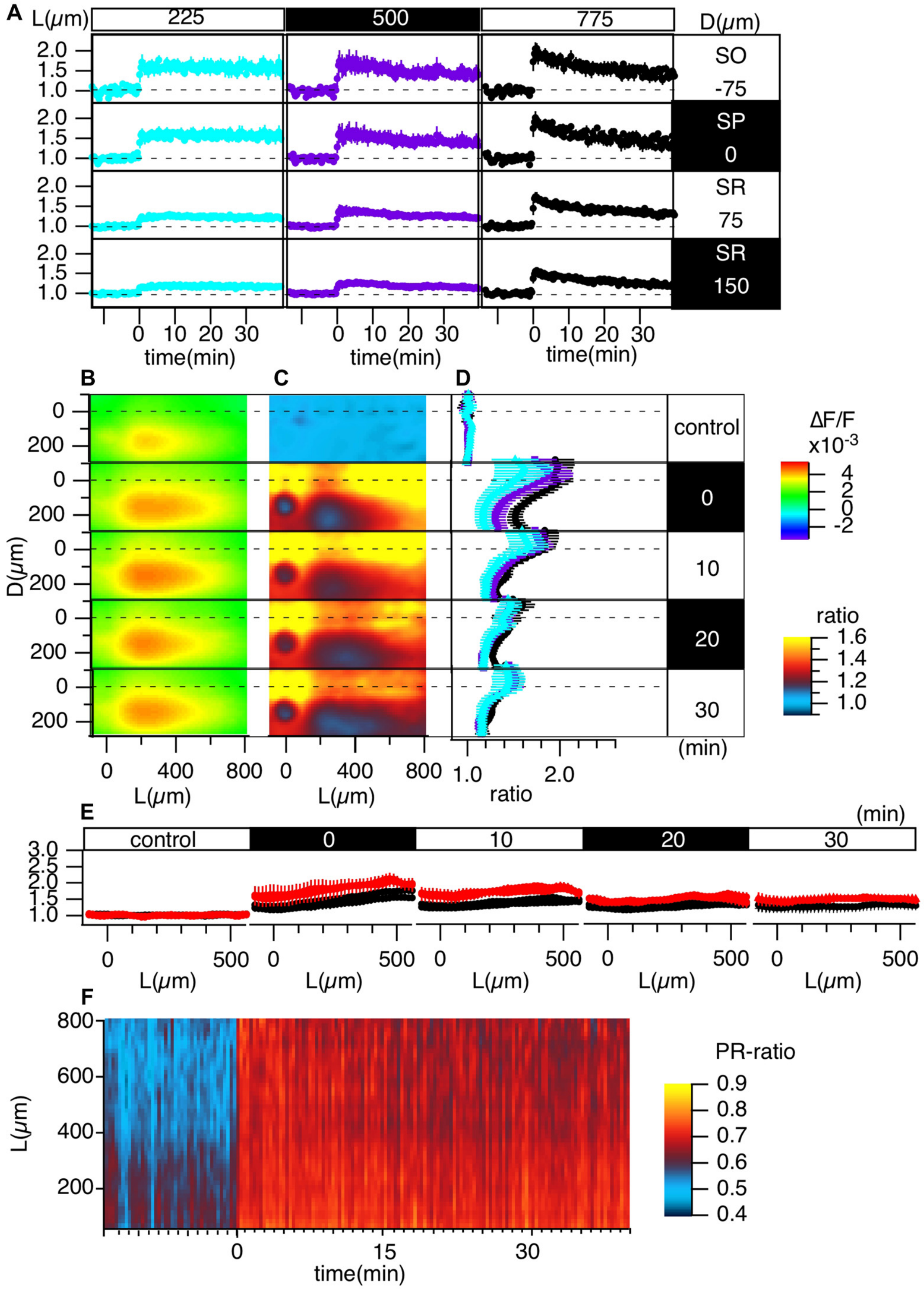

**FIGURE 4 |** Grouped evaluation of TBS-induced LTP. **(A)** The time changes in the normalized peak amplitude of the optical signals at representative points for three different L positions [*L* = 225 (cyan), 500 (purple), 775 (black) μm] and four different D positions (*D* = −75, 0, 75, 150 μm). **(B)** The peak values mapped in the D-L coordinates. **(C)** The LTP ratio in the D-L coordinates. **(D)** The line profiles of C at different L positions [225 (cyan), 500 (purple), 775 (black) μm] at each time point. **(E)** The line profile along the L axis at different time points corresponding to the control recording and recordings made at 0, 10, 20 and 30 min from TBS. **(F)** The time change in the ratio of the line profiles at the SO (*D* = −75) vs. the SR (*D* = 150), i.e., the PRR, along the L axis. *N* = 4, *n* = 12, bars in **(A,D,E)** indicate SEM.

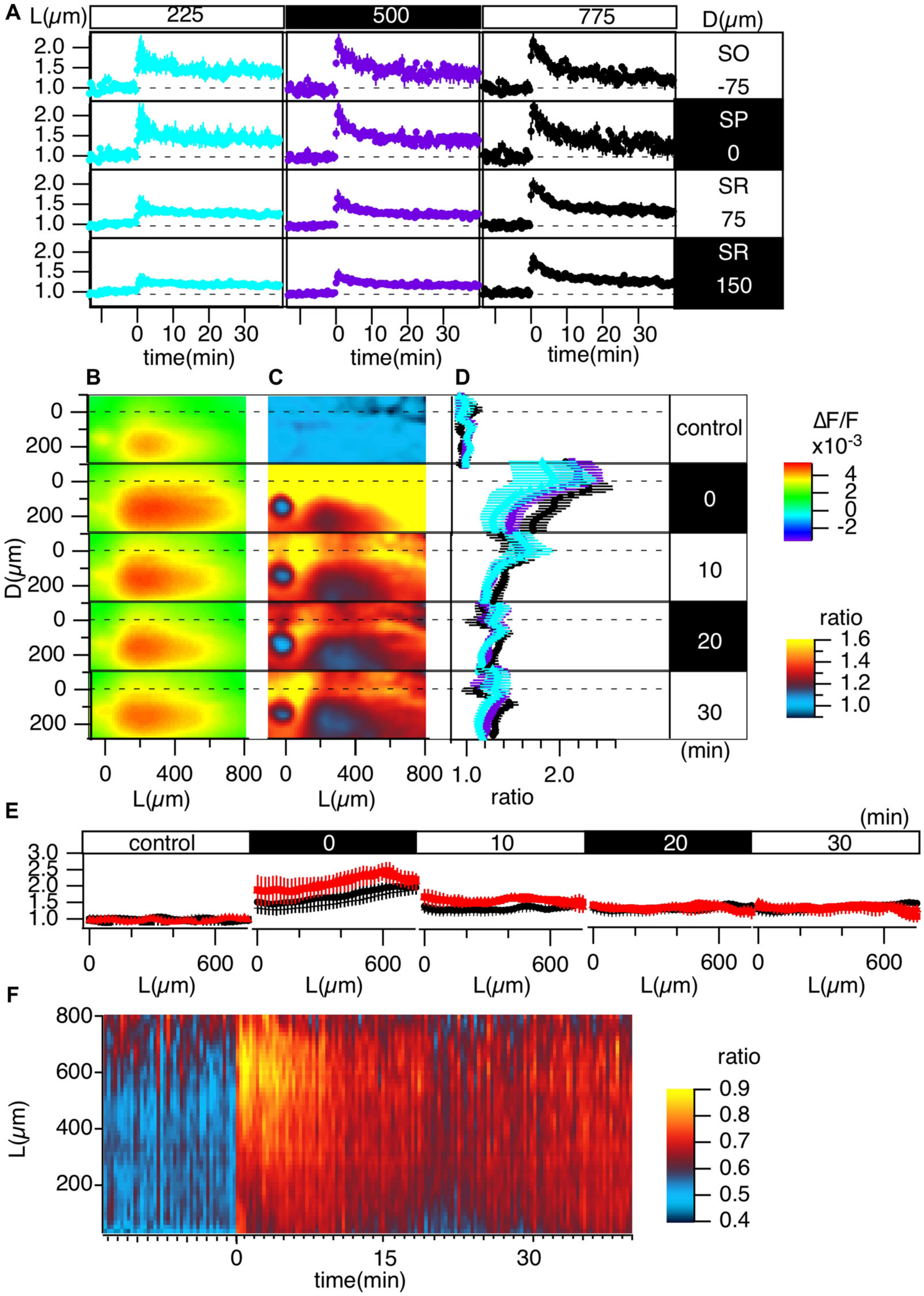

**FIGURE 5 |** Grouped evaluation of high-frequency stimulation (HFS)-induced LTP. The same analysis of LTP is shown in **Figure 3**, but the induction protocol is 100 pulses of 100 Hz (HFS). **(A)** The time changes in normalized peak amplitude of the optical signals at representative points at three different L positions [*L* = 225 (cyan), 500 (purple), 775 (black) μm] and four different D positions (*D* = −75, 0, 75, 150 μm). **(B)** The peak values mapped in the D-L coordinates. **(C)** The LTP ratio in the D-L coordinates. **(D)** The line profiles of C at different L positions [225 (cyan), 500 (purple), 775 (black) μm] at each time point. **(E)** The line profile along the L axis at different time sections for control recordings and recordings made at 0, 10, 20 and 30 min from TBS. **(F)** The time change in the ratio of the line profiles at the SO (*D* = −75) vs. the SR (*D* = 150), i.e., the PRR along the L axis. *N* = 2, *n* = 7, bars in **(A,D,E)** indicate SEM.

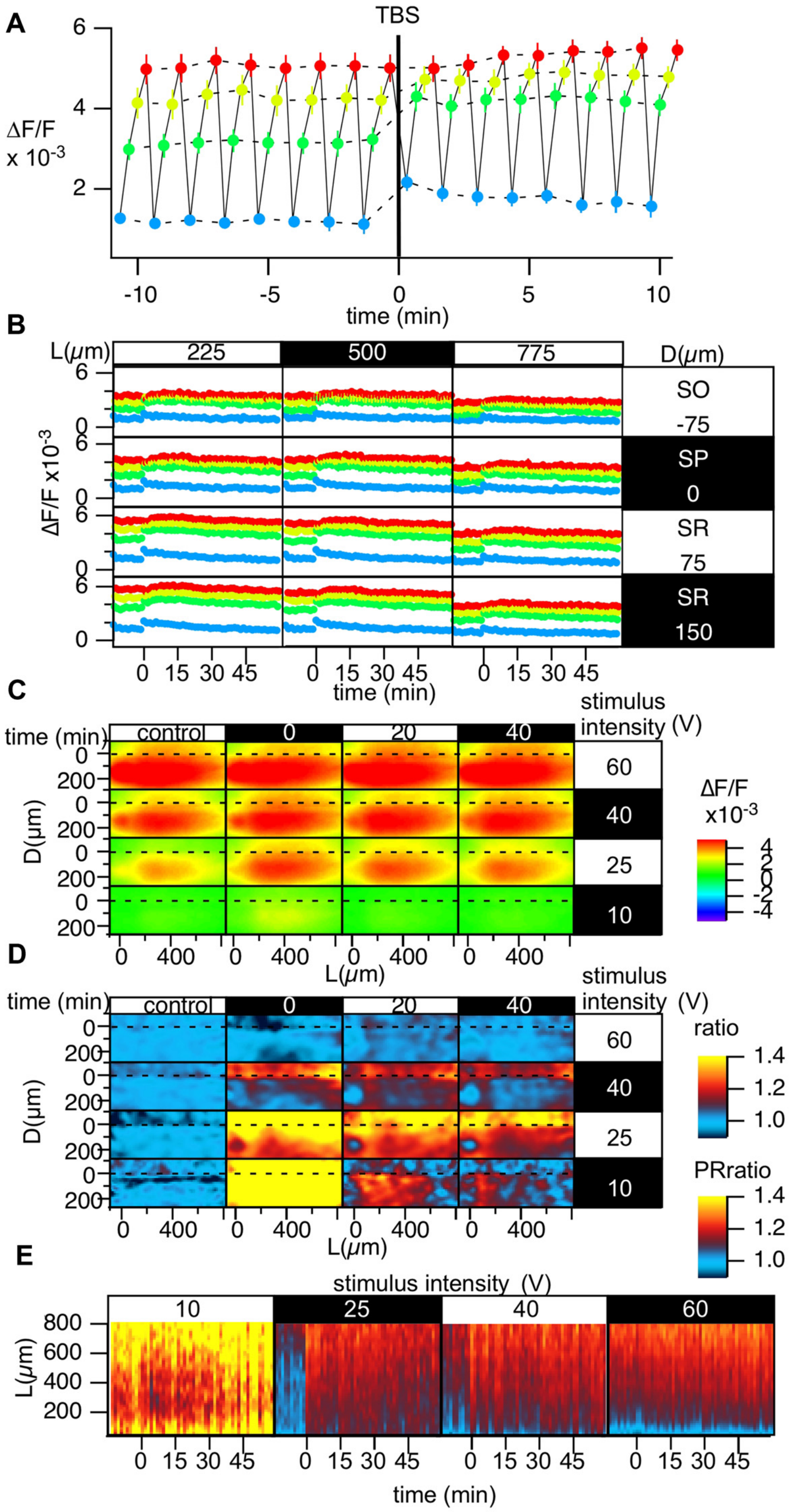

**FIGURE 6 |** Grouped data of the change in the stimulus-response relationship caused by TBS. **(A)** Change in the optically measured stimulus-response relationship measured by altering the stimulus intensity in four steps c[10 (blue), 25 (green), 40 (yellow) and 60 V (red)] every 20 s while performing optical recording in a time-window containing the induction of LTP in a representative point. **(B)** The time courses of the optical response at the representative points in the D-L coordinates while changing the stimulus intensity; the colors of the points correspond to the stimulus intensity [10 (blue), 25 (green), 40 (yellow), and 60 V (red)]. **(C)** The peak of the optical signals mapped in D-L coordinate at different stimulus intensity and different time. **(D)** The degree of LTP in the D-L coordinate plane corresponding to the stimulus intensity. **(E)** Time change in the PRR for each stimulus intensity. *N* = 2, *n* = 10, bars in **(A,B)** indicate SEM.

A 0.05 Hz stimulus was applied to the Schaffer collateral pathway in most of the experimental procedures to monitor synaptic transmission. The IgroPro procedure controlled stimulation patterns through ITC-18 (Instrutech, Longmont, CO, USA) and ESTM-8 (Brainvision, Inc., Tokyo, Japan), and both instruments equip D/A and A/D converters. ITC-18 was used in combination with a linear isolator (A395, WPI Inc., Sarasota, FL, USA; 0–250 μA, 200 μs bipolar), the ESTM-8 has built-in linear isolators to programmatically produce stimulation pulses at different intensities (0–60 V, 300 μs biploar). Neither of these experimental processes interfered with the other. For details regarding the optical recording technique, see our previous article (Tominaga et al., 2000, 2013; Tominaga and Tominaga, 2016).

### Compensation the VSD Signal

The fluorescence signal from the Di-4-ANEPPS dye was adjusted if needed. Generally, the fluorescence of the dye changes for many reasons (Habib-E-Rasul Mullah et al., 2013). Firstly, one might sometimes experience increased fluorescence during the first 10 min of recordings (Habib-E-Rasul Mullah et al., 2013). We have figured out that this relates to the washout of unbound dye. The dim fluorescence at the first phase of perfusion could be the quenching effect of the dye chemical in the aqueous phase. Washing out the dye prevents this change. The second cause is bleaching. The high intensity of the excitation light and the long duration of the illumination can cause this problem. Hence, the high numerical aperture for collecting light is critical. Our recordings in the present experiments did not produce a measurable bleaching effect, judging by the lack of significant time-change of initial fluorescence intensity. The third one should be caused by unknown factors probably relating to the internalization of the dye. We did not see a significant decrease in fluorescence over 12 h but observed a gradual reduction in the sensitivity of the VSD judged by the intensity of the stimulus artifact at the site of stimulation. The optical artifact showed the gradual decrease by two-time constants, while there was no reason for the reduction of the signal. We compensated the reduction in the data shown in **Figures 2**, **3** by applying a double exponent function to the artifact intensity. The same analysis on the following measurements did not show any considerable reduction in sensitivity for 2–3 h. This can be dependent on the intensity of the excitation light because the data in **Figures 2**, **3** recorded at 0.1 ms/frame requires much higher excitation light than the following measurements.

## RESULTS

### The Recording System and the LTP Measured

**Figure 1** illustrates the recording chamber system (Tominaga et al., 2000, 2002, 2013) that allows stable, long-lasting fluorescent recording from slices prepared from rodents (rats and mice). We designed a slice chamber that can fix the slice in place while perfusing enough fluid needed to retain the physiology of the slice preparation. The system consists of a thin plastic ring with a polytetrafluoroethylene (PTFE) membrane filter beneath it; the slice sticks to the membrane without any other devices. The device is essential to keep the slice physiology intact for hours and to avoid any mechanical disturbances from recordings. ACSF is perfused from beneath the slice; the fluid then covers the slice towards the suction pipette. The membrane filter helps distribute the solution from the bottom. The tight sealed solution flow channel ensures the supply of the oxygenated solution (Hájos et al., 2009). The membrane filter becomes transparent when wet so that electrophysiological manipulation can be easily performed. The system is also beneficial in reducing the staining solution needed when loading the VSD because the ring can hold a small aliquot (100–110 μl) of staining solution in the incubation chamber. The slices stick to the membrane rather firmly so that mechanical disturbances are avoided; no weights or holding wires are needed to fix the slice in the submerged recording chamber.

**Figure 2A** shows the recording setup. The excitation light (LEX-2G, Brainvision, Inc., Tokyo, Japan) is equipped with a feedback stabilizing controller to prevent the drift problem, which often occurs in LED illumination (Nishimura et al., 2006). The light is illuminated onto a dichroic mirror and then projected to a water immersion objective lens (×5, NA 0.60, custom made by Olympus and $f = 20$ mm, NA 0.35, Brainvision Inc., Tokyo, Japan). A low-magnification lens with a water immersion objective is suitable to avoid noise from fluid movements while measuring the whole circuit activity. A high NA at low magnification with a substantial focal length (f) requires a large pupil. The combination of two objective lenses with a wide dichroic mirror allows epifluorescence optics with a high numerical aperture. The optics ensured that the excitation light was minimized while capturing a sufficient amount of fluorescence for high-speed imaging (up to 10,000 frames per second, **Figure 2B** right).

The slice chamber system and the optics established long-lasting, stable recording that could follow the late LTP (L-LTP; **Figures 2B–D**) induced by a so-called theta burst stimulus (TBS; 10 bursts of 100 Hz in 4 pulses spaced at 200 ms intervals). We routinely measured the stimulus-response relationships in each slice by changing the stimulus intensity programmatically. However, since the stimulus-response relationships differ depending on the distance from the stimulation electrode, we continued to use 100 μA (200 μsec bipolar) stimulation as the control and TBS that gave an almost half-maximum response in the field electrode. **Figure 2B** shows the representative traces of field excitatory postsynaptic potentials (fEPSPs) and the optical signal at the pixel of the tip of the field electrode (red dot in **Figure 2A** righthand figure) corresponding to the control recording (black) and recordings made 2 (green), 4 (cyan) and 6 h (blue) from TBS. **Figure 2D** shows the series of optical signals (data captured at 10,000 frames/s) showing neural propagation along the CA1 area at each time point (control, 2, 4 and 6 h). There was a distinct increase in activation from the control condition to after TBS, but after 2 h, the amplitude and time change of the activation patterns were consistent. The recordings demonstrate that the optical recording system can follow changes in the physiological activity for an extended period of time.

## Normalization of the Optical Signal in the CA1 Area of the Hippocampus by Layers

We transformed the two-dimensional imaging data obtained from the CA1 area to coordinates along the stratum pyramidale (SP). That is, we converted the imaging data in normal x-y coordinates to coordinates corresponding to the distance from the SP layer (D) and the distance from the site of stimulation near the CA1-CA2 boundary (L). We aimed to read the optical signal based on the assumption that each pyramidal cell lies radially on an arc along the following function (**Figure 3A**).

$$r^2 = (x - x_0)^2 + (y - y_0)^2 \quad (1)$$

$$x = (x_s - x_0)\cos(L/r) - (y_s - y_0)\sin(L/r) + x_0 \quad (2)$$

$$y = (y_s - y_0)\cos(L/r) - (x_s - x_0)\sin(L/r) + y_0 \quad (3)$$

where $x_s$, $y_s$ indicate the (x, y) coordinate for the site of stimulation.

By fitting the line of the SP in an image to an arc, the parameters of the center ($x_0$, $y_0$) and radius (r) of the arc were determined. Once these parameters were determined, we converted the CA1 region in the image to a rectangular area shown in the image of **Figure 3A**. **Figure 3B** shows an example of a fluorescent image of the CA1 area (**Figure 2A**) converted to the D-L coordinates. **Figure 3C** shows the propagation pattern of neuronal activity along the D-L axis. As can be clearly observed in the figure, excitation always ran parallel to the D axis, and excitation began at approximately 150 μm on the D axis.

The conversion (**Figure 3B**) allows us to evaluate image data from different slices in a normalized manner. **Figure 3C** represents an example of the propagation pattern of neuronal activity at four different time points (control, 2, 4 and 6 h). The figure shows that the fitting converted the propagation pattern along the Schaffer collateral to the straight line along the L axis. **Figure 3D** shows the peak values of the optical response at each pixel in the D-L coordinates, and **Figure 3E** shows the time change of the response for 10 h at pixels at different D-L coordinates. The amount of LTP varies depending on the D-L coordinates. **Figure 3F** indicates the uneven distribution of the LTP occurrence, where the pseudo-color code indicates the ratio of LTP at each D-L coordinate. **Figure 3G** shows the line profile of the amplitude of the response shown in **Figure 2D** at $D = -75$ μm (black; stratum oriens [SO]) and $D = 150$ μm (blue; stratum radiatum [SR]) for the control recording (open symbol) and recordings made at 2, 4 and 6 h from TBS (filled symbol). **Figure 3H** shows the ratio of LTP, that is, the line profiles in **Figure 3F** at the same D levels, and time. There was a clear peak in SO at $L = 775$ μm, while the SO signal showed a somewhat steady increase except for in the vicinity of the stimulation. The time course of the response at the representative pixel at $L = 500$ μm SO ($D = -75$ μm) and SR ($D = 150$ μm) and the corresponding point at $L = 775$ μm (**Figure 3I**) show the changes in the response. The signals in SO reflect the occurrence of the spikes. The results highlight the stability of the dynamics of the neural activity in the circuit- and layer-dependent changes in the occurrence of LTP.

## Grouped Data of TBS-Induced LTP

**Figure 4** summarizes the pooled data of the TBS-induced LTP in the D-L coordinates of 12 slices from four animals ($N = 4$, $n = 12$). LTP was more substantial in the SO and SP than in the SR, as shown in **Figure 4A**. **Figures 4C,D** demonstrate this phenomenon more clearly. Spatial heterogeneity also appears in the time course of LTP induction depending on the location along the L axis. That is, the LTP could not be clearly observed for smaller L (225 μm) but was more conspicuous for larger L (775 μm). To determine the change in the input-output (I-O) relationship in cells, we calculated the ratio of the peak values at the SO and the SR, which are shown in **Figure 4F** (i.e., the st. pyramidale-st. radiatum ratio ("PR-ratio"); Tominaga et al., 2009). The PR-ratio changed throughout the entire CA1 area along the L axis when TBS was applied to the Schaffer collateral.

## Comparison of TBS-Induced LTP With HFS-Induced LTP

Several publications highlight the difference between LTP induction and maintenance mechanisms depending on the induction stimulus (Larson and Lynch, 1986; Larson et al., 1986; Huerta and Lisman, 1995; Larson and Munkácsy, 2015). High-frequency stimulus (100 Hz, 1 s) is one of the most common LTP induction stimuli and is known as a "tetanic" stimulus. The maintenance phase of LTP depends on different mechanisms (Korte et al., 1995, 1998; Kang and Schuman, 1996; Smith et al., 2009; Edelmann et al., 2015). We also showed that the induction process of LTP was different depending on the induction stimulus: TBS augmented spike generation, while high-frequency stimulation (HFS) reduced spikes through a GABA-A-dependent mechanism (Tominaga et al., 2000, 2013; Tominaga and Ichikawa, 2002). Here, we compared the differences in LTP in the CA1 area, as shown in **Figure 4**. **Figure 5** illustrates the same experiment as shown in **Figure 4** except that the LTP induction stimulus was HFS.

Short-term potentiation is more explicit in HFS-induced LTP over the entire length of the L axis, while short-term potentiation was not clearly observed in TBS-induced LTP (compare **Figures 4A**, **5A**). The heterogeneous distribution of LTP followed a similar trend when comparing TBS-induced LTP with HFS-induced LTP (compare **Figures 4B,C** to **Figures 5B,C**). That is, the SO showed a more significant response than the SR. The PRR (**Figure 5F**) showed a transient increase at the distal ($L = 775$ μm) region, which differs from the TBS-induced change in PRR (**Figure 4F**).

These results indicate the differences in the spatiotemporal changes in LTP induction depending on the LTP induction stimulus.

## Examination of the Stimulus-Response Relationships During TBS-Induced LTP

The spatial heterogeneity in LTP induction might relate to the I-O relationship of each neuronal element. Hence, we measured LTP induced by four different stimulus intensities (10, 25, 40 and 60 V; **Figure 6**). **Figure 6A** represents the optically measured responses at the representative point at the middle of the D-L coordinates. Altering the stimulus intensity every 20 s resulted in the time change of the optically measured responses shown in **Figure 6A**. TBS (stimulus intensity of 25 V) induced a change in the I-O relationship. **Figure 6B** shows the same recordings at different points on the D-L coordinates. It is evident that the time course corresponding to a smaller stimulus intensity showed a more significant shift, while a higher stimulus intensity corresponded to a smaller shift (**Figures 6C,D**). **Figure 6D** summarizes the degree of LTP at different positions at each stimulus intensity at three different time points. As evident in the figure, for the higher stimulus intensity (60 V), LTP was not significant. At stimulus intensities of 40 and 25 V, the difference between the SR and the SO was evident, and LTP was more substantial in the distal region, as shown in **Figures 3**, **4**. For the smaller stimulus intensity, LTP was more substantial in the vicinity of the stimulus site (**Figure 6D**). This result may suggest that LTP was conspicuous when the first S-R relation was steep. The heterogeneity of LTP might, at least in part, reflect the original S-R relationship. The change in the PR-ratio was also evident at the middle stimulus intensity but was not evident at the weakest and strongest stimulus intensities (**Figure 6E**).

# DISCUSSION

We have described and demonstrated an optical recording method with VSD that allows us to record long-term modifications of neural circuits in slice preparations. In the present article, we measured changes accompanied by LTP induction in the CA1 area of mouse hippocampal slices to demonstrate the usefulness of the method. The results indicated that we could follow changes in neural activity in the CA1 area for a long period of time (12 h) with repetitive exposure of the excitation light needed to achieve recording at 0.1 ms/frame for 400 ms. The results show that the method can be successfully applied measure L-LTP (Huang et al., 1996; Kandel, 2001) in slice preparations. Additionally, we showed that the technique can be used to convert images from different slices for grouping according to the morphological background of the CA1 area. The method also highlights the difference in LTP induction by TBS and HFS (**Figures 4**, **5**). It was also shown that the LTP depend on the original stimulus-response relationship (**Figure 6**). The method will be useful for comparing slices in different test groups, such as genetic modifications, pharmacological treatments and other treatments that can affect hippocampal plasticity changes.

## Optical Recordings From Hippocampal Slices

Since earlier pioneering attempts to apply VSD imaging to mammalian brain tissue (Grinvald et al., 1982), hippocampal slice preparation has been a frequently employed. We can easily assign the optical signals of these preparations to specific membrane elements of the soma and dendrites due to the simple lamellar organization (Witter, 1993). Absorption dyes were often used to show the pharmacological effects of synaptic connections (Ratzlaff and Grinvald, 1991; Barish et al., 1996; Nakagami et al., 1997; Sekino et al., 1997; Kojima et al., 1999; Jin et al., 2002), and a fluorescent dye (Tominaga et al., 2000, 2002, 2013; Mann et al., 2005; Suh et al., 2011; Juliandi et al., 2016; Tominaga and Tominaga, 2016). Absorption dyes (primarily RH482; Momose-Sato et al., 1999; Mochida et al., 2001; Jin et al., 2002; Chang and Jackson, 2006; Chang et al., 2007; Wright and Jackson, 2014) and a fluorescent dye (Tominaga et al., 2000) have also been tried in long-term recordings.

We prefer using Di-4-ANNEPS (Fluhler et al., 1985; Loew et al., 1992) among several other types of fluorescent dyes. This dye is more highly soluble in lipid solutions than in aqueous solutions, which allows the dye to remain longer in the membrane. This characteristic is necessary to achieve long-term recordings, especially for *in vitro* preparations where the physiological solution continuously perfuses the brain slice and causes "washout" of the dye. The washout and unequal staining of slice preparations can cause changes in the signal magnitude that are not due to physiological activity. Fluorescent dyes are advantageous in this regard if the signal is measured relative to the initial amount of light. It is also noticeable that the time-course of the optical signal obtained with Di-4-ANEPPS is different from that recorded with some absorption dye [Grinvald et al., 1982; (RH-155) and Momose-Sato et al., 1999; NK3630 (RH482)]. The absorption dye recordings, especially RH-155, have optical components sensitive to dihydrokainate (DHK; an inhibitor for glial glutamate transporters GLT-1) application and thus include the glial signal (Kojima et al., 1999). The optical signal with Di-4-ANEPPS did not have such components (Tominaga et al., 2002). On the other hand, the absorption dye might have less phototoxicity because of its nature. Hence, one might need to choose which types of dye suit the experiments, depending on the purpose and the possible outcome of the measurements. If the recording system did not cause significant phototoxicity, the fluorescent dye would be better because of less contamination of the glial signal and other intrinsic optical components.

## Implication of Heterogeneity in LTP Induction

There were at least two spatial differences in the degree of LTP. The first is the difference between the SO-SP and the SR, that is, the SO-SP always showed higher LTP than the SR. The SO-SP optical signal mostly reflects the membrane potential events in the soma (Tominaga et al., 2009), which reflect the all-or-none action potential firing property, and thus, that the stimulus-response relationships have a steeper slope than the SR (Tominaga et al., 2000).

The other spatial difference is the L axis, that is, LTP at distal sites is more significant than at proximal sites. The increase in LTP depending on the distance from the stimulating site might reflect the increasing interneuron involvement in the circuit activity. Distant cells receive more inhibition than proximal cells, and this possibility must be tested in future research.

## TBS and HFS

Hippocampal LTP is believed to be a synaptic model of learning and memory (Bliss and Gardner-Medwin, 1973; Bliss and Collingridge, 1993). Tetanic HFS was the first stimulation paradigm that was used to induce LTP in the hippocampus circuit. However, there are arguments that the stimulation pattern is too artificial because such activity is not common *in vivo* in the brain. Rodents show theta activity while exploring novel objects, and the place cell is formed in the phase of these theta oscillation (O'Keefe and Dostrovsky, 1971; Larson and Munkácsy, 2015). The stimulation paradigm that mimics theta activity, i.e., TBS, successfully induced LTP in CA1 synapses (Larson and Lynch, 1986; Larson et al., 1986). TBS is believed to induce different types of LTP (Larson and Munkácsy, 2015).

During the induction phase of LTP, we found that TBS triggers more action potentials but that HFS suppresses action potentials during the stimulus (Tominaga et al., 2002). Both responses involve GABA-a receptor activation (Tominaga and Tominaga, 2010, 2016). The HFS primarily induces long-lasting depolarizing GABA-a potentials (Kaila et al., 1997, 2014; Voipio and Kaila, 2000), where increased conductance inhibits action potential firing by shunting (Tominaga and Tominaga, 2010).

In the present study, LTP induced by TBS and HFS showed different spatiotemporal patterns, and whether or not LTP differs during in the maintenance phase may be important.

## Applicability of the VSD Imaging Analysis of LTP

LTP remains a critical measure for assessing neural function in animal models of neuropsychiatric diseases, including AD and ASD (Monday and Castillo, 2017; Monday et al., 2018). The presented method allows detailed differences possibly caused by pathology and other factors to be shown. The spatiotemporal differences in LTP can introduce arbitrary error, showing differences in the assay that must be avoided.

The spatiotemporal differences in LTP reflect the E/I balance in the circuit. These diseases are closely related to the E/I balance of the circuit (Gogolla et al., 2009; Takesian and Hensch, 2013; Murray et al., 2014). Hence, the spatiotemporal pattern changes during LTP induction (Jackson, 2013; Stepan et al., 2015) could be an important target to measure the pathology of diseases.

Finally, the use of a genetically encoded voltage indicator (GEVI) could significantly advance this field through cell type-specific expression (Vranesic et al., 1994; Knöpfel, 2008, 2012).

# AUTHOR CONTRIBUTIONS

TT designed the research. YT, MT and TT performed the research. YT and TT developed the software and analyzed the data and wrote the article.

# FUNDING

TT received the JSPS KAKENHI Grant Number (JP16H06532, JP16K21743, JP16H06524, JP16K0038, JP15K00413) from MEXT and grants from the Ministry of Health, Labour and Welfare [MHLW-kagaku-ippan-H27 (15570760), H30 (18062156)].

# ACKNOWLEDGMENTS

We thank Dr. Michinori Ichikawa for discussion and help with system development. We also thank Ms. Naoko Maeda for technical assistance. This manuscript was edited for English language by American Journal Experts (AJE).

# REFERENCES

Anticevic, A., and Murray, J. D. (2017). Rebalancing altered computations: considering the role of neural excitation and inhibition balance across the psychiatric spectrum. *Biol. Psychiatry* 81, 816–817. doi: 10.1016/j.biopsych.2017.03.019

Barish, M. E., Ichikawa, M., Tominaga, T., Matsumoto, G., and Iijima, T. (1996). Enhanced fast synaptic transmission and a delayed depolarization induced by transient potassium current blockade in rat hippocampal slice as studied by optical recording. *J. Neurosci.* 16, 5672–5687. doi: 10.1523/JNEUROSCI.16-18-05672.1996

Bliss, T. V., and Collingridge, G. L. (1993). A synaptic model of memory: long-term potentiation in the hippocampus. *Nature* 361, 31–39. doi: 10.1038/361031a0

Bliss, T. V., and Gardner-Medwin, A. R. (1973). Long-lasting potentiation of synaptic transmission in the dentate area of the unanaesthetized rabbit following stimulation of the perforant path. *J. Physiol.* 232, 357–374. doi: 10.1113/jphysiol.1973.sp010274

Busche, M. A., and Konnerth, A. (2016). Impairments of neural circuit function in Alzheimer's disease. *Philos. Trans. R. Soc. B Biol. Sci.* 371:20150429. doi: 10.1098/rstb.2015.0429

Canitano, R., and Pallagrosi, M. (2017). Autism spectrum disorders and schizophrenia spectrum disorders: excitation/inhibition imbalance and developmental trajectories. *Front. Psychiatry* 8:69. doi: 10.3389/fpsyt.2017.00069

Chang, P. Y., and Jackson, M. B. (2006). Heterogeneous spatial patterns of long-term potentiation in rat hippocampal slices. *J. Physiol.* 576, 427–443. doi: 10.1113/jphysiol.2006.112128

Chang, P. Y., Taylor, P. E., and Jackson, M. B. (2007). Voltage imaging reveals the CA1 region at the CA2 border as a focus for epileptiform discharges and long-term potentiation in hippocampal slices. *J. Neurophysiol.* 98, 1309–1322. doi: 10.1152/jn.00532.2007

Cohen, L. B., Hille, B., and Keynes, R. D. (1970). Changes in axon birefringence during the action potential. *J. Physiol.* 211, 495–515. doi: 10.1113/jphysiol.1970.sp009289

Cohen, L. B., Keynes, R. D., and Hille, B. (1968). Light scattering and birefringence changes during nerve activity. *Nature* 218, 438–441. doi: 10.1038/218438a0

Davila, H. V., Salzberg, B. M., Cohen, L. B., and Waggoner, A. S. (1973). A large change in axon fluorescence that provides a promising method for measuring membrane potential. *Nat. New Biol.* 241, 159–160. doi: 10.1038/newbio241159a0

Edelmann, E., Cepeda-Prado, E., Franck, M., Lichtenecker, P., Brigadski, T., and Leßmann, V. (2015). Theta burst firing recruits BDNF release and signaling in postsynaptic CA1 neurons in spike-timing-dependent LTP. *Neuron* 86, 1041–1054. doi: 10.1016/j.neuron.2015.04.007

Fluhler, E., Burnham, V. G., and Loew, L. M. (1985). Spectra, membrane binding, and potentiometric responses of new charge shift probes. *Biochemistry* 24, 5749–5755. doi: 10.1021/bi00342a010

Gogolla, N., Leblanc, J. J., Quast, K. B., Südhof, T. C., Fagiolini, M., and Hensch, T. K. (2009). Common circuit defect of excitatory-inhibitory balance in mouse models of autism. *J. Neurodev. Disord.* 1, 172–181. doi: 10.1007/s11689-009-9023-x

Grinvald, A., Cohen, L. B., Lesher, S., and Boyle, M. B. (1981). Simultaneous optical monitoring of activity of many neurons in invertebrate ganglia using a 124-element photodiode array. *J. Neurophysiol.* 45, 829–840. doi: 10.1152/jn.1981.45.5.829

Grinvald, A., Frostig, R. D., Lieke, E., and Hildesheim, R. (1988). Optical imaging of neuronal activity. *Physiol. Rev.* 68, 1285–1366. doi: 10.1152/physrev.1988.68.4.1285

Grinvald, A., Manker, A., and Segal, M. (1982). Visualization of the spread of electrical activity in rat hippocampal slices by voltage-sensitive optical probes. *J. Physiol.* 333, 269–291. doi: 10.1113/jphysiol.1982.sp014453

Habib-E-Rasul Mullah, S., Komuro, R., Yan, P., Hayashi, S., Inaji, M., Momose-Sato, Y., et al. (2013). Evaluation of voltage-sensitive fluorescence dyes for monitoring neuronal activity in the embryonic central nervous system. *J. Membr. Biol.* 246, 679–688. doi: 10.1007/s00232-013-9584-1

Hájos, N., Ellender, T. J., Zemankovics, R., Mann, E. O., Exley, R., Cragg, S. J., et al. (2009). Maintaining network activity in submerged hippocampal slices: importance of oxygen supply. *Eur. J. Neurosci.* 29, 319–327. doi: 10.1111/j.1460-9568.2008.06577.x

Hill, D. K., and Keynes, R. D. (1949). Opacity changes in stimulated nerve. *J. Physiol.* 108, 278–281. doi: 10.1113/jphysiol.1949.sp004331

Huang, Y. Y., Nguyen, P. V., Abel, T., and Kandel, E. R. (1996). Long-lasting forms of synaptic potentiation in the mammalian hippocampus. *Learn. Mem.* 3, 74–85. doi: 10.1101/lm.3.2-3.74

Huerta, P. T., and Lisman, J. E. (1995). Bidirectional synaptic plasticity induced by a single burst during cholinergic theta oscillation in CA1 *in vitro*. *Neuron* 15, 1053–1063. doi: 10.1016/0896-6273(95)90094-2

Ichikawa, M., Iijima, T., Matsumoto, G., and Ono, T. (1993). "Real-time optical recording of neuronal activities in the brain," in *Brain Mechanisms of Perception and Memory*, eds T. Ono, L. R. Squire, M. E. Raichle, D. I. Perrett and M. Fukuda (New York, NY: Oxford University Press), 638–648.

Isaacson, J. S., and Scanziani, M. (2011). How inhibition shapes cortical activity. *Neuron* 72, 231–243. doi: 10.1016/j.neuron.2011.09.027

Jackson, M. B. (2013). Recall of spatial patterns stored in a hippocampal slice by long-term potentiation. *J. Neurophysiol.* 110, 2511–2519. doi: 10.1152/jn.00533.2013

Jin, W., Zhang, R.-J., and Wu, J. Y. (2002). Voltage-sensitive dye imaging of population neuronal activity in cortical tissue. *J. Neurosci. Methods* 115, 13–27. doi: 10.1016/s0165-0270(01)00511-8

Juliandi, B., Tanemura, K., Igarashi, K., Tominaga, T., Furukawa, Y., Otsuka, M., et al. (2016). Reduced adult hippocampal neurogenesis and cognitive impairments following prenatal treatment of the antiepileptic drug valproic acid. *Stem Cell Reports* 5, 996–1009. doi: 10.1016/j.stemcr.2015.10.012

Kaila, K., Lamsa, K., Smirnov, S., Taira, T., and Voipio, J. (1997). Long-lasting GABA-mediated depolarization evoked by high-frequency stimulation in pyramidal neurons of rat hippocampal slice is attributable to a network-driven, bicarbonate-dependent $K^+$ transient. *J. Neurosci.* 17, 7662–7672. doi: 10.1523/JNEUROSCI.17-20-07662.1997

Kaila, K., Ruusuvuori, E., Seja, P., Voipio, J., and Puskarjov, M. (2014). GABA actions and ionic plasticity in epilepsy. *Curr. Opin. Neurobiol.* 26, 34–41. doi: 10.1016/j.conb.2013.11.004

Kandel, E. R. (2001). The molecular biology of memory storage: a dialogue between genes and synapses. *Science* 294, 1030–1038. doi: 10.1126/science.1067020

Kang, H., and Schuman, E. M. (1996). A requirement for local protein synthesis in neurotrophin-induced hippocampal synaptic plasticity. *Science* 273, 1402–1406. doi: 10.1126/science.273.5280.1402

Knöpfel, T. (2008). Expanding the toolbox for remote control of neuronal circuits. *Nat. Methods* 5, 293–295. doi: 10.1038/nmeth0408-293

Knöpfel, T. (2012). Genetically encoded optical indicators for the analysis of neuronal circuits. *Nat. Rev. Neurosci.* 13, 687–700. doi: 10.1038/nrn3293

Kojima, S., Nakamura, T., Nidaira, T., Nakamura, K., Ooashi, N., Ito, E., et al. (1999). Optical detection of synaptically induced glutamate transport in hippocampal slices. *J. Neurosci.* 19, 2580–2588. doi: 10.1523/JNEUROSCI.19-07-02580.1999

Korte, M., Carroll, P., Wolf, E., Brem, G., Thoenen, H., and Bonhoeffer, T. (1995). Hippocampal long-term potentiation is impaired in mice lacking brain-derived neurotrophic factor. *Proc. Natl. Acad. Sci. U S A* 92, 8856–8860. doi: 10.1073/pnas.92.19.8856

Korte, M., Kang, H., Bonhoeffer, T., and Schuman, E. (1998). A role for BDNF in the late-phase of hippocampal long-term potentiation. *Neuropharmacology* 37, 553–559. doi: 10.1016/s0028-3908(98)00035-5

Larson, J., and Lynch, G. (1986). Induction of synaptic potentiation in hippocampus by patterned stimulation involves two events. *Science* 232, 985–988. doi: 10.1126/science.3704635

Larson, J., and Munkácsy, E. (2015). Theta-burst LTP. *Brain Res.* 1621, 38–50. doi: 10.1016/j.brainres.2014.10.034

Larson, J., Wong, D., and Lynch, G. (1986). Patterned stimulation at the theta frequency is optimal for the induction of hippocampal long-term potentiation. *Brain Res.* 368, 347–350. doi: 10.1016/0006-8993(86)90579-2

Loew, L., Cohen, L., Dix, J., Fluhler, E., Montana, V., Salama, G., et al. (1992). A naphthyl analog of the aminostyryl pyridinium class of potentiometric membrane dyes shows consistent sensitivity in a variety of tissue, cell, and model membrane preparations. *J. Membr. Biol.* 130, 1–10. doi: 10.1007/bf00233734

Mann, E. O., Tominaga, T., Ichikawa, M., and Greenfield, S. A. (2005). Cholinergic modulation of the spatiotemporal pattern of hippocampal activity *in vitro*. *Neuropharmacology* 48, 118–133. doi: 10.1016/j.neuropharm.2004.08.022

Mochida, H., Sato, K., Sasaki, S., Yazawa, I., Kamino, K., and Momose-Sato, Y. (2001). Effects of anisomycin on LTP in the hippocampal CA1: long-term analysis using optical recording. *Neuroreport* 12, 987–991. doi: 10.1097/00001756-200104170-00025

Momose-Sato, Y., Sato, K., Arai, Y., Yazawa, I., Mochida, H., and Kamino, K. (1999). Evaluation of voltage-sensitive dyes for long-term recording of neural activity in the hippocampus. *J. Membr. Biol.* 172, 145–157. doi: 10.1007/s002329900592

Monday, H. R., and Castillo, P. E. (2017). Closing the gap: long-term presynaptic plasticity in brain function and disease. *Curr. Opin. Neurobiol.* 45, 106–112. doi: 10.1016/j.conb.2017.05.011

Monday, H. R., Younts, T. J., and Castillo, P. E. (2018). Long-term plasticity of neurotransmitter release: emerging mechanisms and contributions to brain function and disease. *Annu. Rev. Neurosci.* 41, 299–322. doi: 10.1146/annurev-neuro-080317-062155

Murray, J. D., Anticevic, A., Gancsos, M., Ichinose, M., Corlett, P. R., Krystal, J. H., et al. (2014). Linking microcircuit dysfunction to cognitive impairment: effects of disinhibition associated with schizophrenia in a cortical working memory model. *Cereb. Cortex* 24, 859–872. doi: 10.1093/cercor/bhs370

Nakagami, Y., Saito, H., and Matsuki, N. (1997). Optical recording of trisynaptic pathway in rat hippocampal slices with a voltage-sensitive dye. *Neuroscience* 81, 1–8. doi: 10.1016/s0306-4522(97)00161-9

Nishimura, M., Shirasawa, H., and Song, W.-J. (2006). A light-emitting diode light source for imaging of neural activities with voltage-sensitive dyes. *Neurosci. Res.* 54, 230–234. doi: 10.1016/j.neures.2005.12.002

O'Keefe, J., and Dostrovsky, J. (1971). The hippocampus as a spatial map. Preliminary evidence from unit activity in the freely-moving rat. *Brain Res.* 34, 171–175. doi: 10.1016/0006-8993(71)90358-1

Persico, A. M., and Bourgeron, T. (2006). Searching for ways out of the autism maze: genetic, epigenetic and environmental clues. *Trends Neurosci.* 29, 349–358. doi: 10.1016/j.tins.2006.05.010

Peterka, D. S., Takahashi, H., and Yuste, R. (2011). Imaging voltage in neurons. *Neuron* 69, 9–21. doi: 10.1016/j.neuron.2010.12.010

Ratzlaff, E. H., and Grinvald, A. (1991). A tandem-lens epifluorescence macroscope: hundred-fold brightness advantage for wide-field imaging. *J. Neurosci. Meth.* 36, 127–137. doi: 10.1016/0165-0270(91)90038-2

Ross, W. N., Salzberg, B. M., Cohen, L. B., and Davila, H. V. (1974). A large change in dye absorption during the action potential. *Biophys. J.* 14, 983–986. doi: 10.1016/s0006-3495(74)85963-1

Sekino, Y., Obata, K., Tanifuji, M., Mizuno, M., and Murayama, J. (1997). Delayed signal propagation via CA2 in rat hippocampal slices revealed by optical recording. *J. Neurophysiol.* 78, 1662–1668. doi: 10.1152/jn.1997.78.3.1662

Smith, J. P., Lal, V., Bowser, D., Cappai, R., Masters, C. L., and Ciccotosto, G. D. (2009). Stimulus pattern dependence of the Alzheimer's disease amyloid-42 peptide's inhibition of long term potentiation in mouse hippocampal slices. *Brain Res.* 1269, 176–184. doi: 10.1016/j.brainres.2009.03.007

Stepan, J., Dine, J., and Eder, M. (2015). Functional optical probing of the hippocampal trisynaptic circuit *in vitro*: network dynamics, filter properties, and polysynaptic induction of CA1 LTP. *Front. Neurosci.* 9:160. doi: 10.3389/fnins.2015.00160

Suh, J., Rivest, A. J., Nakashiba, T., Tominaga, T., and Tonegawa, S. (2011). Entorhinal cortex layer III input to the hippocampus is crucial for temporal association memory. *Science* 334, 1415–1420. doi: 10.1126/science.1210125

Takesian, A. E., and Hensch, T. K. (2013). Balancing plasticity/stability across brain development. *Prog. Brain Res.* 207, 3–34. doi: 10.1016/B978-0-444-63327-9.00001-1

Tanemura, K., Murayama, M., Akagi, T., Hashikawa, T., Tominaga, T., Ichikawa, M., et al. (2002). Neurodegeneration with tau accumulation in a transgenic mouse expressing V337M human tau. *J. Neurosci.* 22, 133–141. doi: 10.1523/JNEUROSCI.22-01-00133.2002

Tominaga, T., and Ichikawa, M. (2002). Experimental apparatus for sliced specimen of biological tissue and specimen holder. *U.S. Patent* US 6,448,063 B2.

Tominaga, Y., Ichikawa, M., and Tominaga, T. (2009). Membrane potential response profiles of CA1 pyramidal cells probed with voltage-sensitive dye optical imaging in rat hippocampal slices reveal the impact of GABA$_A$-mediated feed-forward inhibition in signal propagation. *Neurosci. Res.* 64, 152–161. doi: 10.1016/j.neures.2009.02.007

Tominaga, T., Kajiwara, R., and Tominaga, Y. (2013). VSD imaging method of *ex vivo* brain preparation. *J. Neurosci. Neuroeng.* 2, 211–219. doi: 10.1166/jnsne.2013.1051

Tominaga, T., and Tominaga, Y. (2010). GABAA receptor-mediated modulation of neuronal activity propagation upon tetanic stimulation in rat hippocampal slices. *Pflugers Arch.* 460, 875–889. doi: 10.1007/s00424-010-0870-9

Tominaga, T., and Tominaga, Y. (2016). Paired burst stimulation causes GABA$_A$ receptor-dependent spike firing facilitation in CA1 of rat hippocampal slices. *Front. Cell. Neurosci.* 10:9. doi: 10.3389/fncel.2016.00009

Tominaga, T., Tominaga, Y., and Ichikawa, M. (2002). Optical imaging of long-lasting depolarization on burst stimulation in area CA1 of rat hippocampal slices. *J. Neurophysiol.* 88, 1523–1532. doi: 10.1152/jn.2002.88.3.1523

Tominaga, T., Tominaga, Y., Yamada, H., Matsumoto, G., and Ichikawa, M. (2000). Quantification of optical signals with electrophysiological signals in neural activities of Di-4-ANEPPS stained rat hippocampal slices. *J. Neurosci. Methods* 102, 11–23. doi: 10.1016/s0165-0270(00)00270-3

Uhlhaas, P. J., and Singer, W. (2012). Neuronal dynamics and neuropsychiatric disorders: toward a translational paradigm for dysfunctional large-scale networks. *Neuron* 75, 963–980. doi: 10.1016/j.neuron.2012.09.004

Voipio, J., and Kaila, K. (2000). GABAergic excitation and K$^+$-mediated volume transmission in the hippocampus. *Prog. Brain Res.* 125, 329–338. doi: 10.1016/s0079-6123(00)25022-x

Vranesic, I., Iijima, T., Ichikawa, M., Matsumoto, G., and Knöpfel, T. (1994). Signal transmission in the parallel fiber-Purkinje cell system visualized by high-resolution imaging. *Proc. Natl. Acad. Sci. U S A* 91, 13014–13017. doi: 10.1073/pnas.91.26.13014

Witter, M. P. (1993). Organization of the entorhinal—hippocampal system: a review of current anatomical data. *Hippocampus* 3, 33–44.

Wright, B. J., and Jackson, M. B. (2014). Long-term potentiation in hilar circuitry modulates gating by the dentate gyrus. *J. Neurosci.* 34, 9743–9753. doi: 10.1523/JNEUROSCI.0814-14.2014

**Conflict of Interest Statement**: The authors declare that the research was conducted in the absence of any commercial or financial relationships that could be construed as a potential conflict of interest.

frontiers
in Cellular Neuroscience

ORIGINAL RESEARCH
published: 05 December 2018
doi: 10.3389/fncel.2018.00465

# Photolysis of a Caged, Fast-Equilibrating Glutamate Receptor Antagonist, MNI-Caged γ-D-Glutamyl-Glycine, to Investigate Transmitter Dynamics and Receptor Properties at Glutamatergic Synapses

***Francisco Palma-Cerda[1], George Papageorgiou[2], Boris Barbour[3], Céline Auger[1] and David Ogden[1,2]****

*[1]Brain Physiology Lab, UMR8118 Université Paris Descartes, Paris, France, [2]The Francis Crick Institute, London, United Kingdom, [3]Institut de Biologie de l'Ecole Normale Supérieure (IBENS), Ecole Normale Supérieure, CNRS, INSERM, PSL University, Paris, France*

***Edited by:***
*Marco Canepari,*
*UMR5588 Laboratoire*
*Interdisciplinaire de Physique (LIPhy),*
*France*

***Reviewed by:***
*Annalisa Scimemi,*
*University at Albany, United States*
*Julie Perroy,*
*Centre National de la Recherche*
*Scientifique (CNRS), France*

****Correspondence:***
*David Ogden*
*david.ogden@parisdescartes.fr*

***Received:*** *01 August 2018*
***Accepted:*** *15 November 2018*
***Published:*** *05 December 2018*

***Citation:***
*Palma-Cerda F, Papageorgiou G, Barbour B, Auger C and Ogden D (2018) Photolysis of a Caged, Fast-Equilibrating Glutamate Receptor Antagonist, MNI-Caged γ-D-Glutamyl-Glycine, to Investigate Transmitter Dynamics and Receptor Properties at Glutamatergic Synapses.*
*Front. Cell. Neurosci. 12:465.*
*doi: 10.3389/fncel.2018.00465*

Fast uncaging of low affinity competitive receptor antagonists can in principle measure the timing and concentration dependence of transmitter action at receptors during synaptic transmission. Here, we describe the development, synthesis and characterization of MNI-caged γ-D-glutamyl-glycine (γ-DGG), which combines the fast photolysis and hydrolytic stability of nitroindoline cages with the well-characterized fast-equilibrating competitive glutamate receptor antagonist γ-DGG. At climbing fiber-Purkinje cell (CF-PC) synapses MNI-caged-γ-DGG was applied at concentrations up to 5 mM without affecting CF-PC transmission, permitting release of up to 1.5 mM γ-DGG in 1 ms in wide-field flashlamp photolysis. In steady-state conditions, photoreleased γ-DGG at 0.55–1.7 mM inhibited the CF first and second paired EPSCs by on average 30% and 60%, respectively, similar to reported values for bath applied γ-DGG. Photolysis of the L-isomer MNI-caged γ-L-glutamyl-glycine was ineffective. The time-course of receptor activation by synaptically released glutamate was investigated by timed photolysis of MNI-caged-γ-DGG at defined intervals following CF stimulation in the second EPSCs. Photorelease of γ-DGG prior to the stimulus and up to 3 ms after showed strong inhibition similar to steady-state inhibition; in contrast γ-DGG applied by a flash at 3–4 ms post-stimulus produced weaker and variable block, suggesting transmitter-receptor interaction occurs mainly in this time window. The data also show a small and lasting component of inhibition when γ-DGG was released at 4–7 ms post stimulus, near the peak of the CF-PC EPSC, or at 10–11 ms. This indicates that competition for binding and activation of AMPA receptors occurs also during the late phase of the EPSC, due to either delayed transmitter release or persistence of glutamate in the synaptic region. The results presented here first show that MNI-caged-γ-DGG has properties suitable for use as a synaptic probe at high concentration and that its photolysis can resolve timing and extent of transmitter activation of receptors in glutamatergic transmission.

**Keywords: photolysis, synaptic transmission, caged fast antagonist, glutamate receptor, climbing fiber, Purkinje cell, cerebellum, nitroindoline**

## INTRODUCTION

The time scale and spatial distribution of transmitter release are important in determining both the speed and independence of information transfer between pre- and postsynaptic elements in synaptic transmission. Synapses with a single or few release sites and short-lived transmitter transients show greater independence and postsynaptic specificity than multisite synapses that activate a larger postsynaptic volume. This distinction has been formalized as synaptic vs. parasynaptic ("spillover" or volume transmission; Szapiro and Barbour, 2007, 2009; Coddington et al., 2014) and relates directly to the time for which transmitter interacts with postsynaptic receptors following release. Fast, timed application of an antagonist to the post-synaptic receptors would enable dissection of the time-course of receptor activation to distinguish modes of transmission. However, there are few examples of caged photolabile derivatives of receptor antagonists applied in neuroscience, although they are potentially useful tools in probing synaptic function on the time scale of transmission. They offer the possibility of timed release and competition with transmitter binding at postsynaptic receptors, thereby giving time-resolved data of transmitter concentration at the target receptors. With further development of selective ligands there is the possibility of targeting specific signaling pathways as has been done with selective agonists (Palma-Cerda et al., 2012).

To be useful caged antagonists require fast photochemistry relative to the synaptic timescale, with uncaging rates >10,000 $s^{-1}$ following a light pulse. Additionally, to facilitate repeated applications in wide-field photolysis, it is also desirable that the photoreleased antagonist dissociates rapidly from receptors, requiring a low affinity, contrary to the high affinity generally useful for pharmacological studies at synapses. Because of the dependence of block on transmitter concentration, the low affinity competitive receptor antagonists also permit a measure of the relative concentration of the competing neurotransmitter during transmission. Here, we report the development and application of a fast-equilibrating caged glutamate receptor antagonist to study excitatory synaptic mechanisms. Photolysis is with the well-established nitroindoline photochemistry, which is both fast (half-time for release 0.15 μs; Morrison et al., 2002) and stable to hydrolysis (Papageorgiou et al., 1999). Nitroindoline photochemistry has been applied to synaptic physiology since 1999 and is well established as an effective experimental tool in neuroscience.

Previous use of the low-affinity antagonist γ-D-glutamylglycine (γ-DGG, Davies and Watkins, 1981) has been in the analysis of L-glutamate concentration and time-course at synapses. In one study, Liu et al. (1999) applied a concentration-ratio analysis to show low affinity competitive antagonism by γ-DGG with L-glutamate at hippocampal AMPA-R synapses (estimated equilibrium dissociation constant $K$ = 0.55 mM) and used the dependence of block on glutamate concentration to show fast equilibration of γ-DGG with receptors. At climbing fiber-Purkinje cell (CF-PC) synapses Wadiche and Jahr (2001) used the glutamate concentration dependence of γ-DGG block to test multivesicular release during paired responses. The analysis was based on fast application patch data and kinetic simulations, estimating a fast dissociation rate constant of $10^4$ $s^{-1}$. The use of low affinity antagonists to assess neurotransmitter concentration and time-course (Clements et al., 1992) has been evaluated by Beato (2008) at glycinergic synapses and reviewed by Scimemi and Beato (2009). In simulations they showed a correlation between transmitter concentration and exposure time that prevents separate determination and requires additional information, such as the effects of transporter inhibition, to obtain independent parameter estimate. Furthermore, independent determination of the postsynaptic gating properties is required for analysis to estimate transmitter timing and concentration; these are usually obtained from patch experiments and do not take account of possible differences between excised patch and post-synaptic receptor properties, resulting for instance from different receptor subunit/auxiliary protein compositions. In this context the precise timing and quantitation of photorelease proposed here would be useful since data are gathered at the synapse of interest.

In this report, we describe the chemical synthesis and characterization of MNI-caged γ-DGG and tests for interference with synaptic transmission at high (mM) concentration at cerebellar climbing fiber to Purkinje cell synapses. Both enantiomers γ-DGG and γ-LGG were prepared in caged form. The latter endogenous dipeptide (Kanazawa et al., 1965) served as a readily available model reagent in the synthesis and has been reported to have a lower affinity for glutamate receptors (Francis et al., 1980; Davies and Watkins, 1981), making it useful as a control probe. Structures of the two caged compounds are shown in the **Supplementary Information**. The results show that MNI-caged γ-DGG can be used at concentrations up to 5 mM to release mM concentrations by flashlamp or laser photolysis and that timing of competition with synaptic L-glutamate can be resolved with 1 ms precision with flashlamp photolysis. This article describes the properties of MNI-caged γ-DGG in relation to synaptic investigations and presents results of transmitter timing and duration at the CF-PC synapse with wide-field flashlamp photolysis. Photolysis of MNI-caged amino acids is readily adapted to localized laser photolysis (Trigo et al., 2009) to yield faster time and better spatial resolution.

# MATERIALS AND METHODS

## Ethical Approval

Sprague–Dawley rats were provided by Janvier (St Berthevin, France) and subsequently housed in agreement with the European Directive 2010/63/UE regarding the protection of animals used for experimental and other scientific purposes. Experimental procedures were approved by the French Ministry of Research and the ethical committee for animal experimentation of Paris Descartes.

## Slice Preparation

Experiments were made with parasagittal slices 200 μm thick cut from the cerebellum of Sprague-Dawley rats, age 12–21 days. Slices were prepared and stored at 34°C throughout in a solution containing (mM): 115 NaCl, 2.5 KCl, 1.3 $NaH_2PO_4$, 26 $NaHCO_3$, 0.1 L-ascorbic acid, 25 glucose, 1 $MgSO_4$, 2 $CaCl_2$ equilibrated with 95% $O_2$–5% $CO_2$.

## Electrophysiological Recording

A Hepes-buffered saline was used containing a low concentration of bicarbonate to maintain intracellular pH, composition (mM): 130 NaCl, 4 KCl, 2.5 $NaHCO_3$, 10 Hepes, 25 glucose, 0.1 ascorbic acid, 1 mM $MgSO_4$ and 2 mM $CaCl_2$, pH 7.3 with NaOH, perfused at 5 mL/min. Once a recording was established perfusion was stopped and the cage, dissolved at 20 mM in Hepes-buffered isotonic saline, added to the bath volume. Air was blown over the surface of the static bath solution to produce mixing of the caged compound; ambient $pCO_2$ is equilibrated at 2.5 mM bicarbonate and pH is controlled by Hepes. The presence of bicarbonate facilitates intracellular pH regulation by $CO_2$ diffusion across the membrane. The intracellular solution for Purkinje neurons was (in mM): 150 K gluconate, 10 Hepes, 0.01 EGTA, 2.5 $MgCl_2$, 2 $ATPNa_2$ and 0.4 GTPNa, 5 mM QX314, pH adjusted to 7.3 with KOH and osmolality to 300 mosmol/kg. Alexa 488 20 μM was included to record cell morphology (Andor Ixon EMCCD; Oxford, UK). Recordings were at 21–24°C. The preparation was viewed with a Zeiss Axioskop1FS (Oberkochen, Germany) with Olympus 40× 0.8w objective. To avoid photolysis, transmitted illumination was long pass filtered at 425 nm. The optical arrangement is described in **Supplementary Figure S2**.

Recording pipettes had resistances of 2.5–3.5 MΩ. Whole cell voltage clamp recordings from Purkinje neurons were with an Axopatch 200B amplifier (Molecular Devices, San Jose, CA, USA). Series resistance was 7–10 MΩ and compensated 60%–80%. The pipette potential was held at −60 to −30 mV, data were not corrected for the junction potential of 12 mV. Data acquisition was with a CED P1401 interface (Cambridge Electronic Design, Cambridge, UK) LP filtered at 3 kHz, sampled at 50 kHz with WINWCP (Dr. John Dempster, University of Strathclyde) and analyzed in Igor Pro 7 (Wavemetrics, Lake Oswego, OR, USA).

For climbing fiber (CF) stimulation, cathodal pulses of 50 μs duration and supramaximal amplitude were delivered from a constant voltage stimulator (DS2, Digitimer, Welwyn UK) through glass pipettes with 2 MΩ resistance filled with bath solution, positioned at the surface of the slice in the granule cell layer. Voltage thresholds were 30–70 V (15–35 μA) determined regularly during recordings. The stimulus comprised two pulses separated by 40 ms or 150 ms to test paired pulse depression. To inhibit Na-current in the Purkinje neuron with CF stimulation the intracellular solution contained 5 mM QX314.HCl salt. The extracellular solution was supplemented with 3 μM SR 95531 and 50 μM D-AP5 to block GABAA and NMDA receptors, respectively, or as specified in Figure legends.

## Flash Photolysis

Flash photolysis was through the condenser of the transmitted light path with a Xenon Arc Flashlamp (Rapp Optoelectronic, Hamburg, Germany) producing a 0.5–1.5 ms light pulse, bandpass filtered 275–395 nm, energy measured as 120 mJ on discharge at 300V with three capacitors. Because of the high cage concentration it is not feasible to use epi-illumination for near UV wide spectrum photolysis, the light is absorbed too strongly by mM cage over 3 mm pathlength. The optical arrangement and calibration procedures are summarized in **Supplementary Figure S2**. The flashlamp was coupled with a 3 mm liquid light guide into the transmitted-illumination path by a silica lens and 425 nm LP dichroic reflector and focused by a silica condenser through the slice to illuminate uniformly a 200 μm diameter region at the top surface. Calibration of photolysis was in separate experiments by comparison with photolysis of caged fluorophore NPE-HPTS (the nitrophenylethyl ether of HPTS) which becomes fluorescent on uncaging to release free HPTS (exc 470/40 nm, em 525/50 nm; see **Supplementary Figure S2** caption in **Supplementary Information**; also Canepari et al., 2001). Briefly, NPE-HPTS at 100 μM in borate buffer (10 mM pH 9) is suspended by stirring into Sylgard 184 resin to form vesicles of 5–20 μm diameter that cure to form a thin layer on coverslips. The progressive increase in fluorescence in each vesicle with consecutive flashlamp pulses depends on the efficiency of photolysis in the microscope at the flashlamp parameters used, the conversion/flash obtained by fitting an exponential under conditions where bleaching of released HPTS is minimal. The conversion of MNI-glutamate relative to NPE-HPTS with wide-field flashlamp illumination and band-pass near UV filter was determined as 2.1, and will be the same for MNI-caged γ-DGG or MNI-caged γ-LGG, since no additional chromophores are present. A further correction was applied for transmission of photolysis light through the slice, estimated from transmission of the flashlamp pulse as 32% in the molecular layer of cerebellar slices 200 μm thick from 18 day rats, 40% at 15 days and 44% at 13 days. At the end of the experiment the bath concentration of MNI-γ-DGG was measured in a microliter spectrophotometer (Nanodrop, ThermoFisher Scientific) from the absorbance at 322 nm with molar absorption coefficient 4800 $M^{-1}cm^{-1}$. To obtain the concentration released, the cage concentration was multiplied by the conversion/flash of NPE-HPTS at the flash intensity used, multiplied by the factor of 2.1 for relative efficiencies of MNI-glutamate to NPE-HPTS with this excitation spectrum, and by the transmission factor through the slice dependent on the age of the animal. Measurements of several vesicles in the microscope field showed that photolysis was uniform over the 200 μm field viewed by the camera (Andor Ixon, Oxford Instruments, Oxford, UK). Conversion efficiencies for MNI-caged-γ-DGG at the flashlamp settings used here, as in **Figures 1A,B**, were estimated as 14%/flash for 300 V one capacitor and 30%/flash for 300 V three capacitors in 13-day 200-μm thick slices.

## Drugs

Drugs used were D-AP5, SR 95531, NBQX, Cyclothiazide, Amiloride and QX314.HCl from Tocris Bioscience UK or Sigma-Aldrich.

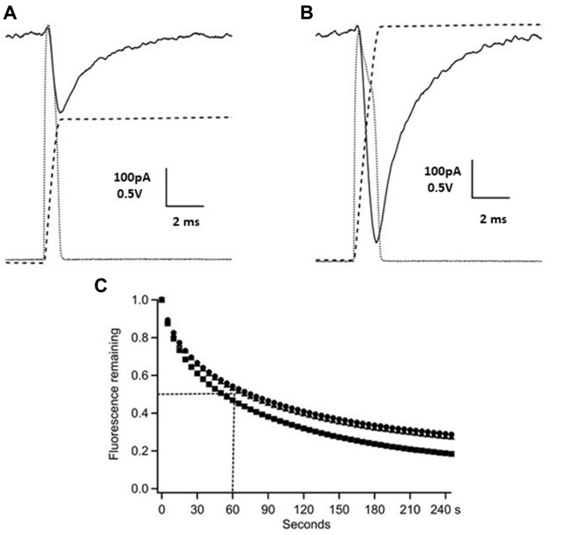

**FIGURE 1 |** Time-course of γ-D-glutamyl-glycine (γ-DGG) concentration during and following photorelease. Panels **(A,B)** show photodiode records of the flash (dotted gray traces, scale bar 0.5 V) and their integrals over the pulse representing the time-course of the γ-DGG concentration (dashed traces), and the whole cell current generated by photolysis of MNI-caged γ-DGG in a Purkinje neuron at −60 mV (black traces, scale bar 100 pA). Panel **(A)** shows the response to a low intensity flash as used in synaptic experiments, producing 14% conversion to release γ-DGG and proton concentrations of 0.65 mM. Panel **(B)** shows the response to a strong flash releasing 1.3 mM γ-DGG and protons. The bath concentration of MNI-caged γ-DGG was 4.6 mM in **(A,B)**. **(C)** Following wide-field photolysis of NPE-HPTS the time-course of diffusional loss of HPTS fluorescence was monitored from a region defined by an aperture in a conjugate image plane corresponding to 10 μm in the slice. HPTS and amino acids have similar diffusion coefficients in extracellular space. A single flash released HPTS from 100 μM NPE-HPTS equilibrated in the slice. Fluorescence of photoreleased HPTS (em 525/50 nm) from the 10 μm spot was measured every 5 s thereafter, corrected for background counts and normalized to the maximum fluorescence immediately after the flash. The data are from three trials, the dotted lines show the mean half-time for the fluorescence decline, estimated as 60 s; the time-course is expected to be similar for photoreleased γ-DGG.

## Chemical Synthesis and Photochemistry of MNI-Caged γ-D-Glutamylglycine

Synthesis and purification of both D and L optical isomers of MNI-caged γ-glutamylglycine were based on published protocols for MNI-glycine (Papageorgiou et al., 2011) and for substituted nitroindolines (Papageorgiou and Corrie, 2000). Full experimental details of the synthesis of the two isomers and their structural verification are given in the **Supplementary Information (Data sheet 1)**, together with circular dichroism spectra (**Supplementary Figure S1**) to confirm the configurations. The photocleavage reaction is outlined in **Scheme 1** (below).

# RESULTS

## Time-Course of γ-DGG Concentration Following Photorelease From MNI-Caged γ-DGG

Flashlamp photolysis releases ligand over a large field and it is important for interpretation of results to know the time-course of release and the persistence of released γ-DGG in the photolysis region. The release of carboxylate ligands from nitroindoline-caged precursors was shown by nanoseconds laser flash photolysis to have a halftime of 150 ns (Morrison et al., 2002). Thus, on the 0.1 ms timescale relevant for synaptic function, photolysis closely follows the light intensity, the quantity of γ-DGG released and its concentration in the irradiated volume are given by the time integral of the flash. A photodiode was used to monitor light intensity applied by photolysis. The photodiode output (dotted gray traces) and their integral (dashed traces) are shown in **Figure 1** for low (300 V, one capacitor, panel **A**) and high energy (three capacitors, panel **B**) flashes. Simultaneous voltage clamp recording in the Purkinje neuron shows transient current (black solid traces) evoked by photolysis; these are discussed below. The γ-DGG concentrations immediately after the flash were calculated from the photolysis efficiency at the flashlamp energy used and the bath concentration of MNI-caged γ-DGG measured by spectrometry at the end of the recording. The photolysis efficiencies were calculated for low or high flash energy from independent experiments in the same microscope as described above in the "Materials and Methods" section and in **Supplementary Information**.

## Time-Course of Diffusional Loss of Photoreleased γ-DGG From the Irradiated Region

After fast release the concentration of γ-DGG in the region of the Purkinje neuron will decline by diffusional exchange of photoreleased γ-DGG between the irradiated volume, approximately 10 μl, and the bulk bath volume of 1.5 ml. This will determine the concentration of γ-DGG adjacent to synaptic sites with time following photorelease. The highly polar fluorophore HPTS (pyranine) photoreleased in extracellular space has previously been used to measure diffusion within tissues (Xia et al., 1998); it has a diffusion coefficient

330 $\mu m^2 s^{-1}$, similar to that estimated for synaptic L-glutamate (Nielsen et al., 2004). HPTS was photoreleased from NPE-caged-HPTS releasing fluorophore quickly and uniformly over the field of view (rate of photolysis of 550 $s^{-1}$ at pH 7 following the flash; Jasuja et al., 1999). The fluorescence was monitored after the flash at 5 s intervals with 100 ms camera frames over an aperture placed in a conjugate image plane corresponding to 10 μm (referred to the specimen plane) and corresponding in size to a PC soma. The results are shown for three slices in **Figure 1C**, giving an average half-time for diffusional loss from the region of the cell of 60 s. In relation to the paired pulse protocol used here the concentration of HPTS over an interval of 50 or 150 ms declined to 90%–95%, and in the 30 s interval between paired stimuli declined to 60%–70% of the concentration released by photolysis associated with the preceding paired pulse stimulation. Rapid mixing of the bath between experimental protocols was by a perfusion tube and remote syringe.

## Transient Inward Current During Photolysis Due to Proton Release

The photolysis of MNI-caged γ-DGG shown in **Figures 1A,B** evokes a transient inward current. Release of 0.5 or 1 mM of either γ-DGG (shown in **Figures 1A,B**, **2B**) or γ-LGG (not shown) generated transient currents of approximately 0.25 nA and 0.6 nA amplitude that followed closely the light intensity in rise-time, and subsequently declined with a fast milliseconds time-course. As shown in **Scheme 1**, the photolysis of MNI-caged γ-DGG generates γ-DGG, a proton and a nitrosoindole by-product in stoichiometric proportion. Each of these products could activate the transient inward current observed on photolysis. γ-DGG released at high concentration by fast photolysis might bind and activate AMPA, Kainate or NMDA receptors on a milliseconds timescale, functioning as a weak or partial agonist. By comparison with the γ-DGG evoked currents however, photorelease of L-glutamate (3 μM or 7 μM) from MNI-caged L-glutamate to generate similar peak amplitudes evoked currents with much slower onset and decline (**Figure 2A**), suggesting that activation of AMPA-receptors by γ-DGG or γ-LGG is not responsible for the fast current. Moreover, photorelease of γ-DGG or γ-LGG at 0.5 mM or 1 mM in presence of NBQX (30 μM, **Figure 2B**) and D-AP5 (50 μM, data not shown) evoked transient currents with the same amplitudes as control. As a further test for AMPA receptor activation and rapid desensitization, the effect of cyclothiazide (100 μM), a blocker of AMPA receptor desensitization, affected neither amplitude nor time-course of the currents. The data show that γ-DGG is not acting as a weak agonist at AMPA-Kainate receptors nor promoting desensitization, supporting the conclusion from steady-state experiments that it acts as a fast-competitive antagonist (Liu et al., 1999; Wadiche and Jahr, 2001).

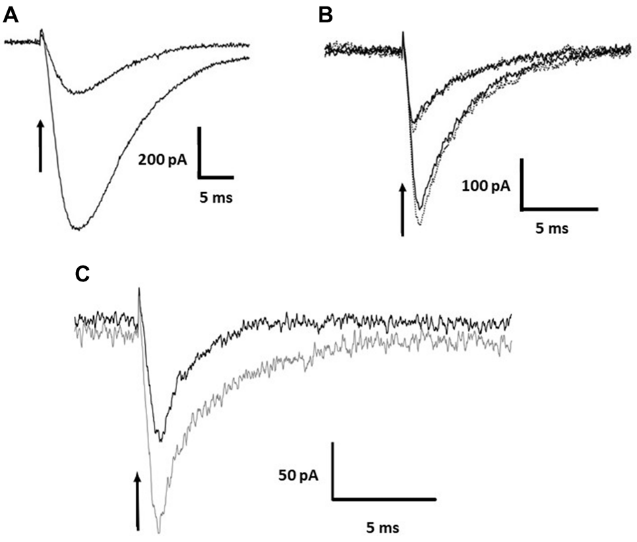

**FIGURE 2 |** Current evoked by photolysis of MNI-caged γ-DGG or MNI-caged γ-LGG. **(A)** Currents evoked by photorelease of L-glutamate at 3 μM and 7 μM in a Purkinje cell. **(B)** Currents of similar amplitude evoked by photorelease of 0.5 or 1.0 mM γ-DGG, in the absence (solid black traces) or presence (dotted gray traces) of the AMPA/Kainate receptor antagonist NBQX (30 μM). Currents evoked by γ-DGG are faster than the glutamate evoked currents and are not affected by the high affinity AMPA receptor competitive antagonist NBQX, indicating that γ-DGG is not an agonist of AMPA/Kainate receptors. **(C)** To test for an effect of the protons co-released with γ-DGG and γ-LGG (see **Scheme 1**), photorelease of 1.0 mM γ-LGG was compared in saline buffered with 70 mM HEPES (black trace) or 10 mM HEPES (gray trace). High proton buffering reduced the amplitude of the currents. Time of release indicated by the arrow.

A second possibility to account for the transient current may be the activation of a proton-gated channel or proton exchanger by the $H^+$ released stoichiometrically with γ-DGG during photolysis, shown in **Scheme 1**. A first test was to increase the pH buffering from 10 mM HEPES (buffer capacity 5 mM/pH at pH 7.3) to 70 mM, a 7-fold greater equilibrium buffer capacity. The result is illustrated in **Figure 2C**. The peak amplitude in 70 mM HEPES (black trace) was reduced to 50% of that in

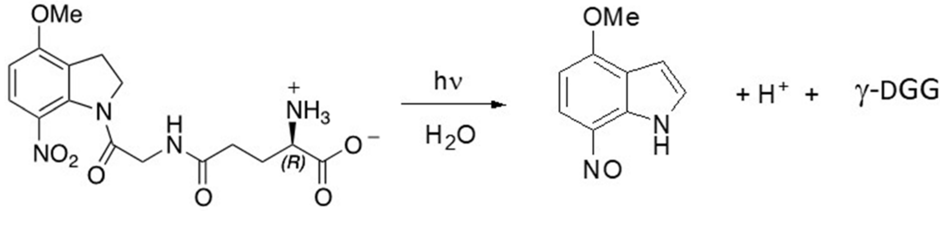

**SCHEME 1 |** Photolysis of MNI-caged γ-DGG releases γ-DGG, a nitrosoindole by-product and a proton for each caged molecule photolysed.

10 mM HEPES (gray trace), and the decay of the current was shortened from 5 ms to 2 ms, indicating a role of protons in the activation of the current. However, the partial inhibition and faster time-course of the currents by high HEPES concentration suggest that the kinetics of buffering by HEPES is too slow to bind protons on the timescale of photorelease.

ASIC channels are known to be present in Purkinje neurons and to respond rapidly to protons (Lingueglia et al., 1997). As a further test of the activation of a proton gated channel, an inhibitor of ASIC channels, IEPA, an analog of amiloride, was tested at the concentration of 30 μM. In two PC the current was inhibited by 30%, however tests of recovery were not possible because the concentration that could be applied was limited by toxicity of the vehicle DMSO. Amiloride itself also produced incomplete inhibition at high concentration, tested at concentrations up to 500 μM. ASIC channels are the most likely candidates for the observed current however known blockers amiloride and derivatives tested here were ineffective and the origin of this conductance will require further pharmacological testing.

Finally, the nitrosoindole by-product generated by the photolysis reaction could in principle be responsible for the transient current. This possibility cannot easily be tested independently since there are no fast-acting reagents available to quench potential oxidative actions. The reducing thiols DTT and glutathione have been shown to react too slowly to be useful in this context (half-time 120 s; Papageorgiou et al., 2008). Evidence from previous experiments however, has suggested that any interference by the nitroso by-products are slow and not on the time-course of the photolysis pulse (Papageorgiou et al., 2011). Thus, it is unlikely that the fast currents are generated by this product of the photolysis reaction.

The evidence suggests that the transient conductance activated upon photolysis of MNI-caged γ-DGG is due to activation of ASIC channels and other conductances, such as electrogenic exchangers, by the protons released stoichiometrically with γ-DGG. Current evoked by proton release during photolysis of MNI-caged ligands has not been demonstrated previously because L-glutamate or other agonists have not been applied with wide-field photolysis at the high concentrations used here for release of γ-DGG.

## Tests for Interference of MNI-Caged γ-DGG With Climbing Fiber-Purkinje Cell (CF-PC) Synaptic Transmission

Although MNI-caged ligands have been widely used and evaluated since 1999 the concentrations of cage used here are high and were tested for interference with synaptic transmission at CF-PC synapses. The example presented in **Figure 3** shows paired CF EPSCs separated by 150 ms before (black trace) and 5 min after addition of MNI-caged γ-DGG to give a concentration of 4.6 mM in the bath (gray trace). The threshold for CF stimulation and the synaptic charge of the first and second EPSC of the pair were compared before and after addition of MNI-caged γ-DGG; data in seven cells with 2.7–5.2 mM caged γ-DGG showed charge in the first EPSC was 0.97 ± 0.023 (SD) of pre-cage control and 0.99 ± 0.018 in the second. No change of stimulation threshold was observed immediately following addition of the cage, although threshold often increased progressively during the experiment.

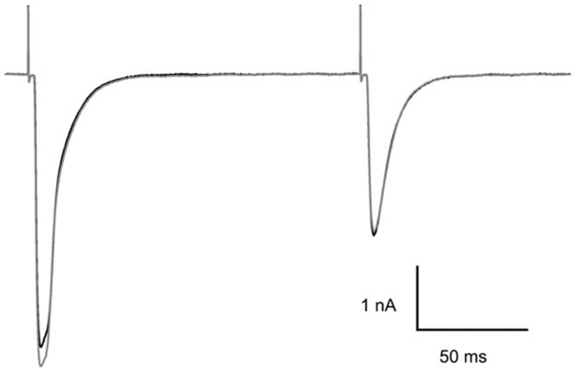

**FIGURE 3 |** Effect of MNI-caged γ-DGG on CF-PC synaptic transmission. Paired pulse stimulation at 150 ms interval before (black trace) and 5 min after addition of 4.6 mM MNI-caged γ-DGG to the bath (gray trace). Pipette potential −40 mV, 21°C.

## Block of Climbing Fiber Transmission at Constant γ-DGG Concentration Generated by Photolysis

γ-DGG is a low affinity competitive antagonist that binds to receptors with fast kinetics similar to L-glutamate. Consequently, there is competition between γ-DGG and L-glutamate that reaches equilibrium on the time-scale of the synaptic glutamate concentration transient; this property has been used to estimate changes in the amount of transmitter released from the reduced inhibition by γ-DGG at high glutamate concentration (Liu et al., 1999; Wadiche and Jahr, 2001). The CF-PC synapse shows short-term depression attributed to reduced transmitter release in the second pulse of a pair, resulting in reduced competition and greater fractional block by equal concentrations of γ-DGG in the second compared to the first response (Wadiche and Jahr, 2001). The slow diffusion of γ-DGG from the region of photolysis of MNI-caged-γ-DGG shown above permits estimates of the block at near steady concentration following flash photolysis and may be compared with published steady state data. In experiments to test this, CF were stimulated on a 30 s cycle with pairs of stimuli separated by 40 ms. After acquiring control data over two or more cycles, γ-DGG was released by photolysis coinciding with the first stimulus of a pair. Since γ-DGG diffuses slowly from the region of photolysis the concentration remained high during the second stimulus. The steady state inhibition was calculated by subtraction of the EPSC in γ-DGG from the control followed by normalization to the control EPSC amplitude.

The results are illustrated in **Figure 4** which shows the EPSCs elicited by a pair of CF stimuli separated by 40 ms in the presence of MNI-caged γ-DGG before (gray trace, control) and after photolysis timed with the first stimulus (black trace). The fraction of current blocked by γ-DGG was

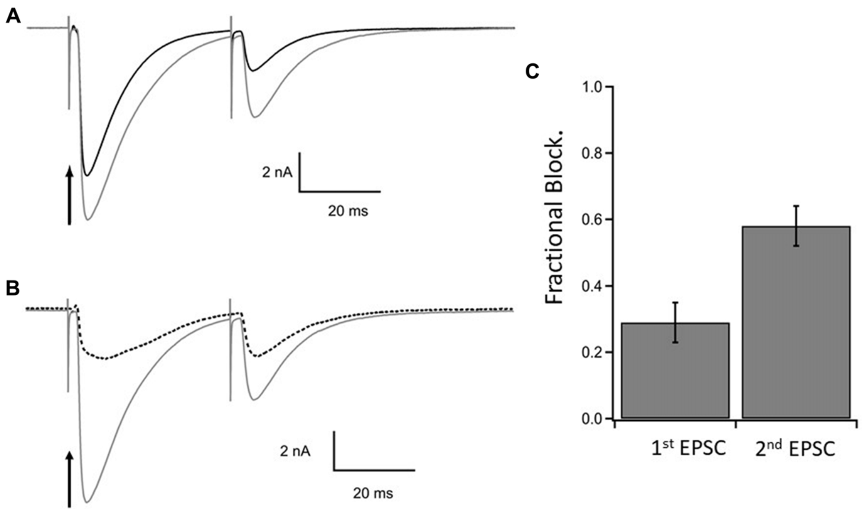

**FIGURE 4 |** Steady state inhibition of climbing fiber paired pulse EPSCs. **(A)** Control paired EPSCs in gray and test EPSCs in black following photorelease of 1.1 mM γ-DGG at the time of stimulation of the first EPSC. Paired stimulations 40 ms interval. γ-DGG inhibits the second EPSC more than the first. **(B)** The current blocked by γ-DGG (dashed line) was obtained by subtracting test (black trace) from control (gray trace) and is compared to control. **(C)** Fractional block of the peak current of 1st and 2nd EPSC following a flash to release γ-DGG at the first stimulus; data from 10 cells, Mean ± SEM. Range of γ-DGG concentrations released 0.55–1.7 mM. Note that diffusional loss of photoreleased γ-DGG is negligible on this time scale (see **Figure 1C**). Panels **(B,C)** show that the γ-DGG blocked component is a greater fraction of the control in the second EPSC than the first, indicating a lower competing transmitter concentration in the second EPSC.

obtained by subtracting the current recorded after photolysis from the control, giving the γ-DGG-sensitive current (dotted traces in **Figure 4B**). Data from 10 cells are summarized in the bar graph **Figure 4C**. The average fractional block of the first pulse was 0.29 ± 0.06 (SEM) and of the second by 0.60 ± 0.06 (SEM) respectively, measured in **Figure 4C** at the peak current. The greater block of the second EPSC is consistent with the interpretation that transmitter release and concentration are less in the second pulse than the first during paired pulse depression at CF-PC synapses (Wadiche and Jahr, 2001).

## Timed Inhibition of the CF EPSC by Photoreleased γ-DGG: Delayed Release and Sustained Transmitter Presence

The fast photorelease of γ-DGG from MNI-caged-γ-DGG was used here to probe transmitter action at postsynaptic receptors during the CF EPSC in order to test the timing and duration of release, and the possible contribution of receptor activation late in the EPSC. The analysis was made on the second of paired EPSCs with 150 ms interval in a 30 s stimulus cycle. The second EPSC was used because the smaller second EPSCs are less affected by poor voltage clamp spatial uniformity. The flashlamp pulse was 1 ms duration (see low intensity flash of **Figure 1A**) and delayed by 0–10 ms with respect to the CF stimulation. The protocol and results are illustrated by the records shown in **Figure 5**, traces in gray are controls and in black after photorelease of 0.74 mM γ-DGG at the times indicated. Timing was set with respect to the stimulus, the γ-DGG concentration rising with the integral of light intensity over 1 ms from the time indicated, as shown in **Figure 1A** and **Figure 6B**. Release prior to transmitter binding to postsynaptic receptors is predicted to produce block similar to the steady state block shown for the second EPSC in **Figure 4**. Release of γ-DGG after transmitter release will produce inhibition if transmitter is present and postsynaptic receptors are available.

Each panel of **Figure 5** shows the EPSC recorded with photolysis triggered at the time indicated following CF stimulation (black traces), superimposed with the control EPSC recorded 30 s earlier (gray traces). The results show that γ-DGG release with 0–1 ms or 2–3 ms delay from the stimulus resulted in a reduced peak amplitude, similar to the steady state inhibition of 60% described in **Figure 4C**. At longer delays γ-DGG released over 4–5 ms, 5–6 ms, 6–7 ms from the stimulus showed the same peak EPSC as control but a faster decay. γ-DGG released in the interval 3–4 ms reduced the peak amplitude of the EPSC much less than at earlier times and speeds the decline, indicating competition with transmitter during this interval. The records are superimposed in **Figure 6A** to permit comparison of changes in the EPSC waveform.

The block by γ-DGG was quantified by integrating the EPSC to obtain the total synaptic charge in the absence and presence of γ-DGG release. The charge blocked by γ-DGG was obtained by subtracting the integrals and then normalizing to control so as to permit comparisons among experiments. The data were integrated over the whole EPSC (from the CF stimulus for 60 ms; data in **Figure 6B**) or from the time of the flash (to 60 ms post-stimulus; **Figure 6C**).

The data from eight cells are summarized in **Figure 6B** as the fraction of synaptic charge blocked by γ-DGG photorelease at different times delayed with respect to the stimulus. The fraction of EPSC charge blocked by γ-DGG is given for each delay as Mean ± SD of 4–8 determinations plotted at the end of the

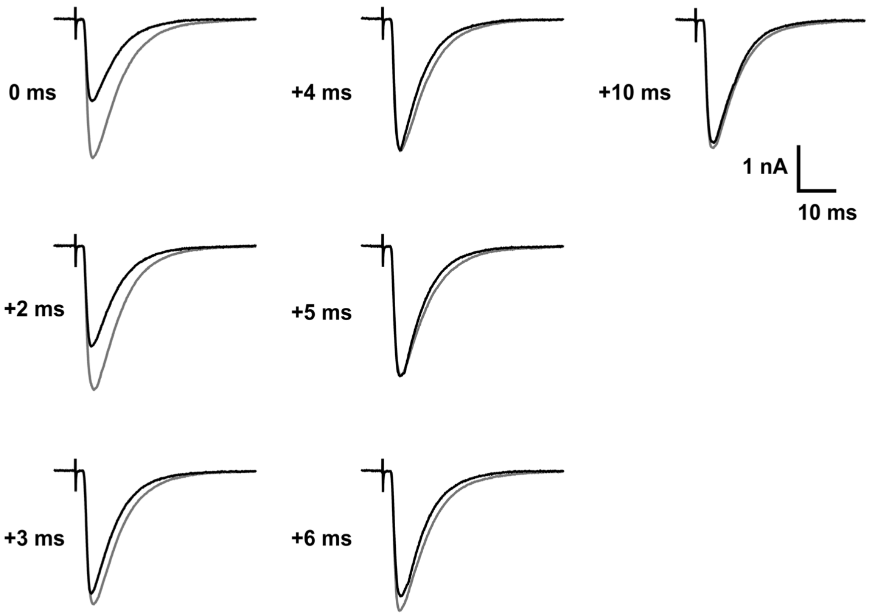

**FIGURE 5 |** Timed inhibition of CF-PC EPSC by photorelease of γ-DGG. Each panel shows the second EPSCs of a pair separated by 150 ms, the control (gray traces) and 30 s later with photorelease of 0.74 mM γ-DGG (black traces), released in a 1 ms flash from the indicated times relative to the stimulus. The bath contained 5.9 mM MNI-caged γ-DGG. At early times (0 and 2 ms delay from the stimulus) inhibition is comparable to steady-state inhibition. At later times of γ-DGG release (triggered at 3–10 ms) the EPSC approaches the control EPSC peak and only the decay is affected. Age 14 days, −50 mV, 24°C.

flash. The γ-DGG concentration range was 0.34–0.74 mM. The results show that release of γ-DGG in the intervals 0–1 ms and 2–3 ms after the stimulus produced block at similar levels, both with mean 60%, and similar to the steady-state block of the second EPSC shown in **Figure 4C**. This indicates that receptor activation by transmitter release had not started after 3 ms from the stimulus. γ-DGG released over the interval 3–4 ms after the stimulus produced a reduced mean block of 40%, indicating competition with transmitter for a shorter time in this interval. Also, the SD is larger, approximately double that seen at other time points, indicating jitter in the timing of transmitter release between measurements. Later, with γ-DGG release at 4–5 ms and 5–6 ms, the block is smaller and less variable. The data therefore suggest that glutamate binding of postsynaptic receptors in competition with photoreleased γ-DGG occurs mainly at 3–4 ms following CF stimulation, a time corresponding to the initial rise of the EPSC. A second observation from **Figure 6B** (seen also in **Figures 5**, **6A**) is the continued inhibition by γ-DGG when released at 5–6 ms, close to the peak EPSC, or at longer delays. This suggests that transmitter is available to bind free receptors late in the EPSC. As a better measure of γ-DGG block at late times the data were expressed as the fraction of EPSC charge blocked relative to control by integrating and comparing the EPSC charge only over the period following the flash. The results plotted in **Figure 6C** show a substantial fraction, average 23%, of the EPSC charge is blocked by γ-DGG released at 6 ms and later times post-stimulus. Although the change in EPSC is small at 5–6 ms and later, the synaptic charge is significant and the observations nonetheless indicate the presence of transmitter at the later time points. The results imply receptor availability and reactivation by transmitter, due either to delayed release or persistence in the synapse. It may be noted that late in the EPSC the fractional block at low transmitter concentration is expected to be constant in absence of competition, simply related to the concentration of γ-DGG and its equilibrium constant for receptor binding (Liu et al., 1999).

## DISCUSSION

MNI-caged-γ-DGG was developed as a tool to probe the activation of postsynaptic receptors during transmission at glutamatergic synapses, to investigate the roles of spillover or volume transmission and the functional independence of synaptic sites. A main purpose of the experiments reported was the verification of MNI-caged-γ-DGG as a probe suitable for testing receptor activation in synaptic and parasynaptic transmission. The CF-PC synapse was studied as a single connection permitting an assessment of the new cage. No detrimental effects of the cage itself were seen on CF-PC transmission, as judged by threshold for stimulation, synaptic properties or short-term plasticity tested by paired pulse depression, at concentrations up to 5 mM of MNI-caged γ-DGG or MNI-caged γ-LGG. The cages synthesized and purified with the methods described above and in **Supplementary Information** were soluble in physiological saline at 20 mM concentration, enabling use from stock solutions. It is also important that there was no loss of chiral specificity in the synthesis, as shown by the results of CD spectrometry (see SI, **Supplementary Figure S1**). The MNI cages have well tested properties of hydrolytic stability (Papageorgiou et al., 1999),

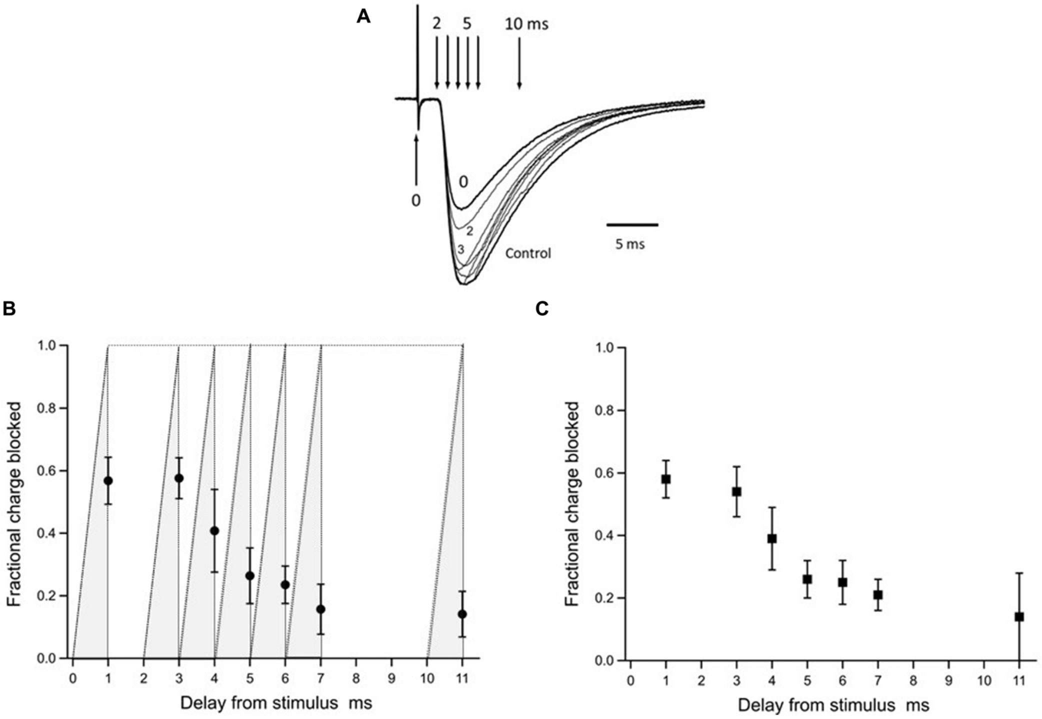

**FIGURE 6 |** Inhibition by γ-DGG photoreleased during the EPSC: estimating the timing of the synaptic transmitter transient. Panel **(A)** shows the EPSCs presented in **Figure 5** superimposed for comparison of the time-course; the record obtained by release of γ-DGG between 0 and 1 ms, coincident with the stimulus, is marked 0; records corresponding to release over 2–3 ms and 3–4 ms post-stimulus are labeled 2 and 3 respectively. Vertical arrows indicate the trigger timing of photolysis pulses releasing γ-DGG as delay times from the stimulus. Panel **(B)** summarizes data from 4 to 8 cells of the fraction of total synaptic charge blocked by γ-DGG. Data are Mean ± SD plotted at the end of the 1 ms photolysis pulse. The integration of the light pulse is indicated by the gray shading for each data point and represents the time-course of γ-DGG concentration increase during the flash, uniform over the microscope field. To obtain the fractional charge blocked by γ-DGG test EPSCs were integrated over 60 ms following the stimulus, subtracted from and normalized to the integral of control EPSCs recorded 30 s earlier. MNI-caged-γ-DGG concentration range 2.7–5.9 mM, γ-DGG released range 0.34–0.74 mM. Panel **(C)** to quantify γ-DGG fractional block late in the EPSC, integrations were made from the time of the flash to 60 ms, subtracted from and normalized to the same period in control. To control for the proton current artifact a record was taken with the flash but without stimulation and subtracted from the test records obtained with stimulation. As a further check the records in **(C)** were integrated from 1 ms after the flash, requiring no subtraction of initial current. Results with or without subtraction were similar. Animal ages 13 days in **(A)**, 13–14 days in **(B,C)**. Temperature 21–24°C.

sub-microsecond release (Morrison et al., 2002) and good pharmacological properties at glutamate synapses (Canepari et al., 2001; Trigo et al., 2009; Palma-Cerda et al., 2012). The ability to use high concentrations without detrimental effects on excitability or transmitter release, the known efficiency with 405 nm laser photolysis of the MNI-cages (Trigo et al., 2009), and the time-resolution of photolysis suggest MNI-caged- γ-DGG is a useful synaptic probe.

To our knowledge, this is the first study that tests the fast release of a fast equilibrating antagonist at AMPA-Kainate and NMDA receptors and we were interested to know whether transient activation of receptors might be apparent under these release conditions. There was no partial agonist activity of γ-DGG seen when applied at mM concentration by photorelease on a sub-millisecond timescale. This indicates that the receptor binding of γ-DGG does not induce conformation changes that result in transient channel gating and desensitization. It is consistent with the equilibrium data of Liu et al. (1999) that γ-DGG has properties of a competitive receptor antagonist, apparently showing no efficacy for channel gating. We also tested the ability of MNI-caged-LGG to block CF-PC synapses upon photolysis, the results confirming that γ-LGG is much less potent than γ-DGG at similar high concentrations.

The immediate physiological results presented here, an analysis of the EPSC at the CF-PC synapse, show two interesting aspects. The first is a long delay of 3–4 ms from the stimulus to the first evidence of receptor activation. Since the stimulus site is close, within 50 μm of the Purkinje soma, the conduction delay is predicted to be short, less than 100 μs. At synapses where the delay from presynaptic spike to postsynaptic activation has been measured it is 0.5–1 ms at room temperature (Katz and Miledi, 1965; Forsythe, 1994). The delay from stimulus to release here is therefore approximately 1 ms longer than can be accounted for by synaptic delay and conduction velocity in small myelinated fibers. It may point to other processes such as additional conduction delays in the CF terminals that may delay release.

The second finding is a late component of receptor activation occurring after the major period of activation at 3–4 ms post-stimulus. Vesicular release is known to continue at a reduced rate for several milliseconds after the peak release at about 1 ms (Katz and Miledi, 1965; Trigo et al., 2012) and may contribute a late component. An additional factor contributing to the activation of postsynaptic current late in the EPSC may be persistence of glutamate in the synapse. The CF terminals are protected by Bergmann glial processes and glutamate transporters at high density on both the PC and the glial membranes which will quickly buffer and take up the transmitter. The experiments here were done at 21–24°C and both release and uptake will be slower compared with physiological temperature (Auger and Attwell, 2000). The relative contributions of the two mechanisms are not addressed here and will be better examined at physiological temperature.

The possibility that γ-DGG acts at presynaptic glutamate receptors to modify transmitter release as well as postsynaptically has not been excluded. Presynaptic effects were tested by Wadiche and Jahr (2001) by monitoring transporter currents, with the finding that these were unaffected by addition of 2 mM γ-DGG. However, the transporter currents in their study were isolated by a high concentration of NBQX which would mask an effect of γ-DGG on presynaptic AMPA-K receptors. While ruling out direct effects of γ-DGG on release, the possibility of block by γ-DGG of receptor mediated modulation of transmission by presynaptic AMPA-K or NMDAR is difficult to test. There are, however, no reports of presynaptic AMPAR or NMDAR at climbing fiber terminals.

We have noted previously a selectivity of γ-DGG for Bergmann glial AMPAR with about 10-fold higher affinity than Purkinje AMPAR (Bellamy and Ogden, 2005). This may relate to the different receptor composition, GluA1 and GluA4 in Bergmann glia and GluA1, GluA2 and GluA3 in Purkinje neurons, and the presence of auxiliary proteins, particularly TARP γ2. Thus, there is the additional possibility of time resolved experiments with pharmacological specificity for AMPA receptors of different subunit and auxiliary protein composition by the photorelease of γ-DGG at low or high concentrations to distinguish receptor types pharmacologically. Further, evidence has been presented that kinetic parameters and functional affinity of AMPAR for transmitter L-glutamate differs among TARP vs. non-TARP associated receptors (Zhang et al., 2014; Carbone and Plested, 2016; Devi et al., 2016). If the affinity for L-glutamate differs among AMPA-R of different compositions and gating mode, the estimates of transmitter concentration with steady-state application of γ-DGG will be modified due to competition and to differences in affinity.

An important result obtained here in the context of uncaging methodology was the activation in Purkinje cells of a small fast inward current gated by mM release of protons. Protons are released during nitrobenzyl and nitroindoline photolysis stoichiometrically with the ligand, however usually the concentrations are low and, in the case of local laser photolysis, rapidly dissipated by diffusion. The high concentrations released over a large volume here are unusual. The data shown in **Figure 2** indicate that even raising the buffer capacity from 10 mM to 70 mM HEPES was not effective in completely suppressing the current; even if the protonation rate is high in aqueous solution, estimated as $10^{10}$ L.mole$^{-1}$.s$^{-1}$, the pK of 7.3 indicates a deprotonation rate in the milliseconds range for HEPES. Further, the normal bicarbonate-$CO_2$ buffer is known to have kinetics on a second timescale and will be ineffective on a millisecond timescale. These considerations apply also to the strong alkalinization produced by photolysis of DMnitophen and NPE-EGTA to release Ca intracellularly (Trigo et al., 2012). The origin of the inward current activated by protons here is not clear. ASIC channels are known to be present in Purkinje neurons and to respond rapidly to protons (Lingueglia et al., 1997), however known blockers amiloride and derivatives tested here were ineffective. Other possibilities are electrogenic transporters with coupled proton flux or proton permeabilities which may be tested pharmacologically.

The time resolution in the experiments reported here is determined by the 1 ms duration of the flashlamp discharge, measured for each record to determine the precise timing of γ-DGG release but longer than the 0.1 ms limit imposed by equilibration in receptor binding by γ-DGG (Liu et al., 1999; Wadiche and Jahr, 2001). The flashlamp provides widefield photolysis and was necessary because of the large field of CF dendritic innervation. At small synaptic contacts laser photolysis over a smaller area will give time resolution of 0.1 ms with MNI-caged γ-DGG at individual synapses with the methods described by Trigo et al. (2009). As well as improved time resolution, the extent of photolysis is greater with laser activation, permitting greater economy with the cage and better control of the concentration released.

Recently the time resolution of tethered genetically encoded fluorescent glutamate reporters has been improved to the milliseconds level (Helassa et al., 2018) providing another way to investigate transmitter concentration profiles at single synapses. The two approaches are complementary, the present method more readily applicable because there is no requirement for transgene or viral labeling. Combining the two approaches is unlikely because of the strong bleaching action of near-UV on the GFP reporter fluorescence.

Although MNI cages have properties of speed, stability and pharmacological inertness it is generally known that they are very inefficient in two-photon photolysis, requiring high concentrations and high intensities, releasing a few percent of the cage concentration at non-toxic intensities. The two-photon cross-section measured by us and in other studies is 0.05 GM, whereas the cross-section required for 50% photolysis in the laser spot is two orders larger at the threshold for non-toxic exposure, an average power of 5 mW. Phototoxicity of ultra-short pulsed irradiation is seen presynaptically, characterized by aberrant release at average powers greater than 5 mW (Hopt and Neher, 2001; Kiskin et al., 2002). Two-photon excitation of MNI-caged-γ-DGG to release useful concentrations of γ-DGG would be phototoxic and too localized to be useful in testing distributed transmitter release.

In conclusion, we present the synthesis and evaluation of a fast-caged antagonist MNI-caged-γ-DGG and the methods to apply it in the analysis of synaptic transmission in this case with wide-field photolysis at the CF-PC synapse. The results define the time-window of receptor activation by transmitter, present evidence for a delay in transmission or release, and persistence of receptor activation by transmitter late in the EPSC.

## AUTHOR CONTRIBUTIONS

FP-C, GP, BB, CA and DO contributed to the conception and design of the study. GP synthesized and characterized reagents. FP-C and DO performed experiments and analyzed data. DO wrote the first draft of the manuscript. All authors contributed to manuscript revision, read and approved the submitted version.

## FUNDING

The research was supported by the ANR (FP-C, CA, DO; ANR-16-CE16-0016), the CNRS and Université Paris Descartes (DO, CA), the UK Medical Research Council and Francis Crick Institute (GP). BB was supported by Idex PSL Research University (ANR-11-IDEX-0001-02), Labex (ANR-10-LABX-54 MEMOLIFE) and Fondation pour la Recherche Médicale (DEQ20160334927).

## ACKNOWLEDGMENTS

We thank the animal facility at Universite Paris Descartes St. Peres for animal care. We thank Dr. Steve Martin (Francis Crick Institute) for expert help with CD spectra. We gratefully acknowledge the contribution of Dr. John E.T. Corrie to the chemical synthesis, and for advice, discussion and encouragement.

## SUPPLEMENTARY MATERIAL

The Supplementary Material for this article can be found online at: https://www.frontiersin.org/articles/10.3389/fncel.2018.00465/full#supplementary-material

## REFERENCES

Auger, C., and Attwell, D. (2000). Fast removal of synaptic glutamate by postsynaptic transporters. *Neuron* 28, 547–558. doi: 10.1016/s0896-6273(00)00132-x

Beato, M. (2008). The time course of transmitter at glycinergic synapses onto motoneurons. *J. Neurosci.* 28, 7412–7425. doi: 10.1523/JNEUROSCI.0581-08.2008

Bellamy, T. C., and Ogden, D. (2005). Short-term plasticity of Bergmann glial cell extrasynaptic currents during parallel fiber stimulation in rat cerebellum. *Glia* 52, 325–335. doi: 10.1002/glia.20248

Canepari, M., Nelson, L., Papageorgiou, G., Corrie, J. E. T., and Ogden, D. (2001). Photochemical and pharmacological evaluation of 7-nitroindolinyl-and 4-methoxy-7-nitroindolinyl-amino acids as novel, fast caged neurotransmitters. *J. Neurosci. Methods* 112, 29–42. doi: 10.1016/s0165-0270(01)00451-4

Carbone, A. L., and Plested, A. J. (2016). Superactivation of AMPA receptors by auxiliary proteins. *Nat. Commun.* 8:10178. doi: 10.1038/ncomms10178

Clements, J. D., Lester, R. A., Tong, G., Jahr, C. E., and Westbrook, G. L. (1992). The time course of glutamate in the synaptic cleft. *Science* 258, 1498–1501. doi: 10.1126/science.1359647

Coddington, L. T., Nietz, L. K., and Wadiche, J. I. (2014). The contribution of extrasynaptic signalling to cerebellar information processing. *Cerebellum* 13, 513–520. doi: 10.1007/s12311-014-0554-7

Davies, J., and Watkins, J. C. (1981). Differentiation of kainate and quisqualate receptors in the cat spinal cord by selective antagonism with γ-D (and L)-glutamylglycine. *Brain Res.* 206, 172–177. doi: 10.1016/0006-8993(81)90111-6

Devi, S. P., Howe, J. R., and Auger, C. (2016). Train stimulation of parallel fiber to Purkinje cell inputs reveals two populations of synaptic responses with different receptor signatures. *J. Physiol.* 594, 3705–3727. doi: 10.1113/jp272415

Forsythe, I. D. (1994). Direct patch recording from identified presynaptic terminals mediating glutamatergic EPSCs in the rat CNS, *in vitro*. *J. Physiol.* 479, 381–387. doi: 10.1113/jphysiol.1994.sp020303

Francis, A. A., Jones, A. W., and Watkins, J. C. (1980). Dipeptide antagonists of amino acid-induced and synaptic excitation in the frog spinal cord. *J. Neurochem.* 35, 1458–1460. doi: 10.1111/j.1471-4159.1980.tb09025.x

Helassa, N., Dürst, C.-D., Coates, C., Kerruth, S., Arif, U., Schulze, C., et al. (2018). Ultrafast glutamate sensors resolve high-frequency release at Schaffer collateral synapses. *Proc. Natl. Acad. Sci. U S A* 115, 5594–5599. doi: 10.1073/pnas.1720648115

Hopt, A., and Neher, E. (2001). Highly nonlinear photodamage in two-photon fluorescence microscopy. *Biophys. J.* 80, 2029–2036. doi: 10.1016/s0006-3495(01)76173-5

Jasuja, R., Keyoung, J., Reid, G. P., Trentham, D. R., and Khan, S. (1999). Chemotactic responses of *Escherichia coli* to small jumps of photoreleased L-aspartate. *Biophys. J.* 76, 1706–1719. doi: 10.1016/s0006-3495(99)77329-7

Kanazawa, A., Kakimoto, Y., Nakajima, T., Shimizu, H., Takesada, M., and Sano, I. (1965). Isolation and identification of γ-L-glutamylglycine from bovine brain. *Biochim. Biophys. Acta* 97, 460–464. doi: 10.1016/0304-4165(65)90157-1

Katz, B., and Miledi, R. (1965). The effect of temperature on the synaptic delay at the neuromuscular junction. *J. Physiol.* 181, 656–670. doi: 10.1113/jphysiol.1965.sp007790

Kiskin, N. I., Chillingworth, R., McCray, J. A., Piston, D., and Ogden, D. (2002). The efficiency of two-photon photolysis of a "caged" fluorophore, o-1-(2-nitrophenyl)ethylpyranine, in relation to photodamage of synaptic terminals. *Eur. Biophys. J.* 30, 588–604. doi: 10.1007/s00249-001-0187-x

Lingueglia, E., de Weille, J. R., Bassilana, F., Heurteaux, C., Sakai, H., Waldmann, R., et al. (1997). A modulatory subunit of acid sensing ion channels in brain and dorsal root ganglion cells. *J. Biol. Chem.* 272, 29778–29783. doi: 10.1074/jbc.272.47.29778

Liu, G., Choi, S., and Tsien, R. W. (1999). Variability of neurotransmitter concentration and nonsaturation of postsynaptic AMPA receptors at synapses in hippocampal cultures and slices. *Neuron* 22, 395–409. doi: 10.1016/s0896-6273(00)81099-5

Morrison, J., Wan, P., Corrie, J. E. T., and Papageorgiou, G. (2002). Mechanisms of photorelease of carboxylic acids from 1-acyl-7-nitroindolines in solutions of varying water content. *Photochem. Photobiol. Sci.* 1, 960–969. doi: 10.1039/b206155d

Nielsen, T. A., DiGregorio, D. A., and Silver, R. A. (2004). Modulation of glutamate mobility reveals the mechanism underlying slow-rising AMPAR EPSCs and the diffusion coefficient in the synaptic cleft. *Neuron* 42, 757–771. doi: 10.1016/j.neuron.2004.04.003

Palma-Cerda, F., Auger, C., Crawford, D. J., Hodgson, A. C. C., Reynolds, S. J., Cowell, J. K., et al. (2012). New caged neurotransmitter analogs selective for glutamate receptor sub-types based on methoxynitroindoline and nitrophenylethoxycarbonyl caging groups. *Neuropharmacology* 63, 624–634. doi: 10.1016/j.neuropharm.2012.05.010

Papageorgiou, G., Beato, M., and Ogden, D. (2011). Synthesis and photolytic evaluation of a nitroindoline-caged glycine with a side chain of high negative charge for use in neuroscience. *Tetrahedron* 67, 5228–5234. doi: 10.1016/j.tet.2011.05.045

Papageorgiou, G., and Corrie, J. E. T. (2000). Effects of aromatic substituents on the photocleavage of 1-acyl-7-nitroindolines. *Tetrahedron* 56, 8197–8205. doi: 10.1016/s0040-4020(00)00745-6

Papageorgiou, G., Ogden, D., Barth, A., and Corrie, J. E. T. (1999). Photorelease of carboxylic acids from 1-acyl-7-nitroindolines in aqueous solution: rapid and efficient photorelease of L-glutamate. *J. Am. Chem. Soc.* 121, 6503–6504. doi: 10.1021/ja990931e

Papageorgiou, G., Ogden, D., and Corrie, J. E. T. (2008). An antenna-sensitised 1-acyl-7-nitroindoline that has good solubility properties in the presence of calcium ions and is suitable for use as a caged L-glutamate in neuroscience. *Photochem. Photobiol. Sci.* 7, 423–432. doi: 10.1039/b800683k

Scimemi, A., and Beato, M. (2009). Determining the neurotransmitter concentration profile at active synapses. *Mol. Neurobiol.* 40, 289–306. doi: 10.1007/s12035-009-8087-7

Szapiro, G., and Barbour, B. (2007). Multiple climbing fibers signal to molecular layer interneurons exclusively via glutamate spillover. *Nat. Neurosci.* 10, 735–742. doi: 10.1038/nn1907

Szapiro, G., and Barbour, B. (2009). Parasynaptic signalling by fast neurotransmitters: the cerebellar cortex. *Neuroscience* 162, 644–655. doi: 10.1016/j.neuroscience.2009.03.077

Trigo, F. F., Corrie, J. E. T., and Ogden, D. (2009). Laser photolysis of caged compounds at 405 nm: photochemical advantages, localisation, phototoxicity and methods for calibration. *J. Neurosci. Methods* 180, 9–21. doi: 10.1016/j.jneumeth.2009.01.032

Trigo, F. F., Sakaba, T., Ogden, D., and Marty, A. (2012). Readily releasable pool of synaptic vesicles measured at single synaptic contacts. *Proc. Natl. Acad. Sci. U S A* 109, 18138–18143. doi: 10.1073/pnas.1209798109

Wadiche, J. I., and Jahr, C. E. (2001). Multivesicular release at climbing fiber-Purkinje cell synapses. *Neuron* 32, 301–313. doi: 10.1016/s0896-6273(01)00488-3

Xia, P., Bungay, P. M., Gibson, C. C., Kovbasnjuk, O. N., and Spring, K. R. (1998). Diffusion coefficients in the lateral intercellular spaces of Madin-Darby canine kidney cell epithelium determined with caged compounds. *Biophys. J.* 74, 3302–3312. doi: 10.1016/s0006-3495(98)78037-3

Zhang, W., Devi, S. P., Tomita, S., and Howe, J. R. (2014). Auxiliary proteins promote modal gating of AMPA- and kainate-type glutamate receptors. *Eur. J. Neurosci.* 39, 1138–1147. doi: 10.1111/ejn.12519

**Conflict of Interest Statement**: The authors declare that the research was conducted in the absence of any commercial or financial relationships that could be construed as a potential conflict of interest.

frontiers
in Cellular Neuroscience

REVIEW
published: 17 December 2018
doi: 10.3389/fncel.2018.00469

# Methods for Three-Dimensional All-Optical Manipulation of Neural Circuits

*Emiliano Ronzitti, Valentina Emiliani and Eirini Papagiakoumou**

*Wavefront Engineering Microscopy Group, Photonics Department, Institut de la Vision, Sorbonne Université, Inserm S968, CNRS UMR7210, Paris, France*

Optical means for modulating and monitoring neuronal activity, have provided substantial insights to neurophysiology and toward our understanding of how the brain works. Optogenetic actuators, calcium or voltage imaging probes and other molecular tools, combined with advanced microscopies have allowed an "all-optical" readout and modulation of neural circuits. Completion of this remarkable work is evolving toward a three-dimensional (3D) manipulation of neural ensembles at a high spatiotemporal resolution. Recently, original optical methods have been proposed for both activating and monitoring neurons in a 3D space, mainly through optogenetic compounds. Here, we review these methods and anticipate possible combinations among them.

**Keywords: light-shaping, three-dimensional photostimulation, three-dimensional functional imaging, all-optical neuronal studies, optogenetics, neural circuits**

***Edited by:***
*Marco Canepari,*
*UMR5588 Laboratoire*
*Interdisciplinaire de Physique (LIPhy),*
*France*

***Reviewed by:***
*Albrecht Stroh,*
*Johannes Gutenberg University*
*Mainz, Germany*
*Marco Lorenzo Dal Maschio,*
*Università degli Studi di Padova, Italy*

****Correspondence:***
*Eirini Papagiakoumou*
*eirini.papagiakoumou@inserm.fr*

***Received:*** *04 September 2018*
***Accepted:*** *19 November 2018*
***Published:*** *17 December 2018*

***Citation:***
*Ronzitti E, Emiliani V and Papagiakoumou E (2018) Methods for Three-Dimensional All-Optical Manipulation of Neural Circuits. Front. Cell. Neurosci. 12:469. doi: 10.3389/fncel.2018.00469*

## INTRODUCTION

Controlling and monitoring neuronal activity with a light has become a common practice in many neurobiological studies, throughout the last decade. The continuously expanding toolbox of molecular probes that activate/inhibit (Herlitze and Landmesser, 2007; Airan et al., 2009; Levitz et al., 2013; Klapoetke et al., 2014; Shemesh et al., 2017; Becker et al., 2018; Guruge et al., 2018; Mardinly et al., 2018) or image (Emiliani et al., 2015; Kim et al., 2018) neuronal activity as well as the development of original light-microscopy methods for stimulating these tools (Ronzitti et al., 2017b; Chen et al., 2018c; Yang and Yuste, 2018), has tremendously contributed to the direction of research and has led to innovative experimental concepts (Rickgauer et al., 2014; Carrillo-reid et al., 2016). Photostimulation via optogenetics and/or uncaging (Kwon et al., 2017) is suitable for single cell and, most importantly, circuit studies, since light gives access to a large number of targets simultaneously, at high spatial precision via parallel illumination methods (Papagiakoumou et al., 2010; Packer et al., 2015; Forli et al., 2018; Yang et al., 2018).

Circuit studies are usually performed *in vivo* by light-stimulation at near-infrared to minimize scattering effects and optimize spatial resolution via non-linear multiphoton absorption processes. Ideally, these studies also demand three-dimensional (3D) accessibility both for activation and imaging at physiological time scales (few-ms scale activation and imaging). 3D imaging approaches enable the use of complementary strategies to access volumes extending up to a few hundred μms in the axial direction, by proposing the use of piezo scanners to scan the objectives in specific trajectories (Göbel et al., 2007), acousto-optic deflectors (Reddy et al., 2008; Grewe et al., 2010; Katona et al., 2012; Nadella et al., 2016), tunable lenses (Grewe et al., 2011; Fahrbach et al., 2013; Kong et al., 2015), spatiotemporal multiplexing (Cheng et al., 2011; Ducros et al., 2013), light field microscopy (Prevedel et al., 2014), or Bessel beam excitation (Lu et al., 2017) and reaching tens of Hz imaging frequencies, of neuronal activity *in vivo* (Göbel et al., 2007; Grewe et al., 2011; Katona et al., 2012; Nadella et al., 2016). 3D functional imaging of neurons has more recently been demonstrated at even larger volumes, reaching 0.5 mm in *z*, using a temporally focused Gaussian beam excitation at the size of neuron soma (Prevedel et al., 2016), with large field views up to 5 mm in *xy* (Sofroniew et al., 2016; Stirman et al., 2016) or in two different areas of the brain (Lecoq et al., 2014; Chen et al., 2016).

The development of 3D photoactivation methods is more recent. These systems are based on the use of Computer-Generated Holography (CGH) (Papagiakoumou et al., 2018; Yang and Yuste, 2018). Although this technique was established for the projection of 3D patterns (Piestun et al., 1996; Haist et al., 1997) or diffraction-limited spots (Liesener et al., 2000) via spatial light modulators (SLMs) several years ago, its use in neuroscience for simultaneous activation of multiple targets in two (Lutz et al., 2008; Nikolenko et al., 2008; Dal Maschio et al., 2010) or three dimensions (Yang et al., 2011; Go et al., 2012; Hernandez et al., 2016; Dal Maschio et al., 2017) was established only during the last decade. Thanks to 3D-CGH, used either solely (parallel methods) or in its diffraction-limit version in combination with scanning of the holographic beamlets (hybrid methods) [see (Papagiakoumou, 2013; Ronzitti et al., 2017b) for detailed description of these approaches], it is possible nowadays to activate multiple neurons providing both the adequate temporal resolution, as well as the spatial resolution for single-cell precision (**Figures 1A,B**).

With regards to temporal resolution, it is helpful to define the notion of *temporal precision* in optogenetic activation, i.e., the degree of reproducibility of the occurrence timing of a photo-evoked AP (also indicated as photo-evoked spike jitter) (**Figure 1C**) and *temporal resolution*, i.e., the time needed to photo-evoke an AP, ultimately linked to the maximum achievable light-driven neuronal firing rate (**Figure 1D**). Minimizing those two parameters helps to reproduce precise temporal patterns of activity that in combination with multicell activation, enables to mimic the physiological activity of a network. It has been shown that parallel photoactivation methods (Ronzitti et al., 2017b) can easily achieve short timescales during optogenetic activation (few-ms temporal resolution and sub-ms jitter) (Chaigneau et al., 2016; Ronzitti et al., 2017a; Shemesh et al., 2017; Chen et al., 2018b). Later studies using scanning methods, have also shown a high temporal specificity, reaching a millisecond jitter by using high power in the excitation spots (Yang et al., 2018).

With regards to 3D spatial resolution, scanning methods using 3D-CGH show an intrinsically good spatial resolution, thanks to the small spot size of the excitation beam (close to diffraction limit). Nevertheless, resolution can dramatically decrease when using intensities close to the saturation levels for the opsin, which results in out-of-focus excitation (Rickgauer and Tank, 2009; Andrasfalvy et al., 2010). Parallel methods use illumination shapes that cover the whole cell body, in order to achieve parallel recruitment of all opsins on the cell membrane to improve efficiency (Papagiakoumou et al., 2010). This, however, causes a quick deterioration of the axial resolution, which scales linearly or quadratically with lateral size, for holographic or Gaussian beams, respectively (Oron et al., 2012). Parallel methods can provide a good axial resolution when combined with temporal focusing (TF) (Papagiakoumou et al., 2008, 2010; Oron et al., 2012; Rickgauer et al., 2014). Notably, temporally focused light-shaping methods allow to preserve sharp borders of the excitation pattern (Papagiakoumou et al., 2010), even through scattering media (Bègue et al., 2013; Papagiakoumou et al., 2013). However, because TF works by dispersing the spectral frequencies of a femtosecond light pulse at a specific plane (Oron et al., 2005), special configurations are needed to extend the methods in 3D.

Here we review the methods proposed so far for 3D photoactivation and present the possibilities for combination with 3D imaging modalities, to establish precise and flexible microscopy methods for all-optical manipulation of neural circuits. The methods we present here have mostly been developed for optogenetic photostimulation but in principle, any other photoactivation technique, such as uncaging of caged neurotransmitters, or activation of photoactivable proteins, could benefit from them.

## ALL-OPTICAL MANIPULATION

The very first experiment of all-optical manipulation of neurons was demonstrated by activating cells in neocortical slices via two-photon (2P) uncaging of MNI-glutamate with multiple beamlets generated with a diffractive optical element, or one single beam multiplexed in time, and 2P $Ca^{2+}$ imaging (Nikolenko et al., 2007). Similarly, a few years later in two other papers researchers measured $Ca^{2+}$ signals in neurons while uncaging MNI-glutamate (Dal Maschio et al., 2010; Anselmi et al., 2011). In (Dal Maschio et al., 2010) the optical system incorporated 2P 2D-CGH in the optical path of a commercial 2P scanning microscope and it could exchange holographic or scanning stimulation between the uncaging and imaging beams. In (Anselmi et al., 2011) 3D-CGH with diffraction-limited spots was combined with a remote-focusing system (Botcherby et al., 2007, 2012) to perform functional imaging along tilted dendrites of hippocampal pyramidal neurons in brain slices. Although the first demonstrations of combined activation and imaging of neurons used uncaging, the term *all-optical* is mostly related to the combination of functional imaging and optogenetic activation. In 2014, a milestone was achieved when an important number of scientific studies showing the activation of neurons *in vivo* in rodents via optogenetic molecules and the imaging of $Ca^{2+}$ responses with GCaMP, took place (Vogt, 2015), using either visible (Szabo et al., 2014) or 2P light stimulation (Rickgauer et al., 2014; Packer et al., 2015). More publications followed, using 2D (Carroll et al., 2015; Carrillo-reid et al., 2016; Bovetti et al., 2017; Förster et al., 2017; Forli et al., 2018), and more recently 3D stimulation (Hernandez et al., 2016; Dal Maschio et al., 2017; Mardinly et al., 2018; Yang et al., 2018).

Despite these very important studies, full optical neuronal control remains a challenge in terms of achieving reliable delivery and expression of sensors and actuators in the same neurons, eliminating the cross-talk between imaging and activation,

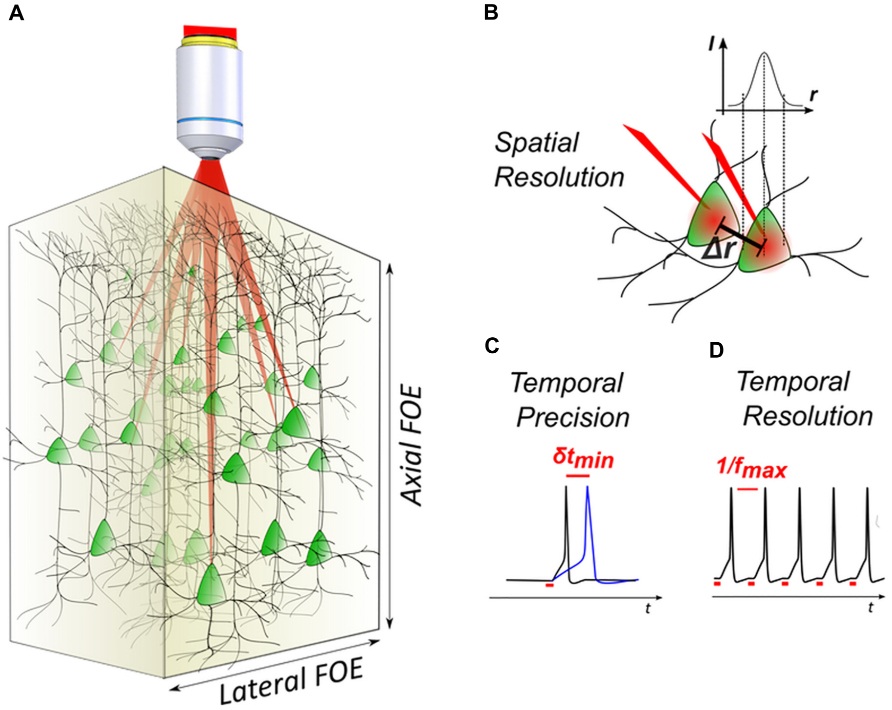

**FIGURE 1 |** 3D light-targeted photostimulation. **(A)** SLM-based multiplexing strategies allow to target opsin-expressing neurons over axial and lateral fields of excitation, extending over a few hundred microns in the brain. **(B)** The photostimulation resolution defines the minimal distance $\Delta r$ between two targets, at which each target can be individually activated. **(C)** Photostimulation temporal performances are linked to the photostimulation temporal precision, that is the timing precision $\delta t$ in evoking action potentials (APs) with repetitive stimulations (i.e., light-evoked spike jitter) and **(D)** the temporal resolution, that is the minimal time interval between two consecutive light-evoked APs (i.e., the maximum light-driven neuronal firing rate $f_{max}$).

and recording and stimulating with a single-neuron and a single-action-potential precision (Emiliani et al., 2015). These problems have been discussed exhaustively in other recent reviews (Emiliani et al., 2015; Ronzitti et al., 2017b; Chen et al., 2018c). Here we will focus on reviewing the recent developments for 3D all-optical manipulation.

# 3D Photoactivation

## Fully Parallel Methods

Fully parallel optical methods proposed for 3D activation in an all-optical configuration have been presented for optogenetics and make use of extended light-pattern formation to cover the entire neuron soma. Light-patterns can be either large Gaussian beams generated by underfilling the objective numerical aperture (NA; low-NA Gaussian beams), or beams created with more flexible light-patterning methods such as CGH, generalized phase contrast (GPC) or amplitude modulation. As already mentioned, the limit of extended light patterns is the deterioration of the axial confinement, an issue that can be solved by using temporal focusing. Common experimental configurations of TF make use of a diffraction grating in a plane conjugate to the focal plane of the microscope objective (image formation plane), separating the spectral frequencies of the laser femtosecond pulses (dispersion of different wavelengths in different angles) (Oron et al., 2005; Zhu et al., 2005). In other words, the image projected at the grating plane is the image formed at the sample plane, while 2P absorption of light projected in any other plane before or after the grating, as it is the case when you generate a 3D pattern distribution, will be strongly weakened by the pulse broadening. This has, until recently, limited TF-light shaping to 2D configurations. Methods have been proposed for axial displacement of the TF plane for Gaussian beams, by introducing group velocity dispersion (Durst et al., 2006, 2008; Dana and Shoham, 2012). However, they are only suitable for remotely displacing one plane and they are not compatible with light-patterning techniques (Leshem et al., 2014), as they can displace the TF plane but not the spatial focusing one.

Hernandez et al. (2016) solved the problem, by introducing the axial displacement mechanism after the grating for TF, which decoupled lateral light shaping from axial displacements. The system used a conventional 2D-CGH with TF for lateral light-patterning and a second SLM placed at a Fourier plane after the grating to introduce the desired axial shift from the original focal plane, via a lens-effect phase modulation. This configuration also enabled the generation of different excitation patterns at distinct axial planes, by addressing the two SLMs in multiple regions, tiled vertically to the direction of dispersion for TF. With this configuration, researchers demonstrated for the first time the generation of multi-plane temporally focused patterns, reaching a volume of 240 × 240 × 260 $\mu m^3$ with the axial confinement varying from 5 μm Full Width Half Maximum (FWHM) at the center of the field of excitation (FOE) to 10 μm at the edges of it, tested with spots of 20 μm in diameter. The number of regions equal to the number of planes to be addressed. The system was used for selective 2P 3D photoconversion of the Kaede protein (Isobe et al., 2010) in the brain of zebrafish larvae (photoconversion at 800 nm with 0.1–4.0 mW/μm$^2$ depending the illumination duration) and for 2D optogenetic activation of ChR2 in zebrafish spinal cord neurons co-expressing GCaMP5G (excitation at 900 nm with 0.6 mW/μm$^2$). Monitoring of Ca$^{2+}$ traces in that case was performed with visible illumination and two-color HiLo imaging (Lim et al., 2008) (at ∼30.8 μW/mm$^2$).

Despite the flexibility of this system, an inherent limitation occurs in the maximum number of axial planes that could be addressed because of the physical tiling of the SLMs, before the quality of the holographic spots get distorted (∼6 planes) (Hernandez et al., 2016). Although this can be sufficient for a number of biological applications (Yang et al., 2016), three new studies, have recently proposed ways to increase both the number of planes and the FOE. They all used the same principle: having a beam-shaping method for creating a 2D temporally focused pattern and using a SLM at a Fourier plane of the TF system for lateral and axial multiplexing of this pattern in several positions in 3Ds via 3D-CGH (**Figure 2A**). 3D-CGH is used to generate arrays of 3D diffraction-limited spots, using variations of the Gerchberg-Saxton algorithm (Gerchberg and Saxton, 1972; Di Leonardo et al., 2007) to calculate the phase profile to address to the SLM.

In two of these works the light-shaping part is a TF-Gaussian beam (Pégard et al., 2017; Sun et al., 2018) (**Figure 2B**). In (Pégard et al., 2017) 3D scanless holographic optogenetics with temporal focusing (3D-SHOT) was used to generate a large number of temporally focused spots, each of them fitting the size of a cell soma of pyramidal neurons (i.e., ∼10–15 μm FWHM lateral size). With this approach, researchers reported the possibility to project hundreds of excitation spots in a total volume of 350 × 350 × 280 μm$^3$. (Sun et al., 2018) presented a very similar approach as the one presented by (Pégard et al., 2017), using a TF experimental configuration with two gratings instead of a single grating and a lens. The beam's lateral size was 2.5 μm in diameter and the axial FWHM of the 2P light intensity was 7.5 μm. This study did not include any biological demonstration. The authors used the generated spots in direct laser writing inside a glass, which relies on non-linear light absorption at the focus. Fabrication was conducted either on the surface or inside standard microscope glass slides. As a novelty, they showed that they were able to place focal points at high lateral proximity (4 ţm) with minimal interference between them. That is thanks to the pulse front tilt effect, a property inherent to TF systems where the arrival time of an ultrashort pulse in a certain plane varies across the beam profile thus creating a tilt between the pulse front and the direction perpendicular to the beam. In this way, adjacent spots can be spatially overlapped (Sun et al., 2018).

Both of these studies use Gaussian beams, which is technically simpler compared to the 3D-CGH-TF system proposed by (Hernandez et al., 2016). However, a considerable drawback of this system is the fact that the laser beam is focused on a line on the SLM used for 3D multiplexing, where the size depends on the linear dispersion of the TF system in the direction of dispersing the spectral frequencies (usually parallel to the optical table), and it equals the monochromatic beam size in the unchirped dimension (vertical to the dispersion direction). In the chirped direction, care is usually given to fill the size of the SLM liquid crystal array, while in the unchirped direction the size of the beam is a few millimeters (2–3 mm) (Durst et al., 2008; Sun et al., 2018). This imposes a restriction to the maximum laser power used before damaging the SLM (and thus to the maximum number of spots that can be projected). To overcome this limitation Pégard et al. (2017) proposed adding an extra lens before dispersing the ultrashort pulses on the TF grating, defocusing the beam on the SLM and thus increasing the illumination area. Nevertheless, the defocusing created a secondary spatial focus in the form of a line that deteriorated the axial propagation of the beam (Pégard et al., 2017; Chen et al., 2018c). In a more advanced version of this method the lens was replaced by a rotating diffuser at an image plane, after the grating. This led to an enlarged illumination of the SLM, without secondary focus effects (Mardinly et al., 2018) and Gaussian beams of 23 μm axial FWHM (axial optical Point Spread Function; PSF) (Pégard et al., 2018). 3D-SHOT was used in this case to simultaneously stimulate neurons co-expressing newly developed excitatory or inhibitory somatic opsins, ST-ChroME or IRES-ST-eGTACR1, respectively, and GCaMP6s in an all-optical configuration (about 50 neurons in three different planes extending to an axial range of 100 μm, 0.13 mW/μm$^2$ or 40 mW per target for activating ST-ChroME neurons, 0.08 mW/μm$^2$ or ∼6 mW per target for IRES-ST-eGTACR1 neurons, illumination with a low-repetition rate laser at 1040 nm for 1 s) (Mardinly et al., 2018).

Higher flexibility and better axial resolution was demonstrated by Accanto et al. who presented a system for multiplexed temporally focused-light shaping (MTF-light shaping), where the beam-shaping part was either 2D-CGH or GPC (Accanto et al., 2018) (**Figure 2C,D**). For MTF-CGH, the optical setup is the same as the one of 3D-CGH-TF (Hernandez et al., 2016), the only difference being the way the multiplexing SLM is addressed. MTF-CGH enabled investigators to generate 15-μm diameter temporally focused holographic spots on 50 independent planes on an excitation field of 300 × 300 × 500 μm$^3$ and an average axial PSF of 11 μm FWHM. The theoretical FOE for the optical parameters they used was 750 × 750 × 990 μm$^3$, but was experimentally limited by the size of the optics used.

In MTF-GPC the beam-shaping part was substituted by a GPC setup (Glückstad, 1996; Papagiakoumou et al., 2010) for projection of high-precision, speckle-less, temporally focused arbitrarily shaped patterns. Notably, the combination of GPC with CGH to extend GPC to 3D was previously reported (Go et al., 2011; Bañas and Glückstad, 2017) but without TF, which is essential for suppressing excitation by the out-of-focus light (Papagiakoumou et al., 2010). In MTF-GPC, characterization of 12-μm diameter TF-GPC spots showed improved axial PSF, compared to MTF-CGH (6 μm FWHM on average on a FOE of 200 × 200 × 200 μm$^3$), as expected for TF-GPC patterns (Papagiakoumou et al., 2010). Similar to the Gaussian beam case, a crucial drawback remains the illumination of the multiplexing SLM with a line. To overcome this, (Accanto et al., 2018) removed the phase contrast filter and used the first SLM of their

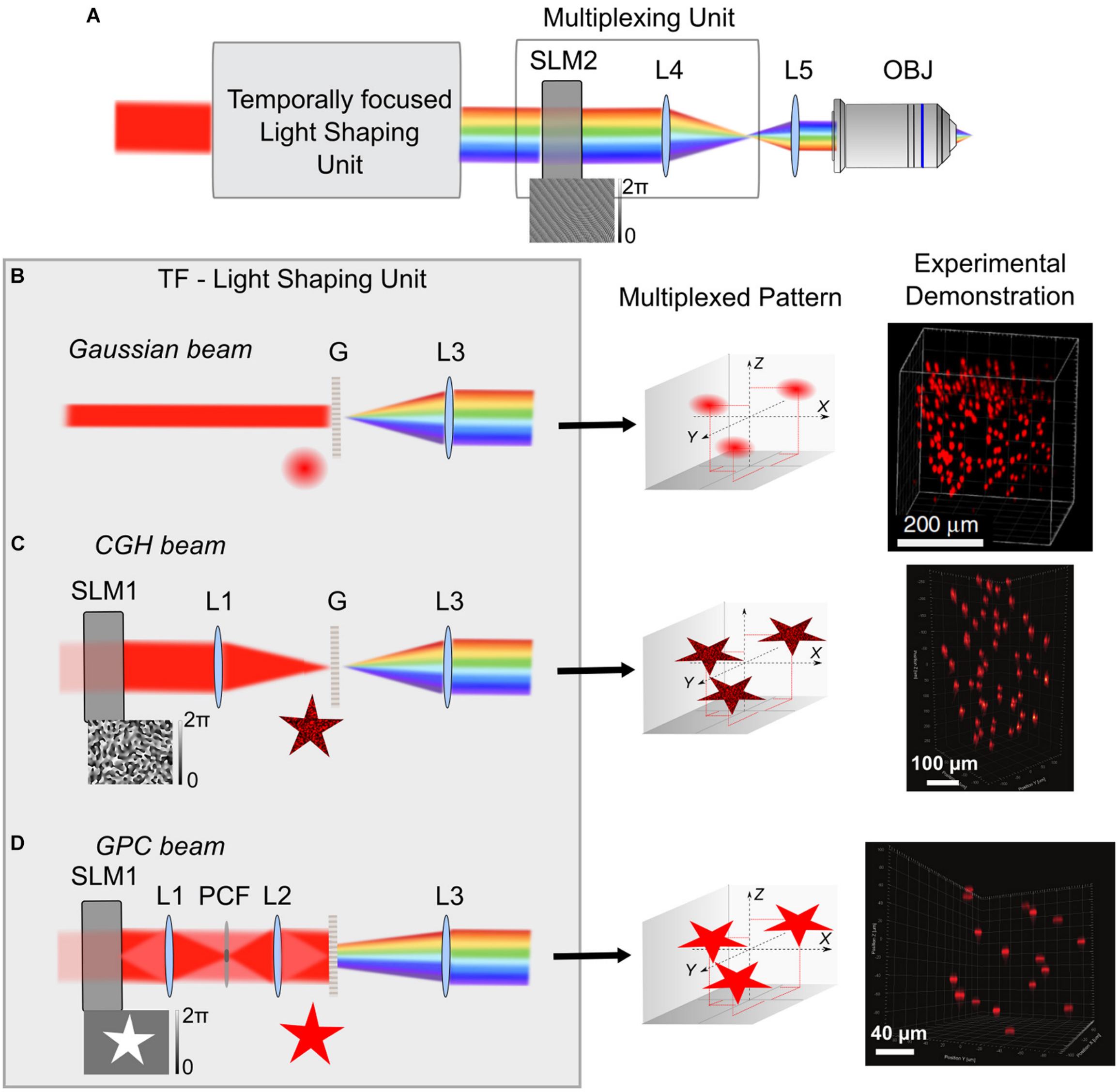

**FIGURE 2 |** 3D multiplexed temporally focused light shaping. **(A)** Optical systems for 3D temporally focused light shaping consist of a light-shaping unit for creating a 2D temporally focused pattern and a multiplexing unit, using a SLM (SLM2) at a Fourier plane of the TF system, to replicate the 2D pattern in several positions in 3D via 3D-CGH (example of a phase profile for projecting 3 diffraction-limited spots in different positions is shown on the bottom of SLM2). After the light-shaping unit, the beam is represented with its spectral frequencies diffracted, because of spectral diffraction by the grating G. After phase modulation on SLM2 the beam is imaged by two lenses (here L4 and L5) to the back aperture of the microscope objective. **(B–D)** Different cases for the TF-light-shaping unit: **(B)** Gaussian beam. In this case the grating is illuminated with a collimated Gaussian beam of a suitable size, usually adjusted with a telescope of lenses (not shown here). Configuration with a non-collimated beam (by introducing a lens prior to the grating) was used by Pégard et al. (2017) in order to increase the illuminated area of SLM2. Middle. Illustration of the example for projection of 3 Gaussian replicas, when the SLM2 is illuminated with the phase profile shown in **A**. Right. Experimental demonstration showing projection of 200 Gaussian beams in a 350 × 350 × 280 $\mu m^3$ volume, adapted from Pégard et al. (2017). **(C)** CGH beam. A SLM (SLM1) and a lens (L1) are used for holographic pattern projection (here, a star), that is then replicated in the 3 different positions (Middle). Right. Experimental demonstration of 50 holographic circular spots of 15 µm diameter in a 300 × 300 × 500 $\mu m^3$ volume, adapted from Accanto et al. (2018). **(D)** GPC beam. SLM1 is used for a binary phase modulation of $\Delta\varphi = \pi$, that is then phase contrasted by the phase contrast filter (PCF), placed at the focal plane of L1. A sharp speckle-free pattern is formed at the grating plane by L2. Middle. 3 replicas for the GPC pattern in the corresponding predefined positions of the multiplexing unit. Right. Experimental demonstration of projection of 17, 12-µm diameter circular GPC spots in a 200 × 200 × 200 $\mu m^3$ volume, adapted from Accanto et al. (2018). L3 Collimating lens.

configuration to perform amplitude and phase modulation. They encoded a pattern in four different areas on the beam-shaping SLM and the pattern of each area was laterally displaced with a different prism-phase effect, such as generating four different lines on the multiplexing SLM after the beams were temporally focused. Addressing the first SLM in different areas enabled the projection of replicas of four different speckle-free patterns in a volume of 300 × 300 × 400 $\mu m^3$, a method referred to as MTF-Multi Shapes. This strategy both increased the illumination area of the multiplexing SLM and allowed more flexibility on

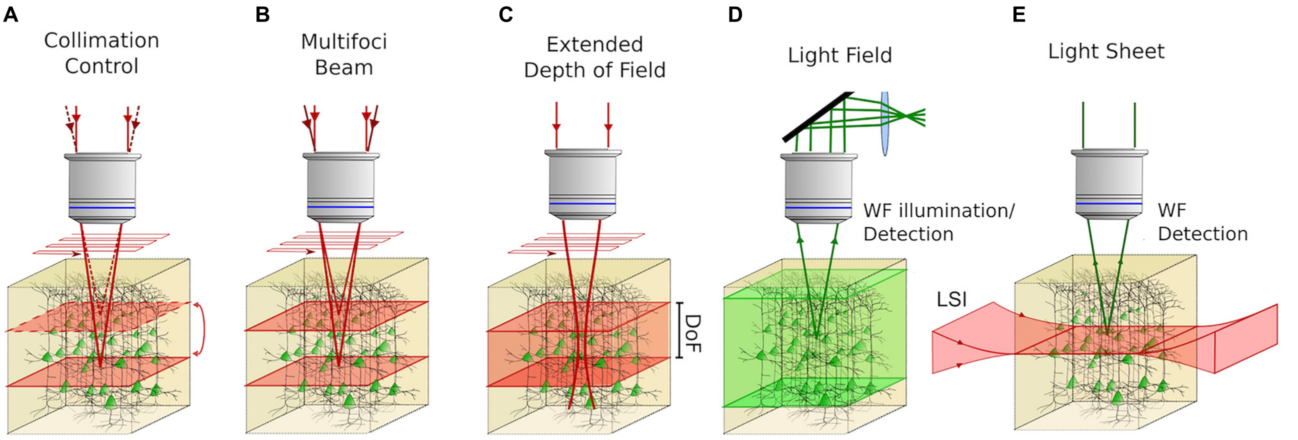

**FIGURE 3 |** Volume imaging techniques with the possibility to be coupled with 3D photostimulation in all-optical approaches. **(A)** Control of the collimation of a scanned 2P beam at the back aperture of the objective enables sequentially addressing different focal planes in an extended volume. **(B)** Multifoci 2P techniques can be used to synchronously scan several planes of the sample providing adequate demixing strategies to distinguish the contribution coming from different planes. **(C)** Extended Depth of Field (EDF) approaches enable imaging entire volumes by 2D scan of an illumination beam, featuring an extended axial point spread function (Depth of Field; DoF). **(D)** Light Field Microscopy enables CCD-recorded volume imaging by modulating the fluorescent signal induced in the sample, upon 1P wide-field (WF) illumination by means of a system of microlenses located in the detection path and computational reconstruction algorithms. **(E)** In Light-Sheet Microscopy 2D scanless imaging is obtained by illuminating the sample with a "sheet" of light in the orthogonal direction of the microscope's optical axis. In this way, optical sectioning is achieved and 3D volume imaging is performed by scanning the light sheet in the axial direction of the microscope. Red light indicates the excitation beam and green light indicates excited fluorescence.

the shape of the projected patterns, similar to that described by (Hernandez et al., 2016).

Evidently, flexibility of the MTF-light shaping methods comes at the cost of simplicity of the optical setup and total cost. For simpler cost-effective solutions in applications where the excitation spot size and form can be predetermined, it is possible to use static lithographically fabricated phase masks (Accanto et al., 2018) to replace the first SLM in MTF-CGH, or a GPC-light shaper (Bañas et al., 2014) to replace the GPC setup in MTF-GPC.

MTF-CGH was used in a multi-cell excitation of photoactivatable GCaMP (paGCaMP) in the central nervous system of the drosophila larvae (photoconversion at 760 nm with 1.0 mW/$\mu$m$^2$, illumination with trains of 10-ms pulses at 50 Hz, total illumination duration: tens of seconds up to 4 min) and to photoconvert Kaede in the zebrafish larva hindbrain (photoconversion at 800 nm with 0.4 mW/$\mu$m$^2$, illumination with trains of 10-ms pulses at 50 Hz, total illumination duration 1–4 min). Parallel illumination of neurons allowed fast photoconversion in both cases, with minimal photoactivation of untargeted neighboring cells. Especially in the case of paGCaMP, neuronal processes of the targeted cells could be clearly distinguished from the background, allowing the possibility to precisely track neuronal morphology (Accanto et al., 2018).

Although the use of TF in neuronal photoactivation with parallel methods has offered the possibility to locally confine the excitation volume, such as to preserve single-cell resolution, this might not be necessary for low-scattering samples, excitation of small size cells or sparse staining. In that case, 3D-CGH alone can be used for the projection of extended light patterns in different planes (Haist et al., 1997; Hernandez et al., 2016). Thus 2P 3D-CGH spots of 6-$\mu$m diameter were used to photoactivate ChR2 in the zebrafish larval neurons, which in combination with 2P GCaMP6s Ca$^{2+}$ imaging, enabled the identification of neuronal ensembles associated with control of tail bending (photoactivation at 920 nm, 0.2 mW/$\mu$m$^2$ or 50 mW per target, circular overlapping photoactivation regions of 18 $\mu$m in diameter) (Dal Maschio et al., 2017). Moreover, the authors performed targeted photoactivatable GFP (paGFP) photoconversion to obtain a morphological reconstruction of individual functionally identified neurons (photoconversion at 750 nm with 0.25 mW/$\mu$m$^2$ or 7 mW per target, 1-s illumination).

Finally, as a general comment we should note that 3D-TF methods using CGH for multiplexing the excitation spot, can produce powerful experimental configurations in volumetric FOEs, with the quality of all spots being the same across the whole FOE, since the spots multiplexed are replicas of the same single original spot. However, for volumes reaching mm-range, care should be taken to homogenize the excitation properties of the projected spots, by taking into account factors such as scattering with increasing depth, SLM-diffraction-efficiency corrections, optical aberrations due to the large defocusing of spots (objective used at its limits) or projection near the borders of the FOE, and spectral aberrations for TF occurring by cropping spectral frequencies in the optics when using large defocus (Hernandez et al., 2016).

## Hybrid Methods

Scanning methods are alternative approaches for neuronal stimulation and have been widely used in 2P optogenetics (Rickgauer and Tank, 2009; Andrasfalvy et al., 2010; Packer et al., 2012; Prakash et al., 2012), mainly for the activation of the slow kinetics opsin, C1V1, and most of the times in a spiral trajectory (Packer et al., 2012, 2015; Carrillo-reid et al., 2016; Yang et al., 2018). They represent the simplest and most immediate solution for many laboratories, since they adopt conventional 2P scanning microscopes based on galvanometric scanners. Nevertheless, the sequential photostimulation limits the achievable temporal resolution (Papagiakoumou, 2013; Ronzitti et al., 2017b) and does not allow the simultaneous activation of multiple targets. The use of resonant scanners or acousto-optic deflectors (AODs) to increase the temporal resolution of scanning methods, is still limited by the necessary dwell time in 2P excitation, especially for slow opsins (Prakash et al., 2012). Moreover, due to their cycling at resonant frequencies (8 kHz), resonant scanners cannot provide the necessary flexibility for arbitrary excitation trajectories, like spiral scans. For simultaneous multicell activation in 3Ds, scanning microscopes can be modified to include a SLM to multiplex the beam prior to the scan via 3D-CGH (Packer et al., 2012; Yang et al., 2018). The holographic pattern, consisting of multiple near-diffraction limited spots (~1 μm in diameter), is then scanned in spiral trajectories on an area covering the size of the cell soma (Rickgauer and Tank, 2009; Packer et al., 2015; Yang et al., 2018).

Studies using hybrid methods in all-optical configurations have so far used C1V1 as optogenetic actuator excited at 1040 nm (Packer et al., 2015; 20–80 mW per target, spirals of 20 ms, 80 MHz repetition rate laser; Yang et al., 2018; 2.2–6.0 mW per target, spirals of 20 ms, low-repetition rate amplified laser). For 3D manipulation of neurons specifically, there is currently only one study where investigators simultaneously photostimulated more than 80 neurons over 150 μm in depth in layer 2/3 of the mouse visual cortex, while simultaneously imaging the activity of the surrounding neurons with GCaMP6s (Yang et al., 2018). The authors photoactivated in three different planes in an axial range of 100 μm selected groups of somatostatin inhibitory interneurons, suppressing the response of nearby pyramidal neurons to visual stimuli in awake animals (6 mW per cell from a low-repetition rate laser, or 6 mW/$\mu$m$^2$, since the surface of the illumination spot in that case is about 1 $\mu$m$^2$, illumination for 2.8 s with 175 continuously repeated spirals, each lasting ~16 ms).

## Maximum Number of Excitation Targets

An estimate of the maximum possible number of targets to address with each approach in the framework of an all-optical experiment, presumes knowledge of the total light losses of an optical system from the laser source to the objective output, which can significantly vary from one system to another. Moreover, the power necessary per target used, can vary according to opsin type, expression level, cell health and activation depth. In general, power losses for parallel illumination methods mainly consist of losses on the SLM(s) and the diffraction grating used for TF. For hybrid methods losses are approximately 2–3 times less than those of parallel ones, since they are mainly due to the use of a single SLM. It has also been reported that parallel approaches need about twice the power used by a spiral scanned beam, to induce a neuronal response with the same properties in both cases (Picot et al., 2018; Yang et al., 2018). Thus, in principle, for the same laser source and systems carefully designed to minimize power losses, hybrid methods are supposed to outmatch parallel ones about 4 times in the maximum number of cells possibly activated (without considering photodamage limits). From what is reported so far in literature, the maximum number of cells that have been simultaneously activated with parallel approaches is 50 neurons (Mardinly et al., 2018), while for hybrid methods this number is reported to be up to 80 (Yang et al., 2018). In the first case, the authors clearly state that they were limited by the available power of their laser system. However, current advances in laser technology can provide fiber amplified systems that deliver up to 60 W maximum average power, allowing for the possibility to greatly increase the above reported numbers.

A fundamental difference between parallel and hybrid 3D multi-target photoactivation methods is the eventual photodamage effects that one can induce by increasing the number of targets and thus the amount of light that is sent to the tissue. As presented in the previously reported cases, in general, parallel illumination approaches use lower illumination intensity [<0.4 mW/$\mu$m$^2$ independently on the opsin type, see also (Chen et al., 2018b)] but higher total average power per target (e.g., for 2P *in vivo* activation 10–45 mW when amplified laser pulses of tens of μJ pulse energy are used from low-repetition rate fiber amplifiers, 30–90 mW when nJ-energy pulses are used from MHz-repetition rate oscillators) than scanning approaches (Chen et al., 2018b; Forli et al., 2018; Mardinly et al., 2018), making them more vulnerable to heating, i.e., linear photodamage. On the other hand, scanning (or hybrid) methods use high intensity (2–6 mW/$\mu$m$^2$) focused beams of low total average power (Yang et al., 2018) (although average powers in the range of 20–80 mW were reported (Packer et al., 2015) when nJ-energy pulses were used from MHz-repetition rate oscillators), making them vulnerable to non-linear photodamage.

For non-linear photodamage, the damage threshold was shown to be inversely proportional to the pulse duration and proportional to the square of the mean power (König et al., 1999). It has been evaluated on the basis of morphological damage for CHO (Chinese Hamster Ovarian) cells to 0.1 J/cm$^2$ (König et al., 1999), or tissue ablation for porcine cornea (Olivié et al., 2008) to 1.5–2.2 J/cm$^2$ for 800–1000 nm. For comparison, an intensity of 80 mW/$\mu$m$^2$ at 80 MHz pulse repetition rate corresponds to a fluence of 0.1 J/cm$^2$. No relevant studies exist for the mouse brain. A recent study on tissue heating, took the standard illumination parameters for either parallel or scanning methods into consideration, showing that the local temperature rise on a target area did not exceed the physiological limits in both cases (<1 K) (Picot et al., 2018). Specifically, to generate an action potential *in vivo,* with a holographic spot of 12-μm diameter at a depth of ~150 μm, illuminating a neuron for 3 ms, at 1030 nm and 0.1 mW/$\mu$m$^2$, the average temperature rise over the spot's surface, is estimated to 0.3 K. Furthermore, comparing the temperature rise for experimental conditions able to generate action potentials with latency in the range of 2–10 ms *in vitro*, it was found that for a holographic spot (3-ms illumination, 0.2 mW/$\mu$m$^2$) the average rise was 1 K, while for a focused beam in a spiral trajectory (3-ms illumination, 31 mW/$\mu$m$^2$) the mean temperature rise was <0.5 K, and the local rise at the center of the spiral was again ∼1 K (Picot et al., 2018). For multi-target excitation, what remains critical is the distance between the different targets: for spots placed at an average distance from their nearest neighbor greater than the thermal diffusion length in tissue $\ell_{\mathrm{th}}=\sqrt{6Dt}$ , where $D$ is the thermal diffusion constant [140 $\mu\mathrm{m}^2/\mathrm{ms}$ (Yizhar et al., 2011), and $t$ the evolved time], the temperature rise remains comparable to the case of the isolated spot (for 3-ms illumination duration, holographic stimulation at an intensity $\leq 0.2$ mW/$\mu\mathrm{m}^2$ enables keeping the induced temperature rise <2 K for activating 100 cells whose inter-soma distance was larger than the thermal diffusion length, which in that case was ∼50 μm). Otherwise, the heat load starts to significantly increase locally (Picot et al., 2018). Moreover, in terms of illumination duration, prolonged stimulation (>1 min) was found to induce substantial brain heating (6–8°C) (Mardinly et al., 2018).

Notably, the considerations of the study by Picot et al. (2018) indicate that the optimal laser repetition rate for 2P optogenetics depends on the adopted illumination method: the very low excitation intensity used in parallel illumination, allows to neglect non-linear damage effects and privileges using low (500 kHz–2 MHz) repetition rate lasers to minimize heating through linear absorption. Scanning approaches on the other hand, require high excitation intensity but enable more efficient heat dissipation because of their small beam spot size; therefore, for short illumination times, a higher repetition rate laser (Ji et al., 2008) should be preferred in order to minimize peak-power-sensitive damages.

## 3D Imaging

In order to combine photostimulation and functional imaging over large neuronal populations in extended volumes, it is necessary to elaborate strategies to decouple and independently control the photostimulation and the imaging plane. An exhaustive presentation of the existing imaging techniques have recently been presented in literature (Ji et al., 2016; Yang and Yuste, 2017). Here we will discuss the techniques that can be combined with 3D photoactivation, in volumetric all-optical studies.

Adoption of approaches for 3D imaging, involving fast mechanical axial movements of the objective lens with piezoelectric positioners (Grewe et al., 2010; Katona et al., 2011), in combination with 3D photoactivation methods can be rather challenging for an independent control of the stimulation and imaging planes. In that case, the microscope objective is shared by both photostimulation and imaging paths, and a 3D all-optical configuration would require a simultaneous readjustment of the axial position of the photostimulation foci, to compensate for the objective shifts. Since 3D photoactivation methods use a SLM to project the excitation spots/patterns to different axial planes at a maximum refresh rate of 3 ms (Yang et al., 2016), a combination of fast piezo-repositioning approaches is feasible in cases where imaging is done in few discrete axial planes (Cossell et al., 2015; Peron et al., 2015; Seelig and Jayaraman, 2015), but not possible when objectives need to be moved over an extended volume in a quasi-continuous way (Grewe et al., 2010; Katona et al., 2011).

Strategies involving the fast repositioning of the imaging focus by modulating the imaging beam divergence (**Figure 3A**), appear to be more convenient for all-optical volume investigations. This can be done by introducing a *lens-effect* in an upstream location of the imaging path, possibly in a plane conjugated to the objective back aperture to obtain a telecentric system. Clearly, the control of laser divergence must be fast enough to be compatible with functional imaging rates. Few technologies are commercially available for high-speed focus control through lenses. They are based either on the curvature change of a flexible-membrane electrically controlled lens (usually referred as Electrically Tunable Lens; ETL) (Grewe et al., 2011) or on ultrasounds propagating in a confined fluid, resulting in a tunable index of refraction gradient lens [usually referred as Tunable Acoustic Gradient (TAG) lens] that behaves like an aspheric lens (Mermillod-Blondin et al., 2008). ETLs have been mainly driven in stepping mode, enabling a ≈15 ms refocus time and can be electronically synchronized with the two-photon scanning imaging acquisition (Grewe et al., 2011). They have been successfully applied in 3D all-optical experiments, enabling simultaneous two-photon imaging and photostimulation on three planes axially spanning over 100 μm in mammals (Yang et al., 2018) and on five planes axially spanning over 32 μm in zebrafish (Dal Maschio et al., 2017). In TAG varifocal lenses, the optical power varies continuously at resonant frequencies, thus enabling much higher speeds with a ≈1 μs switching time, but they require careful control of oscillations through optical-phase locking (Kong et al., 2015). Volume imaging is built up by stacks of *xz* planes (where the fast-axis is along the axial direction) resulting in high-rate volume imaging ranging between 14 Hz ($375 \times 112 \times 130\ \mu\mathrm{m}^3$) and 56 Hz ($60 \times 4 \times 30\ \mu\mathrm{m}^3$).

Alternatively, SLMs or AODs can be used to dynamically control the degree of divergence of the imaging beam. SLM permits wavefront modulation resulting in fast beam refocusing (Dal Maschio et al., 2011) with refreshing rates up to 300 Hz. Importantly, in this case modulation is not limited to beam refocusing but can potentially be combined with more complex wavefront modulations, to correct optical aberrations (Booth, 2014) or to optimize the signal to noise ratio by targeting illumination of the cell (in this latter case in a CCD detection scheme) (Foust et al., 2015; Bovetti et al., 2017; Tanese et al., 2017). In the latter 2P near diffraction-limited stationary laser spots generated through CGH were used to perform scanless high-speed imaging of GCaMP6 activity in neurons *in vivo* on a CCD camera (Bovetti et al., 2017), or voltage imaging on dendritic spines (Tanese et al., 2017). CGH-shaped excitation was also used to improve the signal to noise ratio in voltage imaging experiments of dendrites and axons (Foust et al., 2015).

AODs can also be used for fast 3D beam repositioning. Using two pairs of orthogonal AODs addressed with counter-propagating acoustic waves of linearly varying frequency (chirped waves), it is possible to impress a precise *xy* radial deflection (determined by the center frequencies of the waves) and *z* axial displacement (determined by the amount of chirp) to the illumination beam. Being completely inertia-free, AOD systems can achieve very short commutation (24.5 μs for 3D random access) and dwell (0.05–1.0 μs) times (Kirkby et al., 2010; Nadella et al., 2016). This makes AODs especially well-suited for high-rate random access point- or line-scanning imaging. For instance, in (Katona et al., 2012) the authors recorded responses from a population of individual neurons and glial cells, in the visual cortex of adult anesthetized mice, by automated tissue-drift compensation performed plane by plane, when obtaining a reference z-stack or between 3D random-access scans. They recorded spontaneous activity within $400 \times 400 \times 500\ \mu m^3$ at a frequency up to 56 Hz. In another example (Nadella et al., 2016), researchers performed random-access patch imaging of neurons in layer 2/3 of primary visual cortex in an awake behaving mouse at 50 Hz, as well as the simultaneous dendritic and somatic imaging of pyramidal neurons in the visual cortex of awake mice at 27.9 Hz, by applying *post hoc* movement correction of images. The downside of such systems is that the combination of four AODs in a series is associated with power losses up to 75% (Reddy et al., 2008; Nadella et al., 2016) and requires strategies to compensate the temporal and spatial dispersion (Katona et al., 2012). However, recent developments in the AOD technology allow more efficient and uniform light transmission over larger scan angles when focusing away from the nominal focal plane of the objective (Nadella et al., 2016).

Remote focusing is another approach enabling fast sequential imaging of axially separated planes. It allows remote axial shifting the imaging beam by integrating a classical raster scanning system with an axial scan unit, which comprises of an objective lens and a lightweight mirror (Botcherby et al., 2007, 2012). Since the mirror is imaged on the sample plane, its oscillations are translated in a rapid change of focus in the sample, without physically moving the imaging objective lens. Fast oscillations are enabled by using a custom-built actuator constructed with a pair of galvanometer motors to scan the mirror in the kHz range. Importantly, as the two objectives are disposed to modify the beam wavefront with equal and opposite aberrations, the microscope is resilient to the systematic aberrations introduced by diverging beams that yield large focus shifts. Remote focusing enabled volume imaging of extracellular electrically induced calcium transients in OGB-loaded neurons up to 1 kHz, over a depth of 60 μm (Botcherby et al., 2012). Of note, other systems using remote focusing units, have used voice coil motors to drive the movable mirror at high speed (Rupprecht et al., 2016; Sofroniew et al., 2016).

Other volume imaging approaches, potentially compatible with 3D photostimulation, are based on multi-foci beams sent in parallel on the sample, imaging different planes simultaneously (**Figure 3B**), provided that *ad hoc* read-out demultiplexing strategies are adopted, to distinguish the signal coming from those planes. One possible strategy involves temporally multiplexed beams. Pulsed beams can be sent at different foci with different time delays. If the delays are superior to the fluorescence lifetime decay (in the range of few ns) and inferior to the inter-pulse interval, the fluorescence signal originating from different locations, can be distinguished by temporally demultiplexing the detected signal (Amir et al., 2007; Cheng et al., 2011). Other strategies rely on computational demultiplexing algorithms, which permit simultaneous multi-foci imaging, without introducing any temporal shifts among the beams. In this case, a priori knowledge of the cells distribution and sparsity of cortical neuronal activity, allow demixing signals from different planes, using independent component analysis or non-negative matrix factorization algorithms (Yang et al., 2016).

Further strategies use extended depth of field (EDF) imaging, where the illumination PSF elongates axially (Botcherby et al., 2006). Since several layers of cells are encompassed within the PSF (**Figure 3C**), a lateral scan of such a beam is equivalent to projecting a stack of axially displaced layers in a single plane. Volume imaging is thus enabled at speeds equal to scan-based planar imaging. Very high-volume rates of functional imaging can thus be obtained, provided that neural activity comes from the sparse distribution of neurons, that do not significantly overlap axially and an *a priori* high-resolution mapping of the cells position in the volume, is acquired. Bessel beam based EDF functional volume imaging has been reported *in vivo* at 30 Hz for volumes extending up to 160 μm (Lu et al., 2017).

EDF imaging can also be obtained by engineering the detection PSF. Here, the strategy is conceptually reversed compared to previous approaches: instead of attaining volume imaging by modifying the illumination beam, axial discrimination is achieved by modulating the detected fluorescent signal. Similar to the excitation PSF, the detection PSF can be phase-only modulated with a transparent static phase mask placed at a Fourier plane of the detection path, so that it does not disturb the numerical aperture and the photon throughput of the system (no photon losses). Imaging can then be performed with a CCD and computational tools can be used to recover image information over the entire extended depth of field, as in the case of the elongated excitation PSF. Researchers have shown that the use of cubic phase masks in such configurations, in combination with CGH-based target illumination, allows for simultaneous imaging of fluorescence signals arising from different 3D targeted points (Quirin et al., 2013). Moreover, an *a priori* information of the origin of the fluorescence signal, through targeted excitation with CGH spots, can remove any ambiguity arising from imaging unknown objects with extended axial features (Quirin et al., 2013). Here, the strategy is conceptually reversed compared to previous approaches: instead of attaining volume imaging by modifying the illumination beam, axial discrimination is achieved by modulating the detected fluorescent signal.

Alternatively, volumetric imaging can be obtained in a wide-field illumination configuration using Light Field Microscopy (LFM) (Broxton et al., 2013) (**Figure 3D**). A series of micro lenses are placed at the native image plane (i.e., the plane where a camera is put in standard wide-field configurations) and a relay lens system is used to reimage the lenslets' back focal plane onto a camera (Broxton et al., 2013). Since in-focus and out-of-focus light results in different patterns at the camera, axial localization of the emitters in a sample volume can be obtained by computationally processing the image. The volumetric imaging speed is only limited by the CCD acquisition rate. Despite the high temporal performances, the application of LFM has been restricted to semi-transparent tissues due to scattering limitations (Broxton et al., 2013; Cohen et al., 2014; Prevedel et al., 2014). However, it has recently been proposed in a computational imaging approach, where it is integrated with high-dimensional, structured statistics enabling fast volumetric acquisition *in vivo* in the brains of mammals (Grosenick et al., 2017). If coupled with 3D photoactivation, particular attention needs to be paid when considering photoactivation cross-talk, as contamination induced by a single-photon wide-field imaging beam, may not be negligible.

Finally, light-sheet microscopy (LSM) represents another volumetric imaging approach (**Figure 3E**) particularly suited to whole-brain imaging of small-scale organisms (Keller and Ahrens, 2015; Power and Huisken, 2017), at single-cell imaging resolution (Ahrens et al., 2013). In this case, optical sectioning of the specimen is obtained in a conventional wide-field detection scheme, with an orthogonal illumination of the sample by means of a thin "sheet" of light coming from the side. Since excitation only yields in an axially confined planar portion of the sample, optically sectioned video-rate imaging of specific planes is enabled simply by using a common camera-based detection. 3D photostimulation coupling could be, e.g., envisaged by delivering photostimulation light through the high-NA detection objective. All-optical 3D functional investigations might then be obtained by adopting those LSM volumetric strategies involving axial light-sheet repositioning and varifocal ETL-based detection (Fahrbach et al., 2013) or cubic phase-based extended depth of field detection approaches, combined with imaging deconvolution (Olarte et al., 2015; Quirin et al., 2016). It is worth mentioning that, since the side-on light-sheet needs to uniformly excite a large portion of tissue, LSM is chiefly adopted for imaging of low-scattering media, even if imaging in relatively opaque tissues have been demonstrated in double-sided illumination and detection arrangements (Tomer et al., 2012; Lemon et al., 2015; Ezpeleta et al., 2016). Interestingly, double-sided illumination can be potentially used with one low-NA objective to generate the light-sheet and the other opposite-sided objective chosen with a high NA to address the 3D photostimulation patterns. At last, it should also be considered, that the orthogonal disposition of illumination and detection objectives, ultimately limit the geometric accessibility to the sample compared to other techniques relying on a single objective.

## OUTLOOK

From this overview of the methods for 3D photoactivation and imaging, it is evident that these domains have tremendously advanced over the last few years. However, the combination of all-optical approaches is so far limited to use 2P scanning imaging modalities with an ETL (Dal Maschio et al., 2017; Mardinly et al., 2018; Yang et al., 2018), which is the most straightforward method for multiplane imaging, from those presented.

Nevertheless, the first steps have now been completed and we are entering an era where there will be an increasing demand for high-performance all-optical methods to tackle more complex biological questions. This will certainly prompt further developments for all-optical strategies in large excitation volumes and multi-area microscopes, where it will be possible, for instance, to activate a population of neurons in one area while monitoring the effects in another area of the brain (Lecoq et al., 2014; Chen et al., 2016). Furthermore, for imaging and photoactivation in large depths, development of micro-endoscopes based on miniaturized optics (Zong et al., 2017; Zou et al., 2017; Ozbay et al., 2018), able to perform all-optical manipulations, and use of three-photon excitation (Horton et al., 2013; Chen et al., 2018a; Rodríguez et al., 2018), can be envisioned.

## AUTHOR CONTRIBUTIONS

EP conceived and organized the structure of the manuscript. EP and ER wrote the manuscript and prepared the figures. VE revised and contributed in writing the manuscript.

## FUNDING

EP acknowledges the "Agence Nationale de la Recherche" ANR (Grants ANR-15-CE19-0001-01, 3DHoloPAc) for financial support. ER acknowledges the European Research Council SYNERGY Grant Scheme (HELMHOLTZ, ERC Grant Agreement # 610110). VE acknowledges the National Institutes of Health (NIH) (1UF1NS107574-01), Human Frontier Science Program (HFSP) (RGP0015/2016), Fondation Bettencourt Shueller (Prix Coups d'Élan pour la Recherche Française) and AXA Research Fund.

## REFERENCES

Accanto, N., Molinier, C., Tanese, D., Ronzitti, E., Newman, Z. L., Wyart, C., et al. (2018). Multiplexed temporally focused light shaping for high-resolution multi-cell targeting. *Optica* 5, 1478–1491. doi: 10.1364/OPTICA.5.001478

Ahrens, M. B., Orger, M. B., Robson, D. N., Li, J. M., and Keller, P. J. (2013). Whole-brain functional imaging at cellular resolution using light-sheet microscopy. *Nat. Methods* 10, 413–420. doi: 10.1038/nmeth.2434

Airan, R. D., Thompson, K. R., Fenno, L. E., Bernstein, H., and Deisseroth, K. (2009). Temporally precise in vivo control of intracellular signalling. *Nature* 458, 1025–1029. doi: 10.1038/nature07926

Amir, W., Carriles, R., Hoover, E. E., Durfee, C. G., and Squier, J. A. (2007). Simultaneous imaging of multiple focal planes in scanning two-photon absorption microscope. *Opt. Lett.* 32, 1731–1733. doi: 10.1117/12.731868

Andrasfalvy, B. K., Zemelman, B. V., Tang, J., and Vaziri, A. (2010). Two-photon single-cell optogenetic control of neuronal activity by sculpted light. *Proc. Natl. Acad. Sci. U.S.A.* 107, 11981–11986. doi: 10.1073/pnas.1006620107

Anselmi, F., Ventalon, C., Begue, A., Ogden, D., Emiliani, V., Bègue, A., et al. (2011). Three-dimensional imaging and photostimulation by remote-focusing and holographic light patterning. *Proc. Natl. Acad. Sci. U.S.A.* 108, 19504–19509. doi: 10.1073/pnas.1109111108

Bañas, A., and Glückstad, J. (2017). Holo-GPC: holographic generalized phase contrast. *Opt. Commun.* 392, 190–195. doi: 10.1016/j.optcom.2017.01.036

Bañas, A., Palima, D., Villangca, M., Aabo, T., and Glückstad, J. (2014). GPC light shaper for speckle-free one- and two- photon contiguous pattern excitation. *Opt. Express* 7102, 5299–5310. doi: 10.1364/OE.22.005299

Becker, Y., Unger, E., Fichte, M. A. H., Gacek, D. A., Dreuw, A., Wachtveitl, J., et al. (2018). A red-shifted two-photon-only caging group for three-dimensional photorelease. *Chem. Sci.* 9, 2797–2802. doi: 10.1039/C7SC05182D

Bègue, A., Papagiakoumou, E., Leshem, B., Conti, R., Enke, L., Oron, D., et al. (2013). Two-photon excitation in scattering media by spatiotemporally shaped beams and their application in optogenetic stimulation. *Biomed. Opt. Express* 4, 2869–2879. doi: 10.1364/BOE.4.002869

Booth, M. J. (2014). Adaptive optical microscopy: the ongoing quest for a perfect image. *Light Sci. Appl.* 3:e165. doi: 10.1038/lsa.2014.46

Botcherby, E. J., Juskaitis, R., Booth, M. J., and Wilson, T. (2007). Aberration-free optical refocusing in high numerical aperture microscopy. *Opt. Lett.* 32, 2007–2009. doi: 10.1364/OL.32.002007

Botcherby, E. J., Smith, C. W., Kohl, M. M., Débarre, D., Booth, M. J., Juskaitis, R., et al. (2012). Aberration-free three-dimensional multiphoton imaging of neuronal activity at kHz rates. *Proc. Natl. Acad. Sci. U.S.A.* 109, 2919–2924. doi: 10.1073/pnas.1111662109

Botcherby, E. J. J., Juškaitis, R., Wilson, T., Botcherby, E. J. J., Jus, R., Juskaitis, R., et al. (2006). Scanning two photon fluorescence microscopy with extended depth of field. *Opt. Commun.* 268, 253–260. doi: 10.1016/j.optcom.2006.07.026

Bovetti, S., Moretti, C., Zucca, S., Dal Maschio, M., Bonifazi, P., and Fellin, T. (2017). Simultaneous high-speed imaging and optogenetic inhibition in the intact mouse brain. *Sci. Rep.* 7:40041. doi: 10.1038/srep40041

Broxton, M., Grosenick, L., Yang, S., Cohen, N., Andalman, A., Deisseroth, K., et al. (2013). Wave optics theory and 3-D deconvolution for the light field microscope. *Opt. Express* 21, 25418–25439. doi: 10.1364/OE.21.025418

Carrillo-reid, L., Yang, W., Bando, Y., Peterka, D. S., and Yuste, R. (2016). Imprinting and recalling cortical ensembles. *Science* 353, 691–694. doi: 10.1126/science.aaf7560

Carroll, E. C., Berlin, S., Levitz, J., Kienzler, M. A., Yuan, Z., Madsen, D., et al. (2015). Two-photon brightness of azobenzene photoswitches designed for glutamate receptor optogenetics. *Proc. Natl. Acad. Sci. U.S.A.* 112, E776–E785. doi: 10.1073/pnas.1416942112

Chaigneau, E., Ronzitti, E., Gajowa, A. M., Soler-Llavina, J. G., Tanese, D., Brureau, Y. B. A., et al. (2016). Two-photon holographic stimulation of ReaChR. *Front. Cell. Neurosci.* 10:234. doi: 10.3389/fncel.2016.00234

Chen, B., Huang, X., Gou, D., Zeng, J., Chen, G., Pang, M., et al. (2018a). Rapid volumetric imaging with Bessel-Beam three-photon microscopy. *Biomed. Opt. Express* 9, 1992–2000. doi: 10.1364/BOE.9.001992

Chen, I. W., Papagiakoumou, E., and Emiliani, V. (2018b). Towards circuit optogenetics. *Curr. Opin. Neurobiol.* 50, 179–189. doi: 10.1016/j.conb.2018.03.008

Chen, I.-W., Ronzitti, E., Lee, R. B., Daigle, L. T., Zeng, H., Papagiakoumou, E., et al. (2018c). Parallel holographic illumination enables sub-millisecond two-photon optogenetic activation in mouse visual cortex in vivo. *bioRxiv* [Preprint]. doi: 10.1101/250795

Chen, J. L., Voigt, F. F., Javadzadeh, M., Krueppel, R., and Helmchen, F. (2016). Long-Range population dynamics of anatomically defined neocortical networks. *eLife* 5:e14679. doi: 10.7554/eLife.14679

Cheng, A., Gonçalves, J. T., Golshani, P., Arisaka, K., and Portera-Cailliau, C. (2011). Simultaneous two-photon calcium imaging at different depths with spatiotemporal multiplexing. *Nat. Methods* 8, 139–142. doi: 10.1038/nmeth.1552

Cohen, N., Yang, S., Andalman, A., Broxton, M., Grosenick, L., Deisseroth, K., et al. (2014). Enhancing the performance of the light field microscope using wavefront coding. *Opt. Express* 22, 24817–24839. doi: 10.1364/OE.22.024817

Cossell, L., Iacaruso, M. F., Muir, D. R., Houlton, R., Sader, E. N., Ko, H., et al. (2015). Functional organization of excitatory synaptic strength in primary visual cortex. *Nature* 518, 399–403. doi: 10.1038/nature14182

Dal Maschio, M., De Stasi, A. M., Benfenati, F., and Fellin, T. (2011). Three-dimensional in vivo scanning microscopy with inertia-free focus control. *Opt. Lett.* 36, 3503–3505. doi: 10.1364/OL.36.003503

Dal Maschio, M., Difato, F., Beltramo, R., Blau, A., Benfenati, F., and Fellin, T. (2010). Simultaneous two-photon imaging and photo-stimulation with structured light illumination. *Opt. Express* 18, 18720–18731. doi: 10.1364/OE.18.018720

Dal Maschio, M., Donovan, J. C., Helmbrecht, T. O., and Baier, H. (2017). Linking neurons to network function and behavior by two-photon holographic optogenetics and volumetric imaging. *Neuron* 94, 774–789.e5. doi: 10.1016/j.neuron.2017.04.034

Dana, H., and Shoham, S. (2012). Remotely scanned multiphoton temporal focusing by axial grism scanning. *Opt. Lett.* 37, 2913–2915. doi: 10.1364/OL.37.002913

Di Leonardo, R., Ianni, F., and Ruocco, G. (2007). Computer generation of optimal holograms for optical trap arrays. *Opt. Express* 15, 1913–1922. doi: 10.1364/OE.15.001913

Ducros, M., Goulam Houssen, Y., Bradley, J., de Sars, V., and Charpak, S. (2013). Encoded multisite two-photon microscopy. *Proc. Natl. Acad. Sci. U.S.A.* 110, 13138–13143. doi: 10.1073/pnas.1307818110

Durst, M. E., Zhu, G., and Xu, C. (2006). Simultaneous spatial and temporal focusing for axial scanning. *Opt. Express* 14, 12243–12254. doi: 10.1364/OE.14.012243

Durst, M. E., Zhu, G., and Xu, C. (2008). Simultaneous spatial and temporal focusing in nonlinear microscopy. *Opt. Commun.* 281, 1796–1805. doi: 10.1016/j.optcom.2007.05.071

Emiliani, V., Cohen, A. E., Deisseroth, K., and Häusser, M. (2015). All-optical interrogation of neural circuits. *J. Neurosci.* 35, 13917–13926. doi: 10.1523/JNEUROSCI.2916-15.2015

Ezpeleta, E., Zurutuza, U., and Hidalgo, J. M. G. (2016). Using personality recognition techniques to improve Bayesian spam filtering. *Proces. Leng. Nat.* 57, 125–132. doi: 10.1038/nmeth.2064

Fahrbach, F., Voigt, F., Schmid, B., Helmchen, F., and Huisken, J. (2013). Rapid 3D light-sheet microscopy with a tunable lens. *Opt. Express* 21, 1963–1975. doi: 10.1364/OE.21.021010

Forli, A., Vecchia, D., Binini, N., Succol, F., Bovetti, S., Moretti, C., et al. (2018). Two-photon bidirectional control and imaging of neuronal excitability with high spatial resolution in vivo. *Cell Rep.* 22, 2809–2817. doi: 10.1016/j.celrep.2018.02.063

Förster, D., Dal Maschio, M., Laurell, E., and Baier, H. (2017). An optogenetic toolbox for unbiased discovery of functionally connected cells in neural circuits. *Nat. Commun.* 8:116. doi: 10.1038/s41467-017-00160-z

Foust, A. J., Zampini, V., Tanese, D., Papagiakoumou, E., and Emiliani, V. (2015). Computer-generated holography enhances voltage dye fluorescence discrimination in adjacent neuronal structures. *Neurophotonics* 2:021007. doi: 10.1117/1.NPh.2.2.021007

Gerchberg, R. W., and Saxton, W. O. (1972). A practical algorithm for the determination of the phase from image and diffraction pictures. *Optik* 35, 237–246.

Glückstad, J. (1996). Phase contrast image synthesis. *Opt. Commun.* 130, 225–230. doi: 10.1016/0030-4018(96)00339-2

Go, M. A., Ng, P.-F., Bachor, H. A., and Daria, V. R. (2011). Optimal complex field holographic projection. *Opt. Lett.* 36, 3073–3075. doi: 10.1364/OL.36.003073

Go, M. A., Stricker, C., Redman, S., Bachor, H.-A. A., and Daria, V. R. (2012). Simultaneous multi-site two-photon photostimulation in three dimensions. *J. Biophotonics* 5, 745–753. doi: 10.1002/jbio.201100101

Göbel, W., Kampa, B. M., Helmchen, F., and Go, W. (2007). Imaging cellular network dynamics in three dimensions using fast 3D laser scanning. *Nat. Methods* 4, 73–79. doi: 10.1038/NMETH989

Grewe, B. F., Langer, D., Kasper, H., Kampa, B. M., and Helmchen, F. (2010). High-speed in vivo calcium imaging reveals neuronal network activity with near-millisecond precision. *Nat. Methods* 7, 399–405. doi: 10.1038/nmeth.1453

Grewe, B. F., Voigt, F. F., van 't Hoff, M., Helmchen, F., van 't Hoff, M., Helmchen, F., et al. (2011). Fast two-layer two-photon imaging of neuronal cell populations using an electrically tunable lens. *Biomed. Opt. Express* 2, 2035–2046. doi: 10.1364/BOE.2.002035

Grosenick, L. M., Broxton, M., Kim, C. K., Liston, C., Poole, B., Yang, S., et al. (2017). Identification of cellular-activity dynamics across large tissue volumes in the mammalian brain. *bioRxiv* [Preprint]. doi: 10.1101/132688

Guruge, C., Ouedraogo, Y. P., Comitz, R. L., Ma, J., Losonczy, A., and Nesnas, N. (2018). Improved synthesis of caged glutamate and caging each functional group. *ACS Chem. Neurosci.* 9, 2713–2727. doi: 10.1021/acschemneuro.8b00152

Haist, T., Schönleber, M., and Tiziani, H. (1997). Computer-generated holograms from 3D-objects written on twisted-nematic liquid crystal displays. *Opt. Commun.* 140, 299–308. doi: 10.1016/S0030-4018(97)00192-2

Herlitze, S., and Landmesser, L. T. (2007). New optical tools for controlling neuronal activity. *Curr. Opin. Neurobiol.* 17, 87–94. doi: 10.1016/j.conb.2006.12.002

Hernandez, O., Papagiakoumou, E., Tanese, D., Fidelin, K., Wyart, C., and Emiliani, V. (2016). Three-dimensional spatiotemporal focusing of holographic patterns. *Nat. Commun.* 7:11928. doi: 10.1038/ncomms11928

Horton, N. G., Wang, K., Kobat, D., Clark, C. G., Wise, F. W., Schaffer, C. B., et al. (2013). In vivo three-photon microscopy of subcortical structures within an intact mouse brain. *Nat. Photonics* 7, 205–209. doi: 10.1038/nphoton.2012.336

Isobe, K., Hashimoto, H., Suda, A., Kannari, F., Kawano, H., Mizuno, H., et al. (2010). Measurement of two-photon excitation spectrum used to photoconvert a fluorescent protein (Kaede) by nonlinear Fourier-transform spectroscopy. *Biomed. Opt. Express* 1, 687–693. doi: 10.1364/BOE.1.000687

Ji, N., Freeman, J., and Smith, S. L. (2016). Technologies for imaging neural activity in large volumes. *Nat. Neurosci.* 19, 1154–1164. doi: 10.1038/nn.4358

Ji, N., Magee, J. C., and Betzig, E. (2008). High-speed, low-photodamage nonlinear imaging using passive pulse splitters. *Nat. Methods* 5, 197–202. doi: 10.1038/nmeth.1175

Katona, G., Kaszás, A., Turi, G. F., Hájos, N., Tamás, G., Vizi, E. S., et al. (2011). Roller Coaster Scanning reveals spontaneous triggering of dendritic spikes in CA1 interneurons. *Proc. Natl. Acad. Sci. U.S.A.* 108, 2148–2153. doi: 10.1073/pnas.1009270108

Katona, G., Szalay, G., Maák, P., Kaszás, A., Veress, M., Hillier, D., et al. (2012). Fast two-photon in vivo imaging with three-dimensional random-access scanning in large tissue volumes. *Nat. Methods* 9, 201–208. doi: 10.1038/nMeth.1851

Keller, P. J., and Ahrens, M. B. (2015). Visualizing whole-brain activity and development at the single-cell level using light-sheet microscopy. *Neuron* 85, 462–483. doi: 10.1016/j.neuron.2014.12.039

Kim, E. H., Chin, G., Rong, G., Poskanzer, K. E., and Clark, H. A. (2018). Optical probes for neurobiological sensing and imaging. *Acc. Chem. Res.* 51, 1023–1032. doi: 10.1021/acs.accounts.7b00564

Kirkby, P. A., Srinivas Nadella, K. M., and Silver, R. A. (2010). A compact Acousto-optic lens for 2D and 3D femtosecond based 2-photon microscopy. *Opt. Express* 18, 13721–13745. doi: 10.1364/OE.18.013720

Klapoetke, N. C., Murata, Y., Kim, S. S., Pulver, S. R., Birdsey-Benson, A., Cho, Y. K., et al. (2014). Independent optical excitation of distinct neural populations. *Nat. Methods* 11, 338–346. doi: 10.1038/nmeth.2836

Kong, L., Tang, J., Little, J. P., Yu, Y., Lämmermann, T., Lin, C. P., et al. (2015). Continuous volumetric imaging via an optical phase-locked ultrasound lens. *Nat. Methods* 12, 759–762. doi: 10.1038/nmeth.3476

König, K., Becker, T. W., Fischer, P., Riemann, I., and Halbhuber, K.-J. (1999). Pulse-length dependence of cellular response to intense near-infrared laser pulses in multiphoton microscopes. *Opt. Lett.* 24, 113–115. doi: 10.1364/OL.24.000113

Kwon, T., Sakamoto, M., Peterka, D. S., and Yuste, R. (2017). Attenuation of synaptic potentials in dendritic spines. *Cell Rep.* 20, 1100–1110. doi: 10.1016/j.celrep.2017.07.012

Lecoq, J., Savall, J., Vučiniæ, D., Grewe, B. F., Kim, H., Li, J. Z., et al. (2014). Visualizing mammalian brain area interactions by dual-axis two-photon calcium imaging. *Nat. Neurosci.* 17, 1825–1829. doi: 10.1038/nn.3867

Lemon, W. C., Pulver, S. R., Höckendorf, B., McDole, K., Branson, K., Freeman, J., et al. (2015). Whole-central nervous system functional imaging in larval *Drosophila*. *Nat. Commun.* 6:7924. doi: 10.1038/ncomms8924

Leshem, B., Hernandez, O., Papagiakoumou, E., Emiliani, V., and Oron, D. (2014). When can temporally focused excitation be axially shifted by dispersion? *Opt. Express* 22, 7087–7098. doi: 10.1364/OE.22.007087

Levitz, J., Pantoja, C., Gaub, B., Janovjak, H., Reiner, A., Hoagland, A., et al. (2013). Optical control of metabotropic glutamate receptors. *Nat. Neurosci.* 16, 507–516. doi: 10.1038/nn.3346

Liesener, J., Reicherter, M., Haist, T., and Tiziani, H. J. (2000). Multi-functional optical tweezers using computer-generated holograms. *Opt. Commun.* 185, 77–82. doi: 10.1016/S0030-4018(00)00990-1

Lim, D., Chu, K. K., and Mertz, J. (2008). Wide-field fluorescence sectioning with hybrid speckle and uniform-illumination microscopy. *Opt. Lett.* 33, 1819–1821. doi: 10.1364/OL.33.001819

Lu, R., Sun, W., Liang, Y., Kerlin, A., Bierfeld, J., Seelig, J. D., et al. (2017). Video-rate volumetric functional imaging of the brain at synaptic resolution. *Nat. Neurosci.* 20, 620–628. doi: 10.1038/nn.4516

Lutz, C., Otis, T. S., DeSars, V., Charpak, S., Digregorio, D. A., and Emiliani, V. (2008). Holographic photolysis of caged neurotransmitters. *Nat. Methods* 5, 821–827. doi: 10.1038/nmeth.1241

Mardinly, A. R., Oldenburg, I. A., Pégard, N. C., Sridharan, S., Lyall, E. H., Chesnov, K., et al. (2018). Precise multimodal optical control of neural ensemble activity. *Nat. Neurosci.* 21, 881–893. doi: 10.1038/s41593-018-0139-8

Mermillod-Blondin, A., McLeod, E., and Arnold, C. B. (2008). High-speed varifocal imaging with a tunable acoustic gradient index of refraction lens. *Opt. Lett.* 33, 2146–2148. doi: 10.1364/OL.33.002146

Nadella, K. M. N. S., Roš, H., Baragli, C., Griffiths, V. A., Konstantinou, G., Koimtzis, T., et al. (2016). Random access scanning microscopy for 3D imaging in awake behaving animals. *Nat. Methods* 13, 1001–1004. doi: 10.1038/nMeth.4033

Nikolenko, V., Poskanzer, K. E., and Yuste, R. (2007). Two-photon photostimulation and imaging of neural circuits. *Nat. Methods* 4, 943–950. doi: 10.1038/NMETH1105

Nikolenko, V., Watson, B. O., Araya, R., Woodruff, A., Peterka, D. S., and Yuste, R. (2008). SLM microscopy: scanless two-photon imaging and photostimulation with spatial light modulators. *Front. Neural Circuits* 2:5. doi: 10.3389/neuro.04.005.2008

Olarte, O. E., Andilla, J., Artigas, D., and Loza-Alvarez, P. (2015). Decoupled illumination detection in light sheet microscopy for fast volumetric imaging. *Optica* 2, 702–705. doi: 10.1364/OPTICA.2.000702

Olivié, G., Giguère, D., Vidal, F., Ozaki, T., Kieffer, J.-C., Nada, O., et al. (2008). Wavelength dependence of femtosecond laser ablation threshold of corneal stroma. *Opt. Express* 16, 4121–4129. doi: 10.1364/OE.16.004121

Oron, D., Papagiakoumou, E., Anselmi, F., and Emiliani, V. (2012). Two-photon optogenetics. *Prog. Brain Res.* 196, 119–143. doi: 10.1016/B978-0-444-59426-6.00007-0

Oron, D., Tal, E., and Silberberg, Y. (2005). Scanningless depth-resolved microscopy. *Opt. Express* 13, 1468–1476. doi: 10.1364/OPEX.13.001468

Ozbay, B. N., Futia, G. L., Ma, M., Bright, V. M., Gopinath, J. T., Hughes, E. G., et al. (2018). Three dimensional two-photon imaging of neuronal activity in freely moving mice using a miniature fiber coupled microscope with active axial-scanning. *bioRxiv* [Preprint]. doi: 10.1101/226431

Packer, A. M., Peterka, D. S., Hirtz, J. J., Prakash, R., Deisseroth, K., Yuste, R., et al. (2012). Two-photon optogenetics of dendritic spines and neural circuits. *Nat. Methods* 9, 1171–1179. doi: 10.1038/nmeth.2249

Packer, A. M., Russell, L. E., Dalgleish, H. W. P., and Häusser, M. (2015). Simultaneous all-optical manipulation and recording of neural circuit activity with cellular resolution in vivo. *Nat. Methods* 12, 140–146. doi: 10.1038/nmeth.3217

Papagiakoumou, E. (2013). Optical developments for optogenetics. *Biol. Cell* 105, 443–464. doi: 10.1111/boc.201200087

Papagiakoumou, E., Anselmi, F., Bègue, A., de Sars, V., Glückstad, J., Isacoff, E. Y., et al. (2010). Scanless two-photon excitation of channelrhodopsin-2. *Nat. Methods* 7, 848–854. doi: 10.1038/nmeth.1505

Papagiakoumou, E., Bègue, A., Leshem, B., Schwartz, O., Stell, B. M., Bradley, J., et al. (2013). Functional patterned multiphoton excitation deep inside scattering tissue. *Nat. Photonics* 7, 274–278. doi: 10.1038/nphoton.2013.9

Papagiakoumou, E., de Sars, V., Oron, D., and Emiliani, V. (2008). Patterned two-photon illumination by spatiotemporal shaping of ultrashort pulses. *Opt. Express* 16, 22039–22047. doi: 10.1364/OE.16.022039

Papagiakoumou, E., Ronzitti, E., Chen, I.-W., Gajowa, M., Picot, A., and Emiliani, V. (2018). Two-photon optogenetics by computer-generated holography. *Neuromethods* 133, 175–197. doi: 10.1007/978-1-4939-7417-7_10

Pégard, N., Mardinly, A., Oldenburg, I., Waller, L., and Adesnik, H. (2018). *Partially Coherent Holographic temporal focusing for 3D light sculpting with single neuron resolution. Opt. InfoBase Conf. Pap. Part F*88-B, 4–5. doi: 10.1364/BRAIN.2018.BW2C.2$^{*}$

Pégard, N. M., Oldenburg, I., Sridharan, S., Walller, L., and Adesnik, H. (2017). 3D scanless holographic optogenetics with temporal focusing. *Nat. Commun.* 8:1228. doi: 10.1038/s41467-017-01031-3

Peron, S. P., Freeman, J., Iyer, V., Guo, C., and Svoboda, K. (2015). A cellular resolution map of barrel cortex activity during tactile behavior. *Neuron* 86, 783–799. doi: 10.1016/j.neuron.2015.03.027

Picot, A., Dominguez, S., Liu, C., Chen, I. W., Tanese, D., Ronzitti, E., et al. (2018). Temperature rise under two-photon optogenetic brain stimulation. *Cell Rep.* 24, 1243–1253.e5. doi: 10.1016/j.celrep.2018.06.119

Piestun, R., Spektor, B., and Shamir, J. (1996). Wave fields in three dimensions: analysis and synthesis. *J. Opt. Soc. Am. A* 13, 1837–1848. doi: 10.1364/JOSAA.13.001837

Power, R. M., and Huisken, J. (2017). A guide to light-sheet fluorescence microscopy for multiscale imaging. *Nat. Methods* 14, 360–373. doi: 10.1038/nmeth.4224

Prakash, R., Yizhar, O., Grewe, B., Ramakrishnan, C., Wang, N., Goshen, I., et al. (2012). Two-photon optogenetic toolbox for fast inhibition, excitation and bistable modulation. *Nat. Methods* 9, 1171–1179. doi: 10.1038/nmeth.2215

Prevedel, R., Verhoef, A. J., Pernía-Andrade, A. J., Weisenburger, S., Huang, B. S., Nöbauer, T., et al. (2016). Fast volumetric calcium imaging across multiple cortical layers using sculpted light. *Nat. Methods* 13, 1021–1028. doi: 10.1038/nmeth.4040

Prevedel, R., Yoon, Y.-G., Hoffmann, M., Pak, N., Wetzstein, G., Kato, S., et al. (2014). Simultaneous whole-animal 3D imaging of neuronal activity using light-field microscopy. *Nat. Methods* 11, 727–730. doi: 10.1038/nmeth.2964

Quirin, S., Peterka, D. S., and Yuste, R. (2013). Instantaneous three-dimensional sensing using spatial light modulator illumination with extended depth of field imaging. *Opt. Express* 21, 16007–16021. doi: 10.1364/OE.21.016007

Quirin, S., Vladimirov, N., Yang, C.-T., Peterka, D. S., Yuste, R., and Ahrens, M. B. (2016). Calcium imaging of neural circuits with extended depth-of-field light-sheet microscopy. *Opt. Lett.* 41, 855–858. doi: 10.1364/OL.41.000855

Reddy, G. D., Kelleher, K., Fink, R., and Saggau, P. (2008). Three-dimensional random access multiphoton microscopy for functional imaging of neuronal activity. *Nat. Neurosci.* 11, 713–720. doi: 10.1038/nn.2116

Rickgauer, J. P., Deisseroth, K., and Tank, D. W. (2014). Simultaneous cellular-resolution optical perturbation and imaging of place cell firing fields. *Nat. Neurosci.* 17, 1816–1824. doi: 10.1038/nn.3866

Rickgauer, J. P., and Tank, D. W. (2009). Two-photon excitation of channelrhodopsin-2 at saturation. *Proc. Natl. Acad. Sci. U.S.A.* 106, 15025–15030. doi: 10.1073/pnas.0907084106

Rodríguez, C., Liang, Y., Lu, R., and Ji, N. (2018). Three-photon fluorescence microscopy with an axially elongated Bessel focus. *Opt. Lett.* 43, 1914–1917. doi: 10.1364/OL.43.001914

Ronzitti, E., Conti, R., Zampini, V., Tanese, D., Foust, A. J., Klapoetke, N., et al. (2017a). Sub-millisecond optogenetic control of neuronal firing with two-photon holographic photoactivation of Chronos. *J. Neurosci.* 37, 10679–10689. doi: 10.1523/JNEUROSCI.1246-17.2017

Ronzitti, E., Ventalon, C., Canepari, M., Forget, B. C., Papagiakoumou, E., and Emiliani, V. (2017b). Recent advances in patterned photostimulation for optogenetics. *J. Opt.* 19:113001. doi: 10.1088/2040-8986/aa8299

Rupprecht, P., Prendergast, A., Wyart, C., and Friedrich, R. W. (2016). Remote z-scanning with a macroscopic voice coil motor for fast 3D multiphoton laser scanning microscopy. *Biomed. Opt. Express* 7, 1656–1671. doi: 10.1364/BOE.7.001656

Seelig, J. D., and Jayaraman, V. (2015). Neural dynamics for landmark orientation and angular path integration. *Nature* 521, 186–191. doi: 10.1038/nature14446

Shemesh, O. A., Tanese, D., Zampini, V., Linghu, C., Piatkevich, K., Ronzitti, E., et al. (2017). Temporally precise single-cell resolution optogenetics. *Nat. Neurosci.* 20, 1796–1806. doi: 10.1038/s41593-017-0018-8

Sofroniew, N. J., Flickinger, D., King, J., and Svoboda, K. (2016). A large field of view two-photon mesoscope with subcellular resolution for in vivo imaging. *eLife* 5:e14472. doi: 10.7554/eLife.14472

Stirman, J. N., Smith, I. T., Kudenov, M. W., and Smith, S. L. (2016). Wide field-of-view, multi-region, two-photon imaging of neuronal activity in the mammalian brain. *Nat. Biotechnol.* 34, 857–862. doi: 10.1038/nbt.3594

Sun, B., Salter, P. S., Roider, C., Strauss, J., Heberle, J., and Booth, M. J. (2018). Four-dimensional light shaping?: manipulating ultrafast spatio-temporal foci in space and time. *Light Sci. Appl.* 7:17117. doi: 10.1038/lsa.2017.117

Szabo, V., Ventalon, C., De Sars, V., Bradley, J., and Emiliani, V. (2014). Spatially selective holographic photoactivation and functional fluorescence imaging in freely behaving mice with a fiberscope. *Neuron* 84, 1157–1169. doi: 10.1016/j.neuron.2014.11.005

Tanese, D., Weng, J.-Y., Zampini, V., De Sars, V., Canepari, M., Rozsa, B., et al. (2017). Imaging membrane potential changes from dendritic spines using computer-generated holography. *Neurophotonics* 4:031211. doi: 10.1117/1.NPh.4.3.031211

Tomer, R., Khairy, K., Amat, F., and Keller, P. J. (2012). Quantitative high-speed imaging of entire developing embryos with simultaneous multiview light-sheet microscopy. *Nat. Methods* 9, 755–763. doi: 10.1038/nmeth.2062

Vogt, N. (2015). All-optical electrophysiology in behaving animals. *Nat. Methods* 12:101. doi: 10.1038/nmeth.3272

Yang, S., Papagiakoumou, E., Guillon, M., de Sars, V., Tang, C. M., and Emiliani, V. (2011). Three-dimensional holographic photostimulation of the dendritic arbor. *J. Neural Eng.* 8:46002. doi: 10.1088/1741-2560/8/4/046002

Yang, W., Carrillo-reid, L., Bando, Y., Peterka, D. S., and Yuste, R. (2018). Simultaneous two-photon optogenetics and imaging of cortical circuits in three dimensions. *eLife* 7:e32671. doi: 10.7554/eLife.32671

Yang, W., Miller, J. K., Carrillo-Reid, L., Pnevmatikakis, E., Paninski, L., Yuste, R., et al. (2016). Simultaneous multi-plane imaging of neural circuits. *Neuron* 89, 269–284. doi: 10.1016/j.neuron.2015.12.012

Yang, W., and Yuste, R. (2017). In vivo imaging of neural activity. *Nat. Methods* 14, 349–359. doi: 10.1038/nmeth.4230

Yang, W., and Yuste, R. (2018). Holographic imaging and photostimulation of neural activity. *Curr. Opin. Neurobiol.* 50, 211–221. doi: 10.1016/j.conb.2018.03.006

Yizhar, O., Fenno, L. E., Davidson, T. J., Mogri, M., and Deisseroth, K. (2011). Optogenetics in neural systems. *Neuron* 71, 9–34. doi: 10.1016/j.neuron.2011.06.004

Zhu, G., van Howe, J., Durst, M., Zipfel, W., and Xu, C. (2005). Simultaneous spatial and temporal focusing of femtosecond pulses. *Opt. Express* 13, 2153–2159. doi: 10.1364/OPEX.13.002153

Zong, W., Wu, R., Li, M., Hu, Y., Li, Y., Li, J., et al. (2017). Fast high-resolution miniature two-photon microscopy for brain imaging in freely behaving mice. *Nat. Methods* 14, 713–719. doi: 10.1038/nmeth.4305

Zou, Y., Chau, F. S., and Zhou, G. (2017). Ultra-compact optical zoom endoscope using solid tunable lenses. *Opt. Express* 25, 20675–20688. doi: 10.1364/OE.25.020675

**Conflict of Interest Statement:** The authors declare that the research was conducted in the absence of any commercial or financial relationships that could be construed as a potential conflict of interest.

The handling Editor declared a past co-authorship with the authors.

frontiers
in Cellular Neuroscience

TECHNOLOGY REPORT
published: 08 January 2019
doi: 10.3389/fncel.2018.00514

# Improvements in Simultaneous Sodium and Calcium Imaging

*Kenichi Miyazaki*[1,2], *John E. Lisman*[2,3†] *and William N. Ross*[1,2*]

[1]*Department of Physiology, New York Medical College, Valhalla, NY, United States,* [2]*Marine Biological Laboratory, Woods Hole, MA, United States,* [3]*Department of Biology, Brandeis University, Waltham, MA, United States*

High speed imaging of ion concentration changes in neurons is an important and growing tool for neuroscientists. We previously developed a system for simultaneously measuring sodium and calcium changes in small compartments in neurons (Miyazaki and Ross, 2015). We used this technique to analyze the dynamics of these ions in individual pyramidal neuron dendritic spines (Miyazaki and Ross, 2017). This system is based on high speed multiplexing of light emitting diodes (LEDs) and classic organic indicators. To improve this system we made additional changes, primarily incorporating lasers in addition to the LEDs, more sophisticated imaging protocols, and the use of newer sodium and calcium indicators. This new system generates signals with higher signal to noise ratio (S/N), less background fluorescence, and less photodynamic damage. In addition, by using longer wavelength indicators instead of indicators sensitive in the UV range, it allows for the incorporation of focal uncaging along with simultaneous imaging, which should extend the range of experiments.

**Keywords: sodium, calcium, imaging, dendrite, spine, pyramidal neuron, CCD camera**

***Edited by:***
*Marco Canepari,*
*UMR5588 Laboratoire Interdisciplinaire de Physique (LIPhy), France*

***Reviewed by:***
*Dejan Zecevic,*
*Yale University, United States*
*Leonardo Sacconi,*
*Università degli Studi di Firenze, Italy*

****Correspondence:***
*William N. Ross*
*ross@nymc.edu*

*†Deceased*

***Received:*** *28 September 2018*
***Accepted:*** *10 December 2018*
***Published:*** *08 January 2019*

***Citation:***
*Miyazaki K, Lisman JE and Ross WN (2019) Improvements in Simultaneous Sodium and Calcium Imaging. Front. Cell. Neurosci. 12:514. doi: 10.3389/fncel.2018.00514*

## INTRODUCTION

High speed imaging of ion concentration changes has revolutionized our understanding of many aspects of nervous system function. Before the use of imaging most neuronal activity was recorded using electrodes that detected responses at one site on the neuron, usually the cell body. With imaging, using appropriate indicator molecules, activity can be recorded from many sites, including sites on neurons that are too small or distant, like dendrites or axons, to be penetrated with electrodes. Most progress has occurred using calcium indicators because these are easy to design with appropriate sensitivity and because physiological $[Ca^{2+}]_i$ changes are large compared to the resting $[Ca^{2+}]_i$ in the cell. Experiments using this class of indicator have examined the direct physiological role of $[Ca^{2+}]_i$ changes in different parts of the cell (e.g., calcium entry in presynaptic terminals, calcium entry through postsynaptic receptors, and calcium release from stores in the soma and dendrites). They also used the detected $[Ca^{2+}]_i$ changes as an indicator of electrical activity because action potentials almost always cause measurable $[Ca^{2+}]_i$ changes in all parts of the cell where they propagate. Some experiments have used voltage sensitive dyes (VSDs) to measure electrical activity directly in small compartments, with some experiments detecting subthreshold potential changes in dendritic spines (Popovic et al., 2015; Acker et al., 2016).

Sodium sensitive indicators have also been used to report on the activity of neurons in slices, but with less frequency, in part, because they are relatively less sensitive than calcium indicators, making the measurements more challenging. Nevertheless, there are kinds of experiments where they might be preferred, for example, when trying to detect sodium entry through AMPA receptors, which are not permeable to calcium in most pyramidal neurons. In some ways these kinds of measurements are complementary to calcium measurements, giving additional useful information about synaptic activity and electrical function.

Recently, we developed a method (Miyazaki and Ross, 2015) to simultaneously image $[Ca^{2+}]_i$ and $[Na^{+}]_i$ changes in neurons at high speed and high spatial resolution. It has some resemblance to other approaches to measure two parameters simultaneously (Vogt et al., 2011; Lee et al., 2012), but optimized to detect these two ions. We were able to combine this system with other improvements to detect and analyze these changes in individual dendritic spines on hippocampal pyramidal neurons with sufficient time resolution to follow the physiological calcium ($[Ca^{2+}]_i$) and sodium ion concentration ($[Na^{+}]_i$) changes in those structures (Miyazaki and Ross, 2017). These measurements were the first to use high speed sodium imaging with single spine resolution. Even with this success, however, we thought it would be useful to improve the system to: (a) increase the signal to noise ratio (S/N) of these measurements to reveal additional properties about spines; (b) to decrease background fluorescence to improve the accuracy of the interpretation of the fluorescence measurements in terms of $[Na^{+}]_i$ changes; (c) to reduce the photodynamic damage caused by the fluorescence excitation light to allow for longer experiments; and (d) to allow for the incorporation of uncaging stimulation in addition to electrical stimulation. To this end, we made several improvements to the apparatus. In this article we review the original setup for simultaneous sodium and calcium imaging, pointing out the novel aspects of the system, and we describe the new components, which are responsible for the improvements. We also indicate a few additional changes that we hope to incorporate in the near future.

## MATERIALS AND METHODS

Hippocampal transverse slices were prepared from 2- to 4-week-old Sprague-Dawley rats using techniques regularly followed in our laboratory (Miyazaki and Ross, 2017). All procedures were approved by institutional IACUC committees at New York Medical College and the Marine Biological Laboratory. After incubation, individual slices were placed on the stage of an Olympus BX50WI microscope and viewed with a 20× or 60× water immersion lens. Pyramidal neurons were patched on the soma and filled with combinations of sodium and calcium indicators [either SBFI and Oregon Green Bapta-1 (OGB-1; or OGB-5N), or bis-fura-2 and ANG-2]. Some trial experiments (**Figure 7**) used Cal-630 as the calcium indicator. Synaptic

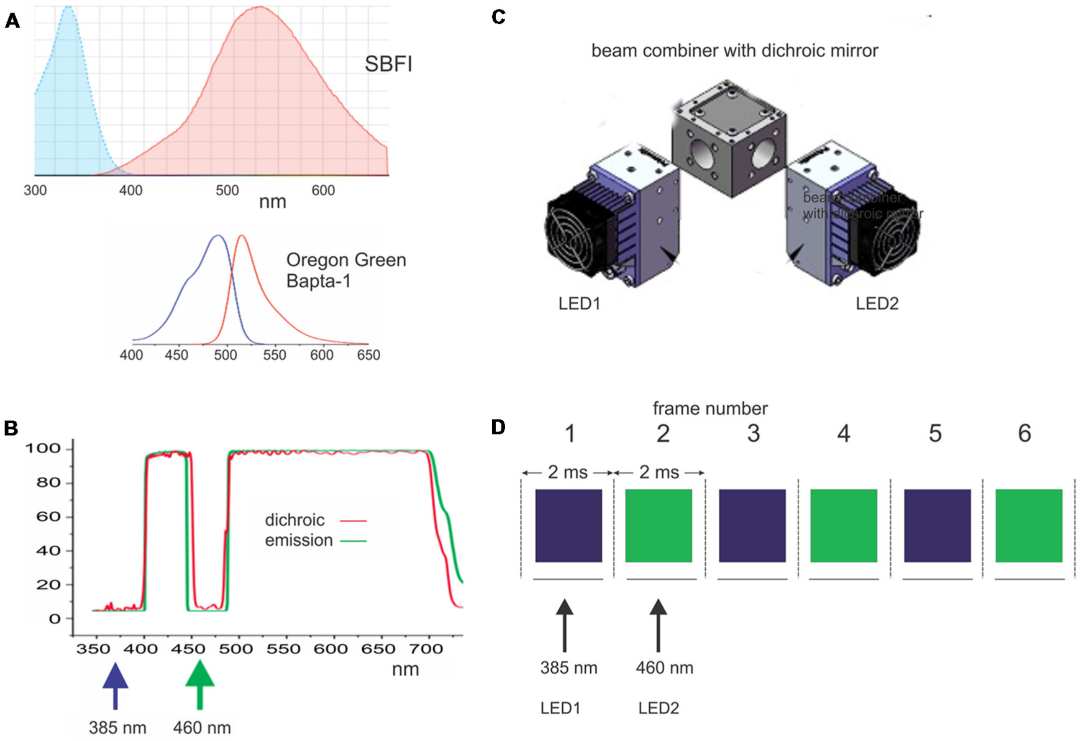

**FIGURE 1 |** Components of the apparatus used to make simultaneous sodium and calcium measurements with light emitting diode (LED) excitation sources. **(A)** Excitation and emission spectra of SBFI (sodium indicator) and Oregon Green Bapta-1 (OGB-1; calcium indicator). Both sets of spectra are plotted on the same wavelength scale to show the separation of the excitation bands. **(B)** Custom dichroic and emission filters used for these two indicators. Note the notch in the filters to pass 460 nm excitation light for OGB-1. **(C)** Two LEDs (385 nm and 460 nm) together with a beam combiner with a dichroic mirror (DM) used to excite the two indicators. **(D)** Pattern of excitation and detection: every 2 ms alternate 1.8 ms LED pulses excite the indicators. The switching is synchronized to the frames of the CCD camera operating at 500 Hz. Adapted from Miyazaki and Ross (2015).

activation was through an external theta-glass electrode placed on the slice ∼10 μm from a dendrite. Fluorescence illumination, through the usual rear fluorescence port of the microscope, was provided by one of several light emitting diodes (LEDs; Miyazaki and Ross, 2015). High speed movies of the fluorescence changes from the indicators were detected by a RedShirtImaging NeuroCCD-SMQ camera (80 × 80 pixel resolution). Data taking was under the control of Neuroplex software supplied by RedShirtImaging. Analysis was under control of a package of programs, SCANDATA, also written in MATLAB. More details are provided in the previous articles (Miyazaki and Ross, 2015, 2017). Newer methods are described below.

# RESULTS

## Simultaneous Imaging Using LEDs

**Figure 1** (modified from Miyazaki and Ross, 2015) shows the main features of the original system for detecting signals using LED excitation. **Figure 1A** shows the excitation and emission spectra for the SBFI and OGB-1 combination of sodium and calcium indicators, with the spectra aligned to the same wavelength scale. **Figure 1B** shows the custom filter set that allows excitation of SBFI at 385 nm and the excitation of OGB-1 at 460 nm. **Figure 1C** shows the arrangement of the LED illuminators with a dichroic mirror (DM) for combining the two outputs. A similar set of spectra and filter combinations are used for the bis-fura-2 and ANG-2 indicator combination (Miyazaki and Ross, 2015). **Figure 1D** shows the pattern of alternating 385 nm and 460 nm LED pulses aligned with the 2 ms frames of the CCD camera. This system has been upgraded slightly from the original system with the addition of a new software to generate the LED pulses, a new computer and data taking software (Turbo-SM) from RedShirtImaging, and an improved version of our analysis software (SCANDATA). We also introduced a feedback system to correct for the slight drift in LED intensity during an experimental trial due to heating of the LED modules.

**Figure 2**, modified from Miyazaki and Ross (2015), shows the measurement of $[Na^+]_i$ and $[Ca^{2+}]_i$ changes in response to a train of five synaptic stimuli. **Figure 2B** shows the response at a region of interest (ROI) in **Figure 2A** as detected by the camera. Each frame alternately records the sodium and calcium signals. When the odd numbered frames and the even numbered frames are separately plotted and aligned with the simultaneously recorded electrical response in the soma it is clear that both $[Na^+]_i$ and $[Ca^{2+}]_i$ changes occurred (**Figure 2C**). The calcium change is precisely aligned with the single synaptically evoked backpropagating action potential (bAP); the sodium signal is slightly delayed, which may be due to the slower kinetics of the NMDA receptor channel and/or sodium diffusion from its source in the spines (Miyazaki and Ross, 2017).

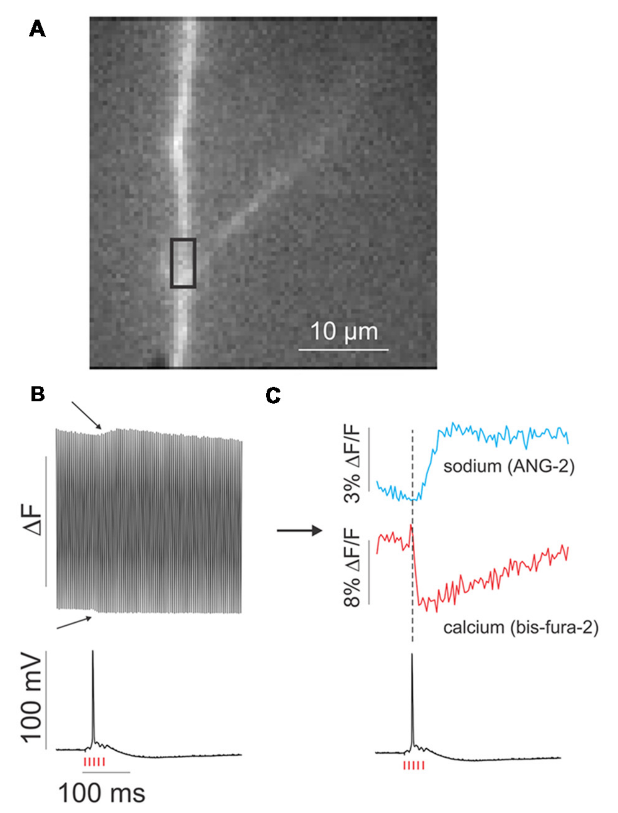

**FIGURE 2 |** Quasi-simultaneous detection of $[Ca^{2+}]_i$ and $[Na^+]_i$ changes in a dendrite in response to synaptic stimulation. **(A)** Fluorescence image of a small region of an apical dendrite of a rat CA1 pyramidal neuron. A region of interest (ROI) is marked with a black rectangle. **(B)** Simultaneous fluorescence response in the ROI and the somatically measured electrical response to a train of five synaptic stimuli at 100 Hz (red hash marks). The fluorescence response switches with each frame, which are excited at alternate wavelengths. The two "bumps" (arrows) correspond to the changes in $[Ca^{2+}]_i$ and $[Na^+]_i$ in response to the stimulation. **(C)** Sodium and calcium signals after separating alternate frames. The calcium transient is matched to the action potential, while the sodium signal is delayed slightly. The calcium signal goes down because bis-fura-2 fluorescence decreases in response to an increase in $[Ca^{2+}]_i$. Adapted from Miyazaki and Ross (2015).

## Simultaneous Imaging Using Laser Spot Illumination

In addition to pursuing experiments using this system, we made some efforts to improve the simultaneous detection of sodium and calcium signals. The new components of the system are shown in **Figure 3**. We added a set of four laser diode modules at 377, 476, 517, and 561 nm, which are combined using DMs into one beam (Versalase, Vortran Laser Technologies). Selection among these lasers, including setting the laser pulse widths and amplitudes, is controlled by a combination of software from Vortran and a package (PULSE) written in MATLAB in our laboratory. The combined outputs of these lasers are focused onto a fiber optic patch cord (50 or 200 μm diameter). The fiber is fed into a custom side port in the fluorescence illuminator of the microscope. A 45° mirror is positioned in the object plane of the illuminator. The mirror transmits 70% of the light from the rear port from the LEDs and 30% of the laser light from the side port from the fiber. This ratio was chosen because the lasers are much brighter than the LEDs and 30% of the peak laser intensity is sufficient for most experiments. The tip of the optical fiber is

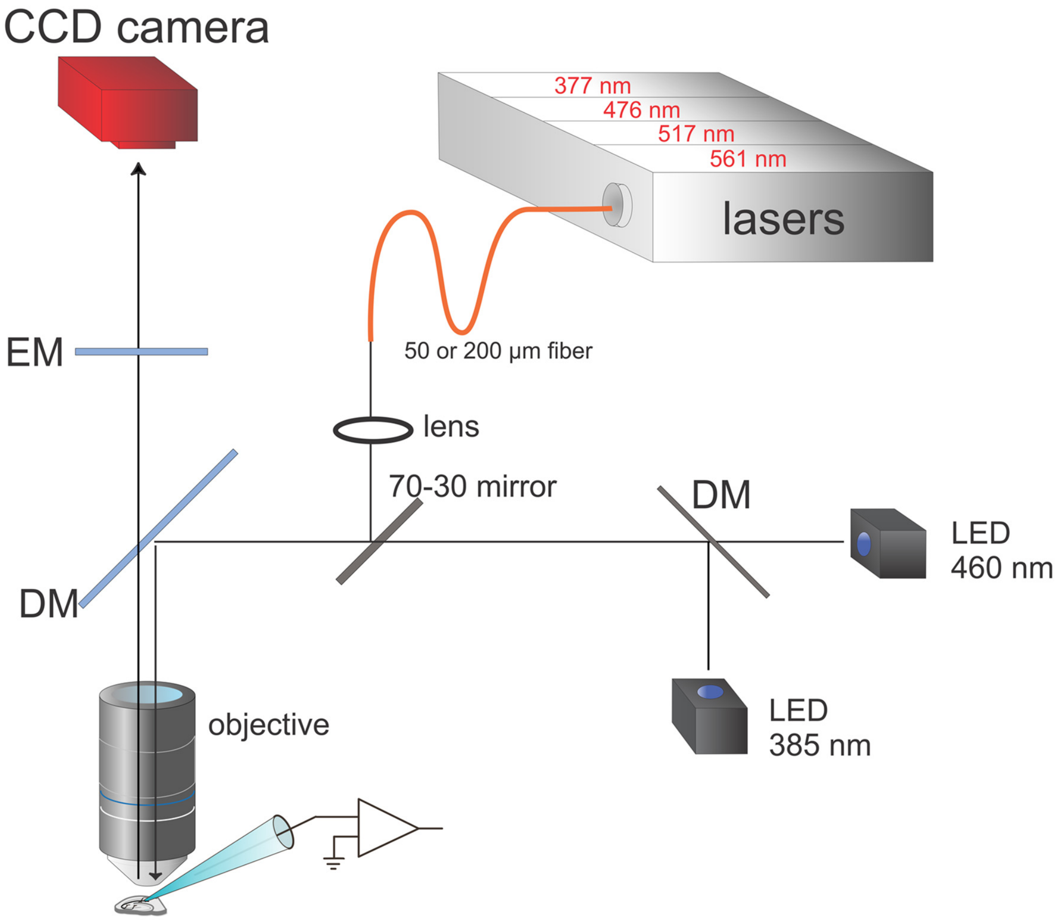

**FIGURE 3 |** Schematic of modified apparatus including both LEDs and lasers. The box at the top contains four lasers at the indicated wavelengths. The laser outputs, which can be separately controlled, are combined and focused onto either a 50 μm or 200 μm diameter fiber optic. The face of the fiber is focused with a lens and the objective onto a region of the slice, after 30% of the light is reflected off a mirror in the microscope body and a special DM in a standard filter cube (see **Figure 1B** for a typical filter set). The LED outputs are combined and 70% of the light passes through to preparation. Software selects combinations of LEDs and lasers to excite the indicator dyes in the cell of interest. The CCD camera (RedShirtImaging, NeuroCCD-SMQ) detects the fluorescence changes with frames synchronized with the laser or LED pulses.

focused onto the image plane of the objective, which contains the cell filled with fluorescent indicators.

We used the lasers to reduce the size of the illumination spot, to improve the S/N, to reduce background illumination, and to minimize photodynamic damage. The smallest spot the LED system can generate is about 100 μm diameter, using the built-in aperture of the Olympus fluorescence illuminator. This is because the LED is a large source and the aperture has a limited constriction range. It is possible that a custom aperture could further reduce the diameter, but it would also reduce the excitation intensity, which was already a limiting factor in obtaining good single spine signals. We did not pursue that direction. In contrast, the laser spot can be focused to a spot of 2.5 μm diameter using the 50 μm fiber optic and the 60× objective. Other illumination techniques (Popovic et al., 2015; Tanese et al., 2017) can achieve diffraction limited spots. That approach is useful for 2-photon uncaging and measurements from single spines, but is not helpful if we are trying to detect optical signals simultaneously from spines and nearby regions.

For both the LED system and the laser system we typically run the camera at 500 Hz, even though it can go faster. Five-hundred hertz is fast enough to distinguish among the time courses of physiological events without introducing additional noise due to a reduction in integration time. Typically, each LED pulse illuminates about 1.8 ms of a 2 ms camera frame; we do not illuminate during the 0.1 ms around the frame transition to prevent contamination of one frame from the light of the preceding frame. Tests confirmed that there was no cross contamination. When we use laser illumination we can make much shorter pulses (~0.1–0.4 ms) because the lasers can be much more intense than a LED; the parameter that matters is the integrated light intensity per frame. We can control this value for each laser by either varying the pulse width or the peak intensity or both. We select this value to be as high as possible without causing significant photodynamic damage.

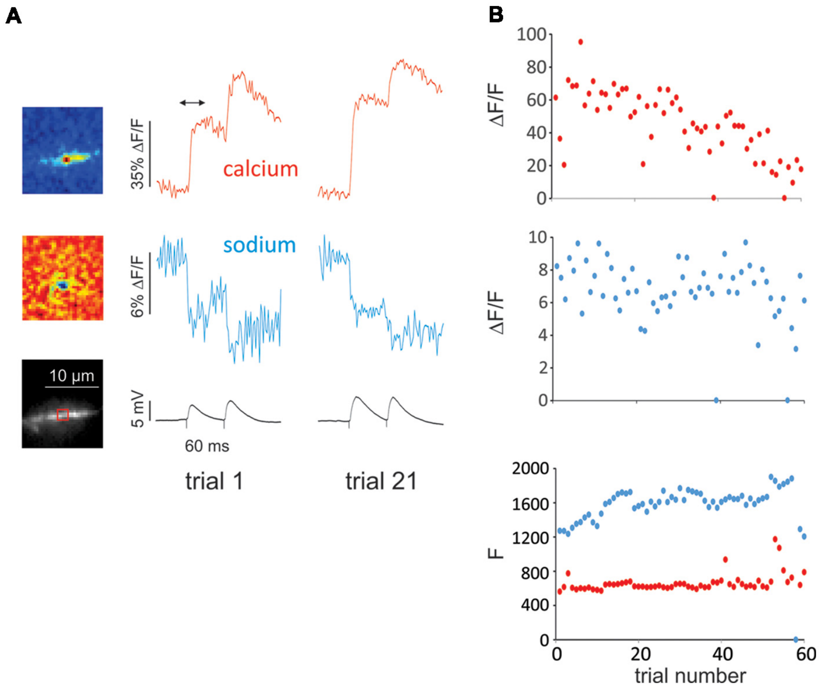

**FIGURE 4 |** Example of experiment with many trials showing little cumulative photodynamic damage reflected in single spine sodium and calcium signals. **(A)** Pseudocolor difference images (top) and image of dendritic region with ROI indicated (bottom). The difference images show the spatial distribution of the calcium and sodium signals from the first of two synaptic stimuli (time marked by arrow above calcium signal) of the first of 60 trials. The cells were filled with 50 μM OGB-1 and 2 mM SBFI from a patch pipette on the soma. The pseudocolor images show that both changes were localized to a small region corresponding to a dendritic spine. The traces show that the signals from trial 1 and trial 21 were about the same. **(B)** Plots of peak signal sizes (ΔF/F) from the first synaptic response and resting fluorescence levels (F) for all 60 trials. The *F* values were measured at the beginning of the traces before stimulation. The peak calcium signal (ΔF/F, red dots) decreased slightly over the many trials; the peak sodium signal (ΔF/F, blue dots) showed little deterioration. In two trials (38 and 55) there was failure in both the sodium and calcium signals (an unusually small number). The *F* values stayed relatively constant until the last few trials. In four trials the resting calcium F levels were high, probably because the trials were preceded by spontaneous synaptic responses. The resting sodium *F* value did not change significantly.

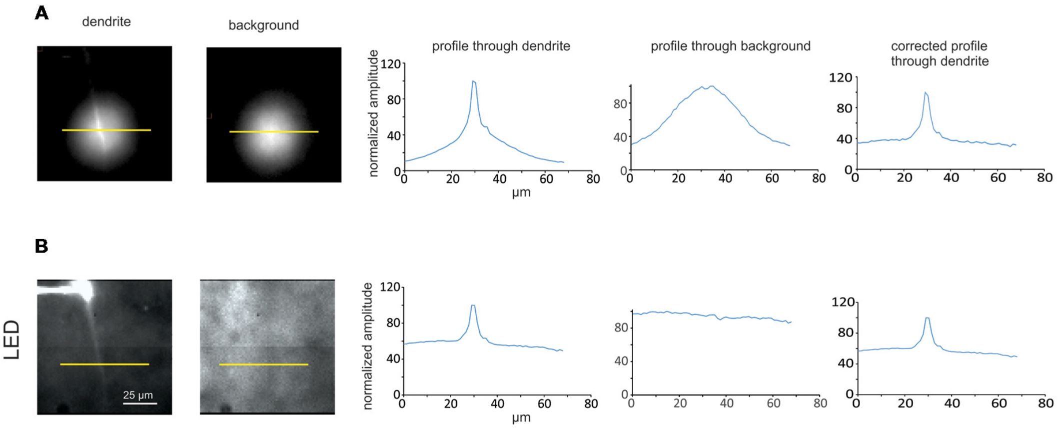

**FIGURE 5 |** Comparison between LED and laser illumination for separating dendrite fluorescence from background. (**A**, left and middle) Images of slices with and without a dendrite in the field of view illuminated by a 377 nm laser through a 200 μm fiber and a 20× objective lens (each image has the same field of view as images in **B**). The cell was filled with 2 mM SBFI from a patch pipette on the soma. The yellow bars indicate lines along which profiles were measured. (**A**, right) Intensity profiles along yellow lines through the two images. The line through the field without the dendrite (background fluorescence) was used to normalize the profile through the dendrite, which is shown in the right trace. (**B**, left and middle) Similar images from the same neuron where the dendrite and background are illuminated by a 385 nm LED. (**B**, right) Similar profiles through the LED illuminated images. Note that the profile through the background is almost flat, which is due to the wide field illumination by the LED. Importantly, the background level using the laser illumination is less than the background when the LED is used.

Spot illumination with the laser also appears to reduce photodynamic damage because only a small volume of the neuron is illuminated. In our experience many more trials can be made with laser spot illumination than with widefield LED illumination using about the same excitation intensity, although it was hard to develop a rigorous way of demonstrating this conclusion. One example is shown in **Figure 4**, where we made over 60 measurements of single spine sodium and calcium signals with little deterioration except at the end. Illuminating the synaptic region does not appear to cause significant photodynamic damage, as assayed by the synaptic electrical response. One possible reason for this good fortune is that the indicator dyes are injected postsynaptically, while the most sensitive metabolic components are in the presynaptic terminal, which does not contain sensitizing fluorophores.

We tried to assay how much focused laser illumination reduces background fluorescence compared to using more widespread LED illumination. For this effort we filled a pyramidal neuron with 2 mM SBFI and searched for a region where a single dendrite could be isolated and in focus (**Figures 5A,B**, left). We measured the profile of fluorescence across the dendrite simultaneously using the 385 nm LED and laser illumination (377 nm) by recording the fluorescence from each source in different camera frames. It is not clear from these profiles how much of the fluorescence comes from the dendrite and how much from the background since the illumination along the profile is not constant and not the same for the LED and laser. To try to correct for this variation we moved to a region of the slice without a dendrite and measured the fluorescence profiles only due to the autofluorescence background of the tissue (**Figures 5A,B**, middle). These autofluorescence profiles should correspond to the illumination profiles of the LED and laser. We then used these profiles to normalize the intensity distribution from the images including the dendrite (**Figures 5A,B**, right). It is clear that after this correction the normalized intensity profile using the laser has less contribution from the background (∼35%) than the background contribution to the profile (∼60%) using the LED, i.e., the background contribution was reduced by ∼40%. In six cells the background contribution using laser illumination was 38 ± 4% and the contribution using LED illumination was 56 ± 4% (SE), i.e., the background was 32% less using the laser. This set of measurements was made using a 200 μm diameter fiber optic, which makes a spot of about 30 μm diameter with the 20× lens. In one experiment when we used the 50 μm diameter fiber optic the background contribution to the profile using the laser was reduced slightly more (∼46%). We did not do sufficient experiments with the 50 μm fiber to determine the statistical validity of this conclusion. Also, these numbers fluctuated depending on the preparation and the depth of the cell, but the lowest background was usually obtained with the 50 μm fiber.

To further compare the two illumination methods we measured sodium and calcium signals using LED and laser excitation simultaneously. In the first example (**Figure 6A**), we recorded the calcium signals at a dendritic location from a single bAP detected with OGB-1 using laser excitation at 476 nm and LED excitation at 460 ± 11 nm. It is clear that the S/N is better with laser excitation and the peak ΔF/F response is about twice the level obtained with the LED. In six cells we found that ΔF/F was 2.4 ± 0.2 (SE) times higher using the laser compared with ΔF/F measured using the LED. The S/N improved by the same amount, which was expected since the major source of noise is shot noise, and the intensity of the laser was adjusted to be about the same as the LED intensity in the center of the dendrite In a similar experiment we compared the sodium signals detected with SBFI from five APs in the axon initial segment region with the two excitation sources (laser at 377 nm and LED at 385 ± 8 nm) using the 60× lens which makes 10 μm diameter spot. Again (**Figure 6B**), it is clear that the S/N and ΔF/F values using the laser signal are better. These improvements are more than be accounted for by the reduction in background

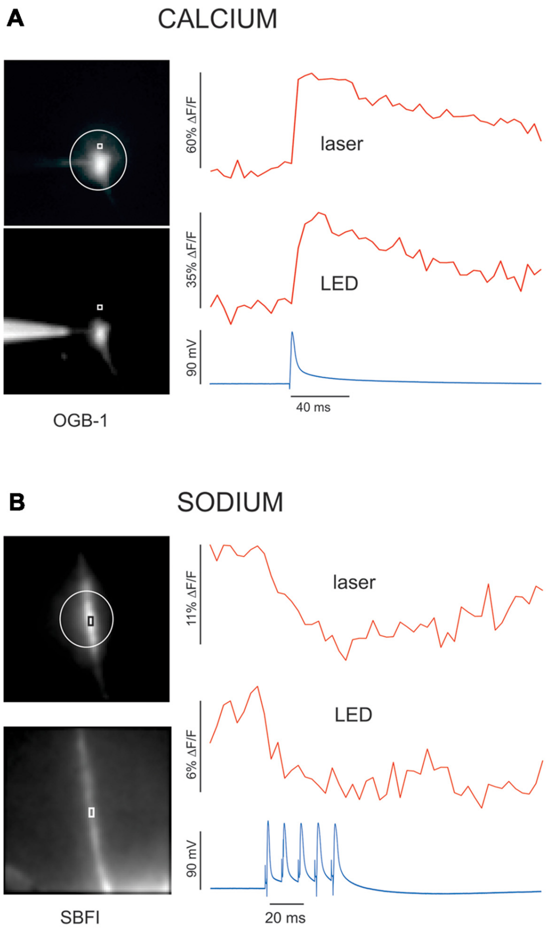

**FIGURE 6 |** The fractional change in fluorescence (ΔF/F) is greater using a laser spot compared to when illumination is with an LED. Using a laser in one channel and an LED in the other, $[Ca^{2+}]_i$ or $[Na^{+}]_i$ changes were measured in alternate channels. The calcium signals (using OGB-1, 200 μm fiber, and 20× lens) in response to a single bAP were measured from a dendritic location in one cell **(A)** and the sodium signals (using SBFI, 200 μm fiber, and 60× lens) in response to five APs were measured from the axon of another cell **(B)**. In each case the laser and LED signals were measured simultaneously in the two channels. For both the sodium and calcium signals the peak ΔF/F response was about twice as large using the laser. Resting fluorescence levels (F) were about the same.

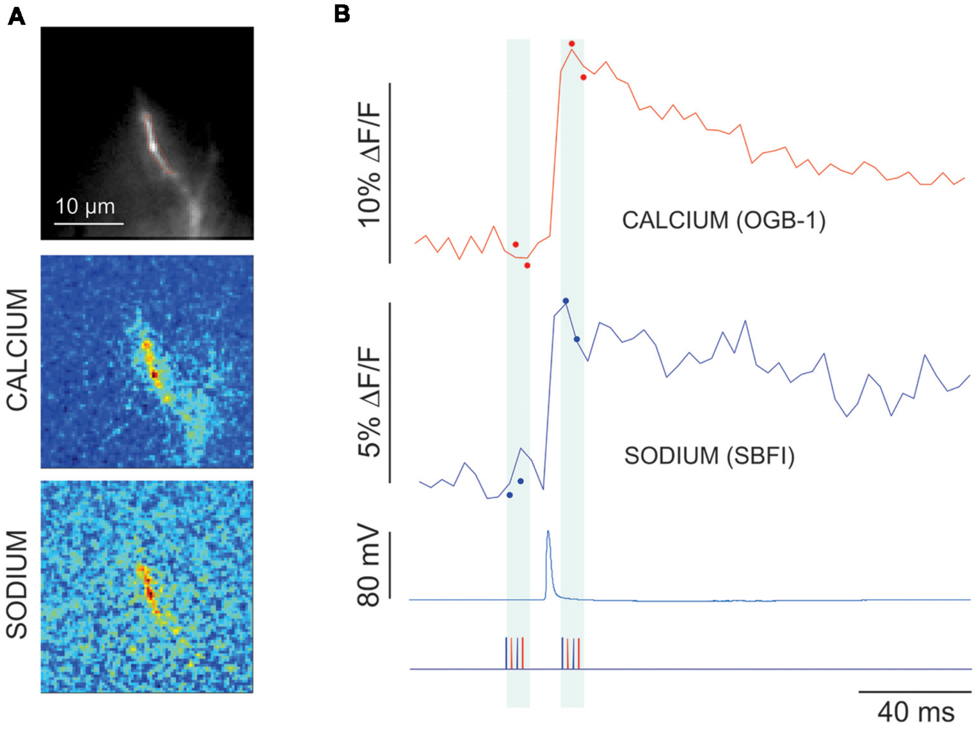

**FIGURE 7 |** Measurement of fluorescence signals using reduced illumination protocol. **(A)** Image using 60× lens of the axon filled with 2 mM SBFI and 50 μM OGB-1, and difference images made by only illuminating four frames (two with 377 nm laser and two with 476 nm laser) before and four frames after a single intrasomatically evoked AP. **(B)** Calcium (red) and sodium (blue) signals taken by limited illumination (closed circles) and full frame illumination (solid lines) from the extended ROI in the left image. Bottom trace shows timing of the light flashes of each wavelength (blue-377 nm; red-476 nm). Sodium trace and image are inverted.

light calculated above. We are not clear about the source of the additional enhancement.

The ability to record signals using laser excitation in one channel and LED excitation in the other is useful for more than just test purposes. For some experiments it is useful to detect signals from one ion over a wide field and signals from the other ion from a spot with better S/N. For example, wide field calcium imaging can be used to identify responding spines, while focal laser excitation can improve the sodium signals from the identified spines.

## Reduction of the Illumination Duration to Reduce Photodynamic Damage

Although the results shown is **Figure 4** suggest that photodynamic damage would not be a problem in many situations, there are certain experiments that might require accurate measurements over longer time periods, e.g., experiments investigating long term potentiation (LTP). Another way of limiting photodynamic damage is to reduce the integrated light per sweep. The simplest way of doing that is just to shorten the sweep as much as possible. We found that we could reduce the effective illumination period even further if we are only interested in the spatial distribution of the peak intensity of the signal and not the complete time course. For example, in an experiment to measure spike-evoked signals in the axon hillock region (**Figure 7**), we illuminated the preparation for a few frames just before electrical stimulation (two frames each for both wavelengths) and for a few frames after the peak of the response (**Figure 7B**, closed circles). We then averaged the set of frames before and after the synaptic stimulation and then subtracted one average from the other (**Figure 7A**, middle and bottom). This difference image corresponds to the spatial distribution of the signal maximum and only requires a few frames of illumination on each side of the response, usually less than a total of 20 ms, which is about 10% of the duration of the trials shown in the other figures in this article. Using this protocol we can record many more trials before significant photodynamic damage is observed. The weakness of this approach is that it does not record the time course of the signals. However, as shown in the figure, we can take other trials using the standard protocol to determine the time course (solid lines). This works if we expect the time course to be approximately the same in different trials. For example, some experiments examining synaptic responses might show significant variability in the amplitude of the signals, while their time courses would be expected to be more constant. Of course, this assumption would have to be tested.

## Improvements Using Long Wavelength Indicators

A complementary approach to improving the sodium and calcium signals is to use better indicators. The best currently

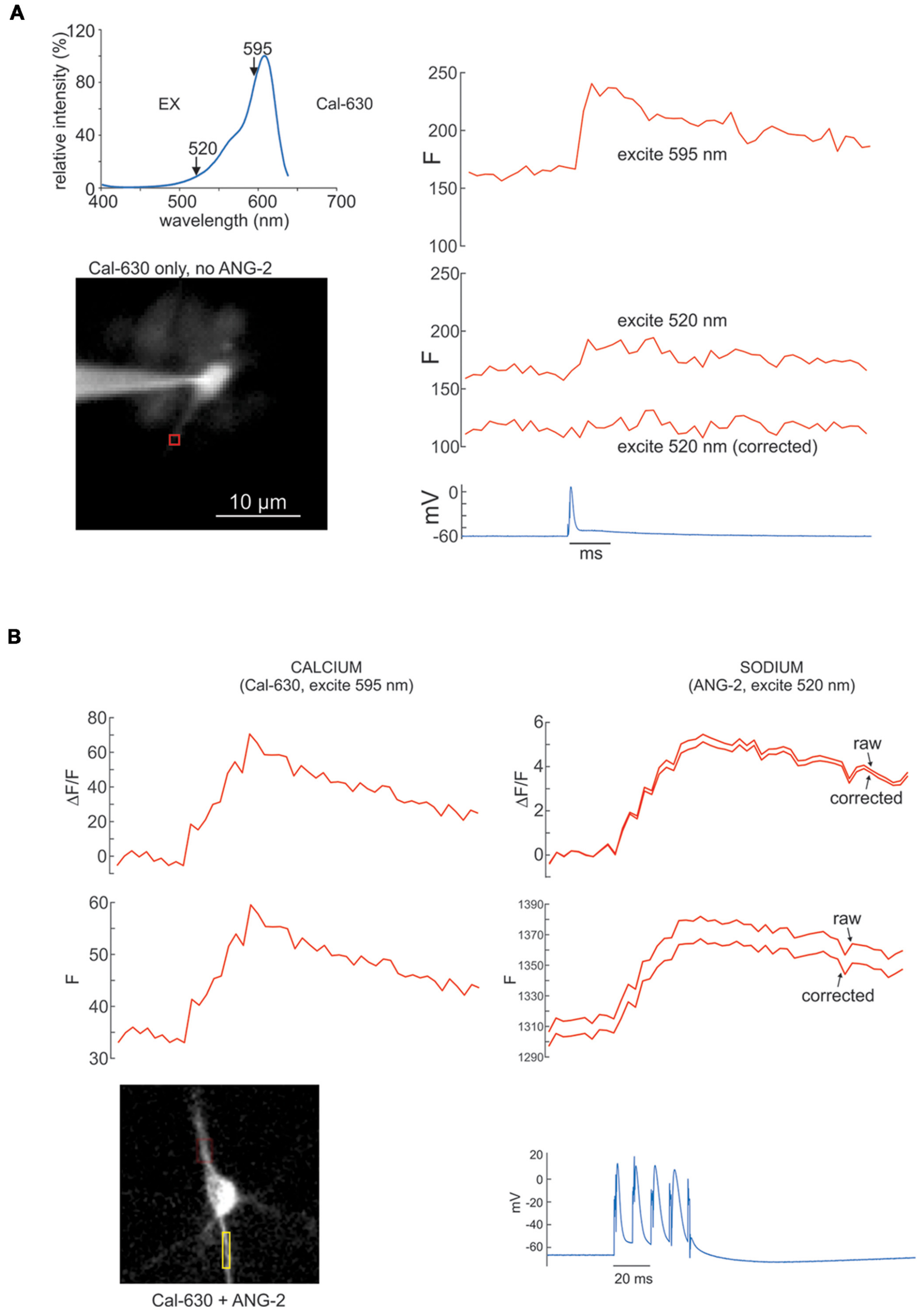

**FIGURE 8 |** Sodium and calcium signals from APs measured with ANG-2 (sodium) and Cal-630 (calcium) with corrections for Cal-630 excitation by ANG-2 excitation light at 520 nm. (**A**, top left) Excitation spectrum of Cal-630. Note that this indicator is strongly excited at 595 nm but there is still some excitation at 520 nm. (**A**, right) Fluorescence responses from a dendritic ROI of a pyramidal neuron filled with 100 µM Cal-630 when stimulated with a single AP. The response at 595 nm is strong but there is still a signal when excited at 520 nm. The "corrected" trace, which shows no signal, was obtained when 29% of the 595 nm signal was subtracted from the 520 nm trace. (**B**, left) ΔF/F and F signals from the axon of a pyramidal neuron in response to four intrasomatically evoked APs. The cell was filled with 200 µM ANG-2 and 100 µM Cal-630, but the fluorescence only comes from the calcium indicator since exciting at 595 nm is outside the excitation band of ANG-2. (**B**, right) Similar responses to the same four APs when the cell was excited at 520 nm. The "raw" traces are the direct fluorescence signals. The "corrected" traces have the contribution of Cal-630 to the signal removed as shown in **(A)**.

available sodium indicator (although not by more than a factor of two) is ANG-2 (currently sold by Ion Indicators). When we use this indicator, which is maximally excited near 513 nm, we have to use a calcium indicator that is excited away from this excitation band if we want to use our simultaneous imaging protocol. The most common calcium indicators that meet this requirement are in the fura series (most often bis-fura-2; Miyazaki and Ross, 2015). These calcium indicators are best excited near 380 nm. However, there are two disadvantages to exciting at this low wavelength. One is that excitation at this wavelength causes more background light due to autofluorescence in the tissue and more photodynamic damage because the lower wavelength photons have more energy and scatter more. Most other commonly used calcium indicators are in the OGB series or Fluo series, and are excited too close to the ANG-2 peak to separate the sodium and calcium signals. Recently, a series of long wavelength calcium indicators has become available (mostly from AATBioquest). One advantage of these new indicators is that that their excitation maxima are far enough towards the red end of the spectrum that there is minimal contamination between the two indicators when ANG-2 (for sodium) is excited at 513 nm. One good indicator in this series is Cal-630, which is best excited at 607 nm (**Figure 8A**). For our experiments we use either 595 nm (the peak of the closest available LED) or 561 nm (the closest available laser line). We also designed custom dichroic and emission filters for this pair of indicators with notches near 595 nm or 561 nm to pass the excitation light with either the LED or laser as we did for the other indicator pairs (Miyazaki and Ross, 2015). Using Cal-630 instead of bis-fura-2 gives good calcium signals (**Figure 8A**) with less background. An additional advantage of this and analogous indicators (e.g., Calbryte-630) for future work is that uncaging experiments can be combined with simultaneous sodium and calcium measurements since there is no need to excite near 375 nm, a wavelength region commonly used to uncage glutamate or other bioactive compounds. Using bis-fura-2 or SBFI would require excitation at this wavelength, which would prevent combining the measurements with uncaging.

One concern with using combinations of indicators is that there might be some contamination of one signal by the other if there is overlap in the excitation spectra. For the bis-fura-2:ANG-2 combination or the SBFI:OGB-1 combination there is almost no overlap in the excitation spectra (Miyazaki and Ross, 2015). In addition, their changes are in the opposite directions for parallel increases in ion concentration. However, when using the ANG-2 and Cal-630 combination there is more concern since the fluorescence changes are in the same direction and there is a small amount of Cal-630 excitation at the ANG-2 excitation peak (520 nm, **Figure 8A**, top). To investigate the Cal-630 fluorescence contamination we measured the signal from a bAP with 520 nm and 595 nm LEDs in a cell filled only with Cal-630 (**Figure 8A**, top). The Cal-630 signal from 520 nm excitation was 29% of the signal from 595 nm excitation. But it is easy to correct for this contamination, since it is always the same percentage of the signal at the preferred wavelength (**Figure 8A**). **Figure 8B** shows an experiment where we applied this correction procedure to the sodium signal measured at 520 nm. In this case the correction was small because the change in fluorescence of Cal-630 was smaller than the ANG-2 fluorescence. In other experiments (not shown) the correction was larger but still quantifiable. This correction procedure is similar to the way the spectra of chemical mixtures are separated into their components in some forms of spectroscopy.

## DISCUSSION

In this article we reviewed our approach to high speed simultaneous sodium and calcium imaging. The original system (Miyazaki and Ross, 2015) using multiplexed LEDs was good enough to detect sodium and calcium signals from dendritic spines in rat hippocampal pyramidal neurons (Miyazaki and Ross, 2017). Building on this system we added spot illumination with lasers. This laser system has improved S/N, less background light and less photodynamic damage. One limitation of this system is that the spot illumination, which can vary from 2.5 μm to 30 μm diameter (depending on the fiber size and the objective lens) does not cover an extensive dendritic region. In this case the experiments may miss details about the spatial extent of synaptic activation on a particular dendrite or if more than one dendrite participates in the response. However, the system is designed in a way that it is easy to switch between LED and laser excitation even while maintaining electrical recording. It can also do a combination of one LED and one laser, which may be advantageous, for example, if the sodium signal is from a focal synaptic site and the calcium signal is from a propagating calcium spike.

We also introduced a new pair of indicators for simultaneous sodium/calcium imaging. This pair (ANG-2, Cal-630) does not require excitation near 380 nm as the previous pairs (bis-fura-2/ANG-2 and SBFI/OGB-1) require. Using this new pair should reduce background autofluorescence and photodynamic damage since both of these problems are greater at shorter wavelengths. In addition, uncaging stimulation (using laser pulses at 379 nm) can be incorporated into the system with no change in hardware.

One property of the laser excitation system, which might be of some value in future experiments, is that the lasers can be pulsed at very high rates, up to 200 MHz, with pulse widths fully under computer control. This property may provide the basis for more patterned excitation that may optimize the S/N of the measurements while minimizing photodynamic damage.

## AUTHOR CONTRIBUTIONS

KM, JL and WR conceived experiments. KM, performed experiments. KM and WR analyzed experiments and wrote manuscript.

## FUNDING

This work was supported in part by National Institutes of Health Grants R21NS085729 (WR), R01NS099122 (WR), and R01NS103168 (JL).

# REFERENCES

Acker, C. D., Hoyos, E., and Loew, L. M. (2016). EPSPs measured in proximal dendritic spines of cortical pyramidal neurons. *eNeuro* 3:ENEURO.0050-15.2016. doi: 10.1523/eneuro.0050-15.2016

Lee, P., Yan, P., Ewart, P., Kohl, P., Loew, L. M., and Bollensdorff, C. (2012). Simultaneous measurement and modulation of multiple physiological parameters in the isolated heart using optical techniques. *Pflugers Arch.* 464, 403–414. doi: 10.1007/s00424-012-1135-6

Miyazaki, K., and Ross, W. N. (2015). Simultaneous sodium and calcium imaging from dendrites and axons. *eNeuro* 2:ENEURO.0092-15.2015. doi: 10.1523/eneuro.0092-15.2015

Miyazaki, K., and Ross, W. N. (2017). Sodium dynamics in pyramidal neuron dendritic spines: synaptically evoked entry predominantly through AMPA receptors and removal by diffusion. *J. Neurosci.* 37, 9964–9976. doi: 10.1523/jneurosci.1758-17.2017

Popovic, M. A., Carnevale, N., Rozsa, B., and Zecevic, D. (2015). Electrical behaviour of dendritic spines as revealed by voltage imaging. *Nat. Commun.* 6:8436. doi: 10.1038/ncomms9436

Tanese, D., Weng, J.-Y., Zampini, V., De Sars, V., Canepari, M., Rozsa, B., et al. (2017). Imaging membrane potential changes from dendritic spines using computer-generated holography. *Neurophotonics* 4:031211. doi: 10.1117/1.nph.4.3.031211

Vogt, K. E., Gerharz, S., Graham, J., and Canepari, M. (2011). High-resolution simultaneous voltage and $Ca^{2+}$ imaging. *J. Physiol.* 589, 489–494. doi: 10.1113/jphysiol.2010.200220

**Conflict of Interest Statement**: The authors declare that the research was conducted in the absence of any commercial or financial relationships that could be construed as a potential conflict of interest.

frontiers
in Cellular Neuroscience

METHODS
published: 17 January 2019
doi: 10.3389/fncel.2018.00530

# A Versatile and Open-Source Rapid LED Switching System for One-Photon Imaging and Photo-Activation

**Edited by:**
Marco Canepari,
UMR5588 Laboratoire
Interdisciplinaire de Physique (LIPhy),
France

**Reviewed by:**
William Ross,
New York Medical College,
United States
Lucy Maree Palmer,
Florey Institute of Neuroscience and
Mental Health, Australia

**Arne Battefeld**[1,2*†‡], **Marko A. Popovic**[1*†‡], **Dirk van der Werf**[3] **and Maarten H. P. Kole**[1,4]

[1] Department of Axonal Signaling, Netherlands Institute for Neuroscience, Royal Netherlands Academy of Arts and Sciences, Amsterdam, Netherlands, [2] Grass Laboratory, Marine Biological Laboratory, Woods Hole, MA, United States, [3] Department of Mechatronics, Netherlands Institute for Neuroscience, Royal Netherlands Academy of Arts and Sciences, Amsterdam, Netherlands, [4] Cell Biology, Faculty of Science, Utrecht University, Utrecht, Netherlands

***Correspondence:**
Arne Battefeld
arne.battefeld@u-bordeaux.fr
Marko A. Popovic
m.popovic@vumc.nl

† These authors have contributed equally to this work

**‡ Present address:**
Arne Battefeld,
UMR 5293, Institut des Maladies
Neurodégénératives, Université
de Bordeaux, Bordeaux, France
Marko A. Popovic,
Molecular Cell Biology
and Immunology, Amsterdam UMC,
Locatie VUmc, Amsterdam,
Netherlands

Combining fluorescence and transmitted light sources for microscopy is an invaluable method in cellular neuroscience to probe the molecular and cellular mechanisms of cells. This approach enables the targeted recording from fluorescent reporter protein expressing neurons or glial cells in brain slices and fluorescence-assisted electrophysiological recordings from subcellular structures. However, the existing tools to mix multiple light sources in one-photon microscopy are limited. Here, we present the development of several microcontroller devices that provide temporal and intensity control of light emitting diodes (LEDs) for computer controlled microscopy illumination. We interfaced one microcontroller with μManager for rapid and dynamic overlay of transmitted and fluorescent images. Moreover, on the basis of this illumination system we implemented an electronic circuit to combine two pulsed LED light sources for fast (up to 1 kHz) ratiometric calcium ($Ca^{2+}$) imaging. This microcontroller enabled the calibration of intracellular $Ca^{2+}$ concentration and furthermore the combination of $Ca^{2+}$ imaging with optogenetic activation. The devices are based on affordable components and open-source hardware and software. Integration into existing bright-field microscope systems will take ∼1 day. The microcontroller based LED imaging substantially advances conventional illumination methods by limiting light exposure and adding versatility and speed.

**Keywords: Arduino, μManager, microscopy, LED, high-speed imaging, Propeller, calcium imaging**

***Received:*** 10 September 2018
***Accepted:*** 21 December 2018
***Published:*** 17 January 2019

**Citation:**
Battefeld A, Popovic MA,
van der Werf D and Kole MHP (2019)
A Versatile and Open-Source Rapid
LED Switching System
for One-Photon Imaging
and Photo-Activation.
Front. Cell. Neurosci. 12:530.
doi: 10.3389/fncel.2018.00530

## INTRODUCTION

The continuous improvement of equipment and methodologies to visualize cells and their fine processes is critical to the advancement of neuroscience research. Cellular membranes are phase objects and with the many layers in intact brain tissue the identification of individual cells and their subcellular processes provides a major challenge. The application of long infrared (IR) wavelengths for visualization of cells in brain tissue reduces light scattering and in combination with different contrast enhancing methods, neuronal processes can be directly visualized (Dodt and Zieglgänsberger, 1990; Stuart et al., 1993; Dodt et al., 1999). Loading unlabeled neurons with chemical fluorescent dyes through the patch pipette further facilitated visualization of processes for targeted subcellular recording (Stuart et al., 1993). More recently, genetic strategies for fluorescence reporter expression (Zhuo et al., 1997; Feng et al., 2000; Mallon et al., 2002) improved experimental targeting of specific cell classes.

Many of the above mentioned approaches benefit from the combination of transmitted light with fluorescence light, but existing hardware solutions have pros and cons. Two-photon or confocal spinning disk microscopy are both ideal to simultaneously monitor subcellular structures and patch pipettes, exert minimal phototoxicity and provide sufficient spatial resolution to identify small diameter structures such as fine dendrites and axons (Nevian et al., 2007; Sasaki et al., 2012; Kole and Popovic, 2016). However, in comparison to one-photon microscopes the equipment is expensive. While conventional one-photon epifluorescence microscopy setups are more affordable they suffer from poor control of the excitation light. For example, conventional arc lamps have a very high luminance output and several emission peaks that are useful for the imaging of various fluorescence proteins. Adjustment of light intensity has to be achieved with neutral density filters. Short exposure times that limit phototoxicity (Icha et al., 2017) have to be established by third party shutters adding cost and potential sources of vibration. Furthermore, the widespread use of IR differential interference contrast (DIC), to improve the contrast of *in vitro* brain slices, prohibits the simultaneous use of transmitted and fluorescence light and requires switching of the analyzer and fluorescence cube. Alternatives for DIC are either the simpler oblique contrast or the Dodt gradient contrast illumination (Dodt et al., 1999) both enabling fluorescence illumination without switching components in the light path.

In recent years, high-power light emitting diodes (LEDs) from commercial suppliers or purpose built solutions (Albeanu et al., 2008; Rösner et al., 2013; Bosse et al., 2015) found their way into microscope illumination systems. High-power LEDs provide a low-noise and high intensity light source for microscopy. Combining LEDs for dual excitation fluorescence allows microsecond rapid switching between excitation wavelengths. Rapid LED switching has previously been shown to allow pseudo-simultaneous imaging of two fluorescence reporters at high speed (Miyazaki and Ross, 2015). However, the possibilities to implement fast pseudo-simultaneous imaging is often limited by the specific equipment. Similarly, a simple system that integrates fluorescence assisted patch-clamping into existing microscope setups is currently lacking.

Here, we present a number of simple and cost-effective solutions based on open-source hardware and LED illumination that can be easily adapted to most microscopes. We created a GitHub repository with instructions, code and circuit diagrams to build these microcontroller devices. First, we show a device that allows the near-continuous overlay of fluorescence and bright-field images for fluorescence assisted patching. Second, we present an extended solution for combining photo-activation and $Ca^{2+}$ imaging. Third, we demonstrate the possibility to perform ratiometric imaging at microseconds speed. The combination of open-source hardware and software provides the backbone for an affordable and versatile system advancing epifluorescence microscopy setups for optical and electrophysiological recordings.

# METHODS

## Animals, Slice Preparation and Whole-Cell Patch Clamp Recordings

This study was carried out in accordance with the recommendations of EU directive 2010/63/EU, Dutch law and the institutional IACUC committee. The protocols involving animal work were approved by the local ethics committees (IACUC or KNAW-DEC). Male Wistar rats at an age between 3 to 7 weeks (Charles River and Janvier) were kept on a 14/10 or 12/12 light/dark cycle. Mice were kept on a 12/12 light/dark cycle. All animals had unrestricted access to food and were fed a standard diet. The following mouse lines were used: R26-CAG-LSL-2XChETA-tdTomato (Jax: #017455) x Rbp4-cre_KL100Gsat/Mmucd (RRID:MMRRC_031125-UCD); PLP-CFP (Hirrlinger et al., 2005; Battefeld et al., 2016). Coronal and parasagittal brain slices (300 μm) were made as described in detail previously (Davie et al., 2006; Battefeld et al., 2016). Whole-cell patch clamp recordings were performed as described previously (Battefeld et al., 2016) and controlled by either AxoGraph X (RRID:SCR_014284, AxoGraph Scientific, Sydney, NSW, Australia) or pClamp (RRID:SCR_011323, Molecular Devices) software.

## Microscope Configuration, Filters and Cameras

For combining fluorescence and transmitted light illumination we used an optical light path that allowed simultaneous imaging without the need for changing fluorescence filter cubes. This prerequisite was fulfilled by either the Dodt gradient contrast (Dodt et al., 1999) or oblique condenser illumination. We tested the equipment on an Examiner A1 (Zeiss, Thornwood, NY, United States) with built in Dodt gradient contrast or an BX51WI (Olympus, Leiderdorp, Netherlands) with an oblique illumination condenser (WI-OBCD, N.A. 0.8). For simultaneous imaging of fluorescence and transmitted light, filter cubes were equipped with an excitation filter 530/30 nm (Chroma, Bellows Falls, VT, United States), a dichroic mirror 550lpxr (Chroma) and a long pass filter 570 nm (FGL570, Thorlabs). We successfully utilized alternative combinations of LED and filtercubes for CFP (U-MCFPHQ, Olympus), GFP (U-MWB, Olympus), and RFP (U-MWG2, Olympus). These standard filter cubes often required replacement of the emission filter with a long-pass emission filter. A sufficient and inexpensive solution is to use a long-pass colored glass filter (from Schott corporation) for the desired cut-on wavelength. The long-pass filter allows the combination of fluorescence with near infra-red light used for the transmitted light. For simultaneous $Ca^{2+}$ imaging and optogenetic activation two fluorescence light paths were arranged on top of each other. This configuration allows independent control of field illumination for $Ca^{2+}$ indicator and optogenetic light paths. Ideally, the field stop opening is kept small for $Ca^{2+}$ imaging to reduce bleaching and phototoxicity and large (fully open) to increase the activation efficiency of light-gated channelrhodopsins. The lower fluorescence light path was routed through the standard fluorescence illuminator (BX-RFA, Olympus). A U-DP coupled to U-DP1XC was mounted on top the BX-RFA. Olympus microscopes that we used for patching and fast imaging were equipped with a dual camera intermediate attachment (U-TRU, Olympus) allowing the connection of two cameras. We have successfully utilized CCD and scientific CMOS (sCMOS) based cameras for fluorescence assisted patching that include Xyla 4.2 (Andor, Concord, MA, United States), CoolSnap EZ (Photometrics, Tucson, AZ, United States), CoolSnap ES2 (Photometrics), and Evolution QEi (QImaging, Surrey, BC, Canada).

## LEDs and LED Driver Hardware

For epifluorescence illumination, we used various combinations of collimated LEDs with peak wavelengths of 340, 420, and 530 nm (all from Thorlabs, Newton, NJ, United States). In addition, we used custom built LEDs with peak wavelengths of 448 nm (SP-01-V4, Luxeonstar) and 590 nm (SP-01-A8, Luxeonstar). As transmitted light source, we used a collimated infrared 730 nm LED (M730L4, Thorlabs) mounted into the transmitted light port. Besides LEDs with single peak wavelengths we successfully used a high-power white LED (LZ1-00CW02, LED Engin Inc., San Jose, CA, United States) that allowed rapid and easy switching between different fluorescence excitation wavelengths without requiring several LEDs for each excitation wavelength. Custom built LEDs were mounted on a heatsink, collimated and arranged into the light path via a cage system similarly as previously described (Albeanu et al., 2008; Bosse et al., 2015). LEDs were equipped with proper cooling (passive heat sinks) and were not driven continuously to increase their lifetime. LEDs were TTL pulse controlled and LED drivers (LEDD1B, Thorlabs) allowed manual adjustment for light intensity in *continuous wave* or *trigger* mode or analog intensity control in *analog modulation* mode. We successfully tested the Cyclops LED driver providing even faster current delivery to LEDs and allowing optical feedback to achieve improved LED intensity stability (open-ephys project, Newman et al., 2015). An application example summarizing utilized LEDs and drivers can be found in **Supplementary Table 1**. As an alternative to LED light sources, other light sources (arc-lamp or laser) in combination with pre-existing mechanical shutters could be used, thereby reducing the need for new hardware. In this case, the TTL pulses trigger opening and closing of shutters or gating of lasers. We successfully used this approach to trigger mechanical shutters of Vincent Associates Inc. (Rochester, NY, United States) or laser light sources (89 North, Williston, VT, United States).

## Single-Cell $Ca^{2+}$ Imaging

For $Ca^{2+}$ imaging experiments, we supplemented the intracellular solution with either 200 μM Cal-590 potassium salt (20518, AAT Bioquest, Sunnyvale, CA, United States) or 200 μM fura-2 pentapotassium salt (F1200, Thermo Fisher Scientific). Cal-590 was excited with a collimated 590 nm LED (Luxeonstar) passed through an excitation filter 538/84 (FF01-538/84-25, Semrock, Rochester, NY, United States) reflected by a 580 nm beam splitter (FF580-FDi01-25x36, Semrock) toward the sample and emission filtered with a 593 nm long-pass filter (FF01-593/LP-25, Semrock). Channelrhodopsin activation combined with $Ca^{2+}$ imaging was performed in juvenile animals (P14 to P20). The channelrhodopsin variant ChETA was activated with a non-optimal excitation wavelength of 448 nm resulting in reduced photo-activation in response to blue activation light. We could not detect optical crosstalk between photo-activation light and the excitation light used for imaging of the red shifted $Ca^{2+}$ indicator Cal-590.

Fura-2 was alternately excited with 340 and 420 nm LEDs that were collimated with a UV-optimized aspheric lens for 340 nm (#33-953, Edmund Optics, York, United Kingdom) and a 1″ plano-convex lens (N-BK7, Thorlabs) for 420 nm. The 420 nm LED was passed through a 420/10 (FF01-420/10-25, Semrock) excitation filter and the 340 nm LED through a 340/22 nm excitation filter (FF01-340/22-25, Semrock) before combining the two light paths by passing/reflecting with a 405 nm dichroic mirror (Di02-R405, Semrock). We replaced the tube lens of U-DPXC1 with a UV passing plano-convex lens (#48-289, Edmund Optics) and placed a round field stop at a focal length of 17.5 cm. Light was reflected by a dichroic mirror (FF458-Di02, Semrock) through a 60× 1.0 NA water immersion objective (LUMPLFLN 60× W, Olympus) to the sample. Emission light was long-pass filtered with a cut-on wavelength of 455 nm. Exciting fura-2 at 420 nm reduced its dynamic range, but still allowed calibration.

For $Ca^{2+}$ imaging we utilized a low resolution (80 × 80 pixel), but highly sensitive NeuroCCD camera (RedShirt Imaging, Decatur, GA, United States) mounted on the front port of U-TRU. This camera was controlled by Neuroplex software (RedShirt Imaging) and imaging time series were recorded in Neuroplex (.da file format). *Post hoc* separation of imaging channels was performed by a script available on github[1].

## Software

We used the Arduino IDE (Arduino CC) with the Teensyduino plugins installed[2] to program Teensy. PropellerIDE software (Parallax) was used to program the microcontroller for POPSAR. We used μManager (RRID:SCR_000415) (Edelstein et al., 2014) for integrating microscope illumination and camera control with TEAMSTER. RedShirt Imaging NeuroCCD cameras were controlled by Neuroplex software (RRID:SCR_016193, v. 10.1.2 and v 10.2.1, RedShirt Imaging) and image acquisition trigger signals were detected by TEAMSTER and SLIDER.

---

[1] https://github.com/Kolelab/Image-analysis

[2] PJRC.com

## Code and Circuit Schematics

We have created an online repository on GitHub[3] which includes all code and circuit schematics described here. Instructions and part lists for building TEAMSTER, POPSAR, and SLIDER are provided.

# RESULTS

Here we present three microcontroller devices that are used for controlling LEDs to provide epifluorescence and transmitted light illumination for microscopes. For targeted patch-clamp recordings from subcellular structures we designed a device that we call TEAMSTER (Teensy Micromanager based timing switch controller). This Arduino based solution can control continuous overlay of transmitted and epifluorescence LEDs on conventional microscopy patch-clamp setups (**Figures 1A–C**). We further adapted the illumination system and designed a device we call POPSAR (Propeller based activity generator). This microcontroller solution allows high-speed (tested up to 1 kHz) imaging with dual excitation LEDs for, e.g., fura-2 based ratiometric imaging on a single camera (**Figure 1D**). To achieve reproducible LED activation currents, we interconnected POPSAR with a device we call SLIDER (Simple light digitizer), which we used to precisely control current intensities for LED drivers (**Figure 1D**).

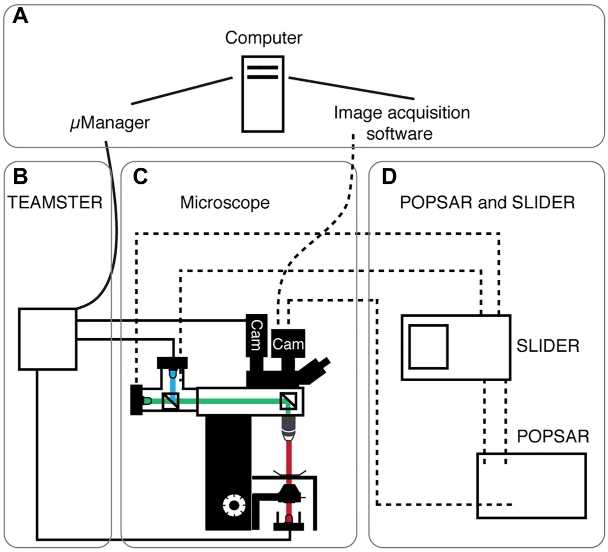

**FIGURE 1 |** System overview of presented microcontrollers. Schematic overview showing the four main modules of the system. **(A)** Computer running μManager and/or specialized image acquisition software. **(B)** The microscope equipped with transmitted light and fluorescence LEDs. Light paths indicated (fluorescence: blue, green; transmitted: red) as well as cameras (Cam). **(C)** TEAMSTER, a microcontroller based and μManager integrated LED timing and switching unit for, e.g., patch-clamp applications (solid lines, see **Figure 2**). **(D)** POPSAR and SLIDER microcontroller for precise LED timing and setting of LED intensities (dashed lines) for, e.g., $Ca^{2+}$ imaging applications (see **Figures 3**, **4**).

## TEAMSTER, a Microcontroller With μManager Integration for Fluorescence-Assisted Patch-Clamp Recordings

As basis of the LED controller device (**Figure 1B**) we utilized an Arduino compatible Teensy microcontroller board (v3.2) that is interfaced with μManager (**Supplementary Figure 1A**). TEAMSTER reads frame exposure signals from the camera to subsequently trigger illumination LEDs. A manual (force) switch was implemented to manually test LED activation. For easier integration into experimental patch-clamp setups we added a foot-switch for controlling fluorescence by user input, which helps to limit fluorescence exposure. TEAMSTER controls the LED pulse durations of transmitted and fluorescence LEDs. By keeping activation times of the transmitted light LED short (25 ms) motion blur that can occur when focusing through a sample is avoided. Once triggered, the fluorescence LED is activated for the full defined frame duration. TEAMSTER is an affordable hardware interface (**Supplementary Table 2**) between the μManager software to control two LED drivers via TTL outputs based on pre-programmed and user selectable modes.

The effectiveness of integrating TEAMSTER into patch-clamp experiments is demonstrated by two examples (**Figure 2**). We used a green LED (530 nm) for epifluorescence excitation and a near-IR LED (730 nm) for transmitted light illumination with either oblique illumination contrast or Dodt contrast. In combination with a long-pass emission filter, fluorescence and transmitted images can then be projected on the same camera. Timing is provided by controlling LEDs via programmed and user selectable modes in μManager. We tested the functionality by targeting cut axon blebs (Shu et al., 2006; Kole et al., 2007) from pyramidal neurons in layer 2/3 and 5, which were filled with Alexa dyes during somatic whole-cell recordings (Kole and Popovic, 2016). After ~30 min neurons were sufficiently filled and the axon bleb could be clearly identified and targeted for electrical recording (**Figures 2B,C**). To live overlay the epifluorescence image of the Alexa dye with a transmitted light image we ran an additional script in μManager. The script assigns look-up tables and continuously refreshes the combined image at up to 10 Hz. This approach allowed us to monitor the neuron morphology and the patch pipettes with a sufficiently high frame rate. We then targeted the fluorescence labeled axon bleb with a second recording pipette. Limiting fluorescence exposure times to short pulses of 50 to 100 ms allowed positioning the pipette on axon blebs without compromising neuron viability. Based on this approach we could successfully record from layer 2/3 pyramidal neuron soma and axon blebs at 128 ± 20 μm distance from the soma that showed a soma-to-axon delay of 140 ± 90 μs (*n* = 5, **Figure 2C**).

Another application of TEAMSTER is targeting of fluorescent protein expressing cells in transgenic animals. To identify fluorescent labeled cells, we used a foot-switch to activate an LED or a mechanical shutter in front of an arc lamp to limit fluorescent

---

[3] https://github.com/Kolelab/Fluorescence-Microscopy-Tools

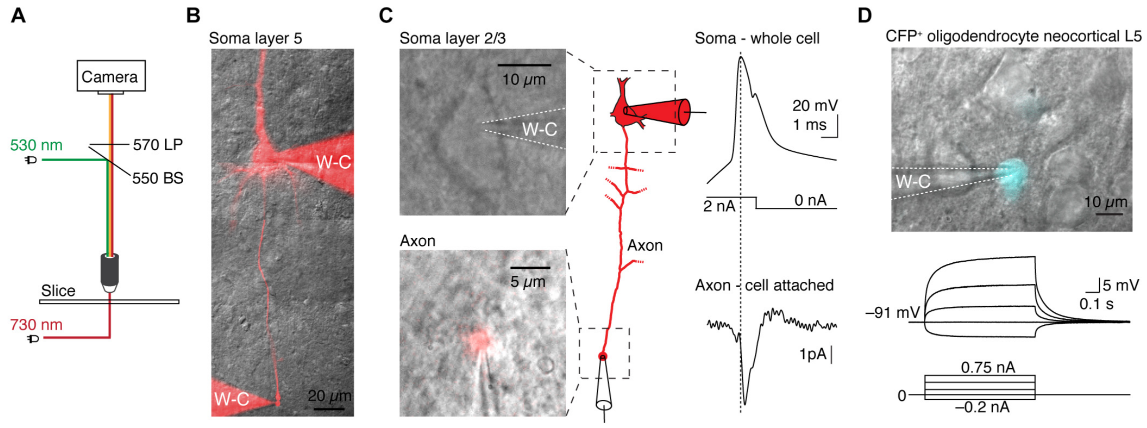

**FIGURE 2 |** Application examples of TEAMSTER, a microcontroller for simultaneous imaging of transmitted and fluorescence light for targeted patch-clamp recordings. **(A)** Schematic showing the light paths for the combination of LEDs for fluorescence (green) and near infrared illumination (red). A long-pass filter allows passing of transmitted and fluorescence light while blocking fluorescence excitation light. **(B)** Example of a layer 5 neuron filled with Alexa dye to visualize the axon and perform a double whole-cell recording from the soma and axon bleb (not shown here). **(C)** Example images of a layer 2/3 neuron soma (top) and a corresponding axon bleb (bottom) identified after loading the neuron with Alexa 555 dye during whole-cell access. μManager was utilized to display a continuous overlay of the bright field image with Alexa 555 fluorescence allowing a cell-attached recording of the axon bleb, shown in the example traces. **(D)** Example of a targeted patch-clamp recording in a transgenic reporter mouse in which oligodendrocytes express CFP (top). Corresponding current-clamp recording of the targeted oligodendrocyte (middle, bottom).

light to the duration of foot-switch push. We routinely used this approach to identify cyan fluorescent protein (CFP) expressing oligodendrocytes in a reporter mouse line (Battefeld et al., 2016, 2019). The example shows a CFP$^+$ oligodendrocyte with a whole-cell recording pipette. The oligodendrocyte showed the typical hyperpolarized resting membrane potential and near passive responses to current injections (**Figure 2D**).

## POPSAR – Splitter for High-Speed Dual Imaging or Simultaneous Imaging and Photo-Activation

Optical recordings of the intracellular Ca$^{2+}$ concentration ($[Ca^{2+}]_i$) are widely used to infer the underlying action potentials and resolve firing patterns of neurons. An advantage of epifluorescence-based imaging approaches is the possibility to image $[Ca^{2+}]_i$ in large fields of view with high (kHz) frame rates using CCD or sCMOS cameras. Combining Ca$^{2+}$ imaging with activation of channelrhodopsins or calibrating $[Ca^{2+}]_i$ requires rapid switching between light sources to avoid cross-talk of imaging channels. To allow pseudo-simultaneous high-speed (up to 1 kHz) imaging with two excitation light sources precise control of LEDs is necessary. Based on a previously published approach (Miyazaki and Ross, 2015) we built an affordable stand-alone implementation that we called POPSAR to rapidly assign alternating frame exposure times to two LEDs (**Figure 1D** and **Supplementary Figure 1B**). This sub 100€ device (**Supplementary Table 3**) is based on the Propeller ASC$^+$ board allowing execution of parallel processes for near real-time computation. This implementation achieves high frame rates as only camera frame exposure ouputs are detected and experimental flexibility as acquisition properties are software coded. We confirmed the functionality of the splitter in two applications that are of use for neuroscience research, first, the combination of Ca$^{2+}$ imaging and photo-activation and second, calibration of $[Ca^{2+}]_i$ using fura-2.

For combining Ca$^{2+}$ imaging and photo-activation we used mice that express the channelrhodopsin variant ChETA (Gunaydin et al., 2010) specifically in layer 5 pyramidal neurons. Channelrhodopsin was activated with a blue LED (448 nm) and $[Ca^{2+}]_i$ imaged simultaneously with the synthetic Ca$^{2+}$ indicator Cal-590 exited with a 590 nm LED (**Figure 3A**). We reasoned that a red-shifted Ca$^{2+}$ indicator should avoid photo-activation of ChETA, which shows little residual activation beyond 575 nm (Gunaydin et al., 2010). We acquired Cal-590 fluorescence at 40 Hz with fluorescent light pulse durations of 10 ms that were initiated every 25 ms. We next tested whether photo-activation can be achieved with either continuous or pulsed stimulation of blue LEDs (**Figure 3B**). Continuous light (448 nm LED) for a 1 s channelrhodopsin activation period abruptly increased the resting fluorescence over the full field of view (**Figure 3C**). As a consequence, the signal-to-noise ratio decreased and we observed non-specific bleaching of the background over the full field of view (imaging traces **Figure 3C**). We could still detect light activated backpropagating action potentials, but the fluorescence change was only ∼3% ΔF/F $[Ca^{2+}]_i$ in the apical dendrite (**Figure 3C**). To improve the signal-to-noise ratio and reduce bleaching we examined whether interleaved light pulses for either imaging or photo-activation can be used. For a duration of 0.5 s, light was pulsed for each channel at a combined frequency of 80 Hz (10 ms light on) or 40 Hz/channel (**Figure 3B**). *Post hoc* separation of the two channels resulted in an excellent signal-to-noise ratio and a Ca$^{2+}$ signal that was free of artifacts from photo-activation light. We observed peak $[Ca^{2+}]_i$ changes of ∼20% ΔF/F at the apical dendrite from light activated backpropagating action

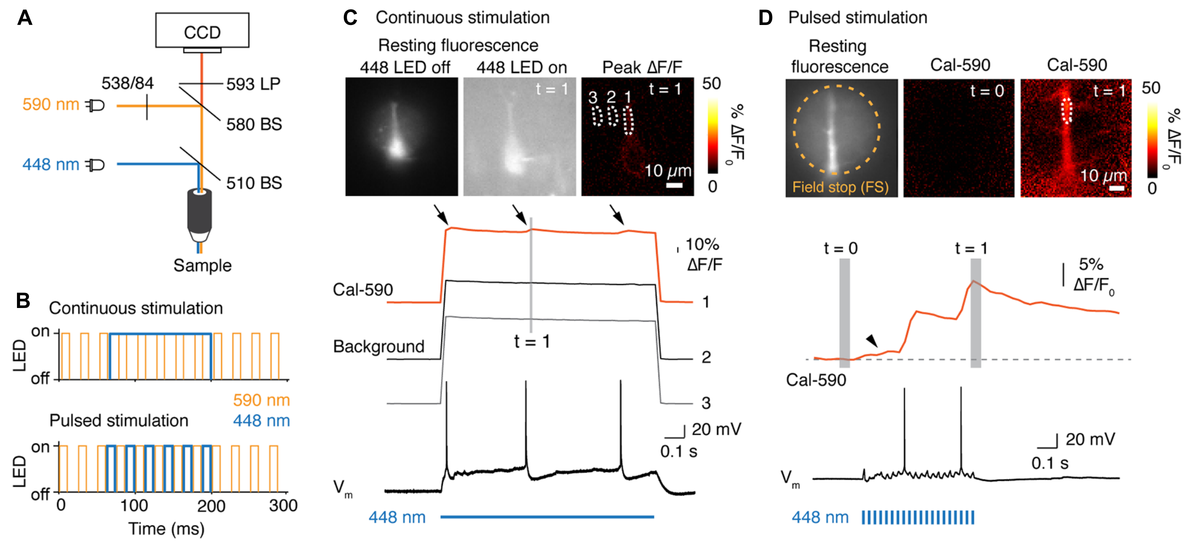

**FIGURE 3 |** POPSAR microcontroller for simultaneous photo-activation of channelrhodopsin and $Ca^{2+}$ imaging. **(A)** Light path schematic with used filters and beam splitters (BS) to achieve photo-activation and epifluorescence imaging. For photo-activation of the channelrhodopsin variant ChETA we used an LED with a center wavelength of 448 nm. $Ca^{2+}$ was imaged with the red indicator Cal-590, excited with a 590 nm (peak) LED. **(B)** Two possible approaches for combining imaging and photo-activation. Photo-activation can either be achieved with continuous light (top) or with pulsed stimulation (bottom). **(C)** Neuronal $Ca^{2+}$ was imaged at 40 Hz. To elicit a backpropagating action potential the ChETA expressing neuron was stimulated with a continuous pulse of light for 1 s. During photo-activation, total light intensity increased, resulting in a low signal to noise ratio of Cal-590 fluorescence. The three $[Ca^{2+}]_i$ peaks (arrows) correspond to the three action potentials (arrows). Continuous LED light leads to an increased total fluorescence and non-specific bleaching of the illuminated field of view. **(D)** Epifluorescence $Ca^{2+}$ imaging at 40 Hz interleaved with photo-activation pulses for ChETA. Images of resting fluorescence, Cal-590 baseline signal and the $[Ca^{2+}]_i$ peak during the second action potential (top). The dendritic $[Ca^{2+}]_i$ dynamics of the selected ROI were plotted (middle) and aligned to the simultaneous electrical recording (bottom). Pulsed stimulation resulted in an increased signal-to-noise ratio and low background fluorescence in absence of stimulation due to red shifted imaging wavelengths. Note the slow increase of $[Ca^{2+}]_i$ during the first activation of ChETA (arrow head in $[Ca^{2+}]_i$ recording).

potentials (**Figure 3D**). Another advantage of a red $Ca^{2+}$ indicator is that cellular structures located at greater depth from the surface can be imaged when compared to shorter wave length indicators. Simultaneous electrical recording confirmed that $Ca^{2+}$ peaks were associated with single action potentials elicited by photo-stimulation (**Figure 3D**). Comparing these two approaches demonstrates that pseudo-simultaneous imaging and photo-activation results in improved $Ca^{2+}$ signals while maintaining functional photo-activation at 40 Hz. Based on these results the latter mode was implemented into the POPSAR source code.

As a second application for POPSAR, we performed ratiometric imaging of fura-2 to, e.g., determine the absolute $[Ca^{2+}]_i$. Calibration of $[Ca^{2+}]_i$ necessitates to drive LEDs with reproducible and fixed current settings. In contrast to similar concepts that are provided in commercial systems which cost several thousand euros, SLIDER is an affordable add-on (∼100 €) as it is based on an Arduino compatible board and standard electronic components (**Figure 1D** and **Supplementary Figure 1C** and **Supplementary Table 4**). SLIDER is connected between POPSAR and the LED drivers allowing fine current adjustment (12 bit resolution) of the individual channels. When fura-2 was excited with two high-power LEDs with peak wavelengths of 340 and 420 nm we could collect the resulting emission with the same camera (**Figure 4A**). The addition of SLIDER introduced minimal delays (∼0.1 μs), which were negligible for an imaging frequency of 80 Hz and we confirmed functionality up to 1 kHz. At 80 Hz each frame was exposed for 10 ms and included an additional 2.5 ms buffer between frames to compensate for theoretical imperfect timing of LED on/off rise times and hardware induced delays (**Figure 4B**). For $Ca^{2+}$ imaging, layer 5 rat pyramidal neurons were loaded with fura-2 during whole-cell patch-clamp recordings and the dye was allowed to diffuse into the neurons (**Figures 4C,D**). Subsequently, we imaged $Ca^{2+}$ changes in the apical dendrite by evoking single action potentials with a somatic current injection. When one LED was switched off, every other frame recorded complete darkness resulting in a saw tooth pattern (**Figure 4E**). Precise timing and absence of crosstalk of the LEDs was confirmed after separating the two fluorescence channels (**Figure 4F**). Finally, we imaged $Ca^{2+}$ with both LEDs resulting in $[Ca^{2+}]_i$ responses of opposite polarities allowing subsequent transformation to a ratio and alignment to the evoked action potential (**Figure 4G**). As short-wave UV light induces phototoxicity, we monitored resting membrane potentials of neurons during imaging recordings. The resting membrane potential was unaffected for 25 ± 8 min, before imaging: −64.7 ± 3.6 mV after imaging: −63.7 ± 4.4 mV ($n = 5$, $p = 0.63$, Wilcoxon signed Rank test). To summarize, we demonstrate the functionality of POPSAR for ratio-metric $Ca^{2+}$ imaging and for combining $Ca^{2+}$ imaging with photo-activation of channelrhodopsins allowing high-speed imaging of subcellular compartments.

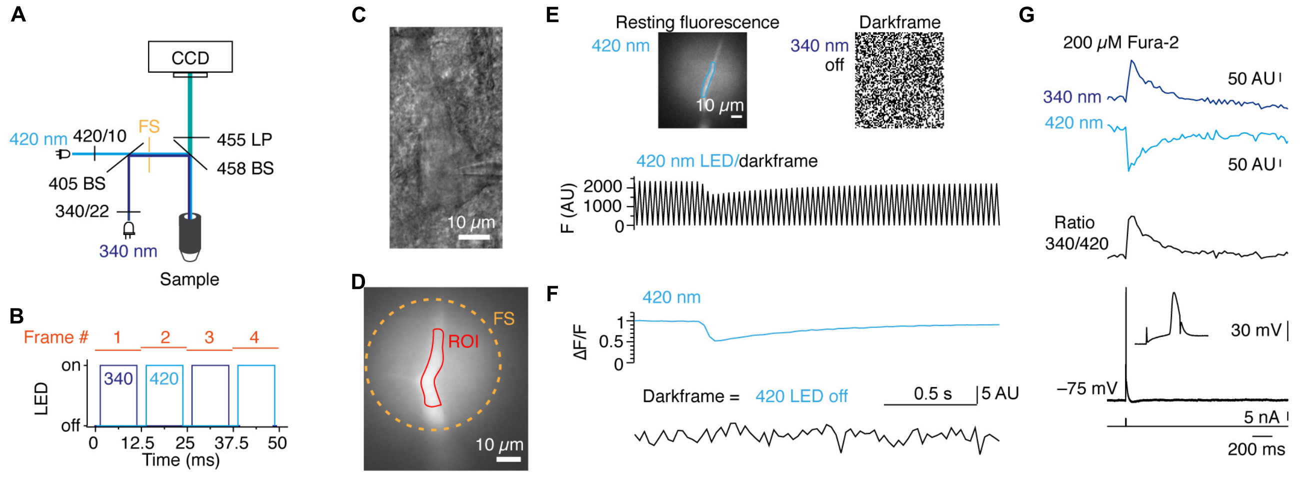

**FIGURE 4 |** POPSAR and SLIDER microcontrollers for pseudo simultaneous ratiometric imaging with analog intensity control for calibration of ion concentrations. **(A)** Schematic of the microscope light path with LEDs, filters, and dichroic mirrors. The two excitation wavelengths were combined into a single light path in which optical elements were improved for UV transmission (see Methods). **(B)** Schematic of the timing of dual LED excitation. The 340 and 420 nm LEDs were switched on for 10 ms in an alternating manner and frames were initiated every 12.5 ms, resulting in an imaging frequency of 80 Hz. **(C)** Oblique illumination contrast image of a rat layer 5 neuron of the somatosensory cortex, recorded in whole-cell configuration and filled with 200 μM fura-2. **(D)** Fluorescence fura-2 image of the apical dendrite from the neuron in **(C)** from which fluorescence traces were extracted. **(E)** Images of 420 nm fluorescence and random noise pattern due to total darkness while the 340 nm LED was switched off. The partial illumination of the apical dendrite by the field stop can be seen and an ROI for signal extraction is indicated (top). Raw 420 nm fluorescence alternating with a dark frame results in a saw tooth pattern of the optical signal (bottom). **(F)** When the two channels are *post hoc* separated non-interfering fluorescence and dark frame signals are obtained. **(G)** Background subtracted fluorescence traces for 340 and 420 nm excitation (top) and 340/420 ratio of the two traces (middle). Voltage traces of corresponding single action potentials evoked by somatic current injection (bottom). The somatic action potential led to a backpropagating action potential into the apical dendrite and evoked $[Ca^{2+}]_i$ changes. Note that between the two excitation wavelengths the polarity of the fura-2 signals is reversed.

## DISCUSSION

In the present study, we describe the development of three microcontroller-based systems for brain slice illumination during patch-clamp recordings and epifluorescence imaging in combination with optogenetic activation. The low-cost devices are built around open-source hardware and free software and can be adapted to conventional microscopes. By using standard TTL commands the microcontrollers provide flexibility to connect a range of equipment and allow to keep existing components, e.g., external shutters. We created a GitHub repository that includes source code, part lists and detailed building instructions enabling the reproduction of the devices and rapid integration into existing microscope systems. If non-commercial LED illumination systems are adopted (Albeanu et al., 2008; Teikari et al., 2012; Bosse et al., 2015) an affordable (<500 €) and versatile microscope illumination system can be achieved for a fraction of the price of commercially available systems. At the same time the end-user remains in full control to adjust software settings to experimental needs and has the flexibility to add and exchange components.

Inspired by a system for rapid simultaneous imaging of two fluorescence probes (Miyazaki and Ross, 2015) we developed POPSAR and demonstrate its full functionality by simultaneous photo-stimulation and $Ca^{2+}$ imaging. Similar LED triggering paradigms were recently implemented in head mounted miniscope solutions (Scott et al., 2018; Stamatakis et al., 2018). Stamatakis et al. (2018) utilized genetically encoded GCaMP6 and a red-shifted opsin. However, in this study channelrhodopsin activation was still observed while the LED for $Ca^{2+}$ imaging was activated. In contrast, in our implementation we used the red-shifted synthetic $Ca^{2+}$ indicator Cal-590 in combination with a blue LED to activate channelrhodopsin. By imaging pseudo-simultaneously and shifting the $Ca^{2+}$ dye excitation into longer orange/red wavelengths we did not observe crosstalk of the two channels (**Figure 3D**). Moreover, POPSAR provides the opportunity to perform $[Ca^{2+}]_i$ calibration by using the ratiometric $Ca^{2+}$ indicator fura-2. To achieve ratiometric fura-2 excitation we used a newly available high-power LED with a peak wavelength of 340 nm in combination with a 420 nm LED. Optimization of the optical path for UV light transmission and utilization of POPSAR and SLIDER for repeatable digital intensity control of LED current settings, revealed excellent performance for imaging frequencies up to 1 kHz. Implementing high-power UV-LEDs provides an efficient approach to investigate dynamic sub-cellular $[Ca^{2+}]_i$ changes in neurons or glial cells (Battefeld et al., 2019). The disadvantage of short wavelength (UV) light is that UV light induces phototoxicity more rapidly than longer wavelengths (Icha et al., 2017). The ability to accurately control and limit UV exposure times, as demonstrated here, was crucial for experiments using UV light.

The rapid LED imaging approaches are a useful tool to improve our understanding of neuronal assemblies, but also come with challenges associated with epifluorescence imaging. In contrast to two-photon imaging, single-photon excitation poses limitations in the control of the z-resolution as excitation light is not restricted outside the optical focus. Moreover, prolonged fluorescence exposure can lead to light induced damage (Icha et al., 2017). Precisely controlling exposure times by pulsing LEDs can thereby reduce overall fluorescence exposure and limit phototoxicity. Another approach of limiting excitation light in a sample is the recently developed wavefront shaping technique that makes use of computer-controlled spatial light modulators (SLM) to spatially restrict laser excitation light in tissue. Computer generated holography has the advantage of improving spatial specificity down to ~10 μm in the axial direction thereby further reducing phototoxicity and increasing the signal-to-noise ratio (Foust et al., 2015). In future applications both laser based spatial control (SLM) and temporal control (TEAMSTER; POPSAR) could be combined to achieve pseudo-simultaneous recording of different indicators from diverse sub-cellular structures. Alternatively, POPSAR could be used for light-based activation of presynaptic terminals while recording optically $Ca^{2+}$ or voltage in postsynaptic dendritic compartments to map the spatial distribution of inputs. These applications would significantly expand the toolset available for neuroscientists. Compared to two-photon microscopy the use of epifluorescence illumination increases light collection, has the cutting-edge advantage of achieving kilohertz acquisition rates, while allowing simultaneous imaging of a large field of view and detection of low intensity fluorescent signals (Jaafari et al., 2014). By changing excitation LEDs and filter combinations one could use a non-ratiometric $Ca^{2+}$ reporter and structural dye to estimate $Ca^{2+}$ concentrations (Delvendahl et al., 2015). In future imaging experiments one could combine two different synthetic $Ca^{2+}$ probes (e.g., OGB-1 and Cal-590) in two neighboring cells thereby allowing dynamic imaging of cell-cell interactions. These applications are under the premise that optical crosstalk is non-existing and the appropriate filters are selected.

In summary, the microcontroller systems we presented here enable rapid and controlled LED excitation, expanding the toolbox for one-photon imaging and addressing new questions in the field of neuroscience.

## AUTHOR CONTRIBUTIONS

AB, MK, and MP designed the research and edited the manuscript. MP wrote the scripts. AB, MP, and DvdW built and tested the hardware. AB acquired the data and drafted the manuscript. All authors contributed to the manuscript and approved the final version.

## FUNDING

This work was supported by grants to MK: European Research Council (FP7/2007-2013)/ERC grant agreement P261114, National Multiple Sclerosis Society grant (RG 4924A1/1) and a NWO-Vici grant 865.17.003. AB received a Grass Fellowship from the Grass Foundation.

## ACKNOWLEDGMENTS

AB thanks the following suppliers for their generosity in providing loan equipment: Zeiss, Luigs & Neumann, Thorlabs, Andor, Chroma, and Molecular Devices. The authors thank Joris Coppens for supporting the development of earlier versions of Arduino based implementations with μManager scripts and the electronics department of the NIN for excellent support and discussions.

## SUPPLEMENTARY MATERIAL

The Supplementary Material for this article can be found online at: https://www.frontiersin.org/articles/10.3389/fncel.2018.00530/full#supplementary-material

## REFERENCES

Albeanu, D. F., Soucy, E., Sato, T. F., Meister, M., and Murthy, V. N. (2008). LED arrays as cost effective and efficient light sources for widefield microscopy. *PLoS One* 3:e2146. doi: 10.1371/journal.pone.0002146

Battefeld, A., Klooster, J., and Kole, M. H. P. (2016). Myelinating satellite oligodendrocytes are integrated in a glial syncytium constraining neuronal high-frequency activity. *Nat. Commun.* 7:11298. doi: 10.1038/ncomms11298

Battefeld, A., Popovic, M. A., de Vries, S. I., and Kole, M. H. P. (2019). High-frequency microdomain $Ca^{2+}$ transients and waves during early myelin internode remodeling. *Cell Rep.* 26, 182–191. doi: 10.1016/j.celrep.2018.12.039

Bosse, J. B., Tanneti, N. S., Hogue, I. B., and Enquist, L. W. (2015). Open LED illuminator: a simple and inexpensive LED illuminator for fast multicolor particle tracking in neurons. *PLoS One* 10:e0143547. doi: 10.1371/journal.pone.0143547.s008

Davie, J. T., Kole, M. H. P., Letzkus, J. J., Rancz, E. A., Spruston, N., Stuart, G. J., et al. (2006). Dendritic patch-clamp recording. *Nat. Protoc.* 1, 1235–1247. doi: 10.1038/nprot.2006.164

Delvendahl, I., Jablonski, L., Baade, C., Matveev, V., Neher, E., and Hallermann, S. (2015). Reduced endogenous $Ca^{2+}$ buffering speeds active zone $Ca^{2+}$ signaling. *Proc. Natl. Acad. Sci. U.S.A.* 112, E3075–E3084. doi: 10.1016/j.neuron.2010.10.026

Dodt, H., Eder, M., Frick, A., and Zieglgänsberger, W. (1999). Precisely localized LTD in the neocortex revealed by infrared-guided laser stimulation. *Science* 286, 110–113. doi: 10.1126/science.286.5437.110

Dodt, H. U., and Zieglgänsberger, W. (1990). Visualizing unstained neurons in living brain slices by infrared DIC-videomicroscopy. *Brain Res.* 537, 333–336. doi: 10.1016/0006-8993(90)90380-T

Edelstein, A. D., Tsuchida, M. A., Amodaj, N., Pinkard, H., Vale, R. D., and Stuurman, N. (2014). Advanced methods of microscope control using μManager software. *J. Biol. Methods* 1:e60. doi: 10.14440/jbm.2014.36

Feng, G., Mellor, R. H., Bernstein, M., Keller-Peck, C., Nguyen, Q. T., Wallace, M., et al. (2000). Imaging neuronal subsets in transgenic mice expressing multiple spectral variants of GFP. *Neuron* 28, 41–51. doi: 10.1016/S0896-6273(00)00084-2

Foust, A. J., Zampini, V., Tanese, D., Papagiakoumou, E., and Emiliani, V. (2015). Computer-generated holography enhances voltage dye fluorescence discrimination in adjacent neuronal structures. *Neurophoton* 2:021007. doi: 10.1117/1.NPh.2.2.021007

Gunaydin, L. A., Yizhar, O., Berndt, A., Sohal, V. S., Deisseroth, K., and Hegemann, P. (2010). technical reports. *Nat. Neurosci.* 13, 387–392. doi: 10.1038/nn.2495

Hirrlinger, P. G., Scheller, A., Braun, C., Quintela-Schneider, M., Fuss, B., Hirrlinger, J., et al. (2005). Expression of reef coral fluorescent proteins in the central nervous system of transgenic mice. *Mol. Cell. Neurosci.* 30, 291–303. doi: 10.1016/j.mcn.2005.08.011

Icha, J., Weber, M., Waters, J. C., and Norden, C. (2017). Phototoxicity in live fluorescence microscopy, and how to avoid it. *Bioessays* 39:1700003. doi: 10.1002/bies.201700003

Jaafari, N., De Waard, M., and Canepari, M. (2014). Imaging fast calcium currents beyond the limitations of electrode techniques. *Biophys. J.* 107, 1280–1288. doi: 10.1016/j.bpj.2014.07.059

Kole, M. H. P., Letzkus, J. J., and Stuart, G. J. (2007). Axon initial segment Kv1 channels control axonal action potential waveform and synaptic efficacy. *Neuron* 55, 633–647. doi: 10.1016/j.neuron.2007.07.031

Kole, M. H. P., and Popovic, M. A. (2016). "Patch-clamp recording from myelinated central axons," in *Advanced Patch-Clamp Analysis for Neuroscientists Advanced Patch-Clamp Analysis for Neuroscientists*, ed. A. Korngreen (New York, NY: Springer New York), 123–138. doi: 10.1007/978-1-4939-3411-9_6

Mallon, B. S., Shick, H. E., Kidd, G. J., and Macklin, W. B. (2002). Proteolipid promoter activity distinguishes two populations of NG2-positive cells throughout neonatal cortical development. *J. Neurosci.* 22, 876–885. doi: 10.1523/JNEUROSCI.22-03-00876.2002

Miyazaki, K., and Ross, W. N. (2015). Simultaneous sodium and calcium imaging from dendrites and axons. *eNeuro* 2:ENEURO.0092-15.2015. doi: 10.1523/ENEURO.0092-15.2015

Nevian, T., Larkum, M. E., Polsky, A., and Schiller, J. (2007). Properties of basal dendrites of layer 5 pyramidal neurons: a direct patch-clamp recording study. *Nat. Neurosci.* 10, 206–214. doi: 10.1038/nn1826

Newman, J. P., Fong, M.-F., Millard, D. C., Whitmire, C. J., Stanley, G. B., and Potter, S. M. (2015). Optogenetic feedback control of neural activity. *eLife* 4:e07192. doi: 10.7554/eLife.07192

Rösner, J., Liotta, A., Schmitz, D., Heinemann, U., and Kovács, R. (2013). A LED-based method for monitoring NAD(P)H and FAD fluorescence in cell cultures and brain slices. *J. Neurosci. Methods* 212, 222–227. doi: 10.1016/j.jneumeth.2012.11.001

Sasaki, T., Matsuki, N., and Ikegaya, Y. (2012). Targeted axon-attached recording with fluorescent patch-clamp pipettes in brain slices. *Nat. Protoc.* 7, 1228–1234. doi: 10.1038/nprot.2012.061

Scott, B. B., Thiberge, S. Y., Guo, C., Tervo, D. G. R., Brody, C. D., Karpova, A. Y., et al. (2018). Imaging cortical dynamics in GCaMP transgenic rats with a head-mounted widefield macroscope. *Neuron* 100, 1045–1058. doi: 10.1016/j.neuron.2018.09.050

Shu, Y., Hasenstaub, A., Duque, A., Yu, Y., and McCormick, D. A. (2006). Modulation of intracortical synaptic potentials by presynaptic somatic membrane potential. *Nature* 441, 761–765. doi: 10.1038/nature04720

Stamatakis, A. M., Schachter, M. J., Gulati, S., Zitelli, K. T., Malanowski, S., Tajik, A., et al. (2018). Simultaneous optogenetics and cellular resolution calcium imaging during active behavior using a miniaturized microscope. *Front. Neurosci.* 12:496. doi: 10.3389/fnins.2018.00496

Stuart, G. J., Dodt, H. U., and Sakmann, B. (1993). Patch-clamp recordings from the soma and dendrites of neurons in brain slices using infrared video microscopy. *Pflugers Arch.* 423, 511–518. doi: 10.1007/BF00374949

Teikari, P., Najjar, R. P., Malkki, H., Knoblauch, K., Dumortier, D., Gronfier, C., et al. (2012). An inexpensive Arduino-based LED stimulator system for vision research. *J. Neurosci. Methods* 211, 227–236. doi: 10.1016/j.jneumeth.2012.09.012

Zhuo, L., Sun, B., Zhang, C. L., Fine, A., Chiu, S. Y., and Messing, A. (1997). Live astrocytes visualized by green fluorescent protein in transgenic mice. *Dev. Biol.* 187, 36–42. doi: 10.1006/dbio.1997.8601

**Conflict of Interest Statement:** The authors declare that the research was conducted in the absence of any commercial or financial relationships that could be construed as a potential conflict of interest.

frontiers
in Cellular Neuroscience

ORIGINAL RESEARCH
published: 06 February 2019
doi: 10.3389/fncel.2019.00020

# Network Plasticity Involved in the Spread of Neural Activity Within the Rhinal Cortices as Revealed by Voltage-Sensitive Dye Imaging in Mouse Brain Slices

*Riichi Kajiwara[1]*, Yoko Tominaga[2] and Takashi Tominaga[2]*

*[1]Department of Electronics and Bioinformatics, School of Science and Technology, Meiji University, Kawasaki, Japan,*
*[2]Laboratory for Neural Circuit Systems, Institute of Neuroscience, Tokushima Bunri University, Sanuki, Japan*

The rhinal cortices, such as the perirhinal cortex (PC) and the entorhinal cortex (EC), are located within the bidirectional pathway between the neocortex and the hippocampus. Physiological studies indicate that the perirhinal transmission of neocortical inputs to the EC occurs at an extremely low probability, though many anatomical studies indicated strong connections exist in the pathway. Our previous study in rat brain slices indicated that an increase in excitability in deep layers of the PC/EC border initiated the neural activity transfer from the PC to the EC. In the present study, we hypothesized that such changes in network dynamics are not incidental observations but rather due to the plastic features of the perirhinal network, which links with the EC. To confirm this idea, we analyzed the network properties of neural transmission throughout the rhinal cortices and the plastic behavior of the network by performing a single-photon wide-field optical recording technique with a voltage-sensitive dye (VSD) in mouse brain slices of the PC, the EC, and the hippocampus. The low concentration of 4-aminopyridine (4-AP; 40 μM) enhanced neural activity in the PC, which eventually propagated to the EC *via* the deep layers of the PC/EC border. Interestingly, washout of 4-AP was unable to reverse entorhinal activation to the previous state. This change in the network property persisted for more than 1 h. This observation was not limited to the application of 4-AP. Burst stimulation to neurons in the perirhinal deep layers also induced the same change of network property. These results indicate the long-lasting modification of physiological connection between the PC and the EC, suggesting the existence of plasticity in the perirhinal-entorhinal network.

**Keywords: perirhinal cortex, entorhinal cortex, optical imaging, voltage-sensitive dye, plasticity**

***Edited by:***
*Srdjan D. Antic,*
*University of Connecticut Health Center, United States*

***Reviewed by:***
*De-Lai Qiu,*
*Yanbian University, China*
*Ruth M. Empson,*
*University of Otago, New Zealand*

****Correspondence:***
*Riichi Kajiwara*
*rdkaji@meiji.ac.jp*

***Received:*** *09 September 2018*
***Accepted:*** *16 January 2019*
***Published:*** *06 February 2019*

***Citation:***
*Kajiwara R, Tominaga Y and Tominaga T (2019) Network Plasticity Involved in the Spread of Neural Activity Within the Rhinal Cortices as Revealed by Voltage-Sensitive Dye Imaging in Mouse Brain Slices. Front. Cell. Neurosci. 13:20. doi: 10.3389/fncel.2019.00020*

## INTRODUCTION

The perirhinal cortex (PC) is a polymodal association area that communicates with neocortical and subcortical areas, such as the sensory, temporal, and insular cortical areas as well as the amygdala, basal ganglia, raphe nucleus, and olfactory bulb (Suzuki, 1996; Kealy and Commins, 2011). Various lesion studies have confirmed that the association between the PC and other brain regions is necessary for fear learning (Corodimas and LeDoux, 1995; Herzog and Otto, 1998;

Kholodar-Smith et al., 2008) and object recognition (Murray et al., 1993; Higuchi and Miyashita, 1996; Buckley and Gaffan, 1998). The PC sends axons to the entorhinal cortex (EC) and acts as an important gateway for hippocampal declarative memory processing (Burwell and Amaral, 1998a; Buffalo et al., 1999; Witter et al., 2000; Burwell, 2001; Squire et al., 2004; van Strien et al., 2009; Cappaert et al., 2015). Therefore, the PC operates in conjunction with the hippocampus *via* the EC, especially when spatial or contextual cues are relevant during encoding of object information (Dere et al., 2007). In fact, the one-trial object recognition test, which examines preference behavior for a novel object without reinforcement stimuli, suggests that the PC is especially critical for the encoding of object information and the maintenance of the object memory trace (Winters and Bussey, 2005). In contrast, hippocampal lesions have only revealed impairments when behavioral trials are performed in a complex spatial environment (Winters et al., 2004; Forwood et al., 2005).

The synchronous neural activation *via* the rhinal cortices between the neocortex and the hippocampus is thus suggested to be essential for the formation and recall of context-dependent memories. However, previous electrophysiological experiments in *ex vivo* isolated brains from guinea pigs and *in vivo* anesthetized cats have indicated that propagation of neural activity between the PC and the EC occurs at an extremely low probability (de Curtis and Paré, 2004; Pelletier et al., 2004, 2005). These groups have investigated the physiological and anatomical properties related to PC-EC connectivity (Biella et al., 2001, 2002, 2010; Uva et al., 2005; Pinto et al., 2006; Apergis-Schoute et al., 2007; Unal et al., 2012). Consistent with this phenomenon, using a voltage-sensitive dye (VSD) imaging technique in rat brain slices, we also found that neural activities in response to PC stimulation did not transmit to the EC even under partial suppression of the GABA-A system (Kajiwara et al., 2003). Moreover, we found that associative inputs from the amygdala promoted the spread of perirhinal activity to the EC by activating neurons in the deep layers of the PC/EC, suggesting a functional "gate" that can control information transfer from the PC to the EC. In regard to the mechanism of the gate, further VSD imaging experiments have been conducted by other groups to examine the network between area 35 of the PC and the lateral EC (LEC; Koganezawa et al., 2008; Willems et al., 2016) and have suggested the importance of the inhibitory system in these cortices. More recently, Willems et al. (2018) investigated the role of interneurons in PC/EC transmission by performing whole-cell recordings of interneurons expressing yellow fluorescent protein (YFP) driven by the parvalbumin promotor-dependent cre-recombinase. They revealed that parvalbumin interneurons are involved in eliciting strong inhibition of principal neurons in the deep layer network. These studies focused on the inhibitory system in the PC/EC; however, the contribution of the increase in the excitability of principal neurons is still poorly understood.

In the PC, many excitatory neurons possess late-spiking properties that have been suggested to result from a slowly inactivating potassium conductance (Beggs et al., 2000; Moyer et al., 2002). Since such neurons have delayed and sustained firing properties in response to long synaptic trains, it is difficult for the PC to initiate EC activation. Low concentrations of 4-aminopyridine(4-AP; less than 200 $\mu$M) reduce the amplitude of a more slowly inactivating D current while sparing the A current (Rudy, 1988; Storm, 1988; Ficker and Heinemann, 1992; Wu and Barish, 1992; Barish et al., 1996). In this article, we examined the effect of a low concentration of 4-AP on the gate, which normally blocks neural transmission from the PC to the EC.

In a preliminary experiment on PC-EC transmission using the VSD imaging method, we noticed that once the PC/EC gate was open, even weak stimulation of the PC easily activated the EC network, and this property persisted throughout the experiment. Recent electrophysiological and VSD imaging studies in isolated whole brains from guinea pigs revealed that paired theta frequency stimulation of two distant neocortical sites resulted in a prolonged response potentiation to the paired inputs (Unal et al., 2012). However, persistent modification of the physiological connectivity between the PC and the EC was not mentioned because the potentiated response in the PC did not drive the entorhinal activity. Here, we also aimed to determine whether plastic changes in PC-EC transmission occur.

A single-photon wide-field optical recording technique can be used to analyze such plastic changes in network dynamics by elucidating what types of changes occur and identifying the critical region for these changes. However, to observe long-lasting modification of the network property, stability to fix the inherent problems of VSD imaging (e.g., toxicity and bleaching of the dye) is required. In the present study, by using a low-magnification epi-fluorescent macroscope to maximize optical efficacy (Tominaga et al., 2018), the long-term transition of the state in the network activity in a slice was stably visualized, and we investigated the plastic behavior in the PC-EC network.

## MATERIALS AND METHODS

All procedures involving animal experiments were approved by the Animal Care and Use Committee of Tokushima Bunri University and Meiji University.

### Brain Slice Preparation and VSD Staining

Adult male C57BL/6 mice aged 12–36 weeks were decapitated under deep isoflurane anesthesia. The brains were quickly cooled in ice-cold oxygenated artificial cerebrospinal fluid (ACSF) containing the following in mM: 124 NaCl, 2.5 KCl, 2 $CaCl_2$, 2 $MgSO_4$, 1.25 $NaH_2PO_4$, 26 $NaHCO_3$, and 10 glucose with a pH of 7.4 when saturated with a mixture of 95% $O_2$ and 5% $CO_2$. After cooling for 5 min, the cerebellum, the brainstem and the frontal third of the brain were removed, and horizontal slices (350 $\mu$m) containing the PC, the EC [including the medial EC (MEC) and the LEC], and the hippocampus were prepared using a vibrating blade microtome (VT1200S, Leica) as described previously (Kajiwara et al., 2003). Each slice was transferred onto a fine-mesh membrane filter (Omni Pore membrane filter, JHWP01300, Millipore) held in place by a thin plexiglass ring (inner diameter, 11 mm; outer diameter, 15 mm, thickness 1–2 mm; Tominaga et al., 2000). Slices placed in the plexiglass ring were transferred to a moist holding chamber continuously supplied with ACSF infused with the $O_2$ and $CO_2$ gas mixture. After 1 h of incubation in this chamber, slices were bath-stained for 25 min with an aliquot of VSD staining solution (100 μl for each slice), consisting of 0.2 mM aminonaphthylethenyl-pyridinium (Di-4-ANEPPS; D-1199, Invitrogen) in 2.7% ethanol, 0.13% Cremophor EL (Sigma-Aldrich Co.), 50% fetal bovine serum (Sigma-Aldrich Co.), and 50% ACSF. The slices were subjected to experiments after incubation at room temperature in normal ACSF for at least 1 h.

## Optical Recording System and Data Processing

The plexiglass ring supporting each slice was placed in an immersion-type recording chamber. Slices were continuously perfused with prewarmed (31°C) and oxygenated ACSF (bubbled with a 95%/5% $O_2/CO_2$ gas mixture) at a rate of 1 ml/min. Custom laboratory-designed epifluorescence optics consisting of two principal lenses were used to view the slices during experiments. The optics consisted of an objective lens for the microscope (×1.6 Leica Micro Systems MZ-APO) and another lens (×0.63 Leica Microsystems MZ-APO) as the projection lens. Excitation light was provided by a halogen lamp source (150 W; MHW-G150LR; Moritex Corp.) projected through an excitation filter ($\lambda = 530 \pm 10$ nm) and reflected onto the hippocampal slice by a dichroic mirror ($\lambda = 575$ nm). Emission fluorescence from the slice was passed through an emission filter ($\lambda > 590$ nm) and projected onto a cMOS camera (MiCAM Ultima; BrainVision, Inc., Tokyo, Japan). Most recordings were made at a frame rate of 0.5 ms/frame.

The fluorescence intensity emitted by the slice prior to stimulation (a prestimulation period usually lasting from 100 to 740 frames) was averaged and used as the reference intensity (F0). The fractional change in fluorescence [$\Delta F(t) = F(t) - F0$] was normalized by the F0 ($\Delta F/F0$) and used as the optical signal. The optical signals referred to in the following sections represent signals filtered in spatial and temporal dimensions with a digital Gaussian kernel of 5 × 5 × 3 (horizontal × vertical × temporal; $\sigma \approx 1$). In some experiments, we observed a slow drift in the baseline signal; in these cases, the drift was compensated for by subtracting a normalized smooth spline curve obtained from optical signals recorded at pixels where no response was observed. We confirmed that this procedure produced steady and flat baseline signals and did not cause an artificial drift in the absence of stimulation.

Recordings were made in a total of 45 slices, and we analyzed optical signals offline using a procedure developed for Igor Pro (WaveMetrics Inc., Portland, OR, USA). The data presented here are drawn from a pool of 29 successful experiments. At a wavelength of 610 nm, the VSD fluorescence decreases in response to depolarization of the membrane. To fit the polarity of the response to conventional membrane potential changes, we expressed the optical signal in a polarity that matched the membrane potential change. For example, decreased fluorescence, which corresponds to depolarization, was represented as a positive deflection. In some experiments, regions of interest (ROIs) consisting of 21–23 VSD signals were selected. The average of the maximum VSD signal amplitudes and the standard deviation of each ROI were calculated. For additional details on the methods, see Tominaga et al. (2000, 2002).

## Stimulation and Field Potential Recording

To investigate the influence of the network activity in the PC on the behavior of EC neurons, we stimulated various sites using a stimulus intensity that caused the maximum response of superficial layers in the PC (100–150 μA for 200 μs, bi-phasic pulse). The position of the stimulating electrode was changed from the rostral (area 36 of the PC) to the caudal area (area 35) close to the boundary between the PC and the EC. The stimulating electrodes were glass electrodes filled with ACSF (1 MΩ). In some experiments, field potential recordings were performed to confirm no photodynamic effect on the field potential amplitude during the optical recording. A glass recording electrode filled with ACSF (1 MΩ, 5-μm inner diameter) was positioned in the entorhinal and perirhinal layers II/III near the rhinal sulcus. A laboratory-made differential amplifier and a general-purpose amplifier (model 440; Brownlee Precision, San Jose, CA, USA) were used for field potential recordings (100× gain, bandpass DC–3 kHz).

## Drugs

A large number of parvalbumin immunoreactive neurons have been observed on the border of the perirhinal area and in the EC (Wouterlood et al., 1995; Miettinen et al., 1996). To investigate the spatiotemporal distribution of excitatory activities between the PC and the EC, synaptic inhibition was partly suppressed by applying a low concentration of the GABA-A antagonist gabazine (0.5–1 μM; SR95531, Sigma-Aldrich Co.). Under such partial suppression of the inhibitory system, we observed perirhinal–entorhinal neural activation without inducing spontaneous paroxysmal activities in rat brain slices (Kajiwara et al., 2003).

In the PC, there are many excitatory neurons possessing late-spiking properties suggested to result from a slowly inactivating potassium conductance (Beggs et al., 2000; Moyer et al., 2002). In some experiments, we perfused brain slices with 40 μM 4-AP (Sigma-Aldrich Co.) to increase the firing rate of principal neurons by blocking potassium channels. 4-AP is a potassium channel blocker that affects A-type (Gutman et al., 2005), D-type (Storm, 1988) and delayed rectifier potassium channels (Gutman et al., 2005). Low concentrations of 4-AP (less than 200 μM) reduce the amplitude of a more slowly inactivating D current while sparing the A current (Rudy, 1988; Storm, 1988; Ficker and Heinemann, 1992; Wu and Barish, 1992; Barish et al., 1996).

# RESULTS

## The Presence of 0.5 μM Gabazine in the Recording Solution Allowed us to Examine the Behavior of the Gate

The neural transmission from the PC to the EC was tested under the perfusion of gabazine, which blocks GABA-A-dependent

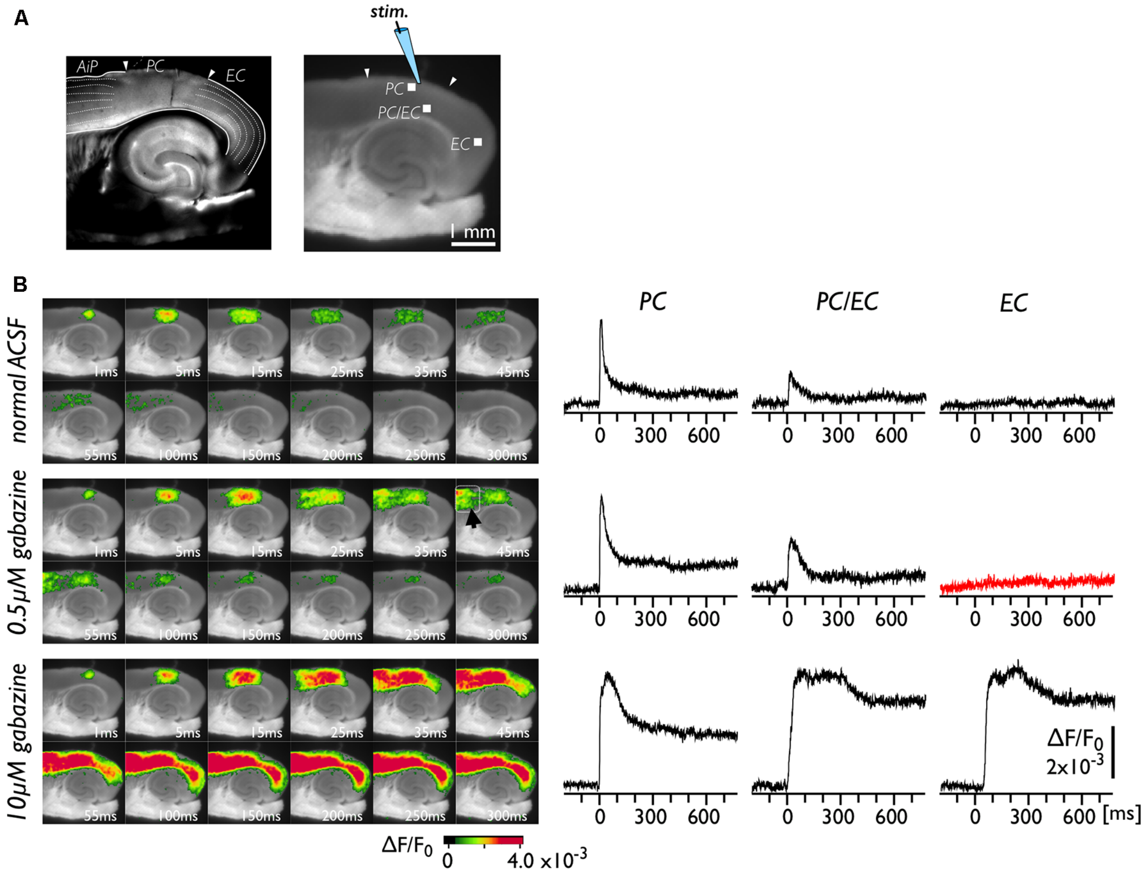

**FIGURE 1 |** Spread of neural activity upon single stimulation of perirhinal cortex (PC) under gabazine treatment. **(A)** Bright-field (left) and fluorescent (right) images of mouse horizontal brain slices. This type of brain slice includes the hippocampus, the entorhinal cortex (EC), the PC, and the insular cortex (AiP). The stimulus electrode was placed in superficial layers in the PC, and the membrane depolarization change was recorded. **(B)** Typical spread pattern of evoked neural activity following electrical stimulation. Sequence of images are the neural activity map after the stimulation obtained under normal solution (upper), 0.5 μM (middle) and 10 μM gabazine treatment (bottom). Depolarization was measured as fractional changes in fluorescence in each pixel; this value is encoded in pseudocolor as indicated in the scale and superimposed on a fluorescent image of the slice. Voltage-sensitive dye (VSD) signal traces of the PC, the PC/EC and the EC in response to the single stimulation are also presented. Electrical stimulation elicited a prolonged response in the EC under 10 μM gabazine (bottom) but did not evoke the EC response under partial suppression of the GABA-A system (0.5 μM; red-trace).

inhibitory transmission in the entire network of the brain slice. **Figure 1A** represents bright-field (left) and fluorescent (right) images of brain slices. The positions of the PC, the EC and the insular cortex (AiP) were identified from the left image with reference to previous literature (Kirkcaldie, 2012; Sills et al., 2012; Willems et al., 2016). A representative experiment is illustrated in **Figure 1B**. We recorded the change in VSD signals in slices following stimulation of the superficial layers of the PC (**Figure 1A**). Under normal conditions (**Figure 1B**, upper), entorhinal activity was not activated by PC stimulation. Because the propagation of neural activity in a slice can be suppressed by local inhibitory neurotransmission (Iijima et al., 1996), we perfused slices with 0.5 μM gabazine (**Figure 1B**, middle). As a result, the evoked neural activity propagated to the AiP (arrowhead in the 45 ms image) but not to the EC (red trace). However, by increasing the concentration of gabazine to 10 μM, we observed apparent neural activity transmission between the PC and the EC (**Figure 1B**, bottom). We performed similar experiments (*n* = 25) and confirmed that 0.5 μM gabazine did not cause entry of perirhinal activity into the EC in our experimental conditions. Hereafter, we used 0.5 μM gabazine to investigate the gate between the PC and the EC.

## Effect of Low-Concentration 4-AP on Neuronal Propagation Across the PC/EC Border

The PC contains many late-spiking neurons, which characteristically possess slowly inactivating potassium channels (Faulkner and Brown, 1999; Beggs et al., 2000; McGann et al., 2001; Moyer et al., 2002). Such neurons might contribute to the blockade of neural transmission to the EC in conjunction with the PC/EC inhibitory system. To obtain evidence in support of this idea, we perfused slices with 40 μM 4-AP in the presence of 0.5 μM gabazine. In the control experiment, we stimulated (five pulses at 40 Hz) the superficial layers of the PC near the PC/EC

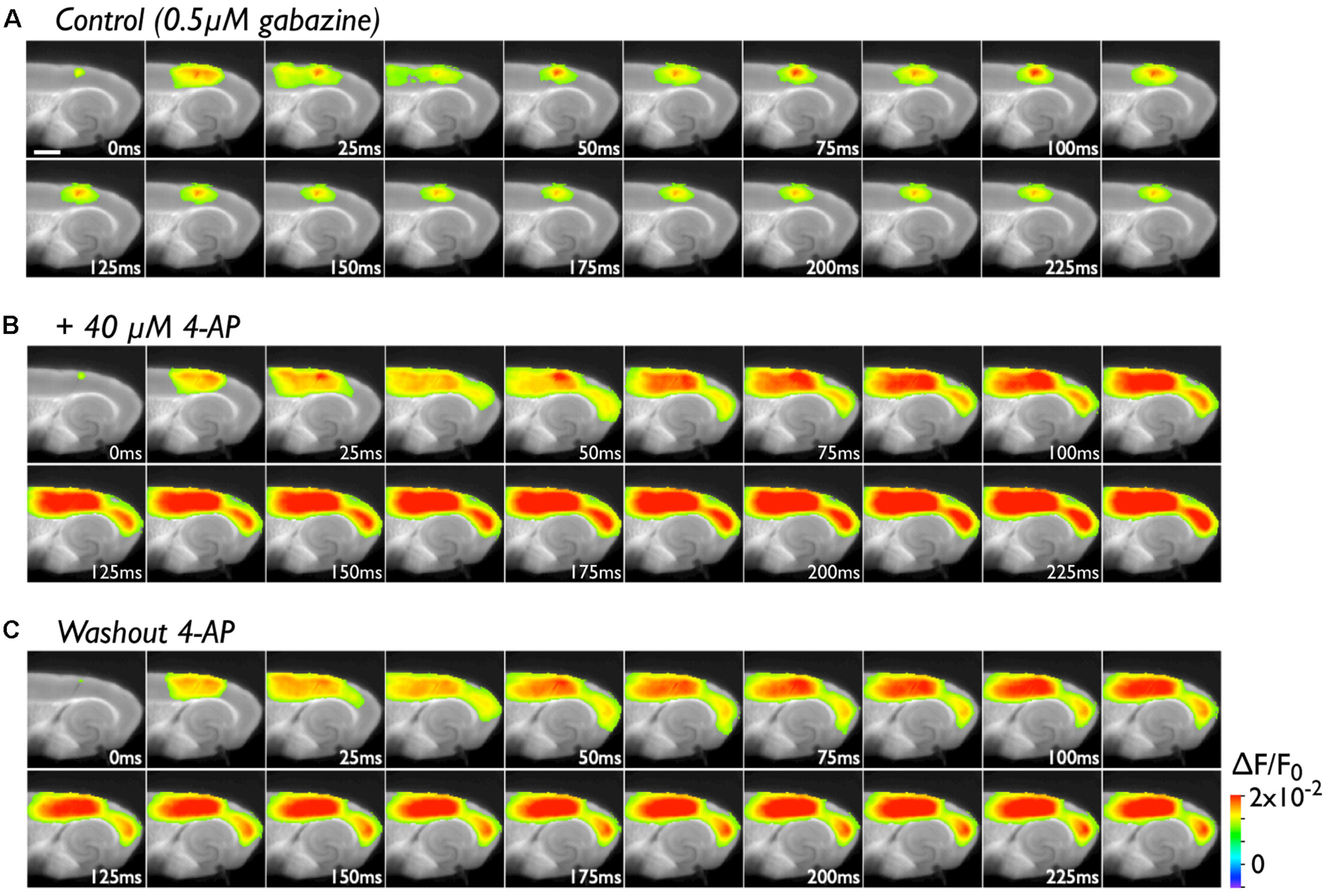

**FIGURE 2 |** The effect of 4-aminopyridine (4-AP) treatment (40 μM) on the initiation of excitation propagation from the PC to the EC. **(A)** Consecutive images showing the spread of neural activity through the cortices upon burst stimulation (40 Hz, 5 pulses) to superficial layers of the PC under the perfusion of gabazine (0.5 μM). The numbers on each image indicate the time after stimulation in milliseconds in the presence of 0.5 μM gabazine. **(B)** The propagation pattern under the coperfusion of 4-AP (40 μM) and gabazine to the same stimulation. **(C)** After 4-AP washout.

border (**Figure 2A**). The responses elicited by a stimulating electrode mainly propagate in the rostrocaudal direction within the stimulated superficial layers for 25 ms. During this period, activity in the superficial layers also propagated to the deep layers of the PC. Repetitive inputs did not cause neural propagation across the PC/EC border. However, entorhinal activity was observed after co-application of 4-AP with gabazine (**Figure 2B**). In this set of experiments, five pulses at 40 Hz were applied to the superficial layers of the PC. Such repetitive pulses caused an increase in the amplitude of perirhinal responses (the VSD signal traces shown in **Figure 3A**) in the presence of 4-AP and gabazine that persisted even after cessation of the 40-Hz stimulus. Moreover, enhancement of the neural activity in the PC triggered neural propagation to the EC. Even after washout of 4-AP, excitation propagation from the PC to the EC was still observed (**Figure 2C**), and it lasted for more than 50 min. Thus, the boundary area between the PC and the EC seems to act as a "gate" for information transfer from the PC to the entorhinal-hippocampal circuit. The data presented here are representative of nine similar experiments.

## Long-Term Continuous VSD Imaging of the Neural Activity Propagation Caused by 4-AP

As shown in **Figure 2**, the increase in excitability at the PC/EC border region induced by 4-AP application caused perirhinal-entorhinal transmission, although partial blockade of GABA-A receptors did not. Our hypothesis is that once the PC/EC gate is open, the PC response can propagate to the EC even when 4-AP is washed out. To investigate the transition of PC/EC network property throughout the experiment, the optical recording system must be sufficiently stable (Barish et al., 1996). By improving the system in many aspects (e.g., optics, staining protocol and performance of the camera), we were able to maintain the slice in a stable condition (Barish et al., 1996; Tominaga et al., 2013; Tominaga and Tominaga, 2016). Thus, we continuously acquired a sequence of images every 2 min for 2 h. **Figure 3** indicates that the 4-AP-induced change in the PC-EC propagation pattern persisted following 4-AP washout. Each image shown in **Figure 3B** is the maximum response

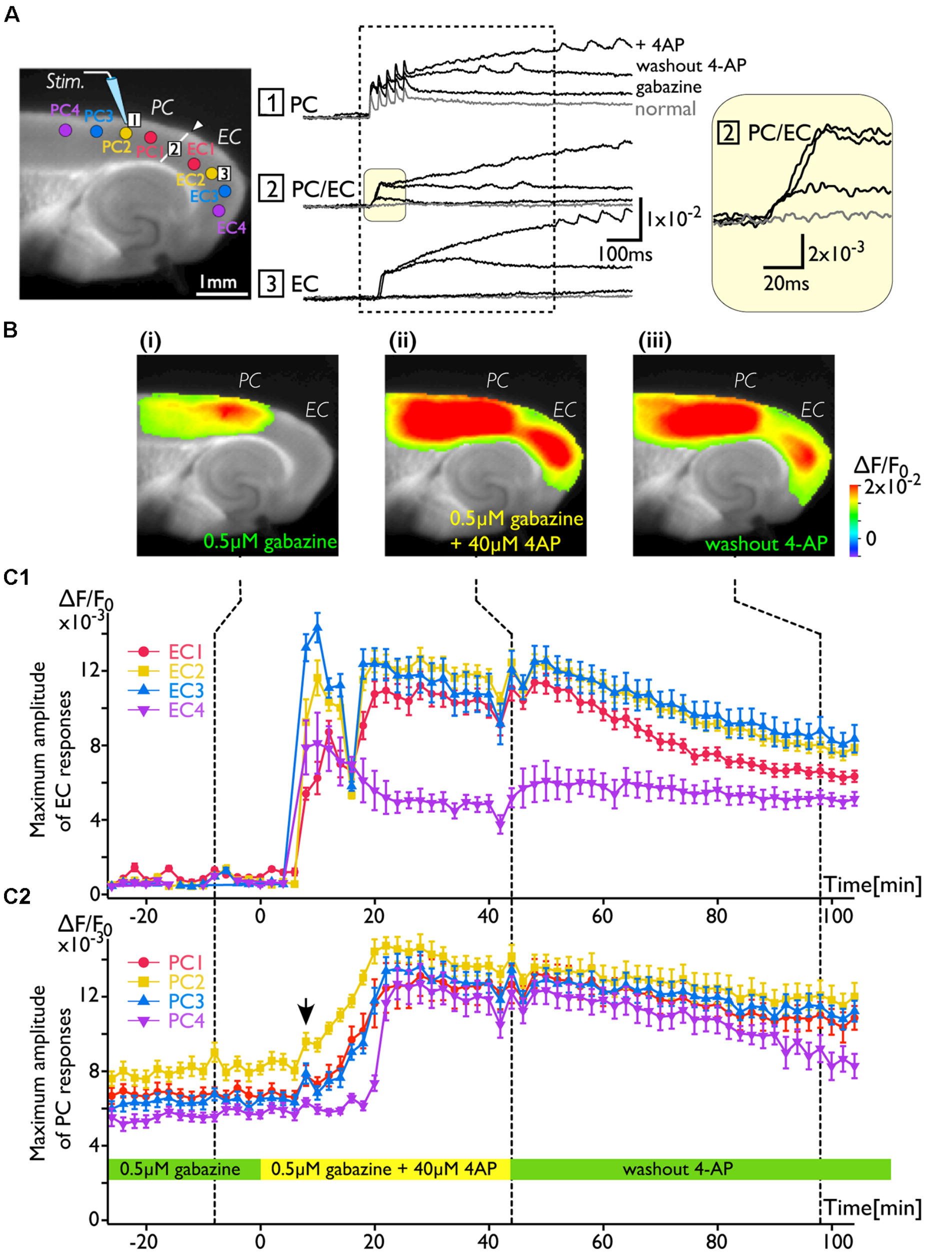

**FIGURE 3 |** The change in the PC-EC network property caused by 4-AP application. VSD imaging was performed every 2 min for 2 h. The recording solution contained gabazine (0.5 μM) throughout the experiment. Perfusion of 4-AP (40 μM) started at 0 ms, and washout started at 44 min. **(A)** The position of the stimulating electrode in the PC is shown in the fluorescent image. Traces are the VSD signals recorded from: (1) the PC; (2) the PC/EC border; and (3) the EC. The VSD signals recorded at −8, 44, and 98 min were superimposed. The inset on the right indicates the initial phase of the depolarization in the PC/EC on an expanded scale. Regions of interest (ROIs) consisting of 21–23 VSD signals were selected from PC1, 2, 3, and 4 and EC1, 2, 3, and 4 (colored circle in the image of **A**). The average of maximum VSD signal amplitudes of 21–23 pixels at each ROI were calculated during the period indicated by the dotted rectangle and plotted in **(C)**. **(B)** Representative maximum response map obtained from the acquisition at the time indicated by the dotted line (**i**: −8 min, **ii**: 44 min, and **iii**: 98 min) in **(C)**. **(C)** Average maximum amplitude plots of ROIs in the EC **(C1)** and the PC **(C2)** throughout the experiment. The error bar represents the standard deviation of maximum amplitudes in a ROI. The averaged maximum value of each ROI displayed a significant increase before and after 4-AP perfusion (*P* values determined using the *t*-test $\ll 10^{-3}$).

map calculated from a sequence of images and shows that the EC was activated after perfusion of 4-AP. Furthermore, we averaged the maximum amplitude of 21–23 pixels at some ROIs selected from the PC and the EC (**Figure 3A**) as an index of the degree of activation in the PC and the EC, respectively. **Figures 3C1,2** illustrate the time series graph in which the maximum values of each ROI were plotted. The averaged maximum value of each ROI displayed a significant increase

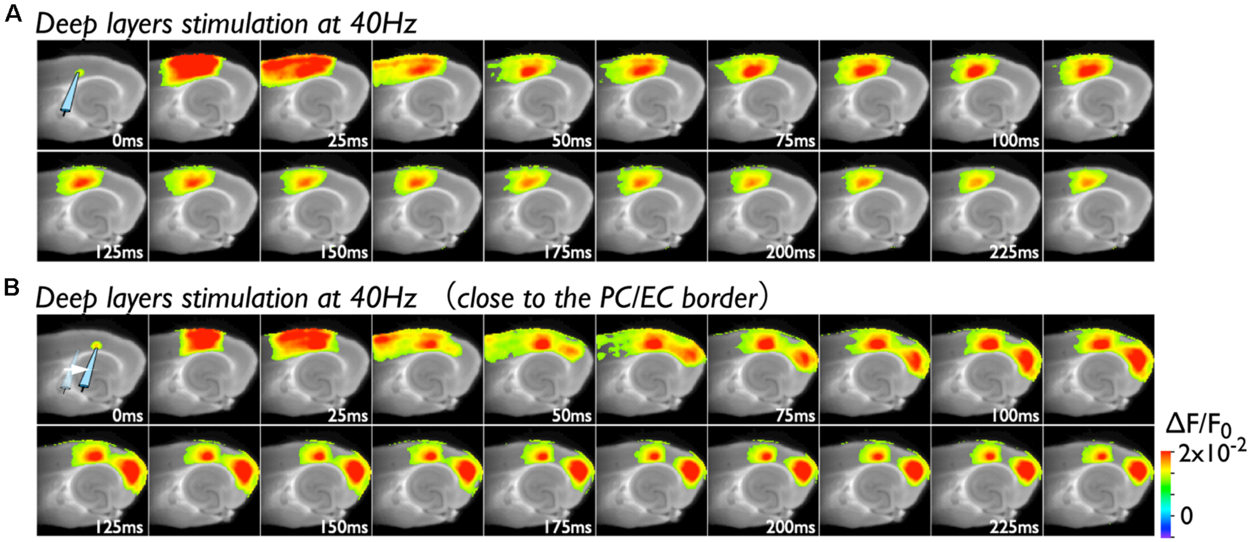

**FIGURE 4 |** Spread of the neural activity from the PC to the EC elicited by deep layer stimulation in the presence of 0.5 μM gabazine. **(A)** The time sequence of the burst stimulation (40 Hz, 5 pulses) to deep layers. The position of the stimulating electrode in the PC is shown in the image at 0 ms. **(B)** Spread of neuronal activity caused by stimulation of the deep layers. The position of the stimulation electrode was moved to the adjacent area of the PC/EC border.

between before and after 4-AP perfusion (*P* values determined using *t*-test $\ll 10^{-3}$). During the experiment, 4-AP was added to the recording solution from 0 to 40 min and then washed out. The maximum response plot of the EC in **Figure 3C1** indicates that 4-AP led to a rapid rise and fall in the EC response (blue and yellow plots) between 8 and 16 min after the initiation of 4-AP perfusion (0 min). During this period, small transient changes (allow head) following the gradual increase were observed in the PC (**Figure 3C2**). From 44 to 100 min, 4-AP was washed out of the solution; however, EC activation was still observed (**Figure 3Biii**), although activation of both the EC and the PC was gradually reduced. At the most medial part of the EC, the value remained stable (purple plots in **Figure 3C1**).

## Neural Propagation From the PC to the EC Caused by Repeated Deep Layer Stimulation at 40 Hz

Because deep layers of the perirhinal area 35 neighboring the EC have been reported to play a key role in neural propagation from the PC to the EC (Kajiwara et al., 2003), we examined the impact of deep layer excitability on the gating property by applying 40 Hz stimulation (**Figure 4**). Initially, we were not able to record neural excitation propagation across the PC/EC border (**Figure 4A**). As shown in **Figure 4B**, however, the increase in excitability at the PC/EC border region caused perirhinal-entorhinal transmission when the position of the stimulation electrode was moved to the PC/EC border (**Figure 4B**). We postulated that once the excitability of neurons at the PC/EC border increased to the level needed to initiate PC-EC transmission, inputs to the superficial layers also transmitted to the EC. We confirmed this hypothesis by the continuous acquisition of the neural activity evoked by alternately applied stimulation to deep or superficial layers every 1 min (**Figure 5**). In this experiment, we placed the stimulating electrodes in both the superficial (sSL) and deep layers (sDL1 or sDL2) of the PC and investigated the contribution of each stimulus to the change in the network response pattern over time according to the stimulation protocol indicated in **Figure 5A**. Regarding the sDL, the position of the electrode was moved from sDL1 to sDL2 (close to the border) at 8 min.

**Figure 5B** represents a maximum amplitude plot of the EC response at ROIs shown in the inset image. EC responses were clearly elicited by sDL2, that is, PC-EC transmission occurred. In addition, sSL elicited an entorhinal response after 13 min, which persisted throughout the experiment. **Figures 5C,D** illustrate the maximum response map and examples of optical signal traces extracted from the PC (trace 1), the PC/EC border (trace 2), and the EC (trace 3, 4, 5). A five-pulse 40-Hz stimulation by sDL1 elicited a sharp large-amplitude response (asterisk) in the PC, whereas a noticeable response in the EC was not observed. However, sDL2 elicited a transient sharp response followed by a slow large-amplitude response at the PC/EC border (trace 2) and in the EC (trace 3, 4), showing an effect of repetitive stimulation (double-asterisk). As shown in **Figure 5Civ**, an EC response was elicited by subsequent application of stimulation to the superficial layers (11th sSL), although not immediately (9th sSL). The optical signal traces of **Figures 5Cii,iv** on an expanded time scale shown in the dotted rectangle in **Figure 5D** indicate that the 1st and/or 2nd pulse of repetitive stimulation of sDL1 contributed to initiation of the EC response (arrow on the black-trace). In contrast, repetitive (1st, 2nd, and 3rd) inputs by the sSL increased the excitability of neurons at the PC/EC border (red-trace 2) and evoked the large-amplitude response in the EC (blue-trace 3) as well as at the PC/EC border itself.

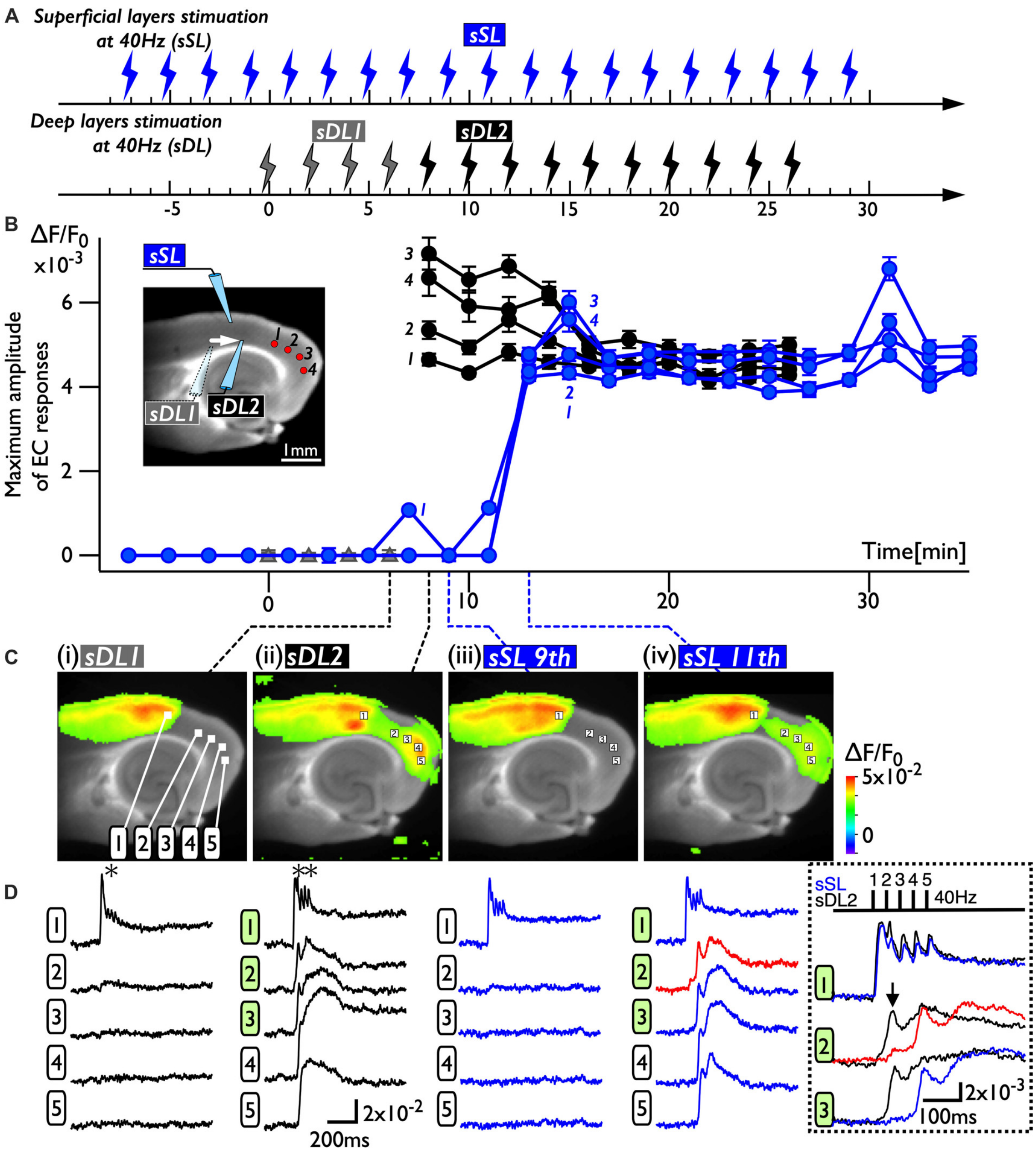

**FIGURE 5 |** The change in the PC-EC network property caused by alternating stimulation of deep and superficial layers. **(A)** The stimulation protocol of the experiment. Burst stimulation (5 pulses at 40 Hz) was applied to the superficial layers (sSL) and deep layers (sDL1 and sDL2) in the PC. At 0, 2, 4, and 6 min, sDL1 was applied, and sDL2 was applied after 8 min. sSL and sDL were alternately applied every 1 min. **(B)** Maximum amplitude plots of ROIs in the EC and a fluorescent image of the slice. The position of the stimulating electrode is indicated in the fluorescent image. The positions of the ROIs are indicated by red circles. The temporal variability of the maximum response induced by stimulation of the deep (black) and superficial (blue) layers is plotted in black and blue, respectively. **(C,D)** Maximum response map **(C)** and representative temporal pattern of the response **(D)** induced by the stimulation of deep layers (**i**: sDL1, **ii**: sDL2) and superficial layers (**iii** and **iv**: sSL9th and sSL 11th). Each number on the image indicates the pixel of the VSD signals extracted. The traces shown in the dotted rectangle indicate the initial phase of the responses in **(ii)** and **(iv)** on an expanded time scale. The five pulses at 40 Hz were applied as indicated above. Black and blue traces represent the response to stimulation of deep layers and superficial layers, respectively. The response at the PC/EC border in response to stimulation of superficial layers is indicated by red.

# DISCUSSION

This study addressed the long-term modification of network activity, termed network plasticity, in mouse perirhinal/entorhinal cortical slices using a recently developed VSD imaging technique (Tominaga et al., 2018). By implementing a low-magnification lens with a high-N.A. in the system, we analyzed the neural activity in a wider field of view and minimized the impact of bleaching of the dye on the long-term recording. The stability of the experimental system enabled us to investigate the dynamics of neural transmission *via* the "gate" in the PC/EC over a long time period and contributed to new findings. First, the increase in neuronal excitability caused by bath application of 4-AP initiated the transmission of perirhinal activity to the EC under conditions in which GABA-A control partially remained. Second, once neural propagation across the perirhinal/entorhinal border was elicited, the network property was changed, and perirhinal neural activity easily propagated to the EC even after 4-AP washout. Third, such a change in the network property was accomplished without 4-AP treatment using repeated burst stimulation of neurons in the deep layers of the PC to initiate neural propagation across the border. Consequently, even ineffective stimulation of the superficial layers of the PC was effective for neural transmission to the EC.

## Inhibitory Control of Neural Propagation Across the Rhinal Sulcus

Based on observations obtained from electrophysiological and imaging studies performed on various brain preparations, such as *in vivo* (Pelletier et al., 2004) and *ex vivo* isolated whole brain (Biella et al., 2002) and brain slice (Kajiwara et al., 2003) preparations, the local network between the PC and the EC is considered to form a wall of inhibition that blocks reciprocal information transfer (de Curtis and Paré, 2004). One of the factors that causes impaired neuronal transmission from the PC to the EC despite the existence of anatomical connections within the PC/EC network is the inhibitory system. Pelletier et al. (2005) reported that repetitive neocortical stimuli or associative stimulus by a conditioning shock to the amygdala enhanced the amplitude of neocortically evoked field potentials in the PC; however, this increased excitability did not augment the responsiveness of entorhinal neurons. They suggested that the increased excitatory drive in the PC was insufficient to overcome the local inhibition. Consistent with this, propagation of perirhinal activity to the EC was observed with a high concentration (10 μM) of a GABA-A antagonist (**Figure 1B**, bottom). However, when the concentration of gabazine was 0.5 μM, entorhinal activity was not evoked by perirhinal stimulation, although neural propagation to the AiP was observed (**Figure 1B**, middle). These observations imply the existence of a unique network structure consisting of different types of inhibitory systems in the PC-EC region. Evidently, a large number of parvalbumin immunoreactive neurons are located in the EC, especially near the border to the PC (Wouterlood et al., 1995; Miettinen et al., 1996). Meanwhile, the PC possesses specific interneuronal structures, with an unusually high proportion of calretinin-positive interneurons (Barinka et al., 2012). Moreover, a combined study of anterograde tracing and GABA immunocytochemistry techniques revealed the characteristic inhibitory networks that should control the impulse traffic from the PC to the EC (Pinto et al., 2006; Apergis-Schoute et al., 2007). Such an inhibitory system at the boundary area between the PC and the EC may be critical for the gate, affecting the information transfer from the PC to the entorhinal-hippocampal circuit (Maurer et al., 2017).

## 4-AP Can Open the Gate for the Neural Transmission From the PC to the EC

The pathway between the PC and the EC is thus under control of the inhibitory system and might form a gate for information transfer from the neocortex to the hippocampus. In addition to disinhibition of the inhibitory system, hyperexcitability of principal neurons in the PC may also affect gate opening. Indeed, even under the weak inhibitory control condition achieved by partial blockade of the GABA-A system, we observed PC-EC transmission by applying associative stimulation, which caused an increase in the excitability of PC neurons (Kajiwara et al., 2003). Because there are many late-spiking neurons in the PC (Faulkner and Brown, 1999; Beggs et al., 2000; McGann et al., 2001; Moyer et al., 2002), a low concentration of 4-AP (40 μM) may have affected the slowly inactivating potassium conductance of these neurons, inducing rapid depolarization of the membrane potential. Certainly, we confirmed that 4-AP application in a solution containing 0.5 μM gabazine induced perirhinal-entorhinal neural transmission (**Figure 2B**). Similar PC-EC propagation has been reported in the ictal/interictal epileptic conditions induced by 4-AP, bicuculine and/or low $Mg^{2+}$ concentrations (Stoop and Pralong, 2000; de Guzman et al., 2004; Zahn et al., 2008). However, it was difficult to identify the critical region for propagation *via* the PC/EC gate because of the limitation of the spatial resolution in electrophysiological methods. By performing the VSD imaging technique in the present study, we successfully observed an increase in the depolarized response in deep layers of the PC/EC (*see the image at 25 ms in **Figure 2B***), suggesting that the physiological connectivity in this area was increased.

## An Increase in the Excitability of Deep Layers at the PC/EC Border Is Necessary for the Gate to Open

Under 4-AP perfusion, the neural activity in response to superficial layer stimulation in the PC propagated to the EC *via* the deep layers at the PC/EC gate. Deep layer stimulation without 4-AP evoked the propagation of the neural response to the EC (**Figure 2Bii**). These results correspond to our previous study performed in rat brain slices (Kajiwara et al., 2003), indicating that repetitive stimulation at 40 Hz of deep layers near the PC/EC border (area 35) triggered the EC response, but stimulation of superficial layers did not. Anatomical studies have indicated that the PC projects heavily to the EC, especially the lateral part (Cappaert et al., 2015), and the projection from the PC terminates preferentially in the superficial layers of the EC (Naber et al., 1997; Burwell and Amaral, 1998b). Why was prominent excitation first observed in deep layers in our studies? A likely explanation is that the VSD imaging in the present study revealed a physiologically activated multi-synaptic pathway, whereas typical anterograde/retrograde tracing studies reveal the majority of the projection fibers, dendrites and cell bodies of principal neurons. Layers II and III of the EC contain a dramatically higher density of parvalbumin-positive fibers, dendrites, and cell bodies than those of the PC (Wouterlood et al., 1995; Miettinen et al., 1996). In our experimental conditions, the remaining GABA-A-mediated transmission by these inhibitory neurons might affect PC-EC neural propagation. Moreover, the PC-EC network is thought to be controlled by a strong feed-forward inhibitory system (Pinto et al., 2006), including various modes, e.g.,: (1) principal cells in perirhinal area 36 (far from the border of the PC/EC) and area 35 (near the border) projecting to inhibitory neurons in each area sequentially (stepwise inhibition); (2) neurons projecting beyond the adjoining area (leap mode); and (3) axons of GABAergic cells extending beyond the area where their soma is located (long-range inhibition). Because the superficial EC neurons receive such multisynaptic innervations as well as direct projections from the PC, deep layers at the PC/EC border under relatively weak inhibitory control may be an alternative pathway to the EC.

## Plasticity of the Neuronal Network in the Rhinal Cortices

As we described above, repetitive 40-Hz stimulation to the deep layers of the PC triggered neural transmission across the PC/EC gate (**Figure 4B**), potentially due to a change in the multisynaptic network involving the transfer of neural activity to the EC from a *steady state* (degree of activation in the PC and EC is “high” and “low”) to an *active state* (“high” and “high”; *i.e., gate-open)*. In support of this idea, superficial layer stimulation did not cause neural transmission across the PC/EC border in the steady state (**Figures 2B**, **5Ciii**). However, once the state was changed to active by deep layer stimulation (**Figure 5Cii**), stimulation of the superficial layers with the same intensity was able to cause an entorhinal response (**Figure 5Civ**). In the active state, repetitive stimulation of the superficial layers was able to depolarize the membrane potential of neurons in the PC/EC border (**Figure 5D**, red-trace). The delay between the onset and the first peak of the optical response elicited by the stimuli to the superficial layers was approximately 100 ms, which is longer than that elicited by deep layer stimulation (30 ms). During this delay, the membrane slowly depolarized. This slow depolarization may be caused by late-spiking neurons in the PC and may be shortened by 4-AP application. Thus, 4-AP was also able to change the state to active and trigger PC-EC neural propagation (**Figures 2**, **3**). In our experimental condition, such a change in the state persisted for a long time, as indicated in **Figures 3C**, **5B**, suggesting the existence of network-scale plasticity in the rhinal cortices, especially at the PC/EC border.

One of the most fundamental principles of plasticity is Hebb’s law. In his book, Hebb (1949) suggests that the two adjacent areas will begin to activate together once a plastic change occurs. Our finding that the repetitive stimulation of the deep layer of the PC causes a persistent change in circuit behavior that allows the spread of activity across the PC/EC border is similar to Hebb’s assumption. Hence, we can also assume that multiple excitatory and inhibitory neurons in this area, probably within the deep layer of the PC/EC border, would exhibit plastic connections. We cannot determine the precise mechanism of plasticity. However, application of a small amount of 4-AP induced the same plastic change, suggesting the involvement of late-spiking neurons in this area. de Guzman et al. (2004) showed 4-AP-induced ictal-like spontaneous activity, which was completely blocked by the addition of NMDA antagonist in the PC, by performing field potential recording of brain slices in an interface-type chamber. In our experimental condition, we did not observe such activity, however, under the current protocol (i.e., perirhinal stimulation under perfusion of 40 $\mu$M 4-AP and 0.5 $\mu$M gabazine), we infrequently observed the evoked oscillatory activity in the restricted region of the PC/EC border at a frequency range from 7 to 40 Hz (unpublished data). In addition, the PC is suggested to be implicated in the processes of epileptogenesis and ictogenesis (Biagini et al., 2013). Thus, the local circuit in the PC, which possesses the ability to induce oscillating activity, may affect the network plasticity through the rhinal cortices. In fact, Zarnadze et al. (2016) reported that gamma rhythms lead to activity-dependent modification of hippocampal networks, and this plasticity was metabotropic glutamate receptor 5 dependent. The plasticity might also involve plastic changes in gap junctions, which have been suggested to exist in the PC (Zlomuzica et al., 2010) and may synchronize neuronal activity and/or accelerate neuronal transmission. Moreover, because synchronous activation of astrocytes has been observed in the rhinal cortices during the spread of epileptic activities (Losi et al., 2016), astrocytes as well as neurons may also be involved in the observed phenomena. Although further experiments are required to confirm this speculative idea, the stable VSD imaging technique with a wide field of view revealed that network-level plastic changes occurred in the PC/EC region, thereby generating new insights into plasticity in this region.

## AUTHOR CONTRIBUTIONS

RK and TT designed the research and wrote the article. TT, YT, and RK performed the research and analyzed the data. YT and TT developed the software.

## FUNDING

This work was supported by Japan Society for the Promotion of Science (JSPS) KAKENHI to RK (16K00380, 17H01810, 16K04923), to TT (16H06532, 16K21743, 16H06524, 15K00413), and Ministry of Health, Labour and Welfare (MHWL) KAKENHI to TT [H27(15570760), H30(18062156)].

## ACKNOWLEDGMENTS

We thank Dr. Michinori Ichikawa for discussion and help with system development. The authors also thank Ms. Yuka Wakayama for technical assistance. This manuscript was edited for English language by American Journal Experts (AJE).

## REFERENCES

Apergis-Schoute, J., Pinto, A., and Paré, D. (2007). Muscarinic control of long-range GABAergic inhibition within the rhinal cortices. *J. Neurosci.* 27, 4061–4071. doi: 10.1523/jneurosci.0068-07.2007

Barinka, F., Salaj, M., Rybář, J., Krajčovičová, E., Kubová, H., and Druga, R. (2012). Calretinin, parvalbumin and calbindin immunoreactive interneurons in perirhinal cortex and temporal area Te3V of the rat brain: qualitative and quantitative analyses. *Brain Res.* 1436, 68–80. doi: 10.1016/j.brainres.2011.12.014

Barish, M. E., Ichikawa, M., Tominaga, T., Matsumoto, G., and Iijima, T. (1996). Enhanced fast synaptic transmission and a delayed depolarization induced by transient potassium current blockade in rat hippocampal slice as studied by optical recording. *J. Neurosci.* 16, 5672–5687. doi: 10.1523/jneurosci.16-18-05672.1996

Beggs, J. M., Moyer, J. R. Jr., McGann, J. P., and Brown, T. H. (2000). Prolonged synaptic integration in perirhinal cortical neurons. *J. Neurophysiol.* 83, 3294–3298. doi: 10.1152/jn.2000.83.6.3294

Biagini, G., D'Antuono, M., Benini, R., de Guzman, P., Longo, D., and Avoli, M. (2013). Perirhinal cortex and temporal lobe epilepsy. *Front. Cell. Neurosci.* 7:130. doi: 10.3389/fncel.2013.00130

Biella, G., Spaiardi, P., Toselli, M., de Curtis, M., and Gnatkovsky, V. (2010). Functional interactions within the parahippocampal region revealed by voltage-sensitive dye imaging in the isolated guinea pig brain. *J. Neurophysiol.* 103, 725–732. doi: 10.1152/jn.00722.2009

Biella, G., Uva, L., and de Curtis, M. (2001). Network activity evoked by neocortical stimulation in area 36 of the guinea pig perirhinal cortex. *J. Neurophysiol.* 86, 164–172. doi: 10.1152/jn.2001.86.1.164

Biella, G., Uva, L., and de Curtis, M. (2002). Propagation of neuronal activity along the neocortical-perirhinal-entorhinal pathway in the guinea pig. *J. Neurosci.* 22, 9972–9979. doi: 10.1523/jneurosci.22-22-09972.2002

Buckley, M. J., and Gaffan, D. (1998). Learning and transfer of object-reward associations and the role of the perirhinal cortex. *Behav. Neurosci.* 112, 15–23. doi: 10.1037/0735-7044.112.1.15

Buffalo, E. A., Ramus, S. J., Clark, R. E., Teng, E., Squire, L. R., and Zola, S. M. (1999). Dissociation between the effects of damage to perirhinal cortex and area TE. *Learn. Mem.* 6, 572–599.

Burwell, R. D. (2001). Borders and cytoarchitecture of the perirhinal and postrhinal cortices in the rat. *J. Comp. Neurol.* 437, 17–41. doi: 10.1002/cne.1267

Burwell, R. D., and Amaral, D. G. (1998a). Cortical afferents of the perirhinal, postrhinal, and entorhinal cortices of the rat. *J. Comp. Neurol.* 398, 179–205. doi: 10.1002/(SICI)1096-9861(19980824)398:2<179::AID-CNE3>3.0.CO;2-Y

Burwell, R. D., and Amaral, D. G. (1998b). Perirhinal and postrhinal cortices of the rat: interconnectivity and connections with the entorhinal cortex. *J. Comp. Neurol.* 391, 293–321. doi: 10.1002/(sici)1096-9861(19980216)391:3<293::aid-cne2>3.0.co;2-x

Cappaert, N. L. M., Van Strien, N. M., and Witter, M. P. (2015). "Hippocampal Formation," in *The Rat Nervous System*, ed. G. Paxinos (Amsterdam: Academic Press), 511–573.

Corodimas, K. P., and LeDoux, J. E. (1995). Disruptive effects of posttraining perirhinal cortex lesions on conditioned fear: contributions of contextual cues. *Behav. Neurosci.* 109, 613–619. doi: 10.1037/0735-7044.109.4.613

de Curtis, M., and Paré, D. (2004). The rhinal cortices: a wall of inhibition between the neocortex and the hippocampus. *Prog. Neurobiol.* 74, 101–110. doi: 10.1016/j.pneurobio.2004.08.005

de Guzman, P., D'Anrtuono, M., and Avoli, M. (2004). Initiation of electrographic seizures by neuronal networks in entorhinal and perirhinal cortices *in vitro*. *Neuroscience* 123, 875–886. doi: 10.1016/j.neuroscience.2003.11.013

Dere, E., Huston, J. P., and De Souza Silva, M. A. (2007). The pharmacology, neuroanatomy and neurogenetics of one-trial object recognition in rodents. *Neurosci. Biobehav. Rev.* 31, 673–704. doi: 10.1016/j.neubiorev.2007.01.005

Faulkner, B., and Brown, T. H. (1999). Morphology and physiology of neurons in the rat perirhinal-lateral amygdala area. *J. Comp. Neurol.* 411, 613–642. doi: 10.1002/(sici)1096-9861(19990906)411:4<613::aid-cne7>3.0.co;2-u

Ficker, E., and Heinemann, U. (1992). Slow and fast transient potassium currents in cultured rat hippocampal cells. *J. Physiol.* 445, 431–455. doi: 10.1113/jphysiol.1992.sp018932

Forwood, S. E., Winters, B. D., and Bussey, T. J. (2005). Hippocampal lesions that abolish spatial maze performance spare object recognition memory at delays of up to 48 hours. *Hippocampus* 15, 347–355. doi: 10.1002/hipo.20059

Gutman, G. A., Chandy, K. G., Grissmer, S., Lazdunski, M., McKinnon, D., Pardo, L. A., et al. (2005). International Union of Pharmacology. LIII. Nomenclature and molecular relationships of voltage-gated potassium channels. *Pharmacol. Rev.* 57, 473–508. doi: 10.1124/pr.57.4.10

Hebb, D. O. (1949). *The Organization of Behavior*. New York, NY: Wiley & Sons.

Herzog, C., and Otto, T. (1998). Contributions of anterior perirhinal cortex to olfactory and contextual fear conditioning. *Neuroreport* 9, 1855–1859. doi: 10.1097/00001756-199806010-00035

Higuchi, S., and Miyashita, Y. (1996). Formation of mnemonic neuronal responses to visual paired associates in inferotemporal cortex is impaired by perirhinal and entorhinal lesions. *Proc. Natl. Acad. Sci. U S A* 93, 739–743. doi: 10.1073/pnas.93.2.739

Iijima, T., Witter, M. P., Ichikawa, M., Tominaga, T., Kajiwara, R., and Matsumoto, G. (1996). Entorhinal-hippocampal interactions revealed by real-time imaging. *Science* 272, 1176–1179. doi: 10.1126/science.272.5265.1176

Kajiwara, R., Takashima, I., Mimura, Y., Witter, M. P., and Iijima, T. (2003). Amygdala input promotes spread of excitatory neural activity from perirhinal cortex to the entorhinal-hippocampal circuit. *J. Neurophysiol.* 89, 2176–2184. doi: 10.1152/jn.01033.2002

Kealy, J., and Commins, S. (2011). The rat perirhinal cortex: a review of anatomy, physiology, plasticity, and function. *Prog. Neurobiol.* 93, 522–548. doi: 10.1016/j.pneurobio.2011.03.002

Kholodar-Smith, D. B., Allen, T. A., and Brown, T. H. (2008). Fear conditioning to discontinuous auditory cues requires perirhinal cortical function. *Behav. Neurosci.* 122, 1178–1185. doi: 10.1037/a0012902

Kirkcaldie, M. (2012). "Neocortex," in *The Mouse Nervous System*, eds. C. R. Watson, G. Paxinos and L. Puelles (San Diego, CA: Academic Press), 52–111.

Koganezawa, N., Taguchi, A., Tominaga, T., Ohara, S., Tsutsui, K.-I., Witter, M. P., et al. (2008). Significance of the deep layers of entorhinal cortex for transfer of both perirhinal and amygdala inputs to the hippocampus. *Neurosci. Res.* 61, 172–181. doi: 10.1016/j.neures.2008.02.007

Losi, G., Marcon, I., Mariotti, L., Sessolo, M., Chiavegato, A., and Carmignoto, G. (2016). A brain slice experimental model to study the generation and the propagation of focally-induced epileptiform activity. *J. Neurosci. Methods* 260, 125–131. doi: 10.1016/j.jneumeth.2015.04.001

Maurer, A. P., Burke, S. N., Diba, K., and Barnes, C. A. (2017). Attenuated activity across multiple cell types and reduced monosynaptic connectivity in the aged perirhinal cortex. *J. Neurosci.* 37, 8965–8974. doi: 10.1523/jneurosci.0531-17.2017

McGann, J. P., Moyer, J. R. Jr., and Brown, T. H. (2001). Predominance of late-spiking neurons in layer VI of rat perirhinal cortex. *J. Neurosci.* 21, 4969–4976. doi: 10.1523/jneurosci.21-14-04969.2001

Miettinen, M., Koivisto, E., Riekkinen, P., and Miettinen, R. (1996). Coexistence of parvalbumin and GABA in nonpyramidal neurons of the rat entorhinal cortex. *Brain Res.* 706, 113–122. doi: 10.1016/0006-8993(95)01203-6

Moyer, J. R. Jr., McNay, E. C., and Brown, T. H. (2002). Three classes of pyramidal neurons in layer V of rat perirhinal cortex. *Hippocampus* 12, 218–234. doi: 10.1002/hipo.1110

Murray, E. A., Gaffan, D., and Mishkin, M. (1993). Neural substrates of visual stimulus-stimulus association in rhesus monkeys. *J. Neurosci.* 13, 4549–4561. doi: 10.1523/jneurosci.13-10-04549.1993

Naber, P. A., Caballero-Bleda, M., Jorritsma-Byham, B., and Witter, M. P. (1997). Parallel input to the hippocampal memory system through peri- and postrhinal cortices. *Neuroreport* 8, 2617–2621. doi: 10.1097/00001756-199707280-00039

Pelletier, J. G., Apergis-Schoute, J., and Paré, D. (2005). Interaction between amygdala and neocortical inputs in the perirhinal cortex. *J. Neurophysiol.* 94, 1837–1848. doi: 10.1152/jn.00260.2005

Pelletier, J. G., Apergis, J., and Paré, D. (2004). Low-probability transmission of neocortical and entorhinal impulses through the perirhinal cortex. *J. Neurophysiol.* 91, 2079–2089. doi: 10.1152/jn.01197.2003

Pinto, A., Fuentes, C., and Paré, D. (2006). Feedforward inhibition regulates perirhinal transmission of neocortical inputs to the entorhinal cortex: ultrastructural study in guinea pigs. *J. Comp. Neurol.* 495, 722–734. doi: 10.1002/cne.20905

Rudy, B. (1988). Diversity and ubiquity of K channels. *Neuroscience* 25, 729–749. doi: 10.1016/0306-4522(88)90033-4

Sills, J. B., Connors, B. W., and Burwell, R. D. (2012). Electrophysiological and morphological properties of neurons in layer 5 of the rat postrhinal cortex. *Hippocampus* 22, 1912–1922. doi: 10.1002/hipo.22026

Stoop, R., and Pralong, E. (2000). Functional connections and epileptic spread between hippocampus, entorhinal cortex and amygdala in a modified horizontal slice preparation of the rat brain. *Eur. J. Neurosci.* 12, 3651–3663. doi: 10.1046/j.1460-9568.2000.00253.x

Squire, L. R., Stark, C. E., and Clark, R. E. (2004). The medial temporal lobe. *Annu. Rev. Neurosci.* 27, 279–306. doi: 10.1146/annurev.neuro.27.070203.144130

Storm, J. F. (1988). Temporal integration by a slowly inactivating $K^+$ current in hippocampal neurons. *Nature* 336, 379–381. doi: 10.1038/336379a0

Suzuki, W. A. (1996). The anatomy, physiology and functions of the perirhinal cortex. *Curr. Opin. Neurobiol.* 6, 179–186. doi: 10.1016/s0959-4388(96)80071-7

Tominaga, T., Kajiwara, R., and Tominaga, Y. (2013). VSD imaging method of *ex vivo* brain preparation. *J. Neurosci. Neuroeng.* 2, 211–219. doi: 10.1166/jnsne.2013.1051

Tominaga, T., and Tominaga, Y. (2016). Paired burst stimulation causes $GABA_A$ receptor-dependent spike firing facilitation in CA1 of rat hippocampal slices. *Front. Cell. Neurosci.* 10:9. doi: 10.3389/fncel.2016.00009

Tominaga, T., Tominaga, Y., and Ichikawa, M. (2002). Optical imaging of long-lasting depolarization on burst stimulation in area CA1 of rat hippocampal slices. *J. Neurophysiol.* 88, 1523–1532. doi: 10.1152/jn.2002.88.3.1523

Tominaga, T., Tominaga, Y., Yamada, H., Matsumoto, G., and Ichikawa, M. (2000). Quantification of optical signals with electrophysiological signals in neural activities of Di-4-ANEPPS stained rat hippocampal slices. *J. Neurosci. Methods* 102, 11–23. doi: 10.1016/s0165-0270(00)00270-3

Tominaga, Y., Taketoshi, M., and Tominaga, T. (2018). Overall assay of neuronal signal propagation pattern with long-term potentiation (LTP) in hippocampal slices from the CA1 area With fast voltage-sensitive dye imaging. *Front. Cell. Neurosci.* 12:389. doi: 10.3389/fncel.2018.00389

Unal, G., Apergis-Schoute, J., and Paré, D. (2012). Associative properties of the perirhinal network. *Cereb. Cortex* 22, 1318–1332. doi: 10.1093/cercor/bhr212

Uva, L., Librizzi, L., Wendling, F., and de Curtis, M. (2005). Propagation dynamics of epileptiform activity acutely induced by bicuculline in the hippocampal-parahippocampal region of the isolated Guinea pig brain. *Epilepsia* 46, 1914–1925. doi: 10.1111/j.1528-1167.2005.00342.x

van Strien, N. M., Cappaert, N. L., and Witter, M. P. (2009). The anatomy of memory: an interactive overview of the parahippocampal-hippocampal network. *Nat. Rev. Neurosci.* 10, 272–282. doi: 10.1038/nrn2614

Willems, J. G., Wadman, W. J., and Cappaert, N. L. (2016). Distinct spatiotemporal activation patterns of the perirhinal-entorhinal network in response to cortical and amygdala input. *Front. Neural Circuits* 10:44. doi: 10.3389/fncir.2016.00044

Willems, J. G. P., Wadman, W. J., and Cappaert, N. L. M. (2018). Parvalbumin interneuron mediated feedforward inhibition controls signal output in the deep layers of the perirhinal-entorhinal cortex. *Hippocampus* 28, 281–296. doi: 10.1002/hipo.22830

Winters, B. D., and Bussey, T. J. (2005). Glutamate receptors in perirhinal cortex mediate encoding, retrieval, and consolidation of object recognition memory. *J. Neurosci.* 25, 4243–4251. doi: 10.1523/jneurosci.0480-05.2005

Winters, B. D., Forwood, S. E., Cowell, R. A., Saksida, L. M., and Bussey, T. J. (2004). Double dissociation between the effects of peri-postrhinal cortex and hippocampal lesions on tests of object recognition and spatial memory: heterogeneity of function within the temporal lobe. *J. Neurosci.* 24, 5901–5908. doi: 10.1523/jneurosci.1346-04.2004

Witter, M. P., Wouterlood, F. G., Naber, P. A., and Van Haeften, T. (2000). Anatomical organization of the parahippocampal-hippocampal network. *Ann. N. Y. Acad. Sci.* 911, 1–24. doi: 10.1111/j.1749-6632.2000.tb06716.x

Wouterlood, F. G., Hartig, W., Bruckner, G., and Witter, M. P. (1995). Parvalbumin-immunoreactive neurons in the entorhinal cortex of the rat: localization, morphology, connectivity and ultrastructure. *J. Neurocytol.* 24, 135–153.

Wu, R. L., and Barish, M. E. (1992). Two pharmacologically and kinetically distinct transient potassium currents in cultured embryonic mouse hippocampal neurons. *J. Neurosci.* 12, 2235–2246. doi: 10.1523/jneurosci.12-06-02235.1992

Zahn, R. K., Tolner, E. A., Derst, C., Gruber, C., Veh, R. W., and Heinemann, U. (2008). Reduced ictogenic potential of 4-aminopyridine in the perirhinal and entorhinal cortex of kainate-treated chronic epileptic rats. *Neurobiol. Dis.* 29, 186–200. doi: 10.1016/j.nbd.2007.08.013

Zarnadze, S., Bäuerle, P., Santos-Torres, J., Böhm, C., Schmitz, D., Geiger, J. R., et al. (2016). Cell-specific synaptic plasticity induced by network oscillations. *Elife* 5:e14912. doi: 10.7554/eLife.14912

Zlomuzica, A., Reichinnek, S., Maxeiner, S., Both, M., May, E., Wörsdörfer, P., et al. (2010). Deletion of connexin45 in mouse neurons disrupts one-trial object recognition and alters kainate-induced γ-oscillations in the hippocampus. *Physiol. Behav.* 101, 245–253. doi: 10.1016/j.physbeh.2010.05.007

**Conflict of Interest Statement**: The authors declare that the research was conducted in the absence of any commercial or financial relationships that could be construed as a potential conflict of interest.

frontiers
in Cellular Neuroscience

ORIGINAL RESEARCH
published: 14 February 2019
doi: 10.3389/fncel.2019.00039

# Single-Neuron Level One-Photon Voltage Imaging With Sparsely Targeted Genetically Encoded Voltage Indicators

**Peter Quicke[1,2,3], Chenchen Song[2], Eric J. McKimm[4], Milena M. Milosevic[4], Carmel L. Howe[1,3], Mark Neil[3,5], Simon R. Schultz[1,3], Srdjan D. Antic[4], Amanda J. Foust[1,3] and Thomas Knöpfel[2,3]***

[1] Department of Bioengineering, Imperial College London, London, United Kingdom, [2] Department of Medicine, Imperial College London, London, United Kingdom, [3] Centre for Neurotechnology, Imperial College London, London, United Kingdom, [4] Institute for Systems Genomics, Stem Cell Institute, UConn Health, Farmington, CT, United States, [5] Department of Physics, Imperial College London, London, United Kingdom

Voltage imaging of many neurons simultaneously at single-cell resolution is hampered by the difficulty of detecting small voltage signals from overlapping neuronal processes in neural tissue. Recent advances in genetically encoded voltage indicator (GEVI) imaging have shown single-cell resolution optical voltage recordings in intact tissue through imaging naturally sparse cell classes, sparse viral expression, soma restricted expression, advanced optical systems, or a combination of these. Widespread sparse and strong transgenic GEVI expression would enable straightforward optical access to a densely occurring cell type, such as cortical pyramidal cells. Here we demonstrate that a recently described sparse transgenic expression strategy can enable single-cell resolution voltage imaging of cortical pyramidal cells in intact brain tissue without restricting expression to the soma. We also quantify the functional crosstalk in brain tissue and discuss optimal imaging rates to inform future GEVI experimental design.

**Keywords: voltage imaging, cerebral cortex, sparse expression, optogenetics, transgenic**

***Edited by:***
*Josef Bischofberger,*
*Universität Basel, Switzerland*

***Reviewed by:***
*Leonardo Sacconi,*
*Università degli Studi di Firenze, Italy*
*Markus Rothermel,*
*RWTH Aachen Universität, Germany*

***Correspondence:**
*Thomas Knöpfel*
*tknopfel@knopfel-lab.net*

***Received:*** *30 November 2018*
***Accepted:*** *24 January 2019*
***Published:*** *14 February 2019*

***Citation:***
*Quicke P, Song C, McKimm EJ, Milosevic MM, Howe CL, Neil M, Schultz SR, Antic SD, Foust AJ and Knöpfel T (2019) Single-Neuron Level One-Photon Voltage Imaging With Sparsely Targeted Genetically Encoded Voltage Indicators. Front. Cell. Neurosci. 13:39. doi: 10.3389/fncel.2019.00039*

## INTRODUCTION

Over the last decade, functional fluorescence imaging has become a key technology in cellular and systems neurosciences (Knöpfel et al., 2006; Scanziani and Häusser, 2009; Knöpfel, 2012; Allen et al., 2017; Chen et al., 2017; Otis et al., 2017; Yang and Yuste, 2017). The most prominent applications include *in vivo* imaging of genetically encoded calcium indicators, such as GCaMPs (Nakai et al., 2001; Chen et al., 2013) that have enabled studies of large numbers of single cells longitudinally (Mank et al., 2008; Chen et al., 2012). Imaging of genetically encoded voltage indicators is less widespread despite being a longstanding goal driven by high expectations. The lag between the development of calcium imaging approaches and voltage imaging technologies is because the latter is more demanding due to several intrinsic constraints (Kulkarni and Miller, 2017). Firstly, in contrast to calcium indicators which are localized in the cytosol of the cells of interest, voltage indicators are localized to their plasma membranes, which account for a tiny fraction of their volume. This limits the number of indicator molecules that can be employed and hence the flux of signaling photons that can be generated. Secondly, voltage signals of interest are typically much faster than the signals provided by calcium indicators and therefore must be imaged at higher frame rates. This is not only an instrumentation challenge but also translates, along with the limited number of dye molecules, into a signal-to-noise ratio (SNR) challenge, as a sufficiently high SNR requires a large number of photons sampled per spatiotemporal bin (e.g., 10,000 photons are required in order for a fluorescence change of 1% to have an SNR of 1).

Optical voltage signals need to be imaged at a frame rate sufficient to resolve the signals of interest (e.g., action potentials or subthreshold fluctuations of membrane voltage). However, the appropriate GEVI imaging sampling rate further depends on the time course of the optical signal generated by the GEVI used. Due to the non-instantaneous kinetics of GEVIs the optical signal is generally low-pass filtered relative to fast voltage signals (i.e., action potentials). Imaging at rates higher than necessary degrades SNR by increasing the proportion of time spent on image readout relative to signal integration and increases accumulated read noise. Increasing frame rates without reducing the SNR also necessitates an increase in illumination intensities, which will increase the bleach rate and reduce the available imaging time. Imaging at frame rates above 100 Hz is also limited by image sensor technology and often requires using fast, low pixel-number charge coupled-device (CCD) cameras, or pixel sub-arrays from most modern sCMOS cameras.

When imaging with wide-field illumination, photons are integrated throughout virtually the whole frame period, and therefore fast fluorescent transients can be detected even if the imaging rate is below the nominal Nyquist rate of the optical signal. This is because the integration of detected photons over the frame period applies an effective low-pass filter to the collected fluorescence signal. This contrasts with laser scanning illumination techniques where photons are collected for each pixel for only a short fraction of the frame rate, and a frame rate above the Nyquist frequency must be used to ensure detection of fast transients. That is, a neuron's action potential may escape detection if it occurs between visits of the neuron by the laser spot in LSM. The choice of wide-field imaging speed appropriate to the indicator and experimental question is therefore important.

Improvement of SNR has been the driving force for much of the previous work on voltage imaging. Recently, new photostable low molecular weight voltage sensitive dyes and genetically encoded voltage indicators (GEVIs) have been developed (Gong et al., 2015; Sepehri Rad et al., 2017; Xu et al., 2017, 2018; Abdelfattah et al., 2018; Adam et al., 2018; Chavarha et al., 2018; Piatkevich et al., 2018; Yi et al., 2018). These have greatly increased sensitivity (fluorescence change with change in membrane voltage), considerably increasing achievable SNRs.

Another feature of voltage indicators adds a third issue that needs to be resolved: as a consequence of their plasma membrane localization, optical voltage signals from adjacent cells cannot be resolved without imaging at sub-micrometer resolution, which is largely impractical for functional fluorescence imaging across multiple neurons. Calcium signals, in contrast, are more easily resolved in intact brain tissue as "blinking" cell bodies that can readily be segregated. Hence, alongside low SNRs, allocation of optical voltage signals to individual cells in intact brain tissue is an inherent problem for voltage imaging.

Formally, the issue of single cell resolution can be described as follows: an optical signal from a cell of interest is compromised by shot noise generated by non-signaling fluorescence emanating from the membranes of other fluorescent cells and tissue autofluorescence (the "background"). The fractional change in collected fluorescence, ΔF/F, will be reduced to $\left(1-f_b\right)\Delta F/F$ where $f_b$ is the fraction of fluorescence arising from non-signaling structures. Background fluorescence also has a detrimental effect on SNR. In a shot noise limited imaging system, SNR will be reduced proportionally to the SNR measured in the absence of background fluorescence ($\mathrm{SNR}_0$) as $\sqrt{\left(1-f_b\right)}SNR_0$ (Knöpfel et al., 2006). Reducing the excitation volume in an attempt to minimize the contribution of fluorescent membranes of adjacent cells and their processes, for instance by using highly localized two-photon laser scanning (2PLS) excitation, reduces the amount of non-signaling fluorescence collected at the cost of very low rates of signal-carrying fluorescence excitation resulting in low SNRs. This makes 2PLS microscopy a poor choice for most voltage imaging applications, although it has been used successfully in some experimental paradigms (Ahrens et al., 2012; Akemann et al., 2013; Chamberland et al., 2017; Chavarha et al., 2018).

In voltage imaging applications aimed at single-cell resolution, instead of limiting fluorescence excitation to small volumes, a practical approach to maximize the contribution of a single cell to the fluorescence measured across an ROI is to limit the spatial overlap of fluorescence from different cells. Targeting a voltage indicator to single or multiple spatially segregated cells has been achieved by intracellular injection or electroporation of low molecular weight dyes (Antic, 2003; Roome and Kuhn, 2018). This approach, however, is limited to a single or a few cells in the microscopic field of view (FOV). Therefore, voltage imaging based on low molecular weight voltage indicators is practically limited to single dye-injected cells or, using unselective staining procedures, to population imaging without single-cell resolution (Grinvald et al., 2003; Antic et al., 2016). We reasoned that sparse labeling of neurons using genetic methods applicable to GEVIs could provide a practical intermediate experimental paradigm allowing multi-cell voltage imaging at single cell resolution (Song et al., 2017). Sparse labeling has the advantage of the single cell labeling approach of reducing or eliminating unwanted background fluorescence, whilst still labeling multiple cells in a FOV. Sparse labeling neurons will create opportunities for multi-cell, single cell resolution imaging aimed toward understanding signal processing in neuronal networks.

Single-cell resolution genetically encoded voltage indicator (GEVI) imaging requires not only sparse, but also strong expression to enable an adequate collected photon flux. Gene delivery via intracortical injection of viruses produces expression patterns where the expression strength and likelihood decreases with increasing distance from the injection site and virus titer. Sparse expression can therefore be achieved with modifications to injection protocols, albeit in a local and highly variable way and with low expression levels (on average <1 virus particle per cell and therefore often only 1 virus per expressing cell). Another strategy to limit the density of indicator expressing membranes is the targeting of a GEVI to specific compartments of the cell. Recent works showed that, indeed, soma targeting of GEVIs can reduce the number of labeled membranes and enable single-cell signals to be extracted from sequences of images (Abdelfattah et al., 2018; Adam et al., 2018). Voltage imaging of naturally sparse cell populations, such as cortical interneurons, at single cell resolution is achievable with standard transgenic mouse lines (Bayguinov et al., 2017). Dual component expression strategies based on Cre-lox (Sauer and Henderson, 1988) and tetracycline response elements (TRE) (Gossen and Bujard, 1992) are especially useful for GEVI imaging experiments aimed at cortical circuit analyses, as these expression strategies label all cells of a genetic class with high expression levels (Madisen et al., 2015). In the case of non-sparse cell classes, in particular cortical pyramidal cells, sparse stochastic targeting can be achieved by controlling activation of a strong expression cassette via the titratable activity of destabilized Cre (Sando et al., 2013; Song et al., 2017). We previously demonstrated this strategy at the morphological level and demonstrated sparse but strong ("Golgi-staining like") expression from a GEVI in a transgenic mouse line (Song et al., 2017). Here we validate this approach for functional voltage imaging which requires higher expression levels than simple anatomical imaging. We show that d-Cre based stochastic expression strategies enables single-cell resolution GEVI imaging in cortical pyramidal cells in acute mouse brain slices. We compare recordings from tissue of mice sparsely expressing in cortical pyramidal cells ("sparse PC line") with recordings from mice which express the GEVI in all pyramidal cells ("pan PC line") using wide-field imaging (**Figure 1A**). We evaluate the achievable SNR, discuss optimal GEVI imaging frame rates and also quantify the functional spread of signals to guide experimenters' choice of the sparsity level. We used early generation GEVIs [VSFP Butterfly 1.2 (Akemann et al., 2012) and chimeric VSFP Butterfly YR (Mishina et al., 2014)] for which transgenic mice suitable for a fully genetic approach were readily available. Our principal conclusions should hold true, and quantifications could be extrapolated, for all recently developed GEVIs covering a spectrum of voltage sensitivities, temporal dynamics, and brightness.

# MATERIALS AND METHODS

## Animals

This study was carried out in accordance with the recommendations of UK Animals (Scientific Procedures) Act 1986 under Home Office Project and Personal Licenses (project licenses 70/7818 and 70/9095). The protocol was approved by the UK Home Office. Transgenic mice were bred to express VSFP Butterfly 1.2 in cortical layer 2/3 pyramidal neurons under the intersectional control of TetO and Cre-recombinase [**Figure 2B**, "sparse PC line," Rasgrf2-dCre; CaMK2A-tTA; Ai78 (Mayford et al., 1996; Harris et al., 2014; Madisen et al., 2015)]. To induce sparse expression through stochastic re-stabilization of destabilized Cre, a titrated total dose of 2E-4 mg/kg Trimethoprim (TMP, Sigma) was given via multiple intra-peritoneal injections over 2 consecutive days as described in Song et al. (2017). For comparison, transgenic mice densely expressing chimeric VSFP-Butterfly in all pyramidal cells were used ["pan PC line," CaMK2A-tTA; tetO-chiVSFP (Song et al., 2018)].

## Slice Preparation

Slices from transgenic mice were prepared at least 2 weeks post TMP injection. 400 μm coronal slices were cut using a Campden Microtome 7000 from 4 mice between 50 and 108 days old in ice cold ACSF oxygenated with 95% $O_2$/5% $CO_2$ containing (in mM): 125 NaCl, 25 $NaHCO_3$, 20 glucose, 2.5 KCl, 1.25 $NaH_2PO_4$, 2 $MgCl_2$, 2 $CaCl_2$. The slices were immediately transferred into NMDG-ACSF (Ting et al., 2014) containing: (in mM) 110 N-Methyl-D glucamine, 2.5 KCl, 1.2 $NaH_2PO_4$, 25 $NaHCO_3$, 25 Glucose, 10 $MgCl_2$, 0.5 $CaCl_2$, adjusted to 300–310 mOsm/kg, pH 7.3–7.4 with HCl, oxygenated with 95% $O_2$/5% $CO_2$ at 36°C for $<12$ min before they were transferred back into the original sodium-containing ACSF for at least an hour rest before imaging.

## Imaging

Healthy fluorescent cells were identified using gradient contrast IR and fluorescence optics. Patch pipettes were pulled to a resistance between 3 and 10 MΩ when filled with the following intracellular solution (in mM): 130 K-Gluconate, 7 KCl, 4 ATP—Mg, 0.3 GTP—Na, 10 Phosphocreatine—Na, 10 HEPES. Cells were patched using a Multiclamp 700B amplifier and signals were digitized using a Power 1401 digitizer. Current pulses were injected to elicit action potentials and fluorescence was imaged at 50−100 Hz using a custom-built epifluorescence microscope (optical path shown in **Figure 1A**).

We excited donor fluorescence of the VSFP FRET fluorescent protein pair with a 490 nm LED (M490L4, Thorlabs) powered by a current driver (Keithley Sourcemeter 1401), collimated with an $f = 16$ mm aspheric lens (ACL25416U0-A, Thorlabs) and filtered with a 475/28 nm excitation filter (FITC-EX01-CLIN-25, Semrock). Intensity at the sample was between 4 and 30 $mW/mm^2$. Fluorescence was collected using a 495 nm long pass dichroic (FF495-Di03, Semrock) along with a 550/88 nm collection filter (FF01-550/88, Semrock), 496 long pass filter (Semrock FF01-496/LP) and IR blocking filter (Semrock, FF01-750/SP) onto a sCMOS camera (512 × 512 pixels with 4 × 4 binning, Orca Flash 4 V2, Hamamatsu). This collected fluorescence from the FRET pair donor fluorophore (mCitrine), meaning membrane depolarizations resulted in decreased fluorescence emission as FRET efficiency increased. Imaging data were acquired using Micromanager (Edelstein et al., 2014). Images recorded at room temperature.

For 500 Hz voltage imaging, a water immersion LUMPlanFl 40× objective with NA 0.8 (Olympus, Japan) was used. Fluorescence was excited with CoolLED, UK, 473 nm. Optical filters were purchased from Chroma Technology (Rockingham, VT, USA). The filter cube contained an exciter 480/40, dichroic 510DRLP, and emitter 535/50 nm. Voltage signals were sampled at 500 Hz with a NeuroCCD camera (80 × 80 pixel configuration) (RedShirtImaging, Decatur, GA). Analysis of optical data, including spatial averaging, high-pass and low-pass filtering, was

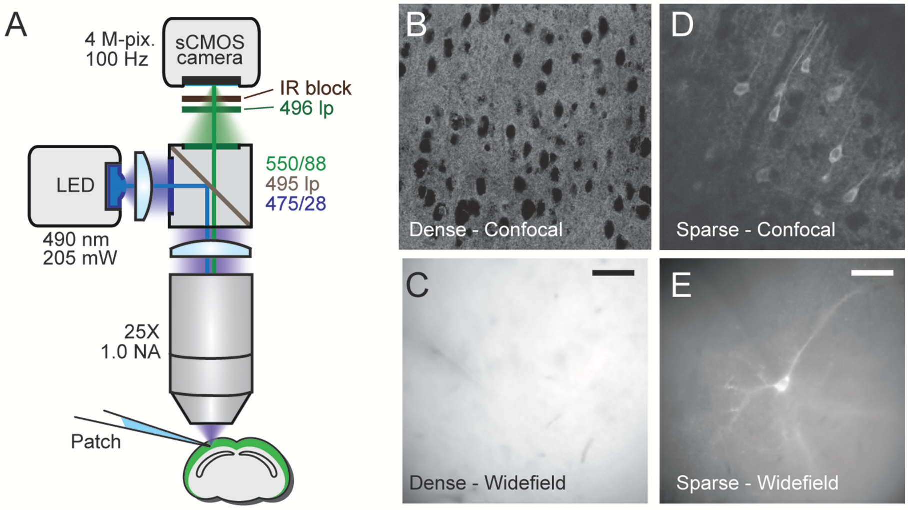

**FIGURE 1 |** Comparison of densely and sparsely expressed GEVIs. **(A)** The microscope set up for wide-field imaging. We used a standard epifluorescence microscope configuration to image patched cells expressing GEVIs in sparsely and densely expressing brain slices. **(B)** A confocal image of a brain slice densely expressing chimeric VSFP-butterfly. Assignment of fluorescence to individual neurons is impossible due to expression in overlapping membranes. **(C)** A wide-field image of a brain slice with the same expression strategy. The problem of assignment is compounded by the lack of optical sectioning, making even cell bodies difficult to discern. **(D)** A confocal image of a brain slice sparsely expressing VSFP butterfly via destabilized-Cre modulated expression. Processes and soma from individual GEVI-expressing cells can be clearly resolved. **(E)** Wide-field image of a brain slice with the same expression strategy. Contrast is decreased due to lack of optical sectioning, but single cells and processes can still be resolved. Scale bar 40 $\mu$m.

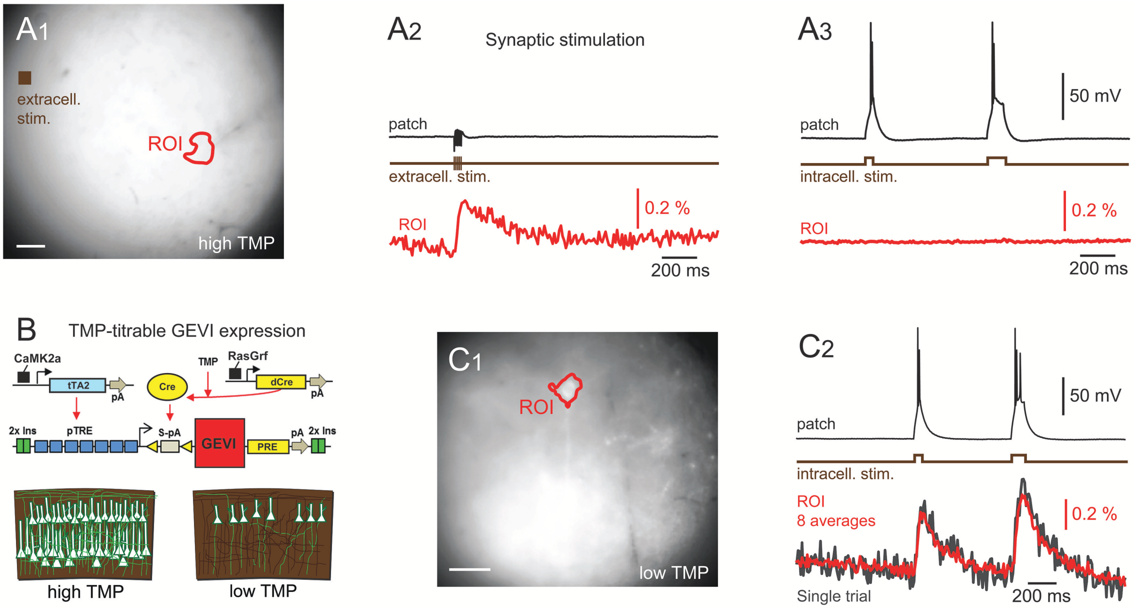

**FIGURE 2 |** d-Cre modulated sparse expression strategies enable single-cell resolution functional imaging. **(A)** Population, but not single-cell, voltage signals are resolved with densely expressed GEVIs. **($A_1$)** A wide-field image showing the patched cell's location and the ROI used to generate the voltage imaging trace. An extracellular stimulation electrode was located as indicated. **($A_2$)** A train of extracellular stimulation evoked responses from many cells, leading to a clear population voltage response in the cellular ROI. **($A_3$)** No single cell voltage signal could be resolved despite averaging of 80 repeated trials of extracellular stimulation. **(B)** The expression strategy used to generate sparse expression in layer 2/3 pyramidal cells. TMP stabilizes destabilized Cre recombinase enabling TRE driven GEVI expression. **($C_1$)** A wide-field image of sparsely expressed GEVI showing the ROI used to calculate the voltage time course. **($C_2$)** Single-cell voltage transients can be clearly resolved with sparse expression. Red time course shows an average of eight repeats, gray shows single trial response. Fluorescence traces shown on inverted *y* axes.

conducted with Neuroplex v. 8.0.0 (RedShirtImaging). Images were recorded at 34 C.

## Image Analysis

Imaging trials were repeated between 5 and 20 times and the individual trial image sequences averaged. Linear fits, $f_i$, were calculated for each pixel, $p_i$, to control for bleaching and the $\Delta F/F_0$ time course was calculated as $(p_i[n] - f_i[n])/(f_i[n] - 1,600)$, where 1,600 is the camera offset for 4 × 4 binning and n is the frame number. Only averaged traces were analyzed and all traces plotted are averages unless explicitly noted. Number of averages for traces are noted in captions. We plot all fluorescence traces on inverted y axes.

Image analysis was conducted with Python. Activation maps were found by considering $\Delta F$ image sequences calculated pixel-wise as $(p_i[n] - f_i[n])$. The image time series was downsampled to 50 Hz by averaging to improve the SNR. To create maps for visualization and segmentation the image sequences were spatiotemporally filtered with a Gaussian filter with sigma of 1 time point/1 pixel 20 ms/1.04 $\mu$m and for functional spread characterization they were temporally filtered with a 3 point median filter. 2D activation maps were then found from 3D image sequences by summing the frames collected during stimulation periods.

ROIs for time series analysis were found by segmenting the activity maps. Each map was thresholded using an automatic criterion (Yen et al., 1995), before a single round of binary closing and then dilation. The largest connected component was then selected as the somatic ROI.

For trials where a long depolarizing stimulus was used the signal size was calculated as the 5th percentile value of the fluorescence time course during the stimulus period with the median value of the previous 10 time points subtracted. For single spike trials the signal size of the first spike in a spike train was calculated differently to the others due to the easier estimation of the fluorescence value immediately preceding. The first spike signal size was calculated as the maximum value in the 50 ms after the stimulus (the stimulus period) with the median value of the preceding 10 time points subtracted. For subsequent spikes in the spike train the signal size was calculated as the minimum of the 50 ms following the stimulus with the maximum of the 20 ms time points before the stimulus subtracted. The noise level of traces was calculated as the standard deviation of 20 samples before the stimulus was applied.

### Frame Rate Analysis

To examine the effect of decreased sampling rate on GEVI traces we took an example $\Delta F/F_0$ trace acquired at 500 Hz and downsampled it by averaging. To avoid overestimating the noise level for larger averaging periods we first flattened the trace to remove bleaching remnants by dividing it by a polynomial fit to the trace with the voltage signals removed. We then calculated $n$ downsampled traces for downsampling by integer factors of 1, 2, 3, 4, 5, 10, and 20, where each of the $n$ traces corresponds to a different downsampling phase. We calculated the noise level as the standard deviation of $100/n$ points with no voltage signal and the signal level as the peak value during the stimulus period subtracted by the median value of the $20/n$ preceding points. AP timing detection jitter was calculated as the imaging frame period multiplied by the range in frame number of the location of the optical AP signal peak. Least-squares log-log-linear fits were then calculated for the noise and 1-signal size.

### Signal Spread Analysis

We estimated the sparsity level required to separate signals between adjacent cells using the mean autocorrelation of the activation maps. Autocorrelations of spatially unfiltered maps were calculated and a 1-pixel central peak arising from noise in the image was removed by replacing the central pixel with the mean of the surrounding pixels. The autocorrelation images were then normalized to between 0 and 1, rotated such that their longest axis faced the same direction before taking an average over all cells. This generated a roughly elliptical autocorrelation image with orthogonal axes representing our estimate of the largest and smallest signal mixing lengths. We calculated the amplitude of the crosstalk for a neuron at the origin due to other neurons at positions $\boldsymbol{r}_i$ to be equal to $1 - \sqrt{\frac{P}{P_T}} \sim 1 - \sqrt{1/(1 + 2\sum_i ACF(\mathbf{r}_i))}$ (see **Supplementary Methods**). We can therefore use the longest and shortest axis of our measured ACF to estimate the best and worst-case mixing fraction, respectively.

# RESULTS

## Voltage Imaging With Densely and Sparsely Targeted GEVIs

As explained in the introduction, it is difficult to optically resolve fluorescent plasma membranes if a GEVI is targeted to all cells in a dense population of neurons, such as cortical pyramidal cells. To illustrate this, **Figure 1** shows a comparison of images obtained from two transgenic mouse models using confocal and wide-field microscopy (**Figure 1A**). In the first mouse line, the GEVI is targeted to all cortical pyramidal cells ("pan PC line," see Methods). In the second line of mice, the GEVI is targeted to a small subset of (mainly) layer 2/3 pyramidal cells ["sparse PC line" (Harris et al., 2014)]. In the case of the non-sparsely targeted tissue (pan PC), confocal microscopy resolves individual cells bodies by negative contrast of their non-fluorescent cytosol (**Figure 1B**). Plasma membranes of adjacent cells cannot be differentiated and the bulk of fluorescence emerges from neuronal processes (dendrites and axons) that are not structurally resolved (**Figure 1B**). Wide-field microscopy of this tissue (pan PC) reveals a sea of fluorescence with virtually no cellular structural details (**Figure 1C**). In contrast, images of cortical tissue from the sparse PC line resolve the plasma membranes of cell bodies and processes both in confocal (**Figure 1D**) and in wide-field microscopy (**Figure 1E**).

To demonstrate that optical voltage signals can readily be recorded in slices from pan PC mice using wide-field imaging, we employed synaptic activation of a large number of optically unresolved neurons (**Figure 2A$_1$**). Optical voltage signals were resolved in single trials over a cell body sized region of interest (ROI) in response to extracellular electrical stimulation (5, 0.5 ms pulses at 100 Hz, electrode ∼360 μm from cell body, **Figure 2A$_2$**). This experiment demonstrates that population voltage signals can be recorded across "cell body sized" ROIs in the brain slices of pan PC mice. We then tested whether the optical signal of a single cell can be resolved in the same preparation using wide-field imaging. To this end we patched a layer 2/3 cortical pyramidal cell in current clamp mode. Imaging during intracellular injection of positive current pulses (two pulses of 50 and 100 ms duration, current amplitude adjusted to induce spiking) did not reveal an optical signal across the cellular ROI despite a noise floor of only 0.004% $\Delta F/F_0$ after averaging the images from up to 80 trials (**Figure 2A$_3$**). This suggests that single cell-level optical voltage signals are masked by the large shot noise produced by the non-signaling fluorescence of neighboring cells.

To verify this prediction, we switched to tissue from the sparse PC line (**Figure 2B**), where single cells can be resolved even with wide-field epi-illumination fluorescence microscopy (**Figure 2C$_1$**). As with the above experiments using pan PC tissue, we patched a single fluorescent cell and imaged while the cell was depolarized by direct current injection through the patch electrode, readily resolving optical voltage signals at the single cell level (**Figure 2C$_2$**).

In response to long lasting depolarizing current injections (50–500 ms, adjusted to induce one or more APs), we resolved voltage signals in single trials ($n = 12$ out of 15 cells attempted). In response to short single spike-triggering current pulses (0.5 ms current injections to induce spiking at 20 Hz), we observed signals ($n = 4$ cells out of 4 cells attempted), with 2 cells with a signal-to-noise ratio consistent with spike detection without trial averaging (see below). Overall, we resolved single cell voltage signals in 13 patched cells in 13 slices at imaging depths of up to 77 μm.

Interestingly, maps of GEVI responses (ΔF images, see Methods) reveal cellular structures that are not always readily apparent in raw wide-field images. Maps of GEVI responses allow identification of processes belonging to active cells (**Figure 3**). We calculated response maps (**Figures 3B,D**) from our ΔF image series by averaging 7–30 frames during stimulus periods, depending on the stimulus length. As the GEVI fluorescence decreases on membrane depolarization, pixels containing signal have a negative value in response to the stimulus whilst pixels containing only noise average to zero (see Methods section). The response maps clearly reflect the anatomy of the patched cells; dendrites and their branches can also be seen when they lie in the plane of focus. 6/13 cells were imaged with one or more other cells in the FOV and in these cases the active cell can be clearly distinguished in the activity map from the adjacent GEVI-labeled cells (**Figure 3**, see also below, **Figure 6**). We used these activity maps to automatically segment the cell soma from the image sequences by thresholding the activity maps. We then calculated the cell's fluorescence time course as the mean time course of the pixels within the segmented region (**Figures 3E,F**).

## Signal-To-Noise Ratio

Comparing experimentally assessed SNR values between different imaging systems and preparations is complicated by differing fluorescence collection efficiencies, illumination conditions, and GEVI expression levels. Optical signals collected with high quality sCMOS cameras operating in a high photon count regime [>>10 photons per pixel per frame (Li et al., 2016)] are shot noise limited. With our measured baseline noise levels <1%, we clearly image in this regime. This means that we can write the SNR as $SNR \propto \frac{\Delta F}{F}\sqrt{n}$, where ΔF/F is the fractional change in fluorescence, or GEVI sensitivity, and n is the number of collected fluorescence photons. Increasing the illumination intensity increases the number of photons collected, increasing SNR, but in doing so increases the rate of bleaching of the sample, thus reducing the available imaging time. This makes fair GEVI evaluation and selection difficult as data from disparate labs must be collated and compared. A practical way to increase comparability of data from different systems, is to take the rate of photobleaching into account. Bleach rates can be used to normalize across different illumination intensities and facilitate comparison across different GEVIs with different photostabilities. The bleach rate, dC/dt, is proportional to $-I_{ex}\Phi_B C$ , where $I_{ex}$ is the illumination intensity, $\Phi_B$ the bleaching quantum yield, and C the concentration of unbleached GEVIs. Ideally the quantum yield of bleaching would be measured for each GEVI as it would allow independent comparison of expression density; however, this is not known for the GEVI used in this study or, to our knowledge, any other GEVI. Normalizing the SNR to the bleach rate, however, can help to control for the GEVIs bleaching propensity and concentration along with the illumination level in one step with an easily calculable number.

To this end, we estimated the signal size, the bleaching rate and the SNR of the optical signals across a segmented ROI. The median bleach rate over the cellular ROIs was 0.52%/s and the 90th and 10th percentiles were 0.98 and 0.23%/s (calculated using a linear fit of baseline fluorescence). We calculated the signal and noise levels for 9/15 cells for which we collected data at 100 Hz with comparable stimulus regimes, and used image sequences of the average of four trials for each cell in the analysis. **Table 1** summarizes the signal, noise, SNR and bleach corrected SNR values measured for long depolarizing stimuli (100 ms pulse duration, **Figure 3E**) and AP inducing stimuli (**Figure 3F**). The values are reported as median [10th percentile, 90th percentile]. We plot the individual measured values in **Figure 4**.

These SNR values come from an early generation GEVI with low sensitivity. As SNR increases linearly with indicator sensitivity, our values and conclusions can easily be scaled for more recent GEVIs with much higher reported sensitivity under similar experimental conditions.

## Effect of Sampling Rate

As discussed in the introduction, due to the integration of photons during the whole frame period, slow camera frame rates may be compatible with GEVI-based AP detection, especially for experiments that can tolerate low precision of AP onset timing. To investigate these predictions, we imaged at 500 Hz using a fast, low resolution (80 × 80 pixel) CCD camera (**Figure 5A**, images). Three brief current pulses (pulse duration = 2 ms, pulse interval = 100 ms) were delivered via a patch pipette to drive a triplet of action potentials (**Figure 5A**, whole-cell). We examined

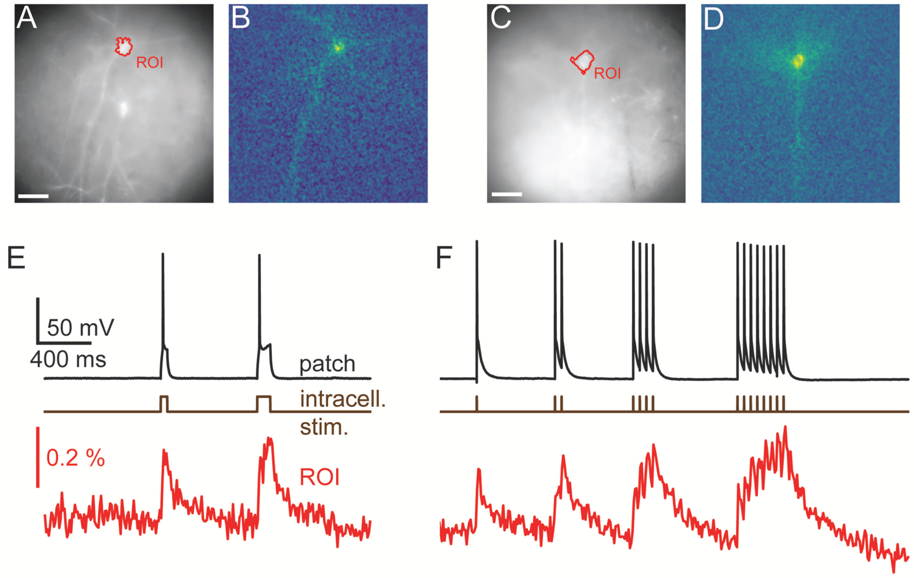

**FIGURE 3 |** Imaging reveals dendritic structure. Wide-field **(A,C)** and activity maps **(B,D)** of two cortical pyramidal cells. Activity maps were generated by calculating the integral over stimulated video frames and pick out an individual cells dendritic structure, including basal and apical dendrites, from adjacent cells. **(E,F)** the average time courses from the videos used to calculate the activity maps. Optical traces are averages of 12 **(E)** and 10 **(F)** repeats, scale bars 40 μm. Fluorescence traces shown on inverted y axes.

**TABLE 1 |** Signal, Noise, and SNR values.

| Stimulus type | Signal size (%) | Noise level (%) | SNR | Bleach corrected SNR | Number of cells |
|---|---|---|---|---|---|
| 100 ms depolarization | 0.59 [0.33, 0.82] | 0.07 [0.03, 0.13] | 10.0 [3.5, 23.9] | 11.8 [3.6, 42.4] | 9 |
| Action potential | 0.14 [0.04, 0.28] | 0.04 [0.02, 0.07] | 3.1 [1.8, 4.8] | 13.5 [7.1, 21.0] | 4 |

the peak SNR of AP related signals for a voltage imaging trace imaged at 500 Hz and integer downsamples by $n$ of the $n$-point moving average. A fluorescent time course containing 3 AP-evoked fluorescence transients was downsampled by averaging to frequencies as low as 25 Hz (**Figure 5B**) and the signal and noise were measured (**Figures 5C,D**). The noise and signal varied with the relative phase of the downsampling. The mean downsampled noise level was well fit by a power law model of the form $A_2x^{b2}$ (log-log linear $r^2 = 0.999$), with $b_2 = 0.45 \approx 0.5$ as predicted by theory (Gans and Gill, 1983). The mean downsampled peak signal was also well fit by a power law fit of $1 - A_1x^{b1}$ ($r^2 = 0.995$), with $b_1 = -0.13$. Combining these and plotting again the SNR gave a predicted ideal imaging speed for spike detection of 99 Hz (**Figure 5E**). We note, however, that the ideal imaging speed may be much higher if precise information about AP shape or spike timing (see spike jitter as a function of imaging rate, **Figure 5F**) is desired and a hypothetical GEVI with very fast kinetics is used.

We validated this analysis by modeling the GEVI signal as a series of decaying exponentials. We calculated the fraction of aliased power compared to total sampled power as a function of sampling frequency when sampling by integrating through the sampling period. We found that severe aliasing occurs when the sampling period used is more than approximately half the decay constant of the optical signal. The signal in **Figure 5A** was well fit with an exponential decay with a time constant of 12.0 ms. This predicts a frame rate of around 167 Hz is sufficient to avoid significant aliasing. The optical signals recorded at 100 Hz are slower, as they were recorded at room temperature, as opposed to 34 C for the 500 Hz traces. For these, 100 Hz imaging is sufficiently high to prevent significant aliasing.

## Signal Spread

In order to guide future levels of sparsity we developed a method to estimate the level of signal mixing between cells as a function of distance. Neurons are highly variable in shape and, in the cortex, their extent varies with the orientation of the imaging focal plane relative to the cortical column. **Figure 6A** shows an example ROI containing a patched, stimulated cell adjacent to unpatched cells. The fluorescent voltage response in **Figure 6B** shows a clear transient in the time course over the patched cell. Fluorescent time courses from ROIs over adjacent unpatched cells show a small amount of crosstalk, disappearing for more distant cells. This indicates that time courses from adjacent cells can be discriminated, albeit with some signal mixing depending on distance.

In order to quantify the expected level of this signal mixing we considered how the time course of one neuron of interest would

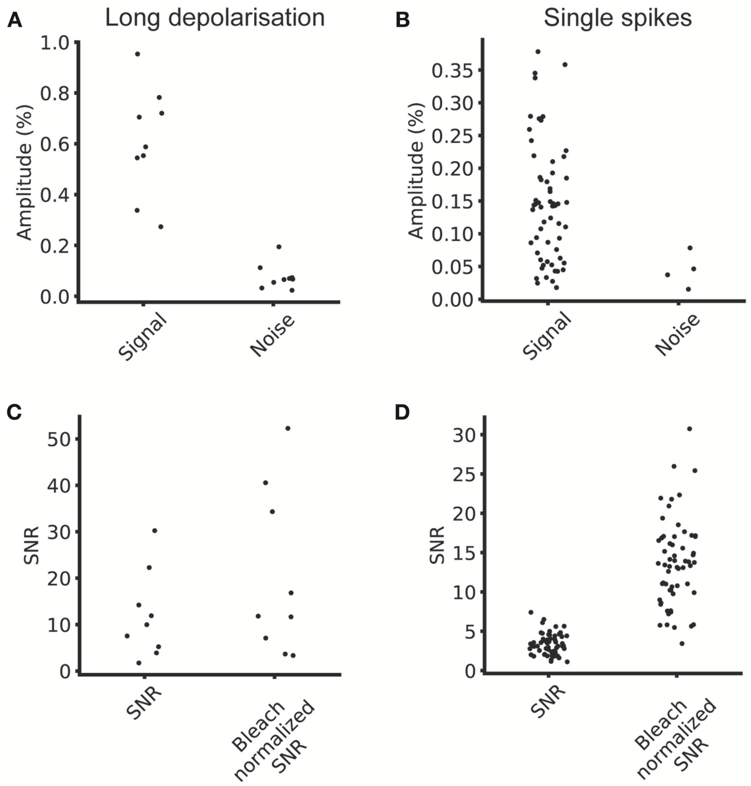

**FIGURE 4 |** Signal and noise levels. **(A)** Average signal and noise amplitudes for individual cells for five repeats at 100 Hz. **(B)** Single spike signal amplitude and noise amplitude for five repeats at 100 Hz. **(C)** SNR and bleach corrected SNR for long depolarizing stimulus. **(D)** SNR and bleach normalized SNR for single spike stimulus.

be affected by being surrounded by $i$ other neurons separated by distances, $r_i$, of the same shape and with similar fluorescent time courses. We wanted to quantify crosstalk, that is the signal amplitude (square root of the signal power, P, $\sqrt{P} = \sqrt{\int s^2 dt}$), arising from adjacent neurons when averaging signal from a ROI over a target neuron as a fraction of the total signal. This crosstalk was calculated (see **Supplementary Methods**) to be given by $1 - \sqrt{\frac{P}{P_T}} \sim 1 - \sqrt{1/(1+2\sum_i ACF(\mathbf{r}_i))}$, where ACF(r) is the spatial autocorrelation function of the neurons' activity ($\Delta$F) map, such as in **Figures 3B,D**, **6C**, evaluated at distance r. P and $P_T$ correspond to the signal power from the target neuron and total measure power, respectively. We calculated autocorrelations from the activation maps of signal-containing pixels (**Figure 6C**), which allowed us to simply average different cells together. We averaged all the autocorrelations together after aligning their longest axes to average out cell-structure specific features caused by different dendritic shapes (**Figure 6E**). To quantify the amount of crosstalk expected in sparse imaging we first calculated the width for each cell where the autocorrelation fell to 50% of its central value (**Figure 6F**). This 50% cutoff represents the distance at which the crosstalk it contributes to an adjacent neuron would be 50% of the signal power or 25% of signal amplitude (where signal amplitude is the square root of the signal power). The 50% cut-offs of the neurons recorded ranged from 15 to 135 μm. The large range in the values can be attributed to differences in imaging depth and dendritic structure. We plot the mean falloff in the autocorrelation in **Figure 6G**. Using this, we calculated the crosstalk for two cells separated by 100 μm the proportion of the total signal amplitude accounted for by the cell of interest when trying to image a single cell as between 20 and 22%. For cells on a hexagonal grid of side length 100 μm the crosstalk was found to be 52–55%.

## DISCUSSION

We have shown that destabilized Cre recombinase (dCre) based expression strategies enable single-cell resolution voltage imaging of cortical pyramidal cells in acute brain slices. This expands the current repertoire of single-cell voltage imaging from interneurons and other naturally sparse cell classes to non-sparse layer 2/3 cortical pyramidal cells. We have not verified this approach with other cell classes, although we expect no differences in the strategy relevant to functional imaging. This powerful approach allows the sparsity of expression to be varied by the titration of the dosage of TMP which stabilizes the dCre and, in combination with strong transgene inducers systems, such as tetO, enables sparse but strong GEVI expression. Different levels of sparsity allow the experimenter to trade off the level of population sampling and functional crosstalk between cellular voltage traces. The level of sparsity can also be adapted to the imaging approach used, with increased specificity

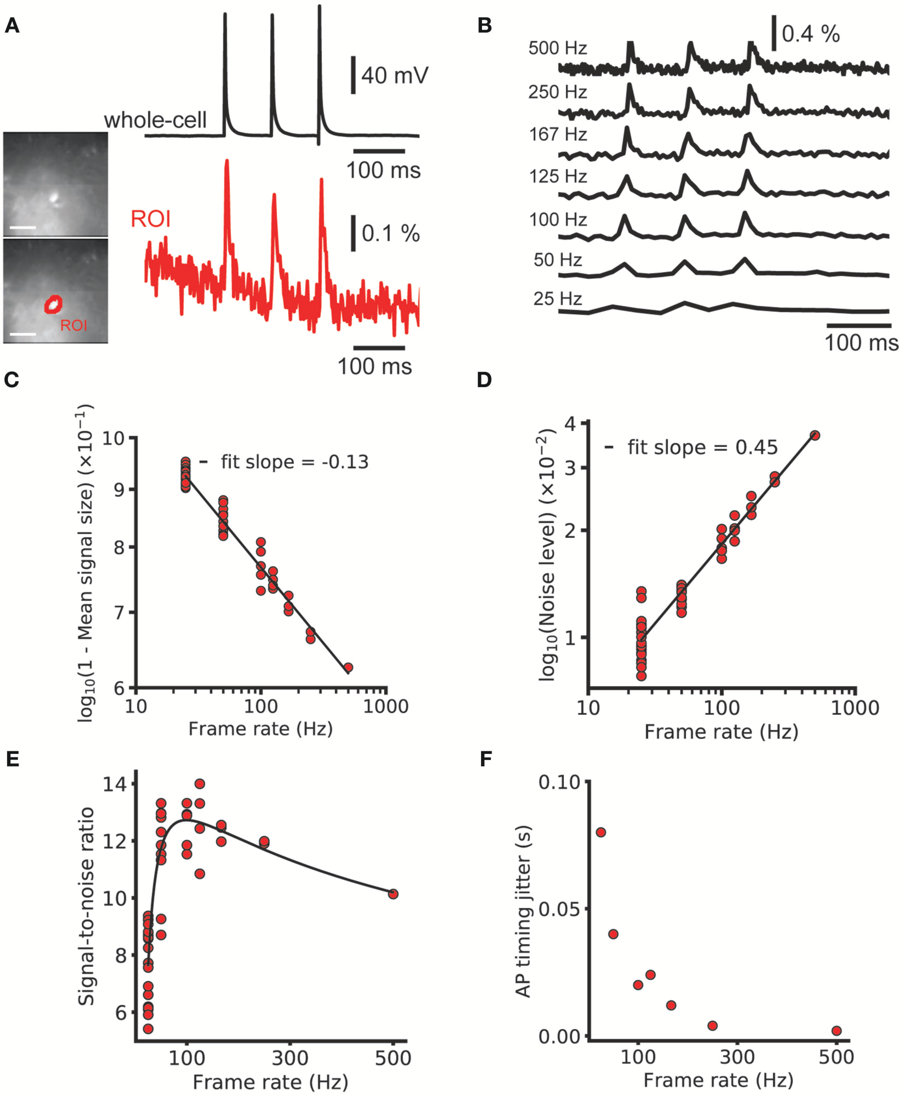

**FIGURE 5 |** Effect of frame rate on SNR and spike timing estimation. Decreasing the imaging rate in wide-field imaging reduces the temporal accuracy and AP shape information but increases the SNR. **(A)** Image of a brain slice from sparse GEVI mouse obtained at 500 Hz frame rate (80 × 80 pixels). Simultaneous electrical recording from cell body (black) and optical recording (red). Average of nine trials. **(B)** A 500 Hz ΔF/F trace with 3 single-spike transients and down samples by averaging. Signal size, noise level and AP timing estimation accuracy all decrease with mean downsampling. **(C,D)** Power law fits to 1 − signal size and the noise level. The noise level scales approximately with the square as expected from Poisson statistics. **(E)** The signal to noise ratio and power law fits plotted on linear axes. Fits give an optimal frame rate for spike detection SNR of 99 Hz. Note that this curve is the result of the division of the log-log linear fits in **(C,D)** and not a fit to the plotted points. **(F)** The bounds on spike timing estimation for different frame rates. Fluorescence traces shown on inverted y axes.

from, for example, holographic imaging allowing denser cellular expression (Foust et al., 2015).

Although in this specific implementation, signal averaging was often needed in order to resolve single-AP voltage transients, an issue common to many voltage imaging applications due to low sensitivity of earlier generation GEVIs, such as those used here. However, this genetic approach is, at least conceptually, not restricted to particular GEVIs, and could be used with any of the more sensitive GEVIs that have been recently reported (Abdelfattah et al., 2018; Adam et al., 2018; Piatkevich et al., 2018; Yi et al., 2018). We anticipate that these new GEVIs, combined with the sparse transgenic strategy used in the current study, will yield better single trial spike detection performance.

As wide-field single photon excitation was used, the imaging depth was limited by the scattering of both excitation and emission light. We were able to record from cells at depths up to 77 μm in slice, although at these depths there was severe broadening of the functional signal due to scattering. This scattering will limit wide-field *in vivo* imaging in mice to superficial cortical layers. Two-photon excitation would improve this performance, however, this would require optimizing both the GEVI for two-photon excitation, and also using improved

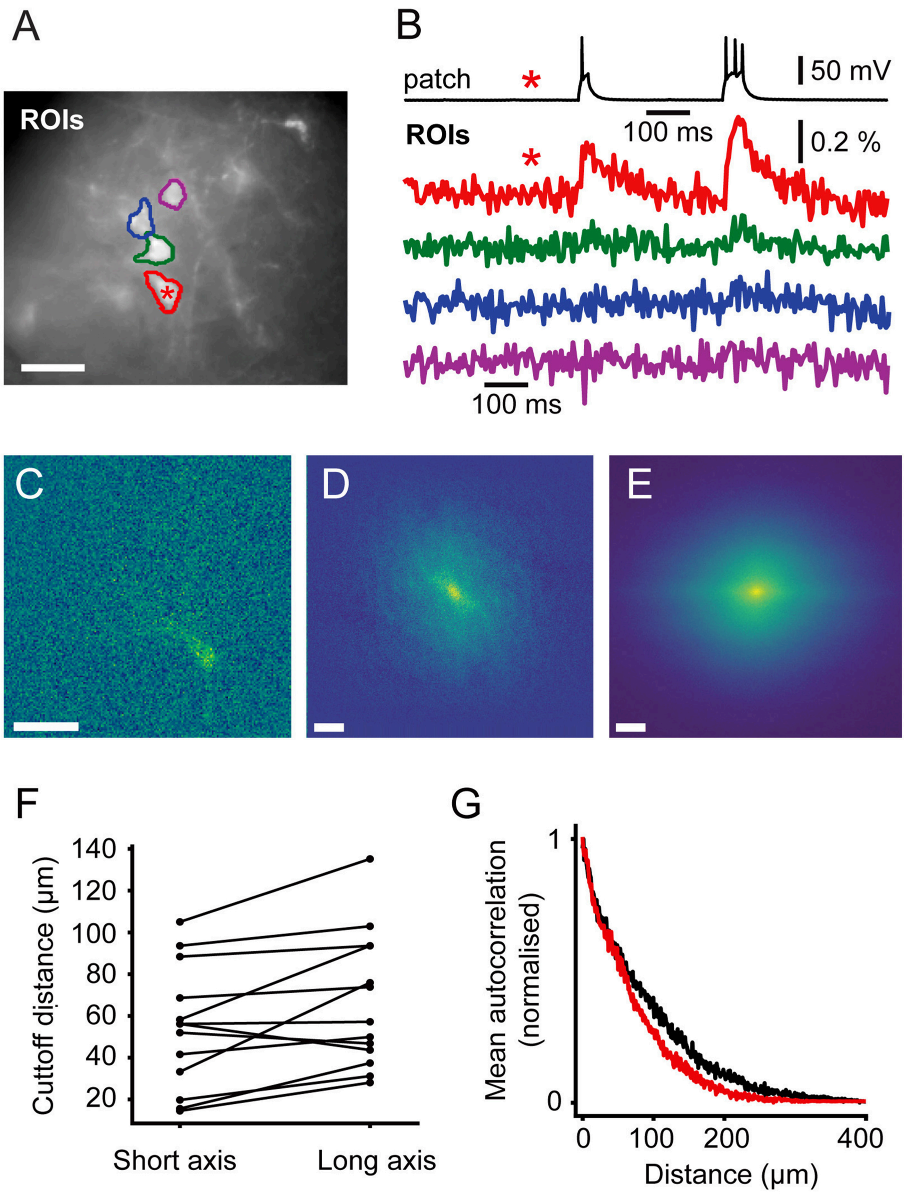

**FIGURE 6 |** Signal Spread. Autocorrelation of activity maps can be used to estimate crosstalk. **(A)** Wide-field image of a patched neuron (red roi) with other neurons in the FOV. **(B)** Electrophysiological and fluorescent trace from the patched active cell (red and black) and fluorescent traces from ROIs over adjacent cells (green, blue and magenta). A small amount of crosstalk can be seen in the time courses of the adjacent cells. **(C)** A spatially unfiltered activity map of the same neuron calculated by measuring the sum over frames during the depolarizing stimulus. **(D)** The 2D spatial autocorrelation of the activity map. This represents the fraction of signal power arising from the patched neuron at different separations. **(E)** The mean of rotationally aligned autocorrelations of all measured cells. **(F)** The length of the long and short 50% cut-offs for all cells. **(G)** The profile of the mean autocorrelation for the long (black) and short (red) axes. Scale bars 40 µm.

imaging methods to increase traditional two-photon imaging's meager photon budget (Cheng et al., 2011; Prevedel et al., 2016; Chavarha et al., 2018; Quicke et al., 2018; Schuck et al., 2018). Contributing to the difficulties of two-photon voltage imaging, as each pixel is sampled for only a short fraction of the frame rate, full Nyquist-rate sampling of the indicator kinetics must be used to avoid aliasing of high frequency voltage transients.

Soma targeting of voltage indicators, as seen in recent GEVI studies (Abdelfattah et al., 2018; Adam et al., 2018) is likely to greatly reduce the mixing of functional signals by restricting the possible spatial sources of contaminating signal. This comes at the cost, however, of eliminating the ability to reveal somato-dendritic physiology. In multi-site voltage imaging experiments, successful soma targeting will eliminate important clues about input signals generated by dendritic neuropil.

We analyzed how far functional signals from fully labeled (not soma-targeted) active cells spread in order to guide future experimental designs. To choose a specific sparsity level, however, experimenters must also consider other factors, such as the characteristics of the membrane dynamics of the studied cell class, as well as the specific experimental question. More crosstalk can be tolerated, and therefore more dense cells studied, if factors, such as AP amplitude can be used to discriminate between signals from different cells and subthreshold fluctuations are less important.

Sparse transgenic approaches could also be beneficial to opsin photostimulation approaches. Light shaping methods using computer generated holography (Papagiakoumou et al., 2008; Pégard et al., 2017) or generalized phase contrast (Papagiakoumou et al., 2010) can benefit from sparsely expressed opsins to better confine excitation to a single cell or subsets of cells. Previous studies have already used soma-restricted expression (Shemesh et al., 2017) or exploited naturally sparse cell classes (Papagiakoumou et al., 2013; Ronzitti et al., 2017) to improve single-cell targeting with optogenetic actuation. Sparse expression strategies as used here could also help with excitation confinement whilst enabling holographic dendritic stimulation of individual cells (Yang et al., 2011).

## DATA AVAILABILITY STATEMENT

The datasets generated for this study are available on request to the corresponding author.

## AUTHOR CONTRIBUTIONS

PQ, CS, SA, AF, and TK conceived and designed the experiments. PQ, CS, EM, MM, and CH performed experiments. PQ, SA, MN, SS, AF, and TK designed the analysis. PQ, SA, and TK analyzed the data and wrote the paper. All authors contributed to manuscript revision and approved the final manuscript.

## ACKNOWLEDGMENTS

We thank Yu Liu and Navjeevan Soor for their technical assistance. This work was supported by the following grants: Engineering and Physical Sciences Research Council (EP/L016737/1); Engineering and Physical Sciences Research Council Imperial College Impact Acceleration Account (EP/K503733/1); National Institutes of Health (U01NS090501, U01NS099573, U01MH109091); Wellcome Trust Seed Award (201964/Z/16/Z); Royal Academy of Engineering Research Fellowship (RF1415/14/26); Biotechnology and Biology Research Council (BB/K001817/1, BB/R009007/1); The Royal Society (TA\R1\170047).

## SUPPLEMENTARY MATERIAL

The Supplementary Material for this article can be found online at: https://www.frontiersin.org/articles/10.3389/fncel.2019.00039/full#supplementary-material

## REFERENCES

Abdelfattah, A. S., Kawashima, T., Singh, A., Novak, O., Mensh, B. D., Paninski, L., et al. (2018). Bright and photostable chemigenetic indicators for extended *in vivo* voltage imaging. *bioRxiv [Preprint]*. doi: 10.1101/436840

Adam, Y., Kim, J. J., Lou, S., Zhao, Y., Brinks, D., Wu, H., et al. (2018). All-optical electrophysiology reveals brain-state dependent changes in hippocampal subthreshold dynamics and excitability. *bioRxiv [Preprint]* 281618. doi: 10.1101/281618

Ahrens, K. F., Heider, B., Lee, H., Isacoff, E. Y., and Siegel, R. M. (2012). Two-photon scanning microscopy of *in vivo* sensory responses of cortical neurons genetically encoded with a fluorescent voltage sensor in rat. *Front. Neural Circuits* 6:15. doi: 10.3389/fncir.2012.00015

Akemann, W., Mutoh, H., Perron, A., Park, Y. K., Iwamoto, Y., and Knöpfel, T. (2012). Imaging neural circuit dynamics with a voltage-sensitive fluorescent protein. *J. Neurophysiol.* 108, 2323–2337. doi: 10.1152/jn.00452.2012

Akemann, W., Sasaki, M., Mutoh, H., Imamura, T., Honkura, N., and Knöpfel, T. (2013). Two-photon voltage imaging using a genetically encoded voltage indicator. *Sci. Rep.* 3, 1–7. doi: 10.1038/srep02231

Allen, W. E., Kauvar, I. V., Chen, M. Z., Richman, E. B., Yang, S. J., Chan, K., et al. (2017). Global representations of goal-directed behavior in distinct cell types of mouse neocortex. *Neuron* 94, 891–907.e6. doi: 10.1016/j.neuron.2017.04.017

Antic, S. D. (2003). Action potentials in basal and oblique dendrites of rat neocortical pyramidal neurons. *J. Physiol.* 550, 35–50. doi: 10.1113/jphysiol.2002.033746

Antic, S. D., Empson, R. M., and Knöpfel, T. (2016). Voltage imaging to understand connections and functions of neuronal circuits. *J. Neurophysiol.* 116, 135–152. doi: 10.1152/jn.00226.2016

Bayguinov, P. O., Ma, Y., Gao, Y., Zhao, X., and Jackson, M. B. (2017). Imaging voltage in genetically-defined neuronal subpopulations with a cre recombinase-targeted hybrid voltage sensor. *J. Neurosci.* 37, 9305–9931. doi: 10.1523/JNEUROSCI.1363-17.2017

Chamberland, S., Yang, H. H., Pan, M. M., Evans, S. W., Guan, S., Chavarha, M., et al. (2017). Fast two-photon imaging of subcellular voltage dynamics in neuronal tissue with genetically encoded indicators. *Elife* 6, 1–35. doi: 10.7554/eLife.25690

Chavarha, M., Villette, V., Dimov, I., Pradhan, L., Evans, S., Shi, D., et al. (2018). Fast two-photon volumetric imaging of an improved voltage indicator reveals electrical activity in deeply located neurons in the awake brain. *bioRxiv [Preprint]* 445064. doi: 10.1101/445064

Chen, Q., Cichon, J., Wang, W., Qiu, L., Lee, S. J. R., Campbell, N. R., et al. (2012). Imaging neural activity using Thy1-GCaMP transgenic mice. *Neuron* 76, 297–308. doi: 10.1016/j.neuron.2012.07.011

Chen, T., Wardill, T. J., Sun, Y., Pulver, S. R., Renninger, S. L., Baohan, A., et al. (2013). Ultra-sensitive fluorescent proteins for imaging neuronal activity. *Nature* 499, 295–300. doi: 10.1038/nature12354

Chen, T. W., Li, N., Daie, K., and Svoboda, K. (2017). A map of anticipatory activity in mouse motor cortex. *Neuron* 94, 866–879.e4. doi: 10.1016/j.neuron.2017.05.005

Cheng, A., Gonçalves, J. T., Golshani, P., Arisaka, K., and Portera-Cailliau, C. (2011). Simultaneous two-photon calcium imaging at different depths with spatiotemporal multiplexing. *Nat. Methods* 8, 139–142. doi: 10.1038/nmeth.1552

Edelstein, A. D., Tsuchida, M. A., Amodaj, N., Pinkard, H., Vale, R. D., and Stuurman, N. (2014). Advanced methods of microscope control using μManager software. *J. Biol. Methods* 1:10. doi: 10.14440/jbm.2014.36

Foust, A. J., Zampini, V., Tanese, D., Papagiakoumou, E., and Emiliani, V. (2015). Computer-generated holography enhances voltage dye fluorescence discrimination in adjacent neuronal structures. *Neurophotonics* 2:021007. doi: 10.1117/1.NPh.2.2.021007

Gans, P., and Gill, J. B. (1983). Examination of the convolution method for numerical smoothing and differentiation of spectroscopic data in theory and in practice. *Appl. Spectrosc.* 37, 515–520. doi: 10.1366/0003702834634712

Gong, Y., Huang, C., Li, J. Z., Grewe, B. F., Zhang, Y., Eismann, S., et al. (2015). High-speed recording of neural spikes in awake mice and flies with a fluorescent voltage sensor. *Science* 350, 1361–1366. doi: 10.1126/science.aab0810

Gossen, M., and Bujard, H. (1992). Tight control of gene expression in mammalian cells by tetracycline-responsive promoters. *Proc. Natl. Acad. Sci. U S A.* 89, 5547–5551. doi: 10.1073/pnas.89.12.5547

Grinvald, A., Arieli, A., Tsodyks, M., and Kenet, T. (2003). Neuronal assemblies: single cortical neurons are obedient members of a huge orchestra. *Biopolymers* 68, 422–436. doi: 10.1002/bip.10273

Harris, J. A., Hirokawa, K. E., Sorensen, S. A., Gu, H., Mills, M., Ng, L. L., et al. (2014). Anatomical characterization of Cre driver mice for neural circuit mapping and manipulation. *Front. Neural Circuits* 8:76. doi: 10.3389/fncir.2014.00076

Knöpfel, T. (2012). Genetically encoded optical indicators for the analysis of neuronal circuits. *Nat. Rev. Neurosci.* 13, 687–700. doi: 10.1038/nrn3293

Knöpfel, T., Díez-García, J., Akemann, W. (2006). Optical probing of neuronal circuit dynamics: genetically encoded versus classical fluorescent sensors. *Trends Neurosci.* 29, 160–166. doi: 10.1016/j.tins.2006.01.004

Kulkarni, R. U., and Miller, E. W. (2017). Voltage imaging: pitfalls and potential. *Biochemistry* 56, 5171–5177. doi: 10.1021/acs.biochem.7b00490

Li, L., Li, M., Zhang, Z., and Huang, Z.-L. (2016). Assessing low-light cameras with photon transfer curve method. *J. Innov. Opt. Health Sci.* 09:1630008. doi: 10.1142/S1793545816300081

Madisen, L., Garner, A. R., Shimaoka, D., Chuong, A. S., Klapoetke, N. C., Li, L., et al. (2015). Transgenic mice for intersectional targeting of neural sensors and effectors with high specificity and performance. *Neuron* 85, 942–958. doi: 10.1016/j.neuron.2015.02.022

Mank, M., Santos, A. F., Direnberger, S., Mrsic-Flogel, T. D., Hofer, S. B., Stein, V., et al. (2008). A genetically encoded calcium indicator for chronic *in vivo* two-photon imaging. *Nat. Methods* 5, 805–811. doi: 10.1038/nmeth.1243

Mayford, M., Bach, M. E., Huang, Y. Y., Wang, L., Hawkins, R. D., and Kandel, E. R. (1996). Control of memory formation through regulated expression of a CaMKII transgene. *Science* 274, 1678–1683. doi: 10.1126/science.274.5293.1678

Mishina, Y., Mutoh, H., Song, C., and Knöpfel, T. (2014). Exploration of genetically encoded voltage indicators based on a chimeric voltage sensing domain. *Front. Mol. Neurosci.* 7:78. doi: 10.3389/fnmol.2014.00078

Nakai, J., Ohkura, M., and Imoto, K. (2001). A high signal-to-noise Ca(2+) probe composed of a single green fluorescent protein. *Nat. Biotechnol.* 19, 137–141. doi: 10.1038/84397

Otis, J. M., Namboodiri, V. M., Matan, A. M., Voets, E. S., Mohorn, E. P., Kosyk, O., et al. (2017). Prefrontal cortex output circuits guide reward seeking through divergent cue encoding. *Nature* 543, 103–107. doi: 10.1038/nature21376

Papagiakoumou, E., Anselmi, F., Bègue, A., De Sars, V., Glückstad, J., Isacoff, E. Y., et al. (2010). Scanless two-photon excitation of channelrhodopsin-2. *Nat. Methods* 7, 848–854. doi: 10.1038/nmeth.1505

Papagiakoumou, E., Bègue, A., Leshem, B., Schwartz, O., Stell, B. M., Bradley, J., et al. (2013). Functional patterned multiphoton excitation deep inside scattering tissue. *Nat. Photonics* 7, 274–278. doi: 10.1038/nphoton.2013.9

Papagiakoumou, E., de Sars, V., Oron, D., and Emiliani, V. (2008). Patterned two-photon illumination by spatiotemporal shaping of ultrashort pulses. *Opt. Express* 16:22039. doi: 10.1364/OE.16.022039

Pégard, N. C., Mardinly, A. R., Oldenburg, I. A., Sridharan, S., Waller, L., and Adesnik, H. (2017). Three-dimensional scanless holographic optogenetics with temporal focusing (3D-SHOT). *Nat. Commun.* 8:1228. doi: 10.1038/s41467-017-01031-3

Piatkevich, K. D., Jung, E. E., Straub, C., Linghu, C., Park, D., Suk, H., et al. (2018). A robotic multidimensional directed evolution approach applied to fluorescent voltage reporters. *Nat. Chem. Biol.* 14, 352–360. doi: 10.1038/s41589-018-0004-9

Prevedel, R., Verhoef, A. J., Pernía-Andrade, A. J., Weisenburger, S., Huang, B. S., Nöbauer, T., et al. (2016). Fast volumetric calcium imaging across multiple cortical layers using sculpted light. *Nat. Methods* 13, 1021–1028. doi: 10.1038/nmeth.4040

Quicke, P., Reynolds, S., Neil, M., Knöpfel, T., Schultz, S. R., and Foust, A. J. (2018). High speed functional imaging with source localized multifocal two-photon microscopy. *Biomed. Opt. Express* 9:3678. doi: 10.1364/BOE.9.003678

Ronzitti, E., Conti, R., Zampini, V., Tanese, D., Foust, A. J., Klapoetke, N., et al. (2017). Submillisecond optogenetic control of neuronal firing with two-photon holographic photoactivation of chronos. *J. Neurosci.* 37, 10679–10689. doi: 10.1523/JNEUROSCI.1246-17.2017

Roome, C. J., and Kuhn, B. (2018). Simultaneous dendritic voltage and calcium imaging and somatic recording from Purkinje neurons in awake mice. *Nat. Commun.* 9:3388. doi: 10.1038/s41467-018-05900-3

Sando, R., Baumgaertel, K., Pieraut, S., Torabi-Rander, N., Wandless, T. J., Mayford, M., et al. (2013). Inducible control of gene expression with destabilized Cre. *Nat. Methods* 10, 1085–1088. doi: 10.1038/nmeth.2640

Sauer, B., and Henderson, N. (1988). Site-specific DNA recombination in mammalian cells by the Cre recombinase of bacteriophage P1. *Proc. Natl. Acad. Sci. U S A.* 85, 5166–5170. doi: 10.1073/pnas.85.14.5166

Scanziani, M., and Häusser, M. (2009). Electrophysiology in the age of light. *Nature* 461, 930–939. doi: 10.1038/nature08540

Schuck, R., Go, M. A., Garasto, S., Reynolds, S., Dragotti, P. L., and Schultz, S. R. (2018). Multiphoton minimal inertia scanning for fast acquisition of neural activity signals. *J. Neural Eng.* 15:025003. doi: 10.1088/1741-2552/aa99e2

Sepehri Rad, M., Choi, Y., Cohen, L. B., Baker, B. J., Zhong, S., Storace, D. A., et al. (2017). Voltage and calcium imaging of brain activity. *Biophys. J.* 113, 2160–2167. doi: 10.1016/j.bpj.2017.09.040

Shemesh, O. A., Tanese, D., Zampini, V., Linghu, C., Piatkevich, K., Ronzitti, E., et al. (2017). Temporally precise single-cell-resolution optogenetics. *Nat. Neurosci.* 20, 1796–1806. doi: 10.1038/s41593-017-0018-8

Song, C., Do, Q., Antic, S., and Knöpfel, T. (2017). Transgenic Strategies for sparse but strong expression of genetically encoded voltage and calcium indicators. *Int. J. Mol. Sci.* 18:1461. doi: 10.3390/ijms18071461

Song, C., Piscopo, D. M., Niell, C. M., and Knöpfel, T. (2018). Cortical signatures of wakeful somatosensory processing. *Sci. Rep.* 8:11977. doi: 10.1038/s41598-018-30422-9

Ting, J. T., Daigle, T. L., Chen, Q., and Feng, G. (2014). Acute brain slice methods for adult and aging animals: application of targeted patch clamp analysis and optogenetics. *Methods Mol. Biol.* 1183, 221–242. doi: 10.1007/978-1-4939-1096-0_14

Xu, F., Shi, D. Q., Lau, P. M., Lin, M. Z., and Bi, G. Q. (2018). Excitation wavelength optimization improves photostability of ASAP-family GEVIs. *Mol. Brain* 11:32. doi: 10.1186/s13041-018-0374-7

Xu, Y., Zou, P., and Cohen, A. E. (2017). Voltage imaging with genetically encoded indicators. *Curr. Opin. Chem. Biol.* 39, 1–10. doi: 10.1016/j.cbpa.2017.04.005

Yang, S., Papagiakoumou, E., Guillon, M., de Sars, V., Tang, C. M., and Emiliani, V. (2011). Three-dimensional holographic photostimulation of the dendritic arbor. *J. Neural. Eng.* 8:046002. doi: 10.1088/1741-2560/8/4/046002

Yang, W., and Yuste, R. (2017). *In vivo* imaging of neural activity. *Nat. Methods* 14, 349–359. doi: 10.1038/nmeth.4230

Yen, J. C., Chang, F. J., and Chang, S. (1995). A new criterion for automatic multilevel thresholding. *IEEE Trans. Image Process.* 4, 370–378. doi: 10.1109/83.366472

Yi, B., Kang, B. E., Lee, S., Braubach, S., and Baker, B. J. (2018). A dimeric fluorescent protein yields a bright, red-shifted GEVI capable of population signals in brain slice. *Sci. Rep.* 8:15199. doi: 10.1038/s41598-018-33297-y

**Conflict of Interest Statement:** The authors declare that the research was conducted in the absence of any commercial or financial relationships that could be construed as a potential conflict of interest.

frontiers in Cellular Neuroscience

CORRECTION
published: 07 May 2019
doi: 10.3389/fncel.2019.00202

# Corrigendum: Single-Neuron Level One-Photon Voltage Imaging With Sparsely Targeted Genetically Encoded Voltage Indicators

**Peter Quicke**[1,2,3], **Chenchen Song**[2], **Eric J. McKimm**[4], **Milena M. Milosevic**[4], **Carmel L. Howe**[1,3], **Mark Neil**[3,5], **Simon R. Schultz**[1,3], **Srdjan D. Antic**[4], **Amanda J. Foust**[1,3] and **Thomas Knöpfel**[2,3]*

[1] Department of Bioengineering, Imperial College London, London, United Kingdom, [2] Department of Medicine, Imperial College London, London, United Kingdom, [3] Centre for Neurotechnology, Imperial College London, London, United Kingdom, [4] Institute for Systems Genomics, Stem Cell Institute, UConn Health, Farmington, CT, United States, [5] Department of Physics, Imperial College London, London, United Kingdom

**Keywords: voltage imaging, cerebral cortex, sparse expression, optogenetics, transgenic**

OPEN ACCESS

**Edited and reviewed by:**
Josef Bischofberger,
Universität Basel, Switzerland

***Correspondence:**
Thomas Knöpfel
tknopfel@knopfel-lab.net

**Specialty section:**
This article was submitted to
Cellular Neurophysiology,
a section of the journal
Frontiers in Cellular Neuroscience

**Received:** 17 April 2019
**Accepted:** 23 April 2019
**Published:** 07 May 2019

**Citation:**
Quicke P, Song C, McKimm EJ, Milosevic MM, Howe CL, Neil M, Schultz SR, Antic SD, Foust AJ and Knöpfel T (2019) Corrigendum: Single-Neuron Level One-Photon Voltage Imaging With Sparsely Targeted Genetically Encoded Voltage Indicators.
Front. Cell. Neurosci. 13:202.
doi: 10.3389/fncel.2019.00202

**A Corrigendum on**

**Single-Neuron Level One-Photon Voltage Imaging With Sparsely Targeted Genetically Encoded Voltage Indicators**
*by Quicke, P., Song, C., McKimm, E. J., Milosevic, M. M., Howe, C. L., Neil, M., et al. (2019). Front. Cell. Neurosci. 13:39. doi: 10.3389/fncel.2019.00039*

In the original article, there was an error. The in-line equation for the signal-to-noise ratio in the presence of a fluorescence background was incorrectly printed as $\sqrt{(1-f_b)} * SNR_0$, where it should have been printed as $\sqrt{(1-f_b)}SNR_0$.

A correction has been made to the **Introduction**, paragraph six:

"Formally, the issue of single cell resolution can be described as follows: an optical signal from a cell of interest is compromised by shot noise generated by non-signaling fluorescence emanating from the membranes of other fluorescent cells and tissue autofluorescence (the "background"). The fractional change in collected fluorescence, ΔF/F, will be reduced to $(1-f_b)\,\Delta F/F$ where $f_b$ is the fraction of fluorescence arising from non-signaling structures. Background fluorescence also has a detrimental effect on SNR. In a shot noise limited imaging system, SNR will be reduced proportionally to the SNR measured in the absence of background fluorescence ($SNR_0$) as $\sqrt{(1-f_b)}SNR_0$ (Knöpfel et al., 2006). Reducing the excitation volume in an attempt to minimize the contribution of fluorescent membranes of adjacent cells and their processes, for instance by using highly localized two-photon laser scanning (2PLS) excitation, reduces the amount of non-signaling fluorescence collected at the cost of very low rates of signal-carrying fluorescence excitation resulting in low SNRs. This makes 2PLS microscopy a poor choice for most voltage imaging applications, although it has been used successfully in some experimental paradigms (Ahrens et al., 2012; Akemann et al., 2013; Chamberland et al., 2017; Chavarha et al., 2018)."

The authors apologize for this error and state that this does not change the scientific conclusions of the article in any way. The original article has been updated.

## REFERENCES

Ahrens, K. F., Heider, B., Lee, H., Isacoff, E. Y., and Siegel, R. M. (2012). Two-photon scanning microscopy of *in vivo* sensory responses of cortical neurons genetically encoded with a fluorescent voltage sensor in rat. *Front. Neural Circuits* 6:15. doi: 10.3389/fncir.2012.00015

Akemann, W., Sasaki, M., Mutoh, H., Imamura, T., Honkura, N., and Knöpfel, T. (2013). Two-photon voltage imaging using a genetically encoded voltage indicator. *Sci. Rep.* 3, 1–7. doi: 10.1038/srep02231

Chamberland, S., Yang, H. H., Pan, M. M., Evans, S. W., Guan, S., Chavarha, M., et al. (2017). Fast two-photon imaging of subcellular voltage dynamics in neuronal tissue with genetically encoded indicators. *Elife* 6, 1–35. doi: 10.7554/eLife.25690

Chavarha, M., Villette, V., Dimov, I., Pradhan, L., Evans, S., Shi, D., et al. (2018). Fast two-photon volumetric imaging of an improved voltage indicator reveals electrical activity in deeply located neurons in the awake brain. *bioRxiv [Preprint]* 445064. doi: 10.1101/445064

Knöpfel, T., Díez-García, J., and Akemann, W. (2006). Optical probing of neuronal circuit dynamics: genetically encoded versus classical fluorescent sensors. *Trends Neurosci.* 29, 160–166. doi: 10.1016/j.tins.2006.01.004

frontiers
in Cellular Neuroscience

REVIEW
published: 26 February 2019
doi: 10.3389/fncel.2019.00053

# Optimizing Strategies for Developing Genetically Encoded Voltage Indicators

*Madhuvanthi Kannan*[1,2]*, *Ganesh Vasan*[1,2] *and Vincent A. Pieribone*[1,2,3]*

[1] The John B. Pierce Laboratory, New Haven, CT, United States, [2] Department of Cellular and Molecular Physiology, Yale School of Medicine, Yale University, New Haven, CT, United States, [3] Department of Neuroscience, Yale School of Medicine, Yale University, New Haven, CT, United States

Genetically encoded optical indicators of neuronal activity enable unambiguous recordings of input-output activity patterns from identified cells in intact circuits. Among them, genetically encoded voltage indicators (GEVIs) offer additional advantages over calcium indicators as they are direct sensors of membrane potential and can adeptly report subthreshold events and hyperpolarization. Here, we outline the major GEVI designs and give an account of properties that need to be carefully optimized during indicator engineering. While designing the ideal GEVI, one should keep in mind aspects such as membrane localization, signal size, signal-to-noise ratio, kinetics and voltage dependence of optical responses. Using ArcLight and derivatives as prototypes, we delineate how a probe should be optimized for the former properties and developed along other areas in a need-based manner. Finally, we present an overview of the GEVI engineering process and lend an insight into their discovery, delivery and diagnosis.

**Keywords: genetically encoded voltage indicators, ArcLight, *Ci*VSD, voltage sensitivity, membrane potential**

OPEN ACCESS

***Edited by:***
*Bradley James Baker,*
*Korea Institute of Science and Technology (KIST), South Korea*

***Reviewed by:***
*Robert N. S. Sachdev,*
*Humboldt-Universität zu Berlin, Germany*
*Bernd Kuhn,*
*Okinawa Institute of Science and Technology Graduate University, Japan*

***Correspondence:**
*Madhuvanthi Kannan*
*m.kannan@yale.edu*
*Vincent A. Pieribone*
*vincent.pieribone@yale.edu*

***Received:*** *30 July 2018*
***Accepted:*** *04 February 2019*
***Published:*** *26 February 2019*

***Citation:***
*Kannan M, Vasan G and Pieribone VA (2019) Optimizing Strategies for Developing Genetically Encoded Voltage Indicators. Front. Cell. Neurosci. 13:53. doi: 10.3389/fncel.2019.00053*

## INTRODUCTION

To understand the brain is to understand how individual neurons process information – all the way from the tips of dendrites to the soma, and onward to the nerve terminals. The real challenge, however, is to decode information processing in every neuron in the context of its neighbors or, in other words, intact neural circuits because neuronal interactions form the basis of sense perceptions, behavior and consciousness.

In mammals, neural ensembles consisting of thousands of neurons are often involved during a complex process such as reconstructing a visual scene or maneuvering in the local environment. To decode information processing during such behaviors, it becomes necessary to obtain simultaneous electrical recordings of input–output activity patterns from all participating neurons at single-cell resolution.

Conventional electrophysiology relies on the use of patch electrodes (intracellular) and multi-electrode arrays (MEAs) (extracellular) to measure electrical events that accompany neuronal signal processing. Patch electrodes can measure both subthreshold synaptic potentials as well as action potentials (APs) but can only record from a handful of neurons at a time. MEAs, on the other hand, consist of hundreds of electrical contacts, and can be used to obtain voltage recordings from several hundred neurons simultaneously. Current extracellular probes can allow for nearly a thousand densely spaced individual recording sites, providing a high spatial resolution for electrical measurements (Jun et al., 2017). However, parsing signals from individual neurons is not straightforward, as most sites sample signals from multiple neurons. Besides, the technique does not allow for targeted recordings in specific cells, cell types or subcellular compartments (Buzsaki, 2004; Spira and Hai, 2013).

The limitations of electrode-based techniques have largely been mitigated by optical approaches to monitoring neuronal activity, such as using synthetic dyes and genetically encoded fluorescent indicators. Using the latter, it is now possible to simultaneously record unambiguously from as many as 500 neurons in three-dimensional space, in awake and behaving animals, while preserving cellular resolution with multiphoton laser scanning modalities (Huber et al., 2012; Katona et al., 2012). Genetically encoded indicators can be engineered to selectively target distinct cell types and subcellular compartments, and to do so at precise stages of development. Genetically encoded calcium and voltage indicators [GECIs and genetically encoded voltage indicators (GEVIs), respectively] enable longitudinal imaging of activity in labeled neurons (Denk et al., 1996; Mainen et al., 1999; Mao et al., 2008; Tian et al., 2009; Mittmann et al., 2011; Chen et al., 2012; Wachowiak et al., 2013; Dana et al., 2014; Rothermel and Wachowiak, 2014; Zhu et al., 2014; Lur et al., 2016), and are the method of choice for functional imaging in subcellular compartments, e.g., dendritic spines inaccessible to electrodes, and organisms less-suited for patch-clamp experiments, such as *Drosophila* and *Caenorhabditis elegans* (Tian et al., 2009; Akerboom et al., 2012; Yoshihara, 2012; Kovacevic et al., 2013).

## COMPARISON OF GENETICALLY ENCODED CALCIUM AND VOLTAGE SENSORS

Since their development in the late 1990s, fluorescent activity indicators have seen extensive improvements in sensitivity and kinetics (Miyawaki et al., 1997; Romoser et al., 1997; Gong et al., 2015; Chamberland et al., 2017; Kannan et al., 2018; Piatkevich et al., 2018), and are beginning to complement electrode-based studies to understand fundamental aspects of neurophysiology.

Calcium indicators are molecular fusions of a calcium sensor, such as calmodulin or troponin C, and a fluorescent reporter protein (FP). GECIs are cytosolic proteins, which, upon binding intracellular $Ca^{2+}$, undergo conformational changes that modulate the fluorescence output of the FP. In some instances, a conformational change in the calcium-binding domain modulates instead the fluorescence resonance energy transfer (FRET) between a pair of donor and acceptor fluorophores. Modern GECIs include the GCaMPs and RCaMPs, GECOs, and Cameleons (Nagai et al., 2004; Palmer et al., 2006; Tian et al., 2009; Zhao et al., 2011; Akerboom et al., 2013; Chen et al., 2013). Because they detect intracellular $Ca^{2+}$, whose levels fluctuate during APs, GECIs provide an indirect measure of suprathreshold neuronal activity.

In contrast, GEVIs are fluorescent transmembrane proteins that can directly sense voltage fluctuations across the membrane during activity and synaptic transmission. The voltage-sensing domain (VSD) in GEVIs may be derived from transmembrane proteins such as ion channels, voltage-sensitive phosphatases or microbial opsins, and is fused to a single FP or a FRET-FP pair (Jin et al., 2012; Gong et al., 2013, 2014; Flytzanis et al., 2014; Hochbaum et al., 2014; St-Pierre et al., 2014; Zou et al., 2014; Piao et al., 2015; Abdelfattah et al., 2016). Opsin-based probes can also function as standalone GEVIs that report activity by virtue of their native albeit dim fluorescence (Gong et al., 2013; Flytzanis et al., 2014; Hochbaum et al., 2014).

Genetically encoded voltage indicators exhibit voltage-dependent fluorescence change via one of two distinct mechanisms: (1) by drawing on a conformational change in the voltage sensor or (2) by coupling with active state transitions during the photocycle of pigment retinal, the chromophore in voltage-sensitive opsins. GEVIs that fall under the type 1 category include ArcLight, VSFPs, ASAP1/2, Bongwoori and FlicR1 (Dimitrov et al., 2007; Akemann et al., 2012; Jin et al., 2012; St-Pierre et al., 2014; Piao et al., 2015; Abdelfattah et al., 2016), whereas those part of the type 2 category comprise derivatives of *Archaerhodopsin* (Arch), such as QuasArs, Archers, Archons, and FRET-opsin indicators, namely, QuasAr-mOrange2, MacQ-mCitrine, and Ace2N-mNeon, among others (Flytzanis et al., 2014; Gong et al., 2014, 2015; Hochbaum et al., 2014; Zou et al., 2014; Piatkevich et al., 2018). The different GEVI templates are illustrated in **Figure 1**.

As sensors of membrane potential, GEVIs are not limited to detecting APs unlike calcium indicators but can also report hyperpolarizations, subthreshold depolarizations such as those associated with synaptic transmission and sustained depolarizations that represent transient activated states. Further, while calcium indicators exhibit slow kinetics (∼50–75 ms for the fast GECI GCaMP6f) and can only resolve spikes at or below 20 Hz (Chen et al., 2013), GEVIs can provide superior temporal resolution, capable of detecting spikes at frequencies greater than 100 Hz (Gong et al., 2015).

## INNOVATING A GENETICALLY ENCODED VOLTAGE INDICATOR

Owing to their distinctive subcellular localization and mechanism of action, the criteria to engineer voltage indicators are inherently different from calcium indicators, spurring unique challenges in their design, development, and testing.

Voltage indicators require robust trafficking signals to ensure adequate and exclusive membrane expression, a prerequisite for high signal-to-noise ratios (SNR) in optical recordings – the ratio of the peak of optical response to the standard deviation of baseline fluorescence ($F_0$). Precise subcellular targeting is especially crucial for voltage indicators because useful voltage signals emerge but from a limited area of the cell (the membrane) as compared to the large volume of cytoplasm available for calcium detection.

Likewise, enhancing the sensitivity of voltage indicators is particularly challenging. The sensitivity of a probe per unit voltage change is expressed as the fraction of fluorescence change ($\Delta F$) to baseline fluorescence. Calcium indicators

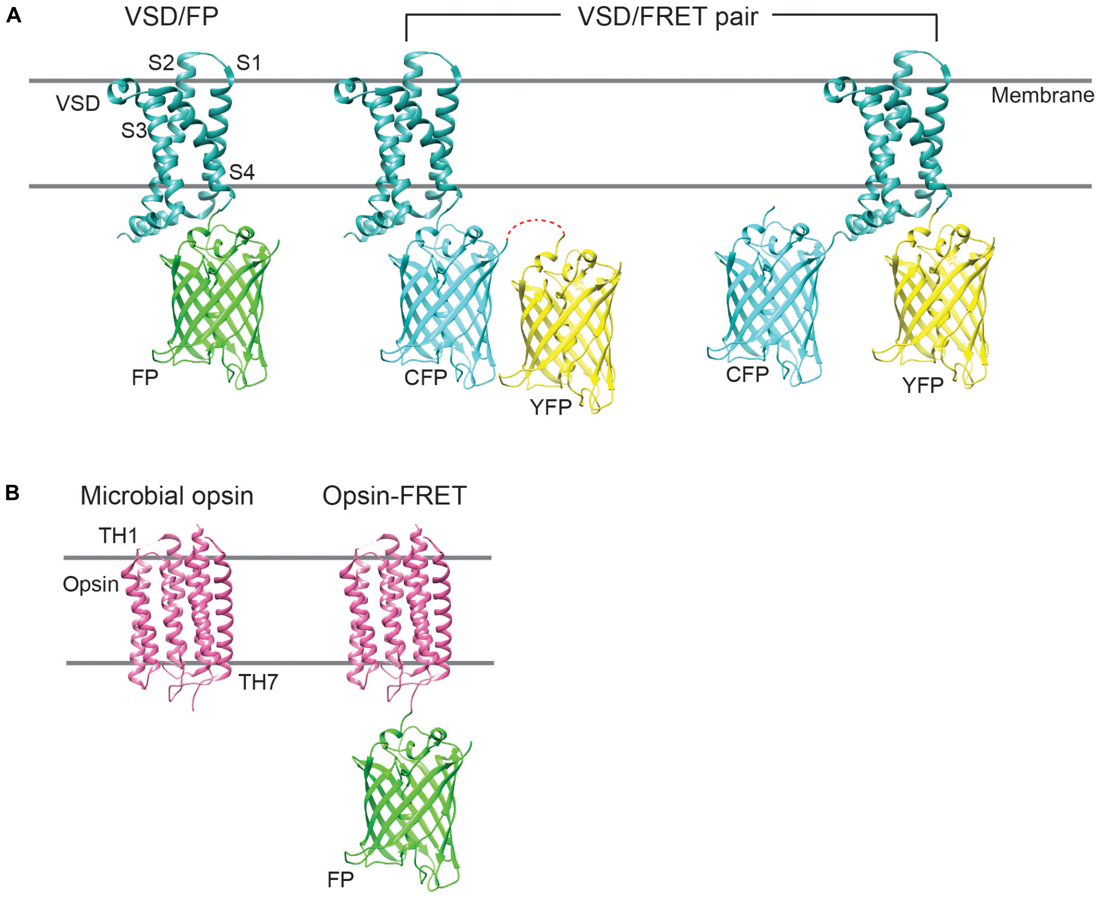

**FIGURE 1 |** Cartoon showing the different GEVI designs. **(A)** The majority of type 1 GEVIs consist of a molecular fusion of an isolated VSD, derived from a voltage-sensitive phosphatase, and a single FP, or a FRET FP pair. In FRET constructs, the FPs may be fused in tandem or to either terminus of the VSD. CFP, cyan fluorescent protein; YFP, yellow fluorescent protein. **(B)** Type 2 GEVIs comprise standalone microbial opsins, which possess seven transmembrane helices (TH1–TH7), or opsin-FRET constructs, where the opsin may be fused to a fluorophore. Microbial opsins exhibit broad absorption spectra (500–700 nm) and serve to "quench" the fluorescence of the appended fluorophore, during voltage fluctuations.

exhibit large sensitivities as the slow kinetics of successive calcium transients allows for cumulative increases in fluorescence response amplitudes. Spike-induced calcium transients have short rise times but prolonged decays. Fast AP trains cause individual transients to summate or, in other words, ride on top of one another (Smetters et al., 1999). Thus, during high frequency AP bursts (>∼20 Hz), GECIs bind the built-up calcium over several hundred milliseconds, much after the underlying spikes have decayed, resulting in long-lasting responses with large $\Delta F/F_0$ values. Indeed, the exact kinetics (on and off rates) and dynamic range of sensitivities of an indicator depend on its effective concentration, $Ca^{2+}$-binding affinity, and cellular calcium-buffering properties. Nevertheless, GCaMP variants exhibit fractional fluorescence changes of up to 500% for a train of 10 APs and 1000–1700% for 160 APs in cultured neurons, when in fact their $\Delta F/F_0$ values for single APs are merely 10–30% (Tian et al., 2009; Chen et al., 2013). Their large *in vitro* sensitivities further make calcium probes favorable for *in vivo* experiments where they provide high SNRs against background fluorescence and signal attenuation in thick tissue. Voltage fluxes, on the other hand, are extremely rapid – a neuronal AP lasts for less than a few milliseconds. The sensitivity of GEVIs is thus measured as the $\Delta F/F_0$ for a single AP. Contemporary GEVIs have modest sensitivities of 40–80% $\Delta F/F_0$ in cultured cells for 100 mV depolarization (≈AP amplitude) (Jin et al., 2012; Hochbaum et al., 2014; Piao et al., 2015; Yang et al., 2016; Piatkevich et al., 2018). The responses are further dampened *in vivo* due to background fluorescence and light scattering. To enhance signal sizes by at least an order of magnitude, embarking on high-throughput engineering and testing endeavors becomes inevitable.

As direct sensors of membrane potential, GEVIs can be tailored to be sensitive to hyperpolarization. However, the voltage range across which a probe's sensitivity spans is variable. In many cases, it can be shifted to more negative potentials by carrying out specific mutations in the VSDs (Dimitrov et al., 2007; Baker et al., 2012; Piao et al., 2015). Full optimization of the voltage-dependence of optical responses requires careful consideration of experimental needs and appropriate engineering of the voltage sensor.

In the following sections, we will review the characteristics of an ideal GEVI and the current standing of probes.

## Membrane Localization

To report changes in cellular membrane potential, voltage indicators must reside in the plasma membrane. They capitalize on the cell's secretory protein trafficking machinery to be transported here (Lippincott-Schwartz et al., 2000). Secretory proteins that are synthesized and assembled at the endoplasmic reticulum (ER) are exported to the Golgi complex where they undergo maturation. They are eventually packaged into post-Golgi vesicles and translocated along microtubules – fine cylindrical structures that constitute the scaffolding of a cell. Sometimes, misfolded proteins and proteins that tightly bind chaperones (protein-folding assistors) can be entrapped in the ER or Golgi complex, leading to intracellular aggregates. By contributing to voltage-insensitive background fluorescence, these aggregates can dampen the SNR of voltage signals in optical recordings.

The first-generation type 1 GEVIs FlaSh and its derivative Flare, VSFP1 and SPARC, were tandem fusions of a voltage-gated potassium or sodium channel and a single FP or a FRET-FP pair (Siegel and Isacoff, 1997; Sakai et al., 2001; Ataka and Pieribone, 2002; Baker et al., 2007). These GEVIs exhibited intense intracellular aggregation in cultured human embryonic kidney (HEK) cells and hippocampal neurons, with less than 5% fluorescence at the plasma membrane. The intracellular fluorescence often displayed a "web-like" pattern, a classic phenotype suggestive of ER retention (Baker et al., 2007) (**Figure 2**). Likely due to their poor membrane localization, these early probes exhibited extremely poor voltage sensitivity in neurons both *in vitro* and *in vivo*.

To overcome the issue of aggregation, which was thought to arise from improper folding of multimeric or modular channel proteins, the clunky ion channels of the first-generation GEVIs were replaced by the self-contained, monomeric VSD of a transmembrane phosphatase isolated from the sea squirt *Ciona intestinalis* (abbr. *Ci*VSD) (Dimitrov et al., 2007) (**Figure 2**). *Ci*VSD is a four-pass transmembrane protein (S1–S4 α helices), which can independently function as a voltage sensor (Murata et al., 2005).

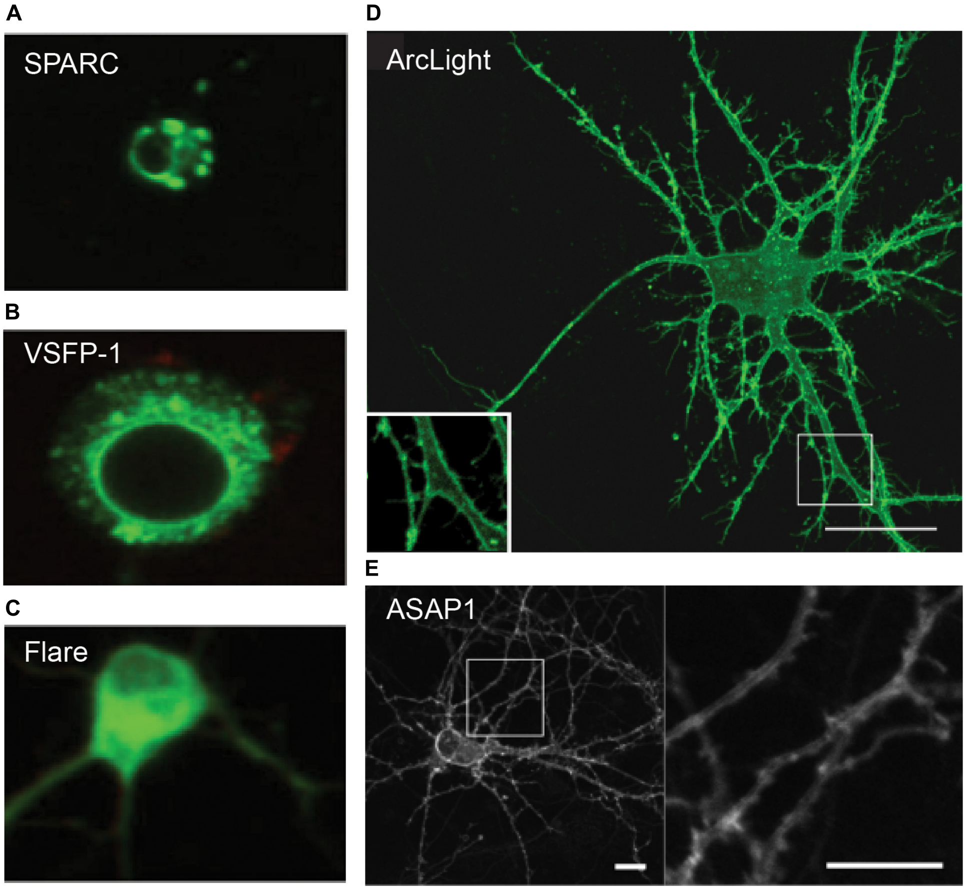

**FIGURE 2 |** Confocal images of GEVI expression in dissociated hippocampal neurons. **(A–C)** Ion channel-based GEVIs SPARC, VSFP-1 and Flare exhibit poor membrane localization and "web-like" intracellular aggregates, suggestive of protein retention in the ER. **(D,E)** VSD-based voltage sensors Arclight and ASAP1 show excellent membrane expression, which is clearly visible even in subcellular compartments such as dendrites (insets). Scale bars = 10 μm (Baker et al., 2007; Jin et al., 2012; St-Pierre et al., 2014).

Subsequently, orthologs from other species such as chicken, zebrafish, mouse, human and frog have each been cloned in place of *Ci*VSD as putative voltage sensors. The resultant probes show distinct characteristics, with the chicken (abbr. *Gg*VSD) and zebrafish VSDs (abbr. *Dr*VSD) having profound effects on GEVI kinetics (Baker et al., 2012; Han et al., 2013; St-Pierre et al., 2014).

The majority of VSD-based GEVIs – VSFP2, VSFP-Butterfly, Mermaid, ArcLight, Bongwoori and FlicR1 – contain *Ci*VSD as the voltage sensor fused to a green or red FP, or a FRET-FP pair (Dimitrov et al., 2007; Tsutsui et al., 2008; Akemann et al., 2012; Jin et al., 2012; Piao et al., 2015; Abdelfattah et al., 2016). When the FP or FRET pair is fused to either intracellular terminus of the VSD (S1 or S4), GEVIs show predominant membrane localization in non-neuronal and hippocampal cultures. Membrane localization appears to be impaired when the FP is inserted in the extracellular loop between S3 and S4 domains. This is, however, not the case for a similar FP insertion within *Gg*VSD in the fast voltage sensor ASAP1 (St-Pierre et al., 2014).

Opsin-based indicators have similarly suffered from intracellular aggregation in cultured neurons and brain slices, warranting the need for pixel weighing algorithms for fluorescence response quantification. These algorithms selectively average fluorescence changes across pixels that are informative (membranal) while deemphasizing the contribution from voltage-insensitive background (Hochbaum et al., 2014).

Aside from the voltage sensor, the choice of FP in membrane-targeted fusion proteins also affects membrane expression. Red FPs, such as dsRED, mCherry, and mOrange from the mushroom anemone *Discosoma* (class Anthozoa) have a greater tendency to aggregate, whereas FPs isolated from the jellyfish *Aequorea victoria*, such as the widely used green fluorescent protein (GFP) and its derivatives, generally traffic better (Arrenberg et al., 2009; Gong et al., 2014). Circular permuted (cp) FPs, in which the N- and C-terminal fragments are transposed to make them more permissive to regulation by conformational changes, tend to be more challenging to fold, and voltage probes incorporating cpFPs have a greater propensity to aggregate (Barnett et al., 2012; Abdelfattah et al., 2016).

Appending ER export (FCYENEV) and membrane trafficking (KSRITSEGEYIPLDQIDINV) peptide signals from the inward-rectifier potassium channel $K_{ir}2.1$ to the C-terminus of microbial opsins, has been shown to reduce intracellular aggregates and improve membrane expression in mammalian cells (Gradinaru et al., 2008, 2010). Accordingly, novel GEVIs are engineered to incorporate these peptides as fusion tags (Gong et al., 2014).

Finally, when overexpressing voltage indicators, it is important to carefully evaluate any adverse effects on membrane properties. As GEVIs introduce charge carriers in the membrane, their expression likely affects membrane capacitance – a measure of the charge stored across the membrane – which can in turn affect downstream physiological processes. Capacitive effects of GEVIs are reported to be minimal at expression levels normally achieved. Nevertheless, it is important to thoroughly quantify passive membrane properties and estimate AP widths while developing new indicators (Jin et al., 2012; St-Pierre et al., 2014; Gong et al., 2015).

## Sensitivity

The sensitivity of optical indicators is a critical parameter in functional imaging. As outlined above, it is also the most challenging to improve while engineering GEVIs.

### The Need for Large Voltage Sensitivity

The optical signal size is an important determinant of a probe's performance for the following reasons.

First, a probe's sensitivity directly contributes to the SNR of the optical signals. High SNR is indispensable for reliable data interpretation, including identification of subthreshold events and high-fidelity spike detection. Second, a large sensitivity in preliminary screens with cultured cells ensures that the optical signal is discernible in thick brain slices and *in vivo* experiments, where fluorescence responses are attenuated by tissue absorption, scattering, auto-fluorescence and out-of-focus fluorescence (see section "Signal-to-Noise Ratio"). Third, large optical signals circumvent the need to average responses across multiple sweeps. They hence allow imaging under physiological conditions where responses may vary from trial to trial. A probe that yields a conspicuous signal in single trials allows detection of non-stationary events such as spontaneous APs and AP bursts.

### Enhancing the Voltage Sensitivity of GEVIs

ArcLight was one of the first described GEVIs to exhibit a large sensitivity – its fluorescence output decreases by as much as 40% $\Delta F/F_0$ during 100 mV depolarization steps in HEK cells, 5% in response to APs in cultured neurons and acute brain slices and 2% *in vivo* in the mouse olfactory bulb (Jin et al., 2012; Cao et al., 2013; Kunst et al., 2014; Klein et al., 2015; Storace et al., 2015). ASAPs and Arch-based indicators have also been engineered to exhibit large response amplitudes (Yang et al., 2016; Chamberland et al., 2017; Piatkevich et al., 2018).

#### *Targeting the FP or VSD*

ArcLight's parental probe was constructed by fusing a pH-sensitive GFP variant, ecliptic pHluorin, to the C-terminus of *Ci*VSD. It exhibited a marginal sensitivity of $-1.3\%$ $\Delta F/F_0$ per 100 mV depolarization in HEK cells. Subsequently, a serendipitous discovery – an unintended substitution of alanine with aspartic acid at position 227 in the β-barrel of GFP (A227D) – led to an improved variant with a $\Delta F/F_0$ of $-18\%$ per 100 mV (Jin et al., 2012) (**Figure 3A**).

Replacing ecliptic pHluorin in ArcLight with superecliptic pHluorin (SEP), which contains the mutations F64L and S65T from enhanced GFP (eGFP), abates the acquired sensitivity but $\Delta F/F_0$ can be restored by simply reintroducing 227D (**Figure 3B**). Importantly, substituting the aspartic acid with any of the other 18 amino acids either completely or partially dampens the optical signal. The other negatively charged amino acid glutamic acid, which has an additional carbon, retains but a third of the improved sensitivity ($-6\%$ $\Delta F/F_0$ per 100 mV), suggesting that both negative charge *and* reduced steric effects from the compact side chain of aspartic acid are critical for the voltage response (Jin et al., 2012).

In addition to A227D, other residues specific to SEP and/or ecliptic pHluorin seem to play a role in ArcLight's voltage

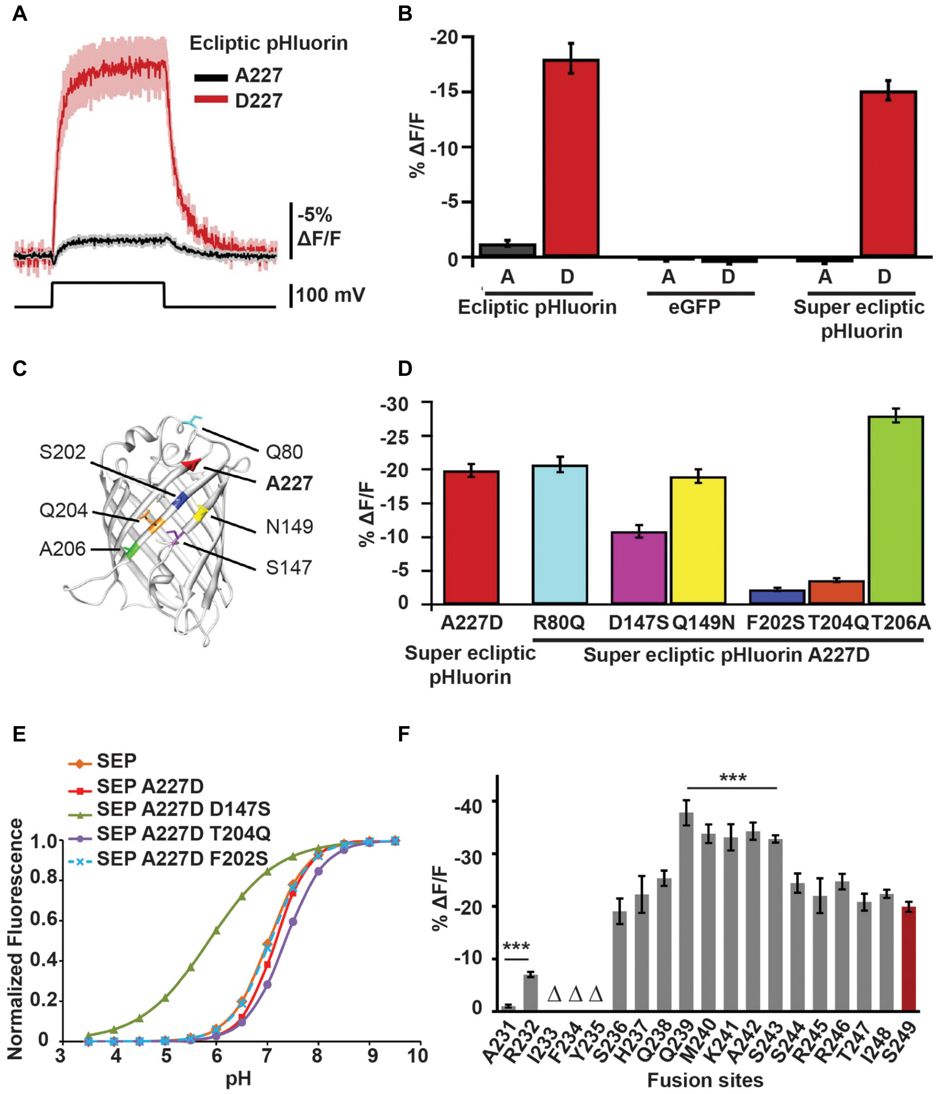

**FIGURE 3 |** Mutations in the FP sequence as well changes to the *Ci*VSD-FP linker length contribute to ArcLight's voltage sensitivity. **(A)** Fluorescence responses to 100 mV depolarization of HEK cells transfected with *Ci*VSD-ecliptic pHluorin or *Ci*VSD-ecliptic pHluorin A227D. **(B)** 100 mV step responses (mean ± SEM) of HEK cells expressing 227A or 227D variants of each of *Ci*VSD-ecliptic pHluorin, *Ci*VSD-eGFP or *Ci*VSD-SEP. **(C)** Crystal structure of eGFP (PDB ID 1EMG) highlighting A227 as well as the six most dissimilar residues between SEP and eGFP. The SEP versions are indicated. Note that all four critical residues 147, 227, 202, and 204 reside on the same barrel surface of the fluorophore. **(D)** Fluorescence responses (mean ± SEM) of *Ci*VSD-SEP variants harboring mutations at indicated residues in **(C)**. These mutations serve to replace the SEP amino acids with corresponding residues found in eGFP. **(E)** pH sensitivity curves of SEP and SEP mutants containing eGFP residues at indicated sites. **(F)** Mean response amplitudes to 100 mV depolarization of ArcLight derivatives with modified linker length. Groups that significantly differ from ArcLight S249 are indicated with asterisks. Δ refers to sensors showing poor membrane localization (Jin et al., 2012; Han et al., 2014).

sensitivity. This is because an ArcLight based on eGFP/A227D, which differs from SEP by nine mutations, fails to produce a voltage signal.

Loss-of-function studies reveal that in fact three mutations in the β-barrel unique to pHluorins – S147D, S202F, and Q204T – are necessary for ArcLight's voltage-dependent fluorescence response. Introducing these mutations, together with A227D, is sufficient to make an eGFP-based ArcLight as sensitive as the SEP/227D-based sensor (Han et al., 2014) (**Figures 3C,D**).

However, to date, it remains unclear how these amino acids transduce voltage changes into a fluorescent signal. Some plausible mechanisms have been suggested based on the interaction of the FP with the membrane, pH sensitivity and oligomerization.

Two-photon polarization microscopy of ArcLight-transfected HEK cells suggests that the SEP/227D exhibits linear dichroism, meaning that the fluorophore is likely oriented parallel to the surface of the membrane. This observation together with GFP's crystal structure data, which shows that all the four critical residues have outward-facing side chains and belong in adjacent β strands (same surface) of the GFP barrel, lead us to speculate that a voltage-dependent conformational change in the *Ci*VSD may swing the FP closer to the membrane and modulate the strength of interactions between the barrel and the membrane. Reversible changes in the strength of these interactions may in turn affect the chromophore environment and its deprotonated (fluorescent) state.

Further, SEP exhibits fluorescence changes as a function of pH (**Figure 3E**). D147 serves as an intrinsic pH sensor that base-shifts the pH sensitivity curve, bringing the pKa of GFP (the pH at half-maximal fluorescence) to near neutral, the ambient pH of the membrane. It also steepens the slope of the curve ($>1$). A slope greater than one suggests that even subtle changes in pH, as would be expected to occur during an AP when protons are mobilized by an electric field, can produce a large change in fluorescence. Whether or not ArcLight's voltage sensitivity indeed arises from SEP's pH sensing remains elusive. Substitution of other FPs with similar pH curves, such as ratiometric pHluorin or YFP, fails to generate voltage-sensitive variants even in the presence of A227D. It is possible that mutations unique to SEP are crucial for ArcLight's sensitivity and the absence of these mutations may result in small pH changes being rapidly buffered. Nevertheless, the pH sensitivity of SEP does not appear to solely modulate ArcLight's responses because mutations in *Ci*VSD can independently tune its sensitivity to different voltage ranges (see section "Voltage Dependence of Optical Responses").

Lastly, FP oligomerization may also have an impact on voltage sensitivity. Insertion of a tandem SEP downstream of *Ci*VSD dramatically reduces the response size and flips the polarity of the optical signal ($+2\%$ $\Delta F/F_0$ per 100 mV). In contrast, in the proton-channel-SEP/227D-based indicator Pado, mutation of a putative FP dimerization site diminishes its sensitivity, suggesting that dimerization normally stabilizes the optical signal (Kang and Baker, 2016). It is unclear, however, whether SEP/227D does exist as dimers in intact GEVIs and if so, why dimerization has different effects in different scaffolds.

A more definitive elucidation of the mechanism requires electron microscopy and X-ray crystallization studies to determine the structure of the intact GEVI before and during depolarization. However, membrane proteins are rather challenging to crystallize in their native folded state (Parker and Newstead, 2016).

Likewise, multiple mutations in the opsin core comprising the vicinity of the chromophore have been shown to result in large improvements in voltage sensitivity in Arch-based indicators (Hochbaum et al., 2014; Piatkevich et al., 2018).

The primary sequence of the VSD has also been shown to regulate voltage sensitivity. Recently, a single mutation R415Q in the S4 helix of *Gg*VSD in ASAP uncovered a new variant ASAP2s with strikingly large sensitivity ($-38\%$ $\Delta F/F_0$ per 100 mV) to depolarizing voltage steps. The response represents a 66% improvement over the parental template ASAP1 ($-23\%$ $\Delta F/F_0$ per 100 mV) (Chamberland et al., 2017). However, the mutation affected response kinetics, slowing down the rise time from 2.9 to 5.2 ms. This observation is not entirely surprising considering that movements of the S4 helix are speculated to partake in voltage-sensing (see section "Source of VSD").

Together, these findings point to the important role of the primary amino acid sequence in regulating an indicator's voltage performance.

#### *Targeting the linker*

Aside from the VSD and FP, changing the length and composition of the AA sequence in the linker between the two domains has often led to dramatic improvements in voltage sensitivity.

Shortening the linker between the S4 helix of *Ci*VSD and SEP/227D doubled the response amplitude of ArcLight (∼35–40% versus 18% $\Delta F/F_0$ per 100 mV). This was achieved by truncating the linker, one amino acid at a time from residue S249 of the VSD, and bringing SEP closer to S4, until the optical response reached saturation viz. between positions S243 and Q239 (**Figure 3F**).

Similarly, a substitution and a deletion involving two amino acids (A147S ΔA148) in the linker between the S3 helix and FP in ASAP1, enhanced its optical signal to ∼45% from 30% $\Delta F/F_0$ per 50 mV, albeit for responses to hyperpolarization (Yang et al., 2016).

Fluorescence resonance energy transfer sensors rely even more on optimal linker lengths (and AA composition) since FRET efficiency is inversely proportional to the sixth power of the distance between donor and acceptor FPs. A type 2 GEVI QuasAr-mOrange2, for instance, was derived by progressively shortening the linker by truncating not only the C-terminus of the voltage sensor cum FRET quencher QuasAr, but also the N-terminus of the FRET donor mOrange2, followed by randomization of two residues at the intersection (Zou et al., 2014).

Although reducing linker lengths in most cases enhances performance by allowing conformational changes in the VSD to better pervade the FP, bringing the two motifs too close to each other can also interfere with their vibrational freedom and dampen the sensitivity. For instance, bringing the FP closer than Q239 of *Ci*VSD diminishes ArcLight's voltage sensitivity. Moreover, large deletions in the VSD and/or FP can adversely affect protein folding and expression (Han et al., 2014; Zou et al., 2014). We have observed that unconventional FPs, with structures distinct from the classic barrel, tend to require longer linkers. This can be achieved by introducing one or a few randomized (NNK) codons at the junction and selecting the insertional mutants for improved voltage sensitivity.

#### *Polarity of the optical signal*

Most contemporary GEVIs, except the Arch family of standalone opsins and FlicR1, exhibit a decrease in fluorescence following depolarization. These probes, with negatively sloped voltage-fluorescence relationships ($\Delta V/\Delta F$ curves), are brighter at resting conditions than during an AP. Their high baseline fluorescence can be disadvantageous because fluorophores are prone to photobleaching even under ambient illumination intensities, and the loss of fluorescence (reduced photon count) can have a negative impact on SNR. Besides, out-of-focus fluorescence from nearby resting neurons can increase noise levels, further dampening the SNR, in wide-field recordings from intact tissue. For instance, in an *in vivo* olfaction study in the fly, extraneous ArcLight fluorescence from non-coplanar glomeruli contaminated the signals from regions-of-interest (ROIs) comprising the relevant glomeruli on the surface of the antennal lobe. The poor SNR led to odorant responses that were inconsistent with published extracellular recordings in peripheral sensilla. The problem was partially overcome by limiting ArcLight expression in specific glomeruli by genetic targeting (Cao et al., 2013).

Low baseline fluorescence, on the contrary, correlates well with high SNRs, as is the case with the most advanced GCaMP variants (Chen et al., 2013). GCaMPs respond to APs by increasing their fluorescence output compared to resting levels.

Recent work from our lab demonstrates that specific FP mutations can reverse the polarity of the optical signal. Substituting three residues in ArcLight's SEP with hydrophobic amino acids (D389A, H390A, and Y442V) yields a novel probe with a positively sloped $\Delta V/\Delta F$ curve. While 389A serves to flip the polarity, the others, also on the same surface of the β-barrel, enhance the response amplitude in the same direction. Hydrophilic or polar residues at these sites, however, revert the polarity to that of ArcLight. The finding bolsters the argument that voltage-sensitive movements in *Ci*VSD modulate the strength of interactions between the FP and the hydrophobic membrane and suggests that both voltage sensitivity and polarity of optical responses can be altered by targeting the fluorophore (Platisa et al., 2017).

The red voltage indicator FlicR1 also shows a positive response to depolarization (Abdelfattah et al., 2016). FlicR1 consists of *Ci*VSD fused to cp-mApple. It is unclear whether the reversal is due to mApple's sequence and geometry, which are distinct from the GFP family, or its circular permutation. A previous study has shown that circular permutation can have bidirectional effects on polarity with some *Ci*VSD/cp-eGFP-based scaffolds exhibiting positive and others negative responses to depolarization (Barnett et al., 2012).

### *Implications of signal size for in vivo experiments*

Their large dynamic range of sensitivities make calcium indicators ideal for routine *in vivo* imaging. In contrast, only a few GEVIs with substantial sensitivities have been demonstrated to work *in vivo* (Cao et al., 2013; Carandini et al., 2015; Gong et al., 2015; Storace et al., 2015; Yang et al., 2016). Low sensitivity is particularly problematic for wide-field (one-photon) microscopy, where out-of-focus fluorescence diminishes SNR (Flusberg et al., 2008; Mukamel et al., 2009).

ArcLight was first imaged *in vivo* in *Drosophila*. Here, the probe was genetically targeted to specific olfactory sensory neurons (OSNs) by driving ArcLight expression from promoters of cell-specific olfactory receptor genes. Odorant tuning of presynaptic OSNs and their glomerular projections was studied using wide-field imaging with a blue laser (488 nm). Optical signals were collected at 125 Hz using a low-noise charge-coupled device (CCD) camera. As expected from established electrical recordings of sensilla, the different ArcLight-expressing OSN subtypes exhibited excitatory responses (up to −5% $\Delta F/F_0$) to select odorants, with a high degree of odorant tuning. The signals were discernible in single-trial recordings and reported the relative differences in the strength of responses to different odorants and different doses. For instance, the glomerulus DC2 exhibited a stronger response to 3-octanol than 1-butanol (−5% versus −2% $\Delta F/F_0$). Additionally, ArcLight also revealed inhibitory responses in VA1v with similar sensitivity (Cao et al., 2013) (**Figure 4**).

ASAP2f, which was engineered to exhibit a large sensitivity and improved kinetics, has been used to delineate visual response properties in the fly with superior sensitivities of up to −10% $\Delta F/F_0$ in averaged sweeps. The data, acquired using a two-photon microscope, provided a high spatial resolution for subcellular imaging (Yang et al., 2016).

Likewise, Ace2N-mNeon, a high-speed FRET-opsin indicator consisting of *Acetabularia* opsin and mNeonGreen, could report orientation tuning properties in sparsely labeled mouse visual cortical neurons with response amplitudes of −3% $\Delta F/F_0$ per AP. The probe, which exhibits ∼−10% $\Delta F/F_0$ per AP in cultured neurons, has superior kinetics that compensates for the apparent low sensitivity and enhances spike detection rates *in vivo* (Gong et al., 2015).

Although wide-field imaging can dampen the SNR by confounding optical signals with out-of-focus fluorescence, targeting probes to specific cell types can minimize non-specific labeling and improve image quality. Such low-noise recordings are conducive for isolating individual responses in single trials. In addition, they are beneficial for measuring activity in certain cell types, which are inaccessible to electrodes, such as *Drosophila* circadian clock neurons (Cao et al., 2013).

Optical recordings in mice are also facilitated by targeted expression of indicators in genetically identified populations, followed by thinned skull preparations or cranial window implants to enable imaging through intact tissue. Live imaging in mice, however, entails such issues as movement artifacts from breathing and pulsations of blood vessels, hemodynamic artifacts from light absorption ($\lambda < 650$ nm) by hemoglobin, and green autofluorescence from endogenous chromophores nicotinamide adenine dinucleotide and flavoproteins. All of the above can essentially contaminate the signals and can be especially problematic when using blue-shifted indicators. Some of these issues can be resolved by engineering red-shifted probes, applying temporal and spatial filtering strategies, or ratiometric imaging with FRET indicators. However, in the long run, enhancing the sensitivity and SNR is key to improving event detection *in vivo*. Indeed, the field saw a huge surge in the use of GECIs after GCaMP3 was described, which then displayed a large enough dynamic range of sensitivities from ∼10 to ∼120% $\Delta F/F_0$ for APs and spike detection probabilities that correlate with response sizes (Tian et al., 2012).

## Signal-to-Noise Ratio

The SNR of voltage signals provides a measure of an indicator's fidelity to detect the incidence (and timing) of individual spikes and subthreshold signals. A large SNR allows for event detection from single trials, eliminating the need for averaging. The SNR of optical recordings depends on intrinsic properties of an indicator such as brightness, quantum yield and excitation/emission wavelengths, as well as extrinsic factors

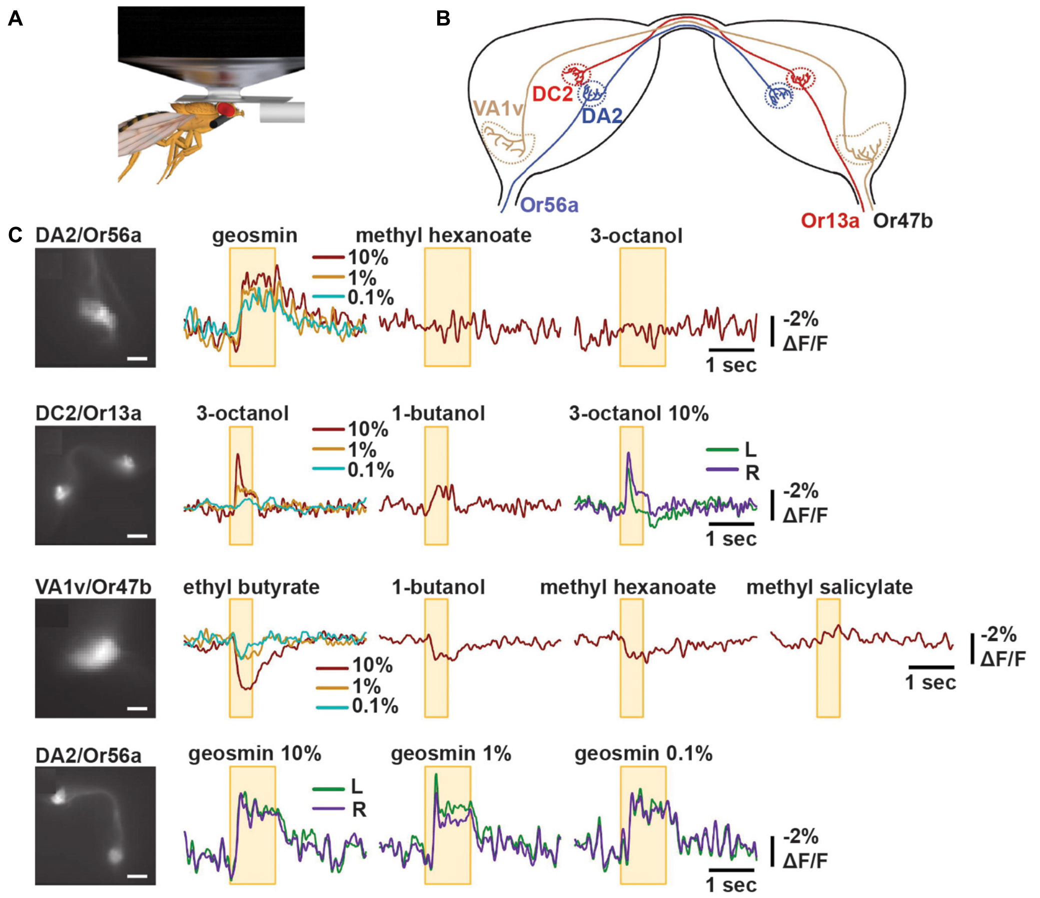

**FIGURE 4 |** ArcLight reports odorant responses in single trial recordings in *Drosophila*. **(A)** Schematic representation of *in vivo* imaging experiment of *Drosophila* antennal lobe following odorant presentation. **(B)** Schematic diagram of bilateral antennal lobes displaying projections of OSNs expressing Or56a, Or13a, or Or47b to their respective glomeruli. **(C)** Representative optical recordings of membrane activity at presynaptic terminals of OSNs following indicated odor application. The yellow box indicates the time of odor application. The colors indicate the different odorant concentrations 10, 1, or 0.1% or recordings obtained from the left (L) or right (R) glomeruli. Scale bars = 10 μm (panel 2 and 4) and 20 μm (panel 1 and 3) (Cao et al., 2013).

such as protein expression, membrane trafficking, illumination intensity, sources of noise, emission filter, numerical aperture (NA) of the objective and choice of detector.

## Choice of Fluorescent Protein

An essential first step in engineering a probe is choosing an FP with a high fluorescence quantum yield (φ), brightness, which is the product of φ and extinction coefficient (ε), and photostability. FPs such as eGFP, mNeonGreen, mCitrine, and mRuby have high φ (0.5–0.8) and brightness (60–90) and make excellent probes with high SNRs (Jin et al., 2012; St-Pierre et al., 2014; Zou et al., 2014; Gong et al., 2015; Bajar et al., 2016). In contrast, Arch derivatives, which operate as standalone GEVIs, have fluorescence φ of the order of $10^{-4}$ to $10^{-3}$. Although opsins can still yield high-SNR signals under high illumination intensities (880 mW $\text{mm}^{-2}$ to 8 W $\text{mm}^{-2}$, 18–80 times that required for GFP-based probes) and when combined with sensitive electron-multiplying-CCD or complementary metal oxide semiconductor (cMOS) detectors (Flytzanis et al., 2014; Hochbaum et al., 2014), they are impractical for studying intact tissue because high light intensities can cause sample heating, photodamage and tissue autofluorescence. They have since been adapted into opsin-FRET probes where they are fused to standard fluorophores to enable improved detection under standard conditions.

Photostability, defined as the time to photobleach to half-fluorescence under constant illumination, is another factor that impairs the SNR, especially during long recording sessions. Photostable probes exhibit low to moderate bleaching during an experiment and do not require extensive bleach-correction to isolate the signals. GFP-based indicators tend to photobleach faster than opsins, a limitation attributable to the properties of currently available fluorophores.

The spectral properties of an FP also have an impact on the SNR for *in vivo* imaging. Optical signals, especially from blue-shifted probes ($\lambda < 650$ nm) are prone to attenuation from absorption and scattering in the brain and exhibit low contrast amid green tissue autofluorescence. Red-shifted probes are less subject to loss from absorption or scattering and the attenuation coefficient at 600–700 nm is about a half of that at 500 nm. As a result, their optical transmittance (tissue penetration) is almost twice as high (Flock et al., 1992; Al-Juboori et al., 2013).

One should bear in mind, however, that the optical and spectral properties of an FP may not apply to an engineered GEVI because fusing an FP with VSD and mutating its primary sequence can influence protein folding and chromophore environment to substantially modify the native fluorophore.

## Probe Expression

Exclusive expression of GEVIs in the plasma membrane is important to minimize contamination of useful signals with intracellular fluorescence refractory to voltage changes. To some extent, this can be achieved by inserting membrane-trafficking signals into the coding sequence or coopting pH-sensitive fluorophores, such as ecliptic pHluorin and SEP, whose fluorescence is "eclipsed" in acidic intracellular compartments. In addition, adequate transgene expression requires the use of appropriate vectors for gene delivery such as recombinant adeno-associated viruses (rAAVs) or plasmid DNA for *in utero* electroporation.

It is also important to achieve sparse expression of indicators in select neurons to reduce background fluorescence from dampening the SNR. For some types of neurons such as cortical pyramidal cells and interneurons, layer-specific expression can be achieved by delivery of plasmid DNA to embryos carried by timed-pregnant mice via *in utero* electroporation (Wang and Mei, 2013; De Marco Garcia and Fishell, 2014). Specific neuronal subtypes can also be targeted by exploiting differences in their gene expression profiles. Using cell-type specific promoters together with combinatorial gene targeting strategies such as Cre recombinase/loxP or tetracycline transactivation (tTA) systems, it is possible to both spatially and temporally regulate indicator expression.

## Optical Instrumentation

As with any fluorescence microscopy, the SNR in functional imaging also depends on the optical setup.

High numerical aperture (NA) ($\sim$1.2) objectives can deliver more excitation photons and collect more fluorescent photons, thereby enhancing signal brightness and resolution [resolvable distance $R = \lambda/(2 \times NA)$] (Piston, 1998). When coupled with high-resolution detectors, they enable better identification of ROIs. Illumination intensities should be adequate to overcome shot-noise limitations from stochastic fluctuations in photon counts. Yet, the light intensity should not be overpowering as it can accelerate photobleaching, cause sample heating and phototoxicity. Likewise, emission filters should be carefully chosen to minimize fluorescence contamination with excitation light, which can drastically obscure the signals. FPs with large Stokes shift – the difference between the absorption and emission maxima – are useful for avoiding spectral overlap (Piatkevich et al., 2010, 2013; Chu et al., 2016).

The choice of detector is another factor that can influence the SNR. CCD cameras such as those offered by RedShirt Imaging, LLC are particularly suited for high speed imaging at up to 2 kHz, or 5 kHz with 3 pixel × 3 pixel binning, and enable detection of optical responses to APs. Given their high quantum efficiency ($>$80%) – a measure of the percentage of photons detected – and low read noise, these cameras provide SNRs close to the theoretical maximum.

Although conventional one-photon microscopy provides fast acquisition rates because photons are sampled in parallel, two-photon laser scanning is a better option for *in vivo* imaging as it provides superior SNR due to three-dimensional optical sectioning and enhanced spatial resolution. Type 1 VSD-based indicators such as ArcLight and ASAP2f have been successfully used for imaging slow, subcellular voltage dynamics *in vivo* (Cao et al., 2013; Storace et al., 2015; Yang et al., 2016). For instance, ArcLight reports odorant responses in populations of olfactory glomeruli with a sensitivity of about $-1$ to $-2\%$ $\Delta F/F_0$ in single trial recordings under two-photon microscopy as with widefield imaging (Storace et al., 2015). However, the large pixel dwell times of contemporary lasers and low frame rates (10–100 Hz) preclude their use in imaging responses to rapid voltage fluctuations viz. APs ($<$1–2 ms duration). To overcome this issue, random access scanning, which permits fast acquisition rates of up to 1 kHz, has recently been demonstrated to work well with a novel ASAP variant ASAP2s. Nevertheless, while the large sensitivity of ASAP2s ($-15\%$ $\Delta F/F$ per AP under widefield imaging conditions) was recapitulated under two-photon microscopy, the probe suffered more profoundly from photobleaching during laser scanning compared to one-photon imaging (Chamberland et al., 2017).

It is unclear whether opsin-based GEVIs are optimized for two-photon imaging. Recent studies have demonstrated that opsin GEVIs such as Arch-based indicators, Ace-mNeon and MacQ-mCitrine perform poorly under laser scanning microscopy. A prevailing hypothesis is that the femtosecond pulsed laser likely interferes with rhodopsin photocycle and opsin GEVIs may not be held in their voltage-sensitive state during the "dark" phase (Brinks et al., 2015; Chamberland et al., 2017).

As an alternative imaging modality, a powerful fiber-optic technique has recently been shown to enable cell-type specific recordings of transmembrane voltage dynamics using opsin-FRET indicators. The 0-D recording technique, dubbed Transmembrane electrical measurements performed optically or TEMPO, allows for fluorescence activation by laser beams delivered via optic fibers and signal detection by photoreceivers coupled to lock-in amplifiers. The technique offers a sensitivity approaching theoretical limits imposed by photon-shot noise (Marshall et al., 2016).

One could, in principle, use high-speed epifluorescence imaging to record spikes *in vivo* but the data will require heavy post-processing to distinguish voltage responses from background fluorescence. Besides, the images will still provide little spatial information, which can only be inferred from the processed signals. In the study describing Ace2N-mNeon, optical responses to spontaneous firing *in vivo* were captured using wide-field imaging at up to 2 kHz acquisition rate. The neurons were located by the electrical activity from a juxtacellular electrode. The images were subjected to background subtraction and voltage responses were selectively extracted from pixels that exhibited the top 20% SNR values, which mostly corresponded to the somata of interest (Gong et al., 2015).

## Response Kinetics

Improving the speed of voltage indicators to follow individual APs and resolve fast spike trains can maximize their usefulness in neuroscience research. However, as mentioned above, advances in imaging modalities must complement GEVI engineering directed at improving response kinetics.

In ArcLight and other VSD-based GEVIs, the kinetics is largely controlled by voltage-sensing movements of the VSD. In response to voltage fluctuations, VSDs exhibit "gating" charge movements, which as part of native ion channels and voltage-sensitive phosphatases, facilitate channel gating or enzyme activation. Structural studies show that voltage-activation of *Ci*VSD causes the S4 helix to slide upward by ∼5 Å along its main axis, and rotate by ∼60°, to mobilize the putative gating charges – a series of evenly-spaced arginines (Mannuzzu et al., 1996; Yang et al., 1996; Li et al., 2014) (**Figures 5A,B**). This conformational change is hypothesized to pervade the FP in voltage indicators, thereby modulating their fluorescence output.

In contrast, the voltage sensitivity of opsin-based indicators does not depend on movements of the sensor but instead on changes in the protonated state of the chromophore retinal. These changes are thought occur near instantaneously during voltage transients, and as result, most standalone opsins and opsin-FRET GEVIs exhibit accelerated kinetics in the sub-millisecond timescales.

### Source of VSD

Fast kinetics was first observed in the ion channel-based voltage indicator SPARC. SPARC consists of rat skeletal sodium channel rNav1.4 fused to eGFP, which is inserted in the intracellular loop between its second and third domains. The fast kinetics of the fluorescence response (exponential rise time τ-on <1 ms; <0.5% $\Delta F/F_0$ per 100 mV) reflects the fast voltage-dependent gating charge movements, likely in transmembrane domains I and II (Ataka and Pieribone, 2002).

Most *Ci*VSD-based probes have slow rise times lasting tens of milliseconds and slower decays of about 80–100 ms (Dimitrov et al., 2007; Tsutsui et al., 2008; Perron et al., 2009; Jin et al., 2012). ArcLight-Q239, the variant with the shortest linker and maximum sensitivity, exhibits double exponential kinetics with on-times of 9 (τ1) and 48 (τ2) ms, and off-times of 17 (τ1) and 60 (τ2) ms (per 100 mV). The fast components (τ1s) during rise and decay make up 50 and 80% of the total amplitude, respectively.

Several approaches have been shown to alter the kinetics of VSD-based probes. One of them has been to simply replace *Ci*VSD with orthologs. Substituting *Dr*VSD or *Gg*VSD, for

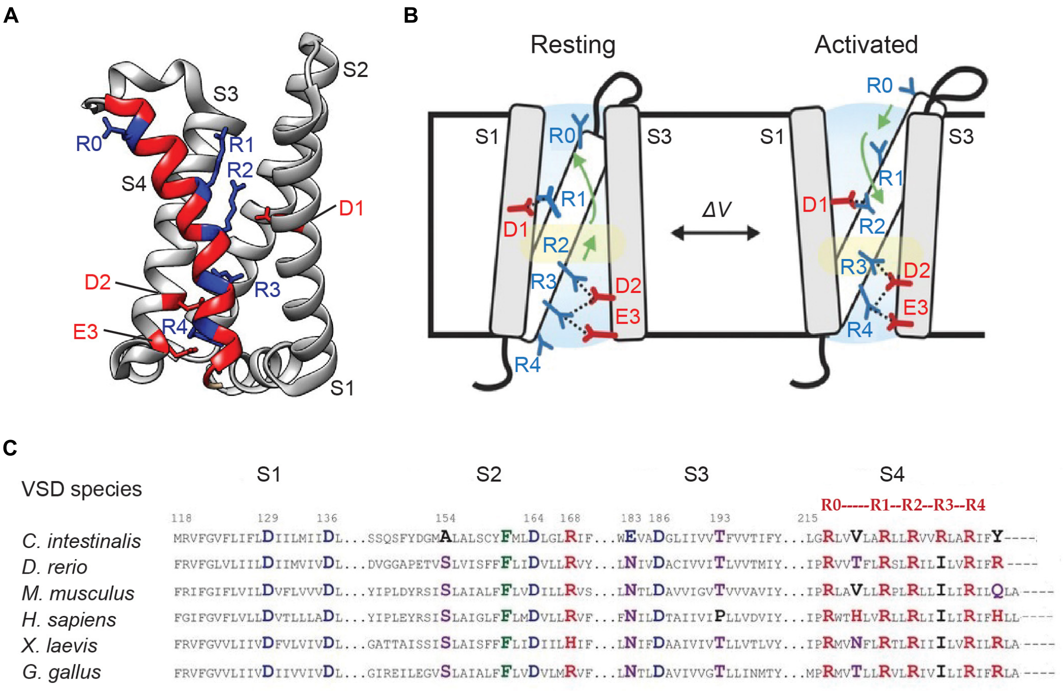

**FIGURE 5 |** Genetically encoded voltage indicators kinetics and voltage dependence of optical responses largely depend on voltage-sensitive conformational changes in its VSD. **(A)** Crystal structure of the VSD of *Ciona intestinalis* voltage sensitive phosphatase (PDB ID 4G7V). The four transmembrane helices S1–S4 are shown. S4 is highlighted in red. The position of the gating arginines R1–R4 (every third amino acid starting at 223) as well as the outermost S4 arginine R0 (position 217 in *Ci*VSD) are shown in blue. The countercharges D1 (on S2 helix), D2 and E3 (on S3 helix) are indicated in red. **(B)** A mechanistic model of voltage sensing in *Ci*VSD. The activated UP state is accompanied by a 5 Å S4 down movement and a ∼60° counterclockwise rotation of the entire helix. The arginines are then stabilized by successive negative countercharges, from R1–D1, R2–D2, and R3–D3 pairings in the resting or DOWN state to R2–D1, R3–D2, and R4–E3 in the UP configuration. **(C)** Sequence alignment of the VSD transmembrane segments of voltage sensitive phosphatase orthologs. Positive, negative and polar residues are indicated in red, blue, and purple, respectively. The numbering follows that of the *Ciona* homolog (Li et al., 2014; Piao et al., 2015).

instance, generates ArcLight variants with faster and simpler kinetics (single exponential) with τ-on and τ-off time constants of ∼5 and ∼9 ms, respectively. These variants, however, exhibit reduced sensitivities, compared to the *Ci*VSD variant, presumably due to altered interactions between the VSD orthologs and SEP 227D. Nevertheless, the chicken ArcLight can detect APs in cultured neurons in single trials with a sensitivity of ∼−3% $\Delta F/F_0$ and resolve simulated APs at 100 Hz in HEK cells (Han et al., 2013).

The zebrafish and chicken VSDs similarly boost response kinetics as part of other GEVI scaffolds. For instance, Zahra, a fusion between *Dr*VSD and CFP/YFP FRET pair, exhibits time constants of ∼3.5–5 ms per 100 mV depolarization, a significant improvement over its predecessor *Ci*VSD-based VSFP2.1 (Dimitrov et al., 2007; Baker et al., 2012). Similarly, another FRET-based sensor Mermaid, displays improved kinetics that compares to *Gg*VSD-ArcLight when *Ci*VSD is replaced with the chicken ortholog (Tsutsui et al., 2008; Han et al., 2013). *Gg*VSD also imparts superior kinetics to ASAP1/2, in which a cp-superfolder GFP is inserted in the extracellular S3–S4 loop. Although ASAP1/2 display double exponential kinetics, the responses are dominated by fast components (τ1 = 2 ms) (St-Pierre et al., 2014).

In contrast, frog and human VSDs impair ArcLight's kinetics by generating responses slower than the *Ciona* version (τ-on = 11 and 70 ms, τ-off = 155 and 70 ms, respectively) (**Figures 6A,B**). It is intriguing why different VSD orthologs exhibit differential kinetics. In part, the discrepancies appear to stem from variations

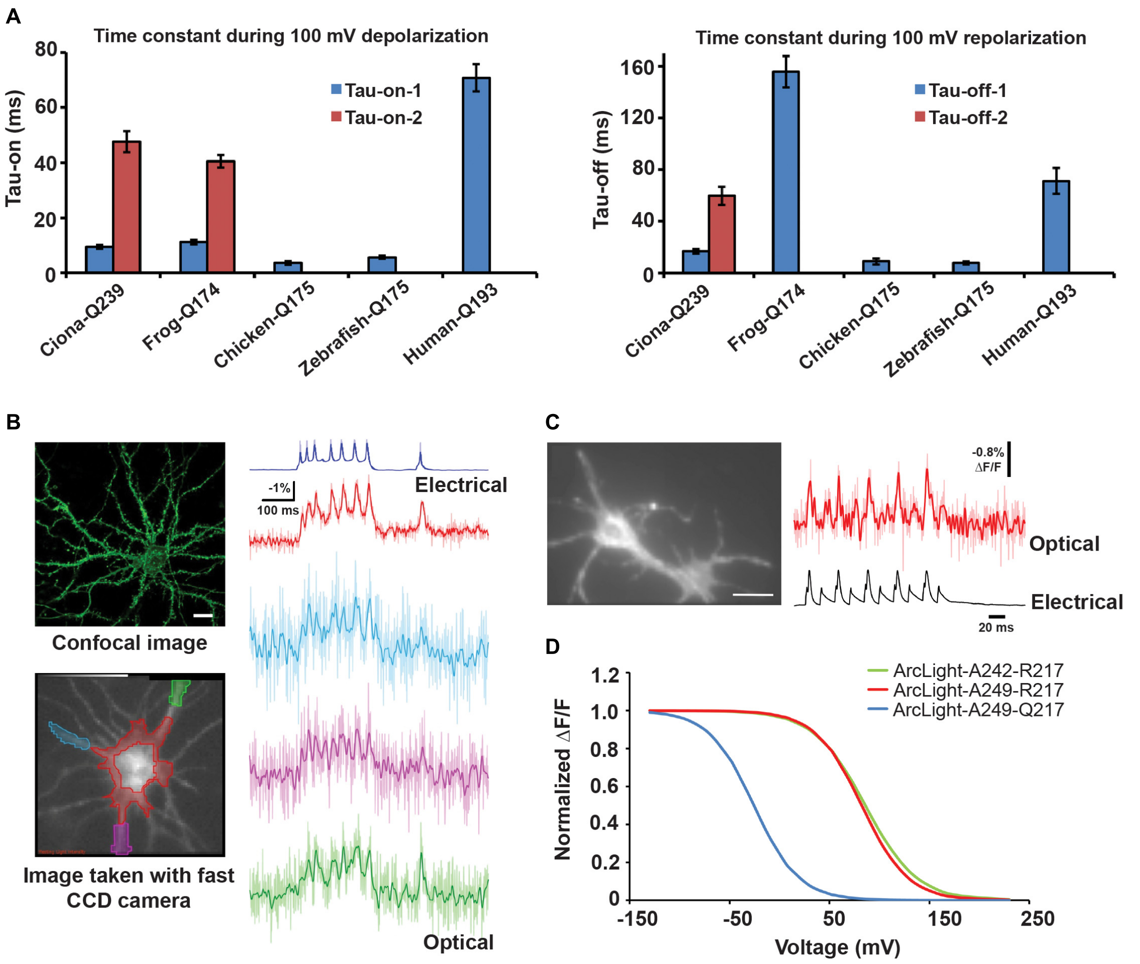

**FIGURE 6 |** Changing the VSD species or circular permutation of FP enhances GEVI kinetics **(A)** τ-on and τ-off of optical responses to 100 mV depolarization in HEK cells transfected with ArcLight derivatives based on frog, chicken, zebrafish or human voltage sensitive phosphatase ortholog. **(B)** Top left: confocal image of cultured hippocampal neuron expressing chicken ArcLight. Scale bar = 20 μm. Bottom left: An 80 × 80 fast CCD camera image of a neuron from which electrical and optical recordings in the right panel were obtained. The ROIs are color coded to match those of the respective optical traces. Right: Single trial recordings of evoked APs using chicken ArcLight. The somatic and neurite recordings were low-pass filtered with a 95 and 50 Hz Gaussian filter, respectively. The unfiltered traces are shown as light-colored lines. **(C)** Left: Wide-field image of a hippocampal neuron expressing ElectricPk. Scale bar = 15 μm. Right: Single (light red trace) and averaged (red trace) optical and electrical responses to evoked APs in the neuron on the left. The optical responses were captured using a NeuroCCD camera (RedShirt Imaging, LLC) at 2 kHz. **(D)** Normalized $\Delta V/\Delta F$ curves for ArcLight derivatives A242–R217, S249–R217, and S249–Q217. 242 and 249 represent sites of FP fusion on the *Ci*VSD linker. 217 refers to the outermost arginine on the S4 helix (Barnett et al., 2012; Han et al., 2013, 2014).

in their primary sequence, which may affect the speed of gating charge movements.

Sequence alignment of VSD orthologs from 29 species reveals that while several residues across the helices are highly conserved, with strikingly similar arginine repeats in S4, conspicuous differences exist at some of these sites. Combinatorial mutations of the variable residues in *Ci*VSD (**Figure 5C**) led to the development of the fast SEP/227D-containing sensor Bongwoori. The *Ci*VSD in Bongwoori contains mutations in S2 and S4 helices (A154D/R229I), which enhance its kinetics, as well as the S4 mutation R217Q, which augments sensitivity to negative potentials. The probe exhibits a similar τ-on (∼8 ms) as ArcLight, but the fast component constitutes a larger fraction of the total exponential decay (91% versus 50%). Its τ-off is 7 ms (Piao et al., 2015).

### Circular Permutation of FP

Voltage indicator kinetics are not only limited by movements of the voltage sensor but also the efficiency and speed of coupling between the sensor and the fluorophore during these movements.

Circular permutation of the FP, regardless of VSD species, enhances response kinetics. ElectricPK, a fast voltage sensor, was discovered during a screen for voltage sensitivity among a series of *Ci*VSD-cp-eGFP scaffolds. This probe, and in fact many other candidates from the screen, exhibited fast on and off rates of ∼2 ms. ElectricPK can reliably resolve short, high frequency depolarization pulses in HEK cells, and APs in hippocampal neurons, with discrete optical responses, unobscured by accumulating baseline drift (Barnett et al., 2012) (**Figure 6C**).

Similarly, the *Ci*VSD-cp-mApple fusion protein FlicR1 exhibits fast kinetics (τ1 = ∼3 ms), with responses dominated by fast components. FlicR1 was developed by random mutagenesis and contains eight mutations in its VSD. It is hence unclear whether the increase in speed is an outcome of circular permutation alone or additional changes to the kinetics of the VSD (Abdelfattah et al., 2016). This is also the case for ASAP1/2, where both VSD species and FP assembly are propitious to accelerated voltage-sensing.

Upon voltage activation, *Ci*VSD appears to undergo multiple structural rearrangements. While the initial response is fast and involves the gating charge movement, it is followed by other slower and plausibly voltage-independent transitions. These two components of VSD dynamics are mirrored in the FP and hence the GEVI's fluorescence output (Kohout et al., 2008; Villalba-Galea et al., 2009). The consensus is that FPs of slower probes reminisce both types of VSD movements whereas those of faster probes capture only the former. Circular-permuted FPs, in particular, effectively couple with the fast movements as they are more vulnerable to barrel distortions and rapidly destabilize given their sub-optimal configuration.

### Kinetics of the Ideal Voltage Sensor

Given that APs are rapid events, one may predict that a GEVI with sub-millisecond kinetics can adeptly resolve a quick succession of APs, providing precise information on both spike incidence and timing. Indeed, opsin-based GEVIs with sub-millisecond kinetics, arising from retinal state transitions of microsecond time-scales, provide superior temporal resolution for spike detection (Maclaurin et al., 2013; Gong et al., 2014, 2015; Zou et al., 2014). However, spike detection fidelity for a probe $d'$ has been shown to depend not on the temporal accuracy of overlap between the optical signal and AP waveform, but rather on the duration of the optical signal, even if it exceeds that of the underlying spike (Wilt et al., 2013).

Under photon shot-noise limited conditions, contemporary detectors offer $d'$ that is dependent on signal size $\Delta F/F$, brightness of the sensor $F_0$ and signal decay time τ such that $d' \approx (\Delta F/F) \bullet \sqrt{(F_0\tau)/2}$ (Wilt et al., 2013). In addition to improving the sensitivity and brightness of the probes, prolonging the decay time of the optical signal improves $d'$, as it allows for additional signal photons to be collected per event, above background. Thus, an optical indicator with a swift rise capable of precisely sensing spike onset, but protracted decay, can effectively improve spike detection. Nevertheless, such indicators may fail to provide accurate spike timing information, when spikes arrive at frequencies greater than the resolvable limit of the indicator.

In sum, when choosing an indicator for its response kinetics, one may want to consider experimental priorities such as whether a given biological question warrants precise spike detection, spike timing estimation or assessment of subthreshold voltage changes. While fast GEVIs may be well-suited for the former type of questions, slower GEVIs may be valuable tools for studying input patterns in local circuits, such as voltage changes from synaptic transmission, and slow population-wide voltage oscillations.

## Voltage Dependence of Optical Responses

The overarching goal of GEVI engineering is to develop optical indicators that are sensitive to both depolarization and hyperpolarization, provide absolute measures of voltage change and operate in the physiological voltage range for neurons (voltage of half-maximal fluorescence response $V_{1/2} \approx -70$ mV). All of these can be achieved by optimizing a probe's $\Delta V/\Delta F$ curve.

The properties of the $\Delta V/\Delta F$ curve are also determined by a GEVI's voltage sensing motif. Since native VSDs are activated by membrane depolarization, the voltage dependence of gating charge movements is shifted toward positive potentials. This means that GEVIs incorporating wild type VSDs would operate only at highly depolarizing voltages. However, it is possible to expand a VSD's sensitivity range to include less depolarizing and even hyperpolarizing voltages. For example, in the *Shaker* potassium channel, neutralization of the outermost positive charge in S4 (R362Q) produces gating charge movements even at voltages below −70 mV (hyperpolarization) (Seoh et al., 1996). Analogous mutations in phosphatase-derived VSDs similarly broaden their sensitivity enhancing the usefulness of GEVIs over a wide range of voltages.

The *Ci*VSD mutation R217Q, and the corresponding *Gg*VSD and *Dr*VSD mutations (R153Q), increase GEVI sensitivity to hyperpolarizing potentials and result in leftward shifts of the $\Delta V/\Delta F$ curve (**Figure 6D**). Accordingly, these mutations have been widely adopted in a number of probes (Dimitrov et al., 2007; Tsutsui et al., 2008; Baker et al., 2012; Han et al., 2013, 2014; Piao et al., 2015). Neutralization of a countercharge (D164) in the S2 helix also enhances responsiveness to negative voltages (Piao et al., 2015). By increasing sensitivity to hyperpolarization, these mutations serve to place the $V_{1/2}$ closer to the resting membrane potential. In practice, however, $V_{1/2}$ is highly variable across GEVIs and in many probes, still leans toward depolarization (∼−35 to −3 mV) (Tsutsui et al., 2008; Jin et al., 2012; Piao et al., 2015). The discrepancy suggests that additional factors such as the coupling between the VSD and FP may play a role in determining the voltage dependence of optical responses.

Aside from negative shifts, the slope of the $\Delta V/\Delta F$ curve is another indicator of a probe's sensitivity across different voltages. For instance, a probe with a large slope that exhibits a large $\Delta F$ for small voltage fluctuations, may be useful for monitoring subthreshold voltage changes, whereas, a GEVI with a smaller slope, showing the same absolute $\Delta F$ but upon larger voltage changes may be appropriate for detecting spikes. At least one factor that seems to affect the slope of the $\Delta V/\Delta F$ curve is the presence of charged residues in S2 (Piao et al., 2015). However, further studies are required to better understand the voltage dependence of optical responses to be able to better tailor GEVIs to meet specific experimental needs.

## CONCLUSION

In the two decades since their discovery, we have begun to understand the challenges associated with GEVI engineering and are striving toward making better probes with enhanced membrane expression, voltage sensitivities and SNR, while also tailoring their speed and dynamic voltage range to fulfill experimental needs. Because each GEVI comes with its own unique advantages and serves distinct purposes in the laboratory, it may be hard to envision an ideal probe that combines the best qualities of all existing probes and provides a unanimous solution for all experimental demands. The goal of GEVI development instead should be to capitalize on a given probe's potential and maximize its utility by strategic and rigorous engineering.

Genetically encoded voltage indicators engineering involves at least three steps – development, delivery and diagnosis. The development starts with analyzing protein crystal structures, where available, and sifting through large volumes of literature to design a preliminary scaffold. The genetic sequence of the putative voltage indicator then needs to be engineered by directed evolution, and the mutants tested iteratively for their performance. While in the past, low to moderate-throughput efforts have focused on manual hierarchical screening for brightness and voltage responsiveness, significant strides have been made to automate these processes and improve throughput. It is now possible to democratize voltage engineering using robotic systems and serially optimize millions of variants for multiple parameters such as brightness, membrane localization and voltage sensitivity (Piatkevich et al., 2018). Likewise, in our laboratory, we have developed semi-automated microscopic systems that are equipped with field electrodes and sensitive detectors to simultaneously optimize indicator constructs in a 96-well plate format for voltage responses, brightness and localization in high throughput and high content (Kannan et al., 2018).

Once a probe is adequately optimized for reporting neuronal activity and characterized in cell culture, the next step is to deliver it in animals to monitor its usefulness in intact circuits *in vivo*. This can be accomplished by injecting recombinant viruses or electroporating plasmid DNA, encoding the engineered GEVI. The choice of promoter, use of inducible regulators of gene expression, and timing of gene delivery can target indicator expression to specific cell types at defined stages of development.

The last step is diagnosis. Although much of the innovation happens early on during discovery, diagnosis is perhaps the most creative phase of GEVI development. It involves designing an experimental paradigm which allows one to explore the entire gamut of applications where an indicator may be of use. A probe may be used as a reporter of spontaneous or stimulus-evoked activity, developmental or experience-dependent plasticity, learning and memory or other forms of behavior. The surgical and optical setup may also need to be customized for the probe. Novel red and far-red indicators may need to be adequately demonstrated for their ability to be multiplexed with blue-shifted optogenetic tools and other types of indicators with minimal optical cross-talk.

Genetically encoded voltage indicators engineering requires a revisit to the fundamentals of voltage-dependent mechanisms, distinct from cellular calcium signaling, and an understanding and appreciation of the advantages of voltage probes to inspire us during the arduous process of innovation. Considering the steady advances in probe engineering and anticipated developments in imaging technologies, we are probably closer to our destination now than ever before.

## AUTHOR CONTRIBUTIONS

MK, GV, and VP wrote the manuscript. MK and GV prepared the figures.

## REFERENCES

Abdelfattah, A. S., Farhi, S. L., Zhao, Y., Brinks, D., Zou, P., Ruangkittisakul, A., et al. (2016). A bright and fast red fluorescent protein voltage indicator that reports neuronal activity in organotypic brain slices. *J. Neurosci.* 36, 2458–2472. doi: 10.1523/JNEUROSCI.3484-15.2016

Akemann, W., Mutoh, H., Perron, A., Park, Y. K., Iwamoto, Y., and Knopfel, T. (2012). Imaging neural circuit dynamics with a voltage-sensitive fluorescent protein. *J. Neurophysiol.* 108, 2323–2337. doi: 10.1152/jn.00452.2012

Akerboom, J., Carreras Calderon, N., Tian, L., Wabnig, S., Prigge, M., Tolo, J., et al. (2013). Genetically encoded calcium indicators for multi-color neural activity imaging and combination with optogenetics. *Front. Mol. Neurosci.* 6:2. doi: 10.3389/fnmol.2013.00002

Akerboom, J., Chen, T. W., Wardill, T. J., Tian, L., Marvin, J. S., Mutlu, S., et al. (2012). Optimization of a GCaMP calcium indicator for neural activity imaging. *J. Neurosci.* 32, 13819–13840. doi: 10.1523/JNEUROSCI.2601-12.2012

Al-Juboori, S. I., Dondzillo, A., Stubblefield, E. A., Felsen, G., Lei, T. C., and Klug, A. (2013). Light scattering properties vary across different regions of the adult mouse brain. *PLoS One* 8:e067626. doi: 10.1371/journal.pone.0067626

Arrenberg, A. B., Del Bene, F., and Baier, H. (2009). Optical control of zebrafish behavior with halorhodopsin. *Proc. Natl. Acad. Sci. U.S.A.* 106, 17968–17973. doi: 10.1073/pnas.0906252106

Ataka, K., and Pieribone, V. A. (2002). A genetically targetable fluorescent probe of channel gating with rapid kinetics. *Biophys. J.* 82, 509–516. doi: 10.1016/S0006-3495(02)75415-5

Bajar, B. T., Wang, E. S., Lam, A. J., Kim, B. B., Jacobs, C. L., Howe, E. S., et al. (2016). Improving brightness and photostability of green and red fluorescent proteins for live cell imaging and FRET reporting. *Sci. Rep.* 6:20889. doi: 10.1038/srep20889

Baker, B. J., Jin, L., Han, Z., Cohen, L. B., Popovic, M., Platisa, J., et al. (2012). Genetically encoded fluorescent voltage sensors using the voltage-sensing domain of *Nematostella* and danio phosphatases exhibit fast kinetics. *J. Neurosci. Methods* 208, 190–196. doi: 10.1016/j.jneumeth.2012.05.016

Baker, B. J., Lee, H., Pieribone, V. A., Cohen, L. B., Isacoff, E. Y., Knopfel, T., et al. (2007). Three fluorescent protein voltage sensors exhibit low plasma membrane expression in mammalian cells. *J. Neurosci. Methods* 161, 32–38. doi: 10.1016/j.jneumeth.2006.10.005

Barnett, L., Platisa, J., Popovic, M., Pieribone, V. A., and Hughes, T. (2012). A fluorescent, genetically-encoded voltage probe capable of resolving action potentials. *PLoS One* 7:e043454. doi: 10.1371/journal.pone.0043454

Brinks, D., Klein, A. J., and Cohen, A. E. (2015). Two-photon lifetime imaging of voltage indicating proteins as a probe of absolute membrane voltage. *Biophys. J.* 109, 914–921. doi: 10.1016/j.bpj.2015.07.038

Buzsaki, G. (2004). Large-scale recording of neuronal ensembles. *Nat. Neurosci.* 7, 446–451. doi: 10.1038/nn1233

Cao, G., Platisa, J., Pieribone, V. A., Raccuglia, D., Kunst, M., and Nitabach, M. N. (2013). Genetically targeted optical electrophysiology in intact neural circuits. *Cell* 154, 904–913. doi: 10.1016/j.cell.2013.07.027

Carandini, M., Shimaoka, D., Rossi, L. F., Sato, T. K., Benucci, A., and Knopfel, T. (2015). Imaging the awake visual cortex with a genetically encoded voltage indicator. *J. Neurosci.* 35, 53–63. doi: 10.1523/JNEUROSCI.0594-14.2015

Chamberland, S., Yang, H. H., Pan, M. M., Evans, S. W., Guan, S., Chavarha, M., et al. (2017). Fast two-photon imaging of subcellular voltage dynamics in neuronal tissue with genetically encoded indicators. *eLife* 6:e25690. doi: 10.7554/eLife.25690

Chen, Q., Cichon, J., Wang, W., Qiu, L., Lee, S. J., Campbell, N. R., et al. (2012). Imaging neural activity using Thy1-GCaMP transgenic mice. *Neuron* 76, 297–308. doi: 10.1016/j.neuron.2012.07.011

Chen, T. W., Wardill, T. J., Sun, Y., Pulver, S. R., Renninger, S. L., Baohan, A., et al. (2013). Ultrasensitive fluorescent proteins for imaging neuronal activity. *Nature* 499, 295–300. doi: 10.1038/nature12354

Chu, J., Oh, Y., Sens, A., Ataie, N., Dana, H., Macklin, J. J., et al. (2016). A bright cyan-excitable orange fluorescent protein facilitates dual-emission microscopy and enhances bioluminescence imaging in vivo. *Nat. Biotechnol.* 34, 760–767. doi: 10.1038/nbt.3550

Dana, H., Chen, T. W., Hu, A., Shields, B. C., Guo, C., Looger, L. L., et al. (2014). Thy1-GCaMP6 transgenic mice for neuronal population imaging in vivo. *PLoS One* 9:e0108697. doi: 10.1371/journal.pone.0108697

De Marco Garcia, N. V., and Fishell, G. (2014). Subtype-selective electroporation of cortical interneurons. *J. Vis. Exp.* 90:e51518. doi: 10.3791/51518

Denk, W., Yuste, R., Svoboda, K., and Tank, D. W. (1996). Imaging calcium dynamics in dendritic spines. *Curr. Opin. Neurobiol.* 6, 372–378. doi: 10.1016/S0959-4388(96)80122-X

Dimitrov, D., He, Y., Mutoh, H., Baker, B. J., Cohen, L., Akemann, W., et al. (2007). Engineering and characterization of an enhanced fluorescent protein voltage sensor. *PLoS One* 2:e0440. doi: 10.1371/journal.pone.0000440

Flock, S. T., Jacques, S. L., Wilson, B. C., Star, W. M., and Van Gemert, M. J. (1992). Optical properties of intralipid: a phantom medium for light propagation studies. *Lasers Surg. Med.* 12, 510–519. doi: 10.1002/lsm.1900120510

Flusberg, B. A., Nimmerjahn, A., Cocker, E. D., Mukamel, E. A., Barretto, R. P., Ko, T. H., et al. (2008). High-speed, miniaturized fluorescence microscopy in freely moving mice. *Nat. Methods* 5, 935–938. doi: 10.1038/nmeth.1256

Flytzanis, N. C., Bedbrook, C. N., Chiu, H., Engqvist, M. K., Xiao, C., Chan, K. Y., et al. (2014). Archaerhodopsin variants with enhanced voltage-sensitive fluorescence in mammalian and *Caenorhabditis elegans* neurons. *Nat. Commun.* 5:4894. doi: 10.1038/ncomms5894

Gong, Y., Huang, C., Li, J. Z., Grewe, B. F., Zhang, Y., Eismann, S., et al. (2015). High-speed recording of neural spikes in awake mice and flies with a fluorescent voltage sensor. *Science* 350, 1361–1366. doi: 10.1126/science.aab0810

Gong, Y., Li, J. Z., and Schnitzer, M. J. (2013). Enhanced archaerhodopsin fluorescent protein voltage indicators. *PLoS One* 8:e066959. doi: 10.1371/journal.pone.0066959

Gong, Y., Wagner, M. J., Li, J. Z., and Schnitzer, M. J. (2014). Imaging neural spiking in brain tissue using FRET-opsin protein voltage sensors. *Nat. Commun.* 5:3674. doi: 10.1038/ncomms4674

Gradinaru, V., Thompson, K. R., and Deisseroth, K. (2008). eNpHR: a natronomonas halorhodopsin enhanced for optogenetic applications. *Brain Cell Biol.* 36, 129–139. doi: 10.1007/s11068-008-9027-6

Gradinaru, V., Zhang, F., Ramakrishnan, C., Mattis, J., Prakash, R., Diester, I., et al. (2010). Molecular and cellular approaches for diversifying and extending optogenetics. *Cell* 141, 154–165. doi: 10.1016/j.cell.2010.02.037

Han, Z., Jin, L., Chen, F., Loturco, J. J., Cohen, L. B., Bondar, A., et al. (2014). Mechanistic studies of the genetically encoded fluorescent protein voltage probe ArcLight. *PLoS One* 9:e0113873. doi: 10.1371/journal.pone.0113873

Han, Z., Jin, L., Platisa, J., Cohen, L. B., Baker, B. J., and Pieribone, V. A. (2013). Fluorescent protein voltage probes derived from ArcLight that respond to membrane voltage changes with fast kinetics. *PLoS One* 8:e081295. doi: 10.1371/journal.pone.0081295

Hochbaum, D. R., Zhao, Y., Farhi, S. L., Klapoetke, N., Werley, C. A., Kapoor, V., et al. (2014). All-optical electrophysiology in mammalian neurons using engineered microbial rhodopsins. *Nat. Methods* 11, 825–833. doi: 10.1038/nmeth.3000

Huber, D., Gutnisky, D. A., Peron, S., O'connor, D. H., Wiegert, J. S., Tian, L., et al. (2012). Multiple dynamic representations in the motor cortex during sensorimotor learning. *Nature* 484, 473–478. doi: 10.1038/nature11039

Jin, L., Han, Z., Platisa, J., Wooltorton, J. R., Cohen, L. B., and Pieribone, V. A. (2012). Single action potentials and subthreshold electrical events imaged in neurons with a fluorescent protein voltage probe. *Neuron* 75, 779–785. doi: 10.1016/j.neuron.2012.06.040

Jun, J. J., Steinmetz, N. A., Siegle, J. H., Denman, D. J., Bauza, M., Barbarits, B., et al. (2017). Fully integrated silicon probes for high-density recording of neural activity. *Nature* 551, 232–236. doi: 10.1038/nature24636

Kang, B. E., and Baker, B. J. (2016). Pado, a fluorescent protein with proton channel activity can optically monitor membrane potential, intracellular pH, and map gap junctions. *Sci. Rep.* 6:23865. doi: 10.1038/srep23865

Kannan, M., Vasan, G., Huang, C., Haziza, S., Li, J. Z., Inan, H., et al. (2018). Fast, in vivo voltage imaging using a red fluorescent indicator. *Nat. Methods* 15, 1108–1116. doi: 10.1038/s41592-018-0188-7

Katona, G., Szalay, G., Maak, P., Kaszas, A., Veress, M., Hillier, D., et al. (2012). Fast two-photon in vivo imaging with three-dimensional random-access scanning in large tissue volumes. *Nat. Methods* 9, 201–208. doi: 10.1038/nmeth.1851

Klein, M., Afonso, B., Vonner, A. J., Hernandez-Nunez, L., Berck, M., Tabone, C. J., et al. (2015). Sensory determinants of behavioral dynamics in drosophila thermotaxis. *Proc. Natl. Acad. Sci. U.S.A.* 112, E220–E229. doi: 10.1073/pnas.1416212112

Kohout, S. C., Ulbrich, M. H., Bell, S. C., and Isacoff, E. Y. (2008). Subunit organization and functional transitions in Ci-VSP. *Nat. Struct. Mol. Biol.* 15, 106–108. doi: 10.1038/nsmb1320

Kovacevic, I., Orozco, J. M., and Cram, E. J. (2013). Filamin and phospholipase C-epsilon are required for calcium signaling in the *Caenorhabditis elegans* spermatheca. *PLoS Genet.* 9:e1003510. doi: 10.1371/journal.pgen.1003510

Kunst, M., Hughes, M. E., Raccuglia, D., Felix, M., Li, M., Barnett, G., et al. (2014). Calcitonin gene-related peptide neurons mediate sleep-specific circadian output in Drosophila. *Curr. Biol.* 24, 2652–2664. doi: 10.1016/j.cub.2014.09.077

Li, Q., Wanderling, S., Paduch, M., Medovoy, D., Singharoy, A., Mcgreevy, R., et al. (2014). Structural mechanism of voltage-dependent gating in an isolated voltage-sensing domain. *Nat. Struct. Mol. Biol.* 21, 244–252. doi: 10.1038/nsmb.2768

Lippincott-Schwartz, J., Roberts, T. H., and Hirschberg, K. (2000). Secretory protein trafficking and organelle dynamics in living cells. *Annu. Rev. Cell Dev. Biol.* 16, 557–589. doi: 10.1146/annurev.cellbio.16.1.557

Lur, G., Vinck, M. A., Tang, L., Cardin, J. A., and Higley, M. J. (2016). Projection-specific visual feature encoding by layer 5 cortical subnetworks. *Cell Rep.* 14, 2538–2545. doi: 10.1016/j.celrep.2016.02.050

Maclaurin, D., Venkatachalam, V., Lee, H., and Cohen, A. E. (2013). Mechanism of voltage-sensitive fluorescence in a microbial rhodopsin. *Proc. Natl. Acad. Sci. U.S.A.* 110, 5939–5944. doi: 10.1073/pnas.1215595110

Mainen, Z. F., Malinow, R., and Svoboda, K. (1999). Synaptic calcium transients in single spines indicate that NMDA receptors are not saturated. *Nature* 399, 151–155. doi: 10.1038/20187

Mannuzzu, L. M., Moronne, M. M., and Isacoff, E. Y. (1996). Direct physical measure of conformational rearrangement underlying potassium channel gating. *Science* 271, 213–216. doi: 10.1126/science.271.5246.213

Mao, T., O'connor, D. H., Scheuss, V., Nakai, J., and Svoboda, K. (2008). Characterization and subcellular targeting of GCaMP-type genetically-encoded calcium indicators. *PLoS One* 3:e01796. doi: 10.1371/journal.pone.0001796

Marshall, J. D., Li, J. Z., Zhang, Y., Gong, Y., St-Pierre, F., Lin, M. Z., et al. (2016). Cell-type-specific optical recording of membrane voltage dynamics in freely moving mice. *Cell* 167, 1650–1662.e15. doi: 10.1016/j.cell.2016.11.021

Mittmann, W., Wallace, D. J., Czubayko, U., Herb, J. T., Schaefer, A. T., Looger, L. L., et al. (2011). Two-photon calcium imaging of evoked activity from L5 somatosensory neurons in vivo. *Nat. Neurosci.* 14, 1089–1093. doi: 10.1038/nn.2879

Miyawaki, A., Llopis, J., Heim, R., Mccaffery, J. M., Adams, J. A., Ikura, M., et al. (1997). Fluorescent indicators for Ca2+ based on green fluorescent proteins and calmodulin. *Nature* 388, 882–887. doi: 10.1038/42264

Mukamel, E. A., Nimmerjahn, A., and Schnitzer, M. J. (2009). Automated analysis of cellular signals from large-scale calcium imaging data. *Neuron* 63, 747–760. doi: 10.1016/j.neuron.2009.08.009

Murata, Y., Iwasaki, H., Sasaki, M., Inaba, K., and Okamura, Y. (2005). Phosphoinositide phosphatase activity coupled to an intrinsic voltage sensor. *Nature* 435, 1239–1243. doi: 10.1038/nature03650

Nagai, T., Yamada, S., Tominaga, T., Ichikawa, M., and Miyawaki, A. (2004). Expanded dynamic range of fluorescent indicators for Ca(2+) by circularly permuted yellow fluorescent proteins. *Proc. Natl. Acad. Sci. U.S.A.* 101, 10554–10559. doi: 10.1073/pnas.0400417101

Palmer, A. E., Giacomello, M., Kortemme, T., Hires, S. A., Lev-Ram, V., Baker, D., et al. (2006). Ca2+ indicators based on computationally redesigned calmodulin-peptide pairs. *Chem. Biol.* 13, 521–530. doi: 10.1016/j.chembiol.2006.03.007

Parker, J. L., and Newstead, S. (2016). Membrane protein crystallisation: current trends and future perspectives. *Adv. Exp. Med. Biol.* 922, 61–72. doi: 10.1007/978-3-319-35072-1_5

Perron, A., Mutoh, H., Akemann, W., Gautam, S. G., Dimitrov, D., Iwamoto, Y., et al. (2009). Second and third generation voltage-sensitive fluorescent proteins for monitoring membrane potential. *Front. Mol. Neurosci.* 2:5. doi: 10.3389/neuro.02.005.2009

Piao, H. H., Rajakumar, D., Kang, B. E., Kim, E. H., and Baker, B. J. (2015). Combinatorial mutagenesis of the voltage-sensing domain enables the optical resolution of action potentials firing at 60 Hz by a genetically encoded fluorescent sensor of membrane potential. *J. Neurosci.* 35, 372–385. doi: 10.1523/JNEUROSCI.3008-14.2015

Piatkevich, K. D., Hulit, J., Subach, O. M., Wu, B., Abdulla, A., Segall, J. E., et al. (2010). Monomeric red fluorescent proteins with a large Stokes shift. *Proc. Natl. Acad. Sci. U.S.A.* 107, 5369–5374. doi: 10.1073/pnas.0914365107

Piatkevich, K. D., Jung, E. E., Straub, C., Linghu, C., Park, D., Suk, H. J., et al. (2018). A robotic multidimensional directed evolution approach applied to fluorescent voltage reporters. *Nat. Chem. Biol.* 14, 352–360. doi: 10.1038/s41589-018-0004-9

Piatkevich, K. D., Malashkevich, V. N., Morozova, K. S., Nemkovich, N. A., Almo, S. C., and Verkhusha, V. V. (2013). Extended stokes shift in fluorescent proteins: chromophore-protein interactions in a near-infrared TagRFP675 variant. *Sci. Rep.* 3:1847. doi: 10.1038/srep01847

Piston, D. W. (1998). Choosing objective lenses: the importance of numerical aperture and magnification in digital optical microscopy. *Biol. Bull.* 195, 1–4. doi: 10.2307/1542768

Platisa, J., Vasan, G., Yang, A., and Pieribone, V. A. (2017). Directed evolution of key residues in fluorescent protein inverses the polarity of voltage sensitivity in the genetically encoded indicator arclight. *ACS Chem. Neurosci.* 8, 513–523. doi: 10.1021/acschemneuro.6b00234

Romoser, V. A., Hinkle, P. M., and Persechini, A. (1997). Detection in living cells of Ca2+-dependent changes in the fluorescence emission of an indicator composed of two green fluorescent protein variants linked by a calmodulin-binding sequence. A new class of fluorescent indicators. *J. Biol. Chem.* 272, 13270–13274. doi: 10.1074/jbc.272.20.13270

Rothermel, M., and Wachowiak, M. (2014). Functional imaging of cortical feedback projections to the olfactory bulb. *Front. Neural Circuits* 8:73. doi: 10.3389/fncir.2014.00073

Sakai, R., Repunte-Canonigo, V., Raj, C. D., and Knopfel, T. (2001). Design and characterization of a DNA-encoded, voltage-sensitive fluorescent protein. *Eur. J. Neurosci.* 13, 2314–2318. doi: 10.1046/j.0953-816x.2001.01617.x

Seoh, S. A., Sigg, D., Papazian, D. M., and Bezanilla, F. (1996). Voltage-sensing residues in the S2 and S4 segments of the Shaker K+ channel. *Neuron* 16, 1159–1167.

Siegel, M. S., and Isacoff, E. Y. (1997). A genetically encoded optical probe of membrane voltage. *Neuron* 19, 735–741. doi: 10.1016/S0896-6273(00)80955-1

Smetters, D., Majewska, A., and Yuste, R. (1999). Detecting action potentials in neuronal populations with calcium imaging. *Methods* 18, 215–221. doi: 10.1006/meth.1999.0774

Spira, M. E., and Hai, A. (2013). Multi-electrode array technologies for neuroscience and cardiology. *Nat. Nanotechnol.* 8, 83–94. doi: 10.1038/nnano.2012.265

Storace, D. A., Braubach, O. R., Jin, L., Cohen, L. B., and Sung, U. (2015). Monitoring brain activity with protein voltage and calcium sensors. *Sci. Rep.* 5:10212. doi: 10.1038/srep10212

St-Pierre, F., Marshall, J. D., Yang, Y., Gong, Y., Schnitzer, M. J., and Lin, M. Z. (2014). High-fidelity optical reporting of neuronal electrical activity with an ultrafast fluorescent voltage sensor. *Nat. Neurosci.* 17, 884–889. doi: 10.1038/nn.3709

Tian, L., Hires, S. A., and Looger, L. L. (2012). Imaging neuronal activity with genetically encoded calcium indicators. *Cold Spring Harb. Protoc.* 2012, 647–656. doi: 10.1101/pdb.top069609

Tian, L., Hires, S. A., Mao, T., Huber, D., Chiappe, M. E., Chalasani, S. H., et al. (2009). Imaging neural activity in worms, flies and mice with improved GCaMP calcium indicators. *Nat. Methods* 6, 875–881. doi: 10.1038/nmeth.1398

Tsutsui, H., Karasawa, S., Okamura, Y., and Miyawaki, A. (2008). Improving membrane voltage measurements using FRET with new fluorescent proteins. *Nat. Methods* 5, 683–685. doi: 10.1038/nmeth.1235

Villalba-Galea, C. A., Sandtner, W., Dimitrov, D., Mutoh, H., Knopfel, T., and Bezanilla, F. (2009). Charge movement of a voltage-sensitive fluorescent protein. *Biophys. J.* 96, L19–L21. doi: 10.1016/j.bpj.2008.11.003

Wachowiak, M., Economo, M. N., Diaz-Quesada, M., Brunert, D., Wesson, D. W., White, J. A., et al. (2013). Optical dissection of odor information processing in vivo using GCaMPs expressed in specified cell types of the olfactory bulb. *J. Neurosci.* 33, 5285–5300. doi: 10.1523/JNEUROSCI.4824-12.2013

Wang, C., and Mei, L. (2013). In utero electroporation in mice. *Methods Mol. Biol.* 1018, 151–163. doi: 10.1007/978-1-62703-444-9_15

Wilt, B. A., Fitzgerald, J. E., and Schnitzer, M. J. (2013). Photon shot noise limits on optical detection of neuronal spikes and estimation of spike timing. *Biophys. J.* 104, 51–62. doi: 10.1016/j.bpj.2012.07.058

Yang, H. H., St-Pierre, F., Sun, X., Ding, X., Lin, M. Z., and Clandinin, T. R. (2016). Subcellular imaging of voltage and calcium signals reveals neural processing in vivo. *Cell* 166, 245–257. doi: 10.1016/j.cell.2016.05.031

Yang, N., George, A. L. Jr., and Horn, R. (1996). Molecular basis of charge movement in voltage-gated sodium channels. *Neuron* 16, 113–122. doi: 10.1016/S0896-6273(00)80028-8

Yoshihara, M. (2012). Simultaneous recording of calcium signals from identified neurons and feeding behavior of *Drosophila melanogaster*. *J. Vis. Exp.* 62:3625. doi: 10.3791/3625

Zhao, Y., Araki, S., Wu, J., Teramoto, T., Chang, Y. F., Nakano, M., et al. (2011). An expanded palette of genetically encoded Ca(2)(+) indicators. *Science* 333, 1888–1891. doi: 10.1126/science.1208592

Zhu, Y., Xu, J., Hauswirth, W. W., and Devries, S. H. (2014). Genetically targeted binary labeling of retinal neurons. *J. Neurosci.* 34, 7845–7861. doi: 10.1523/JNEUROSCI.2960-13.2014

Zou, P., Zhao, Y., Douglass, A. D., Hochbaum, D. R., Brinks, D., Werley, C. A., et al. (2014). Bright and fast multicoloured voltage reporters via electrochromic FRET. *Nat. Commun.* 5:4625. doi: 10.1038/ncomms5625

**Conflict of Interest Statement:** The authors declare that the research was conducted in the absence of any commercial or financial relationships that could be construed as a potential conflict of interest.

frontiers in Cellular Neuroscience

ORIGINAL RESEARCH
published: 15 March 2019
doi: 10.3389/fncel.2019.00098

# Calcium Dynamics in Dendrites of Hippocampal CA1 Interneurons in Awake Mice

*Ruggiero Francavilla, Vincent Villette†, Olivier Martel and Lisa Topolnik**

*Department of Biochemistry, Microbiology and Bio-informatics, Faculty of Science and Engineering, Neuroscience Axis, CHU de Québec Research Center (CHUL), Laval University, Québec, PQ, Canada*

Hippocampal inhibitory interneurons exhibit a large diversity of dendritic $Ca^{2+}$ mechanisms that are involved in the induction of Hebbian and anti-Hebbian synaptic plasticity. High resolution imaging techniques allowed examining somatic $Ca^{2+}$ signals and, accordingly, the recruitment of hippocampal interneurons in awake behaving animals. However, little is still known about dendritic $Ca^{2+}$ activity in interneurons during different behavioral states. Here, we used two-photon $Ca^{2+}$ imaging in mouse hippocampal CA1 interneurons to reveal $Ca^{2+}$ signal patterns in interneuron dendrites during animal locomotion and immobility. Despite overall variability in dendritic $Ca^{2+}$ transients (CaTs) across different cells and dendritic branches, we report consistent behavior state-dependent organization of $Ca^{2+}$ signaling in interneurons. As such, spreading regenerative CaTs dominated in dendrites during locomotion, whereas both spreading and localized $Ca^{2+}$ signals were seen during immobility. Thus, these data indicate that while animal locomotion is associated with widespread $Ca^{2+}$ elevations in interneuron dendrites that may reflect regenerative activity, local CaTs that may be related to synaptic activity become apparent during animal quiet state.

**Keywords: GABAergic inhibition, interneuron, dendrite, calcium, excitatory current, regenerative activity, behavior**

***Edited by:***
*Marco Canepari,*
*UMR5588 Laboratoire Interdisciplinaire de Physique (LIPhy), France*

***Reviewed by:***
*Rory McQuiston,*
*Virginia Commonwealth University, United States*
*Veronica Egger,*
*University of Regensburg, Germany*

****Correspondence:***
*Lisa Topolnik*
*Lisa.Topolnik@bcm.ulaval.ca*

***†Present address:***
*Vincent Villette*
*Institut de Biologie de l'École Normale Supérieure (IBENS), École Normale Supérieure, CNRS, INSERM, PSL Research University, Paris, France*

***Received:*** *02 November 2018*
***Accepted:*** *27 February 2019*
***Published:*** *15 March 2019*

***Citation:***
*Francavilla R, Villette V, Martel O and Topolnik L (2019) Calcium Dynamics in Dendrites of Hippocampal CA1 Interneurons in Awake Mice. Front. Cell. Neurosci. 13:98. doi: 10.3389/fncel.2019.00098*

## INTRODUCTION

Neuronal dendrites exhibit a large variety of voltage- and ligand-gated ion conductances and, therefore, may operate as independent signaling devices (Branco and Häusser, 2011). Calcium ($Ca^{2+}$) signaling represents an important aspect of dendritic integration. It may have different spatial and temporal ranges of action, and can exert various functions from induction of synaptic plasticity and local tuning of neuronal firing to the regulation of the expression of genes involved in neurodegenerative processes (Verkhratsky, 2005; Higley and Sabatini, 2008; Camiré and Topolnik, 2012; Camiré et al., 2012; Topolnik, 2012). Due to methodological limitations, our current knowledge about the functional organization of dendritic $Ca^{2+}$ signals stems mostly from experiments on glutamatergic principal cells (PCs; Regehr and Tank, 1990; Markram and Sakmann, 1994; Schiller et al., 1997; Golding et al., 2002; Losonczy and Magee, 2006; Sheffield and Dombeck, 2015; Sheffield et al., 2017). In hippocampal CA1 area, the dendrites of PCs express voltage-gated $Ca^{2+}$ and sodium ($Na^+$) channels and NMDA receptors. These mechanisms are involved in generation of dendritic regenerative activity in form of back-propagating somatic action potentials (bAPs) and local $Ca^{2+}$ and $Na^+$ spikes generated in single or multiple dendritic branches (Spruston et al., 1995; Magee and Johnston, 1997; Ariav et al., 2003; Gasparini et al., 2004; Losonczy and Magee, 2006; Grienberger et al., 2014). Activated by spatially and temporally coincident patterns of activity, these mechanisms may provide for membrane depolarization and supralinear $Ca^{2+}$ signal required for induction of Hebbian forms of synaptic plasticity and important for place field firing (Magee and Johnston, 1997; Golding et al., 2002; Sheffield and Dombeck, 2015; Sheffield et al., 2017).

Local circuit GABAergic inhibitory interneurons in hippocampal regions control the integration and transfer of information during different network and behavioral states (Klausberger and Somogyi, 2008; Somogyi, 2010; Pelkey et al., 2017). These cells exhibit a large repertoire of voltage- and ligand-gated $Ca^{2+}$ mechanisms, which are regulated differentially by changes in pre- and postsynaptic activity, and provide a means for a highly dynamic and versatile regulation of synaptic plasticity (Topolnik et al., 2005, 2006, 2009; Evstratova et al., 2011; Camiré and Topolnik, 2014; Hainmueller et al., 2014). In most interneurons, bAPs and, accordingly, the $Ca^{2+}$ transients (CaTs) evoked by bAPs (bAP-CaTs) decline with distance from the soma due to a large $K^+$ and low $Na^+$ channel density (Aponte et al., 2008; Hu et al., 2010; Evstratova et al., 2011; Camiré and Topolnik, 2014). This means that only proximal synapses may be influenced by bAPs and are likely to exhibit the spike-timing-dependent forms of plasticity (Sjöström et al., 2008). This situation, however, may change rapidly, dependent on the level of on-going activity. In fact, bAP-CaTs can be boosted locally on a different time scale by the activation of additional voltage- and ligand-dependent $Ca^{2+}$ mechanisms (Topolnik et al., 2009; Evstratova et al., 2011; Chiovini et al., 2014). Moreover, some CA1 interneurons, for example fast-spiking parvalbumin-expressing cells (including basket and bistratified cells) can exhibit large amplitude $Ca^{2+}$ elevations in the absence of voltage-dependent dendritic mechanisms. In particular, we showed that $Ca^{2+}$ entry through GluA2-lacking $Ca^{2+}$-permeable AMPA receptors (CP-AMPARs) followed by $Ca^{2+}$ release from internal stores is important for generating the supralinear $Ca^{2+}$ signals, which control the direction of long-term plasticity at excitatory synapses located distally (Camiré and Topolnik, 2014). Other cell types, for example the CA1 *oriens lacunosum-moleculare* (OLM) cells, may have a relatively high density of $Na^+$ channels in their dendrites and, subsequently, exhibit more wide-spread back-propagation of somatic APs (Topolnik et al., 2009) or even dendritic $Na^+$ spike initiation (Martina et al., 2000), which can be tightly controlled *via* dendritic inhibition (Tyan et al., 2014; Francavilla et al., 2015). Taken together, these studies reveal a highly dynamic nature of dendritic $Ca^{2+}$ signaling in interneurons. Yet, *in vivo* dendritic $Ca^{2+}$ activity in these cells received little attention (Katona et al., 2011; Chiovini et al., 2014), and its regulation and functional significance during different patterns of network oscillations and behavioral states remain to be explored in details.

To begin examining the functional aspects of interneuron dendritic computations *in vivo*, here we performed two-photon $Ca^{2+}$ imaging in CA1 *oriens/alveus* (O/A) interneurons of awake head-fixed animals running on a treadmill. We found that dendritic CaTs (dCaTs) exhibit the behavior-state fluctuations, such as regenerative activity during locomotion and dendrite-autonomous local signals during immobility. This state-dependent $Ca^{2+}$ signaling suggests that distinct forms of synaptic plasticity can be induced in interneurons of awake mice during different behavioral states.

## MATERIALS AND METHODS

### Mouse Surgery and Training

Experiments were performed on male C57BL/6 mice (P50–70) according to the procedures approved by the Animal Protection Committee of Université Laval (protocol #15-097-1). Mice were anesthetized deeply with ketamine/xylazine mixture (10/100 mg/kg) and fixed in a stereotaxic frame. A small (~0.5–1.0 mm) craniotomy was made over the hippocampus (AP: 2.1, ML: 1.8). For single cell dendritic imaging a low titer AAV1.Syn.GCaMP6f.WPRE.SV40 (Penn Vector Core) was diluted [1:4 in phosphate buffer saline (PBS, Gibco)] and injected (one injection of 100 nL) at a depth of ~1,250 μm below the dura surface, resulting in the expression of GCaMP6f in a sparse population of CA1 neurons (Chen et al., 2013).

After 4–6 days of recovery, a 3-day water restriction procedure was applied (0.8–1.0 mL/day) followed by a hippocampal window and head-plate implantation surgery (as described in Dombeck et al., 2010; Villette et al., 2017). Briefly, a bottom glass cannula (2 mm diameter) was inserted on top of dorsal hippocampus after cortex aspiration and secured with kwick-sil at tissue interface and Superbond at the skull level. Head plate was oriented using a 4-axis micromanipulator (MX10L, Siskiyou) and fixed with several layers of Superbond and dental cement (Villette et al., 2017). For dorsal hippocampus, a 7–13° medio-lateral angle was applied. Mice were allowed to recover for several days with post-operative pain killer treatment (Buprenorphine, 0.1 mg/kg, 48 h).

Behavioral handling with head fixation and training in a circular treadmill system (one ~10–15 min session per mouse per day) began ~5 days after window implantation and continued until mice routinely ran back and forth and demonstrated stable running speed values as described previously (Villette et al., 2017). Mouse locomotion speed and direction on the treadmill were monitored using an optical quadrature encoder (HEDS-5645#A06, Avago Technology). The immobility periods were determined as periods with no animal motion for at least 3 s. The locomotion periods were defined as periods of animal locomotion with a speed >2.0 cm/s for at least 3 s. Data was recorded using a Digidata1440A (Molecular Devices) data acquisition system (Clampex 10.2), which allowed synchronizing the animal speed and two-photon image frame timing (using the external trigger at 10,000 sampling frequency) and an AxoScope software (v10.5, Axon Instrument).

### Two-Photon Imaging of Interneuron Soma and Dendrites

Two-photon imaging was performed using Leica SP5 two-photon confocal microscope, the Ti:Sapphire laser (Chameleon Ultra II, Coherent) tuned to 900 nm and a 25× objective (0.95 NA, 2.5 mm working distance, Leica Microsystems). The laser power was modulated using a Pockels cell and reached at the sample (after the objective) 10–75 mW. Green GCaMP6f fluorescence was routed to external photomultiplier tubes (PMTs) (non-descanned detectors, Leica Microsystems). The Leica LAS software was used for microscope control and image acquisition. Image series (128 × 128 pixels, 0.5 ms per line field of view of 207 × 207 μm) in each plane were acquired at 47 Hz in single plane acquisitions. Imaging sessions lasted up to 30 ± 15 min and then the mouse was placed back in its home cage. $Ca^{2+}$ imaging time-series were followed by z-series from each cell to obtain a detailed information on the imaged dendrites using the following parameters: 1 μm z-stack step size, 512 × 512 pixels per frame, 1 ms/line. The interneuron cell bodies were typically located 20–70 μm below the alveus surface.

## Data Analysis and Statistics

Analysis was performed using IgorPro (v.6.3, Wave Metrics) and custom scripts written in MatLab (The MathWorks). The time-series were motion corrected using whole frame cross-correlation, as described previously (Dombeck et al., 2010; Villette et al., 2017). Only dendrites that could be unambiguously traced back to soma were included in the analysis. Dendritic branches were traced off-line using Leica LAS software ($n$ = 10 interneurons; 11 cells were excluded from the analysis because of a high brain motion during morphological z-series preventing accurate dendrite tracing). The dendritic distance to soma was calculated along the dendrite using the maximal projections of morphological z-series.

For CaT analysis, regions of interest (ROIs) were drawn manually on the mean soma or dendrite images following the outline of the structure of interest, and traces of ΔF/F vs. time were generated for each ROI as previously described (Villette et al., 2017; Francavilla et al., 2018). All CaTs occurring during immobility or consistent runs (speed >2 cm/s; longer than 3 s) were included in the analysis. Both average CaTs for the entire period of immobility or run as well as peak CaTs during individual events were analyzed. The local event detection was performed semi-automatically using the TaroTools toolbox in IgorPro. First, all events with peak amplitude exceeding the mean ± 2 SD level of the ΔF/F trace were selected from both somatic and dendritic traces recorded simultaneously. Then ΔF/F traces obtained from soma and dendrites were aligned and local dCaTs were defined as those occurring in the absence of concomitant somatic CaTs (sCaTs) within a 25-ms window. Cross-correlation analysis in IgorPro was used for correlation of dendritic and sCaTs with speed. The data are presented as mean ± SEM. The sample size was determined in preliminary experiments in compliance with ethical guidelines to reduce the number of animals used. Statistical significance between groups was determined using a Student $t$-test (in case of normal data distribution) or Mann-Whitney test (if the distribution of data was not normal as reported by the Shapiro-Wilk test).

# RESULTS

To study dendritic $Ca^{2+}$ signals in hippocampal interneurons during different behavioral states, we performed chronic two-photon $Ca^{2+}$ imaging of CA1 O/A interneurons labeled with a genetically-encoded calcium indicator GCaMP6f in head-restrained mice running on a circular treadmill (**Figure 1A**). Interneurons were identified based on the soma location within CA1 O/A and horizontally oriented dendrites located within the same focal plane (**Figure 1B**). Therefore, all imaging and analysis were performed only on horizontally oriented O/A interneurons and their dendritic arbors (128 dendritic segments of 10 μm each from 39 branches, $n$ = 9 cells, 3.4 ± 0.3 min per interneuron per imaging session, one or two imaging sessions/cell, five mice) during immobility and locomotion. The imaging fields of view (207 × 207 μm) were selected to have in average 3–5 cells with clearly identifiable dendritic branches connected to the interneuron soma in the same focal plane (**Figure 1B**). The imaged dendritic branches had a mean length of 43.3 ± 5.1 μm from the soma (range: 7–145 μm; typical dendrite length in O/A interneurons ∼200 μm) with a mean of 3.0 ± 0.6 branching points (range: 0–8).

According to previous reports, sCaTs result mainly from the AP firing, where the number of underlying APs correlates with fluorescence change (Kerr et al., 2005; Greenberg et al., 2008; Tian et al., 2009; Chen et al., 2013; Sheffield and Dombeck, 2015; Sheffield et al., 2017). Thus, in line with previous reports on the phase-dependent recruitment of different types of O/A interneurons during locomotion and immobility (Lapray et al., 2012), most O/A interneurons showed sCaTs throughout different behavior states (**Figure 1C**). Moreover, the mean sCaTs were significantly higher during locomotion than during immobility ($P$ < 0.001; Mann-Whitney test; **Figure 1D**), consistent with phase-coupled rhythmic recruitment of O/A interneurons during theta oscillations associated with locomotion (Lapray et al., 2012; Katona et al., 2014; Lovett-Barron et al., 2014). This difference in the amplitude of sCaTs between the two behavioral states was not due to different basal somatic fluorescence ($F_0$; **Figure 1E**).

Similar to sCaTs, dCaTs were detected during both locomotion and immobility (**Figure 1C**). Most of our recordings have focused on proximal dendritic branches (5–50 μm from the soma, 59%) made by primary dendrites, with the rest being secondary and tertiary dendritic branches extending up to 145 μm from soma (**Figure 1F**). While the basal fluorescence $F_0$ was similar in dendrites during locomotion and immobility (**Figure 1E**), the amplitude of individual dCaTs varied across cell, individual dendritic segments and behavioral states (**Figure 1C**). The latter could not be associated with inter-cellular difference in GCaMP6f expression as variance in the basal fluorescence ($F_0$) was similar in soma and dendrites when compared between different cells and behavioral states ($sCaT_{Loc}$-$F_0$: CV = 0.41, $sCaT_{Imm}$-$F_0$: CV = 0.45, $dCaT_{Loc}$-$F_0$: CV = 0.39, $dCaT_{Loc}$-$F_0$: CV = 0.39; $n$ = 9 cells). Overall, like in soma, the average amplitude of dCaTs was significantly higher during locomotion ($dCaT_{Loc}$: $n$ = 128 segments/10 cells; $dCaT_{Imm}$: $n$ = 112 segments/nine cells; $P$ < 0.001; Mann-Whitney test; **Figure 1D**), but it was also considerably smaller than in soma ($P$ < 0.001; Mann-Whitney test; **Figure 1D**).

As CaTs in dendrites of O/A interneurons can result from activation of local excitatory inputs (Topolnik et al., 2005, 2006) and regenerative activity (spread of bAPs or

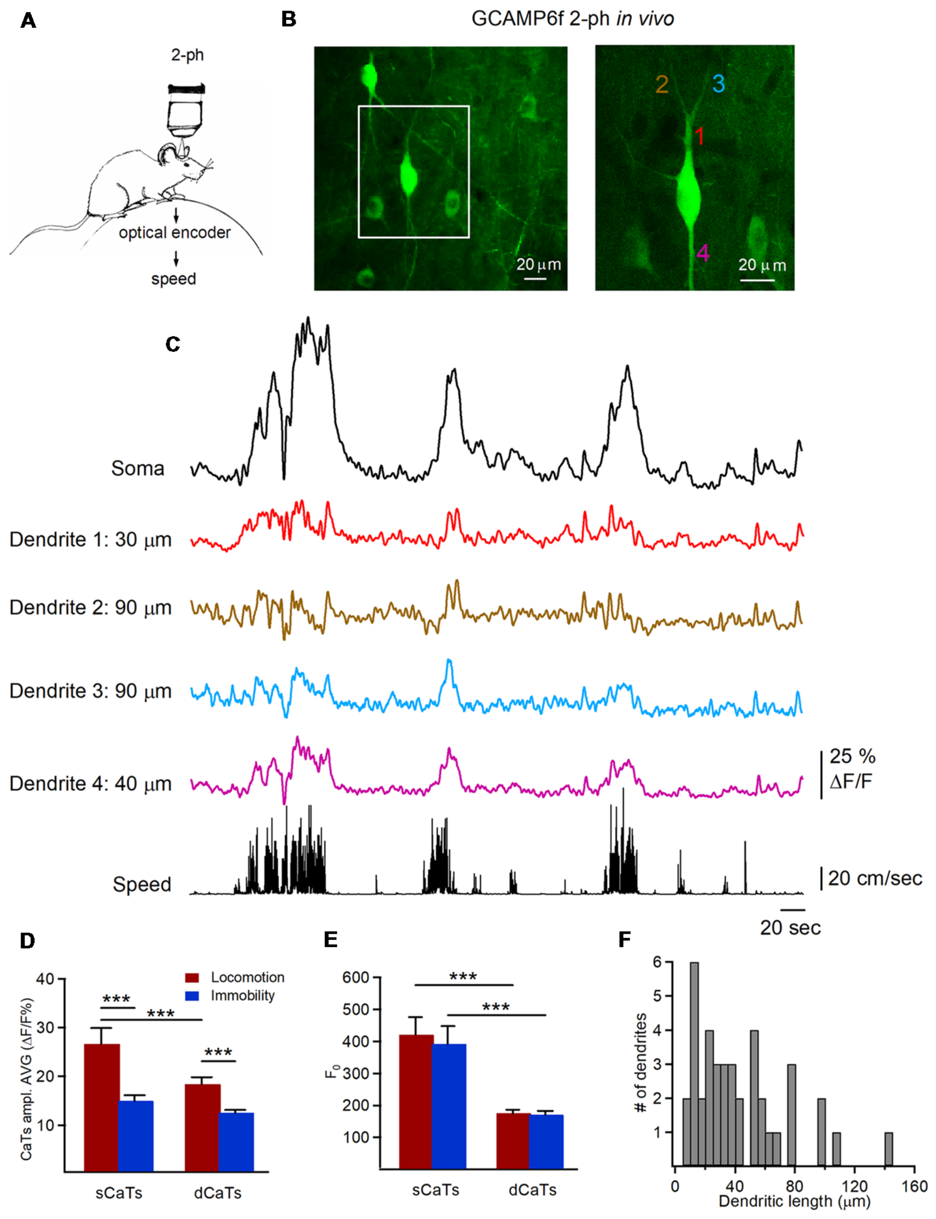

**FIGURE 1 |** Two-photon imaging of dendritic $Ca^{2+}$ transients (dCaTs) in hippocampal CA1 oriens/alveus (O/A) interneurons of awake mice. **(A)** Schematic of two-photon $Ca^{2+}$-imaging and animal speed recording in awake head-restrained mice. **(B)** Two-photon images of the GCaMP6f-expressing interneurons in CA1 O/A (maximal projection of a 100-μm Z-stack) acquired at a high laser power to illustrate the cell morphology. The area depicted with a white square is expanded on the right. The numbers of different color indicate different dendritic branches (20 μm each), from which $Ca^{2+}$ imaging data were obtained **(C)**. **(C)** Representative examples of soma and dCaTs, which were recorded in different dendritic branches and at different distance from the soma along with the animal speed (bottom black trace). Recordings of dCaTs were obtained from dendrites illustrated in (**B**; right). **(D)** Summary bar graphs of average amplitude for somatic CaTs (sCaTs) and dCaTs during locomotion and immobility, $^{***}P < 0.001$. **(E)** Summary bar graphs of basal fluorescence ($F_0$) in soma and dendrites during locomotion and immobility, $^{***}P < 0.001$. **(F)** Summary cumulative histogram of the dendritic length (distance from the soma) at which recordings of dCaTs were obtained.

local dendritic spikes; Martina et al., 2000; Topolnik et al., 2009), which can be characterized by different spatial extent (Sheffield and Dombeck, 2015), we examined the properties of CaTs during different behavioral states (**Figures 2**, **3**). Consistent with activation of local postsynaptic glutamate receptors, we observed small amplitude dCaTs restricted to single dendritic microdomains, with no apparent spread to neighboring dendritic segments or soma, which were defined as synaptic dCaTs (peak amplitude: 12.3 ± 0.7% ΔF/F; spatial extent: 21.4 ± 10.4 μm, $n = 10$ cells; **Figures 2A,B**). However, more frequently we observed large amplitude dCaTs that occurred synchronously with sCaTs (peak amplitude up to 50.0% ΔF/F, $n = 10$ cells; **Figures 2C,D**) and could be detected in the entire recorded branch (up to 100 μm

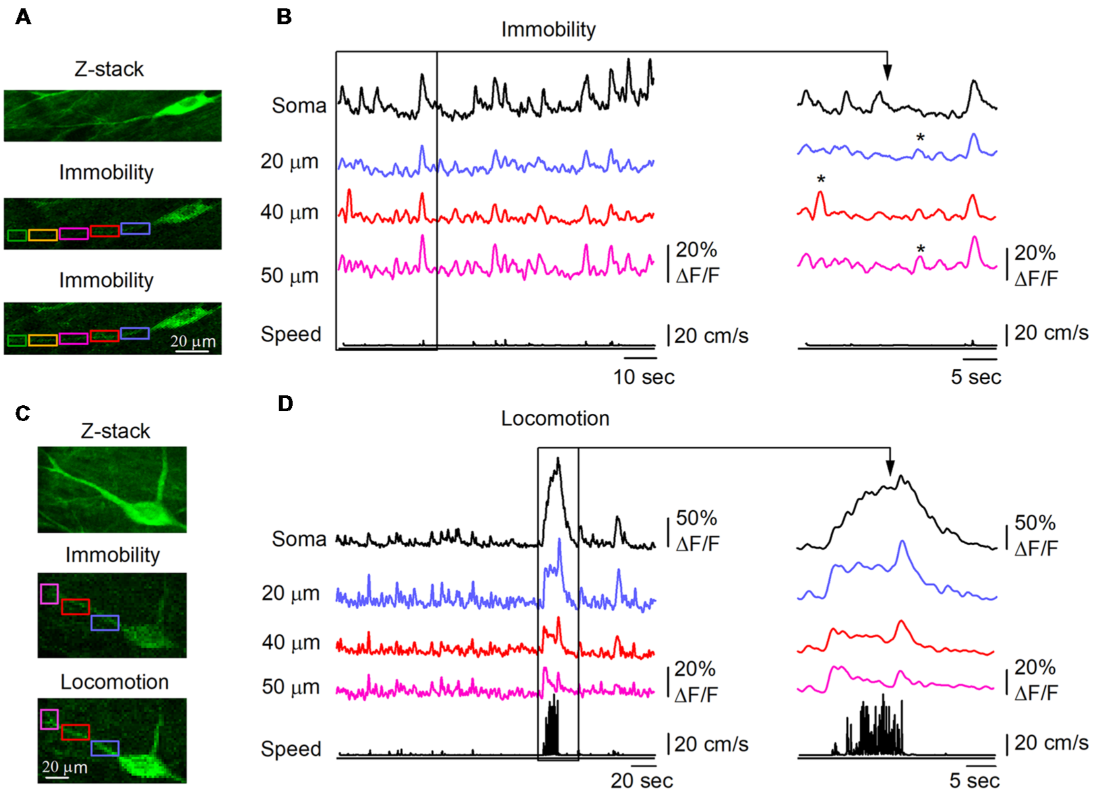

**FIGURE 2 |** Behavior state-dependent CaTs in dendrites of O/A interneurons. **(A)** Representative two-photon images showing the interneuron morphology (top, maximal projection of a 10-µm *Z*-stack) and Ca$^{2+}$ signals in soma and dendrites during immobility. Rectangle areas of different color indicate the dendritic regions of interest (ROIs) where dCaTs were analyzed. **(B)** Example traces of sCaTs and dCaTs recorded in some ROIs depicted in **(A)** during immobility along with the animal speed (black bottom trace). Local dCaTs that were not detected in soma are shown expanded on the right (labeled with stars). Panels **(C,D)** are the same as **(A,B)** but recordings were obtained for a second neighboring cell during locomotion period. CaTs recorded during locomotion are also expanded on the right.

from soma; **Figure 2D**). These events were considered as regenerative that could be evoked either by bAPs or dendritic spikes or both.

We then compared dendritic Ca$^{2+}$ activity during locomotion with that during immobility. During locomotion, both soma and dendrites showed Ca$^{2+}$ elevations, which were simultaneously detected over large dendritic distances (up to 100 µm from soma; **Figures 3A,B**). Using sCaTs as a surrogate measure of AP firing (Dombeck et al., 2010; Chen et al., 2013), we explored whether somatic AP firing was associated with dendritic regenerative activity in interneurons. First, during many run episodes with somatic firing, spreading dCaTs were observed (**Figure 3A**). These events were similar in amplitude to local synaptic dCaTs (15.4 ± 0.7% ΔF/F) but showed a strong linear correlation with sCaTs (**Figure 3C**), and declined with distance from the soma ($r$ = –0.25, Pearson correlation, $P < 0.01$, **Figure 3B**), indicating that they were likely evoked by bAPs. Furthermore, in six out of nine cells, somatic Ca$^{2+}$ activity correlated well with animal running speed (**Figure 3D**). Similarly, all proximal (<50 µm from soma) and some more distal (50–100 µm from soma) dendritic branches in these cells showed a positive correlation between dCaT amplitude and the running speed (**Figure 3E**). Taken together, these data indicate that during locomotion, dendritic Ca$^{2+}$ signals in O/A interneurons correlate well with somatic activity and animal speed.

During immobility, small amplitude dCaTs often occurred independently of soma and remained localized within individual dendritic segments, indicative of local synaptic activity (peak amplitude dCaTs: 12.0 ± 0.7% ΔF/F, $n$ = 22 segments/10 cells; **Figure 4A**, shown with red arrowheads). These data suggest that local isolated dendritic activity, such as postsynaptic Ca$^{2+}$ elevations, can be more frequently seen in interneurons during immobility than during locomotion state. Local CaTs were detected in both proximal and distal dendrites and had the same amplitude across dendritic tree (**Figure 4B**). Similar to dendritic Ca$^{2+}$ activity during locomotion, some small amplitude dCaTs were recorded simultaneously with sCaTs likely in relation to somatic firing during immobility, and could spread between neighboring segments (**Figure 4C**). Also, some sCaTs did not invade dendrites, indicative of local inhibition (**Figure 4C**). Overall, during immobility, dCaTs showed no significant correlation with sCaTs (Pearson correlation coefficient: $r$ = 0.3033; $P$ = 0.2536; $n$ = 18 segments/nine cells; **Figure 4D**), indicating that they were likely associated with activation of local Ca$^{2+}$ mechanisms. The most distant dendritic sites were also the least coupled to soma (**Figure 4D**), consistent

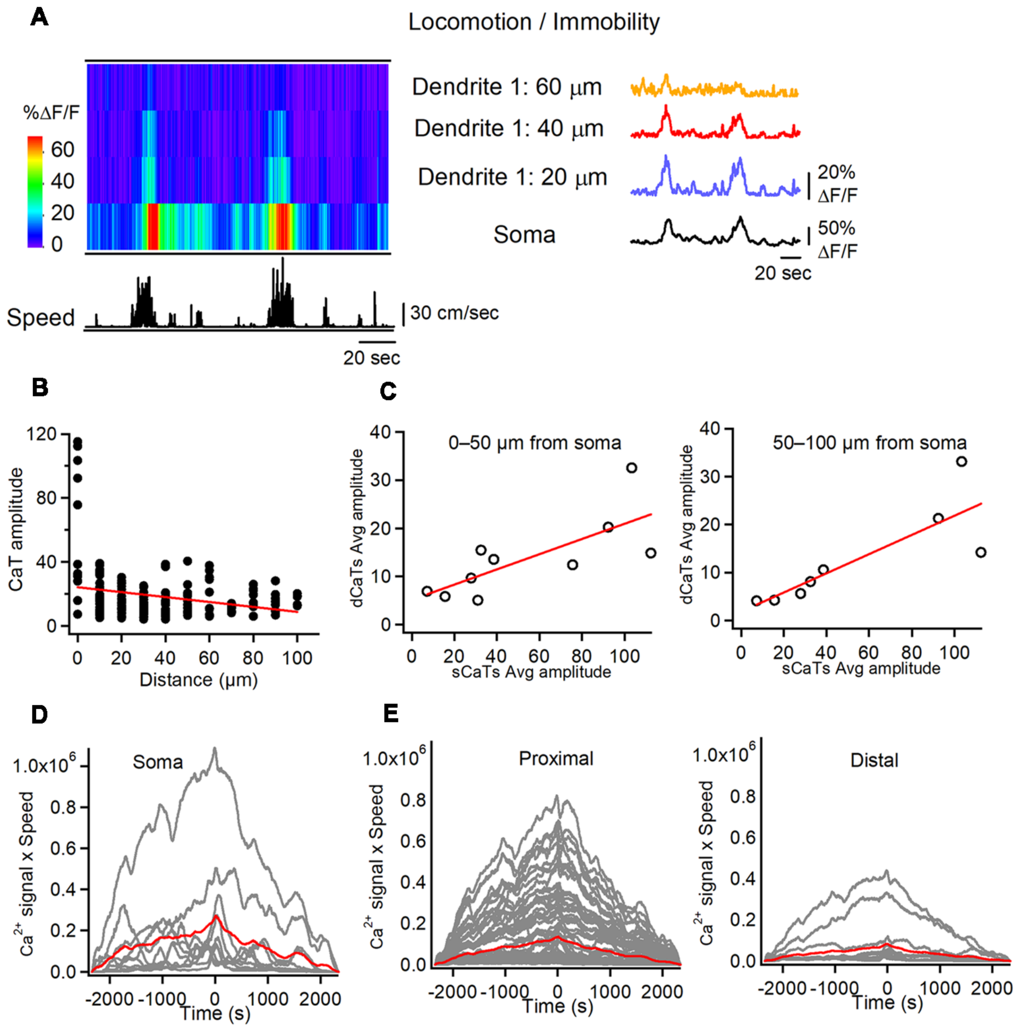

**FIGURE 3 |** Soma-dendrite coupling in O/A interneurons during locomotion. **(A)** Representative heat-map of soma-dendrite $Ca^{2+}$ activity in soma and dendrites along with the animal speed trace (left) and corresponding CaTs recorded in soma and dendrites during locomotion/immobility periods. Note large amplitude sCaTs that propagate to proximal dendrites (<60 µm from soma). **(B)** Summary plot illustrating the average dCaT amplitude as a distance from soma in comparison to that of sCaT (distance = 0) in different cells during locomotion. Red line is a linear regression fit to the data, indicating a significant decline in CaT amplitude with distance from the soma. **(C)** Summary plots illustrating relationships between dCaTs and sCaTs in proximal (0–50 µm from soma; left) and more distal (50–100 µm from soma; right) dendrites. Red lines correspond to a linear regression fit to the data, indicating a significant positive relationship between the sCaT and dCaT amplitude during locomotion. **(D,E)** Cross-correlation functions between the sCaTs **(D)** and dCaTs (**E**, proximal vs. distal) with animal running speed. Red traces indicate the mean cross-correlation functions ($n = 9$ cells).

with previous observations *in vitro* (Camiré and Topolnik, 2014). Thus, in average, the soma-dendrite coupling likely *via* bAPs was stronger during locomotion, while the local synaptic activity dominated in interneuron dendrites during immobility.

Furthermore, during immobility state, dCaTs were more variable within a given cell. Overall, the variance in dCaTs was significantly higher in segments showing local events than in segments showing spreading events (**Figure 4E**). As some dendritic segments showed both local events during immobility and spreading dCaTs during locomotion, we assumed that summation of postsynaptic and bAP-CaTs could occur in such segments during locomotion. If this hypothesis is true, then larger dCaTs in such segments could be associated with coincident pre- and postsynaptic activity and induction of Hebbian forms of plasticity. To explore this idea further, we compared the amplitude of local dCaTs in such segments during immobility with that of spreading events during locomotion (**Figures 4F,G**). Our data showed that the mean amplitude of dCaTs in such segments increased significantly with locomotion (from 12.0 ± 0.7% ΔF/F to 15.2 ± 0.9% ΔF/F; $P < 0.05$; $n = 22$ segments; Mann-Whitney test; **Figures 4F,G**), with the majority of individual segments showing switch from small amplitude local events to considerable dCaTs (increase to 173.1 ± 17.3% of local dCaT, $n = 13/22$ segments), indicative of significant summation of dCaTs during spreading events. The remaining segments showed no change (98.5 ± 4.6% of local

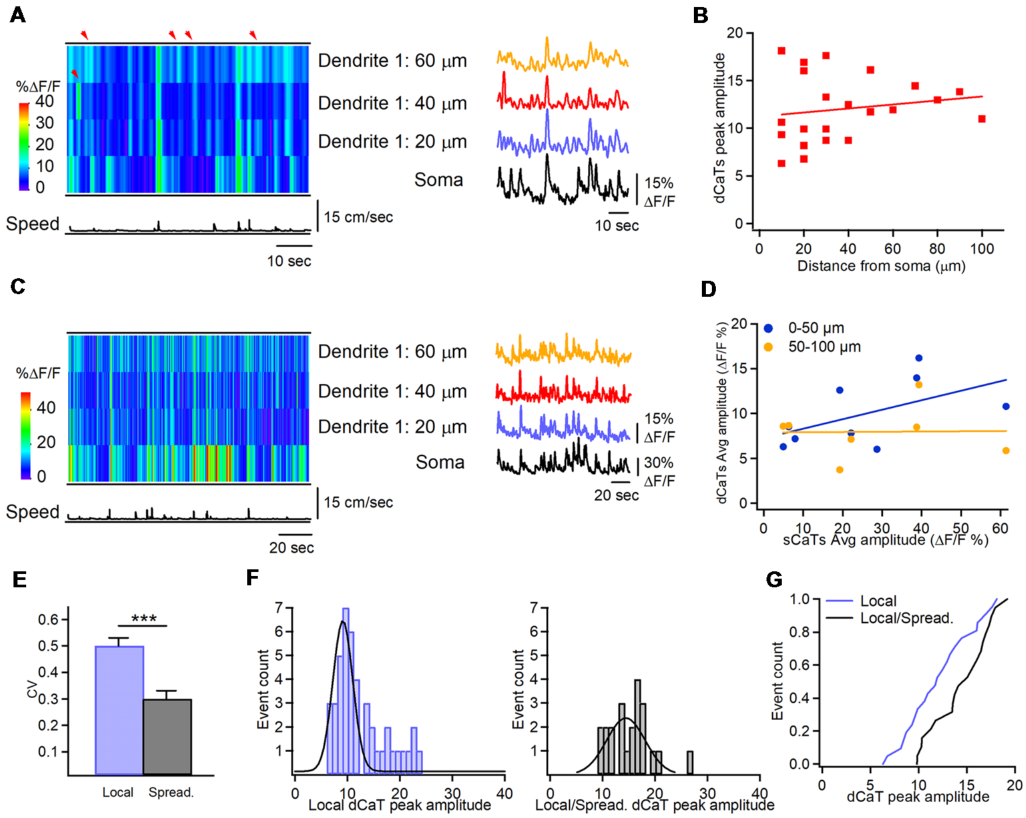

**FIGURE 4 |** Soma-dendrite coupling during immobility. **(A)** Representative heat-map of $Ca^{2+}$ activity in soma and dendrites along with the animal speed trace (left) and corresponding CaTs recorded in soma and dendrites during immobility, showing localized dCaTs that are not seen in soma (indicated with red arrowheads). **(B)** Summary plot showing the peak amplitude of dendritic local events as a function of distance from soma. Red line corresponding to a linear regression fit shows no significant relationship between the dCaT amplitude and distance from the soma. Panel **(C)** is the same as in **(A)** but during higher activity in the soma. Note the soma-dendrite spread of $Ca^{2+}$ signals during some but not all events. **(D)** Summary plot illustrating relationships between dCaTs and sCaTs in proximal (0–50 µm from soma; blue) and more distal (50–100 µm from soma; yellow) dendrites. Lines are the linear regression fits to the corresponding sets of data, indicating no significant relationship between the sCaT and dCaT amplitude during immobility. **(E)** Summary bar graphs of the coefficient of variation for the peak amplitude of local vs. spreading events. Note a significantly higher variance of local events (***$P < 0.001$; $n = 22$ segments, nine cells). **(F)** Cumulative histograms of the peak amplitude for local dCaTs during immobility (left) and spreading dCaTs within the same dendritic segments during locomotion (right), with Gaussian fits to the data sets. **(G)** Cumulative distributions of dCaT peak amplitude for local and spreading events, recorded within the same dendritic segments during immobility and locomotion, respectively. Note a significantly highly amplitude of spreading events during locomotion.

dCaT, $n = 5/22$ segments) or a slight decrease in dCaTs (decrease to 79.4 ± 8.3% of local dCaT, $n = 4/22$ segments) when compared to the local events. Taken together, these data point to a dominant summation of dCaTs during spreading events, but also highlight the segment-specific variability in local dendritic signaling, likely due to specific spatio-temporal arrangements of excitatory and inhibitory inputs converging onto interneuron dendrites.

## DISCUSSION

Using high-resolution two-photon imaging, we explored dendritic $Ca^{2+}$ activity in hippocampal O/A interneurons of awake mice during locomotion and immobility. Our data showed that, despite a large variability in dCaTs across the cells as well as within different dendritic segments of the same interneuron, dendritic $Ca^{2+}$ activity in interneurons reflects the animal behavior, as different types of $Ca^{2+}$ signals and dendrite-soma interactions were observed in specific behavioral states. As a rule, $Ca^{2+}$ signals had larger amplitude and could invade the entire dendritic tree in the focus of observation during locomotion. While this type of $Ca^{2+}$ activity was also present during immobility, the signal amplitude was significantly lower in both soma and dendrites. Moreover, a significant fraction of dendrites showed spatially restricted CaTs, which were not seen by soma. Based on these data, we propose a scenario in which high soma-dendrite coupling, likely due to bAPs or regenerative activity and associated dCaTs, may facilitate the spike-timing-dependent or Hebbian forms of synaptic plasticity in O/A interneurons during animal locomotion. In contrast, during animal quiet state, this type of activity can be reduced or even replaced by local dendritic $Ca^{2+}$ signaling, which, if occurs at the hyperpolarized level of membrane potential, may facilitate the anti-Hebbian plasticity mechanisms.

Dendritic $Ca^{2+}$ signals in interneurons are more complex than in PCs as they arise from activation of different mechanisms, including the postsynaptic $Ca^{2+}$-permeable receptors, such as

NMDA, CP-AMPAR (Goldberg et al., 2003a,b; Topolnik et al., 2005), kainate (Cossart et al., 1998, 2002) or α7 nicotinic acetylcholine receptors (Griguoli et al., 2013), different types of voltage-gated $Ca^{2+}$-channels (VGCCs; Goldberg et al., 2004; Topolnik et al., 2009) and peri- and extrasynaptic group I metabotropic glutamate receptors (mGluR1/mGluR5; Topolnik et al., 2005, 2006; Camiré et al., 2012; Hainmueller et al., 2014). Activation of these $Ca^{2+}$ sources usually triggers events of relatively small amplitude with different kinetic properties (from relatively fast to slow for ionotropic vs. metabotropic receptors), which are restricted to individual dendritic microdomains or branches. Consistent with activation of local excitatory inputs within single dendritic segments, spatially restricted postsynaptic dCaTs were observed in our study *in vivo* during both locomotion and immobility states. In addition, bAP-CaTs can be reliably evoked in proximal dendrites of CA1 interneurons *in vitro via* VGCCs and $Ca^{2+}$ release (Topolnik et al., 2009; Evstratova et al., 2011). Our data *in vivo* indicate that such events may dominate during locomotion and, to a less extend, during immobility. Also, the $Ca^{2+}$ -induced $Ca^{2+}$ release (CICR) events of large amplitude can be generated in some interneurons at rest (e.g., fast-spiking cells; Camiré and Topolnik, 2014), and can be seen during immobility given an overall lower spiking activity of O/A interneurons (Lapray et al., 2012; Varga et al., 2012). In summary, many $Ca^{2+}$ sources can interact in interneuron dendrites depending on the level of on-going network activity and the functional state of a given $Ca^{2+}$ source, indicating that dendritic $Ca^{2+}$ activity in interneurons *in vivo* may be even more diverse than *in vitro*.

Indeed, we demonstrate significant variability in interneuron dCaTs *in vivo*. First, we found that different dendritic segments of the same cell could demonstrate different types of dCaTs likely due to a high diversity of post- and extra-synaptic $Ca^{2+}$ mechanisms expressed across dendritic arbors (Camiré and Topolnik, 2012; Camiré et al., 2012; Topolnik and Camiré, 2019) and a different degree of bAP propagation or bAP-CaT signal amplitude due to activity-dependent regulation of these processes *via* synaptic inhibition (Tyan et al., 2014; Francavilla et al., 2018) or mGluR5-dependent modulation (Topolnik et al., 2009). In addition, the dCaT variability could arise from different types of O/A interneurons sampled in our study, including somatostatin-expressing OLM, bistratified and long-range projecting cells (Sik et al., 1995; Halasy et al., 1996; Jinno et al., 2007) as well as horizontal basket (Maccaferri, 2005) or trilaminar (Ferraguti et al., 2005) cells. The detailed cell type-specific organization of dendritic $Ca^{2+}$ signaling remains still to be examined in the *in vitro* and *in vivo* studies. However, regardless of the inter-cell and intra-cell variability, dCaTs in our study showed consistent behavior state-dependent organization, indicating that similar mechanisms may drive dendritic $Ca^{2+}$ activity in different inhibitory cell types during a particular behavior state.

During locomotion, high power theta oscillations are detected in the CA1 hippocampus, with different types of O/A interneurons exhibiting rhythmic phase-dependent firing (Lapray et al., 2012; Varga et al., 2012; Katona et al., 2014). Dendrites of different types of O/A interneurons receive theta-modulated excitatory input from CA1 PCs, which almost linearly increase their firing rate with the animal speed (McNaughton et al., 1983; Czurkó et al., 1999; Buzsáki, 2002). Accordingly, analysis of somatic and proximal dendritic $Ca^{2+}$ events revealed a good correlation between these signals and the animal speed in O/A interneurons. In addition, the local inhibitory inputs that terminate onto O/A interneuron dendrites are made by the type 3 interneuron-specific interneurons (IS3; Acsády et al., 1996; Chamberland et al., 2010; Tyan et al., 2014) and the long-range projecting vasoactive intestinal peptide (VIP)-expressing GABAergic neurons (VIP-LRPs; Francavilla et al., 2018). While IS3 cells may fire periodically during theta-run epochs, their activation is often delayed and is rather irregular (Luo et al., 2019), indicating that dendritic IS3 inhibitory input may not be efficient in controlling interneuron dendrites during locomotion. The VIP-LRPs are, in turn, the theta-off cells and do not participate in dendritic input modulation during theta (Francavilla et al., 2018). Thus, interneuron dendrites are likely disinhibited during theta-run epochs, which may facilitate the spread of bAPs or local spikes and generation of widespread dCaTs, as observed in our study.

During animal quiet state and consummatory behavior, large irregular activity (LIA) with periodic sharp-wave-associated ripples (SWRs, 120–250 Hz) are recorded in the CA1 hippocampus, with CA1 PCs firing mostly during SWRs. The IS3 and VIP-LRP cells are active during LIA but do not participate to SWRs (Francavilla et al., 2018; Luo et al., 2019), indicating that interneuron dendrites are mostly inhibited during animal quiet state with short periods of disinhibition and excitatory drive received during SWRs. Our findings of significantly reduced dCaTs during immobility are in line with these observations. It remains to be determined whether the spatially restricted dCaTs detected in our study are associated with SWRs.

Dendritic $Ca^{2+}$ activity in interneurons has been consistently associated with induction of Hebbian and anti-Hebbian long-term potentiation (LTP; Perez et al., 2001; Lamsa et al., 2005, 2007; Topolnik et al., 2006; Topolnik, 2012; Camiré and Topolnik, 2014; Hainmueller et al., 2014). In this context, our observations of highly variable dCaTs in interneurons of awake mice imply that distinct forms of synaptic plasticity may be induced across different cells and synaptic inputs terminating onto specific dendritic segments. Given a prevalent regenerative dCaTs during locomotion, we propose that Hebbian LTP can be induced in O/A interneurons during locomotion, thus enhancing their somatic firing (Perez et al., 2001; Lamsa et al., 2005; Croce et al., 2010). During immobility, when the dendritic inhibitory drive to O/A interneurons is increased (Francavilla et al., 2018; Luo et al., 2019), the local membrane potential is likely hyperpolarized. Accordingly, the strong excitatory inputs arriving during SWRs and associated with local dCaTs may induce bidirectional plasticity depending on the $Ca^{2+}$ sources involved (Lamsa et al., 2007; Griguoli et al., 2013; Camiré and Topolnik, 2014). This simplified scenario does not consider other potential mechanisms that may operate during different behavioral states, including the septo-hippocampal cholinergic, glutamatergic and GABAergic projections as well as modulation of local dendritic conductances. Additional studies will be required to directly reveal how different types of dendritic Ca$^{2+}$ activity induce synaptic plasticity *in vivo* and which learning rules may be specific for interneurons in behaving animals performing cognitive tasks.

## AUTHOR CONTRIBUTIONS

RF and VV performed the experiments. RF, OM and LT analyzed the data. RF and LT wrote the manuscript.

## FUNDING

This work was supported by the Canadian Institutes of Health Research (award id MOP-137072, MOP-142447) and the Natural Sciences and Engineering Research Council of Canada (NSERC). VV was supported by the Savoy Foundation Postdoctoral fellowship.

## ACKNOWLEDGMENTS

We thank Dimitry Topolnik for excellent technical assistance.

## REFERENCES

Acsády, L., Görcs, T. J., and Freund, T. F. (1996). Different populations of vasoactive intestinal polypeptide-immunoreactive interneurons are specialized to control pyramidal cells or interneurons in the hippocampus. *Neuroscience* 73, 317–334. doi: 10.1016/0306-4522(95)00609-5

Aponte, Y., Bischofberger, J., and Jonas, P. (2008). Efficient Ca2+ buffering in fast-spiking basket cells of rat hippocampus. *J. Physiol.* 586, 2061–2075. doi: 10.1113/jphysiol.2007.147298

Ariav, G., Polsky, A., and Schiller, J. (2003). Submillisecond precision of the input-output transformation function mediated by fast sodium dendritic spikes in basal dendrites of CA1 pyramidal neurons. *J. Neurosci.* 23, 7750–7758. doi: 10.1523/jneurosci.23-21-07750.2003

Branco, T., and Häusser, M. (2011). Synaptic integration gradients in single cortical pyramidal cell dendrites. *Neuron* 69, 885–892. doi: 10.1016/j.neuron.2011.02.006

Buzsáki, G. (2002). Theta oscillations in the hippocampus. *Neuron* 33, 325–340. doi: 10.1016/S0896-6273(02)00586-X

Camiré, O., Lacaille, J. C., and Topolnik, L. (2012). Dendritic signaling in inhibitory interneurons: local tuning via group I metabotropic glutamate receptors. *Front. Physiol.* 3:259. doi: 10.3389/fphys.2012.00259

Camiré, O., and Topolnik, L. (2012). Functional compartmentalisation and regulation of postsynaptic Ca2+ transients in inhibitory interneurons. *Cell Calcium* 52, 339–346. doi: 10.1016/j.ceca.2012.05.001

Camiré, O., and Topolnik, L. (2014). Dendritic calcium nonlinearities switch the direction of synaptic plasticity in fast-spiking interneurons. *J. Neurosci.* 34, 3864–3877. doi: 10.1523/JNEUROSCI.2253-13.2014

Chamberland, S., Salesse, C., Topolnik, D., and Topolnik, L. (2010). Synapse-specific inhibitory control of hippocampal feedback inhibitory circuit. *Front. Cell. Neurosci.* 4:130. doi: 10.3389/fncel.2010.00130

Chen, T. W., Wardill, T. J., Sun, Y., Pulver, S. R., Renninger, S. L., Baohan, A., et al. (2013). Ultrasensitive fluorescent proteins for imaging neuronal activity. *Nature* 499, 295–300. doi: 10.1038/nature12354

Chiovini, B., Turi, G. F., Katona, G., Kaszás, A., Pálfi, D., Maák, P., et al. (2014). Dendritic spikes induce ripples in parvalbumin interneurons during hippocampal sharp waves. *Neuron* 82, 908–924. doi: 10.1016/j.neuron.2014.04.004

Cossart, R., Epsztein, J., Tyzio, R., Becq, H., Hirsch, J., Ben-Ari, Y., et al. (2002). Quantal release of glutamate generates pure kainate and mixed AMPA/kainate EPSCs in hippocampal neurons. *Neuron* 35, 147–159. doi: 10.1016/s0896-6273(02)00753-5

Cossart, R., Esclapez, M., Hirsch, J. C., Bernard, C., and Ben-Ari, Y. (1998). GluR5 kainate receptor activation in interneurons increases tonic inhibition of pyramidal cells. *Nat. Neurosci.* 1, 470–478. doi: 10.1038/2185

Croce, A., Pelletier, J. G., Tartas, M., and Lacaille, J. C. (2010). Afferent-specific properties of interneuron synapses underlie selective long-term regulation of feedback inhibitory circuits in CA1 hippocampus. *J. Physiol.* 588, 2091–2107. doi: 10.1113/jphysiol.2010.189316

Czurkó, A., Hirase, H., Csicsvari, J., and Buzsáki, G. (1999). Sustained activation of hippocampal pyramidal cells by 'space clamping' in a running wheel. *Eur. J. Neurosci.* 11, 344–352. doi: 10.1046/j.1460-9568.1999.00446.x

Dombeck, D. A., Harvey, C. D., Tian, L., Looger, L. L., and Tank, D. W. (2010). Functional imaging of hippocampal place cells at cellular resolution during virtual navigation. *Nat. Neurosci.* 13, 1433–1440. doi: 10.1038/nn.2648

Evstratova, A., Chamberland, S., and Topolnik, L. (2011). Cell type-specific and activity-dependent dynamics of action potential-evoked Ca2+ signals in dendrites of hippocampal inhibitory interneurons. *J. Physiol.* 589, 1957–1977. doi: 10.1113/jphysiol.2010.204255

Ferraguti, F., Klausberger, T., Cobden, P., Baude, A., Roberts, J. D., Szucs, P., et al. (2005). Metabotropic glutamate receptor 8-expressing nerve terminals target subsets of GABAergic neurons in the hippocampus. *J. Neurosci.* 25, 10520–10536. doi: 10.1523/JNEUROSCI.2547-05.2005

Francavilla, R., Luo, X., Magnin, E., Tyan, L., and Topolnik, L. (2015). Coordination of dendritic inhibition through local disinhibitory circuits. *Front. Synaptic Neurosci.* 7:5. doi: 10.3389/fnsyn.2015.00005

Francavilla, R., Villette, V., Luo, X., Chamberland, S., Muñoz, E., Camiré, O., et al. (2018). Connectivity and network state-dependent recruitment of long-range VIP-GABAergic neurons in the mouse hippocampus. *Nat. Commun.* 9:5043. doi: 10.1038/s41467-018-07162-5

Gasparini, S., Migliore, M., and Magee, J. C. (2004). On the initiation and propagation of dendritic spikes in CA1 pyramidal neurons. *J. Neurosci.* 24, 11046–11056. doi: 10.1523/JNEUROSCI.2520-04.2004

Goldberg, J. H., Lacefield, C. O., and Yuste, R. (2004). Global dendritic calcium spikes in mouse layer 5 low threshold spiking interneurones: implications for control of pyramidal cell bursting. *J. Physiol.* 558, 465–478. doi: 10.1113/jphysiol.2004.064519

Goldberg, J. H., Tamas, G., Aronov, D., and Yuste, R. (2003a). Calcium microdomains in aspiny dendrites. *Neuron* 40, 807–821. doi: 10.1016/s0896-6273(03)00714-1

Goldberg, J. H., Yuste, R., and Tamas, G. (2003b). Ca2+ imaging of mouse neocortical interneurone dendrites: contribution of Ca2+-permeable AMPA and NMDA receptors to subthreshold Ca2+ dynamics. *J. Physiol.* 551, 67–78. doi: 10.1113/jphysiol.2003.042598

Golding, N. L., Staff, N. P., and Spruston, N. (2002). Dendritic spikes as a mechanism for cooperative long-term potentiation. *Nature* 418, 326–331. doi: 10.1038/nature00854

Greenberg, D. S., Houweling, A. R., and Kerr, J. N. (2008). Population imaging of ongoing neuronal activity in the visual cortex of awake rats. *Nat. Neurosci.* 11, 749–751. doi: 10.1038/nn.2140

Grienberger, C., Chen, X., and Konnerth, A. (2014). NMDA receptor-dependent multidendrite Ca(2+) spikes required for hippocampal burst firing *in vivo*. *Neuron* 81, 1274–1281. doi: 10.1016/j.neuron.2014.01.014

Griguoli, M., Cellot, G., and Cherubini, E. (2013). In hippocampal oriens interneurons anti-hebbian long-term potentiation requires cholinergic signaling via 7 nicotinic acetylcholine receptors. *J. Neurosci.* 33, 1044–1049. doi: 10.1523/jneurosci.1070-12.2013

Hainmueller, T., Krieglstein, K., Kulik, A., and Bartos, M. (2014). Joint CP-AMPA and group I mGlu receptor activation is required for synaptic plasticity in dentate gyrus fast-spiking interneurons. *Proc. Natl. Acad. Sci. U S A* 111, 13211–13216. doi: 10.1073/pnas.1409394111

Halasy, K., Buhl, E. H., Lorinczi, Z., and Tamas, G. (1996). Synaptic target selectivity and input of GABAergic basket and bistratified interneurons in the CA1 area of the rat hippocampus. *Hippocampus* 6, 306–329. doi: 10.1002/(sici)1098-1063(1996)6:3<306::aid-hipo8>3.0.co;2-k

Higley, M. J., and Sabatini, B. L. (2008). Calcium signaling in dendrites and spines: practical and functional considerations. *Neuron* 59, 902–913. doi: 10.1016/j.neuron.2008.08.020

Hu, H., Martina, M., and Jonas, P. (2010). Dendritic mechanisms underlying rapid synaptic activation of fast-spiking hippocampal interneurons. *Science* 327, 52–58. doi: 10.1126/science.1177876

Jinno, S., Klausberger, T., Marton, L. F., Dalezios, Y., Roberts, J. D., Fuentealba, P., et al. (2007). Neuronal diversity in GABAergic long-range projections from the hippocampus. *J. Neurosci.* 27, 8790–8804. doi: 10.1523/JNEUROSCI.1847-07.2007

Katona, G., Kaszás, A., Turi, G. F., Hájos, N., Tamás, G., Vizi, E. S., et al. (2011). Roller coaster scanning reveals spontaneous triggering of dendritic spikes in CA1 interneurons. *Proc. Natl. Acad. Sci. U S A* 108, 2148–2153. doi: 10.1073/pnas.1009270108

Katona, L., Lapray, D., Viney, T. J., Oulhaj, A., Borhegyi, Z., Micklem, B. R., et al. (2014). Sleep and movement differentiates actions of two types of somatostatin-expressing GABAergic interneuron in rat hippocampus. *Neuron* 82, 872–886. doi: 10.1016/j.neuron.2014.04.007

Kerr, J. N., Greenberg, D., and Helmchen, F. (2005). Imaging input and output of neocortical networks *in vivo*. *Proc. Natl. Acad. Sci. U S A* 102, 14063–14068. doi: 10.1073/pnas.0506029102

Klausberger, T., and Somogyi, P. (2008). Neuronal diversity and temporal dynamics: the unity of hippocampal circuit operations. *Science* 321, 53–57. doi: 10.1126/science.1149381

Lamsa, K., Heeroma, J. H., and Kullmann, D. M. (2005). Hebbian LTP in feed-forward inhibitory interneurons and the temporal fidelity of input discrimination. *Nat. Neurosci.* 8, 916–924. doi: 10.1038/nn1486

Lamsa, K. P., Heeroma, J. H., Somogyi, P., Rusakov, D. A., and Kullmann, D. M. (2007). Anti-hebbian long-term potentiation in the hippocampal feedback inhibitory circuit. *Science* 315, 1262–1266. doi: 10.1126/science.1137450

Lapray, D., Lasztoczi, B., Lagler, M., Viney, T. J., Katona, L., Valenti, O., et al. (2012). Behavior-dependent specialization of identified hippocampal interneurons. *Nat. Neurosci.* 15, 1265–1271. doi: 10.1038/nn.3176

Losonczy, A., and Magee, J. C. (2006). Integrative properties of radial oblique dendrites in hippocampal CA1 pyramidal neurons. *Neuron* 50, 291–307. doi: 10.1016/j.neuron.2006.03.016

Lovett-Barron, M., Kaifosh, P., Kheirbek, M. A., Danielson, N., Zaremba, J. D., Reardon, T. R., et al. (2014). Dendritic inhibition in the hippocampus supports fear learning. *Science* 343, 857–863. doi: 10.1126/science.1247485

Luo, X., Guet-McCreight, A., Francavilla, R., Villette, V., and Topolnik, L. (2019). Synaptic properties and network state-dependent recruitment of VIP-expressing interneuron-specific interneurons in the CA1 hippocampus. *bioRxiv* [Preprint]. doi: 10.1101/433136

Maccaferri, G. (2005). Stratum oriens horizontal interneurone diversity and hippocampal network dynamics. *J. Physiol.* 562, 73–80. doi: 10.1113/jphysiol.2004.077081

Magee, J. C., and Johnston, D. (1997). A synaptically controlled, associative signal for Hebbian plasticity in hippocampal neurons. *Science* 275, 209–213. doi: 10.1126/science.275.5297.209

Markram, H., and Sakmann, B. (1994). Calcium transients in dendrites of neocortical neurons evoked by single subthreshold excitatory postsynaptic potentials via low-voltage-activated calcium channels. *Proc. Natl. Acad. Sci. U S A* 91, 5207–5211. doi: 10.1073/pnas.91.11.5207

Martina, M., Vida, I., and Jonas, P. (2000). Distal initiation and active propagation of action potentials in interneuron dendrites. *Science* 287, 295–300. doi: 10.1126/science.287.5451.295

McNaughton, B. L., Barnes, C. A., and O'Keefe, J. (1983). The contributions of position, direction, and velocity to single unit activity in the hippocampus of freely-moving rats. *Exp. Brain Res.* 52, 41–49. doi: 10.1007/bf00237147

Pelkey, K. A., Chittajallu, R., Craig, M. T., Tricoire, L., Wester, J. C., and McBain, C. J. (2017). Hippocampal GABAergic inhibitory interneurons. *Physiol. Rev.* 97, 1619–1747. doi: 10.1152/physrev.00007.2017

Perez, Y., Morin, F., and Lacaille, J. C. (2001). A hebbian form of long-term potentiation dependent on mGluR1a in hippocampal inhibitory interneurons. *Proc. Natl. Acad. Sci. U S A* 98, 9401–9406. doi: 10.1073/pnas.161493498

Regehr, W. G., and Tank, D. W. (1990). Postsynaptic NMDA receptor-mediated calcium accumulation in hippocampal CA1 pyramidal cell dendrites. *Nature* 345, 807–810. doi: 10.1038/345807a0

Schiller, J., Schiller, Y., Stuart, G., and Sakmann, B. (1997). Calcium action potentials restricted to distal apical dendrites of rat neocortical pyramidal neurons. *J. Physiol.* 505, 605–616. doi: 10.1111/j.1469-7793.1997.605ba.x

Sheffield, M. E. J., Adoff, M. D., and Dombeck, D. A. (2017). Increased prevalence of calcium transients across the dendritic arbor during place field formation. *Neuron* 96, 490.e5–504.e5. doi: 10.1016/j.neuron.2017.09.029

Sheffield, M. E. J., and Dombeck, D. A. (2015). Calcium transient prevalence across the dendritic arbour predicts place field properties. *Nature* 517, 200–204. doi: 10.1038/nature13871

Sik, A., Penttonen, M., Ylinen, A., and Buzsaki, G. (1995). Hippocampal CA1 interneurons: an *in vivo* intracellular labeling study. *J. Neurosci.* 15, 6651–6665. doi: 10.1523/jneurosci.15-10-06651.1995

Sjöström, P. J., Rancz, E. A., Roth, A., and Häusser, M. (2008). Dendritic excitability and synaptic plasticity. *Physiol. Rev.* 88, 769–840. doi: 10.1152/physrev.00016.2007

Somogyi, P. (2010). "Hippocampus: intrinsic organisation," in *Handbook of Brain Microcircuits*, eds G. Shepherd and S. Grillner (Oxford: Oxford University Press), 148–664.

Spruston, N., Schiller, Y., Stuart, G., and Sakmann, B. (1995). Activity-dependent action potential invasion and calcium influx into hippocampal CA1 dendrites. *Science* 268, 297–300. doi: 10.1126/science.7716524

Tian, L., Hires, A. S., Mao, T., Huber, D., Chiappe, M. E., Chalasani, S. H., et al. (2009). Imaging neural activity in worms, flies and mice with improved GCaMP calcium indicators. *Nat. Methods* 6, 875–881. doi: 10.1038/nmeth.1398

Topolnik, L. (2012). Dendritic calcium mechanisms and long-term potentiation in cortical inhibitory interneurons. *Eur. J. Neurosci.* 35, 496–506. doi: 10.1111/j.1460-9568.2011.07988.x

Topolnik, L., Azzi, M., Morin, F., Kougioumoutzakis, A., and Lacaille, J. C. (2006). mGluR1/5 subtype-specific calcium signalling and induction of long-term potentiation in rat hippocampal oriens/alveus interneurones. *J. Physiol.* 575, 115–131. doi: 10.1113/jphysiol.2006.112896

Topolnik, L., and Camiré, O. (2019). Non-linear calcium signalling and synaptic plasticity in interneurons. *Curr. Opin. Neurobiol.* 54, 98–103. doi: 10.1016/j.conb.2018.09.006

Topolnik, L., Chamberland, S., Pelletier, J. G., Ran, I., and Lacaille, J. C. (2009). Activity-dependent compartmentalized regulation of dendritic Ca2+ signaling in hippocampal interneurons. *J. Neurosci.* 29, 4658–4663. doi: 10.1523/jneurosci.0493-09.2009

Topolnik, L., Congar, P., and Lacaille, J. C. (2005). Differential regulation of metabotropic glutamate receptor- and AMPA receptor-mediated dendritic Ca2+ signals by presynaptic and postsynaptic activity in hippocampal interneurons. *J. Neurosci.* 25, 990–1001. doi: 10.1523/jneurosci.4388-04.2005

Tyan, L., Chamberland, S., Magnin, E., Camiré, O., Francavilla, R., David, L., et al. (2014). Dendritic inhibition provided by interneuron-specific cells controls the firing rate and timing of the hippocampal feedback inhibitory circuitry. *J. Neurosci.* 34, 4534–4547. doi: 10.1523/jneurosci.3813-13.2014

Varga, C., Golshani, P., and Soltesz, I. (2012). Frequency-invariant temporal ordering of interneuronal discharges during hippocampal oscillations in awake mice. *Proc. Natl. Acad. Sci. U S A* 109, E2726–E2734. doi: 10.1073/pnas.1210929109

Verkhratsky, A. (2005). Physiology and pathophysiology of the calcium store in the endoplasmic reticulum of neurons. *Physiol. Rev.* 85, 201–279. doi: 10.1152/physrev.00004.2004

Villette, V., Levesque, M., Miled, A., Gosselin, B., and Topolnik, L. (2017). Simple platform for chronic imaging of hippocampal activity during spontaneous behaviour in an awake mouse. *Sci. Rep.* 7:43388. doi: 10.1038/srep43388

**Conflict of Interest Statement**: The authors declare that the research was conducted in the absence of any commercial or financial relationships that could be construed as a potential conflict of interest.

frontiers
in Cellular Neuroscience

ORIGINAL RESEARCH
published: 19 June 2019
doi: 10.3389/fncel.2019.00274

# Measuring Sharp Waves and Oscillatory Population Activity With the Genetically Encoded Calcium Indicator GCaMP6f

**Pinggan Li[1,2†], Xinling Geng[2,3†], Huiyi Jiang[2,4], Adam Caccavano[5], Stefano Vicini[5] and Jian-young Wu[2*]**

[1] Department of Pediatric Neurology, Sun Yat-sen Memorial Hospital, Sun Yat-sen University, Guangzhou, China, [2] Department of Neuroscience, Georgetown University, Washington, DC, United States, [3] School of Biomedical Engineering, Capital Medical University, Beijing, China, [4] Department of Pediatrics, The First Hospital of Jilin University, Changchun, China, [5] Department of Pharmacology and Physiology, Georgetown University, Washington, DC, United States

GCaMP6f is among the most widely used genetically encoded calcium indicators for monitoring neuronal activity. Applications are at both the cellular and population levels. Here, we explore two important and under-explored issues. First, we have tested if GCaMP6f is sensitive enough for the detection of population activity with sparse firing, similar to the sensitivity of the local field potential (LFP). Second, we have tested if GCaMP6f is fast enough for the detection of fast network oscillations critical for the encoding and consolidation of memory. We have focused this study on the activity of the hippocampal network including sharp waves (SWs), carbachol-induced theta oscillations, and interictal-like spikes. We compare simultaneous LFP and optical GCaMP6f fluorescent recordings in Thy1-GCaMP6f mouse hippocampal slices. We observe that SWs produce a clear population GCaMP6f signal above noise with an average magnitude of 0.3% $\Delta F/F$. This population signal is highly correlated with the LFP, albeit with a delay of 40.3 ms (SD 10.8 ms). The population GCaMP6f signal follows the LFP evoked by 20 Hz stimulation with high fidelity, while electrically evoked oscillations up to 40 Hz were detectable with reduced amplitude. GCaMP6f and LFP signals showed a large amplitude discrepancy. The amplitude of GCaMP6f fluorescence increased by a factor of 28.9 (SD 13.5) between spontaneous SWs and carbachol-induced theta bursts, while the LFP amplitude increased by a factor of 2.4 (SD 1.0). Our results suggest that GCaMP6f is a useful tool for applications commonly considered beyond the scope of genetically encoded calcium indicators. In particular, population GCaMP6f signals are sensitive enough for detecting synchronous network events with sparse firing and sub-threshold activity, as well as asynchronous events with only a nominal LFP. In addition, population GCaMP6f signals are fast enough for monitoring theta and beta oscillations (<25 Hz). Faster calcium indicators (e.g., GCaMP7) will further improve the frequency response for the detection of gamma band oscillations.

OPEN ACCESS

**Edited by:**
Srdjan D. Antic,
University of Connecticut Health
Center, United States

**Reviewed by:**
Katsushige Sato,
Komazawa Women's University,
Japan
Maxim Volgushev,
University of Connecticut,
United States

***Correspondence:**
Jian-young Wu
wuj@georgetown.edu

† These authors have contributed
equally to this work

**Specialty section:**
This article was submitted to
Cellular Neurophysiology,
a section of the journal
Frontiers in Cellular Neuroscience

**Received:** 04 February 2019
**Accepted:** 05 June 2019
**Published:** 19 June 2019

**Citation:**
Li P, Geng X, Jiang H,
Caccavano A, Vicini S and Wu J-y
(2019) Measuring Sharp Waves and
Oscillatory Population Activity With
the Genetically Encoded Calcium
Indicator GCaMP6f.
Front. Cell. Neurosci. 13:274.
doi: 10.3389/fncel.2019.00274

The advantage of population optical over LFP recordings are that they are non-contact and free from stimulation artifacts. These features may be particularly useful for high-throughput recordings and applications sensitive to stimulus artifact, such as monitoring responses during continuous stimulation.

**Keywords: GCaMP, calcium signals, hippocampal slice, voltage-sensitive dye imaging, local field potential recordings, theta oscillation, hippocampal sharp wave**

## INTRODUCTION

Fluorescent calcium signals are widely used for monitoring neuronal activity in the brain thanks to the availability of genetically encoded indicators. GCaMP6f is among the best calcium indicators to date, with high sensitivity, high fluorescent yield and relatively fast response time (Chen et al., 2013). There are two principal applications of GCaMP6f: to visualize somatic calcium transients due to bursts of action potentials (Svoboda et al., 1997; Chen et al., 2013; Muto et al., 2013; Dana et al., 2014), and monitoring population activity via calcium fluorometry (Cui et al., 2013; Kupferschmidt et al., 2017). Two important issues related to the measurement of population activity remain less explored: (1) Is GCaMP6f sensitive enough for detecting population events with sparse neuronal firing and sub-threshold synaptic activity? (2) Is GCaMP6f fast enough for detecting physiologically relevant network oscillations?

For the sensitivity issue, we ask whether the population GCaMP6f signal is comparable to local field potential (LFP) recordings, i.e., capable of detecting network activity in which only a small fraction of neurons fire action potentials, while the majority of neurons only have subthreshold potentials. This is of concern as GCaMP fluorescence appears to primarily reflect supra-threshold somatic $Ca^{2+}$ influx (Helmchen and Tank, 2015), together with intracellular calcium induced by action potentials (Grienberger and Konnerth, 2012). In contrast, the principal source of the LFP may rather reflect subthreshold dendritic synaptic currents (Helmchen and Tank, 2015). However, while the $Ca^{2+}$ signals from individual synapses are small, a population signal from the integration of a large number of dendrites in the neuropil might become detectable, given that the sensitivity and fluorescent yield of GCaMP6f are both excellent.

Concerning the frequency response, the time course of somatic calcium transients is about 1 s (Chen et al., 2013; Dana et al., 2014; Miyawaki et al., 2014), which is too slow for detecting most network oscillations. In a recent report (Xing and Wu, 2018), 2 Hz but not 10 Hz GCaMP signals were detectable. However, the rise time of calcium transients is much faster than 1 s and may be able to follow fast oscillations. Measurements with the organic calcium indicator magnesium green showed <1 ms rise time (Regehr, 2000). When action potentials occur, the duration of intracellular calcium transients are long and dependent on intracellular buffering and clearance (Neher, 2013; Helmchen and Tank, 2015). In contrast, during a network oscillation with low calcium influx on average in the population, we argue that the time course will be more related to faster rise time than the slower decay time, and in particular the response time of the calcium indicator, or about 40 ms for GCaMP6f (Chen et al., 2013), as the onset time of the channels and the rate of calcium influx would be only a few milliseconds (Demuro and Parker, 2004; Shuai and Parker, 2005). When only a small fraction of neurons fire action potentials in the population, the majority of neurons should have a rate of calcium influx related to the opening probability of low voltage activated channels (LVAs) (Reviewed by Catterall, 2000; Grienberger and Konnerth, 2012). The opening probability of the LVA channels should be correlated to the fluctuation of membrane potential. In theory, recording fast oscillations in neuronal populations with calcium indicators is possible during sparse firing, when only a small fraction of neurons fire action potentials, most neurons have subthreshold membrane potential fluctuations, and the ability of intracellular calcium buffering/clearance is much greater than the calcium influx rate. The response time of GCaMP6f (∼40 ms) could in theory permit the detection of oscillations up to 25 Hz.

Hippocampal sharp waves (SWs) are spontaneous network events in which a small fraction of neurons fire action potentials (Ylinen et al., 1995; Csicsvari et al., 1999a,b; Mizuseki and Buzsaki, 2013) while the majority of neurons receive subthreshold excitatory and inhibitory synaptic input (Hajos et al., 2013). The summation of excitatory and inhibitory post-synaptic potentials (EPSPs/IPSPs) generates a clear voltage source/sink pair in LFP recordings (Maier et al., 2009), reviewed by Buzsaki (2015). In this report we test if spontaneous SWs can be seen in the GCaMP signal, events with sparse firing and sub-threshold synaptic activity. We speculate that the population summation of calcium influx during these events is detectable in GCaMP6f optical recordings.

We compared simultaneously recorded LFP and fluorescent GCaMP6f signals in Thy1-GCaMP6f mouse hippocampal slices during SWs, interictal spikes and carbachol-induced theta oscillations. Population activation by electric stimulation was also used to test the frequency response characteristics of GCaMP6f population signals.

We observed that SWs can be clearly detected optically in the population GCaMP6f signal. The GCaMP signals were highly correlated with LFP-detected events with a delay of 40.3 ms (SD 10.8 ms). The GCaMP signal followed evoked network activity below 20 Hz with high fidelity, while activity up to 40 Hz were still detectable with reduced amplitude. The population GCaMP6f and LFP signals showed a large amplitude discrepancy. The amplitude of GCaMP6f fluorescence increased by a factor of 28.9 (SD 13.5) between spontaneous SWs and carbachol-induced theta bursts, while the LFP amplitude increased by a factor of 2.4 (SD 1.0).

Our results suggest that the population GCaMP6f signal has a sensitivity comparable to that of the LFP and may be even more sensitive than the LFP for detecting network events with low amplitude but disproportionally large GCaMP6f fluorescence, likely arising from asynchronous activity. We also found that the population GCaMP6f signal is fast enough for monitoring theta (4–7 Hz) and beta (14–25 Hz) oscillations in slice, and the detection limit can be as high as 40 Hz. These results suggest that optical recordings of population GCaMP6f signals may be useful for detecting network activity complementary to LFP recordings. They may have particular utility in situations where the confound of electrode disruption and stimulus artifacts need to be minimized. In addition, they have the power to monitor activity in multiple distinct anatomical sites concurrently. Our results also have implications for the interpretation of *in vivo* data obtained with the increasingly widespread use of GCaMP based photometry (Cui et al., 2013; Kupferschmidt et al., 2017).

# MATERIALS AND METHODS

## Slice Preparation

P21–P33 male and female C57BL/6J-Tg (Thy1-GCaMP6f) GP5.5 Dkim/J. mice (Jax 024276) mice were used to prepare paired hippocampal hemi-slices in accordance with a protocol approved by the Institutional Animal Care and Use Committee at Georgetown University Medical Center. Following deep isoflurane anesthesia, animals were rapidly decapitated. The whole brain was subsequently removed and chilled in iced (0°C) sucrose-based artificial cerebrospinal fluid (sACSF) containing (in mM) 252 sucrose; 3 KCl; 2 $CaCl_2$; 2 $MgSO_4$; 1.25 $NaH_2PO_4$; 26 $NaHCO_3$; 10 dextrose; bubbled with 95% $O_2$, 5% $CO_2$. Hippocampal slices (480 μm thick) were cut in horizontal sections from dorsal to ventral brain with a vibratome (Leica, VT1000S). Slices were incubated in ACSF for at least 2 h before each experiment. ACSF used for maintenance and recording contained (in mM) 132 NaCl; 3 KCl; 2 $CaCl_2$; 2 $MgSO_4$; 1.25 $NaH_2PO_4$; 26 $NaHCO_3$; 10 dextrose; bubbled with 95% $O_2$, 5% $CO_2$ at 26°C.

## Local Field Potential (LFP) Recording

Local Field Potential (LFP) recordings were done in a submerged chamber, and slices were placed on a mesh that allowed perfusion on both sides at a high flow rate (10–30 ml/min) (Hajos and Mody, 2009; Maier et al., 2009). All recordings were done with low resistance glass microelectrodes (∼150 kΩ tip resistance). The electrodes were pulled with a Sutter P87 puller with six controlled pulls and filled with 0.5 M NaCl in 1% agar, which prevents leakage of the electrode solution that could potentially alter the tissue surrounding the electrode tip. The recording electrode was placed in CA1 stratum *pyramidale*, where SWs have large amplitudes (Maier et al., 2009) in healthy slices.

## GCaMP Fluorescent Recording

The GCaMP signals were recorded by a 464-channel photodiode array (WuTech Instruments). The two-stage amplifier circuits in the diode array subtract the resting light intensity and amplify the small optical signals 100 times before digitization. This achieves a 21-bit effective dynamic range to fully digitize a signal of ∼0.5% $\Delta F/F$. [For a recent review of the two-stage imaging system, see Liang et al. (2015)].

The $\Delta F/F$ is defined as $(F_x - F_0)/F_0$, where $F_x$ is the signal trace from each detector and $F_0$ is the baseline fluorescent intensity. The signals were digitized at 1,616 frames/s. In some experiments, only the center of the field of view was sampled at 3,000 Hz, in order to preserve the high frequency components in the signal. The LFP and stimulation signals were sampled and digitized concurrently with the VSD signals. Optical imaging was performed on an upright microscope (Olympus BX51 WI) with an epi-illumination arrangement: excitation light (470 nm LED, ThorLabs) passes a GFP filter cube (Chroma, excitation 425–475 nm, dichroic mirror 480 and emission filter 485 long pass). The GCaMP signals were imaged at two spatial resolutions: A 20× objective (0.95 NA, Olympus) permitted the concurrent imaging of more localized cellular activity and population signals from the same tissue, and a 10× objective (0.30 NA, AMscopes) allowed for imaging all hippocampal subfields in the same field of view. The aperture of the diode array was 19 mm in diameter; containing a hexagonal arrangement of 464 optic fibers. The diameter of the fiber was 750 μm. Each detector on the array (pixel) collected florescent signals from an area of 37.5 μm in diameter with the 20× objective, and about 75 μm in diameter with the 10× objective. The total beam power of the LED was ∼350 mW at 1A. The fluorescent intensity on each detector was about 20,000 photoelectrons/ms for the 20× objective. Illumination intensity at the sample was $<20$ mW/mm$^2$.

## Voltage-Sensitive Dye (VSD) Imaging

Voltage-sensitive dye imaging was used to validate the response time of the GCaMP signal (**Figure 3**). In three slices, VSD and GCaMP signals are from the same tissue and imaged by the same diode array. The slices were stained by an oxonol dye, NK3630 (Nippon Kankoh-Shikiso Kenkyusho Co., Ltd., Japan), as an indicator of transmembrane potential. Slices were stained with 5–10 μg/ml of the dye dissolved in ACSF for 120 min (26°C). During staining, the ACSF was circulated and bubbled with 95% $O_2$, 5% $CO_2$. After staining, the slices were transferred back to the incubation chamber for at least 1 h before each experiment. NK3630 binds to the external surface of the membrane of all cells and reports their membrane potential change [for a recent review of the diode array and NK3630, see Liang et al. (2015)]. The absorption spectrum of the dye shifts linearly with the changes in the membrane potential (Ross et al., 1977). The VSD signal in this report is the change in absorption of light with a 705 nm wavelength. The detectable signals are a change in light intensity that is roughly 0.01–0.1% of the resting light intensity. Staining with this dye does not cause noticeable changes in spontaneous or evoked neuronal activity (Jin et al., 2002; Huang et al., 2004), and stained slices maintain viability for up to 24 h. In 705 nm recording light, NK3630 molecules do not generate fluorescence, so no noticeable phototoxicity is detected (Jin et al., 2002).

The VSD signals were recorded by the same diode array. With a transillumination arrangement, neurons through the whole thickness of the slice (480 μm) contribute relatively equally to the VSD signal. A tungsten filament lamp was used for illumination and a 705/10 nm interference filter (Chroma) was placed in the illumination path during optical recording.

During imaging experiments, the slice was continuously perfused in a submersion chamber with ACSF (same as the incubation solution) at 26°C and at a rate of more than 20 mL/min. Intermittent VSD imaging trials were performed, with 2–3 min intervals between trials.

### Stimulation

Stimulation to the CA3 area was provided with a concentric metal electrode (FHC CBDSE 75). Stimulation pulse was 0.1 ms wide generated by a Master 8 stimulator (AMPI). The stimulation current was 20–100 μA generated by an isolator (AMPI).

### Data Analysis

Digital filters were applied offline. To automatically detect the amplitude and peak time of the SW events in fluorescent signals (e.g., **Figure 1D**), we first digitally filtered the simultaneously recorded LFP signals between 1–30 Hz, then a threshold was set manually above the baseline noise to identify the majority of SW events in the LFP. Using a window between −50 and 100 ms of the LFP peak, the peak of the fluorescent signal was identified as the SW peak. Custom programs were written in MATLAB and Labview for digital filtering, threshold detection, and determining the amplitude and frequency distributions. For figure preparation, various bandpass ranges were chosen for the LFP and GCaMP signals to minimize filtering whenever possible. These specific ranges have been identified in figure legends.

In experiments with high frequency stimulation, in which the amplitude of the response was too small for quantification (**Figure 3E**), we used the root mean square (RMS) power in place of the amplitude. The RMS was calculated with the following equation:

$$X_{RMS} = \sqrt{\frac{1}{N}\sum_{n=1}^{N}|X_n|^2}$$

where $X_n$ is the signal amplitude at the sample point $n$, $X_{RMS}$ is the RMS power in a period of $N$ sampling points.

Statistics were conducted in Graphpad Prism 8.0. To compare differences in means we first checked normality and lognormality of data with Shapiro-Wilk tests. Differences in means of two groups were assessed by unpaired $t$-tests for parametric distributions, and Mann-Whitney for non-parametric distributions. For more than two groups we compared means via 1-way ANOVA with the Tukey multiple comparisons correction, or Kruskal-Wallis with Dunn's multiple comparisons test as appropriate. Error bars displayed are either SD or SEM, as indicated in figure legend. $^{*}p < 0.05$, $^{**}p < 0.01$, $^{***}p < 0.001$, $^{****}p < 0.0001$.

## RESULTS

### Spontaneous SWs Are Detectable in the Population GCaMP Signal

Spontaneous SWs reliably occur in hippocampal slices as reported by our previous papers and other groups (Kubota et al., 2003; Maier et al., 2003; Colgin et al., 2004; Behrens et al., 2005; Jiang et al., 2018; Sun et al., 2018). Our first goal was to test if SWs can be detected in the GCaMP6f signal in hippocampal slices from Thy1-GCaMP6f mice.

To test this, we positioned the slices with the end of the supra-pyramidal mossy fiber bundle at the center of the field of view of the diode array (**Figure 1A**), as this marks the boundary between CA3 and CA2 (Blackstad et al., 1970; Gaarskjaer, 1978). In Thy1-GCaMP6f mice the mossy fibers showed bright green fluorescence, due to the high expression in granule cells, providing a landmark for the outside limit of CA3 ("M" in **Figure 1A**). CA2 could also be clearly identified as a darker region devoid of fluorescent cell bodies. In this way, CA3, CA2, and CA1 could be clearly delineated. By positioning the end of the mossy fiber bundle at the center of the field of view, the 464 detectors on the diode array covered a large area including CA3, CA2, and CA1 (yellow hexagon in **Figure 1A**).

We observed one-to-one correlations between SW events detected in the LFP and GCaMP signals. In contrast to localized cellular calcium transients (Miyawaki et al., 2014), the population SW signals were reliably seen over a large area of hippocampal tissue spanning CA3, CA2, and CA1 (**Figures 1B,C**). Under a 20× objective, each optical detector received light from an area of 37.5 μm in diameter, so that the population signals we refer to in this report are a summation of the $\Delta F/F$ from both somatic and dendritic areas for a number of neurons under each optical detector.

Sharp wave peaks in the GCaMP signal were visible across trials, with a range in $\Delta F/F$ of 0.1–1.0% (**Figure 1C**). The signal-to-noise ratio was >10, allowing clearly distinguishable events above noise. LFP signals were simultaneously recorded with the GCaMP signals, both sampled at 1,616 Hz. From 11 slices we recorded 6,500 SW events optically, all with a one-to-one correspondence between LFP and optical recording of the GCaMP signals, with an average $\Delta F/F \sim 0.3\%$.

### Signal Polarity of SWs Across Hippocampal Layers

A notable difference between LFP and GCaMP recordings of SWs is the signal polarity in different laminar areas. LFP signals from str. *oriens* and str. *radiatum* have opposite polarities (Maier et al., 2009), as they form a current source-sink pair around str. *pyramidale* (Johsdon and Wu, 1994). This polarity reversal is obviously not observable in the $\Delta F/F$ (**Figure 1B**). GCaMP signals from soma (str. *pyramidale*) and neuropil (polymorphic or molecular layers) have the same polarity (increased $\Delta F/F$

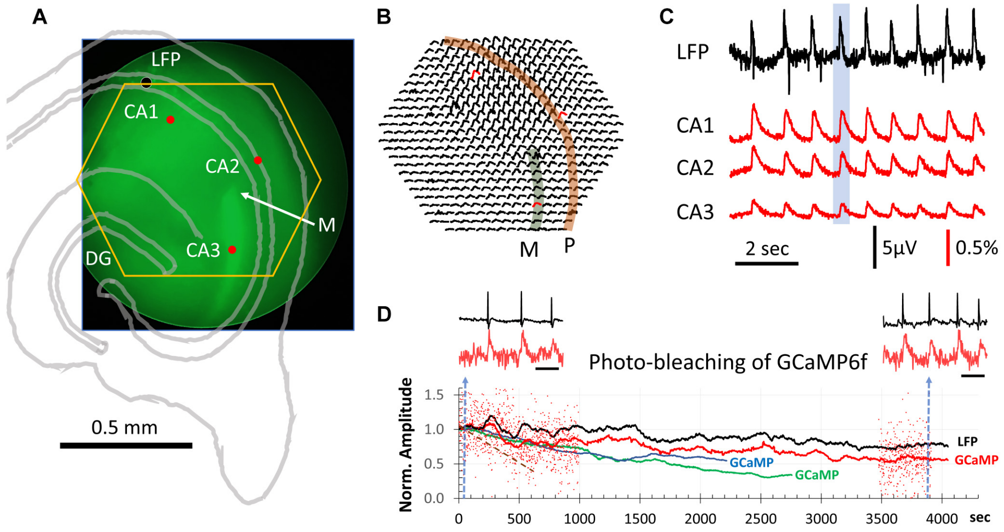

**FIGURE 1 |** GCaMP population signals of SWs across hippocampal subfields. **(A)** Slice positioning over the diode array. The end of mossy fibers (M) and lack of GCaMP6f expression in CA2 was used to identify the three hippocampal subfields CA1-3. The yellow hexagon marks the field of view of the diode array. The black dot marks the location of the LFP electrode. These structures were also outlined with an image of transmitted light (gray lines). **(B)** $\Delta F/F$ from all 464 diodes during a SW event. This SW was one of the 9 occurring during a 9-s recording sweep (blue box in **C**). Note that GCaMP signals of SWs were seen over a large area across CA1, CA2, and CA3. Str. *pyramidale* (P, orange band) and mossy fiber bundle (M. f\green band) are identified overlaying the signals. **(C)** LFP signals were simultaneously recorded with the GCaMP signals (both sampled at 1,616 Hz). Signals from three detectors in CA1, CA2 and CA3 [red dot/traces in panels **(A,B)**] plotted together with the LFP recording (filtered 0.1–30 Hz). The amplitude of SWs in the GCaMP signal were on average 0.3% $\Delta F/F$ with a signal-to-noise $>10$. From 11 slices we recorded ~6,500 SW events optically, all with a clear one-to-one correspondence between LFP and optical GCaMP signals. **(D)** Decline of optical signals over long recording periods due to photobleaching. Red dots mark the relative amplitude of individual SWs from one slice recording. For clarity, events are only shown for the first 1,000 and last 500 s. The relative $\Delta F/F$ amplitude is normalized to the average amplitude of the first 100 events at the beginning of light exposure. Black and red traces are averages of the LFP and GCaMP signals, respectively, in a sliding 100-event window. Blue and green traces are GCaMP signals from two additional animals. Brown broken line: another slice with exposure at 6 times the light intensity for 660 s. Left and right insets: LFP and GCaMP signals from one slice before and after 4300 s of continuous light exposure. Blue broken line in panel **(D)** marks the sample time of the two traces. Note that amplitude reduction due to photobleaching is not obvious in individual SWs, as spontaneous SWs have a large variation in amplitude. Scale bar for inset = 1 s.

at SW onset), suggesting that the calcium signals increase irrespective of current flow direction in the population.

## Photo-Bleaching Limits Long Recording Times

Continuous exposure to light while recording causes bleaching of the GCaMP fluorescent protein. We did observe a gradual reduction in SW amplitude with exposure time. To test the limits of optical recordings of SWs, we recorded continuously for over an hour (4,300 s). In a representative experiment (**Figure 1D**), the excitation light intensity was reduced to 1/4 of the intensity used in **Figure 1C**. Under this light intensity the SWs were still reliably detected, while the dark noise (noise in the electronics) became larger (**Figure 1D**, inset red traces). After long exposure, the amplitude of SWs in the optical signal reduced but were still distinguishable from noise. Because amplitude of spontaneous SWs varies over a large range (**Figure 1D**, red dots), amplitude reduction by photo-bleaching was often difficult to see from individual SW events. However, when the average of 100 SWs were plotted (**Figure 1D**, red curve), a clear trend of amplitude reduction in the optical signal was seen, compared to the simultaneously recorded LFP amplitude (**Figure 1D**, black curve). Similar long-duration recordings were performed in three slices from three animals (**Figure 1D**, blue and green traces). In these experiments the illumination intensity was kept constant, revealing slightly different rates of amplitude reduction. From these results we determined that reliable optical recordings were possible for at least 1,500 s of recording time with continuous illumination, equivalent to 100 15 s trials or 1,000–2,000 spontaneous SWs. At the illumination intensity 6 times greater than in **Figure 1D** (red, green, and blue), the bleaching rate was much faster, with the amplitude reduced to 50% in 660 s of exposure (**Figure 1D**, brown dashed line).

## Time Delay Between GCaMP and VSD Signals

GCaMP signals showed a significant delay compared to LFPs (**Figures 2A,B**, top traces). The peak of the population GCaMP6f signal lagged behind the peak of the LFP signal by 40.3 ms on average (SD 10.8 ms, $n$ = 84 SWs, in two slices from two animals) (**Figure 2C**). The delay time from two recording locations (**Figure 2A**, location a, b, ~1.2 mm apart along the CA1 str. *pyramidale*) was similar (**Figure 2B**, top traces), suggesting that the delay was not caused by spreading of the SW along the CA1 zone.

The delay time of the GCaMP6f population signal was verified with voltage-sensitive dye recordings. In three animals we stained the slices with the voltage sensitive dye NK3630.

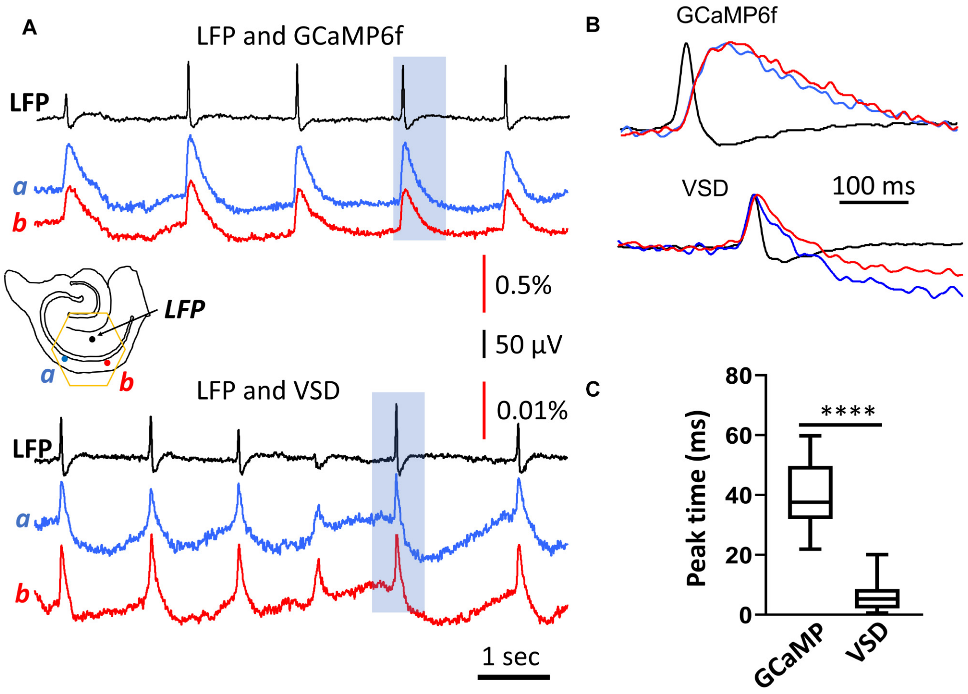

**FIGURE 2 |** Rise time of the population GCaMP6f signal. **(A)** LFP and GCaMP/VSD recordings of SWs in the same tissue. LFP (black trace, filtered 0.2–50 Hz) were highly correlated with events detected optically at two different CA1 locations either with GCaMP6f (blue and red traces, top, filtered 0.2–50 Hz) or VSD (blue and red traces, top, filtered 0.2–50 Hz). Note the different y-scale for GCaMP and VSD traces, GCaMP events were about 50 times larger and slower. Black arrows mark the SWs displayed in expanded time scale in panel **(B)** GCaMP signals showed a marked delay compared to the LFP, which was not observed in the VSD signals from the same tissue. **(C)** Box and whisker plots of the peak delay time between LFP and optical signals. As expected, GCaMP signals showed a longer delay time of 40.3 ms (SD 10.8 ms, $n = 84$ SWs, in two slices from two animals) compared to VSD delay time of 5.7 ms (SD 4.1 ms, $n = 82$ SWs from same slices), a significant difference of $p < 0.0001$ (Mann-Whitney).

The dye staining did not affect the spontaneous SW rate of occurrence or amplitude. The dye absorption signal measured at 705 nm emission wavelength was able to detect SWs. The VSD signal associated with a SW event was manifested by an increase in absorption at 705 nm, in accordance with the previously established nature of voltage imaging with absorption dyes, where dye molecules bind to the neuronal membrane with depolarized membrane potential (Ross et al., 1977). The VSD signal of SWs was fast with the peak correlating well with the LFP (**Figures 2A,B**, bottom traces). The VSD signal showed an insignificant delay to the LFP, 5.7 ms (SD 4.1 ms, $n = 82$ SWs, in two slices from two animals), demonstrating a good correlation between the population summation of membrane potential and LFP signal during SW events.

The GCaMP and VSD signals in **Figure 2** were measured from the same tissue in different recording trials. In the same tissue the VSD and the GCaMP signals were independent as the 705 nm light did not excite the GCaMP6f proteins. The GCaMP signals were measured at 500–530 nm (excited by 470 nm), and there is no significant contribution of VSDs at this wavelength.

A wavelength independent "intrinsic" optical signal was also seen at 705 nm in the VSD measurements. The intrinsic signal was slower and with a reversed polarity compared to the VSD signals at the 705 nm (Jin et al., 2002). The downward deflection in the VSD (**Figures 2A,B** bottom traces) were associated with this intrinsic optical signal.

Comparing with the VSD signals, the time delay in population GCaMP6f signals was likely dictated by the response of the GCaMP protein. The delay times in our population measurements were comparable to the delay times obtained using intracellular calcium measurements; a 40 ms rise time (Chen et al., 2013).

## Population GCaMP Signal Can Detect 20–40 Hz Evoked Activity

If individual calcium transients are far from saturation, the measured rise time of ∼40 ms of the population GCaMP6f optical signal should in theory allow following up to 20 Hz of network oscillations in the tissue. It may also be possible to detect higher frequency signals at attenuated amplitude. To test the frequency response of GCaMP6f population signals, we applied electrical stimulation to CA3 and measured the evoked population response in CA1. The stimulation intensity was low, adjusted to produce evoked LFP responses within the same amplitude range as spontaneous SWs in the same tissue (**Figure 3A**). Evoked GCaMP signals were observed in the CA3 and CA1 areas (**Figure 3A**, red and orange traces). When two stimuli

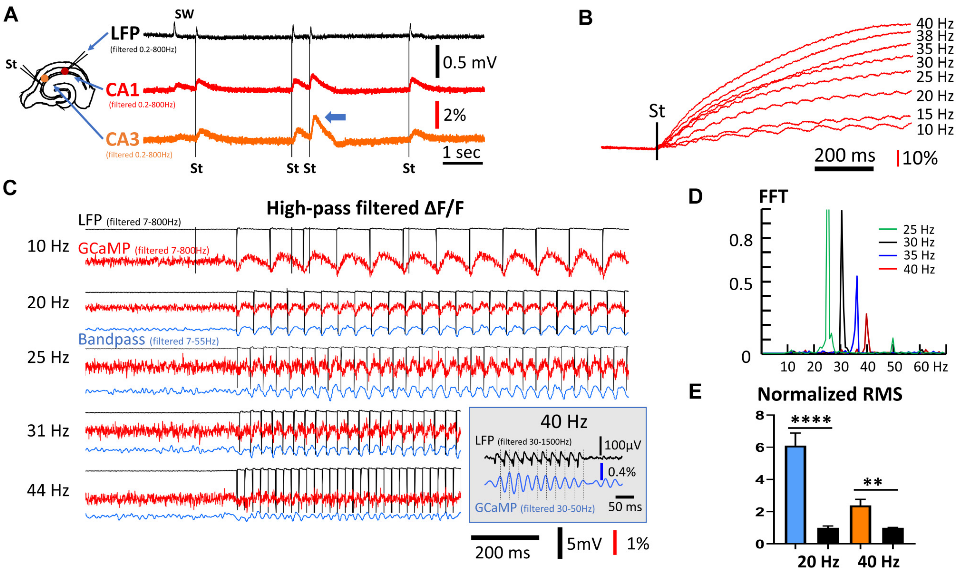

**FIGURE 3 |** Frequency response of population GCaMP signals. **(A)** GCaMP signals in response to mild electric stimuli. Left: The arrangement for the stimulation and recording. Stimuli were applied to CA3 and response was recorded in both CA1 and CA3. The stimulation intensity was adjusted so that the evoked response had an amplitude similar to the SW amplitude in the LFP signals. Note that double stimuli induced larger responses to the second shock, even with long inter-stimulus intervals of 500 ms (blue arrow head). **(B)** High frequency stimuli caused a ramp accumulation of GCaMP signals. Note that the ramp signal was much larger and slower than the response to individual stimuli. **(C)** Evoked GCaMP signal to high frequency stimuli. A high frequency component can be seen in wide-band filtered signals (red traces, 7–800 Hz). Narrow band filtered (blue traces, 7–55 Hz) improved signal-to-noise ratio. (Inset) In a follow-up experiment, 10 mild stimuli (1.4× threshold) at 40 Hz was given to CA3. A narrow bandpass filter (30–50 Hz) of the CA1 GCaMP signals reveals a clear one-to-one correlation between individual stimulus pulses (filtered 30–1500 Hz) and the GCaMP response. **(D)** Power spectrum of the GCaMP signals, normalized to the power at 30 Hz. The signal power reduced to ∼50% at 35 Hz and ∼25% at 40 Hz. Green peak at the 50 Hz is the 2nd harmonic of the 25 Hz peak. High frequency, weak stimuli experiments were done on three slices from three animals. Data in panels **(A,D)** are from different slices receiving stimuli of slightly different frequency. **(E)** RMS power quickly reduced in high frequency. The RMS power during 20 or 40 Hz stimulations was normalized to the RMS noise in the same trial when there was no stimulation. Blue and left black bars, narrow band-pass filtered between 5–30 Hz, $n = 8$ trials, three slices from three animals, $^{****}p < 0.0001$ (unpaired $t$-test). Orange and right black bars, narrow band-pass filtered between 25–50 Hz, $n = 9$ trials, three slices from three animals, $^{**}p = 0.0022$ (unpaired $t$-test). Error bars indicate SEM.

were delivered close in time, the response to the second stimulus was larger (**Figure 3A**, arrowhead), suggesting paired-pulse facilitation through buildup of calcium is detectable by population GCaMP signals.

With a train of stimuli of identical intensity, the GCaMP signals summated, forming a much larger rising ramp than the response to individual stimuli (**Figure 3B**). The $\Delta F/F$ amplitude evoked by individual stimuli were on average 0.1%, while the ramp signal from continuous 40 Hz stimulation was ∼100% (comparing **Figures 3B,C**). The ramp rise time was faster with higher stimulation frequency with the same intensity (**Figure 3B**). The large ramp signal suggests an accumulation of calcium. The time course of these long ramps might be caused by the slow clearance of intracellular calcium, while the individual responses may reflect fast calcium influx.

As the rise time of the long ramp signal was much slower than the rise time of individual responses, the ramp signal could be removed by a digital high-pass filter (7–800 Hz) (**Figure 3C**, red traces). The one-to-one relationship between evoked stimulation and GCaMP signal was maintained up to a frequency of 40 Hz. Responses to stimulation <30 Hz were clearly seen in high-pass filtered signals, while frequencies between 30 and 44 Hz were distinguishable by further band-pass filtering between 7 and 55 Hz (**Figure 3C**, blue traces). One-to-one correlations between stimulus and GCaMP signals were clearly seen at 31 Hz but not at 44 Hz. In a follow-up experiment, 10 mild stimuli (1.4× threshold) at 40 Hz was given to CA3, and a narrow bandpass filter (30–50 Hz) was used on the CA1 GCaMP signals. Under this condition a clear one-to-one correlation between individual stimulus pulses and the GCaMP response was identified (**Figure 3C**, inset). Response to the 40 Hz stimuli was further verified with a fast Fourier transform (FFT) (**Figure 3D**). While the 40 Hz FFT peak was much smaller compared to that of lower frequencies, the peak was clearly distinguishable from background noise. The frequency peaks show about a 50% reduction between 35 and 40 Hz. RMS power was calculated from data collected from three animals receiving 20 and 40 Hz stimulation (**Figure 3E**), demonstrating that the 40 Hz GCaMP6f signal was significantly higher than the RMS power of background noise ($p = 0.0022$, unpaired $t$-test, $n = 9$ trials from three slices from three mice).

## Amplitude Discrepancy Between GCaMP and LFP Signals

Exceptionally large GCaMP signals were occasionally observed during population events, while the LFP signals of the same

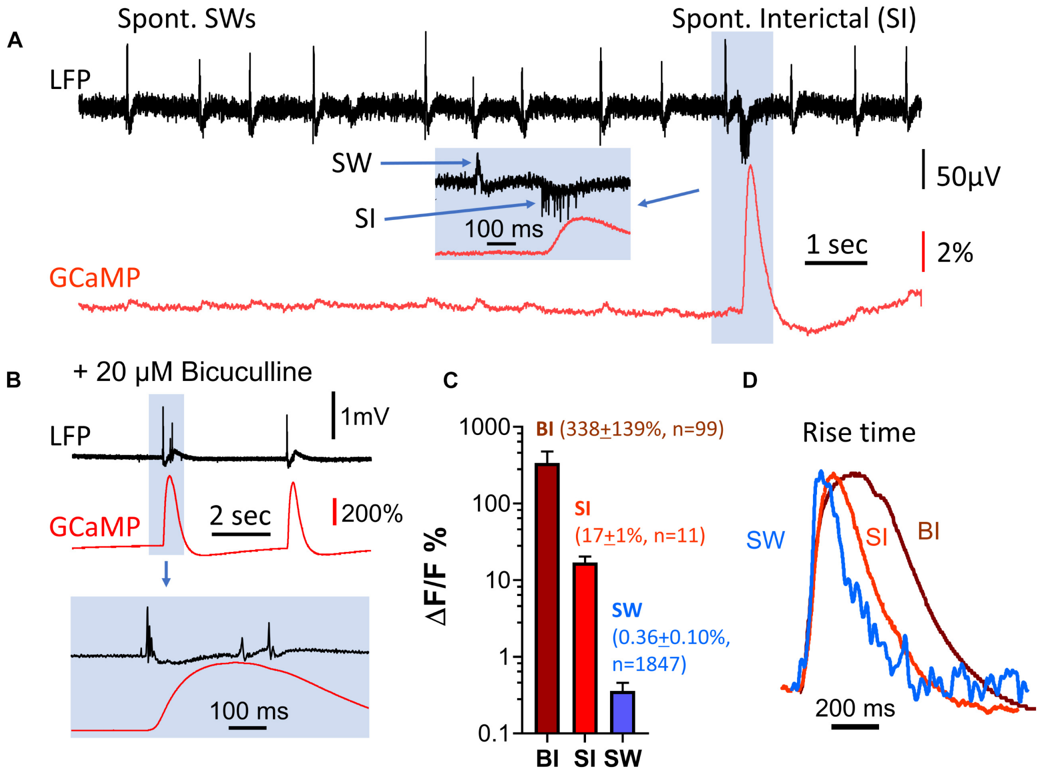

**FIGURE 4 |** Amplitude discrepancy between LFP and GCaMP signals during interictal-like events. **(A)** Spontaneous interictal events (blue box) rarely occur in healthy slices, and are associated with a low LFP peak amplitude but disproportionally large GCaMP fluorescence. The GCaMP signal was measured from the CA1 area, in a region of interest approximately 0.1 mm in diameter surrounding the location of the LFP electrode. *Inset (blue box)*: expanded time scale of the event, showing cellular spiking and the LFP peak of the interictal event. **(B)** Interictal-like events induced by bath supply of 20 μM bicuculline. Bottom traces display event highlighted in blue box above on expanded time scale. **(C)** Comparison of GCaMP6f $\Delta F/F$ amplitude for three types of events. BI: bicuculline-induced interictal-like spike, average $\Delta F/F = 338$ (SD 139%, $n = 99$ events from four slices from four animals). SI: spontaneous interictal event, average $\Delta F/F = 17\%$ (SD 1%, $n = 11$ events from one slice from one animal), SW: sharp wave, average $\Delta F/F = 0.36\%$ (SD 0.10%, $n = 1847$ events from the same slice with SIs). Error bars indicate SD. **(D)** Rise time of sharp wave (SW), spontaneous interictal events (SI) and bicuculline-induced interictal-like spikes (BI). The amplitude of the three events differ by a factor of ~600 but have similar initial rise times. Note that the decay time of the three events are different. These traces are averages of $n = 100$ SWs from one animal; $n = 11$ SIs from the same animal; $n = 10$ BIs from a different animal.

events were relatively small. These spontaneous interictal events had an amplitude of $\Delta F/F = 17\%$ (SD 1%, $n = 11$), almost 50 times greater than the amplitude of SWs in the same tissue [$\Delta F/F = 0.36\%$ (SD 0.10%, $n = 1847$)] (**Figure 4**). In contrast, the LFP signals of SWs and interictal spikes had similar amplitudes, but interictal spikes exhibited reversed polarity and increased extracellular spiking (**Figure 4A**, inset).

Spontaneous interictal events only occurred occasionally in 2 out of 11 slices examined, and their occurrence rate was low. In one characteristic slice, 1,847 SWs were recorded over 36 min, with only 11 spontaneous interictal events detected. To further investigate the discrepancy between amplitudes in the LFP and GCaMP6f signals, we examined induced interictal-like events with the $GABA_A$ receptor antagonist bicuculline. 20 μM bicuculline in ACSF was used to induce interictal-like spikes in four slices from four animals ($n = 99$ events, **Figure 4B**). The amplitudes of GCaMP events associated with bicuculline-induced interictal spikes were almost 1,000 times greater than the amplitudes of the SW events, while the LFP signal had a relative increase ranging from 5 to 20, demonstrating a large discrepancy in relative signal increases between GCaMP and LFP (**Figure 4C**).

Notably, the rise time, defined as the time for the signal to rise from 10 to 60% of peak, was about 40 ms for all three event types (spont. SW, spont. interictal, bicuculline-induced), despite the large amplitude differences in these events (**Figure 4D**). This suggests that the onset time of the optical population signal in all three cases is limited by the response time of GCaMP6f.

## Population GCaMP Signal Can Detect Carbachol-Induced Theta Oscillations

Carbachol-induced theta oscillations and related population events were next explored to further investigate the ability of GCaMP6f to monitor physiologically relevant hippocampal oscillations. When the perfusant was switched from normal ACSF to one containing 40 μM of the cholinergic agonist carbachol, spontaneous SWs disappeared and short bursts of theta oscillations (4–7 Hz) emerged, as recorded by the LFP electrode (**Figures 5A,B**). High amplitude GCaMP peaks were

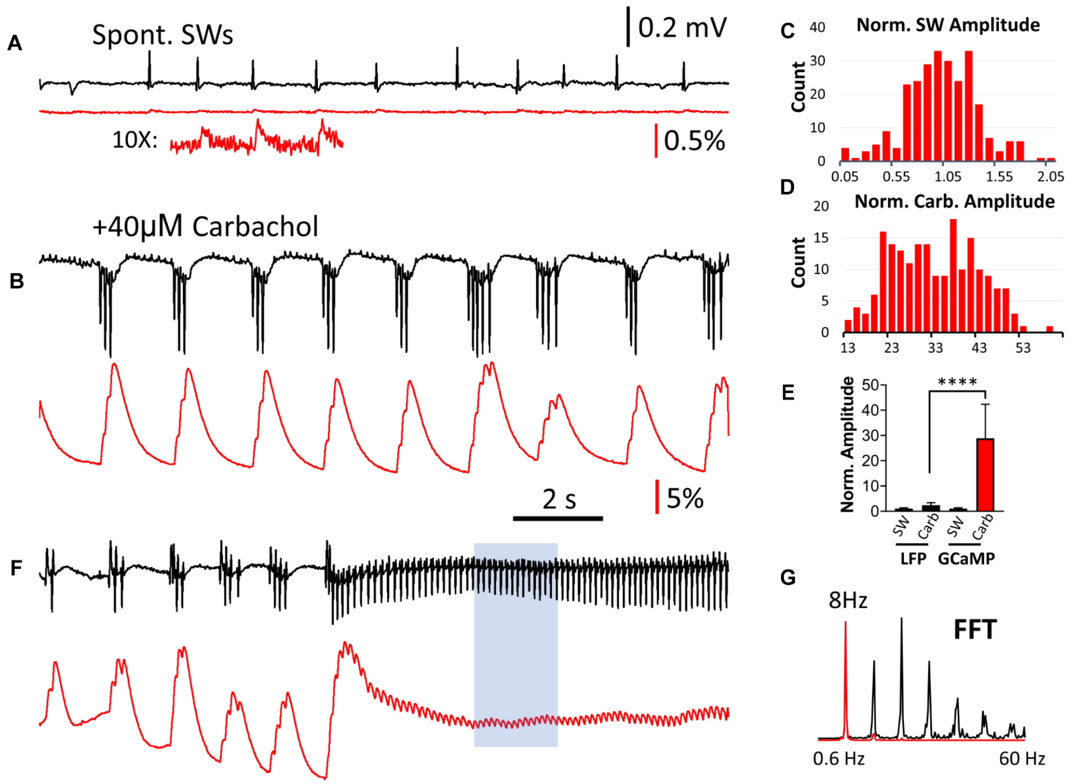

**FIGURE 5 |** Comparison of LFP and GCaMP signals during carbachol-induced theta oscillations. **(A)** Spontaneous SWs when the slice is bathed in normal ACSF, compared with **(B)** Induced theta bursts recorded from the same tissue after bath administration of 40 μM of the cholinergic agonist carbachol. The LFP and GCaMP signals are drawn on the same scales for panels **(A,B)**. On this amplitude scale the GCaMP SW events are very small, but can be clearly seen with 10× amplification (**A**, Inset). Note that the polarity of the LFP signals were reversed during theta bursts, and a group of three or more spikes in the LFP was merged into a single large peak with GCaMP. **(C)** Amplitude distribution of SWs in the GCaMP signals ($n = 260$ SWs, four slices from four animals), first normalized to the average amplitude from each slice and then pooled together in the distribution chart. **(D)** Amplitude distribution of carbachol-induced theta bursts in GCaMP signals ($n = 252$ bursts, four slices from four animals). The amplitude was normalized to the average SW amplitude in each slice. Note that the majority of bursts were 13–30 times larger than the SW in the same tissue. **(E)** Amplitude discrepancy: When LFP and GCaMP signals during bursts were normalized to the average amplitude of SWs in the same tissue, The increase in GCaMP was 28.9 (SD 13.5, $n = 252$ bursts, four slices from four animals) while the LFP was only 2.37 (SD 1.02, $n = 252$ bursts, four slices from four animals). Significant difference in medians from the Kruskal-Wallis test, $p < 0.0001$ (Dunn's multiple comparisons correction between LFP and GCaMP during carbachol show $p < 0.0001$). Error bars indicate SD. **(F)** Continuous theta cycles developed with continued carbachol perfusion. These ∼8 Hz oscillations were seen in both LFP and GCaMP signals. **(G)** An FFT of a sub-section of this signal (**F**, blue box) revealed a clear peak at 8 Hz in both the LFP and GCaMP6f signals, as well as higher harmonics.

observed during these theta bursts, and like interictal-like events, there was a large discrepancy between the change in amplitude in the LFP and GCaMP signals. The GCaMP signal accumulated with successive theta cycles (**Figure 5B**). While both SW and carbachol-induced bursts had a wide range of amplitude in GCaMP signal (**Figures 5C,D**), the amplitude of the carbachol-induced burst was on average greater than the amplitude of SW events by a factor of 28.9 (SD 13.5, $n = 252$ bursts, four slices from four animals) (**Figure 5E**). In contrast, the amplitude of LFP events increased by a factor of only 2.38 (SD 1.02, $n = 252$ bursts, four slices from four animals), further demonstrating the large amplitude discrepancy between LFP and GCaMP signals.

With continued carbachol perfusion, theta oscillations with continuous cycles developed (**Figure 5F**). These ∼8 Hz oscillations were seen in both LFP and GCaMP signals with one-to-one oscillation. An FFT of a sub-section of this signal (**Figure 5F**, blue box) revealed a clear peak at 8 Hz in both the LFP and GCaMP6f signals, as well as higher harmonics (**Figure 5G**).

## Population GCaMP Signal During Transition Period of Elevated and Asynchronous Activity

The large amplitude discrepancy between the LFP and GCaMP6f signals led us to investigate if GCaMP6f can be used to detect population activity insensitive to the LFP. Elevation of asynchronous firing in a neuronal population should generate only a nominal LFP, with asynchronous currents canceling each other out in the volume conductor surrounding the neurons. However, the GCaMP6f signal in this population would be expected to be high, due to the accumulation of calcium from elevated activity. With even higher levels of activity, depolarization block can lead to a cessation of firing and

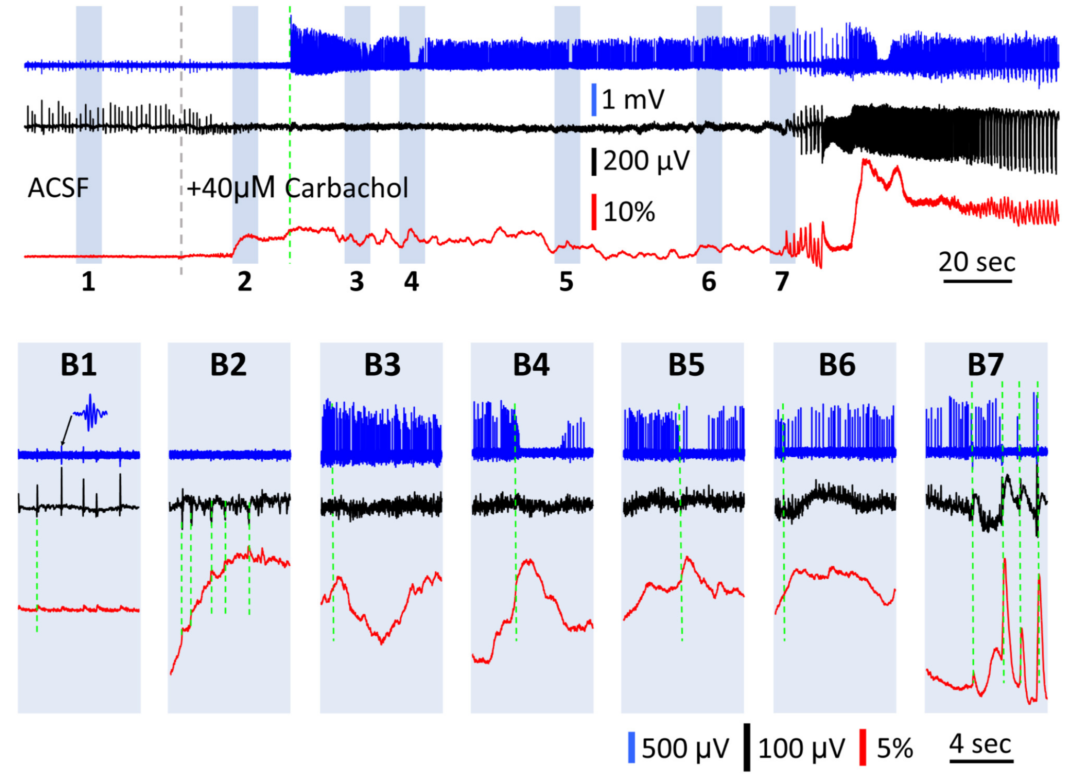

**FIGURE 6 |** GCaMP signals during the transition between SWs and carbachol induced bursts. **(A)** A 5 min recording of the transition period between spontaneous SWs and carbachol-induced theta oscillations. Blue trace shows the LFP filtered between 60–1,500 Hz (data sampled at 3,000 Hz), to isolate neuronal spikes from nearby cells. Black trace shows the LFP filtered between 0.1–30 Hz to isolate SWs (initial period) and theta bursts (final period). Red trace shows the GCaMP signal filtered between 0.1–30 Hz. Gray broken line marks the onset of 40 µM carbachol perfusion. Green broken line marks the onset of high spiking activity in the filtered blue trace. Particular periods of interest highlighted 1–7 to display on expanded time scale in panels **(B)**. **(B1)** Spontaneous SWs with coincident low amplitude GCaMP peaks (green dashed line) and nested ripple oscillations (inset) before carbachol administration. After carbachol administration, the GCaMP signal had slow and large fluctuations up to $\Delta F/F$ = 30%, or about 40 times the SW signals **(B2–B6)**. **(B2)** A period showing one-to-one correlations between observed peaks in the GCaMP and LFP signals (green dashed lines). **(B3–B6)** Periods showing minimal correlation between LFP and GCaMP fluctuations (comparing black and red traces, green dashed line marks onset of GCaMP peaks). **(B4,B5)** Periods showing anti-correlation between spiking rate and GCaMP fluctuations (comparing blue and red traces, green dashed line marks onset of GCaMP peaks). **(B7)** Onset of theta oscillations, showing large GCaMP peaks, high correlations between LFP and GCaMP, and synchronous bursts of spikes.

detectable activity in the LFP, yet with GCaMP6f, the elevated calcium that results from this should be readily detectable.

There was a transition period between SWs and carbachol-induced bursts, in which the GCaMP signal had large fluctuations while the LFP signal displayed only low amplitude peaks (**Figure 6**). Upon 40 µM carbachol administration, SWs abruptly stopped (**Figure 6A**, gray dashed line). A transition period of 3–4 min occurred, during which the GCaMP signal had slow and large fluctuations up to $\Delta F/F$ = 30%, or about 40 times the SW signals (**Figure 6B1** vs. **Figures 6B2–B6**). Meanwhile, the amplitude of the small peaks in the LFP was only 1/3–1/2 of that of the SW (**Figure 6B1** vs. **Figure 6B2**, red traces). These fluctuations only occurred after carbachol was added and SWs stopped (observed in two preparations) and became larger until organized theta bursts emerged (**Figure 6B7**). At times, one-to-one correlations were observed between peaks in the GCaMP and LFP signals (**Figure 6B2**). At other times however, these GCaMP signals displayed dynamics not readily apparent in the LFP recording (**Figures 6B3–B6**). Spikes from nearby neurons were detectable with the LFP electrode in some preparations (**Figure 6**, blue traces, sampled at 3000 Hz and filtered 60–1500 Hz). Spiking rate increased after carbachol, indicating elevated population activity. Peaks in GCaMP6f were also correlated to sudden drops in the firing frequency of neurons (**Figures 6B4,B5**). More obvious correlations between reduction in spiking and GCaMP peaks were seen when theta bursts developed (**Figure 6B7**), potentially from depolarization block or inhibition. Together these observations suggest that in highly excitable and asynchronous environments, GCaMP6f can reveal dynamics not detectable in the LFP, which alone is an incomplete snapshot of population activity.

## Cellular Transients Compared to Population Signals

Finally, we wanted to verify that compared to the population GCaMP6f signal, cellular calcium transients were large, localized

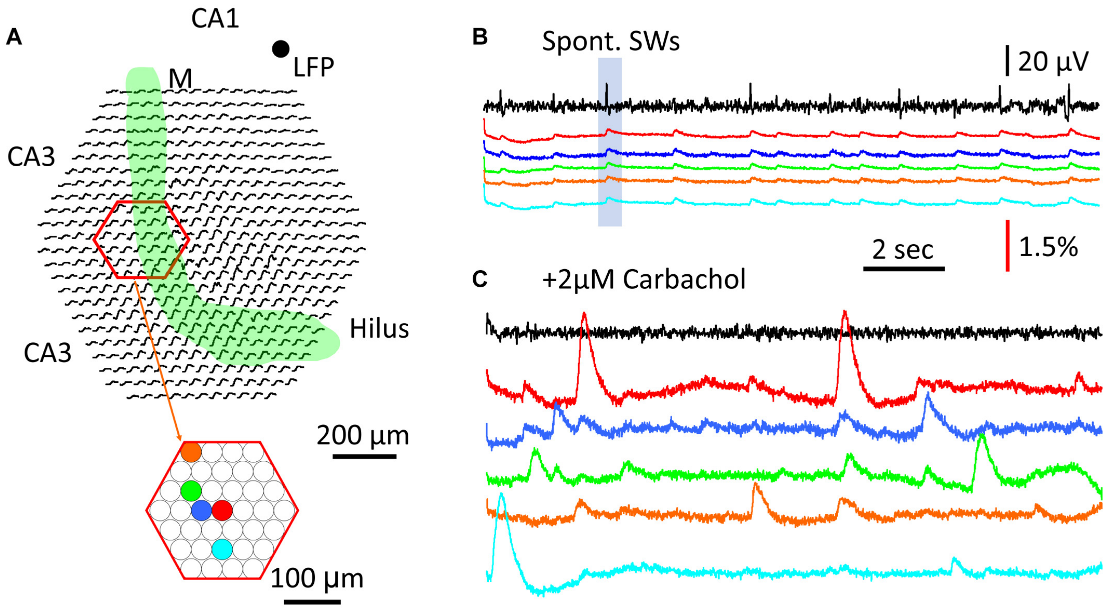

**FIGURE 7 |** Comparison between cellular transients and population GCaMP signal. **(A)** Schematic diagram of the imaging field. Green band marks the mossy fiber bundle. Red hexagon marks a subset of optical detectors imaging the CA3 pyramidal cell layer. Color dots mark five individual optical detectors; signals on these detectors are displayed in the color traces in panels **(B,C)**. **(B)** Traces of LFP (black) and GCaMP (colors) signals during SW events. LFP was recorded from a location in CA1, marked by the black dot on the top right of panel **(A)**. Color traces were from optical detectors (color dots in panel **A**). Blue box marks the particular SW event with optical recordings from the all detectors (black traces in the imaging field in panel **A**), demonstrating that a large fraction of optical detectors around the mossy fiber bundle show SW signals. **(C)** Cellular $Ca^{2+}$ transients recorded from individual detectors in the CA3 pyramidal layer. Color traces are from the same detectors in panels **(A)**. The signals in panels **(B,C)** were from the same tissue, during normal ACSF and 2 μM carbachol, respectively, a low concentration to promote activity but insufficient to induce theta busts. Note that the cellular $Ca^{2+}$ transients were often localized to individual detectors, and of high amplitude and longer duration than the population SW signals in panels **(A,B)**.

to the soma, and with longer duration as previously reported (Miyawaki et al., 2014; Norimoto et al., 2018). In contrast, the population GCaMP signals in the same tissue were expected to be small, distributed over a large area, and with shorter duration.

To test this, a region of CA3 str. *pyramidale* was imaged for cellular calcium transients (**Figure 7A**, red hexagon). Five detectors were chosen to show both SW population signals (**Figure 7B**) and cellular transients (**Figure 7C**). In normal ACSF the SW signals were seen in all five detectors (**Figure 7B**) as well as in most of the detectors throughout the imaging area (SW marked in shaded blue box in **Figure 7B** displayed over all detectors in **Figure 7A**). Later, 2 μM carbachol was added to the perfusion solution to promote cellular spiking, a low concentration that was found to be insufficient to induce theta bursts. Under this condition, localized large calcium transients were observed under one or a few detectors, suggesting cellular transients from spiking of individual neurons. Because the diode array had a low spatial resolution, these calcium transients cannot be attributed to individual CA3 neurons. However, these large signals were localized to one or a few detectors; e.g., the signals on neighboring red, blue, and green detectors only showed small crosstalk (**Figure 7C**), suggesting that the source of the signals was highly localized to the soma or dendrites of distinct CA3 neurons. In contrast, SW signals were distributed over the entire field of view.

The large and localized calcium transients showed a duration of 1–2 s, consistent with cellular calcium transients reported by other groups [e.g., (Dana et al., 2014; Miyawaki et al., 2014)]. The amplitude, spatial distribution, and time course of these local calcium signals all varied, suggesting differing sources.

## DISCUSSION

Our results suggest that $Ca^{2+}$ imaging of population activity can be a useful tool for monitoring activity critical for the consolidation and encoding of memory, e.g., SWs (**Figure 1**) and theta oscillations (**Figure 5**). By reliably detecting SW events, these data demonstrate that GCaMP6f is sensitive enough to detect population activity with sparse spiking and subthreshold activity. With appropriate amplification and filtering of the population signal, we observed that the temporal limit of population $Ca^{2+}$ imaging is close to the response time of the GCaMP6f protein (40 ms), enabling detection of oscillations up to 20 Hz (**Figure 3**). The range in amplitude for detected population signals with our method spans 3000-fold, from $\Delta F/F = 0.1–300\%$ and exhibits a dynamic range different from the accompanying changes to the LFP. In particular, it may be more sensitive than the LFP during highly elevated and asynchronous activity, where the interpretation of the LFP is often ambiguous (**Figure 6**).

## Temporal Limitations of Population GCaMP6f Signals

The rise time of the population GCaMP6f signal was measured to be 40.3 ± 10.8 ms, which is slower than organic calcium indicators [e.g., Cal-520, Rhof-4, (Lock et al., 2015) reviewed by Grienberger and Konnerth (2012)]. These data indicate that this response time is the major limitation for GCaMP6f to measure fast oscillations. Our results suggest that the speed of GCaMP6f is sufficient for measuring oscillations below 20 Hz, while this can be pushed up to 40 Hz with offline signal processing. A better solution for detecting gamma oscillations would be faster calcium sensitive proteins (Helassa et al., 2015, 2016; Dana et al., 2018).

## Population Signal vs. Cellular Transients

One major question raised by our results is whether the integration of CA1 cellular calcium transient would reproduce the population calcium signal seen during SWs. Cellular calcium imaging during SWs has been performed by the Ikegaya group from a large number of neurons with calcium transients in the CA1 area (Norimoto et al., 2012, 2018; Miyawaki et al., 2014). A careful analysis in these studies (Miyawaki et al., 2014) found that while 79% of neurons displaying calcium transients participated in SW events, each SW event only recruited ∼4% of these neurons. Additionally, each neuron participated in only ∼5% of SW events. Since ∼70% of neurons have calcium transients with and without SWs, it is unclear if integrating the individual cellular calcium transients would generate the population signal we observed in this report [see Figure 4 of Miyawaki et al. (2014)]. A large fraction of uncorrelated cellular transients would only contribute to the background fluorescence.

In contrast, the majority of CA1 neurons receive both excitatory and inhibitory synaptic inputs during every SW event (Hajos et al., 2013). The calcium influx in the presynaptic compartments of both excitatory and inhibitory neurons in the CA1 neuropil would contribute to the population GCaMP6f signal locked to the LFP, given that each CA3 neuron projects to 2/3 of the CA1 area and makes 30,000 to 60,000 excitatory synapses onto CA1 neurons (Li et al., 1994; Wittner et al., 2007). The post-synaptic response of the CA1 neurons might also have activate low threshold calcium channels [reviewed by Catterall (2000)] and contribute to the population calcium signal. The current imaging method cannot distinguish whether the signals are from pre- or post-synaptic calcium influx. Our signals are most likely from both, in addition to the regenerative calcium dynamics in the dendritic tree (dendritic calcium spikes). Further experiments are needed to distinguish the source of the population calcium signal.

Cellular calcium transients reach $\Delta F/F$ = 30–2000% when recorded under a dark background with confocal or two photon microscopes. Under bright field fluorescent imaging the background is no longer dark so the fractional change would be greatly reduced. In our wide-field fluorescent imaging the cellular calcium transients range from 2 to 5 times the population GCaMP signals (**Figure 7**). The population signal of SWs is a small intensity change over a brighter background (a light flux of ∼10,000 photoelectrons/ms) which would saturate EMCCDs.

## Greater Dynamic Range of Population GCaMP Signal

GCaMP6f and LFP signals showed a striking amplitude discrepancy during population events (**Figures 4–6**). Spontaneous and bicuculline-induced interictal events, as well as carbachol-induced theta oscillations showed a much greater $Ca^{2+}$ than LFP response. We hypothesize this greater dynamic range in $\Delta F/F$ values compared to the LFP to be due to the population GCaMP6f signal increasing more linearly with increased cellular participation. The LFP will be limited in magnitude due to precise synchrony of voltage-gated and synaptic currents, as well as volume conduction throughout the slice. In contrast, the much slower kinetics of $Ca^{2+}$, and the sensitivity of GCaMP6f to depolarized voltages renders the population GCaMP6f signal more sensitive than the LFP in highly active and/or asynchronous environments.

This high amplitude GCaMP6f signal likely reflects increased population firing rate and not artifact, as we never observed such increases outside of interictal events or carbachol administration. The decay time of GCaMP6f is about 200 ms (Chen et al., 2013), therefore, all calcium transients within the decay period should accumulate and contribute to the population signal. In addition to this, the continued accumulation of intracellular calcium will lengthen the population signal. Individual neurons' calcium transients last on average 1 s for GCaMP6f [**Figure 7**, see also (Chen et al., 2013; Dana et al., 2014) as well as measurements with organic calcium indicators (Miyawaki et al., 2014)]. These long duration intracellular calcium transients are limited by calcium buffering/elimination processes (Helmchen and Tank, 2015).

The accumulation of the population GCaMP signal was also clearly seen in the ramp-like signals in **Figure 3B**, where repetitive stimuli caused a rising ramp, with the ramp slope becoming steeper with higher stimulus frequencies. The ramp signal was much slower and larger compared to the signal induced by individual stimuli. This might partially explain the amplitude discrepancy. In contrast to the population accumulation, on a single cell level, post-synaptic potentials and the GCaMP6 signal time course are much better correlated (Kupferschmidt and Lovinger, 2015).

The accumulation of population GCaMP signals may offer a sensitive indicator for the "spiking density" in the population. Spiking density here refers to an increased firing rate on a temporal scale of ∼100 ms, which is distinct from the more common concept of synchrony, or coincident firing on a millisecond temporal scale. With this definition, high spiking density would not necessarily result in high LFP peaks, as sodium and potassium currents could negate each other if the firing rates between neurons are not closely synchronous.

## Population GCaMP Signals for Detecting Asynchronous Population Activity

During the transition between SW and theta oscillations (**Figure 6**), the LFP showed only a nominal signal while the population GCaMP signal exhibited large fluctuations. Four observations in **Figure 6** suggest that the fluctuations are not noise. First, correlations can be seen between small LFP peaks and GCaMP signals (**Figure 6B2**), indicating that the fluctuations were not random. Second, the fluctuations only occurred during the transition between the SW and the theta oscillations (**Figure 6A**), but never during SW states. Third, the fluctuations gradually increased to become large peaks with one-to-one correlation with LFP bursts (**Figure 6B7**), suggesting the population firing gradually became organized into theta oscillations. Fourth, while the LFP only displayed nominal peaks during the transition, the LFP electrode often picked up spikes from nearby neurons. The high firing rate of nearby neurons suggests an asynchronous state in the population (**Figure 6A**). In addition, the reduction of cellular firing was weakly correlated to GCaMP6f fluctuations (**Figures 6B4,B5,B7**).

## SWs vs. Epileptiform Activity

There is an active debate whether *in vitro* SWs are more reflective of epileptiform or other pathological events (Karlocai et al., 2014; Buzsaki, 2015). We demonstrated that the two events have large differences in GCaMP6f characteristics. Spontaneous interictal events, while rare, can happen without changing the bath solution or the excitability of the slices in our preparation (**Figure 3A**). While the LFP did display altered shapes between the events, the GCaMP6f response was even more highly divergent, indicating that they are different types of events. This provides evidence that *in vitro* SWs are distinct from epileptiform activity.

## Limitations and Advantages of the Diode Device

In contrast to many calcium imaging experiments, we employed a diode array for our measurements. The limiting factor for the sensitivity of the device is the dark noise of the electronics. The intensity of excitation light needs to be high enough so the signal can be distinguished from the dark noise. Bleaching of GCaMP6f fluorescence is a major limitation for the method. In order to achieve $>30$ min of optical recording time, the excitation light needs to be adjusted as low as possible while maintaining sufficient signal to noise. Under light illumination intensity, the dark noise becomes a major limitation for small signals. When approximately 100 mW of LED light output was used through a $10 \times 0.3$ NA objective, which delivers $<1$ mW/cm$^2$ onto the tissue, resulting in dark noise about 20% of the SW peaks. Higher excitation power may also get better sensitivity with a trade-off in optical recording time. However, 30 min of light exposure was more than enough for many experiments.

The high dynamic range of the diode array is a main advantage. For detecting 0.1% $\Delta F/F$ on top of 100% background fluorescent light, a 16–20 bit effective dynamic range would be needed. Such high dynamic range is necessary for detecting small population signal with a sensitivity comparable to LFP.

Some of our results are compatible with a recent *in vivo* photometry study (Kupferschmidt et al., 2017), in which high frequency stimuli generated a slow accumulative response and faster individual responses, and epileptiform events displayed high amplitude GCaMP6s signals. We were able to resolve fast signals up to 30 Hz on single trials, and able to record small signals ($\sim$0.1 $\Delta F/F$) during hippocampal SWs. This is due to the diode array having a higher dynamic range and signal-to-noise ratio than photomultiplier-based devices. Further work is needed to verify if the high signal-to-noise ratio can be achieved under *in vivo* conditions with optical fibers.

# CONCLUSION

In conclusion, this work demonstrates that population GCaMP signals offer a useful complementary approach to image small and fast population activity, with comparable sensitivity to LFP recordings. A planned future direction is *in vivo* imaging of spontaneously occurred theta (4–8 Hz), alpha/mu (7–13 Hz) and beta (15–20 Hz) oscillations. Faster calcium sensors may allow more robust detection and monitoring of gamma oscillations in the 40 Hz range. GCaMP permits multiple-site no-contact recordings, revealing spatiotemporal dynamics of neuronal oscillations. In addition, optical signals are not disturbed by the artifact of electrical stimulation, suitable for applications requiring simultaneous recording and stimulation, e.g., augmenting EEG oscillations by transcranial repetitive AC or magnetic stimulation [Zhai group 2019, current biology 2019], which currently no other methods can achieve.

# ETHICS STATEMENT

This study was carried out in accordance with the laboratory animal welfare guidelines, NIH Office of Laboratory Animal Welfare. The protocol was approved by the Institutional Animal Care and Use Committee of Georgetown University Medical Center.

# AUTHOR CONTRIBUTIONS

PL, HJ, and JYW conducted the experiments. All authors participated in the data analysis and the composition of the manuscript.

# FUNDING

This study was supported by the Georgetown University Dean's Toulmin Pilot award FY18 to JYW, the Scientific Research Common Program of Beijing Municipal Commission of Education No. KM201810025015 and the National Natural Science Foundation of China No. 61302035 to XG. AC was supported by the NIH/NCATS TL1 TR001431 and the NIH/NIA F31 AG062030. The content is solely the responsibility of the authors and does not necessarily represent the official views of the National Institutes of Health.

# REFERENCES

Behrens, C. J., van den Boom, L. P., de Hoz, L., Friedman, A., and Heinemann, U. (2005). Induction of sharp wave-ripple complexes in vitro and reorganization of hippocampal networks. *Nat. Neurosci.* 8, 1560–1567. doi: 10.1038/nn1571 doi: 10.1038/nn1571

Blackstad, T. W., Brink, K., Hem, J., and Jeune, B. (1970). Distribution of hippocampal mossy fibers in the rat. An experimental study with silver impregnation methods. *J. Comp. Neurol.* 138, 433–449. doi: 10.1002/cne.901380404

Buzsaki, G. (2015). Hippocampal sharp wave-ripple: a cognitive biomarker for episodic memory and planning. *Hippocampus* 25, 1073–1188. doi: 10.1002/hipo.22488

Catterall, W. A. (2000). Structure and regulation of voltage-gated calcium channels. *Annu. Rev. Cell Dev. Biol.* 16, 521–555. doi: 10.1146/annurev.cellbio.16.1.521

Chen, T. W., Wardill, T. J., Sun, Y., Pulver, S. R., Renninger, S. L., Baohan, A., et al. (2013). Ultrasensitive fluorescent proteins for imaging neuronal activity. *Nature* 499, 295–300. doi: 10.1038/nature12354

Colgin, L. L., Kubota, D., Jia, Y., Rex, C. S., and Lynch, G. (2004). Long-term potentiation is impaired in rat hippocampal slices that produce spontaneous sharp waves. *J. Physiol.* 558(Pt 3), 953–961. doi: 10.1113/jphysiol.2004.068080

Csicsvari, J., Hirase, H., Czurko, A., Mamiya, A., and Buzsaki, G. (1999a). Fast network oscillations in the hippocampal CA1 region of the behaving rat. *J. Neurosci.* 19:RC20.

Csicsvari, J., Hirase, H., Czurko, A., Mamiya, A., and Buzsaki, G. (1999b). Oscillatory coupling of hippocampal pyramidal cells and interneurons in the behaving Rat. *J. Neurosci.* 19, 274–287. doi: 10.1523/jneurosci.19-01-00274.1999

Cui, G., Jun, S. B., Jin, X., Pham, M. D., Vogel, S. S., Lovinger, D. M., et al. (2013). Concurrent activation of striatal direct and indirect pathways during action initiation. *Nature* 494, 238–242. doi: 10.1038/nature11846

Dana, H., Chen, T. W., Hu, A., Shields, B. C., Guo, C., Looger, L. L., et al. (2014). Thy1-GCaMP6 transgenic mice for neuronal population imaging in vivo. *PLoS One* 9:e108697. doi: 10.1371/journal.pone.0108697

Dana, H., Sun, Y., Mohar, B., Hulse, B., Hasseman, J. P., Tsegaye, G., et al. (2018). High-performance GFP-based calcium indicators for imaging activity in neuronal populations and microcompartments. *bioRxiv* [Preprint]. doi: 10.1101/434589

Demuro, A., and Parker, I. (2004). Imaging the activity and localization of single voltage-gated Ca(2+) channels by total internal reflection fluorescence microscopy. *Biophys. J.* 86, 3250–3259. doi: 10.1016/S0006-3495(04)74373-74378

Gaarskjaer, F. B. (1978). Organization of the mossy fiber system of the rat studied in extended hippocampi. II. Experimental analysis of fiber distribution with silver impregnation methods. *J. Comp. Neurol.* 178, 73–88. doi: 10.1002/cne.901780105

Grienberger, C., and Konnerth, A. (2012). Imaging calcium in neurons. *Neuron* 73, 862–885. doi: 10.1016/j.neuron.2012.02.011

Hajos, N., Karlocai, M. R., Nemeth, B., Ulbert, I., Monyer, H., Szabo, G., et al. (2013). Input-output features of anatomically identified CA3 neurons during hippocampal sharp wave/ripple oscillation in vitro. *J. Neurosci.* 33, 11677–11691. doi: 10.1523/JNEUROSCI.5729-12.2013

Hajos, N., and Mody, I. (2009). Establishing a physiological environment for visualized in vitro brain slice recordings by increasing oxygen supply and modifying aCSF content. *J. Neurosci. Methods* 183, 107–113. doi: 10.1016/j.jneumeth.2009.06.005

Helassa, N., Podor, B., Fine, A., and Torok, K. (2016). Design and mechanistic insight into ultrafast calcium indicators for monitoring intracellular calcium dynamics. *Sci. Rep.* 6:38276. doi: 10.1038/srep38276

Helassa, N., Zhang, X. H., Conte, I., Scaringi, J., Esposito, E., Bradley, J., et al. (2015). Fast-response calmodulin-based fluorescent indicators reveal rapid intracellular calcium dynamics. *Sci. Rep.* 5:15978. doi: 10.1038/srep15978

Helmchen, F., and Tank, D. W. (2015). A single-compartment model of calcium dynamics in nerve terminals and dendrites. *Cold Spring Harb. Protoc.* 2015, 155–167. doi: 10.1101/pdb.top085910

Huang, X., Troy, W. C., Yang, Q., Ma, H., Laing, C. R., Schiff, S. J., et al. (2004). Spiral waves in disinhibited mammalian neocortex. *J. Neurosci.* 24, 9897–9902. doi: 10.1523/jneurosci.2705-04.2004

Jiang, H., Liu, S., Geng, X., Caccavano, A., Conant, K., Vicini, S., et al. (2018). Pacing hippocampal sharp-wave ripples with weak electric stimulation. *Front. Neurosci.* 12:164. doi: 10.3389/fnins.2018.00164

Jin, W., Zhang, R. J., and Wu, J. Y. (2002). Voltage-sensitive dye imaging of population neuronal activity in cortical tissue. *J. Neurosci. Methods* 115, 13–27. doi: 10.1016/s0165-0270(01)00511-8

Johsdon, D., and Wu, M.-S. (1994). *Foundations of Cellular Neurophysiology*. Cambridge, MA: MIT Press.

Karlocai, M. R., Kohus, Z., Kali, S., Ulbert, I., Szabo, G., Mate, Z., et al. (2014). Physiological sharp wave-ripples and interictal events in vitro: what's the difference? *Brain* 137(Pt 2), 463–485. doi: 10.1093/brain/awt348

Kubota, D., Colgin, L. L., Casale, M., Brucher, F. A., and Lynch, G. (2003). Endogenous waves in hippocampal slices. *J. Neurophysiol.* 89, 81–89. doi: 10.1152/jn.00542.2002

Kupferschmidt, D. A., Juczewski, K., Cui, G., Johnson, K. A., and Lovinger, D. M. (2017). Parallel, but dissociable, processing in discrete corticostriatal inputs encodes skill learning. *Neuron* 96, 476–489.e475. doi: 10.1016/j.neuron.2017.09.040

Kupferschmidt, D. A., and Lovinger, D. M. (2015). Inhibition of presynaptic calcium transients in cortical inputs to the dorsolateral striatum by metabotropic GABA(B) and mGlu2/3 receptors. *J. Physiol.* 593, 2295–2310. doi: 10.1113/JP270045

Li, X. G., Somogyi, P., Ylinen, A., and Buzsaki, G. (1994). The hippocampal CA3 network: an in vivo intracellular labeling study. *J. Comp. Neurol.* 339, 181–208. doi: 10.1002/cne.903390204

Liang, J., Xu, W., Geng, X., and Wu, J. Y. (2015). Monitoring population membrane potential signals from neocortex. *Adv. Exp. Med. Biol.* 859, 171–196. doi: 10.1007/978-3-319-17641-3_7

Lock, J. T., Parker, I., and Smith, I. F. (2015). A comparison of fluorescent Ca(2)(+) indicators for imaging local Ca(2)(+) signals in cultured cells. *Cell Calcium* 58, 638–648. doi: 10.1016/j.ceca.2015.10.003

Maier, N., Morris, G., Johenning, F. W., and Schmitz, D. (2009). An approach for reliably investigating hippocampal sharp wave-ripples in vitro. *PLoS One* 4:e6925. doi: 10.1371/journal.pone.0006925

Maier, N., Nimmrich, V., and Draguhn, A. (2003). Cellular and network mechanisms underlying spontaneous sharp wave-ripple complexes in mouse hippocampal slices. *J. Physiol.* 550(Pt 3), 873–887. doi: 10.1113/jphysiol.2003.044602

Miyawaki, T., Norimoto, H., Ishikawa, T., Watanabe, Y., Matsuki, N., and Ikegaya, Y. (2014). Dopamine receptor activation reorganizes neuronal ensembles during hippocampal sharp waves in vitro. *PLoS One* 9:e104438. doi: 10.1371/journal.pone.0104438

Mizuseki, K., and Buzsaki, G. (2013). Preconfigured, skewed distribution of firing rates in the hippocampus and entorhinal cortex. *Cell Rep.* 4, 1010–1021. doi: 10.1016/j.celrep.2013.07.039

Muto, A., Ohkura, M., Abe, G., Nakai, J., and Kawakami, K. (2013). Real-time visualization of neuronal activity during perception. *Curr. Biol.* 23, 307–311. doi: 10.1016/j.cub.2012.12.040

Neher, E. (2013). Quantitative aspects of calcium fluorimetry. *Cold Spring Harb. Protoc.* 2013, 918–924. doi: 10.1101/pdb.top078204

Norimoto, H., Makino, K., Gao, M., Shikano, Y., Okamoto, K., Ishikawa, T., et al. (2018). Hippocampal ripples down-regulate synapses. *Science* 359, 1524–1527. doi: 10.1126/science.aao0702

Norimoto, H., Mizunuma, M., Ishikawa, D., Matsuki, N., and Ikegaya, Y. (2012). Muscarinic receptor activation disrupts hippocampal sharp wave-ripples. *Brain Res.* 1461, 1–9. doi: 10.1016/j.brainres.2012.04.037

Regehr, W. (2000). "Monitoring presynaptic calcium dynamics with membrane-permeant indicators," in *Imaging Neurons: A Laboratory Manual*, eds R. Yuste, F. Lanni, and A. Konnerth (New York, NY: Cold Spring Harbor Laboratory Press).

Ross, W. N., Salzberg, B. M., Cohen, L. B., Grinvald, A., Davila, H. V., Waggoner, A. S., et al. (1977). Changes in absorption, fluorescence, dichroism, and Birefringence in stained giant axons: optical measurement of membrane potential. *J. Membr. Biol.* 33, 141–183. doi: 10.1007/bf01869514

Shuai, J., and Parker, I. (2005). Optical single-channel recording by imaging calcium flux through individual ion channels: theoretical considerations and limits to resolution. *Cell Calcium* 37, 283–299. doi: 10.1016/j.ceca.2004.10.008

Sun, Z. Y., Bozzelli, P. L., Caccavano, A., Allen, M., Balmuth, J., Vicini, S., et al. (2018). Disruption of perineuronal nets increases the frequency of sharp wave ripple events. *Hippocampus* 28, 42–52. doi: 10.1002/hipo.22804

Svoboda, K., Denk, W., Kleinfeld, D., and Tank, D. W. (1997). In vivo dendritic calcium dynamics in neocortical pyramidal neurons. *Nature* 385, 161–165. doi: 10.1038/385161a0

Wittner, L., Henze, D. A., Zaborszky, L., and Buzsaki, G. (2007). Three-dimensional reconstruction of the axon arbor of a CA3 pyramidal cell recorded and filled in vivo. *Brain Struct. Funct.* 212, 75–83. doi: 10.1007/s00429-007-0148-y

Xing, X., and Wu, C. F. (2018). Unraveling synaptic GCaMP signals: differential excitability and clearance mechanisms underlying distinct Ca(2+) dynamics in tonic and phasic excitatory, and aminergic modulatory motor terminals in *Drosophila*. *eNeuro* 5:ENEURO.0362-17.2018. doi: 10.1523/ENEURO.0362-17.2018

Ylinen, A., Bragin, A., Nadasdy, Z., Jando, G., Szabo, I., Sik, A., et al. (1995). Sharp wave-associated high-frequency oscillation (200 Hz) in the intact hippocampus: network and intracellular mechanisms. *J. Neurosci.* 15(Pt 1), 30–46. doi: 10.1523/jneurosci.15-01-00030.1995

**Conflict of Interest Statement:** WuTech Instruments is a company owned by JYW. The diode array used in this research is a gift of WuTech Instruments.

The remaining authors declare that the research was conducted in the absence of any commercial or financial relationships that could be construed as a potential conflict of interest.

frontiers in Cellular Neuroscience

REVIEW
published: 16 July 2019
doi: 10.3389/fncel.2019.00321

# Primer to Voltage Imaging With ANNINE Dyes and Two-Photon Microscopy

*Bernd Kuhn* and Christopher J. Roome*

*Okinawa Institute of Science and Technology Graduate University, Okinawa, Japan*

ANNINE-6 and ANNINE-6plus are voltage-sensitive dyes that when combined with two-photon microscopy are ideal for recording of neuronal voltages *in vivo*, in both bulk loaded tissue and the dendrites of single neurons. Here, we describe in detail but for a broad audience the voltage sensing mechanism of fast voltage-sensitive dyes, with a focus on ANNINE dyes, and how voltage imaging can be optimized with one-photon and two-photon excitation. Under optimized imaging conditions the key strengths of ANNINE dyes are their high sensitivity (0.5%/mV), neglectable bleaching and phototoxicity, a linear response to membrane potential, and a temporal resolution which is faster than the optical imaging devices currently used in neurobiology (order of nanoseconds). ANNINE dyes in combination with two-photon microscopy allow depth-resolved voltage imaging in bulk loaded tissue to study average membrane voltage oscillations and sensory responses. Alternatively, if ANNINE-6plus is applied internally, supra and sub threshold voltage changes can be recorded from dendrites of single neurons in awake animals. Interestingly, in our experience ANNINE-6plus labeling is impressively stable *in vivo*, such that voltage imaging from single Purkinje neuron dendrites can be performed for 2 weeks after a single electroporation of the neuron. Finally, to maximize their potential for neuroscience studies, voltage imaging with ANNINE dyes and two-photon microscopy can be combined with electrophysiological recording, calcium imaging, and/or pharmacology, even in awake animals.

**Keywords: voltage-sensitive dye, VSD, voltage imaging, ANNINE, electrochromism, solvatochromism, membrane potential, two-photon**

***Edited by:***
*Josef Bischofberger,*
*University of Basel, Switzerland*

***Reviewed by:***
*Srdjan D. Antic,*
*University of Connecticut Health Center, United States*
*Dejan Zecevic,*
*Yale University, United States*

****Correspondence:***
*Bernd Kuhn*
*bkuhn@oist.jp*

***Specialty section:***
*This article was submitted to Cellular Neurophysiology, a section of the journal Frontiers in Cellular Neuroscience*

***Received:*** *23 May 2019*
***Accepted:*** *01 July 2019*
***Published:*** *16 July 2019*

***Citation:***
*Kuhn B and Roome CJ (2019) Primer to Voltage Imaging With ANNINE Dyes and Two-Photon Microscopy. Front. Cell. Neurosci. 13:321. doi: 10.3389/fncel.2019.00321*

## INTRODUCTION

ANNINE-6 and ANNINE-6plus are voltage-sensitive dyes successfully implemented for *in vivo* imaging with two-photon microscopy in bulk loaded tissue (Kuhn et al., 2008) as well as in dendrites of single neurons (Roome and Kuhn, 2018). ANNINE dyes (Hübener et al., 2003; Kuhn and Fromherz, 2003; Fromherz et al., 2008) were developed and designed based on elaborate physical chemistry studies and theoretical models in the laboratory of Peter Fromherz (Ephardt and Fromherz, 1991, 1993; Fromherz and Heilemann, 1992; Fromherz, 1995; Röcker et al., 1996). ANNINE-6 was first synthesized in 1996, but it took several years of optimizations until effective protocols for voltage imaging (Kuhn et al., 2004) and labeling (Kuhn et al., 2008; Pages et al., 2011; Roome and Kuhn, 2014, 2018) were established. Here, we describe the design and voltage-sensing mechanism of fast voltage-sensitive dyes, specifically of ANNINE dyes, and how to optimize voltage imaging. In a second publication, we supply protocols for different *in vitro* and *in vivo* applications (Kuhn and Roome, 2019).

## DESIGN AND MEMBRANE LABELING OF FAST VOLTAGE-SENSITIVE DYES

The cytosol of all living cells has a negative electrical potential in relation to the extracellular space (which is at ground). The cytosol is conductive due to ions and it is electrically isolated from the extracellular space by a lipid bilayer; the cell membrane. Therefore, the interior of a cell is typically equipotential and the negative electrical potential drops across the membrane. For neurons, the potential across the membrane at rest is around −60 mV, and a typical action potential rapidly reverses the membrane potential to +40 mV. A change of 100 mV seems small, but since this membrane potential change occurs across a narrow cellular membrane, approximately 5 nm in width, the electric field change across the membrane during an action potential is dramatic; ∼200,000 V/cm (for comparison: the dielectric strength of dry air is 30,000 V/cm).

Such potentials and potential changes are typically measured using an electrode placed in the cytosol and compared against an extracellular bath electrode. However, if we want to design an optical probe that senses the potential locally, it must be physically located inside the membrane or, at least, within the Debye length of the membrane (i.e., the length constant of the electrostatic field generated by charges close to the membrane surface that attenuates into the surrounding electrolyte). A molecular probe that randomly diffuses within the conducting cytosol will not be exposed to any significant potential changes, as any potential difference will quickly shift charges until the cytosol is equipotential again. Therefore, fast voltage-sensitive dyes (Loew et al., 1978; Loew and Simpson, 1981; Fluhler et al., 1985), like ANNINE-6 (Hübener et al., 2003) or ANNINE-6plus (Fromherz et al., 2008) (**Figure 1A**), are designed to be incorporated into the cell membrane (**Figure 1B**). To do this, they necessarily comprise of both hydrophobic (from the Greek words hydro = water and phobos = fear) and hydrophilic (from the Greek word philos = love) components. At one end of the dye molecule there are two hydrophobic hydrocarbon chains serving as membrane anchors. At the opposite end there is a positively charged (and therefore hydrophilic) pyridinium group and a positively (or negatively) charged, hydrophilic head group. In between there is a mostly hydrophobic chromophore consisting of aniline and the anellated benzene rings. Such molecules with both hydrophobic and hydrophilic parts are called amphiphilic (from the Greek word amphi = both). The hydrophilic pyridinium and head groups align with membrane lipid head groups while the hydrophobic part of the dye ends up in the hydrophobic core of the membrane. The idea is that the linear design of ANNINE dyes promotes parallel alignment with the lipid molecules of the membrane so that the long axis of the dye is oriented parallel to the electric field across the membrane. However, it is unlikely that this perfect orientation is achieved.

Integration of amphiphilic dyes into the membrane is based on the hydrophobic effect. The hydrophobic effect is predominantly entropy-driven (entropy is a measure for disorder and maximizes at equilibrium): Neighboring non-polar molecules and polar water molecules cannot form hydrogen bonds. This reduces the number of possible hydrogen bonds of polar water molecule with their neighbors. Fewer choices brings more order, or less entropy. As the entropy of a system aims for maximization, the surface between hydrophobic and hydrophilic substances will be minimized corresponding to the largest number of possible choices and highest disorder. Therefore, oily, non-polar substances and water separate into two phases, and an amphiphilic voltage-sensitive dye in an aqueous environment will label a lipid membrane as soon as diffusion brings them in contact. So, in a first approximation, the binding process is entropy driven and binding forces can be neglected. For a detailed explanation of the hydrophobic effect see, for example (Dill and Bromberg, 2011). In general, the membrane binding strength, indicated by the free energy of binding, increases linearly with the length of the hydrophobic alkyl tail (Fromherz and Röcker, 1994; Hinner et al., 2009) and can therefore be easily manipulated.

## EXCITATION AND FLUORESCENCE OF FAST VOLTAGE-SENSITIVE DYES

The excitation and fluorescence of voltage-sensitive dyes follow the same mechanisms as those of other fluorescent dyes but with some specifically optimized features. For a general introduction to the field of molecular fluorescence see Valeur and Berberan-Santos (2013) and Jameson (2014). In short, molecular chromophores consist mainly of carbon atoms joined by conjugated single-double bonds. In the structural formula, this is indicated by alternating single-double bonds between carbon atoms (**Figure 1A**). While bonding electrons in a covalent single bond are localized in an orbital between the two atoms, the electrons of a conjugated single-double bond system are delocalized in an orbital spanning the full conjugated system. Delocalized electrons are weakly bound so that the energy of a photon in the visible wavelength range is enough to bring the electron to an excited state. If a photon interacts with a molecule with conjugated single-double bonds, there is a probability that the photon will be absorbed. If so, the photon will disappear, and the energy and quantum numbers of the photon, which must be preserved, will be transferred to the molecule. To go back to the ground state, the molecule can emit a photon. Again, the overall energy and the quantum numbers of the molecule-photon system must be preserved.

To describe the absorption and emission process, a molecular model applying the Franck-Condon principle is used. The Franck–Condon principle states that electronic transitions in a molecule are very fast in comparison to changes of bonding angles and bonding distances between the nuclei of the molecule. As electronic and nuclear transitions occur on different time scales, they can be separated into different processes. **Figure 1C** show the Franck–Condon energy diagram of a voltage-sensitive dye where molecular energy levels are plotted over a spatial axis

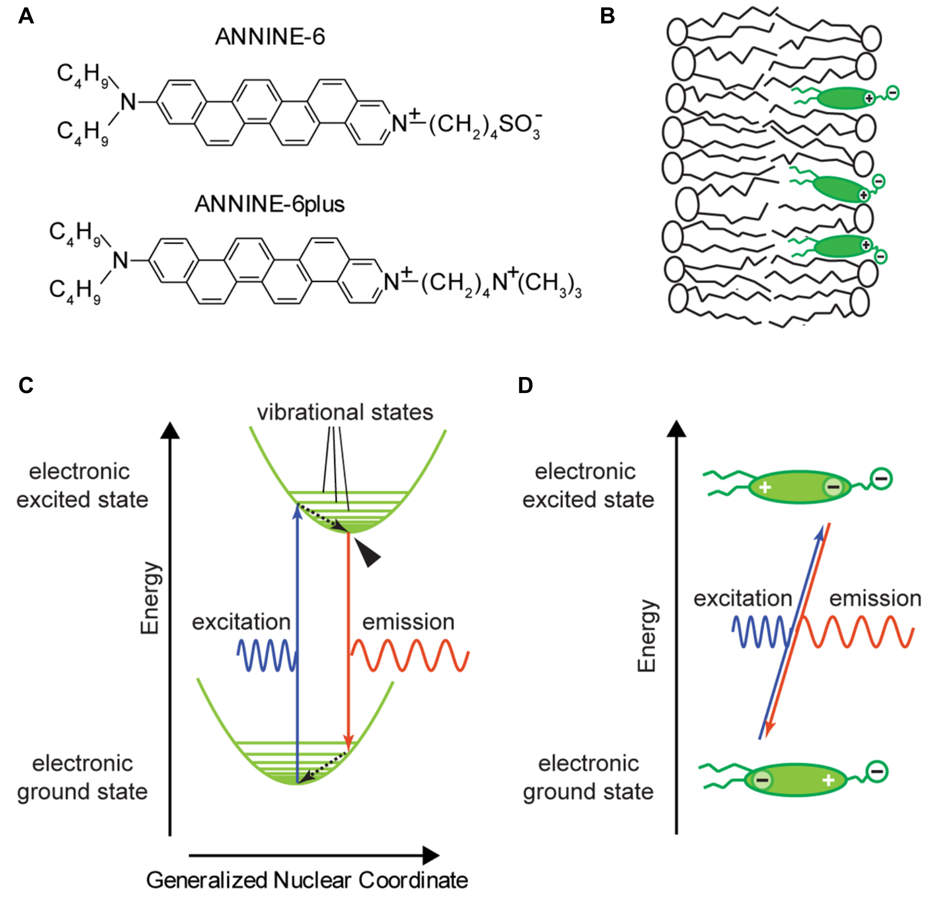

**FIGURE 1 |** ANNINE-6 and ANNINE-6plus; basic properties. **(A)** Structure of ANNINE-6 and ANNINE-6plus. Both have a charged and therefore hydrophilic head group (right) and an uncharged hydrophobic tail (left). ANNINE-6plus is more water soluble than ANNINE-6 due to two positive charges compared to a positive and a negative charge. **(B)** Sketch of a voltage-sensitive dye molecules bound to a lipid membrane. The hydrophilic head groups align with the lipid head groups. The hydrophobic tail and chromophore are surrounded by hydrophobic hydrocarbon chains of the lipid molecules. **(C)** Franck–Condon energy diagram showing electronic ground and excited states over the generalized nuclear coordinate. The Franck–Condon energy diagram indicates that the electron transitions of the excitation and emission process are much faster than the adjustment of the new chromophore conformation, indicated by the generalized nuclear coordinate. After excitation and emission, the molecule vibrates around the new equilibrium position until it relaxes within picoseconds to the vibrational ground state. The vibrational ground state of the electronic excited state from which fluorescence occurs is marked by an arrowhead. Dashed arrows indicate radiationless transitions. **(D)** Charge shift within a voltage-sensitive dye during the absorption and emission process. During the absorption process, the center of charge of the outermost electron of the chromophore shifts from the aniline toward pyridinium. This shift occurs due to the asymmetry of the chromophore. For ANNINE-6 this charge shift is 0.81 nm (Kuhn and Fromherz, 2003). For comparison, the length of the chromophore is about 1.48 nm. During the emission process the electron moves back from pyridinium to aniline.

which represents a generalized nuclear coordinate. Electronic transitions occur on a timescale of femtoseconds ($10^{-15}$ s) and are indicated as vertical arrows corresponding to a change in electron energy, but no change in the generalized nuclear coordinate. The transition between two energy levels occurs with a specific probability. The different probabilities of transition between different levels are reflected in the shape of the spectrum (**Figure 2**). For example, the maximum intensity of the spectrum corresponds to the highest transition probability. After excitation, the molecule vibrates around the new equilibrium state and relaxes to the vibrational ground state on a time scale of typically picoseconds ($10^{-12}$ s). During this relaxation process the molecule passes through a multitude of vibrational levels thereby dissipating the vibrational energy to the local neighborhood of the molecule as heat. The change of the generalized nuclear coordinate of the molecule is interpreted as a change of the size or shape of the molecule. This change will affect the location of the center of charge.

The vibrational ground state of the electronic excited state has a typical lifetime of nanoseconds ($10^{-9}$ s). If a photon is emitted, the molecule arrives at a vibrationally excited, electronic ground state. As the relaxation time is much shorter than the lifetime of the excited state almost all photons are emitted from the vibrational ground state of the excited state (arrowhead in **Figure 1C**). Again, this transition can result in different vibrational levels with different probabilities within the electronic ground state, reflected in the shape of the emission spectrum (**Figure 2**).

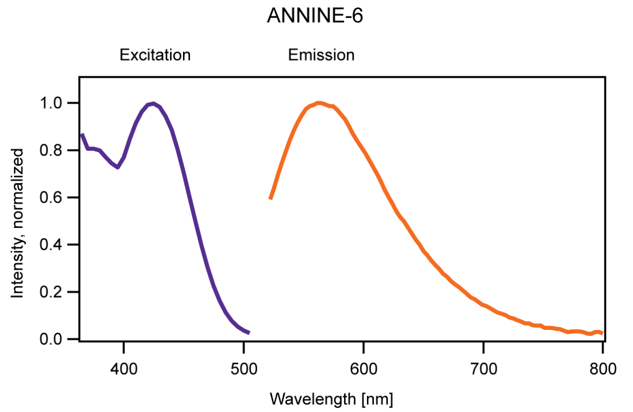

**FIGURE 2 |** One-dimensional excitation (blue) and emission (red) spectrum of ANNINE-6 measured in a neuronal membrane (Kuhn and Fromherz, 2003). The intensity of the excitation spectrum was measured at the peak of the emission spectrum (565 nm). The excitation spectrum acts here as a proxy for the absorption spectrum mentioned in the text. To measure the emission spectrum ANNINE-6 was excited at the peak of the excitation spectrum (420 nm). Both spectra are normalized.

During the relaxation processes following the absorption and emission of a photon, energy is converted into heat. Therefore, the emission spectrum is shifted to lower energy (or longer wavelength) compared to the absorption spectrum. The wavelength difference between excitation and emission peak is called Stokes shift, named after George G. Stokes (1819–1903) who described this wavelength shift for the first time (Stokes, 1952). Electrochromic voltage-sensitive dyes typically have large Stokes shifts. For example, ANNINE-6 and ANNINE-6plus show a Stokes shift of about 145 nm in a cell membrane as can be seen in **Figure 2** (excitation maximum at 420 nm, emission maximum at 565 nm). For comparison, the enhanced Green Fluorescent Protein (eGFP) has a Stokes shift of about 25 nm. So, if an electrochromic voltage-sensitive dye is excited at the absorption maximum a significant fraction of the absorbed energy is converted into heat (in the case of ANNINE-6 and ANNINE-6plus, more than 20%), and heat generation should be minimized to avoid damage to the local environment (lipid molecules and membrane proteins).

The emission of a photon after absorption and relaxation is one process of deactivation. However, other processes can also occur, which are not shown in **Figure 1C**. For example, it is possible that the energy dissipates without emission of a photon. Another possible process is intersystem crossing, which causes phototoxicity: Typically, electrons in molecular orbitals are paired (if they are not paired, the molecule is very reactive). Every electron has a quantum mechanical property called spin, which is an intrinsic form of angular momentum. The spin of an electron $\hat{S} = 1/2$. In molecular orbitals occupied by two electrons, the spins are oriented anti-parallel and therefore the overall spin of the system $\hat{S} = 0$. This state is called singlet state because it is associated with only a single energy level. Molecules generally reside in the singlet state. However, molecular oxygen is an exception to the rule. In its ground state the spin of both outermost electrons is parallel and adds up to $\hat{S} = 1$. Such a spin system can be split up by an external magnetic field into three energy levels. Therefore, it is called a triplet state. Now the following can happen: If a dye molecule is in an excited singlet spin state, and a triplet state oxygen molecule is nearby, the molecule can cross over into the triplet state while the oxygen molecule crosses over into the singlet state (Kalyanaraman et al., 1987). Such a process is called intersystem crossing. Singlet oxygen is a very reactive molecule which will quickly oxidize a neighboring molecule and thereby destroy its functionality. This process is especially harmful if membrane proteins are damaged. The dye molecule will remain in the electronic excited triplet state until it dissipates the energy. This can happen either by emission of a photon, a process called phosphorescence, or by a non-radiative process. In both cases, a neighboring molecule is necessary for returning from the electronic-excited triplet state ($\hat{S} = 1$) to the electronic ground and singlet state ($\hat{S} = 0$). The reason for this is that the transition from the triplet state to the electronic ground and singlet state is a quantum mechanically forbidden transition. A second molecule is necessary to conserve the quantum numbers during the transition.

Another important design characteristic of the chromophore of fast voltage-sensitive dyes is the asymmetry of the chromophore (Loew et al., 1978): One nitrogen atom is integrated into a carbon ring (pyridinium) while a second nitrogen atom is attached to the carbon ring (aniline). These molecules are classified as hemicyanine dyes because their chromophore includes nitrogen atoms, but they lack the symmetry of regular cyanine dyes. Most importantly, in the electronic ground state, this asymmetry results in an asymmetric delocalized electron system with the center of a positive charge at the pyridinium group and a delocalized electron at the aniline group (**Figure 1D**, bottom). During the absorption process, the center of positive charge shifts from pyridinium toward aniline, and during the emission process it shifts back to pyridinium. Or, if we consider the movement of an electron, the delocalized electron shifts from aniline toward pyridinium, and during the emission process back to aniline (**Figure 1D**, top). Therefore, this type of voltage-sensitive dye is also called a charge-shift probe.

## MECHANISM OF VOLTAGE SENSITIVITY OF FAST VOLTAGE-SENSITIVE DYES

If the above described charge shift occurs in an external electric field, in this case the electric field over the cell membrane, more or less energy is required for excitation and released during emission because work is done against the external electric field or work is done by the external electric field, respectively (**Figure 3**). This energy change results in an equal, or symmetric spectral shift of the excitation and the emission spectra. For example, if the negative center of charge of the delocalized electron must be moved in the same direction as the electric field (electric field lines emanate from a positive charge toward a negative charge) more excitation energy is needed than

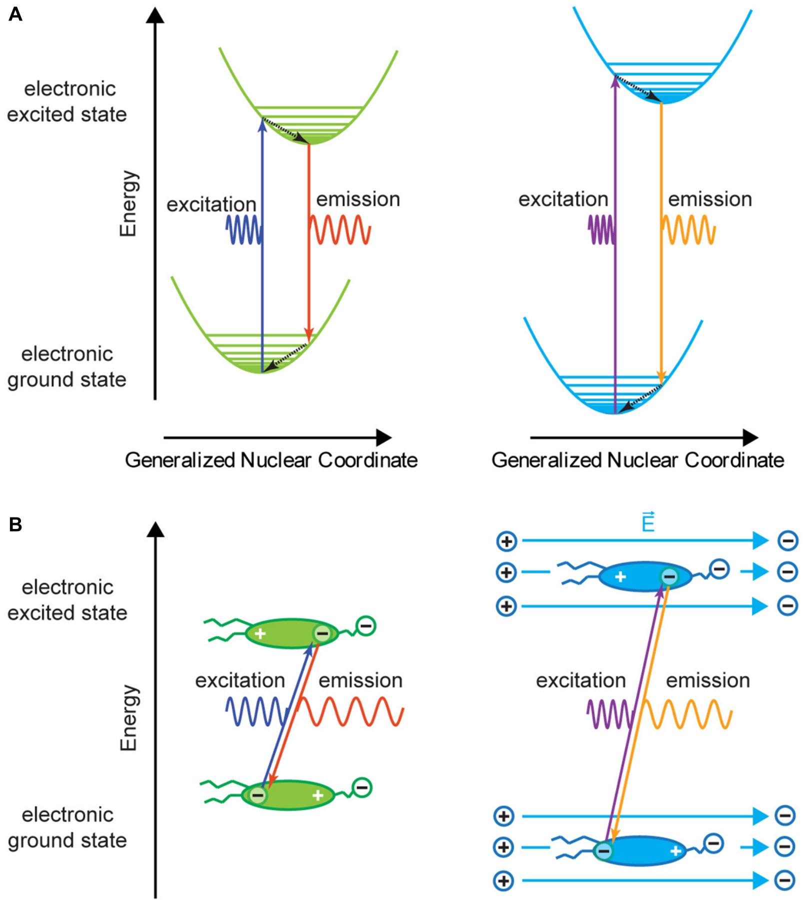

**FIGURE 3 |** Franck–Condon diagram and charge shift without (left) and with (right) external electric field. **(A)** The energy levels in the presence of an external electric field are shifted compared to the energy levels without external electric field. This results in a change in both excitation and emission wavelengths for a given transition. Therefore, for a photon with a given wavelength the absorption probability will be different with and without an external electric field. In general, the energy shift due to the electric field is small compared to the transition energy. **(B)** Charge shift within a voltage-sensitive dye during the absorption and emission process. If the dye molecule is in an external electric field $\vec{E}$, charges within the molecule are slightly shifted (increasing or decreasing the polarization of the molecule) and have different potential energy (**A,B**, right). Therefore, transition energies are shifted compared to transitions without external electric field. In this example, the molecule is more polarized, and excitation and emission spectra will be shifted to higher energy. This corresponds to a spectral blue shift. If the electric field has the opposite direction, a red shift of absorption and emission spectra is expected.

without the external electric field. When the electron drops to a lower energy level, it moves against the external electric field and gains energy so that the emission is also shifted toward higher energy. A voltage-sensitive dye that shows a spectral shift for both excitation and emission is called an electrochromic dye, and if the spectral shift is the same for excitation and emission on an energy-proportional scale it is called a pure electrochromic dye.

From a quantum mechanics point of view, the external electric field will cause splitting and shifting of energy levels of the chromophore. This effect is called molecular Stark effect (Loew et al., 1978; Kuhn and Fromherz, 2003), named after Johannes Stark (1874 – 1957) who discovered this effect in the excited state of hydrogen atoms (Stark, 1914). As the external electric field is small in comparison to intra-molecular electric fields, modulation of the orbital is small and can be approximated as being linear.

Interestingly, conversion of the electric field into the modulation of the optical signal occurs during both the absorption and the emission process. Both occur on a time scale of $10^{-15}$ s. This is the time it takes a photon, whose length equals basically its wavelength, to pass by a molecule with speed of light. However, the readout is delayed by the lifetime of the excited state which is in the nanosecond range. In the case of ANNINE-6plus, the fluorescence lifetime is $6.2 \pm 0.1$ ns (Roome and Kuhn, 2018). This high temporal resolution can be used to measure, for example, break-through voltages of membranes with a temporal resolution of 5 ns by ultrafast laser pulse excitation (Frey et al., 2006).

In general, the theoretical limit of voltage imaging with ANNINE dyes is even faster. It can be shortened to the duration of the absorption process ($<10^{-15}$ s). This can be achieved by excitation at the red spectral edge of the absorption spectrum and integration of the full emission spectrum (see Optimizing Voltage

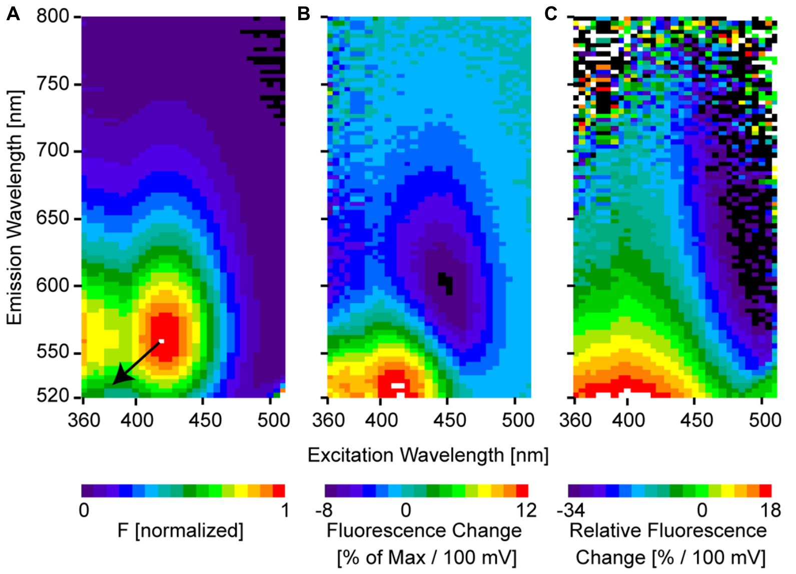

**FIGURE 4 |** Two-dimensional spectra of ANNINE-6. **(A)** Two-dimensional fluorescence spectrum shows the intensity for every excitation-emission wavelength pair. The spectrum was measured from an ANNINE-6-labeled leech neuron. The spectrum is normalized to the maximum. Two such fluorescence spectra were measured, one at rest and another at depolarized membrane potential, with 100 mV potential difference. These two spectra were used to calculate **(B)** the two-dimensional fluorescence change $\frac{\Delta F}{100 mV}$ and **(C)** the two-dimensional relative fluorescence change $\frac{\Delta F}{F}\frac{1}{100 mV}$. The color code indicates the % change per 100 mV. The resulting pattern can be simply explained by a pure diagonal shift of the two-dimensional spectrum indicated by the black arrow in **(A)** (arrow indicates the direction of the shift, but shift is not indicated to scale; the real shift is only about 3–4 nm). An equal energy shift of both, the excitation and the emission spectrum, in response to a change of the external electric field indicates a pure electrochromic mechanism of voltage-sensitivity of ANNINE-6 and ANNINE-6plus (Kuhn and Fromherz, 2003; Fromherz et al., 2008).

Imaging). Thereby, voltage imaging becomes independent of the shift of the emission spectrum and (after deconvolution with the time-resolved fluorescence response) the optical readout reflects the applied voltage during the absorption process only.

The electrochromic effect can be best seen in two-dimensional fluorescence spectra in which the fluorescence intensity is plotted for every excitation wavelength $\lambda_{Ex}$ and emission wavelength $\lambda_{Em}$ pair (**Figure 4A**). Here, we use for convenience a wavelength scale which is proportional to 1/energy. In general, as the spectral shift is proportional to energy it would be better to use an energy-proportional scale, such as a wavenumber scale (1/cm) (Kuhn and Fromherz, 2003), which is widely used in physical chemistry, but rarely in the imaging literature.

For normalization, the two-dimensional fluorescence spectrum $F(\lambda_{Ex}, \lambda_{Em})$ is divided by the global maximum $\mathrm{MAX}(\mathrm{F}(\lambda_{Ex}, \lambda_{Em}))$ (**Figure 4A**):

$$F(\lambda_{Ex}, \lambda_{Em}) = \frac{F_{rest}(\lambda_{Ex}, \lambda_{Em})}{MAX(F_{rest}(\lambda_{Ex}, \lambda_{Em}))}$$

The spectrum measured in the membrane of a cell at resting potential is $F_{rest}$. After measuring $F_{rest}$, the intracellular potential is changed by 100 mV, and a second spectrum is measured ($F_{depolarized}$). Now, the spectral changes induced by the voltage can be analyzed. The two spectra look almost the same at first sight. For example, the largest spectral shift recorded so far (ANNINE-6) for a 100 mV membrane voltage change is only about 3 nm in excitation and 4 nm in emission (spectral shift of excitation and emission in wavenumbers: 160 $\mathrm{cm}^{-1}$). This spectral shift corresponds to a charge shift of 0.81 nm within the chromophore (Kuhn and Fromherz, 2003) (for comparison, the chromophore of ANNINE-6 has a length of 1.48 nm). However, when calculating the fluorescence change $\Delta F(\lambda_{Ex}, \lambda_{Em})$, the shift becomes visible (**Figure 4B**).

$$\Delta F(\lambda_{Ex}, \lambda_{Em})[\%/100\ mV] = \frac{F_{depolarized}(\lambda_{Ex}, \lambda_{Em}) - F_{rest}(\lambda_{Ex}, \lambda_{Em})}{MAX(F_{rest}(\lambda_{Ex}, \lambda_{Em}))} 100\%$$

As expected from a pure shift of the excitation and emission spectra, a region of positive and negative change is located symmetrically to the diagonal through the global maximum of the 2D fluorescence spectrum (red and blue extremes in **Figure 4B**). The unit of fluorescence change is % change relative to the maximal intensity of the two-dimensional spectrum for a voltage change of 100 mV. Importantly, there is no fluorescence change at the global maximum of the 2D fluorescence spectrum and along the diagonal through the global maximum.

Even more interesting than the fluorescence change is the relative fluorescence change $\frac{\Delta F}{F}(\lambda_{Ex}, \lambda_{Em})$ (**Figure 4C**).

$$\frac{\Delta F}{F}(\lambda_{Ex}, \lambda_{Em})[\%/100\ mV] = \frac{F_{depolarized}(\lambda_{Ex}, \lambda_{Em}) - F_{rest}(\lambda_{Ex}, \lambda_{Em})}{F_{rest}(\lambda_{Ex}, \lambda_{Em})} 100\%$$

The relative fluorescence change indicates the % fluorescence change for a voltage change of 100 mV at a given excitation and emission wavelength pair. In general, relative fluorescence change represents information that can be gained by detecting photons when exciting at $\lambda_{Ex}$ and detecting at $\lambda_{Em}$. Additionally, it is normalized to the number of photons, so the % change corresponds to information gain per detected photon. Therefore, relative fluorescence change should be optimized for functional imaging as a crucial factor in the signal-to-noise ratio (see below). Importantly, the largest (positive and negative) relative fluorescence change, which contains the most information about a voltage change, is found at the spectral edges of the 2D spectrum. For example, the intensity at an excitation wavelength of 500 nm and an emission wavelength of 560 nm is less than 10% of the global maximum (**Figure 4A**), but the sensitivity is −34%/100 mV (**Figure 4C**). But, at the absorption and emission peak, 420 and 560 nm, respectively, the sensitivity is 0%/100 mV.

It is important that the voltage-sensitive dye molecules are only on one side of the membrane. If voltage-sensitive dye molecules label both leaflets of the membrane bilayer, the spectral shift in response to the membrane voltage change occurs in opposite directions and therefore the relative fluorescence change will be inverted and will cancel out. For example, for excitation at 500 nm and labeling the outer or inner leaflet of the cell membrane, a negative or positive fluorescence change, respectively, is expected in the range of 550 to 750 nm (**Figure 4B**). Consequently, if dye molecules are equally distributed on both sides of the membrane, the voltage signals of the dye molecules on the two opposing sides of the membrane will cancel each other out. Labeling of both leaflets of the cell membrane can have several reasons: (1) It can occur if dye molecules flip from one membrane leaflet to the other. The flipping probability depends on the hydrophilic and hydrophobic properties of the dye. (2) An inappropriate labeling technique might cause labeling of both membrane leaflets. (3) If single cells are filled with voltage-sensitive dye and, by accident, dye is spilled extracellularly. And (4) due to a net charge of the dye headgroup, dye molecules might flip. For example, externally applied VSD molecules with a positive net charge are attracted by the negative potential inside the cell and might flip to the inside membrane leaflet. Therefore, the voltage signal might even invert (Tsau et al., 1996).

In general, this spectral shift, resulting in positive and negative sensitivity at two diagonal opposing slopes and no change at the global maximum of the 2D excitation/emission spectrum, is different from most other molecular probes. For example, most widely used calcium indicators, like G-CaMP (indicator family developed by J. Nakai) (Ohkura et al., 2012), GCaMP (indicator family of the GENIE Project) (Chen et al., 2013), or fluo dyes (Tsien, 1999), show the same relative fluorescence change for any combination of excitation and emission wavelengths for a given calcium change. Their mechanism is based on a change of absorption cross-section or quantum efficiency. In other cases, the equilibrium between two conformations or binding states of the probe is altered, and the ratio between two emission bands changes, as for the calcium sensitive dye indo-1, for example (Tsien, 1999). Therefore, the intensity or the equilibrium between two distinct excitation or emission spectra changes, but there is typically no spectral shift as in charge-shift probes by electrochromism and solvatochromism (but there are some exceptions, see Tsien, 1999).

A change of the optical voltage signal, as a result of a change of the excitation wavelength, can be shown in an experiment as a clear indicator that a voltage signal was recorded and that the voltage sensing mechanism holds.

## TWO-PHOTON EXCITATION OF VOLTAGE-SENSITIVE DYES

The two-photon absorption probability depends on the change of the molecular dipole moment during the absorption process (Theer et al., 2005; Pawlicki et al., 2009). As the name implies, charge-shift dyes show a large change in polarization during the absorption process and are therefore well suited for two-photon excitation (**Figure 5A**). As with the one-photon process, two-photon absorption depends on the angle between the polarization of the excitation light and the molecular dipole moment, as the oscillations of the light's electric field interact with the electric dipole of the molecule. This is important because voltage-sensitive dye molecules are well aligned in membranes. If the polarization of the excitation light and the dipole moment of the dye are perpendicular to each other, almost no fluorescence will be observed, as can be seen in the cross section of an HEK293 cell (**Figure 5B**) where the adhesion zone and the opposing membrane are invisible while the rim shows bright fluorescence. This effect can be observed with one-photon excitation, but it affects two-photon excitation quadratically because two photons must be oriented in the direction of the molecular dipole moment. Therefore, the polarization of the excitation laser light used for two-photon voltage imaging needs to be carefully considered.

As two photons are involved in the absorption process, quantum-mechanical selection rules for the transition are different from the one-photon case. So far, two-photon absorption spectra cannot be predicted from one-photon absorption spectra. Importantly, however, emission following one- or two-photon excitation is indistinguishable and occurs from the same quantum-mechanical state. Therefore, in both, the one- and two-photon case, the absorbed energy must be sufficient to lift the electron to the electronic excited state. Consequently, the red spectral edge of absorption for two-photon excitation is twice the wavelength of the one-photon case. The energy between the vibrational ground state of the electronic ground state and the vibrational ground state of the first excited state $\bar{\nu}_{00}$ corresponds to 486 nm (20,565 $\mathrm{cm}^{-1}$). With two photons of equal energy this corresponds to a two-photon excitation wavelength for the $\bar{\nu}_{00}$ transition of 972 nm. For voltage imaging ANNINE-6 and derivatives are typically excited at about 510 nm and 1020 nm for one- and two-photon excitation, respectively (Kuhn and Fromherz, 2003; Kuhn et al., 2004) which is both far in the red tail of the absorption spectrum where vibrational energy in the ground state is required to allow a transition.

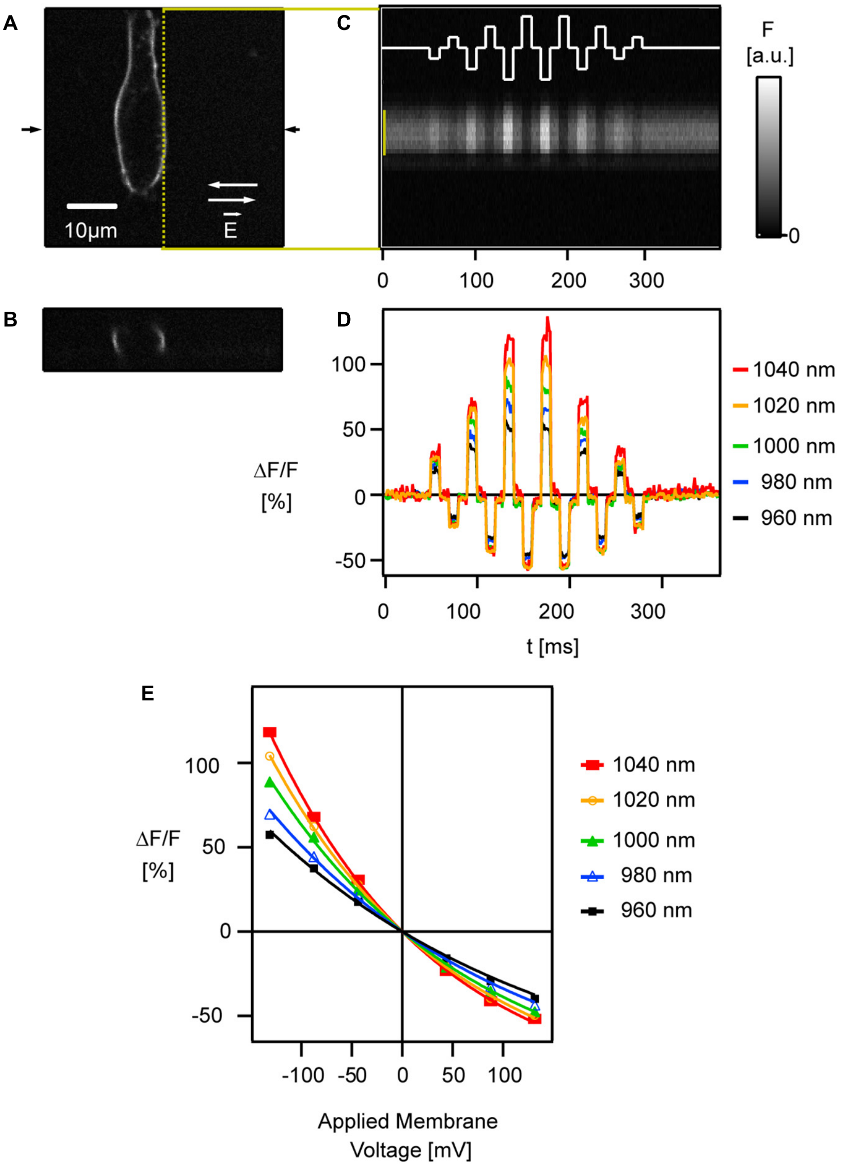

**FIGURE 5 |** Relative fluorescence change of ANNINE-6 increases toward the red spectral edge of two-photon absorption. **(A)** A HEK293 cell labeled with ANNINE-6 is shown in the xy plane and **(B)** the xz plane at the location indicated by arrows in **(A)**. A two-photon line scan was taken along the membrane [yellow dotted line in **(A)**]. **(C)** External electric fields $\vec{E}$ with different amplitudes and direction [white trace, switching directions indicated in **(A)** by white arrows] were applied while scanning along the membrane. The spatio-temporal map shows bright and dark stripes correlating with the applied external electric fields. Intensity gray scale is given in arbitrary units [a.u.]. **(D)** Line scan bands [indicated by yellow bar in **(C)**] were spatially averaged to show relative fluorescence changes corresponding to six different (three positive, three negative) membrane voltage changes. Relative fluorescence changes increase with increasing excitation wavelength, i.e., closer to the red spectral edge of the absorption spectrum. Care was taken that laser polarization was parallel to the main axis of voltage-sensitive dye molecules and therefore perpendicular to the scanned membrane. **(E)** The relative fluorescence change [symbols indicate average voltage response during an electric field pulse at a given wavelength seen in **(D)**] increases linearly in the typical voltage range for biological depolarization and hyperpolarization (±80 mV from resting potential). Only for high voltage changes (>150 mV) the response deviates slightly from being linear. The sensitivity increases with higher excitation wavelength. Modified with permission from Elsevier (Kuhn et al., 2004).

To study the voltage response of ANNINE-6 with two-photon excitation, linescans were acquired along the membrane of a HEK293 cell while applying external electric fields over the cell (**Figure 5C**) (Kuhn et al., 2004).

Also in the two-photon case, the signal is a linear function of the applied membrane voltage within the physiological range (**Figures 5D,E**) (Kuhn et al., 2004). Only if membrane voltages of more than 100 mV are applied, the response becomes slightly non-linear. This non-linearity can be explained by a pure geometric consideration of a linear shift of the excitation and emission spectrum and the resulting response (Kuhn et al., 2004). In other words, the non-linearity is the result of the linear shift of the curved spectrum. As expected, the sensitivity increases near the red spectral edge of absorption (**Figures 5D,E**) as for one-photon excitation (Kuhn et al., 2004).

For the voltage-sensitive dye di4-ANEPPS (Fluhler et al., 1985) and its derivatives, like JPW1114 (Antic and Zecevic, 1995) or JPW3028 (Antic et al., 1999), the optimal wavelengths for one-photon and two-photon excitation at the red spectral edge are 560 and 1120 nm, respectively. This can be estimated from the two-dimensional spectrum of di4-ANEPBS (same chromophore as di4-ANEPPS) and the corresponding fit (Figures 3, 5 in Kuhn and Fromherz, 2003). Thereby, the sensitivity of 16%/100 mV for two-photon excitation at 1060 nm (Acker and Loew, 2013) might increase to over 20%/100 mV above 1120 nm.

## SOLVATOCHROMISM

If absorption and emission spectra are solvent-dependent, a dye shows solvatochromism (Reichardt and Welton, 2011). In principle, all charge-shift voltage-sensitive dyes show solvatochromism because the shift of the charge interacts with the solvent shell of the dye, and a polar solvent like water will have a stronger influence on the charge shift than a non-polar solvent like chloroform. To describe solvatochromism, a model is used where the change of the molecular dipole moment upon excitation interacts with the polarizable environment. This model must be refined for hemicyanine dyes used for voltage imaging. In this refined model an electric point charge and an electric point dipole in the center of a sphere interacts with the solvent (Fromherz, 1995). This Fromherz model describes the experimental solvatochromism data of hemicyanine dyes, like RH-160, di4-ANEPPS, and the ANNINE dyes, exceptionally well, by predicting the shift of the excitation and emission spectra in response to a change of the solvent (Fromherz, 1995; Hübener et al., 2003).

In addition to the spectral changes, the quantum yield of fluorescence depends on the solvent (Ephardt and Fromherz, 1991; Reichardt and Welton, 2011). For example, ANNINE-6plus, as a water-soluble derivative of ANNINE-6, is barely fluorescent in aqueous solutions. Therefore, a pipette for dye-loading is barely visible with one-photon or two-photon excitation, but the dye shows bright fluorescence as soon as the chromophore enters the hydrophobic environment of the membrane.

If we now consider a voltage-sensitive dye molecule in a cell membrane and apply an external electric field, then the voltage-sensitive dye might slightly move in or out of the membrane due to the charged head group. If this happens, the excitation and emission spectra and the quantum yield change because of a change in the local solvent shell of the chromophore, i.e., due to solvatochromism. Sometimes this effect increases the spectral change due to the electrochromic shift, but sometimes it decreases it. A voltage-sensing mechanism based on a combination of electrochromism and solvatochromism depends not only on the electric field over the membrane but also on the local environment of the voltage-sensitive dye molecules and their mobility relative to the membrane-water interface, which is based on hydrophilic and hydrophobic interactions. Therefore, the relative fluorescence change of dyes which show a voltage-sensing mechanism based on a combination of electrochromism and solvatochromism is membrane-dependent. In other words, the lipid composition of the membrane will influence the sensitivity. Also, as a voltage-sensing mechanism based on solvatochromism results from movement of dye molecules at the membrane-water interface, it is not as fast as the pure electrochromic mechanism. This can be neglected for

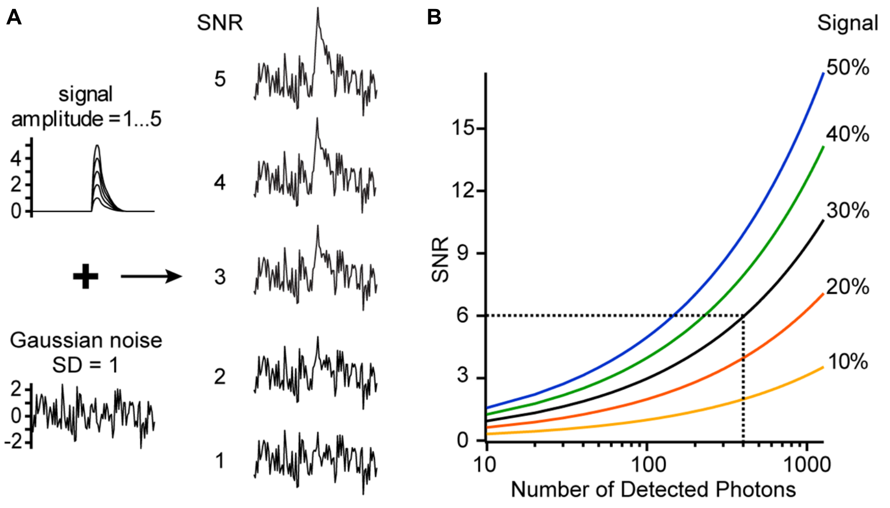

**FIGURE 6 |** Signal-to-noise ratio (SNR). **(A)** Simulated signal traces with different amplitudes (1–5) and a trace with Gaussian noise (*SD* = 1) are added to generate traces of different SNR. **(B)** SNR is shown as a function of the signal (sensitivity multiplied by membrane voltage change, $S\Delta V$[%]) and the number of detected photons. For example, we image with a voltage-sensitive dye which has a sensitivity of 30%/100 mV at a specific excitation wavelength. Now a voltage change of 100 mV occurs in our sample, giving a signal of 30%. At every time point before and after the voltage change, we detect on average 400 photons, resulting in a relative noise level of 5%. Therefore, the measured trace will have a SNR of 6.

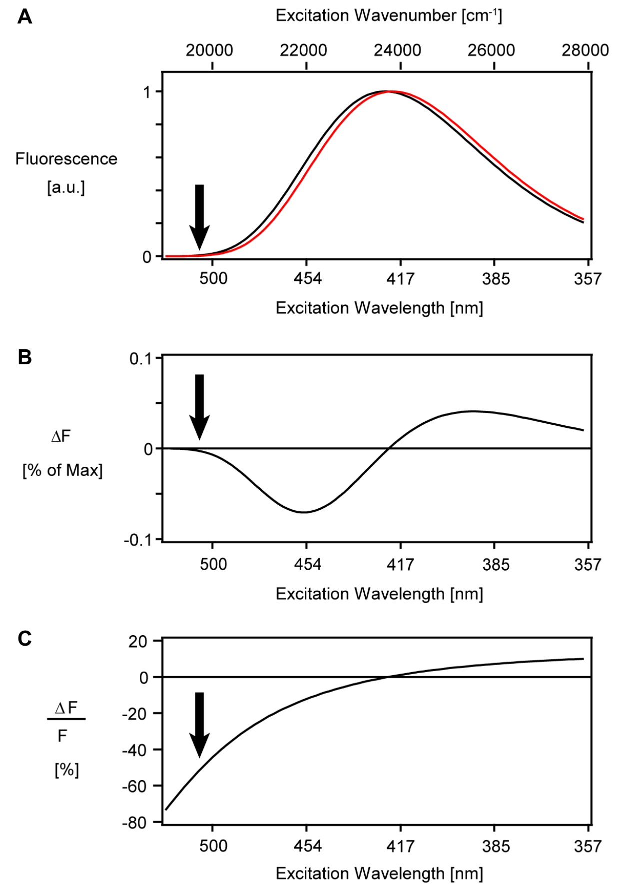

**FIGURE 7 |** Simulation of a pure shift of the excitation spectrum of ANNINE-6. **(A)** A lognormal function (Siano and Metzler, 1969) resembling the ANNINE-6 excitation spectrum (Kuhn and Fromherz, 2003) was blue shifted by about 3 nm (red), equal to a shift of 160 $\text{cm}^{-1}$ in wavenumber. This spectral shift corresponds to a 100 mV membrane voltage change. **(B)** The difference between the two spectra in **(A)** shows extrema at the steepest positive and negative slope. The negative peak amplitude of fluorescence change at 454 nm is only –7% of the peak intensity at 420 nm. **(C)** The simulated relative fluorescence change diverges at the red spectral edge of the excitation spectrum. In reality, the sensitivity has a thermodynamic limit. To image voltage with ANNINE-6 or ANNINE-6plus (which has the same spectral properties), an excitation wavelength of 480 nm or higher is chosen. Arrows indicate a typical excitation wavelength for voltage imaging at 510 nm, corresponding to 1020 nm with two-photon excitation. The absorption coefficient is less than 5% of that at the peak of absorption. The here shown spectra are simulated under the assumption that the full emission spectrum is integrated, and therefore the fluorescence change and relative fluorescence change are independent of the emission wavelength.

neuroscience applications but becomes relevant when imaging in the μs range or faster.

## CHARACTERISTICS OF ANNINE DYES

When we tested the spectral changes of voltage-sensitive dyes in a neuronal membrane with two-dimensional spectroscopy we found that ANNINE-5 (chromophore with 5 rings), ANNINE-6, and their derivatives show a pure electrochromic behavior, as can be concluded from the symmetric shift in excitation and emission (Kuhn and Fromherz, 2003; Fromherz et al., 2008). di4-ANEPB showed a spectral change in response to a voltage change that indicates electrochromism with a small influence of solvatochromism; while RH-421 showed electrochromism with a strong influence of solvatochromism (Kuhn and Fromherz, 2003). This can be seen in the asymmetric shift of the excitation and emission spectrum (Figures 3, 5 and Table 1 in Kuhn and Fromherz, 2003). The only explanation is that ANNINE-5, ANNINE-6, and even the water-soluble ANNINE-6plus do not move in or out of the membrane in response to a membrane voltage change. The absence of a solvatochromic effect during voltage imaging indicates that voltage imaging will be independent of intracellular and extracellular solutions and the membrane composition. We confirmed this membrane-independent voltage-sensing behavior in leech neurons for ANNINE-6 and ANNINE-6plus (Kuhn and Fromherz, 2003; Fromherz et al., 2008) and in HEK293 cells for ANNINE-6 (Kuhn et al., 2004). The linearity of the voltage response was shown in HEK293 cells for ANNINE-6 (Kuhn et al., 2004) and in cultured hippocampal neurons for ANNINE-6plus (Pages et al., 2011). We tested ANNINE dyes with excitation at the red spectral edge of absorption on different setups, in different laboratories, and in different tissues and recorded reliable voltage signals. Cells, tissue, and animals we tested include Ctenophora, Lymnaea stagnalis, sea urchin egg, zebra fish brain, rat brain slice, mouse barrel cortex *in vivo* (Kuhn et al., 2008), and several other cell cultures. ANNINE dyes have also been successfully used in cardiomyocytes (Bu et al., 2009), mouse kidney cells (Chambrey et al., 2013), outer hair cells (Ramamoorthy et al., 2013), plant cells (Flickinger et al., 2010; Berghoefer et al., 2012), T-lymphocyte cells (for electroporation experiments with 5 ns temporal resolution) (Frey et al., 2006), and others.

Another reason – in addition to hydrophobicity – for the absence of dye movement during membrane voltage changes might be the rigid structure of the chromophore, consisting of anellated benzene rings (Hübener et al., 2003). This rigid design was originally chosen to avoid photoisomerization at double bonds (Ephardt and Fromherz, 1993) and rotamerism at single bonds (Röcker et al., 1996) in non-anellated charge-shift dyes, which are associated with radiationless transition and triplet state generation. The rigid design might also contribute to an orderly alignment of the ANNINE molecules to the membrane normal. This is important because the dipole moment of the dye molecule, which is oriented parallel to the axis of the molecule, and the electric field over the membrane are vectors and their interaction, i.e., modulation during a voltage change over the membrane, is proportional to their dot product (multiplication of magnitudes when parallel; zero when perpendicular) (**Figure 1D**).

Interestingly, dye flipping has not been observed so far with ANNINE dyes. This is an important feature and allows for extended imaging periods.

Additionally, so far, no pharmacological side effects were observed in experiments using ANNINE dyes. While some voltage-sensitive dyes like di-4-ANEPPS potentiated GABA action, no such effect was observed for ANNINE-6 and ANNINE-6plus (Mennerick et al., 2010). In another study it was shown that ANNINE-5 is photochemically more stable than RH-421 (Amoroso et al., 2006). It was proposed that this stability arises from the more rigid ring structure than the alternating single-double bonds of RH-421.

## SIGNAL-TO-NOISE RATIO OF VOLTAGE IMAGING

Every measurement is composed of the pure signal and noise (**Figure 6A**). In the case of voltage imaging, the signal (%) is defined by the relative fluorescence change or sensitivity $S$ $(\frac{\%}{mV})$ multiplied by the membrane voltage change $\Delta V$ $(mV)$. Assuming an ideal imaging setup, the noise is caused by fluctuations of the number of detected photons (a non-ideal setup will have additional noise sources like electronic noise or noise due to intensity fluctuations of the excitation light source). Importantly, the incident photon count follows a Poisson distribution. A characteristic of the Poisson distribution is that if the average number of detected photons is $n$, then the expected fluctuations will be the square root of $n$. In other words, the standard deviation of $n$ is $\sqrt{n}$. Therefore, the relative noise level is $\frac{\sqrt{n}}{n}$ or, in %, $\frac{\sqrt{n}}{n}$ 100% .

In voltage imaging experiments, it is necessary to optimize the signal-to-noise ratio (SNR) (Kuhn et al., 2004). The SNR is the ratio of the relative signal (in %) divided by the relative noise (in %) (**Figure 6B**).

$$SNR = \frac{S\Delta V}{\frac{\sqrt{n}}{n}100\%} = \frac{S\Delta V\sqrt{n}}{100\%}$$

This formula is crucial because it shows the importance of the relative fluorescence change or sensitivity $S$ (**Figure 4C**). For example, by doubling the sensitivity, the SNR doubles or, alternatively, only a quarter of photons are needed to reach the same SNR. The number of detected photons $n$ is proportional to the number of dye molecules available, to their absorption coefficient and quantum efficiency, and to the intensity of the excitation light source. This means that $n$ is proportional to the intensity of the fluorescence spectrum (**Figures 2**, **4A**), but the SNR increases only with the square root of $n$.

The equation also shows that, theoretically, any SNR can be reached for any signal $S\Delta V$ by adapting the number of detected photons $n$. The number of detected photons can be easily estimated. In a first approximation, a well set-up two-photon microscope is shot noise-limited. From a background-corrected time course of a constant fluorescence signal, measured in arbitrary units, the mean intensity and standard deviation of the intensity can be calculated. The mean number of photons (n) can then be estimated from this equation:

$$n = \left(\frac{mean}{std}\right)^2$$

Temporal or spatial averaging increases the number of photons taken into account, and therefore reduces the relative noise $(\frac{\sqrt{n}}{n})$ accordingly.

## OPTIMIZING VOLTAGE IMAGING

For all fluorescence imaging, it is important to keep the number of excited dye molecules low, in order to avoid phototoxicity and bleaching. This is especially true for voltage imaging since the probes are close to indispensable membrane proteins. Excited voltage-sensitive dye molecules can cause photochemical reactions (see for example Schaffer et al., 1994) by generating oxidizing singlet oxygen molecules (Kalyanaraman et al., 1987) or, if non-anellated, undergo excited-state isomerization (Fromherz and Heilemann, 1992; Röcker et al., 1996; Amoroso et al., 2006). Therefore, it is important to excite as few dye molecules as possible and to detect as many emitted photons as possible. At the same time, detected photons should carry as much information about the membrane voltage as possible. Therefore, voltage-sensitive dye molecules should only be excited where the sensitivity is highest, and, at the same time, where all generated fluorescence carries a voltage signal with the same sign (positive or negative) (**Figure 4C**).

To convert the spectral shift into a detectable intensity change it is necessary to select an excitation band or line, and a corresponding emission band that optimizes the signal. For electrochromic charge-shift probes, there are always two spectral ranges with high sensitivity (in the following all wavelength bands refer to ANNINE-6 and ANNINE-6plus): One is relatively independent of the excitation wavelength (**Figure 4C**; 360–450 nm), but selective for the emission wavelength range close to the blue spectral edge (**Figure 4C**; 520–550 nm). This spectral range should not be used for voltage imaging because many dye molecules are excited, but only in a narrow spectral range (at the blue edge of the emission spectrum) a large fractional (%) intensity change will occur during a voltage change. The other spectral range is selective for the excitation wavelength (**Figure 4C**; 490–510 nm), but relatively independent of the emission wavelength (**Figure 4C**; 550–750 nm). In this case, all emitted photons originate from a spectral range with high sensitivity, i.e., high information content, with the same sign (in this case, negative relative fluorescence change) and therefore should be selected for detection, using the emission filter.

In case of excitation at the very red spectral edge of the excitation spectrum and collecting all emitted photons, the sensitivity will be independent of the spectral shift of the emission spectrum. **Figure 7A** shows a lognormal function resembling the ANNINE-6 excitation spectrum. A pure shift of the spectrum results in a fluorescence change with extrema at the steepest slopes (**Figure 7B**), and a sensitivity that diverges at the spectral edge (**Figure 7C**).

With the voltage sensitivity increasing more and more toward the red spectral edge, the question remains: Is there a limit of voltage sensitivity for a given dye? The two-dimensional sensitivity spectrum of **Figure 4C** implies a higher and higher sensitivity toward the red spectral edge of absorption until it fades in the noise above an excitation wavelength of 500 nm. Thermodynamic considerations show that there is a theoretical limit of voltage sensitivity for a given dye (Kuhn et al., 2004). In short, the spectral edge is expected to follow a Boltzmann distribution and therefore decay exponentially. This

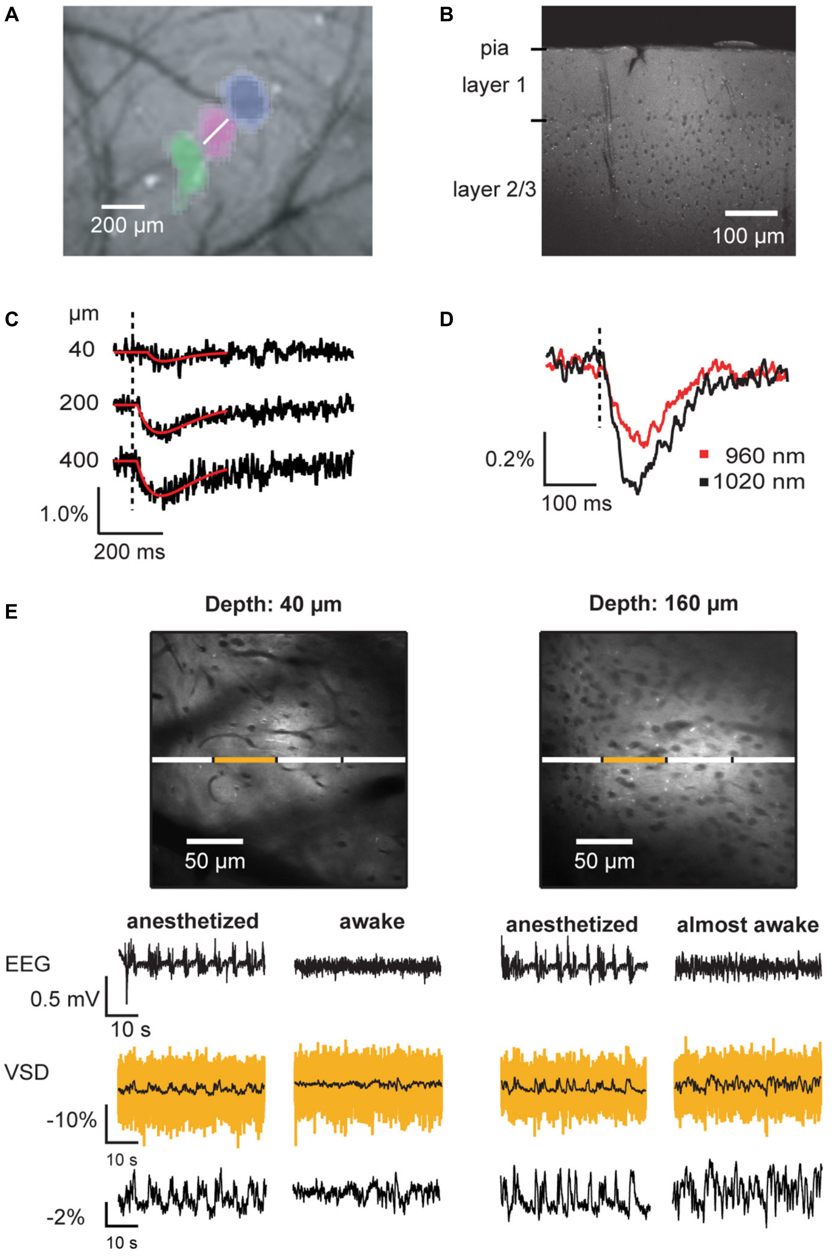

**FIGURE 8 |** Voltage imaging of average membrane potential of neuronal tissue *in vivo*. **(A)** Imaging of intrinsic signals reveals the location of primary responses in barrel cortex. In this montage, three vibrissa responses (green, magenta, blue) in relation to the blood vessel pattern are shown. Following the imaging of intrinsic signals, the brain region of interest was bulk loaded with VSD. **(B)** Two-photon image of a barrel cortex brain slice prepared after *in vivo* bulk-loading with ANNINE-6 shows homogeneous labeling. Somata (here of layer 2/3) and blood vessels remain dark. **(C)** Two-photon linescans performed at the location indicated in **(A)** (white line) at different depths below the brain surface were spatially averaged. Vibrissa stimulation causes an average membrane depolarization, which results in decrease of fluorescence if the dye is bound to the outer leaflet of the membrane and the dye is excited at the red spectral absorption edge. **(D)** Under the same experimental conditions, the excitation wavelength was changed. As expected from a purely electrochromic dye, excitation closer to the spectral edge results in a larger relative fluorescence change. Such an experiment confirms the mechanism of voltage sensing. **(E)** *In vivo* two-photon images of cerebral cortex layer 1 and layer 2/3. Blood vessels and somata appear as dark shadows, as the dye is bound to the outer leaflet of the cell membranes. Line scans allow measurement of local average membrane depolarization in anesthetized and awake animals, which correlates with the local electro-encephalogram (EEG). The yellow trace is the averaged trace of the line scan segment indicated above. The black, overlaid trace is the corresponding filtered trace (boxcar smoothing, 200 ms). The segmentation allows analyzing cross-correlations among neighboring brain segments. For example, cross-correlations among segments are higher in anesthetized than in awake animals (Kuhn et al., 2008). The trace at the bottom shows the relative fluorescence change of the full linescan after filtering with 200 ms boxcar smoothing. EEG signals are biphasic, representing sources and sinks while the VSD signal shows average membrane depolarization (negative fluorescence change). As the neuronal activity de-correlates during the transition from anesthetized to awake state, the average voltage signal becomes noisy (160 µm below the dura mater, right VSD traces) and then flat (40 µm, right VSD traces) in the fully awake animal. Average membrane voltage measurements can be recorded for hours without photo bleaching. Copyright (2008) National Academy of Sciences, United States (Kuhn et al., 2008).

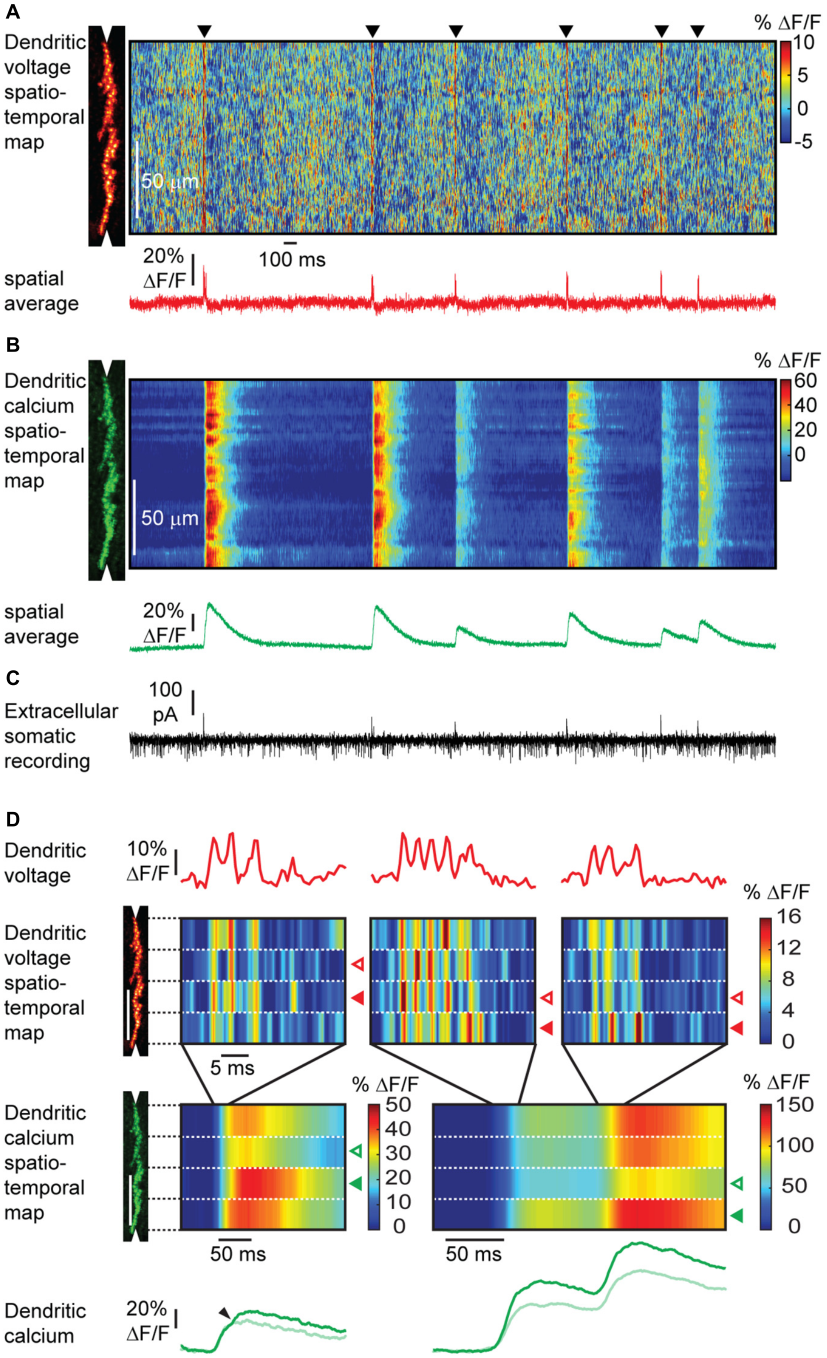

**FIGURE 9 |** Simultaneous voltage and calcium imaging of Purkinje neuron dendrites and electric recording from the soma in the awake mouse. **(A)** A linescan at 2 kHz was taken along the Purkinje neuron dendrite (left) to measure a voltage spatio-temporal map in an awake mouse. Note red vertical lines (black triangles) indicating activation of the full dendritic tree during a complex spike, and background pattern with red 'hotspots' indicating localized subthreshold electrical activity. The spatially averaged dendritic voltage trace shows dendritic complex spikes at high SNR. **(B)** The corresponding dendritic calcium spatio-temporal map shows large transients for every dendritic complex spike. Note the spatial variability of the peak amplitude of calcium transients within single dendritic complex spikes and the amplitude variability between different dendritic complex spikes. **(C)** The access port allowed simultaneous extracellular electrical recordings from the soma while imaging voltage and calcium transients from the dendrites. Simple spikes (somatic $Na^+$ spikes) result in a current sink at the soma, while complex spikes (dendritic $Ca^{2+}$ spikes) result in a dominant current source signal at the soma. **(D)** Different parts of the dendritic tree show a different number of spikelets during the same complex spike event. The number of spikelets correlate with the amplitude of the calcium transients in each part of the dendritic tree. Open arrowheads indicate spatially localized low activity, filled arrowheads high activity. Spatially localized dendritic spikelets during complex spikes correlate with a local boost in the dendritic calcium transient (small arrowheads). Note that the depolarization is caused by the influx of $Ca^{2+}$. Therefore, the voltage and calcium signal should have the same onset. The observed delay in onset of the calcium signal is the result of the dynamics of the calcium indicator GCaMP6f (Roome and Kuhn, 2018).

decay of the spectral tail considers only one vibrational mode of the chromophore and is therefore the steepest possible decay. In more realistic models, additional vibrational modes must be taken into account which would flatten the spectral tail. If this spectral tail is now shifted due to an external electric field, the steepest spectral tail will give the highest voltage sensitivity. Therefore, this simple model of the spectral Boltzmann tail will give us a theoretical thermodynamic limit for voltage sensitivity for a given dye. For ANNINE-6 this limit is −0.77%/mV for extracellular application of the dye and a positive voltage change of the cell (Kuhn and Fromherz, 2003; Kuhn et al., 2004). The highest measured sensitivity for ANNINE-6 is −0.52%/mV (with two-photon microscopy at an excitation wavelength of 1040 nm, corresponding to 520 nm with one-photon excitation) (Kuhn et al., 2004). For comparison, the theoretical limit of voltage sensitivity for di-4-ANEPBS and RH-421 is 0.43%/mV and 0.24%/mV, respectively (Kuhn and Fromherz, 2003; Kuhn et al., 2004).

Excitation at the red spectral edge of absorption has additional advantages which might be interesting for imaging applications other than voltage imaging: (1) The amount of energy converted into heat during the relaxation process after excitation is minimized. (2) The probability for intersystem crossing is minimized, as the energy levels with high probability of crossing might not be excited any more. Both effects reduce phototoxicity and contribute to an extended imaging time and/or increased SNR.

## APPLICATIONS OF TWO-PHOTON VOLTAGE IMAGING WITH ANNINE DYES

With the above described mechanistic understanding and optimizations of two-photon voltage imaging with ANNINE dyes, a wide variety of applications are possible. For example, ANNINE-6 can be bolus loaded *in vivo* and the average membrane potential can be measured (**Figure 8**) (Kuhn et al., 2008). Sensory responses or brain oscillations up to at least 15Hz can be observed.

To overcome labeling of all cell surfaces and a resulting mixture of voltage signals, ANNINE-6plus can be internally loaded into single cells *in vivo* (**Figure 9**) (Roome and Kuhn, 2018). A necessary requirement for this experiment is a chronic cranial window with access port (Roome and Kuhn, 2014) which allows access to the brain to electroporate single neurons, guided by two-photon microscopy. Suprathreshold as well as localized subthreshold events can be detected in dendrites of Purkinje neurons in awake animals with high spatial and temporal resolution. In this case, the labeling after a single electroporation lasts for at least 2 weeks and therefore allows for long-term single neuron imaging experiments. The access port also allows electrical recording, and virus, dye and drug application in combination with the voltage imaging technique. Additionally, voltage imaging with ANNINE dyes can be easily combined with green calcium indicators, specifically GCaMP6 (Roome and Kuhn, 2018). All these experiments can be done without bleaching and with neglectable phototoxicity for many minutes of repetitive laser excitation.

Detailed protocols for these experiments will be available in Multiphoton Microscopy, Springer Nature Neuromethods (Kuhn and Roome, 2019). We hope, that in combination with this paper, it will be possible to adapt the experimental conditions for a wide range of voltage imaging applications on different experimental setups and with different cell types.

## AUTHOR CONTRIBUTIONS

BK and CJR wrote the manuscript.

## ACKNOWLEDGMENTS

The authors thank Espen Hartveit, Steven D. Aird, Neil Dalphin, Ray X. Lee, Mohamed M. Eltabbal, Alisher Duspayev, Claudia Cecchetto, and Leonidas Georgiou for valuable feedback on the manuscript and the Okinawa Institute of Science and Technology Graduate University for internal funding.

## REFERENCES

Acker, C. D., and Loew, L. M. (2013). Characterization of voltage-sensitive dyes in living cells using two-photon excitation. *Methods Mol. Biol.* 995, 147–160. doi: 10.1007/978-1-62703-345-9_11

Amoroso, S., Agon, V. V., Starke-Peterkovic, T., McLeod, M. D., Apell, H. J., Sebban, P., et al. (2006). Photochemical behavior and Na+,K+-ATPase sensitivity of voltage-sensitive styrylpyridinium fluorescent membrane probes. *Photochem. Photobiol.* 82, 495–502. doi: 10.1562/2005-06-08-Ra-569

Antic, S., Major, G., and Zecevic, D. (1999). Fast optical recordings of membrane potential changes from dendrites of pyramidal neurons. *J. Neurophysiol.* 82, 1615–1621. doi: 10.1152/jn.1999.82.3.1615

Antic, S., and Zecevic, D. (1995). Optical signals from neurons with internally applied voltage-sensitive dyes. *J. Neurosci.* 15, 1392–1405. doi: 10.1523/jneurosci.15-02-01392.1995

Berghoefer, T., Flickinger, B., and Frey, W. (2012). Aspects of plant plasmalemma charging induced by external electric field pulses. *Plant Signal Behav.* 7, 322–324. doi: 10.4161/psb.19174

Bu, G., Adams, H., Berbari, E. J., and Rubart, M. (2009). Uniform action potential repolarization within the sarcolemma of in situ ventricular cardiomyocytes. *Biophys. J.* 96, 2532–2546. doi: 10.1016/j.bpj.2008.12.3896

Chambrey, R., Kurth, I., Peti-Peterdi, J., Houillier, P., Purkerson, J. M., Leviel, F., et al. (2013). Renal intercalated cells are rather energized by a proton than a sodium pump. *Proc. Natl. Acad. Sci. U.S.A.* 110, 7928–7933. doi: 10.1073/pnas.1221496110

Chen, T. W., Wardill, T. J., Sun, Y., Pulver, S. R., Renninger, S. L., Baohan, A., et al. (2013). Ultrasensitive fluorescent proteins for imaging neuronal activity. *Nature* 499, 295–300. doi: 10.1038/nature12354

Dill, K. A., and Bromberg, S. (2011). *Molecular Driving Forces: Statistical Thermodynamics in Biology, Chemistry, Physics, and Nanoscience*, 2nd Edn. New York, NY: Garland Science, 629–642.

Ephardt, H., and Fromherz, P. (1991). Anillnopyridinium - Solvent-dependent fluorescence by intramolecular charge-transfer. *J. Phys. Chem.* 95, 6792–6797. doi: 10.1021/j100171a011

Ephardt, H., and Fromherz, P. (1993). Fluorescence of amphiphilic hemicyanine dyes without free double-bonds. *J. Phys. Chem.* 97, 4540–4547. doi: 10.1021/j100119a048

Flickinger, B., Berghofer, T., Hohenberger, P., Eing, C., and Frey, W. (2010). Transmembrane potential measurements on plant cells using the voltage-sensitive dye ANNINE-6. *Protoplasma* 247, 3–12. doi: 10.1007/s00709-010-0131-y

Fluhler, E., Burnham, V. G., and Loew, L. M. (1985). Spectra, membrane-binding, and potentiometric responses of new charge shift probes. *Biochemistry* 24, 5749–5755. doi: 10.1021/bi00342a010

Frey, W., White, J. A., Price, R. O., Blackmore, P. F., Joshi, R. P., Nuccitelli, R., et al. (2006). Plasma membrane voltage changes during nanosecond pulsed electric field exposure. *Biophys. J.* 90, 3608–3615. doi: 10.1529/biophysj.105.072777

Fromherz, P. (1995). Monopole-dipole model for symmetrical solvatochromism of hemicyanine dyes. *J. Phys. Chem.* 99, 7188–7192. doi: 10.1021/j100018a061

Fromherz, P., and Heilemann, A. (1992). Twisted internal charge-transfer in (aminophenyl)pyridinium. *J. Phys. Chem.* 96, 6864–6866. doi: 10.1021/j100196a004

Fromherz, P., Hübener, G., Kuhn, B., and Hinner, M. J. (2008). ANNINE-6plus, a voltage-sensitive dye with good solubility, strong membrane binding and high sensitivity. *Eur. Biophys. J. Biophys. Lett.* 37, 509–514. doi: 10.1007/s00249-007-0210-y

Fromherz, P., and Röcker, C. (1994). Staining of biomembranes with amphiphilic hemicyanine dyes. *Phys. Chem. Chem. Phys.* 98, 128–131. doi: 10.1002/bbpc.19940980120

Hinner, M. J., Marrink, S. J., and de Vries, A. H. (2009). Location, tilt, and binding: a molecular dynamics study of voltage-sensitive dyes in biomembranes. *J. Phys. Chem. B* 113, 15807–15819. doi: 10.1021/jp907981y

Hübener, G., Lambacher, A., and Fromherz, P. (2003). Anellated hemicyanine dyes with large symmetrical solvatochromism of absorption and fluorescence. *J. Phys. Chem. B* 107, 7896–7902. doi: 10.1021/jp0345809

Jameson, D. M. (2014). *Introduction to Fluorescence*. Boca Raton, FL: CRC Press.

Kalyanaraman, B., Feix, J. B., Sieber, F., Thomas, J. P., and Girotti, A. W. (1987). Photodynamic action of merocyanine-540 on artificial and natural cell membranes - involvement of singlet molecular oxygen. *Proc. Natl. Acad. Sci. U.S.A.* 84, 2999–3003. doi: 10.1073/pnas.84.9.2999

Kuhn, B., Denk, W., and Bruno, R. M. (2008). In vivo two-photon voltage-sensitive dye imaging reveals top-down control of cortical layers 1 and 2 during wakefulness. *Proc. Natl. Acad. Sci. U.S.A.* 105, 7588–7593. doi: 10.1073/pnas.0802462105

Kuhn, B., and Fromherz, P. (2003). Anellated hemicyanine dyes in a neuron membrane: molecular Stark effect and optical voltage recording. *J. Phys. Chem. B* 107, 7903–7913. doi: 10.1021/jp0345811

Kuhn, B., Fromherz, P., and Denk, W. (2004). High sensitivity of Stark-shift voltage-sensing dyes by one- or two-photon excitation near the red spectral edge. *Biophys. J.* 87, 631–639. doi: 10.1529/biophysj.104.040477

Kuhn, B., and Roome, C. J. (2019). "Voltage imaging with ANNINE dyes and two-photon microscopy," in *Multiphoton Microscopy*, ed. E. Hartveit (Berlin: Springer). doi: 10.1007/978-1-4939-9702-213

Loew, L. M., Bonneville, G. W., and Surow, J. (1978). Charge shift optical probes of membrane potential - Theory. *Biochemistry* 17, 4065–4071. doi: 10.1021/bi00612a030

Loew, L. M., and Simpson, L. L. (1981). Charge-shift probes of membrane potential - a probable electrochromic mechanism for para-aminostyrylpyridinium probes on a hemispherical lipid bilayer. *Biophys. J.* 34, 353–365. doi: 10.1016/s0006-3495(81)84854-0

Mennerick, S., Chisari, M., Shu, H. J., Taylor, A., Vasek, M., Eisenman, L. N., et al. (2010). Diverse voltage-sensitive dyes modulate GABAA receptor function. *J. Neurosci.* 30, 2871–2879. doi: 10.1523/JNEUROSCI.5607-09.2010

Ohkura, M., Sasaki, T., Sadakari, J., Gengyo-Ando, K., Kagawa-Nagamura, Y., Kobayashi, C., et al. (2012). Genetically encoded green fluorescent Ca2+ indicators with improved detectability for neuronal Ca2+ signals. *PLoS One* 7:e51286. doi: 10.1371/journal.pone.0051286

Pages, S., Cote, D., and De Koninck, P. (2011). Optophysiological approach to resolve neuronal action potentials with high spatial and temporal resolution in cultured neurons. *Front Cell Neurosci* 5:20. doi: 10.3389/fncel.2011.00020

Pawlicki, M., Collins, H. A., Denning, R. G., and Anderson, H. L. (2009). Two-photon absorption and the design of two-photon dyes. *Angew. Chem. Int. Ed.* 48, 3244–3266. doi: 10.1002/anie.200805257

Ramamoorthy, S., Wilson, T. M., Wu, T., and Nuttall, A. L. (2013). Non-uniform distribution of outer hair cell transmembrane potential induced by extracellular electric field. *Biophys. J.* 105, 2666–2675. doi: 10.1016/j.bpj.2013.11.021

Reichardt, C., and Welton, T. (2011). *Solvents and Solvent Effects in Organic Chemistry*. Weinheim: Wiley-VCH.

Röcker, C., Heilemann, A., and Fromherz, P. (1996). Time-resolved fluorescence of a hemicyanine dye: dynamics of rotamerism and resolvation. *J. Phys. Chem.* 100, 12172–12177. doi: 10.1021/jp960095k

Roome, C. J., and Kuhn, B. (2014). Chronic cranial window with access port for repeated cellular manipulations, drug application, and electrophysiology. *Front. Cell. Neurosci.* 8:379. doi: 10.3389/fncel.2014.00379

Roome, C. J., and Kuhn, B. (2018). Simultaneous dendritic voltage and calcium imaging and somatic recording from Purkinje neurons in awake mice. *Nat. Commun.* 9:3388. doi: 10.1038/s41467-018-05900-3

Schaffer, P., Ahammer, H., Müller, W., Koidl, B., and Windisch, H. (1994). Di-4-ANEPPS causes photodynamic damage to isolated cardiomyocytes. *Pflügers Arch.* 426, 548–551. doi: 10.1007/bf00378533

Siano, D. B., and Metzler, D. E. (1969). Band shapes of electronic spectra of complex molecules. *J. Chem. Phys.* 51:1856. doi: 10.1063/1.1672270

Stark, J. (1914). *Elektrische Spektralanalyse Chemischer Atome*. Leipzig: S. Hirzel.

Stokes, G. G. (1952). On the changes of refrangibility of light. *Philos. Trans. R. Soc. Lond.* 142, 463–562.

Theer, P., Kuhn, B., Keusters, D., and Denk, W. (2005). "Two-photon microscopy and imaging," in *Encyclopedia of Molecular Biology and Molecular Medicine*, 2nd Edn, ed. R. A. Meyers (Weinheim: VCH), 61–87.

Tsau, Y., Wenner, P., ODonovan, M. J., Cohen, L. B., Loew, L. M., and Wuskell, J. P. (1996). Dye screening and signal-to-noise ratio for retrogradely transported voltage-sensitive dyes. *J. Neurosci. Methods* 70, 121–129. doi: 10.1016/S0165-0270(96)00109-4

Tsien, R. Y. (1999). "Monitoring cell calcium," in *Calcium as a Cellular Regulator*, eds E. Carafoli and C. B. Klee (New York, NY: Oxford University Press), 28–54.

Valeur, B., and Berberan-Santos, M. N. (2013). *Molecular Fluorescence : Principles and Applications*. Weinheim: Wiley-VCH Verlag GmbH & Co. KGaA.

**Conflict of Interest Statement:** The authors declare that the research was conducted in the absence of any commercial or financial relationships that could be construed as a potential conflict of interest.

frontiers in Cellular Neuroscience

HYPOTHESIS AND THEORY
published: 31 July 2019
doi: 10.3389/fncel.2019.00342

# Using Genetically Encoded Voltage Indicators (GEVIs) to Study the Input-Output Transformation of the Mammalian Olfactory Bulb

**Douglas A. Storace**[1,2]*, **Lawrence B. Cohen**[2,3]* and **Yunsook Choi**[2,3]

[1] Department of Biological Science, Florida State University, Tallahassee, FL, United States, [2] Department of Cellular and Molecular Physiology, Yale School of Medicine, Yale University, New Haven, CT, United States, [3] Center for Functional Connectomics, Korea Institute of Science and Technology, Seoul, South Korea

**Edited by:**
Srdjan D. Antic,
University of Connecticut Health Center, United States

**Reviewed by:**
Diego Restrepo,
University of Colorado Denver, United States
Bernd Kuhn,
Okinawa Institute of Science and Technology Graduate University, Japan

***Correspondence:**
Douglas A. Storace
dstorace@fsu.edu
Lawrence B. Cohen
lawrence.b.cohen@hotmail.com

**Specialty section:**
This article was submitted to Cellular Neurophysiology, a section of the journal Frontiers in Cellular Neuroscience

**Received:** 26 March 2019
**Accepted:** 11 July 2019
**Published:** 31 July 2019

**Citation:**
Storace DA, Cohen LB and Choi Y (2019) Using Genetically Encoded Voltage Indicators (GEVIs) to Study the Input-Output Transformation of the Mammalian Olfactory Bulb. Front. Cell. Neurosci. 13:342. doi: 10.3389/fncel.2019.00342

Genetically encoded voltage indicators (GEVIs) are fluorescent protein reporters of membrane potential. These tools can, in principle, be used to monitor the neural activity of genetically distinct cell types in the brain. Although introduced in 1997, they have been a challenge to use to study intact neural circuits due to a combination of small signal-to-noise ratio, slow kinetics, and poor membrane expression. New strategies have yielded novel GEVIs such as ArcLight, which have improved properties. Here, we compare the *in vivo* properties of ArcLight with Genetically Encoded Calcium Indicators (GECIs) in the mouse olfactory bulb. We show how voltage imaging can be combined with organic calcium sensitive dyes to measure the input-output transformation of the olfactory bulb. Finally, we demonstrate that ArcLight can be targeted to olfactory bulb interneurons. The olfactory bulb contributes substantially to the perception of the concentration invariance of odor recognition.

**Keywords: ArcLight, odors, olfactory bulb, mouse, perception, GEVIs, GECIs**

## INTRODUCTION

Traditional optical imaging techniques using intrinsic signals (Blasdel and Salama, 1986; Grinvald et al., 1986) or organic dyes for measuring voltage (Davila et al., 1973) and calcium (Brown et al., 1975; Tsien, 1980), have limited ability to distinguish the cell types contributing to the signal, except in a few special cases (Tsau et al., 1996; Wenner et al., 1996; Friedrich and Korsching, 1997; Wachowiak and Cohen, 2001). In contrast, protein sensors of neural activity can be genetically targeted to different cell types. Genetically encoded voltage indicators (GEVI) optically report membrane potential in targeted cell types.

GEVIs have been improved in recent years (e.g., Jin et al., 2012; St-Pierre et al., 2014; Gong et al., 2015) and as a result they are starting to be used to answer neurobiological questions. ArcLight is a GEVI that can detect action potentials in cultured mammalian neurons (Jin et al., 2012), *in vivo* in *Caenorhabditis elegans* (Wooltorton et al., 2013) and *Drosophila* (Cao et al., 2013), and population voltage signals in mice (Storace et al., 2015, 2016; Borden et al., 2017; Storace and Cohen, 2017). Bando et al. (2019) compared ArcLight to other GEVIs and reported that ArcLight had the largest signal-to-noise ratio in both 1 and 2-photon imaging from the *in vivo* mouse brain.

In the first section of the paper we show that both the GEVIs and the voltage processes that they follow are faster than the GECIs and the calcium concentration changes that they follow.

In the second section of the paper we describe the use of GEVIs and organic calcium dyes to determine the input-output transformation of the mammalian olfactory bulb. Comparing the input and output of a brain region defines the function(s) carried out by that region. In the third section of the paper we demonstrate that ArcLight can be targeted to an olfactory bulb interneuron. Measurements from different bulb cell types may help determine the mechanisms that shape the input-output transformations.

Typically an odorant is perceived as the same over a substantial range of odorant concentrations (Gross-Isseroff and Lancet, 1988; Krone et al., 2001; Uchida and Mainen, 2007; Homma et al., 2009). This perceptual concentration invariance is essential for animals, including mammals, that use odor to find food, or mates, or family members, or avoid predators, or to make the correct food aversion associations. The input from the nose to the olfactory bulb is a confound of odor quality and odor concentration (Rubin and Katz, 1999; Wachowiak and Cohen, 2001; Bozza et al., 2004). It was not known where in the olfactory sensory system this confound is disambiguated. Each individual olfactory bulb output mitral cell has a very large axon that reaches 12 different olfactory brain regions (Igarashi et al., 2012). Presumably it is in the olfactory bulb and/or in one or more of these cortical areas that this confound is unraveled.

In principle, the input-output comparison can be made using many single cell electrical or optical recordings but this process typically provides only a limited sampling from each animal. An alternative, used in the experiments described below, is to make population recordings with glomerular instead of cellular resolution. In the mouse each glomerulus receives the axon terminals from ∼1,000 olfactory receptor cells in the nose and ∼25 dendritic tufts from output mitral/tufted cells. Simultaneous *in vivo* sampling the odorant responses from 20 glomeruli thus includes the activity of ∼20,000 input cells and ∼500 output cells thereby reducing the sampling noise that occurs when recording from only a few neurons in each preparation. Using glomerular resolution gives up individual cell information in favor of the average response of the populations of the input and output neurons. Measuring population signals typically involves lower temporal resolution recordings and together with the averaging of responses from many neurons results in larger signal-to-noise ratios.

Optical measurements can simultaneously record the input and output in the same glomerulus by using indicators with different excitation or emission spectra, one in the input neurons and the other in the output cells.

Individual neuron recordings with GECIs are well established while single neuron recordings with GEVIs are just beginning. These are described elsewhere (Gong et al., 2015; Lou et al., 2016).

This paper emphasizes population GEVI measurements from the *in vivo* mouse olfactory bulb using ArcLight. Optical recordings from other preparations (Cao et al., 2013; Wooltorton et al., 2013) or using other GEVIs are described elsewhere (Knopfel et al., 2015; St-Pierre et al., 2015; Storace et al., 2015; Kim et al., 2016; Nakajima et al., 2016; Yang et al., 2016; Xu et al., 2017; Deo and Lavis, 2018; dam et al., 2019).

# MATERIALS AND METHODS

## Surgical and Imaging Procedures

All experiments were performed in accordance with relevant guidelines and regulations, including a protocol approved by the Institutional Animal Care and Use Committees of Yale University. For all surgical procedures, male or female adult (40–100 days old) mice were anesthetized with a mixture of ketamine (90 mg $kg^{-1}$) and xylazine (10 mg $kg^{-1}$). Anesthesia was supplemented as needed to maintain areflexia, and anesthetic depth was monitored periodically via the pedal reflex. Animal body temperature was maintained at approximately 37.5°C using a heating pad placed underneath the animal. For recovery manipulations, animals were maintained on the heating pad until awakening. Local anesthetic (1% bupivacaine, McKesson Medical) was applied to all incisions. Respiration was recorded with a piezoelectric sensor.

For virus injections, a small (<1 mm) craniotomy was performed and AAV1 expressing ArcLight or GCaMP (injection volumes between 0.2 and 2 μl) was injected slowly over 10–15 min using a glass capillary (tip diameter 8–15 μm) ∼500 μm below the surface of the bulb. The ArcLight virus was generated at the Penn Vector Core and had a titer of 4.6e12 genome copies (GC) $ml^{-1}$. The GCaMP3 and GCaMP6f virus were acquired from the Penn Vector Core and had titers of 4.7e13 GC $ml^{-1}$ and 4.3e13 GC $ml^{-1}$, respectively. We waited at least 10 days for expression of the virus prior to performing optical measurements.

The venerable, but not very reliable, method first described by Wachowiak and Cohen (2001) was used to load calcium dye into the olfactory sensory neurons. Mice were anesthetized, placed on their back, and an 8 μl mixture of 8/0.2% calcium dye/Triton-X was drawn into a flexible plastic syringe, which was inserted ∼10 mm into the nasal cavity. Using a Hamilton syringe, four injections of 2 μl of the dye/triton mixture was infused into the nose every 3 min. Mice were allowed to recover for at least 4 days prior to optical measurements. The organic calcium dye Fura dextran (F-3029) was from Thermo Fisher Scientific, Waltham, MA, United States. Cal-590 dextran is from AAT Bioquest (Sunnyvale, CA). The excitation spectra of these calcium dyes are well separated from that of many GEVIs and GECIs.

For epifluorescence or 2-photon imaging fluorescence measurements, mice were anesthetized, and the bone above both of the hemi-bulbs was either thinned or removed. The exposure was covered with agarose and then sealed with a glass coverslip.

Epifluorescence imaging was performed by illuminating the dorsal surface of the bulb with 150 W Xenon arc lamp (Opti Quip) on a custom antique Leitz Ortholux II microscope. The light was reflected by a 515 nm long-pass dichroic mirror before being delivered to the sample via an objective lens (various,

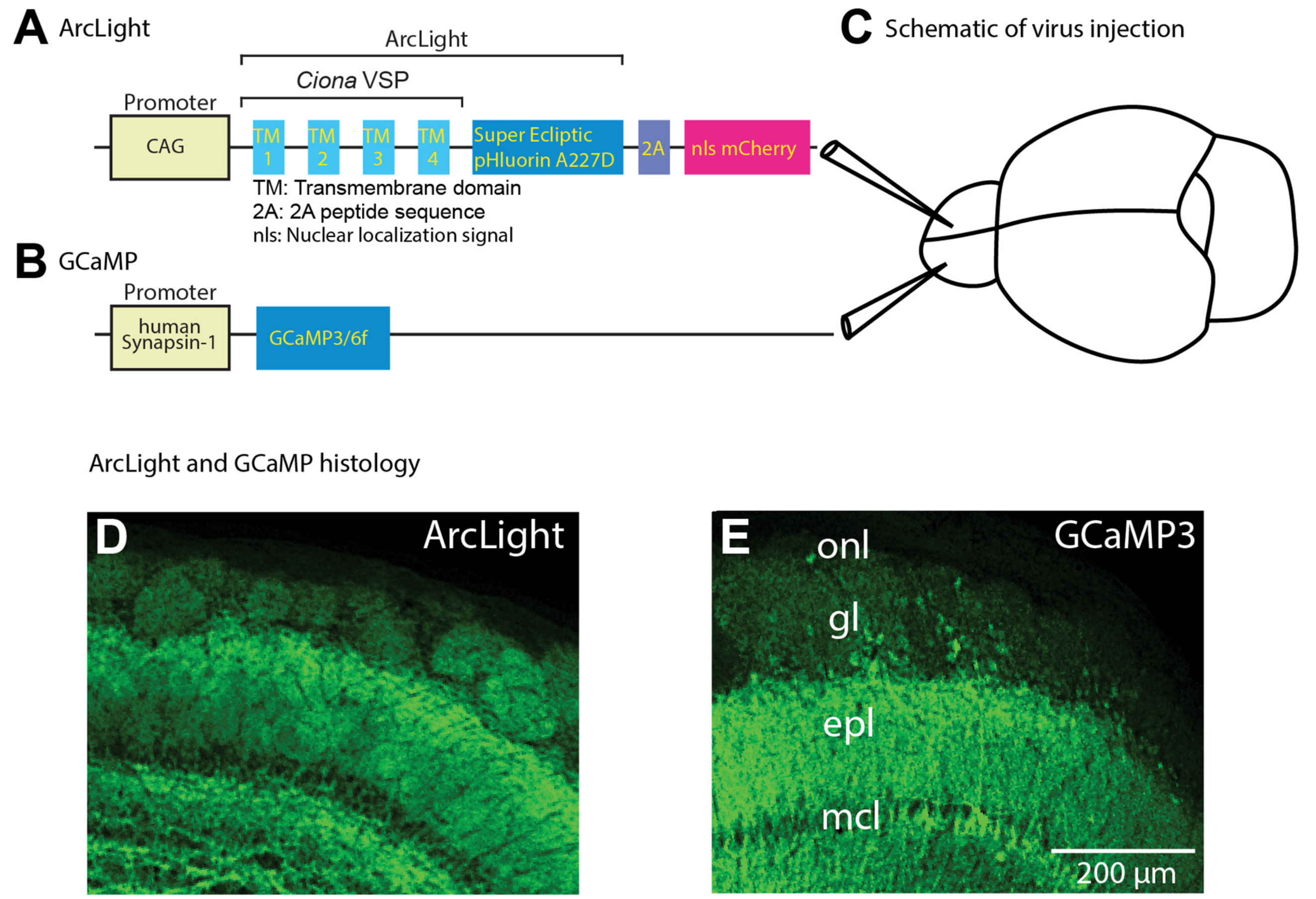

**FIGURE 1 |** Schematic of viral vector constructs, virus injections to target both olfactory bulbs, and histological examination of ArcLight and GCaMP fluorescence. **(A,B)** Schematic drawing of the panel **(A)** ArcLight and **(B)** GCaMP3/6f AAV1 constructs. **(C)** ArcLight and GCaMP AAV vectors were injected into opposite hemibulbs of the same mouse between 10 and 50 days prior to imaging. **(D,E)** Confocal histological images demonstrate the expression patterns resulting from injecting the ArcLight **(D)** and GCaMP3 AAV vectors **(E)**. The scale bar in k also applies to h. onl, olfactory nerve layer; gl, glomerular layer; epl, external plexiform layer; mcl, mitral cell layer. Modified from Storace et al. (2015).

typically a 4× 0.16NA or 10× 0.4NA lens). The fluorescence emission above 530 nm was recorded with a NeuroCCD-SM256 camera (RedShirtImaging, Decatur, GA, United States) with 2 × 2 binning at 40 or 125 Hz.

Two-photon imaging was performed with a modified MOM two-photon laser-scanning microscope (Sutter Instruments). 2-photon excitation was achieved using a Coherent Discovery laser (wavelengths between 940 and 980 nm), and laser scanning was performed with an 8 kHz resonant scanner (Cambridge Technology). Fluorescence was passed through a 510/84 nm bandpass filter and detected with a GaAsP PMT (Hamamatsu, Japan). Power delivered to the sample ranged from 75 to 140 mW as determined using a power meter (Thorlabs) placed underneath the microscope objective.

## AAV Vector

ArcLight A242-2A-nls-mCherry was constructed by fusing ArcLight A242 (Jin et al., 2012) with the self cleaving 2A peptide sequence followed by nuclear localized mCherry (Kim et al., 2012). To allow constitutive expression of the voltage sensor under the CAG promoter in wild type (C57BL/6) mice, ArcLight A242-2A-nls-mCherry was inserted into the aavCAG Jx vector (Gene bank JN898959) in a forward orientation. An adeno-associated virus serotype 1 (AAV1) of the ArcLight construct was produced at the Penn Vector Core at the University of Pennsylvania. For experiments with GCaMP3 and GCaMP6f, we used AAV1s expressing the gene under the human synapsin 1 (**Figure 1B**) promoter (#AV-1-PV1627 and AV-1-PV2822 purchased from the Penn Vector Core). For the TH-Cre targeting experiments, a Cre-dependent ArcLight virus was used (AV1.EF1a.ArcLight.DIO, Penn Vector Core).

## Transgenic Animals

Protocadherin 21 (Pcdh21) (Nagai et al., 2005) embryos were acquired from RIKEN BioResource Center (No. RBRC02189) and recovered by the Yale Genome Editing Center. OMP-GCaMP3 transgenic mice were a gift from T. Bozza. TH-Cre transgenic line were a gift from Matthew McGinley (Jax

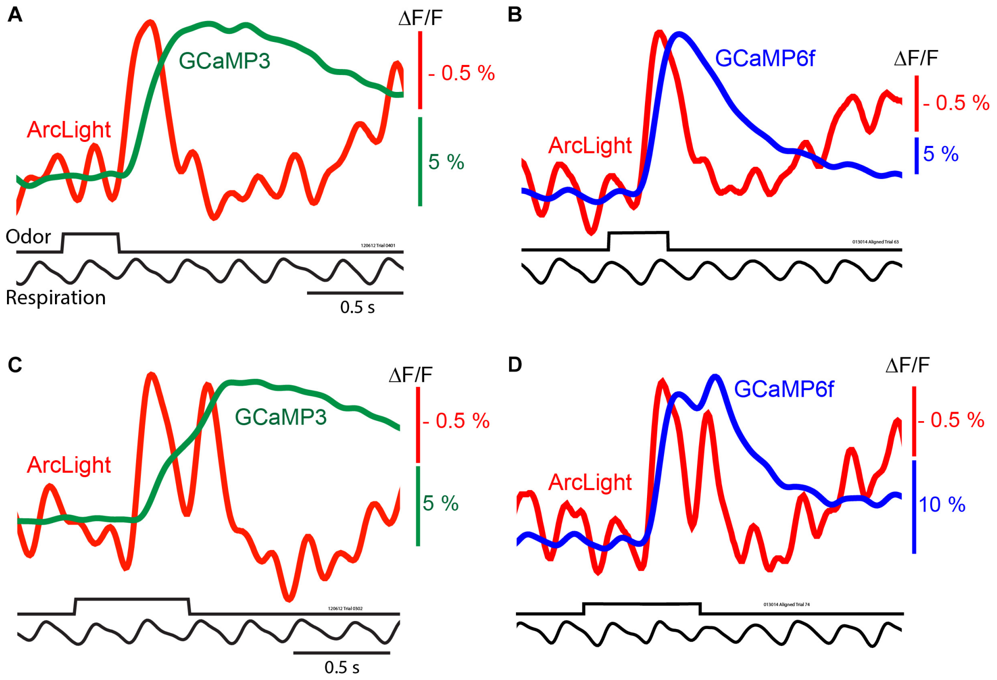

**FIGURE 2 |** *In vivo* measurements of odorant responses in the mouse olfactory bulb using the GEVI ArcLight and two GCaMPs. Left panels **(A,C)** comparing ArcLight and GCaMP3 signals from opposite olfactory bulbs in the same preparation in response to odorant presentations lasting one and two breaths. Right panels **(B,D)** comparing ArcLight and GCaMP6f in response to odorant presentations lasting one and two breaths. The ArcLight signals are substantially faster than those of the GCaMPs. Modified from Storace et al. (2015).

Stock #008601). Thy1-GCaMP6f GP5.11 transgenic mice were acquired from Jax (Stock #024339). Tbx21-Cre transgenic mice were acquired from Jax (Stock #024507) and crossed to a floxed GCaMP6f reporter transgenic mouse (Jax Stock #024105). Animals used in the study were confirmed to express the sensor via genotyping by Transnetyx (Cordova, TN, United States), and by visual inspection (*in vivo* and histologically).

## Data Analysis

For all experiments, odorant-evoked signals were collected in consecutive (1–20) trials separated by a minimum of 45 s. Individual trials were manually inspected and were discarded if they exhibited obvious movement artifact. Trials were averaged after being aligned to the time of the first inspiration following the odorant presentation. Individual glomeruli were visually identified via a frame subtraction analysis that identified stimulus activated glomeruli. The activation maps were generated by subtracting the temporal average of the 1–2 s preceding the stimulus from a 1 s temporal average at the signal peak using frame subtraction in NeuroPlex (RedShirtImaging). Spatial filtering is indicated in the figure legend. The response maps were depixelated for display. Response amplitudes were calculated as the difference between the peak of the response, and the 1–2 s period preceding the stimulus. Fluorescence signals were converted to ΔF/F by dividing the spatial average of each glomerulus by resting fluorescence (the average of the time period prior to the odor presentation).

The input and output measurements in **Figure 5** were performed alternatively using Fura dextran and ArcLight. The 0.04% odor concentration did not evoke any detectable input glomerular response, and was subtracted from the input for the traces and values in (C) and (D). The evoked signal size for each concentration was normalized to the signal evoked at 11% of saturated vapor. To illustrate the similarity of the output maps, in **Figure 5** each output response map was scaled so that all five maps had the same maximum and minimum intensity values. The input map for 11% saturated odor was scaled to have the same maximum and minimum brightness values as the five output maps. The input maps for the lower odorant concentrations were first scaled by the same scaling factors that were used for the output maps and are shown using the same maximum and minimum brightness scale as the 11% odorant map.

The signal-to-noise analysis was performed by measuring the amplitude of the ArcLight response to the first sniff of the odorant vs. the response immediately preceding the odorant. This analysis was performed in 10 preparations in averaged trials that were aligned to the first sniff following the odorant. An ROI that evoked the largest signal for that trial was selected for each preparation.

For the 2-photon input and output measurements in **Figure 7**, glomerular responses were normalized to the signal evoked at the highest odorant concentration (6% of saturated vapor). The responses from all identified individual glomeruli were

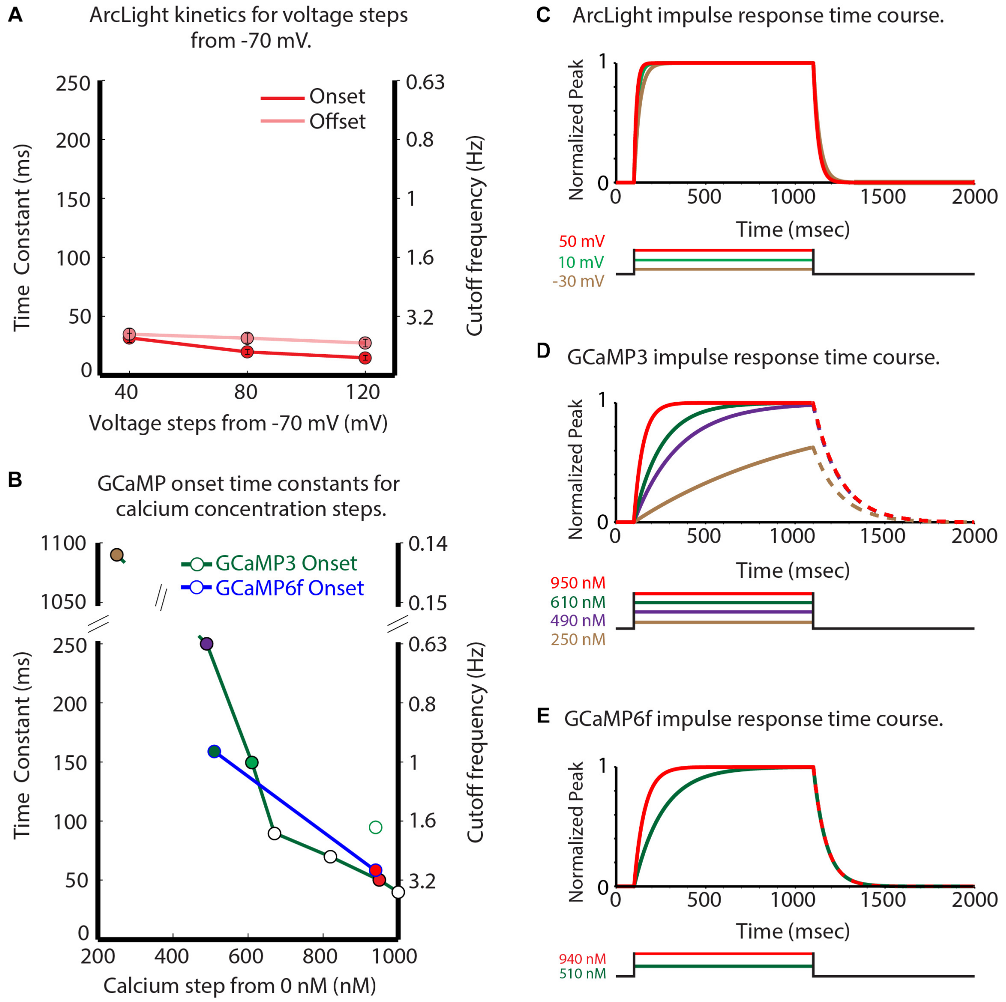

**FIGURE 3 |** Comparison of the GEVI and GECI sensor kinetic properties. Experimentally measured ArcLight values for different depolarizing steps are compared with published and personally communicated values for the GECIs GCaMP3 and GCaMP6f. GCaMP3 and GCaMP6f are considerably slower in their onset response to calcium changes **(B)** than ArcLight is to membrane potential changes. **(A)** ArcLight onset (red) and offset (pink) time constants in response to different depolarizing steps from –70 mV in HEK293 cells. **(B)** The GCaMP3 (green line), and GCaMP6f (blue line) onset time constants in response to different calcium steps (Kim et al., personal communication). **(C–E)** Normalized impulse responses for ArcLight **(C)**, GCaMP3 **(D)**, and GCaMP6f **(E)** to physiologically relevant steps of voltage and calcium. The GCaMP offset rates in panels **(D,E)** are shown as dashed lines to indicate the possibility that they could be sensitive to the magnitude of the calcium change. Modified from Storace et al. (2015).

measured (as in **Figure 7B**), and averaged together to form the values plotted in **Figure 7C**. Statistical significance for **Figure 7** was measured using a Wilcoxon rank sum test comparing the average of input vs. output preparations at each concentration.

For the ArcLight measurements from TH expressing interneurons in **Figure 8**, functional signals were measured in 5 preparations, of which histology was processed and examined to confirm expression in the expected locations in 4 of them. The activity maps in **Figure 8B** are scaled to the minimum and maximum values evoked by the highest odorant concentration. The data in **Figure 8D** come from concentration series performed in 3 of the preparations. For a given odor, all of the activated glomeruli were identified, measured and then averaged together for each odor concentration to give each data point. The $\Delta F/F$ values were normalized to the highest odor concentration used for that preparation (11% of saturated vapor). Responses to 3 odorants were measured in one preparation, only one odorant was used in the other two preparations. The input and output data in **Figure 8D** (red and black lines) are taken from Storace and Cohen (2017). The statistical comparison of the data in **Figure 8D** was performed using a Wilcoxon rank sum test, and similar results were obtained whether the comparisons were performed across preparations ($N = 3$ independent TH measurements), across odor presentations (5 independent TH measurements), or when collapsing all normalized values

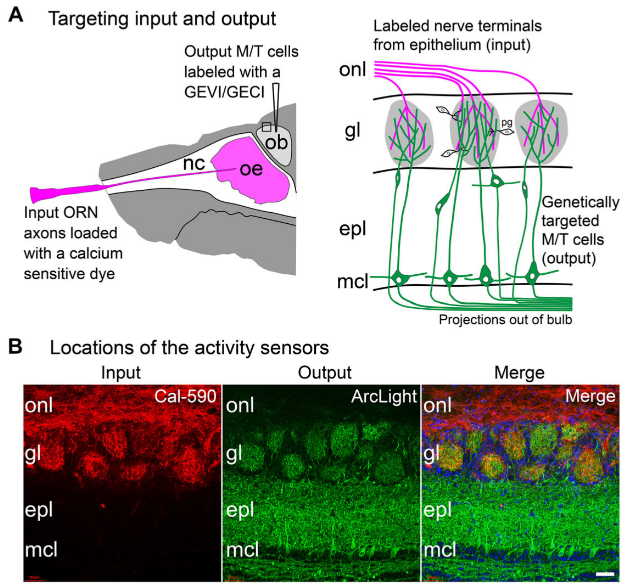

**FIGURE 4 |** Approach to measure both the input and output of the same glomeruli in the mouse olfactory bulb. **(A)** Experimental approach: Left, the olfactory receptor neuron nerve terminal input is labeled via nasal infusion of an organic calcium sensitive dextran dye together with a low concentration of Triton-X. In the same preparation, GEVIs or GECIs were targeted to mitral and tufted output cells using cre-dependent AAVs in a transgenic mouse that expressed cre recombinase in those cells. Right, input and output can be measured independently from the same glomerulus by using activity sensors with substantially different excitation or emission spectra. The signals from the two cell types can be distinguished by changing the excitation or emission wavelengths. **(B)** A doubled labeled histological section showing targeting to input vs. output. In this section, Cal-590 dextran was anatomically targeted to the olfactory receptor nerve terminal input (left) and ArcLight was genetically targeted via AAV injection to the mitral and tufted cell output (middle). The merged image is shown on the right. Both sensors are present in each glomerulus. onl, olfactory nerve layer; gl, glomerular layer; epl, external plexiform layer; mcl, mitral cell layer. Scale bar in panel **(B)**, 50 $\mu$m. Modified from Storace and Cohen (2017).

to the lower odor concentrations (yielding 9 independent TH measurements).

## Odorant Stimuli and Delivery

Odorants (Sigma-Aldrich) were diluted from saturated vapor with cleaned air using a flow dilution olfactometer (Vucinic et al., 2006). The olfactometer provided a constant flow of air blown over the nares. Through a separate set of tubing, odorants were constantly injected into the olfactometer, but sucked away via a vacuum that was switched off during odorant presentation. Different odorants were delivered using separate Teflon tubing. Odorants were delivered at different concentrations (between 0.1 and 6% of saturated vapor). Ethyl tiglate, methyl valerate, 2-heptanone, a mixture of the 3 odorants, and n-butyl acetate were used in these experiments. The time course and relative concentrations of odorants presented by the olfactometer was confirmed using a photo-ionization detector (Aurora Scientific Inc., Aurora, ON, Canada) at the beginning of experiments.

# RESULTS AND DISCUSSION

## Comparing *in vivo* GEVI and GECI Signals From AAV Transfected Mouse Mitral/Tufted Cells

ArcLight was used to record the population voltage signals from mitral and tufted cell dendritic tufts in each glomerulus. ArcLight was expressed using an adeno-associated virus serotype 1 (AAV1) that co-expressed nuclear localized mCherry to facilitate identification of the transduced neurons (**Figure 1A**). GECIs GCaMP3 and GCaMP6f were similarly expressed via AAV transduction. Sensor expression was examined by comparing the fluorescence of the GEVIs and GECIs histologically. The ArcLight (**Figure 1D**) and GCaMP3 (**Figure 1E**) vectors had similar expression patterns in the external bulb layers, and were both largely selective for mitral and tufted neurons (**Figures 1D,E**). We presume that the labeled glomeruli are the result of sensor expression in the mitral/tufted neuron primary dendritic tufts. These AAV1 vectors were selective for restricted cell populations in the bulb: this specificity may be due to a combination of the AAV serotype and the promoter selectivity.

Different odorants evoke distinct spatial and temporal patterns of glomerular activation in the mouse olfactory bulb (Rubin and Katz, 1999; Wachowiak and Cohen, 2001; Spors and Grinvald, 2002). AAV vectors carrying the genes for ArcLight and GCaMP3 or GCaMP6f (**Figures 1A,B**) were injected into separate bulb hemispheres (**Figure 1C**) between 10 and 50 days prior to optical measurements. Expression tended to be widespread in the injected hemispheres.

The ArcLight voltage signals were compared with those from the GECIs GCaMP3 (Tian et al., 2009) and GCaMP6f (Chen et al., 2013) using simultaneous recordings from opposite olfactory bulb hemispheres. Odor-evoked responses could be detected in the glomerular layer in single trials from all three sensors. ArcLight's temporal kinetics were substantially faster than both GCaMPs but the signal-to-noise ratios were lower.

Odorants presented for 0.3 s often coincided with a single inhalation, which resulted in ArcLight and GCaMP3 (**Figure 2A**, red vs. green trace) or ArcLight and GCaMP6f (**Figure 2B**, red vs. blue trace) fluorescence signals that were easily detected in single trials. Depolarizations measured with ArcLight and increases in calcium measured with the GCaMPs are shown as upward signals.

The ArcLight and GCaMP signals had different amplitudes, time courses and signal-to-noise ratios. While ArcLight had a much smaller fractional fluorescence change ($\Delta F/F$) than either GCaMP, ArcLight had a faster onset, rise time, and decay (Storace et al., 2015). With a longer odorant pulse that elicits two odorant inhalations (**Figures 2C,D**) the ArcLight signal returns almost all the way to the baseline between the two inhalations while the GCaMP signals either have only an inflection (**Figure 2C**) or a modest return toward the baseline (**Figure 2D**).

While the signal-to-noise ratios of the ArcLight signals are relatively large, the ArcLight signals in **Figure 2** appear noisier than those of the GCaMPs. We attempted to quantify

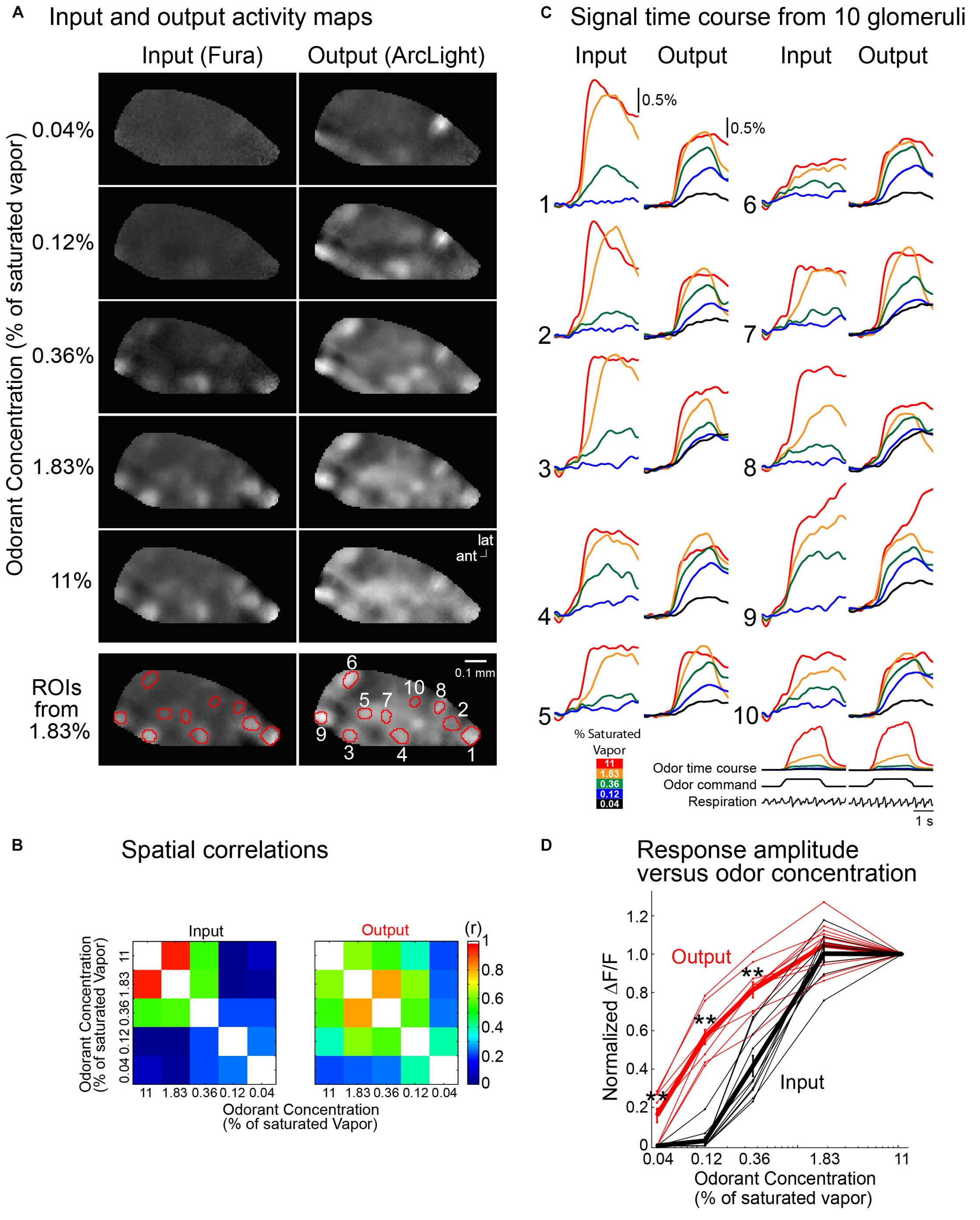

**FIGURE 5 |** Comparing the input and output from ten glomeruli in the same bulb using Fura dextran (input) and the GEVI ArcLight (output). **(A)** Frame subtraction activity maps at five methyl valerate concentrations for input (left) and output (right). The output maps are much more similar to each other in comparison with the input maps. To illustrate the similarity of the output maps, each output response map was scaled so that all five maps had the same maximum and minimum brightness values. The input map for 11% saturated odor was scaled to have the same maximum and minimum brightness values as the five output maps. The input maps for the lower odorant concentrations were first scaled by the same scaling factors that were used for the output maps and are shown using the same maximum and minimum brightness scale as the 11% odorant map. The input map's signals declined much more rapidly with decreasing odorant concentration. The selected glomeruli used for the time course results in panel **(C)** are indicated in the bottom panel (ROIs from 1.83%). **(B)** Spatial correlation of the 1.83% frame subtraction map with the four other odor concentrations. **(C)** Input and output traces of fluorescence vs. time for the ten glomeruli. The input signals decrease more dramatically than those of the output. The traces are low-pass filtered at 1 Hz. Odor time course (measured simultaneously with a photo-ionization detector), odor command pulse and respiration are shown under glomerulus 10. **(D)** Normalized peak fluorescence change vs. odorant concentration for the glomeruli in panel **(C)** (black, input; red, output). The activity maps in panel **(A)** and the traces in panel **(C)** are the average of 4–20 individual trials aligned to the first sniff following odor onset; $^{**}p < 0.001$. ant, anterior; lat, lateral. Modified from Storace and Cohen (2017).

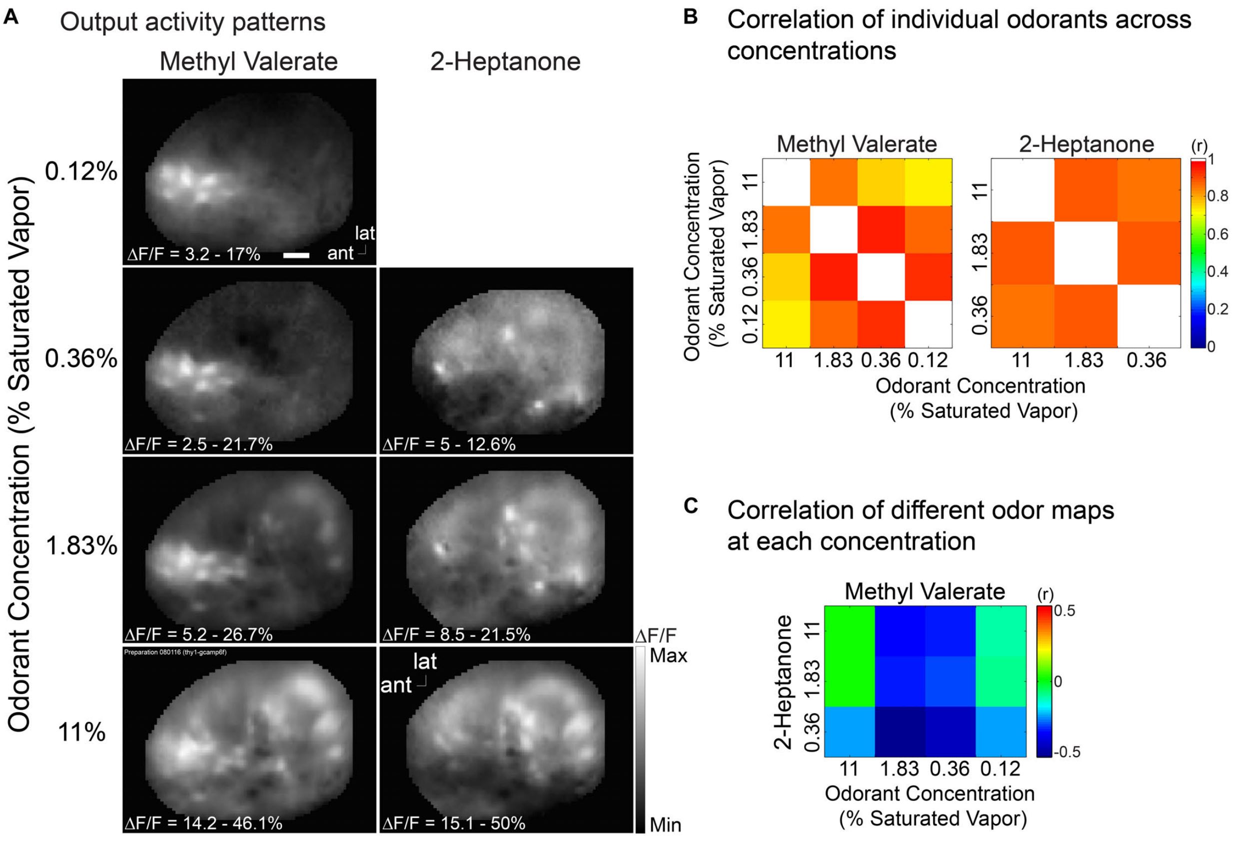

**FIGURE 6 |** Output maps are relatively concentration invariant, but they are odorant specific. **(A)** Output maps in response to two odorants, methyl valerate and 2-heptanone, presented at several concentrations. **(B,C)** Output map correlations evoked by the same **(B)** and different **(C)** odorant. The output maps have a much higher correlation for the same odor than for different odors. This example is from a Thy1-GCaMP6f transgenic mouse in which GCaMP6f is selectively expressed in bulb output neurons (Dana et al., 2014). Similar results were obtained in two other preparations using Pcdh21-Cre transgenic mice. Scale bar in a 250 μm. ant, anterior; lat, lateral. Modified from Storace and Cohen (2017).

the ArcLight signal-to-noise ratio by measuring the difference between the odor-evoked change, and the pre-odor oscillations. On average the largest signal evoked by an odor was 1.83% (±0.17), and the baseline oscillation was 0.47% (±0.05). The fold-change of the odor vs. baseline was 4.07 (±0.28). However some of this baseline "noise" is actually a real respiratory signal which is emphasized more in the ArcLight signals because of the faster ArcLight response (**Figures 2B,D**). We compared the timing of baseline ArcLight and GCaMP signals. Consistent with the notion that the baseline signals are physiological and not movement artifacts, the ArcLight signals preceded the GCaMP signals.

The results from repeated imaging trials were relatively consistent (Storace et al., 2015), which demonstrates that substantial photo-bleaching or photodynamic effects were not present with either ArcLight or the GCaMPs at the incident light intensities which we used. Our comparison of intrinsic signal activity from injected and control hemispheres did not detect a pharmacological effect of ArcLight on normal bulb function. However, continued attention to the possibility of photodynamic and phototoxic effect is desirable. The ArcLight signals were sufficiently large and fast, which made them clearly distinct from the intrinsic light scattering and flavoprotein autofluorescence signals.

## Comparison of ArcLight and GCaMP Sensor Response Speed

The differences in time course and respiration coupling that we found between ArcLight and the two GCaMPs are likely due to a combination of differences in the time courses of the cellular voltage and calcium changes as well as the response speeds of the different sensors. To further understand the differences in signal time courses, we compared the temporal kinetics of the three kinds of protein sensors.

ArcLight had onset and offset time constants of 20 and 30 m s, respectively, for 80 mV depolarizing steps in HEK293 cells (**Figure 3A**). GCaMP3 has onset time constants of 1100 and 250 m s for calcium steps to 250 and 490 nM (**Figure 3B**, green line, time constants of 1100 and 250 m s) (Akerboom et al., 2012). GCaMP6f is about 50% faster for calcium concentration steps to ∼ 510 and ∼ 940 nM (**Figure 3B**, blue line). **Figures 3C–E** compares the temporal responses for ArcLight (C), GCaMP3 (D), and GCaMP6f (E) for selected steps of voltage and calcium.

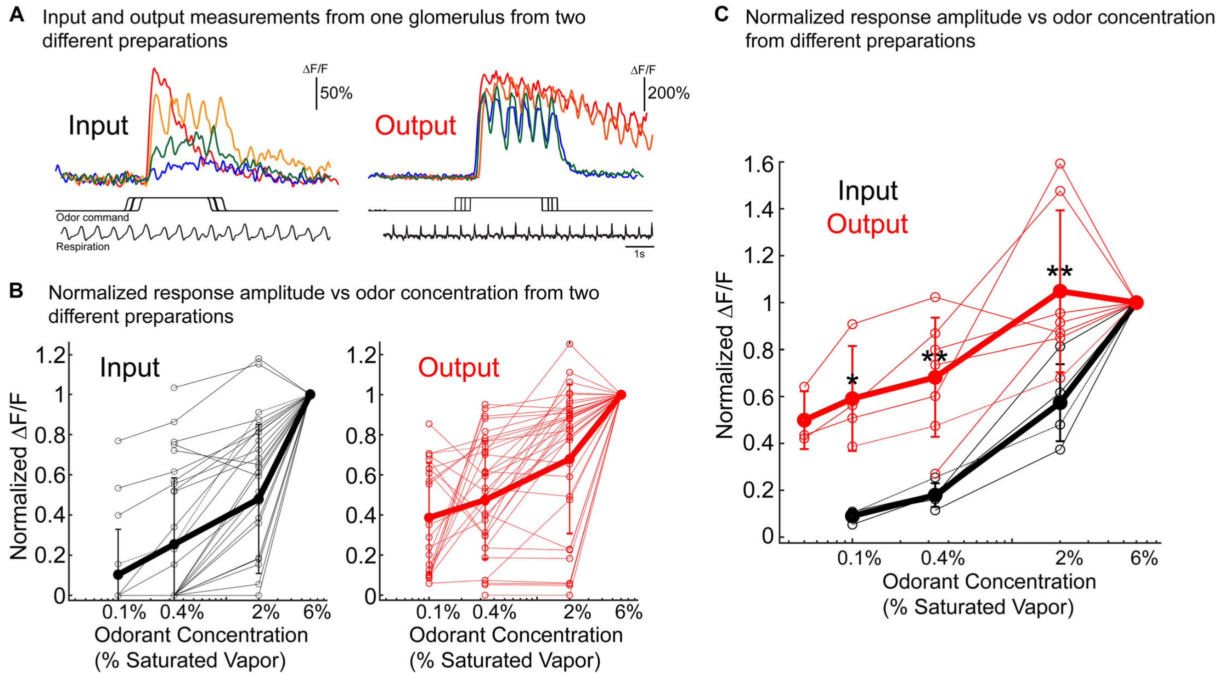

**FIGURE 7 |** Concentration dependence of bulb input and output measured using 2-photon imaging. A different preparation was used for each measurement. OMP-GCaMP3 transgenic mice in which GCaMP3 is endogenously expressed in the olfactory receptor neurons was used for the input measurements. For the output measurements Thy1-GCaMP6f 5.11 or Tbx21-Cre mice that were crossed to a flox-GCaMP6f transgenic mouse. The output results were similar in the two transgenic lines. **(A)** Example results from single glomeruli from preparations in which glomerular input (left) and output (right) were measured in response to the same odor concentration range. The respiration trace is from the 2% single trial for both input and output. The traces in panel **(A)** are taken from single trials. The responses were similar across repeats taken 3 min apart. **(B)** Concentration vs. normalized ΔF/F for all glomeruli measured from the same two preparations used in panel **(A)** (Input: 31 glomeruli; Output: 37 glomeruli). Mean ± SEM is shown as the thick line. The output example in panels **(A,B)** is from a Thy1-GCaMP6f 5.11 preparation. **(C)** Population average concentration vs. normalized ΔF/F. All individual glomeruli were averaged for each preparation (thin lines). The results include measurements from five input preparations and seven output preparations. Wilcoxon rank sum test was used to compare the two distributions (ranksum in MATLAB) $^{*}p < 0.05$ and $^{**}p < 0.01$. The quantification in panels **(B,C)** are from averaged trials.

The GCaMP3 and GCaMP6f decay constants are reported to be ∼150 m s (Sun et al., 2013) and 71 m s (Kim et al., personal communication), respectively. These observations were done when starting at a high calcium concentration, however the effect of different calcium steps on these GECI decay times has not been reported. Clearly, ArcLight has faster kinetics than either of the two GCaMPs, which may explain some of its improved ability to detect individual inspiratory responses.

The ArcLight signal likely reflects the average of all of the mitral/tufted dendritic processes in the glomerular region of interest. Electrode measurements have shown that individual mitral and tufted cells can produce action potentials that are tightly linked to the respiration cycle (Dhawale et al., 2010; Carey and Wachowiak, 2011; Shusterman et al., 2011). Thus, our ArcLight measurements appear to accurately reflect the respiration driven envelope of mitral/tufted cell spiking activity (Rojas-Libano et al., 2014).

The onset and decay kinetics of the GCaMP sensor responses to step changes in calcium result from the calcium binding and unbinding rates. The mechanism generating the ArcLight signal results from a dimerization of the super ecliptic pHluorin of two ArcLight molecules which is then affected by the movement of S4 in the voltage sensitive domain (Kang and Baker, 2016). A pH fluorescent protein like super ecliptic pHluorin is necessary but the ArcLight signal is not the result of a change in pH (Han et al., 2014; Kang and Baker, 2016).

## Determining the Olfactory Bulb Input-Output Transformation

An approach was developed to measure both the input and output of the same glomeruli in the mouse olfactory bulb. Spectrally distinct sensors of neural activity were used; one in the olfactory receptor neurons (input), the other in the mitral and tufted cells (output). This approach employed both anatomical and genetic targeting. Olfactory receptor neurons (input) were labeled via nasal infusion with an organic calcium sensitive dye (**Figure 4A**; Friedrich and Korsching, 1997; Wachowiak and Cohen, 2001). In the same preparation, GEVIs or GECIs were targeted to mitral and tufted (output) cells using cre-dependent AAVs in a transgenic mouse (Protocadherin 21) that expresses cre recombinase in the mitral and tufted cells (**Figure 4A**; Nagai et al., 2005). Appropriate targeting of the sensors in the expected locations was confirmed via histological examination (**Figure 4B**).

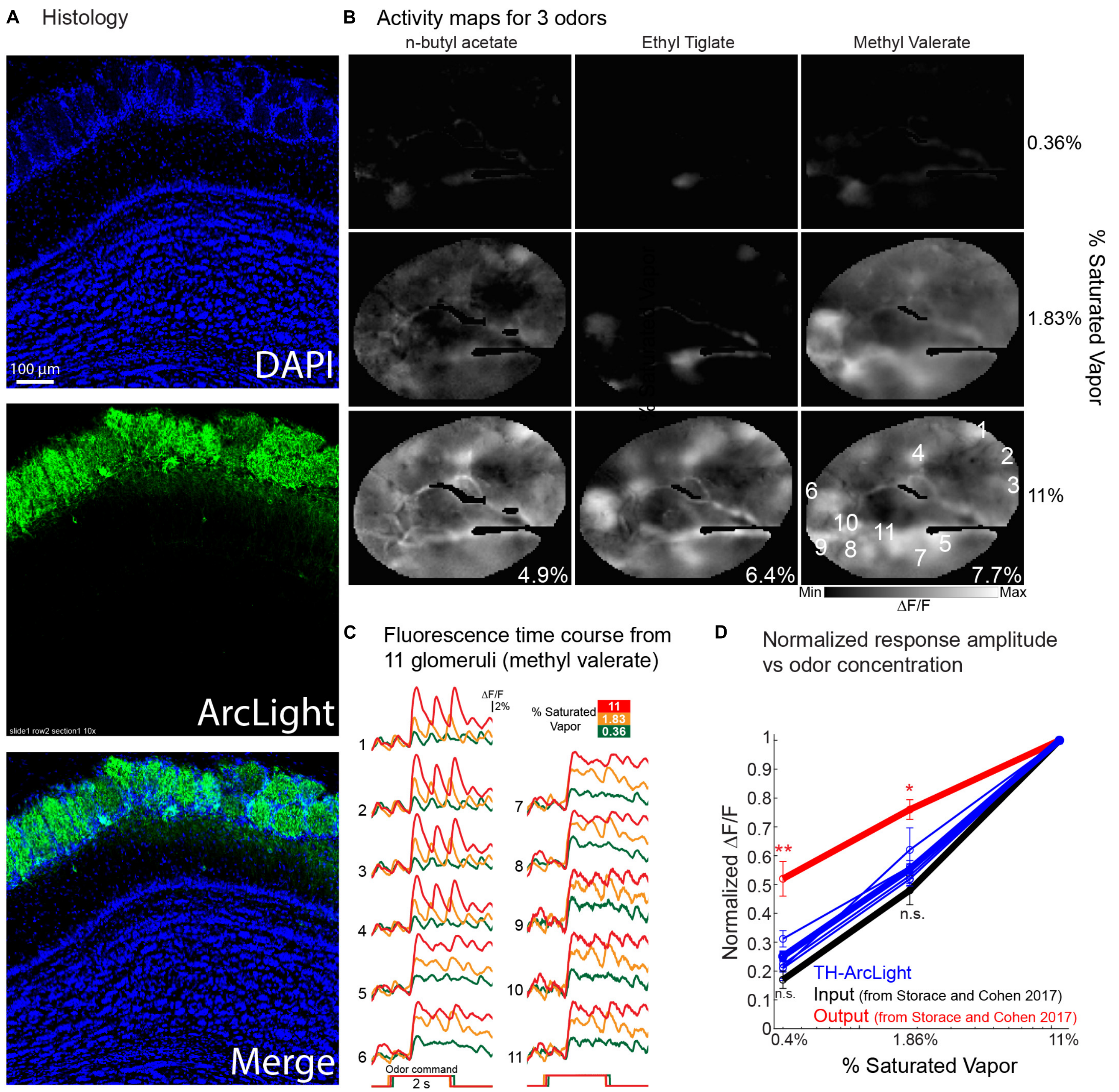

**FIGURE 8 |** Odor-evoked *in vivo* recordings of the GEVI voltage indicator ArcLight from tyrosine hydroxylase (TH) expressing olfactory bulb juxtaglomerular interneurons. **(A)** Histology of cells expressing ArcLight. **(B)** Activity maps evoked by three different odorants at three concentrations. Maps are from an average of 2–4 individual trials that were aligned to the onset of the signal, and were generated by subtracting the ~0.5–1 s during the odor stimulus from the 2 s prior to the stimulus onset. The images were sharpened using high-pass Gaussian filter with a kernel size of 61 × 61 pixels. Activity maps are scaled to the minimum and maximum values evoked by the highest odor concentration. The maximum ΔF/F value for each odor is included in the bottom right of the highest odor concentration map. **(C)** Fluorescence time courses from the 11 glomeruli identified in the middle concentration methyl valerate image in panel **(B)**. The trials are aligned to the onset of the response. **(D)** Normalized response amplitude vs. odor concentration for populations of glomeruli measured from 3 different preparations. TH-ArcLight measurements are from 5 different odorant trials across three preparations. Input and output measurements (red and black lines) are adapted from Storace and Cohen (2017). $^{**}p < 0.01$ and $^{*}p < 0.05$.

Because the input and output sensors had substantially different excitation spectra, input vs. output signals could be measured in the same glomeruli by changing the excitation wavelength. Odor-evoked activity was measured using epi-fluorescence imaging across ~2 log units of odorant concentration in freely breathing anesthetized mice. Input and output measurements were made from the same hemi-bulb using the calcium dye Fura dextran as the input sensor, and the protein voltage sensor ArcLight as the output sensor. The Fura dextran input signal was imaged using 380 nm excitation light. The ArcLight output signals were measured with an excitation light of 480 nm. Fluorescence time courses were recorded from regions of interest corresponding to activated glomeruli. These time courses reflect the population average of the olfactory receptor neuron axon input activity or the population average of the mitral and tufted neuron output activity from individual glomeruli.

In the experiment illustrated in **Figure 5**, signal measurements were made from 10 glomeruli at five odorant concentrations. The output frame subtraction maps at the five odorant concentrations are more similar to each other than are the input maps (**Figure 5A**). The similarity of the input vs. output maps at different odor concentrations was quantified by performing a spatial correlation of each map with one another (**Figure 5B**). The output maps had a significantly higher spatial correlation than the input maps ($p < 0.05$, two-sample $t$-test). The signals from the 10 input and output glomeruli (**Figure 5C**, ROIs) also demonstrate that the input glomeruli have a considerably steeper function of odor concentration than the output glomeruli. The input exhibited no detectable signal at the lowest odorant concentration (0.04% saturated vapor, not shown), and very few had a signal at 0.12% saturated vapor. In contrast, an output signal was detected for all glomeruli at an odorant concentration of 0.04%.

The amplitudes of the odor-evoked input and output signals for each glomerulus were normalized to the response evoked by the highest odorant concentration (11% of saturated vapor). Responses from individual glomeruli are plotted as the thin lines in **Figure 5D**, and the mean evoked signals are shown in the thick lines (red for output; black for input). Reducing the concentration of the odor presentation from 11 to 0.12% reduced the input amplitude to decrease by more than 95%, while the output decreased by only 40% ($p < 0.001$). This result was similarly consistent in a population average across 13 preparations (Storace and Cohen, 2017). Thus both the output activity maps and the output signal size are much less concentration dependent than are the input maps and signals. The olfactory bulb contributes to the perception of concentration invariance of odor recognition.

In another mouse we measured the concentration dependence of the output maps using two different odorants, methyl valerate and 2-heptanone. **Figure 6A** again shows that for each odorant the output maps do not change markedly over a substantial range of odorant concentration. Nonetheless the output maps are markedly different for the two odorants. **Figures 6B,C** show that the map correlations for the individual odorants are relatively large while the correlations across odorants are very small. Thus the bulb contributes to the perception of concentration invariance while maintaining an odorant specific output.

One concern about the results illustrated in **Figures 5C,D** (and in similar figures in Storace and Cohen, 2017) is the possible contribution of the out-of-focus mitral/tufted lateral dendrite signals to the measurements. Accordingly, we have repeated the measurements of input and output concentration dependence using 2-photon microscopy where the depth-of-field is <10 microns instead of the >100 microns of wide-field microscopy. These experiments were carried out using different animals for each input and output measurement. **Figure 7A** illustrates the results from one glomerulus from two different animals. The input signals decline markedly as a function of concentration while the output signal is much less concentration dependent. **Figure 7B** shows a plot of signal size vs. odorant concentration for all of the identified glomeruli in the two preparations used in (a). The normalized response of the output was significantly higher than the input for all tested concentration ($p < 0.05$; Input: 31 glomeruli; Output: 37 glomeruli). **Figure 7C** shows that across a population the average input signal ($N = 5$ preparations; thick black line) declines much more rapidly than the average output signal ($N = 7$ preparations; thick red line) (**Figure 7C**) ($p < 0.05$ using a Wilcoxon rank sum test for all comparisons). The results in **Figure 7** are very similar to those published earlier (Storace and Cohen, 2017) using wide-field microscopy and thus they alleviate the concern that the wide-field conclusion might have been in error because of contamination from mitral/tufted lateral dendrite signals.

We conclude that the olfactory bulb contributes to the perception that the quality of an odorant is considered the same over a range of concentrations. It has been hypothesized that the combination of odorant receptors that are activated by an odorant determines odor identity.

However, previous studies have found that the olfactory bulb glomerular input maps were a confound of odorant identity and concentration (Wachowiak and Cohen, 2001; Bozza et al., 2004). While the activated receptors are critical for odor identification, our results show that odorant identity is determined by the olfactory bulb output. The intensity information may be normalized in the olfactory bulb, and thus the bulb in part removes the qualitative effect of odorant concentration so that odor identity is represented in the output maps. However, the mitral and tufted cell population average still maintains some concentration dependence so that intensity information is not entirely discarded.

The signal-to-noise ratio in the Fura dextran input recordings has a threshold that is ∼5% of the largest signal. If the largest signal represents the activation of ∼1000 olfactory receptor neurons, then the smallest detectable signal would reflect the average activity of less than 50 receptor neurons. The activity of <50 receptor neurons is enough to generate substantial output signals and enough to enable odorant recognition (Homma et al., 2009). However, this argument assumes linearity of the sensor signal with calcium concentration, while calcium signals are typically nonlinear.

The possibility that the olfactory bulb could be involved in normalizing the well-described concentration dependence of the olfactory sensory neurons was proposed by Thomas Cleland (Cleland et al., 2007, 2011). Since that suggestion there is a growing body of supporting evidence across multiple species including *Drosophila* (Asahina et al., 2009), Zebrafish (Niessing and Friedrich, 2010), and mouse (Banerjee et al., 2015; Sirotin et al., 2015; Storace and Cohen, 2017; this paper). A strength of the results in Storace and Cohen (2017) is that the input and output of the olfactory bulb were measured in the same preparation (in some cases simultaneously) allowing a direct comparison to be made. Candidate mechanisms include different types of interneurons with distinct anatomical connections that could facilitate communication across glomeruli, and the ability of some cell types to bidirectionally modulate circuits (Yaksi and Wilson, 2010; Zhu et al., 2013; Banerjee et al., 2015). The results presented here and in other reports (Banerjee et al., 2015; Storace and Cohen, 2017; Bolding and Franks, 2018) also demonstrate that not all concentration information is discarded in the olfactory bulb. It seems likely that the olfactory bulb is performing computations that are critical for downstream targets (e.g., in the Piriform Cortex) to perform invariant object identification. Recent evidence has shown that while the olfactory bulb mitral/tufted cells are relatively concentration invariant, piriform cortex cells are even less sensitivity to concentration, a function that involves feedback from the olfactory cortex to the olfactory bulb (Bolding and Franks, 2018). Thus, concentration invariant odorant perception likely involves dynamic processing across multiple brain regions. Nonetheless, it is clear that the olfactory bulb is involved in a critical processing step to normalize the highly concentration dependent olfactory bulb input.

### *In vivo* ArcLight Signals From a Tyrosine Hydroxylase-Cre Transgenic Mouse

Measuring the contribution of different olfactory bulb cell types may help reveal the mechanisms that shape the transformations occurring in the olfactory bulb. Here, we targeted ArcLight to bulb tyrosine hydroxylase (TH) interneurons with an AAV1 cre dependent ArcLight vector. The TH interneurons are restricted to the glomerular layer and include more than one interneuron type (Pignatelli et al., 2005; Pignatelli and Belluzzi, 2017). **Figure 8A** illustrates the DAPI and ArcLight expression. The ArcLight expression is restricted to cells and processes in the juxtaglomerular layer consistent with the possibility that the expression is restricted to TH periglomerular interneurons.

Activity maps for the odorant responses (**Figure 8B**) were made by subtracting imaging frames prior to the odorant stimulus from frames acquired during the response. Maps for three concentrations of three odorants are illustrated. These maps are very concentration dependent suggesting that they reflect the olfactory receptor cell input to the bulb rather that the mitral/tufted cell output (Banerjee et al., 2015). The time course of the ArcLight fluorescence changes at three concentrations from 11 glomeruli are shown in **Figure 8C** (single trials). **Figure 8D** is a plot of normalized response amplitude vs. odor concentration of the glomerular TH measurements, overlaid with the population input and output measurements from Storace and Cohen (2017).

The normalized TH concentration dependence was not statistically different than the input, and was significantly smaller than the output ($p < 0.05$; Wilcoxon rank sum). While these measurements are from a more limited dataset and performed in different animals, the result support other studies that have proposed that these cells carry the concentration dependent information from the bulb input. These signals may be transmitted throughout the bulb via long-range lateral connections that are found in many of these cells (Aungst et al., 2003; Zhu et al., 2013; Banerjee et al., 2015).

## CONCLUSION

In population measurements from mouse olfactory bulb glomeruli, the ArcLight signals provide important information about membrane potential changes and the perceptual computations carried out in the bulb. In the future we expect that the role of the olfactory bulb in other olfactory perceptions could be determined by using our approach to measure both the input and output. This strategy will help guide investigations into the function of the complex synaptic network of the olfactory bulb. Similar strategies as those used here could be used to understand the input-output transformation of other brain regions.

## DATA AVAILABILITY

The raw data supporting the conclusions of this manuscript will be made available by the authors, without undue reservation, to any qualified researcher.

## ETHICS STATEMENT

All experiments were performed in accordance with relevant guidelines and regulations, including a protocol approved by the Institutional Animal Care and Use Committees of Yale University.

## AUTHOR CONTRIBUTIONS

All authors listed have made a substantial, direct and intellectual contribution to the work, and approved it for publication.

## FUNDING

This work was supported by the World Class Institute (WCI) Program of the National Research Foundation of Korea (NRF) (Grant No. WCI 2009-003), the Korea Institute of Science and Technology (KIST) Grants 2E26190 and 2E26170, and the United States NIH Grants DC005259, NS099691, DC012981, and DC016133.

## REFERENCES

Akerboom, J., Chen, T. W., Wardill, T. J., Tian, L., Marvin, J. S., Mutlu, S., et al. (2012). Optimization of a GCaMP calcium indicator for neural activity imaging. *J. Neurosci.* 32, 13819–13840. doi: 10.1523/JNEUROSCI.2601-12.2012

Asahina, K., Louis, M., Piccinotti, S., and Vosshall, L. B. (2009). A circuit supporting concentration-invariant odor perception in *Drosophila*. *J. Biol.* 8:9. doi: 10.1186/jbiol108

Aungst, J. L., Heyward, P. M., Puche, A. C., Karnup, S. V., Hayar, A., Szabo, G., et al. (2003). Centre-surround inhibition among olfactory bulb glomeruli. *Nature* 426, 623–629. doi: 10.1038/nature02185

Bando, Y., Sakamoto, M., Kim, S., Ayzenshtat, I., and Yuste, R. (2019). Comparative evaluation of genetically encoded voltage indicators. *Cell Rep.* 26, 802–813.e4. doi: 10.1016/j.celrep.2018.12.088

Banerjee, A., Marbach, F., Anselmi, F., Koh, M. S., Davis, M. B., Garcia Da Silva, P., et al. (2015). An interglomerular circuit gates glomerular output and implements gain control in the mouse olfactory bulb. *Neuron* 87, 193–207. doi: 10.1016/j.neuron.2015.06.019

Blasdel, G. G., and Salama, G. (1986). Voltage-sensitive dyes reveal a modular organization in monkey striate cortex. *Nature* 321, 579–585. doi: 10.1038/321579a0

Bolding, K. A., and Franks, K. M. (2018). Recurrent cortical circuits implement concentration-invariant odor coding. *Science* 361:eaat6904. doi: 10.1126/science.aat6904

Borden, P. Y., Ortiz, A. D., Waiblinger, C., Sederberg, A. J., Morrissette, A. E., Forest, C. R., et al. (2017). Genetically expressed voltage sensor arcLight for imaging large scale cortical activity in the anesthetized and awake mouse. *Neurophotonics* 4:031212. doi: 10.1117/1.NPh.4.3.031212

Bozza, T., Mcgann, J. P., Mombaerts, P., and Wachowiak, M. (2004). In vivo imaging of neuronal activity by targeted expression of a genetically encoded probe in the mouse. *Neuron* 42, 9–21. doi: 10.1016/s0896-6273(04)00144-8

Brown, J. E., Cohen, L. B., De Weer, P., Pinto, L. H., Ross, W. N., and Salzberg, B. M. (1975). Rapid changes in intracellular free calcium concentration. *Biophys. J.* 15, 1155–1160. doi: 10.1016/S0006-3495(75)85891-7

Cao, G., Platisa, J., Pieribone, V. A., Raccuglia, D., Kunst, M., and Nitabach, M. N. (2013). Genetically targeted optical electrophysiology in intact neural circuits. *Cell* 154, 904–913. doi: 10.1016/j.cell.2013.07.027

Carey, R. M., and Wachowiak, M. (2011). Effect of sniffing on the temporal structure of mitral/tufted cell output from the olfactory bulb. *J. Neurosci.* 31, 10615–10626. doi: 10.1523/JNEUROSCI.1805-11.2011

Chen, T. W., Wardill, T. J., Sun, Y., Pulver, S. R., Renninger, S. L., Baohan, A., et al. (2013). Ultrasensitive fluorescent proteins for imaging neuronal activity. *Nature* 499, 295–300. doi: 10.1038/nature12354

Cleland, T. A., Chen, S. Y., Hozer, K. W., Ukatu, H. N., Wong, K. J., and Zheng, F. (2011). Sequential mechanisms underlying concentration invariance in biological olfaction. *Front. Neuroeng.* 4:21. doi: 10.3389/fneng.2011.00021

Cleland, T. A., Johnson, B. A., Leon, M., and Linster, C. (2007). Relational representation in the olfactory system. *Proc. Natl. Acad .Sci .U.S.A.* 104, 1953–1958. doi: 10.1073/pnas.0608564104

dam, Y., Kim, J. J., Lou, S., Zhao, Y., Xie, M. E., Brinks, D., et al. (2019). Voltage imaging and optogenetics reveal behaviour-dependent changes in hippocampal dynamics. *Nature* 569, 413–417. doi: 10.1038/s41586-019-1166-7

Dana, H., Chen, T. W., Hu, A., Shields, B. C., Guo, C., Looger, L. L., et al. (2014). Thy1-GCaMP6 transgenic mice for neuronal population imaging in vivo. *PLoS One* 9:e108697. doi: 10.1371/journal.pone.0108697

Davila, H. V., Salzberg, B. M., Cohen, L. B., and Waggoner, A. S. (1973). A large change in axon fluorescence that provides a promising method for measuring membrane potential. *Nat. New Biol.* 241, 159–160. doi: 10.1038/newbio241159a0

Deo, C., and Lavis, L. D. (2018). Synthetic and genetically encoded fluorescent neural activity indicators. *Curr. Opin. Neurobiol.* 50, 101–108. doi: 10.1016/j.conb.2018.01.003

Dhawale, A. K., Hagiwara, A., Bhalla, U. S., Murthy, V. N., and Albeanu, D. F. (2010). Non-redundant odor coding by sister mitral cells revealed by light addressable glomeruli in the mouse. *Nat. Neurosci.* 13, 1404–1412. doi: 10.1038/nn.2673

Friedrich, R. W., and Korsching, S. I. (1997). Combinatorial and chemotopic odorant coding in the zebrafish olfactory bulb visualized by optical imaging. *Neuron* 18, 737–752. doi: 10.1016/s0896-6273(00)80314-1

Gong, Y., Huang, C., Li, J. Z., Grewe, B. F., Zhang, Y., Eismann, S., et al. (2015). High-speed recording of neural spikes in awake mice and flies with a fluorescent voltage sensor. *Science* 350, 1361–1366. doi: 10.1126/science.aab0810

Grinvald, A., Lieke, E., Frostig, R. D., Gilbert, C. D., and Wiesel, T. N. (1986). Functional architecture of cortex revealed by optical imaging of intrinsic signals. *Nature* 324, 361–364. doi: 10.1038/324361a0

Gross-Isseroff, R., and Lancet, D. (1988). Concentration-dependent changes of perceived odor quality. *Chemical. Senses* 13, 191–204. doi: 10.1093/chemse/13.2.191

Han, Z., Jin, L., Chen, F., Loturco, J. J., Cohen, L. B., Bondar, A., et al. (2014). Mechanistic studies of the genetically encoded fluorescent protein voltage probe arclight. *PLoS One* 9:e113873. doi: 10.1371/journal.pone.0113873

Homma, R., Cohen, L. B., Kosmidis, E. K., and Youngentob, S. L. (2009). Perceptual stability during dramatic changes in olfactory bulb activation maps and dramatic declines in activation amplitudes. *Eur. J. Neurosci.* 29, 1027–1034. doi: 10.1111/j.1460-9568.2009.06644.x

Igarashi, K. M., Ieki, N., An, M., Yamaguchi, Y., Nagayama, S., Kobayakawa, K., et al. (2012). Parallel mitral and tufted cell pathways route distinct odor information to different targets in the olfactory cortex. *J. Neurosci.* 32, 7970–7985. doi: 10.1523/JNEUROSCI.0154-12.2012

Jin, L., Han, Z., Platisa, J., Wooltorton, J. R., Cohen, L. B., and Pieribone, V. A. (2012). Single action potentials and subthreshold electrical events imaged in neurons with a fluorescent protein voltage probe. *Neuron* 75, 779–785. doi: 10.1016/j.neuron.2012.06.040

Kang, B. E., and Baker, B. J. (2016). Pado, a fluorescent protein with proton channel activity can optically monitor membrane potential, intracellular pH, and map gap junctions. *Sci. Rep.* 6:23865. doi: 10.1038/srep23865

Kim, J., Zhao, T., Petralia, R. S., Yu, Y., Peng, H., Myers, E., et al. (2012). mGRASP enables mapping mammalian synaptic connectivity with light microscopy. *Nat. Methods* 9, 96–102. doi: 10.1038/nmeth.1784

Kim, T. H., Zhang, Y., Lecoq, J., Jung, J. C., Li, J., Zeng, H., et al. (2016). Long-term optical access to an estimated one million neurons in the live mouse cortex. *Cell Rep.* 17, 3385–3394. doi: 10.1016/j.celrep.2016.12.004

Knopfel, T., Gallero-Salas, Y., and Song, C. (2015). Genetically encoded voltage indicators for large scale cortical imaging come of age. *Curr. Opin. Chem. Biol.* 27, 75–83. doi: 10.1016/j.cbpa.2015.06.006

Krone, D., Mannel, M., Pauli, E., and Hummel, T. (2001). Qualitative and quantitative olfactometric evaluation of different concentrations of ethanol peppermint oil solutions. *Phytother. Res.* 15, 135–138. doi: 10.1002/ptr.716

Lou, S., Adam, Y., Weinstein, E. N., Williams, E., Williams, K., Parot, V., et al. (2016). Genetically targeted all-optical electrophysiology with a transgenic cre-dependent optopatch mouse. *J. Neurosci.* 36, 11059–11073. doi: 10.1523/jneurosci.1582-16.2016

Nagai, Y., Sano, H., and Yokoi, M. (2005). Transgenic expression of cre recombinase in mitral/tufted cells of the olfactory bulb. *Genesis* 43, 12–16. doi: 10.1002/gene.20146

Nakajima, R., Jung, A., Yoon, B. J., and Baker, B. J. (2016). Optogenetic monitoring of synaptic activity with genetically encoded voltage indicators. *Front. Synaptic. Neurosci.* 8:22. doi: 10.3389/fnsyn.2016.00022

Niessing, J., and Friedrich, R. W. (2010). Olfactory pattern classification by discrete neuronal network states. *Nature* 465, 47–52. doi: 10.1038/nature08961

Pignatelli, A., and Belluzzi, O. (2017). Dopaminergic neurones in the main olfactory bulb: an overview from an electrophysiological perspective. *Front. Neuroanat.* 11:7. doi: 10.3389/fnana.2017.00007

Pignatelli, A., Kobayashi, K., Okano, H., and Belluzzi, O. (2005). Functional properties of dopaminergic neurones in the mouse olfactory bulb. *J. Physiol.* 564, 501–514. doi: 10.1113/jphysiol.2005.084632

Rojas-Libano, D., Frederick, D. E., Egana, J. I., and Kay, L. M. (2014). The olfactory bulb theta rhythm follows all frequencies of diaphragmatic respiration in the freely behaving rat. *Front. Behav. Neurosci.* 8:214. doi: 10.3389/fnbeh.2014.00214

Rubin, B. D., and Katz, L. C. (1999). Optical imaging of odorant representations in the mammalian olfactory bulb. *Neuron* 23, 499–511. doi: 10.1016/s0896-6273(00)80803-x

Shusterman, R., Smear, M. C., Koulakov, A. A., and Rinberg, D. (2011). Precise olfactory responses tile the sniff cycle. *Nat. Neurosci.* 14, 1039–1044. doi: 10.1038/nn.2877

Sirotin, Y. B., Shusterman, R., and Rinberg, D. (2015). Neural coding of perceived odor intensity. *eNeuro* 2:ENEURO.0083-15. doi: 10.1523/ENEURO.0083-15.2015

Spors, H., and Grinvald, A. (2002). Spatio-temporal dynamics of odor representations in the mammalian olfactory bulb. *Neuron* 34, 301–315. doi: 10.1016/s0896-6273(02)00644-x

Storace, D., Sepehri Rad, M., Kang, B., Cohen, L. B., Hughes, T., and Baker, B. J. (2016). Toward Better Genetically Encoded Sensors of Membrane Potential. *Trends Neurosci.* 39, 277–289. doi: 10.1016/j.tins.2016.02.005

Storace, D. A., Braubach, O. R., Jin, L., Cohen, L. B., and Sung, U. (2015). Monitoring brain activity with protein voltage and calcium sensors. *Sci. Rep.* 5:10212. doi: 10.1038/srep10212

Storace, D. A., and Cohen, L. B. (2017). Measuring the olfactory bulb input-output transformation reveals a contribution to the perception of odorant concentration invariance. *Nat. Commun.* 8:81. doi: 10.1038/s41467-017-00036-2

St-Pierre, F., Chavarha, M., and Lin, M. Z. (2015). Designs and sensing mechanisms of genetically encoded fluorescent voltage indicators. *Curr. Opin. Chem. Biol.* 27, 31–38. doi: 10.1016/j.cbpa.2015.05.003

St-Pierre, F., Marshall, J. D., Yang, Y., Gong, Y., Schnitzer, M. J., and Lin, M. Z. (2014). High-fidelity optical reporting of neuronal electrical activity with an ultrafast fluorescent voltage sensor. *Nat. Neurosci.* 17, 884–889. doi: 10.1038/nn.3709

Sun, X. R., Badura, A., Pacheco, D. A., Lynch, L. A., Schneider, E. R., Taylor, M. P., et al. (2013). Fast GCaMPs for improved tracking of neuronal activity. *Nat. Commun.* 4:2170. doi: 10.1038/ncomms3170

Tian, L., Hires, S. A., Mao, T., Huber, D., Chiappe, M. E., Chalasani, S. H., et al. (2009). Imaging neural activity in worms, flies and mice with improved GCaMP calcium indicators. *Nat. Methods* 6, 875–881. doi: 10.1038/nmeth.1398

Tsau, Y., Wenner, P., O'donovan, M. J., Cohen, L. B., Loew, L. M., and Wuskell, J. P. (1996). Dye screening and signal-to-noise ratio for retrogradely transported voltage-sensitive dyes. *J. Neurosci. Methods* 70, 121–129. doi: 10.1016/s0165-0270(96)00109-4

Tsien, R. Y. (1980). New calcium indicators and buffers with high selectivity against magnesium and protons: design, synthesis, and properties of prototype structures. *Biochemistry* 19, 2396–2404. doi: 10.1021/bi00552a018

Uchida, N., and Mainen, Z. F. (2007). Odor concentration invariance by chemical ratio coding. *Front. Syst. Neurosci.* 1:3. doi: 10.3389/neuro.06.003.2007

Vucinic, D., Cohen, L. B., and Kosmidis, E. K. (2006). Interglomerular center-surround inhibition shapes odorant-evoked input to the mouse olfactory bulb in vivo. *J. Neurophysiol.* 95, 1881–1887. doi: 10.1152/jn.00918.2005

Wachowiak, M., and Cohen, L. B. (2001). Representation of odorants by receptor neuron input to the mouse olfactory bulb. *Neuron* 32, 723–735. doi: 10.1016/s0896-6273(01)00506-2

Wenner, P., Tsau, Y., Cohen, L. B., O'donovan, M. J., and Dan, Y. (1996). Voltage-sensitive dye recording using retrogradely transported dye in the chicken spinal cord: staining and signal characteristics. *J. Neurosci. Methods* 70, 111–120. doi: 10.1016/s0165-0270(96)00108-2

Wooltorton, J. R., He, L., Salzberg, B. M., and Fang-Yen, C. (2013). *In vivo* optical recording of action potentials in *C. elegans* muscles using arclight, a genetically expressed voltage sensitive fluorescent protein. *Biophys. J.* 104:340a. doi: 10.1016/j.bpj.2012.11.1889

Xu, Y., Zou, P., and Cohen, A. E. (2017). Voltage imaging with genetically encoded indicators. *Curr. Opin. Chem. Biol.* 39, 1–10. doi: 10.1016/j.cbpa.2017.04.005

Yaksi, E., and Wilson, R. I. (2010). Electrical coupling between olfactory glomeruli. *Neuron* 67, 1034–1047. doi: 10.1016/j.neuron.2010.08.041

Yang, H. H., St-Pierre, F., Sun, X., Ding, X., Lin, M. Z., and Clandinin, T. R. (2016). Subcellular imaging of voltage and calcium signals reveals neural processing in vivo. *Cell* 166, 245–257. doi: 10.1016/j.cell.2016.05.031

Zhu, P., Frank, T., and Friedrich, R. W. (2013). Equalization of odor representations by a network of electrically coupled inhibitory interneurons. *Nat. Neurosci.* 16, 1678–1686. doi: 10.1038/nn.3528

**Conflict of Interest Statement:** The authors declare that the research was conducted in the absence of any commercial or financial relationships that could be construed as a potential conflict of interest.

# Advantages of publishing in Frontiers

**OPEN ACCESS**
Articles are free to read
for greatest visibility
and readership

**FAST PUBLICATION**
Around 90 days
from submission
to decision

**HIGH QUALITY PEER-REVIEW**
Rigorous, collaborative,
and constructive
peer-review

**TRANSPARENT PEER-REVIEW**
Editors and reviewers
acknowledged by name
on published articles

**Frontiers**
Avenue du Tribunal-Fédéral 34
1005 Lausanne | Switzerland

**Visit us:** www.frontiersin.org
**Contact us:** info@frontiersin.org | +41 21 510 17 00

**REPRODUCIBILITY OF RESEARCH**
Support open data
and methods to enhance
research reproducibility

**DIGITAL PUBLISHING**
Articles designed
for optimal readership
across devices

**FOLLOW US**
@frontiersin

**IMPACT METRICS**
Advanced article metrics
track visibility across
digital media

**EXTENSIVE PROMOTION**
Marketing
and promotion
of impactful research

**LOOP RESEARCH NETWORK**
Our network
increases your
article's readership